Stimuli-Responsive Molecular Systems – From Theranostic Dendrimers to Responsive Anion Binders

Maynooth University
National University of Ireland Maynooth

A thesis submitted to Maynooth University in fulfilment of the

requirements for the degree of

Doctor of Philosophy

By

Stephen Healy, B.Sc.

Department of Chemistry

Maynooth University

Maynooth

Co. Kildare, Ireland

October 2025

Research Supervisor: Dr. Robert Elmes

Head of Department: Prof. Diego Montagner

Table of Contents

Declaration

I declare that the work presented in this thesis was carried out in accordance with the regulations of Maynooth University. The work is original, except where indicated by reference and has not been submitted before, in whole or in part, to this or any other university for any other degree.

Signed:  Date: 22/10/25

Stephen Healy, B.Sc. (Hons)

Acknowledgements

First and foremost, I'd like to thank my supervisor Dr. Robert Elmes. Thank you for taking a chance on a random email from a lad who honestly had no idea what he was letting himself in for. I am truly grateful to you for having faith in me and for searching for the funding to allow me to pursue a PhD, with that first industry stipend coming in when I had €14.00 left in the account. Your mentorship has been invaluable throughout my time as your PhD student, as well as your optimism, which kept me going through the worst PhD research has to offer. Working with you has been an absolute pleasure.

I would also like to extend my thanks to the all the admin, technical staff and academic staff within the chemistry department. I'd like to give a special mention to Noel and Ria – Noel for your uncanny ability to seemingly fix the unfixable, and Ria for your unending willingness to drop whatever you're doing to helping me deal with whatever health and safety issue I've created for myself.

To Faz, we started together and we're ending together. Thank you for the all the laughs throughout the years, and for the free haircuts, which put every other barber I've had to shame. Thank you for all the gym sessions after a day in the lab, though I never could quite match your dedication to the lifting life. But most importantly, thank you for bringing a bit of quality to the Maynooth staff 5-a-side on Thursdays. Those lads will never see the likes of us again. I hope we cross paths again in the future. It's been a pleasure bro!

The Elmes group - to Wynner, thank you for reigniting my enjoyment in collecting meaningless (but expensive) pieces of cardboard. And for the trips to Carton House, where your golf tips have taken me from being a semi-competent golfer all the way to being a semi-competent golfer. To Gero, thank you for your mentorship in the beginning and for the shared struggle in dendrimer making. I've always said someone had to do it, and it looks like we both did. Collectively known as the two Conors, it was a pleasure working with you lads. Xuanyang, your laid-backness is something I aspire to achieve. Best of luck in the future. Thank you to the past members of the group Luke B, Luke M and Hua for all the advice and support, and best of luck to the current members Emily, Lea and Jordan.

To Adam, I think we'd both agree that being a United fan over the past four years has done more damage to our mental health than the PhD. I'd hoped we could've celebrated more United victories than we did, but we'll always have that FA Cup in 2024. To Rachel, thank you for breathing a new lease of life into the lab. Your professional grade FOMO is a great asset to have in the lab as were always up for the craic when I wasn't bothered working. I don't know who I'm going to aim 90% of my jeering at now, but at least you might be able to get your work done in peace. To Darren, my fellow Meath native, thank you for all the gaming talk and chemistry advice. Now please take my advice and watch Full Metal Alchemist. You'll thank me later. Ciara, being the ladies captain of Rathcore Golf Club is much more prestigious than having a PhD., and you're almost there… just stop hitting it into every possible hazard on the course. And to Joe, who like Nadine Coyle, is not yet known in New Zealand. But who knows, maybe that badminton career will get you there. Finally, thank you to Eoin, Kyle, Keela and Sinead - best of luck with whatever post PhD-life brings.

To my fiancée Jess, words can't truly describe how much your support, love and encouragement have meant to me over the last four years. Thank you for never failing to lift my spirits after the days and weeks of failing experiments. Thank you for helping me focus on the positives when I could only dwell on the negatives, which, given how stubborn I am, might honestly be a C.V. worthy accomplishment. You've pushed me to be the best version of myself, and for that I am truly grateful. None of this would have been possible without having you by my side and I can't wait to see what life bring brings us now that I'm finished.

And last but certainly not least I'd like to thank my family – Pat, Mary and Rachel. Thank you for your unwavering support and encouragement throughout the last four years. Thank you for allowing me to pursue my PhD, and for all the financial support along the way. I'm sure you didn't envision me still being on the family books until I'm 29! I wouldn't be where I am today without you, and I cannot thank you enough.

"It was the best of times, it was the blurst of times" - *C.* Montgomery Burns.

Abstract

With the ever-growing understanding of the complexity of disease progression, be it cancer, microbial or other, comes a rapid need for more targeted treatments plans. Despite these positive advancements however, this is an area that is still in vital need of research. Non-targeted therapies are leading to antimicrobial resistance and chemo resistant cancers which is putting strain on healthcare systems and leading to reduced efficacy of traditional treatments. The development of responsive molecular systems for use in medicinal settings should allow for more patient specific treatments lessened side-effects and early diagnosis/intervention, all of which may lead to improved treatment efficacy. This will be achieved by improving site selective activation of sensors and drugs, which will not only lessen damage to healthy cells, but should also result in increased efficacy meaning lower administered dosages. This thesis will focus on the development of responsive molecular systems for use in diverse areas; from a theranostic agent against glioblastoma multiforme to the design and synthesis of a new strategy towards responsive anion binding based on ring-expansion.

This thesis will open with a literature review (**Chapter 1**) outlining the various strategies employed in the development of responsive systems, with particular emphasis on self-immolative modes of action. The review will also include discussion of the functional groups utilised for the targeting of specific stimuli. The application of these motifs will then be considered within the medicinal context, encompassing both imaging and therapeutic systems. Finally, the review will address the role of molecular responsiveness within supramolecular chemistry, particularly in relation to anion recognition and binding. This section will outline current approaches to the design of responsive binders, which represent distinct, yet conceptually related, strategies to those discussed previously.

Chapter 2 details the design, synthesis and characterisation of two ROS-responsive self-immolative dendrimers for use as cold atmospheric plasma activated theranostics. This compound shows an ability to release its cargo upon reaction with peroxide, demonstrated using UV/Vis and fluorescence spectroscopy, as well as LCMS analysis. It also shows the ability to induce a ‘switch-on’ in cytotoxicity upon exposure to CAP, with the parent compound remaining non-toxic at high concentrations. Furthermore, confocal microscopy shows a ratiometric change in fluorescence output in UMG-251

cells after CAP treatment, exemplifying its utility as a selective theranostic in this cell model.

Chapter 3 then switches to a responsive supramolecular focus, reporting a new strategy for developing responsive anion receptors was established through ring expansion of cyclic squaramides. The optimal scaffold was identified as a medium-sized cyclic squaramide, with side-chain length playing a critical role in enabling controlled intramolecular rearrangements. Using this approach, a series of squaramide–amino acid conjugates were synthesised, and selective ring expansions were achieved under mild conditions. Expanded macrocycles exhibited selective binding towards carboxylate anions, while the unexpanded precursors showed minimal interaction. The binding behaviour varied with macrocycle size, influencing both affinity and stoichiometry. These findings demonstrate that cyclic squaramides provide a versatile and tuneable platform for responsive anion recognition, highlighting the potential of ring expansion strategies in the design of functional supramolecular receptors.

Finally, **Chapter 4** builds upon the findings of **Chapter 3** to enhance the use case of the novel responsive anion binding scaffold and make them more applicable to a biological setting. The aim of this chapter was to modulate the *N*-terminus protecting groups previously used and employ linker chemistry to conjugate NTR and H_2O_2 targeting triggers. This chapter outlines the design and synthesis of this second-generation of responsive anion binders and investigates their ability to undergo ring expansion to allow for a 'switch-on' in anion binding. The design of a potential sensing approach is also discussed.

Abbreviations

AcO^-	Acetate
Br^-	Bromide
CAP	Cold Atmospheric Plasma
$CDCl_3$	Deuterated chloroform
Cl^-	Chloride
COSY	Correlation Spectroscopy
DCM	Dichloromethane
DIPEA	Diisopropylethylamine
DMAP	Dimethylaminopyradine
DMF	Dimethylformamide
DMSO	Dimethylsulfoxide
EDCI	1-Ethyl-3-(3-dimethylaminopropyl)carbodiimide
e.g.	Exempli gratia
Eq.	Equivalents
ESI	Electrospray ionisation
Et al.	Et alia
Et_2O	Diethyl ether
EtOAc	Ethyl acetate
EtOH	Ethanol
F^-	Fluoride
H_2O	Water
H_2O_2	Hydrogen Peroxide
$H_2PO_4^-$	Phosphate
hrs	Hours
HCl	Hydrochloric Acid
HMBC	Heteronuclear Multiple Bond Correlation
HRMS	High Resolution Mass Spectrometry
HSQC	Heteronuclear Single Quantum Coherence

I^-	Iodide
ICT	Internal Charge Transfer
i.e.	Id est
IR	Infrared Spectroscopy
K	Kelvin
K_a	Binding Constant
LC-MS	Liquid Chromatography – Mass Spectrometry
MeCN	Acetonitrile
MeOH	Methanol
MHz	Megahertz
mg	Milligram
min	Minute
mL	Millilitre
NO_2	Nitro group
TEA	Triethylamine
nm	Nanometre
NMR	Nuclear Magnetic Resonance
OH	Hydroxyl group
PBS	Phosphate-buffered saline
Pd/C	Palladium on Carbon
Pet. Ether	Petroleum Ether
$PhCOO^-$	Benzoate
ppm	Parts per million
RNS	Reactive Nitrogen Species
ROS	Reactive Oxygen Species
r.t.	Room Temperature
SO_4^{2-}	Sulphate
TBA	*Tert*-butylammonium
TFA	Trifluoracetic Acid

µL	Microlitre
UV	Ultraviolet
Vis	Visible

Chapter 1

Introduction

1. Introduction

Stimuli-responsive molecular systems are broadly characterised by their ability to change or modulate their structure, chemical properties, or function in response to an external stimulus. In healthcare, the global burden of disease continues to challenge existing systems. Traditional therapies are continuing to show diminishing returns, and non-specific therapies are resulting in multidrug resistance (MDR).[1] The financial implications of these issues are staggering, with antimicrobial resistance alone estimating to cost over $1 trillion by 2030.[2] Similar challenges exist in cancer treatments, where MDR has been implicated in a therapeutic failure of over 90%.[3] Beyond the economic costs, these issues compromise patient care, prolong treatment durations, and reduce overall outcomes.

Stimuli-responsive systems in medicine are a strategy in which therapeutic or diagnostic tools are developed to modulate their output under specific and controlled conditions **(Figure 1.1)**. They have become vital in imaging, enabling tracking of biomarker location or levels for earlier disease detection and a better understanding of the cellular environment. In therapy, stimuli-responsive drugs help overcome MDR and reduce unwanted side effects by minimising damage to healthy cells.

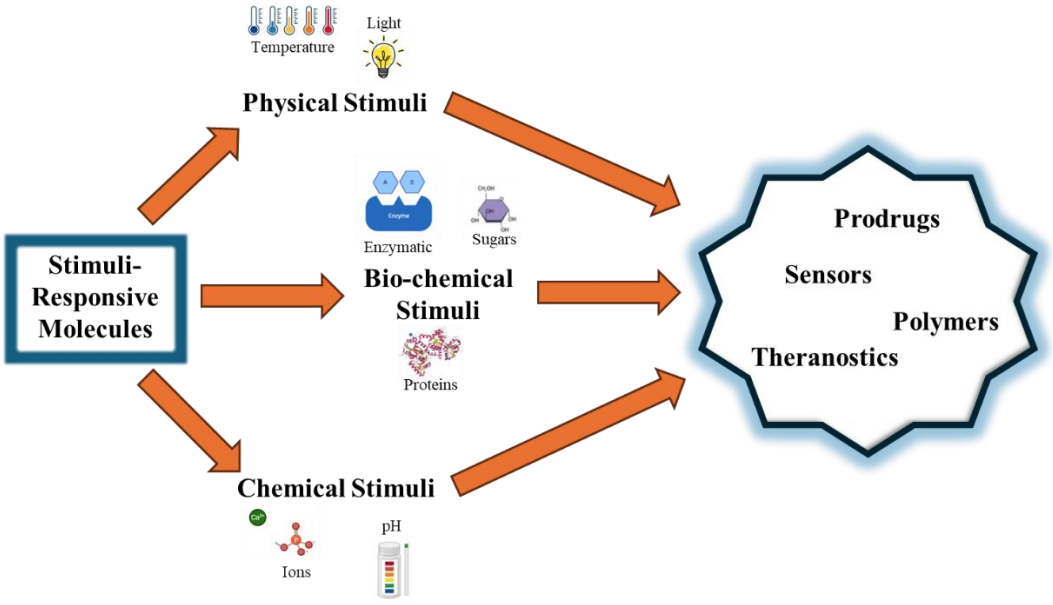

Figure 1.1: Cartoon schematic depicting the variety of stimuli utilised in the activation of stimuli-responsive molecules and their uses.

This chapter discusses the methodologies behind the design, synthesis, and application of synthetic responsive molecular architectures, with particular emphasis on their roles in medicine. It explores how responsive triggers and molecular mechanisms are used to achieve controlled therapeutic and diagnostic outcomes. Advances in biomedical applications of these systems will be examined in detail, along with recent developments in responsive supramolecular systems. Finally, current limitations, future prospects, and the aims of this research project will be outlined.

1.1 Design Strategies for Responsive Function

Building synthetic scaffolds that undergo a structural change upon response to a chosen analyte begins with a simple question; '*what is the chosen target, and by what mechanism will it be recognised and reacted upon?'* The target in question may be a small molecule, anion, biomarker or physical stimulus, and its identification dictates much of the systems subsequent design considerations. The recognition of the marker must operate selectively in the intended environment while avoiding activation in the presence of competing species: a fine balance when aiming to develop an efficient, but selective system. Achieving this often requires molecular architectures in which the recognition unit and the output, or cargo, are linked through a bridge. Among the various design strategies, one particularly versatile approach involves linkers that undergo programmed bond-cleavage events, which allow for a single recognition site to initiate complete molecular disassembly. This 'bridge' is commonly referred to as the self-immolative spacer.

1.1.1 Self-immolative spacers and linkers

Self-immolative spacers are chemical linkers engineered to release a payload through a programmed disassembly process after activation. Put more specifically, in their 2015 review, Schmidt and Julien defined them as "covalent assemblies tailored to correlate the cleavage of two chemical bonds in an inactive precursor".[4] In general, upon reaction with a chosen analyte, the protecting group is cleaved from one end of the spacer and subsequently releases the desired cargo from the other end of the spacer. They were initially introduced as a means by which to overcome limitation in drug delivery,[5] with spatiotemporal control over the release of active therapeutics providing a key advantage over regular therapies. Over recent decades, they have found application across a number of areas for example in polymer science, they enable programmable degradation of materials, contributing to greater sustainability.[6] The elimination of a cargo via self-immolation generally occurs via two pathways: electron-cascade through a spacer, or via an intramolecular cyclisation. Although these pathways both differ from each other in terms of their mechanisms of action, they are both driven by similar factors, notably a release of a thermodynamically favoured by-product, (CO_2), or an increase in entropy. [4,7]

1.1.1.1 Self-immolation based on electron cascade

The vast majority of self-immolative spacers that feature an electronic cascade immolation procedure employ a benzyl linker with an electron donating group, typically a hydroxyl or amino group, *ortho*- or *para*- to the leaving group. This form of elimination is typically referred to as quinone-methide elimination.[8] Quinone methides are quinone analogues whereby one of the carbonyl oxygens are substituted for a methylene group. Aza-quinones are structural analogues, differing by replacing the second carbonyl oxygen for a nitrogen atom (**Figure 1.2**).

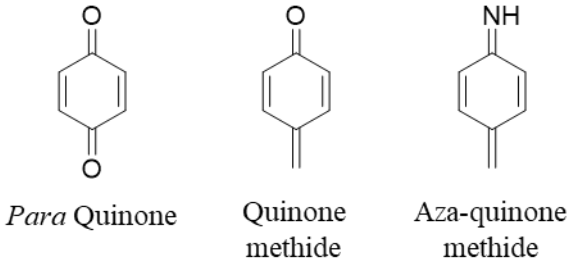

Figure 1.2: Structure of para quinone and its methide analogues

Quinone-methide type elimination is among the most common mechanism of self-immolation employed in molecular design and is typically accessed via a *para*-substituted benzyl derivative. Introduction of an electron donating group at the *para*-position relative to the leaving group increases electron density in the aromatic core. This increased electron density facilitates the intramolecular electron cascade that culminates in the formation of the quinone methide intermediate. This EDG is also essential in the for the immolation process, as it reduces the energy barrier of de-aromatisation by forming the conjugated quinone methide intermediate.[9] However, due to the necessity of the electron donating ability in initiating the elimination, blocking this function can result in completely switching off the immolation process. This is done by replacing or converting the EDG to an EWG, which can be chemically converted to the desired EDG under specific conditions. Therefore, due to the numerous electron-donating groups capable of initiating the process, (hydroxyl-, amino-, thiol-), electron cascade based immolative spacers provide a versatile scaffold about which to build a responsive molecular system.

Typically, the release of the leaving group is following a 1,4- or 1,6- elimination, depending on whether the leaving group is ortho or para to the EDG. As shown in

Figure 1.3, upon stimulation and conversion to the EDG, electron cascade occurs irreversibly. Upon elimination, the quinone methide acts as an excellent Michael acceptor, which can undergo nucleophilic attack at the methylene functional group, which results in the re-aromatisation of the ring.

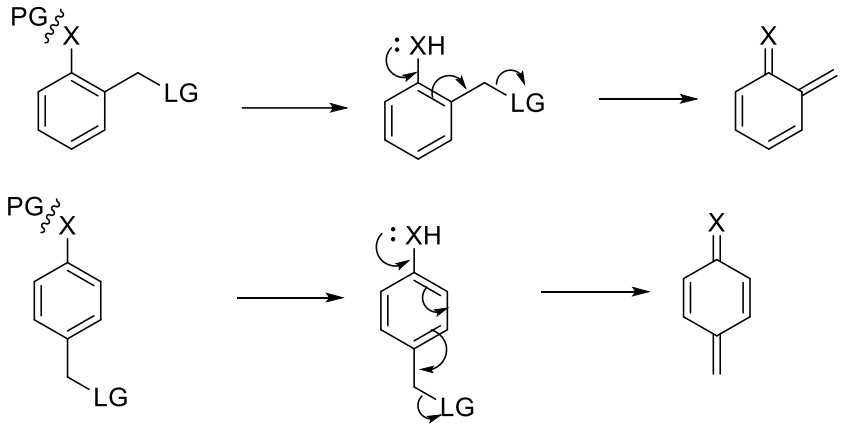

Figure 1.3: Mechanism of electron cascade via quinone-methide type elimination. 1,4-elimination **(top)** and 1,6-elimination **(bottom)**

One important aspect to be considered for the conjugation of the leaving group (LG) to the spacer is the nature of the linker to be employed (**Figure 1.4**). The release of CO_2 is a strong thermodynamic driving force for self-immolation, and as a result, carbamates and carboxylates are commonly employed. This is contrast with ether linkages which facilitate the release of the LG (HO-R in the case of carboxylates and H_2N-R in the case of carbamates) at orders of magnitude slower than their carboxylate counterparts.[10] In work probing these disassembly rates using light activation, Schmidt *et al*. demonstrated that carboxylates and carbamates disassembled significantly faster (2.3 and 3.7 seconds respectively), compared to ethers (> 1600 seconds).[11] Furthermore, stabilisation of the partial positive charge at the benzylic position also increases the rate of disassembly. To this end, incorporation of a methyl group at this position has significantly increased the rate of immolation.[12]

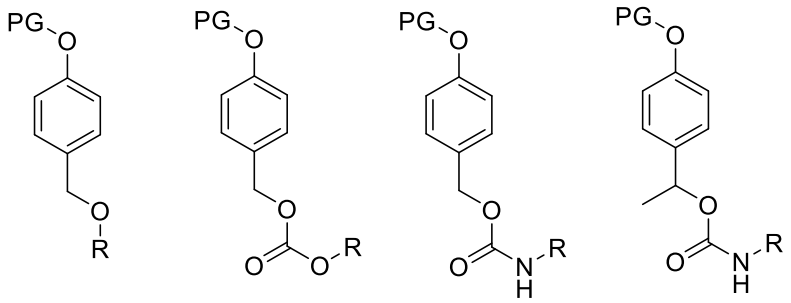

Figure 1.4: Different linkages between leaving group and aromatic core.

Aside from its role in facilitating the electron cascade, the aromatic ring also dictates the distance between the activation site and the leaving group, which can help to avoid steric hindrance. This is often particularly useful in the case of enzyme targeted derivatives, which suffer greatly from steric effects in activation.[13] The distance between the activation site and the leaving group can be increased by extending the conjugation through styryl moiety, with the EDG *para*- to the alkene, which enables a 1,8-elimination pathway. However, simply extending the conjugated system does not always lead to leaving group elimination, with naphthalene and bi-phenyl spacers not undergoing immolation, despite the electron donating ability of the EDG. While this is suggested to be due to the high energy barrier associated with the loss of aromaticity upon immolation,[14] this can be overcome by incorporating a heteroatom into the ring system, which can facilitate the charge delocalisation and resonance stabilisation of the transition state. This can be seen in the case of coumarinyl alcohol systems, which can undergo 1,8-elimination upon activation (**Figure 1.5**).[15]

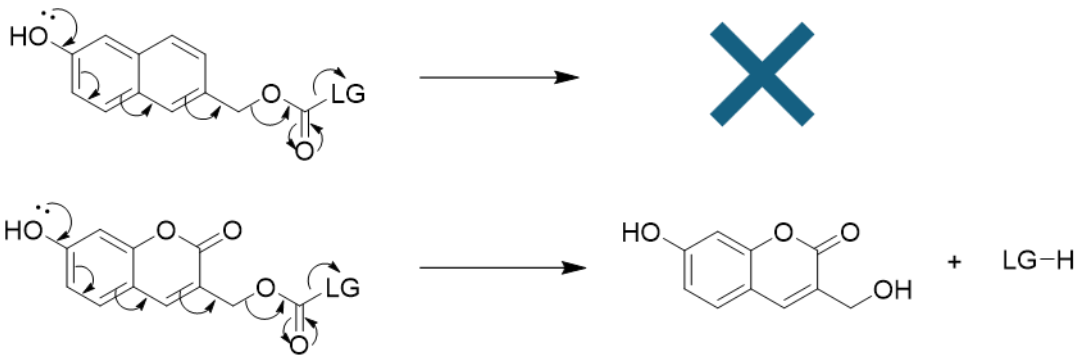

Figure 1.5: Unobserved 1,8-elimination through naphthalene system **(top)**, 1,8-elimination via coumarinyl alcohol **(bottom).**

The heteroaromatic spacer is not limited to benzyl scaffolds, with 5-membered derivatives also seeing use. Indeed, the lower aromatic nature of the 5-membered

heteroaromatics with respect to benzene[16] lowers the energy barrier needed to overcome the loss of aromaticity even further and as a result, would be expected to increase the immolation kinetics.[17] As depicted in **Figure 1.6** their mode of immolation, like the benzyl scaffolds, is a 1,6-elimination upon activation. Due to the lower energy transition states formed during the immolation, 5-membered heteroaromatic scaffolds have been shown to be effective in releasing poor leaving groups upon activation, in comparison to the benzyl derivatives.[18]

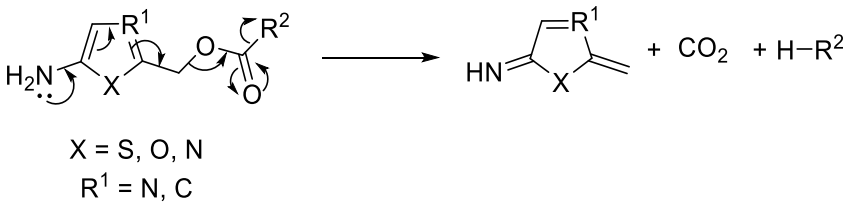

Figure 1.6: Mechanism of electron cascade through 5-membered heteroaromatic spacers.

1.1.1.2 Self-immolation based on cyclisation

In certain self-immolative linker designs, activation proceeds through the liberation of a nucleophilic heteroatom. This heteroatom then undergoes an intramolecular cyclisation with a neighbouring electrophilic site, initiating the disassembly of the linker, shown graphically in **Figure 1.7**. This process usually leads to slower LG release, owing to the slower rate of cyclisation as opposed to electron cascade, with the former often being the rate determining step when both processes are employed in the same system.[19] This lower immolation rate is often governed by the distance between the two activation sites, with longer distances reducing the rate of intramolecular reaction, and also the relative electronegativity and nucleophilicity of the reaction sites.

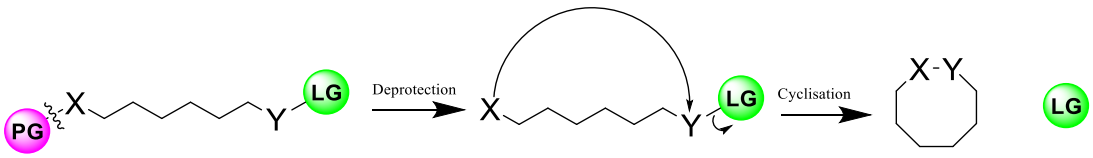

Figure 1.7: General schematic of self-immolation via intramolecular cyclisation.

Similar to electron-cascade based systems, the blocking of immolation can be done by conversion of the nucleophile to a non-nucleophilic entity. As expected, the stronger the nucleophile released, the faster the cyclisation, as is seen in a comparison between amine and thiols with thiols demonstrating more efficient cyclisation. Furthermore,

tuning the electrophilic site also had significant differences in the disassembly rate, with carbonates displaying 10^3 times faster rates than the carbamate analogue.[20] Modification of the α-position of the electrophilic portion of the spacer aims to take advantage of the Thorpe-Ingold effect in order to favour cyclisation. This is clearly seen in the "trimethyl lock" effect, where three interlocking methyl groups induce a large steric strain, and as a result, the electrophilic site (the case below being an amide) is essentially locked into a conformation favourable for nucleophilic attack.[21] This steric strain, which is relieved upon cyclisation leads to rapid release of the leaving group, even for poor electrophiles such as amides (**Figure 1.8**).[22]

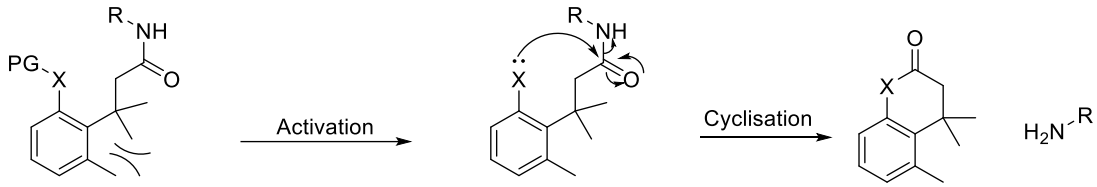

Figure 1.8: General schematic of the trimethyl lock mechanism. Steric strain induced by methyl groups is released upon cyclisation

Building on the self-immolation pathways described above, the next step is to consider the design of triggering units capable of initiating these disassembly processes. The nature of the trigger - whether responsive to chemical, enzymatic or physical stimuli - directly influences the rate and efficacy of the linker cleavage. Subtle changes in electronic properties, steric, or spatial arrangement between the trigger and core can have a marked effect on overall performance. Consequently, this has driven the development of a wide range of trigger motifs, often tailored to the same analyte but optimised for different environments or performance criteria.

1.1.2 Triggering Groups

One of the most important aspects of a responsive system is the decision on which functional group or groups are to be employed as the trigger. This decision will be linked closely to the analyte that has been chosen as the target, and even within that scope, the trigger may differ depending on the specific response required or the payload that is being introduced. Due to the growing research into more selective systems across a magnitude of areas such as medicine, materials chemistry and polymer chemistry, the number of triggering systems being employed is ever growing

(**Figure 1.9**). In fact, the number of ROS responsive systems alone have well over 10 different functional groups to choose from.[23]

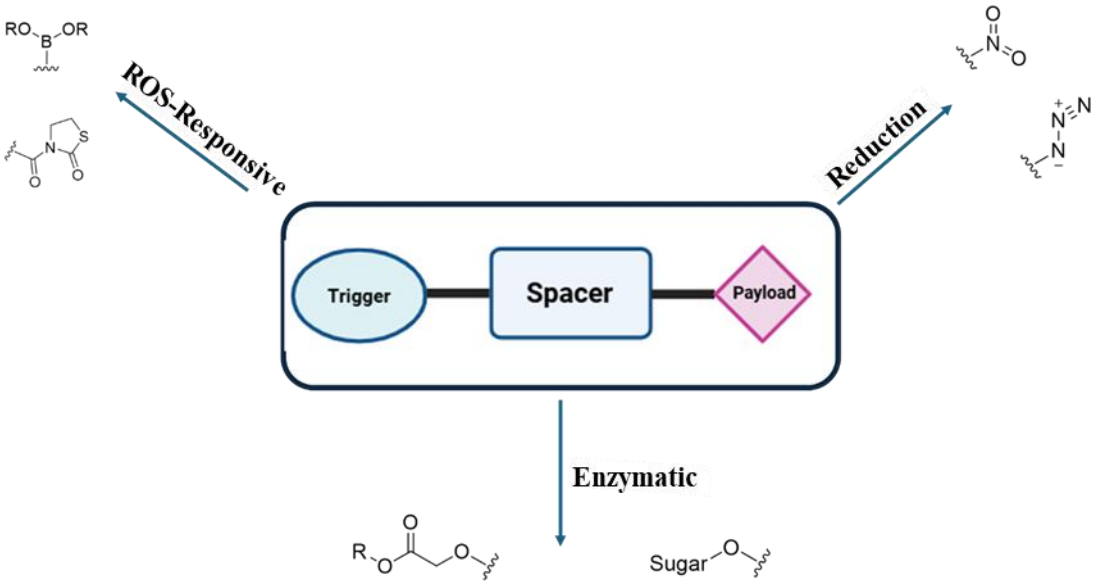

Figure 1.9: Graphical schematic of self-immolative spacers and examples of their protecting groups.

1.1.2.1 ROS-Triggering Groups

Of the numerous ROS-responsive units in use, the boronic ester/acid is one of the most popular and well understood. The elevated levels of ROS within cells are often correlated to significant diseases, such as cancer.[24], and self-immolation systems based on the boronic ester reaction with ROS, such as peroxide, are seeing continued interest. Boronic esters are highly effective ROS triggers, particularly for hydrogen peroxide, owing to the Lewis acid character of the boron centre. The presence of an empty p_z orbital makes them reactive toward nucleophilic species such as water, anions, and other electron-rich species.[25] Boronic esters can easily be installed to a phenyl group, typically through Miyaura borylation between an aryl halide and bis(pinacolato)diboron (B_2pin_2),[26,27] though they can also be directly installed via synthetic pathways beginning with the parent phenol.[28] Once installed, the boronic ester is unable to initialise the electron cascade necessary to facilitate self-immolation. However, upon reaction with H_2O_2 the mechanism follows a Baeyer-Villiger type oxidation, shown in **Figure 1.10** below, whereby peroxide in its anionic form can coordinate to the boron atom forming a boronate complex. This is then followed by an aryl bond migration of the C-B bond to the O-atom, which is then converted to a

phenol via hydrolysis releasing the pinacol boric acid. Re-establishment of the phenol then switches on the electron cascade allowing for self-immolation.

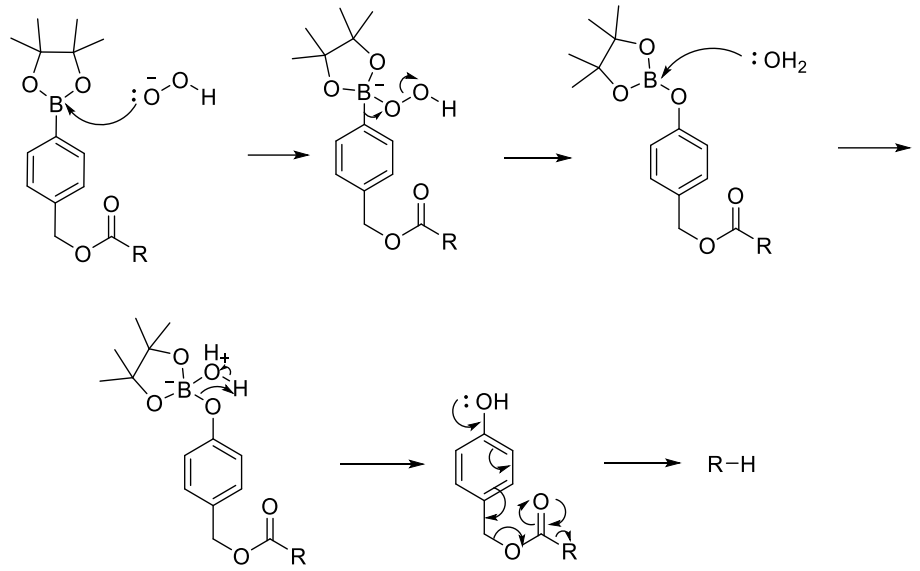

Figure 1.10: Mechanism of action of peroxide mediated boronic ester oxidation

Whilst undoubtedly being the most popular ROS-responsive trigger, arylboronic esters are certainly far from the only one used to target ROS. For the protecting of carboxylic acids for example, thiazolidinones can be used.[29] Installation of the protecting group can be easily done through traditional amide formation, such as coupling reagents.[30] the proposed mechanism follows nucleophilic attack by the hydroperoxide anion on the carbonyl carbon forms a tetrahedral intermediate. This then collapses with the thiozolidinone moiety acts as a good leaving group. The newly formed peroxy acid is rapidly hydrolysed, leading to the release of the free carboxylic acid (**Figure 1.11**). This hydrolysis of the peroxy acid can be carried out under physiological conditions, making thiazolidinone protection an attractive one from a biological context. This strategy, however, and other ROS-responsive units such as thioketals and proline oligomers, have yet to see use in electron cascade-based systems, with the former seeing preferential use in cyclisation-based immolation systems.[31]

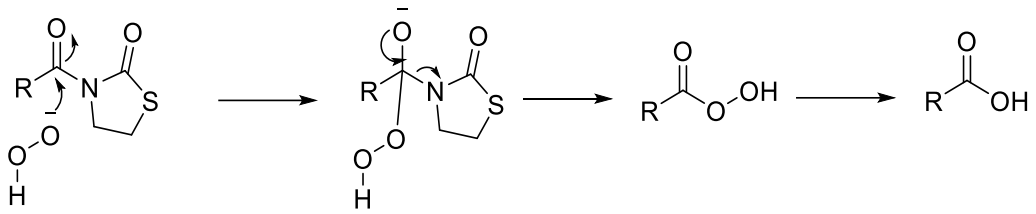

Figure 1.11: Proposed mechanism of action of peroxide mediate oxidative hydrolysis of thiazolidinones.[29]

1.1.2.2 Triggering systems for reductive species

Given that electron cascade–driven self-immolation can be initiated by anilines, reductively triggered self-immolative systems have also been reported. This strategy sees high usage in the targeting of hypoxia and its associated biomarkers, which are increasingly recognised as critical contributors to the progression of diseases such as cancer.[32] As tumour mass expands, oxygen availability diminishes - particularly at the periphery - leading to hypoxic conditions.[33] This environment promotes the overexpression of reductive enzymes such as nitroreductase (NTR).[34] NTR catalyses the reduction of aryl nitro groups to their corresponding amines,[35] making 4-nitrobenzyl derivatives a valuable trigger in the design of NTR-responsive fluorophores and prodrugs. The strongly electron-withdrawing nature of the nitro group decreases electron density in the benzene ring, thereby suppressing self-immolative fragmentation. Upon enzymatic reduction to the corresponding amine, electron donation into the aromatic ring is restored, enabling a 1,6-elimination via an aza-quinone methide intermediate and subsequent release of the active payload (**Figure 1.12**). In a similar fashion, azide groups positioned para to the leaving group are capable of targeting hydrogen sulphide (H_2S) through H_2S mediated azide reduction, as well as standard nitro reduction.[36]

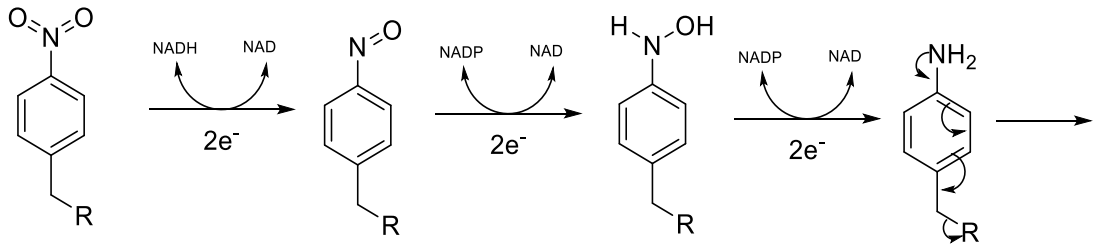

Figure 1.12: Mechanism of action of peroxide mediate boronic ester oxidation

1.1.2.3 Enzyme-Responsive Triggers

Among the various efforts to modify the benzyl spacer for selective biomarker detection, the most significant progress has arguably been made in the development of enzyme-cleavable triggers. This growth is driven not only by the expanding list of enzyme-based biomarkers but also by the synthetic flexibility to functionalise both ends of the linker. In contrast to ROS- and reductive-responsive systems, which typically use the trigger as a terminal masking group, enzyme-responsive linkers offer the unique advantage of dual functionalisation. This allows for the incorporation of additional targeting elements, such as peptides or saccharides, on the opposite end of the cleavage site enhancing selectivity and biological relevance. However, this is not without its own difficulties. Not only does the incorporation of a linker and payload not need to interfere with the peptide's affinity to the chosen receptor, but it also increases the chance for cleavage at sites other than the target.

Enzyme cleavable linkers generally involve the inclusion of an amide or ester bond, (**Figure 1.13**), and can be made site-specific by targeting microenvironments which has upregulation of a specific biomarker. For example, cancer cells are often correlated with upregulation of esterases and amidases.[37,38] The functionalisation of peptides to a benzyl based linker can be easily done by converting the phenol to a carbonate through reaction with acid chlorides, or by conversion to an amide by coupling aniline to a carboxylic acid. The choice of functional group can have drastic effects on the efficacy of the chosen reaction and the overall stability of the molecule itself, with amides being considerably more resistant to hydrolysis compared to carbonates and carbamates.[39]

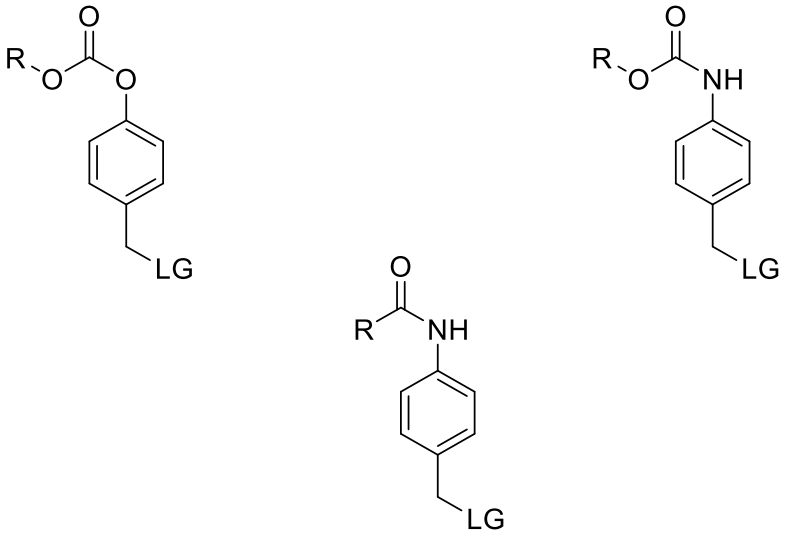

Figure 1.13: Examples of enzyme cleavable triggers.

The diverse range of activation mechanisms available for self-immolative spacers, with the above section only covering a small selection, has made them highly adaptable for biomedical application. These responsive linkers allow for precise control over molecular release, a vital advantage in selective treatments for diseases. This has seen them used in the development of advanced therapeutic and diagnostic tools. The following section will explore how activation mechanisms and self-immolative spacers have been integrated into medical applications.

1.2 Stimuli Responsive Systems in Diagnostics and Therapy.

Despite the tremendous advancements made since the 20th century in our understanding of disease progressions – both in terms of mechanisms at a molecular level and in the development of new therapeutics – this progress has also been met with continuing challenges. Taking cancer for example, while conventional treatments such as surgery, radiotherapy and chemotherapy have significantly improved patient outcomes,[40–42] our overreliance on broad spectrum chemotherapeutics (i.e. cisplatin) has led to phenomena like multidrug resistance (MDR)[43] and the lack of selectivity in these methods has consequences by way of unselective killing of healthy cells.[44] As a result, there is a growing need for more selective and targeted therapeutic approaches. Targeting specific biomarkers expressed in cancer cells can enhance treatment precision and reduce harm to healthy tissue, while early detection strategies are essential for improving prognosis and preventing cancer progression.[24,25] The following sections will explore how triggering chemistry and self-immolative linkers

serve as fundamental components in the design of advanced sensors, prodrugs, and theranostic agents, highlighting their crucial role in enabling more precise, responsive, and effective cancer diagnostics and treatments.

1.2.1 Stimuli Responsive Sensors.

In recent decades, there has been a substantial increase in the volume of research into optical bioimaging technologies for the aim of both early detection of certain diseases such as cancer, but also the *in-situ* monitoring of disease progression or therapeutic efficacy. Not only have these advancements come in the form of higher-resolution power, i.e. super-resolution microscopy,[47] but also in probe development. With the ever-growing understanding of the complexity of molecular events within cells, comes the advantage of identifying biomarkers that may be used in the development of activatable fluorophores. Activatable fluorophores, sometimes named "smart" fluorophores or profluorophores, change their fluorescence behaviour in response to a specific biomarker (enzymes, small molecules).[48] This fluorescence modulation can come in the form of off/on sensors, where reaction with an analyte 'switches-on' fluorescence,[49] or as ratiometric fluorophores, whose fluorescence wavelength changes upon reaction.[50] The chemical scaffolds underpinning activatable fluorophores continue to diversify, with rhodamines, BODIPYs, and coumarins among the most widely employed.[51] In more recent decades, however, the 1,8-naphthalimide core has attracted growing attention due to its exceptional synthetic versatility, enabling its application across a broad range of fluorescence-based systems.

1.2.1.1 The 1,8-naphthalimide.

The 1,8-naphthalimide has become a widely used scaffold around which to design a fluorescent probe, particularly ratiometric sensors, due primarily to its high fluorescence quantum yield, good photostability, large Stokes' shift and excellent chemical modifiability.[52–54] Naphthalimide 'smart' fluorophores are primarily based on derivatives with substitution in the 4-position of the naphthalene portion of the compound. The luminescent properties of naphthalimides are heavily dependent on the Internal Charge Transfer (ICT) and in effect, the electronic characteristics of the substituent, with electron-donating groups leading to strong fluorescent output.[55] Amines and alcohols for example evoke a "push-pull" ICT excited state and lead to broad emission bands from 450 – 550 nm, with primary amines possessing strong

donating character resulting in long wavelength emission of >530 nm.[56] However, conversion to a less effective electron donating group, for example a carbamate, decreases the ICT character of the fluorophore and shifts the emission to shorter wavelengths of < 500 nm. On the more extreme end, inclusion of a nitro-group in the 4-position almost completely shuts off the ICT and renders the fluorophore non-fluorescent (**Figure 1.14**).[57] Furthermore, the fluorescence characteristics of naphthalimides are highly sensitive to solvent, with aqueous and protic solvents leading to dramatic red-shifts in emission compared to in non-polar aprotic organic solvents such as hexane. This increased Stoke's shift has been proposed to be due to intermolecular H-bonding between the naphthalimides and the hydroxy functionalities of water and alcohols, accelerating the interconversion between fluorescent states.[58]

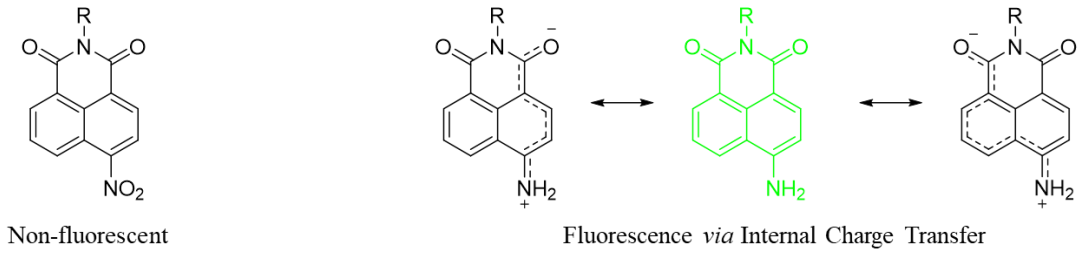

Figure 1.14: Schematic illustration of the influence of 4-position substitution on the ICT behaviour of naphthalimides.

Blocking the ICT behaviour of naphthalimide with a "triggering" group has led to the development of many on/off fluorescent probes. Xu and coworkers were successful in developing an on/off probe for the imaging of NTR within HeLa cells.[59] This design leveraged the ability of NTR to reduce the nitro-functionality to the corresponding amino group, resulting in a switch on in fluorescence at 543 nm. In the aim of detecting peroxynitrite, shown in **Figure 1.15** below, Guo *et el*. developed sensor **1.1** by blocking the ICT behaviour through conjugation of a *p*-aminophenol group in the 4-position, yielding the naphthalimide non-fluorescent.[60] However, reaction with peroxynitrite revealed the 4-amino derivative through *N-/O-* dearylation, switching on the fluorescence. Their design was successfully able to image $^{-}$OONO in both HepG2 cells and live C. elegans in real time.

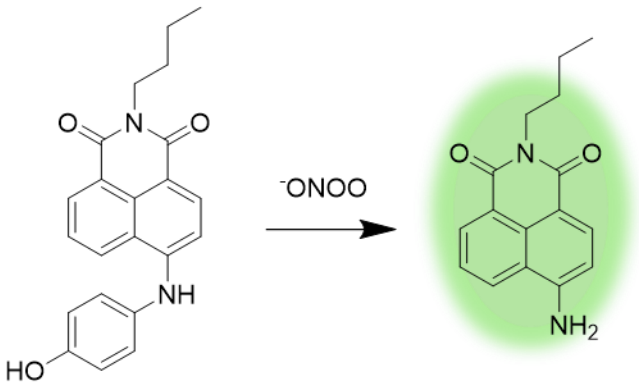

1.1

Figure 1.15: $^{-}$ONOO sensor developed by Guo *et el*.

Ratiometric probes represent the predominant class of naphthalimide-based sensors and are typically developed via conjugation to a linker via the 4-position. The Elmes group has reported a family of naphthalimide-based fluorophores, **1.2** and **1.3,** for the detection of nitroreductase (NTR), aimed at monitoring reductive stress *in cellulo* (**Figure 1.16**).[61] In this design, a nitroimidazole moiety was introduced via a carbamate linker, resulting in blue-shifted emission at 435 nm and 410 nm for the 4- and 3-substituted naphthalimides, respectively. Upon enzymatic reduction by NTR, the nitroimidazole was cleaved through a reduction-triggered self-immolative mechanism, restoring the free amine. This transformation induced a red shift in emission, with the 4-amino derivative exhibiting superior fluorescence intensity. Confocal microscopy confirmed cellular uptake of the fluorophore in HeLa cells and its ability to report on NTR-mediated reductive stress in mammalian systems.

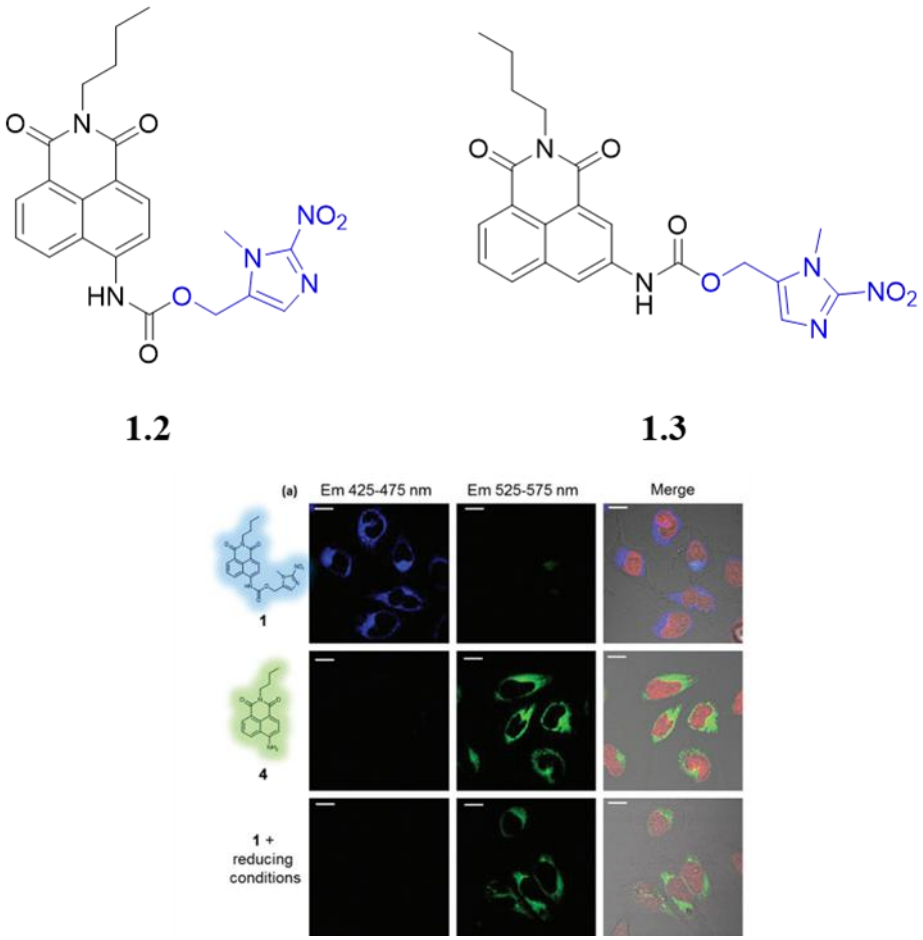

Figure 1.16: Structures of NTR-responsive 1,8-napththalimides developed by the Elmes Group **(top)** and confocal laser scanning microscopy images of **1.2** in HeLa cells **(bottom)**

Additionally, the Elmes group has employed naphthalimide scaffolds in apoptosis detection via caspase-3 activity.[62] In this system, a 4-amino naphthalimide was linked to an Ac-DEVD-PABA peptide substrate. Caspase-3-mediated cleavage of the DEVD sequence-initiated self-immolation through the PABA linker, releasing the free fluorophore. This reaction resulted in a ratiometric fluorescence change with high selectivity for caspase-3.

While the above example involves functionalisation at the amino position, the synthetic flexibility of the naphthalimide scaffold also permits modification at the imide "head" group, enabling the introduction of targeting moieties to enhance fluorophore selectivity for specific biological environments (**Figure 1.17**). For instance, conjugation with a triphenylphosphonium cation has facilitated the selective detection of carbon monoxide within mitochondria.[63] Collectively, the structural

tunability at both the amino and imide positions make naphthalimides a functionally rich and adaptable platform for the development of "smart" fluorophores.

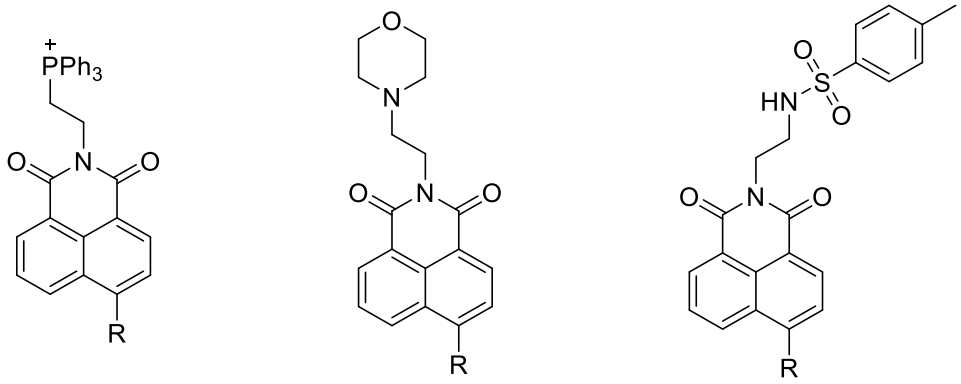

Figure 1.17: Examples of targeting groups which can be functionalised at the imide "head" of naphthalimides.

This strategy of "blocking" essential functional groups to control probe activity also has clear parallels in the therapeutic space. The activity of many pharmaceutical agents often relies on the presence and accessibility of key functional groups within the molecule. Masking or modifying this group can effectively 'switch off' drug activity, while selective restoration of the group can 'switch-on' the therapeutic effect. Such control can improve selectivity, enhance efficacy, and reduce off-target side effects compared to the parent drug. Strategies that exploit this concept are commonly referred to as prodrugs.

1.2.2 Stimuli Responsive Prodrugs

Prodrugs can be broadly defined as pharmacologically inactive compounds that are converted within the body into active drugs through enzymatic or chemical processes. The primary rationale behind the use of prodrugs is to optimise key properties such as absorption, distribution, metabolism, and excretion (ADME) while enhancing the selectivity of the drug for its intended target. This increased specificity improves therapeutic efficacy and reduces adverse effects, such as off-target tissue toxicity.[64]

Although the term 'prodrug' was coined by Adrien Albert in the 1950s,[65] the concept predates this, with examples of prodrug use dating back to the late 1800s. The first synthetic prodrug is often attributed to the development of methenamine in 1899.[66] Prodrugs are designed through various approaches, but the overarching principle remains consistent: the incorporation of a *pro-moiety* containing a triggering group

that activates the drug in response to specific conditions or analytes. Upon activation, this triggering group induces a functional group conversion or releases the active drug via a structural modification, such as self-immolation. This strategy is particularly advantageous in cancer treatment due to the complexity and heterogeneity of cancer types.[67] The distinct biochemical landscape of cancerous tissues, characterised by aforementioned factors such as hypoxia, oxidative stress, and dysregulated enzymatic activity, offers numerous opportunities for selective therapeutic intervention. By strategically incorporating moieties responsive to these tumour-associated biomarkers, prodrugs can be designed to undergo activation preferentially within malignant environments, thereby enhancing target specificity and therapeutic precision.

Targeting Reactive Oxygen Species (ROS) in the tumour microenvironment has become an attractive means to build a prodrug strategy, with cancer cells expressing higher than typical levels of ROS.[24] As such, boronic esters, and their aryl linked derivatives have become a staple of ROS-responsive prodrugs, with aryl boronic esters being incorporated into the structures of FDA approved cytotoxins, such as the camptothecin (CPT) analogue SN-38.[68] In their work Li *et al.* incorporated a boronic acid to SN-38, with their prodrug derivative showing similar and, in some cases, higher potency than the parent compound alone.[69] Doxorubicin (DOX) is another example of an FDA approved drug that has been modified to incorporate a boronic ester, notably to overcome the cardiotoxic side-effects.[70] Prodrug **1.4** below, developed by Labruere and co-workers, fixed an aryl boronic ester to the free amine of DOX, with tumour regression in MiaPaCa-2 tumour models similar for both the prodrug and parent drug.[71] Furthermore, they developed a control compound by replacing the boronic ester with a carboxylic acid and no drug activation was observed, confirming a ROS-initiated mechanism. In a rather unique fashion, Ye *et al*. successfully encapsulated DOX within polymeric micelles, by way of converting the 1,3-diol functional group to a boronic ester, resulting in prodrug **1.5**.[72] Release of β-Lapachone, a known ROS generator,[73] led to the subsequent release of the free drug and displayed significantly enhanced cytotoxic ability compared to free DOX, with LC_{50} values 75% lower. Furthermore, the prodrug displayed significantly higher toxicity in cancer cells when compared to normal cells (**Figure 1.18**).

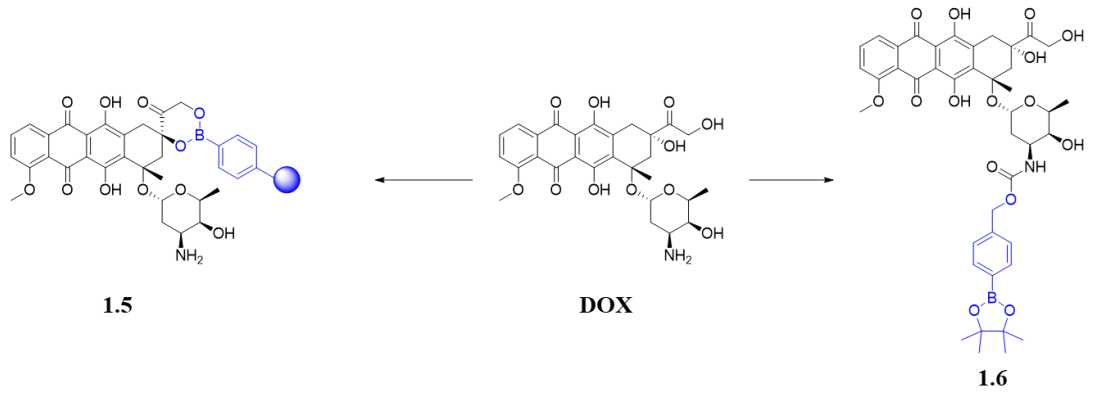

Figure 1.18: Structures of Doxorubicin prodrugs **1.4** and **1.5**

Similar to oxidative stress, hypoxia has also been the target of much prodrug design. DOX again has been shown to be a promising drug for the implementation of a hypoxia-targeting group, such as a disulfide bridge. Disulfide bridges have become a mainstay for the targeting of glutathione (GSH), which has been shown to be upregulated in cancer cells[74]. Prodrug **1.6** below in **Figure 1.19** is a good example showing the increasing sophistication of prodrug architecture. Here, Zhang and coworkers have utilised two immolative mechanisms; the first being a disulfide bridge which undergoes an intramolecular cyclisation upon GSH exposure to release a 4-hydroxybenzyl alcohol DOX derivative. This then immediately undergoes 1-6 elimination via electron cascade to release the active drug.[75] Furthermore, their design incorporates a folic acid targeting moiety on the opposing side of the disulfide bridge, leveraging the higher levels of folate receptors in cancer cells for further selectivity. Their design had better cellular uptake *in vivo* when compared to free DOX, similar cytotoxicity and was also non-toxic prior to activation.

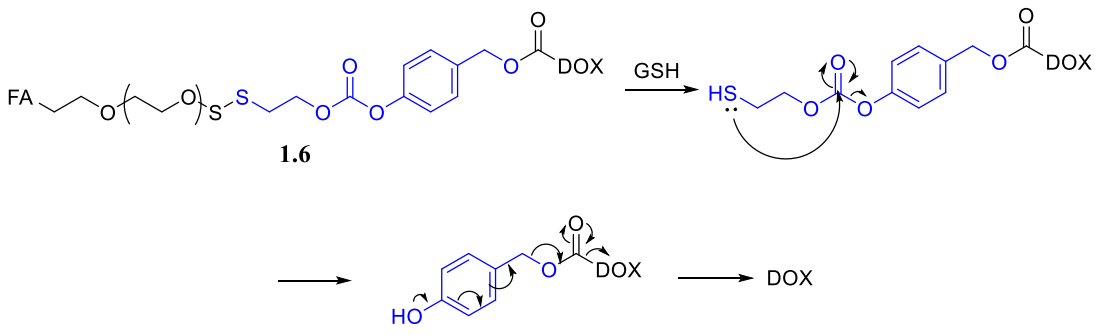

Figure 1.19: Mechanism of action of thiol responsive prodrug **1.6**.

NTR responsive prodrugs for specific cancers have seen development, with some examples making it to phase III clinical trials.[76] Much of the focus on NTR self-

immolative prodrugs has been on the 2-nitroimidazole moiety. One such example is prodrug **1.7** below, a SN-38 derivative, which features a nitroimidazole moiety carbamate linked to a dimethylethylenediamine linker, which itself is carbamate linked to SN-38 (**Figure 1.20**).[77] This, similar to **1.6**, follows two immolation pathways; the NTR initialised 1,6-elimination through the imidazole core, followed by the intramolecular cyclisation-elimination of the active drug. It was reported that the prodrug had good stability in PBS and showed moderate selectivity towards hypoxic cells in comparison to normoxic. Similar reduction based scaffolds have also been employed for nitrofurans, nitropyrrols and nitrothiphenes.[78,79]

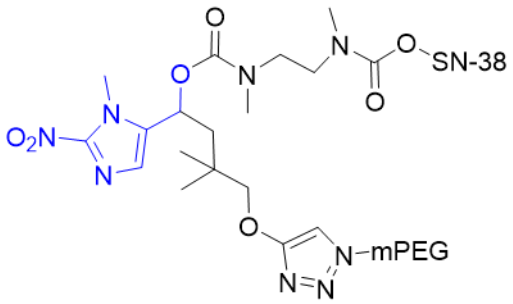

1.7

Figure 1.20: Structure of SN-38 prodrug X

While it's clear that the vast number of self-immolative linkers utilised in drug design, including the ever-growing enzyme responsive families for cancer treatment,[80–83] what is also becoming clear is the complexity of these systems, and how they can be exploited to further enhance efficacy, selectivity or other pharmacokinetic properties. This has also given rise to the ability to employ both a diagnostic and a therapeutic within the same molecule, allowing for real time imaging of drug release and efficacy, in a family of compounds known as theranostics.

1.2.3 Stimuli Responsive Theranostics

The term "theranostic", coined by John Funkhouser, is used to refer to molecular systems which combine therapeutics and diagnostics into a single integrated construct.[84] Theranostic approaches have a number of advantages to traditional methods of imaging and drug delivery, chief of which is the ability to monitor the delivery of the therapeutic agent and confirm its efficacy. This also allows for a more patient focused treatment, which could allow for easing some of the financial burden

on the worlds healthcare systems caused by ineffective treatments.[85] Much like the prodrugs and sensors previously described, its general mechanism of action is based around masking a functional group with an analyte specific trigger, which upon cleavage or functional group conversion, corresponds to both a change in fluorescence behaviour, and the 'switch on' of cytotoxicity.

As with both the smart fluorophores and prodrugs shown previously, the targeting of ROS in the tumour microenvironment continues to be one of the most popular biomarkers in theranostic approaches. Perhaps unsurprising is the continued use of boronic esters as the ROS-responsive unit. To this end, Kim *et al* reported a ROS-responsive theranostic **1.8** consisting of three parts: a boronic ester, SN-38, and a coumarin moiety (**Figure 1.21**). This coumarin moiety acts as both a self-immolative spacer and as the fluorescent reporter.[86] 7-hydroxycoumarin fluorescence is based on its ICT behaviour and this can be blocked by functionalising an electron withdrawing group in the 7-position.[87] Furthermore, its conjugated system allows for electron-cascade self-immolation via 1,8-elimination to release a second molecule upon activation. Upon exposure to H_2O_2, there was an 8.3-fold increase in fluorescence intensity, confirming cleavage of the boronic ester. In order to determine the anticancer effects, colorimetric cell viability assays were carried out in B16F10 and HeLa cell, with cytotoxicity in both cell lines identical to SN-38 upon prodrug activation via endogenous H_2O_2 addition. Furthermore, **1.8** was non-toxic without treatment with H_2O_2. Fluorescence imaging also confirmed the fluorescence activation. A similar design was developed by Ravikumar *et al*. using NO as the anti-cancer agent in conjugation with a coumarin fluorophore.[88]

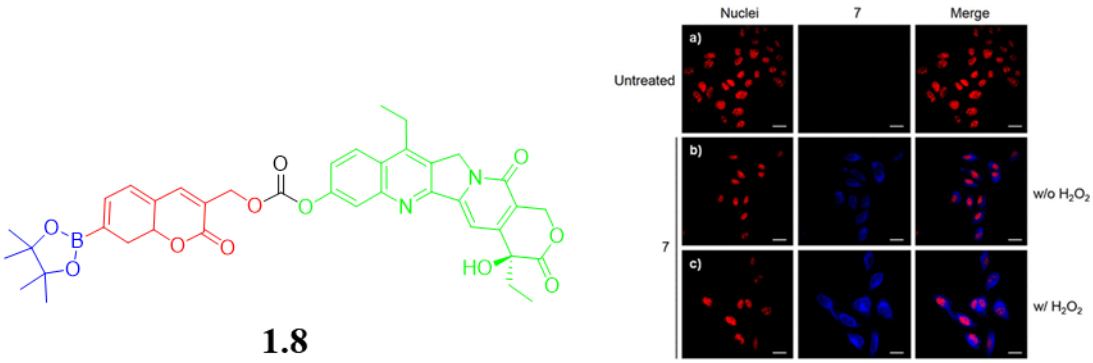

1.8

Figure 1.21: Structure of theranostic **1.8**, and cellular fluorescence images of treated B16F10 cells.

Fluorophores that can both undergo immolation and change their fluorescence characteristics are highly advantageous in theranostic design. In one such example, Cao *et al* developed theranostic **1.9**, which features their novel benzorhodol derivative named LHX, who's fluorescence is switched off through ether linkage of a phenol group to an arylbenzyl spacer.[89] SN-38 is carbonate linked ortho- to the ether link and upon immolation of the spacer, a second 1,6-elimination occurs spontaneously, releasing the active drug (**Figure 1.22**). While cell viability assays showed the probes moderate cytotoxicity in KB cancer cells (>70% at 5 μM), it showed no cytotoxicity in WI38 normal cells, attributed to peroxide induced activation. This was also an improvement on the free drug alone, which was toxic in in both cell lines (<30% cell viability at 5 μM).

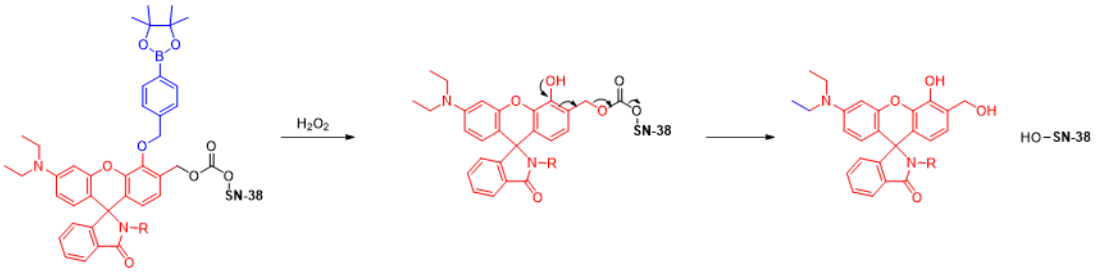

1.9

Figure 1.22: Mode of action of theranostic **1.9**.

Due to the relatively new nature of theranostics, the number of biomarkers used in their activation mechanism remains small. However, the targeting of specific enzymes has also seen use in theranostic approaches. In an early example in 2016 by Zhang and coworkers, theranostic **1.11**, used both NTR and photo-induced isomerisation to release the anticancer drug Gemcitabine, with high selectivity to hypoxic conditions and high cytotoxicity.[90] In a very recent example in 2025, Wu *et al*. utilised the 7-hydroxycoumarin moiety to develop a Evodiamine theranostic, **1.10**, which was released following NTR reduction of the nitrobenzyl moiety (**Figure 1.23**).[91]

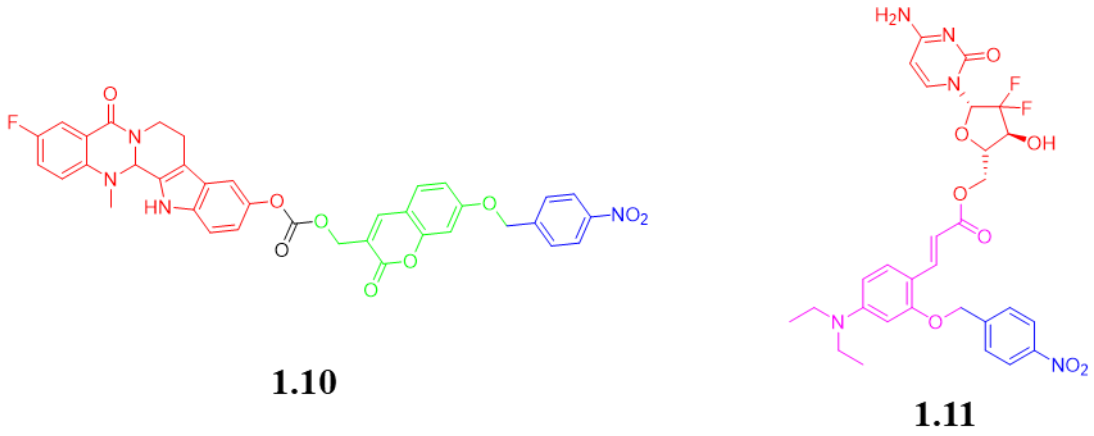

1.10 **1.11**

Figure 1.23: Structures of NTR-responsive theranostics **1.10** and **1.11**.

Wu *et al.* developed a DT-diaphorase activatable theranostic **1.12** (**Figure 1.24**).[92] DT diaphorase can rapidly and selectively reduce quinone moieties,[93] and their work takes advantage of this selectivity to incur an intramolecular cyclisation. This releases a 4-amino benzyl moiety which then undergoes classic aza-quinone methide elimination and subsequently releases CPT. Its ability to act as a theranostic comes from the fluorescence quenching by the quinone via photoinduced electron transfer. Upon the release of CPT the fluorescence is turned on, resulting in a 6-fold increase after 60 minutes. Furthermore, the prodrug showed strong cytotoxicity towards A549 cells, known to over express DT-diaphorase, with a measured LC_{50} of 1.179 µM. This is contrast to an LC_{50} of 80 µM in non-DT-diaphorase overexpressed cells.

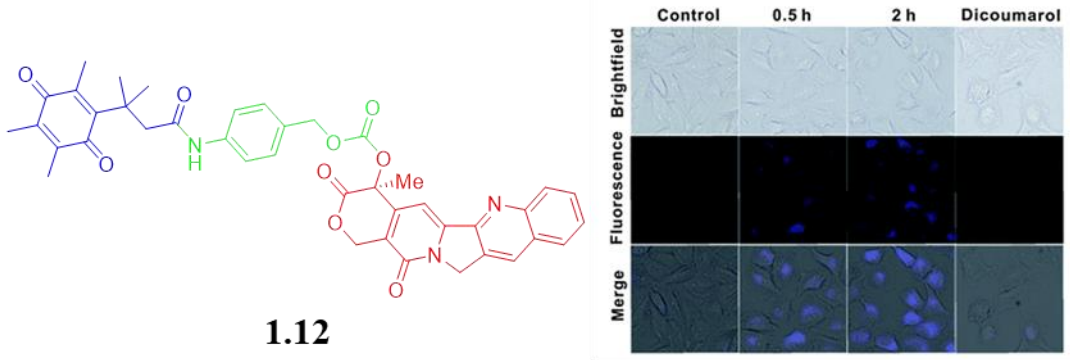

1.12

Figure 1.24: Structure of DT-Diaphorase theranostic X and dicoumarol inhibition study confirming DT-Diaphorase mediated activation.

Despite promising developments, the field of theranostics is in its early stage, with few such agents advancing beyond clinical trials and even fewer achieving regulatory approval.[94,95] This is particularly true for systems based on self-immolative systems, which, while offering elegant solutions for triggered activation, add another layer of

complexity to already multifunctional molecular designs. The integration of diagnostic and therapeutic functions within a single framework poses unique regulatory and translational challenges that traditional clinical trial models are often ill-equipped to manage.[96] Nevertheless, academic interest in theranostic platforms continues to accelerate, as evidenced by the rapid rise in related publications since the term's inception (**Figure 1.25**).

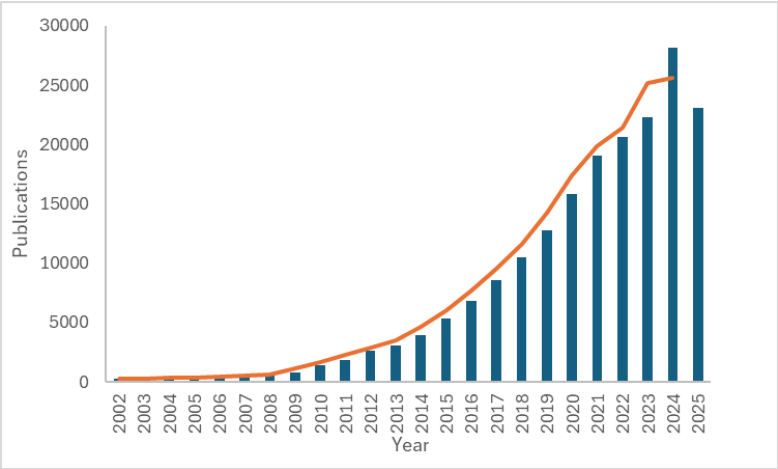

Figure 1.25: Usage of the term "theranostic" in published articles from 2002. Source: PubMed.

While responsive molecular systems have demonstrated considerable promise in medicinal chemistry in terms of drug release and imaging, the principles underlying their design have also increasingly extended further afield, to areas such as supramolecular chemistry. In particular, the use of stimuli-responsive motifs to regulate non-covalent interactions offers opportunities in the development of selective and responsive anion binding.

1.3 Responsive Supramolecular Systems

Since the term "supramolecular chemistry" was first coined in the 1970s by Jean-Marie Lehn, it has become a rapidly growing field of study, even winning the Nobel Prize in Chemistry in both 1987 and 2016.[97] In his 1988 paper, he defined it as "the chemistry of the intermolecular bond, covering the structures and functions of the entities formed by two or more chemical species".[98] Put more broadly, it can be considered the design, synthesis, and investigation of molecules that assemble into larger, well-defined architectures through non-covalent interactions. These structures include, but are not limited to, host-guest complexes and self-assembled structures. A key factor of supramolecular chemistry is that these "weak" interactions are reversible. Since many biological processes are based on these weak interactions, such as the transportation of ions through the cell membrane,[99] much of the inspiration for supramolecular chemistry comes from mimicking these natural processes. This has led to supramolecular systems being the focal point of research for anion binding, sensing and transport.

1.3.1 Anion binding and sensing in supramolecular chemistry

Anions play a key role in role in many aspects of daily life, be it environmental, chemical or biological process. From a biology perspective, anions are fundamental for the maintenance of cellular pH[100] and are key to the distribution of electrical signals throughout the nervous system.[101] Imbalances in these anion concentrations within the body have been shown to play a key role in the development of numerous diseases, with the most common of which being cystic fibrosis, caused by an imbalance of chloride ions.[102] It is this biological importance that has led to significant research into the design and synthesis of molecules that are capable of binding and recognising anions. Non-covalent interactions have been at the forefront of this emerging field of study, particularly the hydrogen bond with the hydrogen bond donor and acceptor motif now a widely established area of anion binding in supramolecular scaffolds. The anion binding capabilities of supramolecular receptors are influenced by a number of factors, such as pK_a of the H-bond donors[103] and preorganisation of the binding pocket.[104] Within this subsection many of these binders focus on the N-H bond. As anion binding Early synthetic anion binders using the N-H bond donor strategy

employed ammonium-based receptors, particularly ureas, thioureas and amides (**Figure 1.26**).

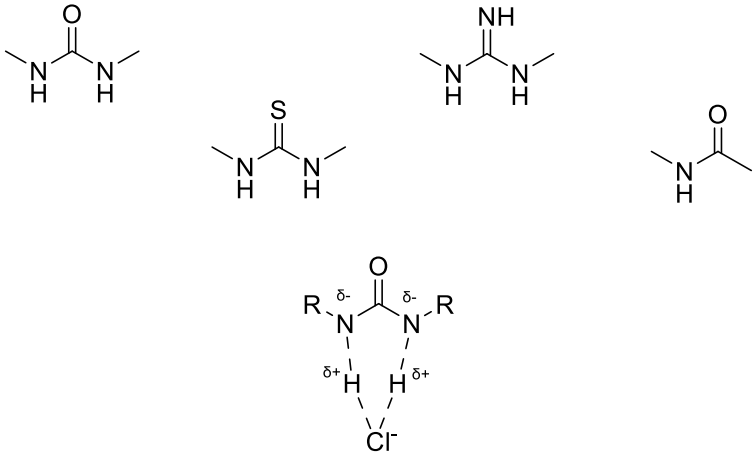

Figure 1.26: Commonly used motifs for H-bonding of anions and schematic of H-bonding interaction between ureas and chloride showing partial charges.

One of the earliest examples of a ammonium-based ion anion receptor was reported by Wilcox *et al.*, in 1992, who showed that compound **1.13**, shown below in **Figure 1.27**, was capable of binding to a number of oxoanions such as sulfonate, oxylate and carboxylate.[105] Studies such as this led to an explosion in interest in the area, such to a point that Gale *et al,* published yearly reports highlighting the advancements in anion receptor chemistry. [106–110]

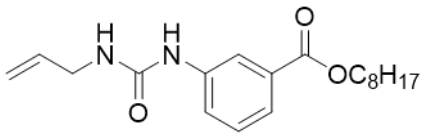

1.13

Figure 1.27: Anion receptor developed by Wilcox *et al.*

Since these earliest examples in the late 1980s, supramolecular scaffolds have evolved in complexity, from simple aryl amides to macrocyclic structures[111], foldamers[112] and supramolecular cages.[113] The integration of fluorescent reporters into these designs has enhanced the use cases of these motifs, moving them from simple anion binders to anion sensors with applications in biological and environmental settings. Moreover, the field has expanded beyond this again, with the development of effective anion transporters, which show promise in addressing channelopathies[114] and serving as

antimicrobial agents.[115] Despite these notable advances that have firmly entrenched supramolecular chemistry in chemical research, efforts to enhance the spatiotemporal control over anion binding behaviour has been comparatively slow.

1.3.2 Responsive anion binding systems

Similar to the theranostic strategies above, the ability to control a desired output (in this case binding affinity) has stark advantages over non-selective strategies. For the most part, most anion binders and transporters are built upon a scaffold that is constantly in a high-affinity state and there is a growing need for research into responsive anion binding methodologies. These systems would have the ability to locally activate under desirable physiological conditions, dependent on the stimuli chosen as the target, and this would allow for deactivation at other sites and prevent undesired side effects and a build-up of resistance.[116,117] Early examples of responsive binder were based on allosterism[118] and metal-ligand coordination,[119] but throughout the last two decades, photo-initiated systems have become the most popular means of activating anion binding.

Using light as the external stimulus provides a high spatiotemporal control over the activation of anion binding, as well as non-invasiveness. In general, these systems are based on photo-induced isomerisation, interconverting a non-binding isomer to one which conformationally allows for efficient binding. One such example is based on a molecular tweezer approach,[120] whereby a pair of anion receptors are positioned far apart from each other in one isomeric configuration and are brought close together under exposure to light of a certain wavelength. Shimasaki *et al.* developed an early example of a stiff-stilbene core which interconverted between an *E*- and *Z*- isomer under irradiation with 365 nm light to go from *E*- to *Z*-, and 410 nm to achieve reverse isomerisation.[121] In testing the binding affinities of both isomers, the *E*- showed an enhanced infinity for Cl^- by a factor of 8 compared to the *Z*- isomer, providing an early example of a responsive binder. Building on this design, Feringa *et al*. developed a *bis*-urea derivative of the stiff-benzene concept in compound **1.14**.[122] Similarly to the early example, the reversible isomerisation under light irradiation showed a significant increase in binding affinity for both acetate and phosphate. It also differed in its binding behaviour, with the *Z*- isomer allowing for a 1:1 binding fit, due to the urea

groups being in close proximity to each other, however the *E*- isomer adopts a 2:1 binding fit, which much lower affinity (**Figure 1.28**).

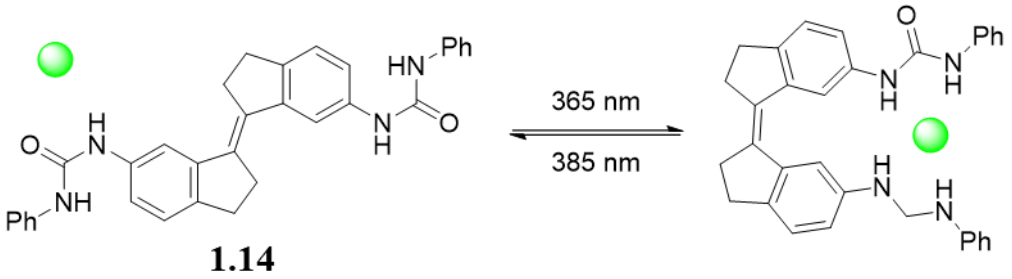

1.14

Figure 1.28: Photo switchable anion receptor developed by Feringa.

Azobenzenes have also emerged as a popular backbone about which to build responsive binders. Despite their popularity however, they suffer from a flaw of being less rigid than their stiff-benzene counterparts.[123] This lack of rigidity results in reversion back to the *E*- isomer in the dark at room temperature, making analysis of the anion binding behaviour of the *Z*- isomer incredibly challenging. Early work into the design of azobenzene based tweezers by Jurczak *et al*. showed that mono and bis urea functionalised derivatives could be interconverted from the *E*- to *Z*- isomer via irradiation at 368 nm.[124] In order to overcome the thermal conversion to the *E*- isomer, Bhosale and co-workers synthesised a naphthalenediimide based receptor **1.15** that could be converted from *E*- to *Z*- by irradiation at 366 nm and subsequently reversed back via irradiation at 500 nm.[125] However, interestingly, upon binding with fluoride, the receptor adopted the *Z*- isomer quantitatively and irreversibly, with ^{1}H NMR studies showing it formed a di-anionic radical species upon addition of excess fluoride (**Figure 1.29**). The binding of fluoride stabilised the complex, with isomerisation back to *E*- occurring only under oxidative conditions.

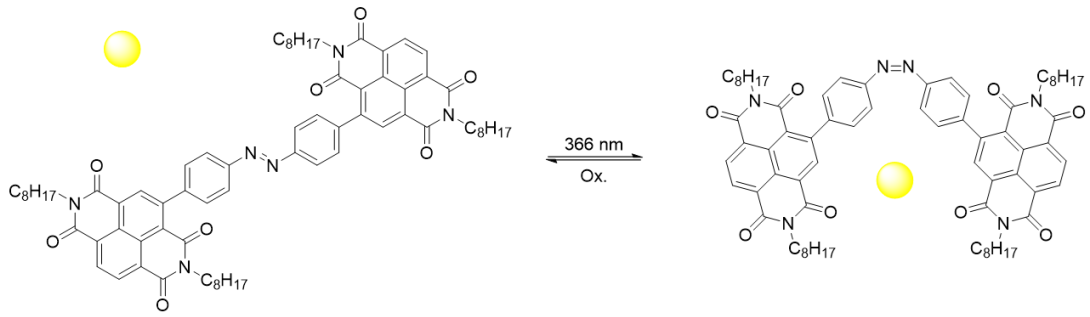

1.15

Figure 1.29: Photoswitchable Fl^- receptor developed by Bhosale.

Although light induced anion binding has been without doubt the most common way of 'switching-on' binding activity, recent research has expanded the scope to include redox-switchable receptors. Beer *et al.* synthesised a series of chloride binders based on a hydroquinone motif (**Figure 1.30**).[126] Their receptor **1.16** displayed a diminished binding affinity when converted from the hydroquinone to the quinone motif, due to the intramolecular hydrogen bond between the amide and the newly formed quinone carbonyl. Although, interestingly, this intramolecular interaction was also seen between the amide carbonyl and the hydroxyl group, leading to an overall lower binding affinity than expected, it was still greater than in the quinone form. Furthermore, this oxidation was reversible, demonstrating the potential of the receptor to be a switchable one. This field of redox-switchable receptors has been expanding over the last five years and is now including probes with on/off fluorescence behaviour upon binding,[127] further enhancing the application of this field of responsive anion binders.

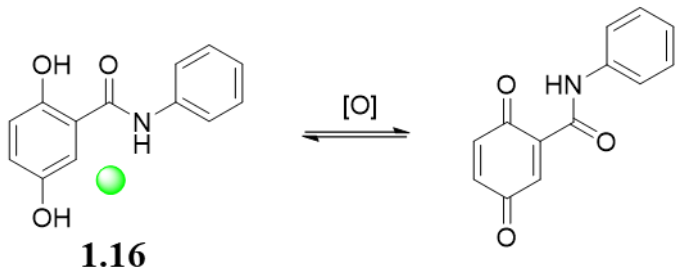

1.16

Figure 1.30: Redox-switchable anion binder **1.16**

Research into responsive anion binding has progressed steadily over the past decade, with ureas dominating much of the field owing to their well-established hydrogen-bonding capabilities. Nonetheless, reliance on a narrow set of binding motifs may

constrain the development of novel strategies, highlighting the need to explore alternative scaffolds. Among these, squaramides have emerged as particularly promising candidates, offering both synthetic versatility and strong, bi-directional binding interactions. These characteristics position squaramides as valuable building blocks for advancing the design of next-generation responsive anion binders and sensors.

1.3.3 The Squaramide

Squaramides have garnered much attention over the past two decades as key scaffolds for the development of novel anion receptors. Structurally, squaramides comprise of a four membered cyclobutadione ring, featuring two carbonyl hydrogen bond acceptors and two N-H hydrogen bond donors (**Figure 1.31**). It is this system of functional groups which makes squaramides incredibly auspicious in the field of anion binding and recognition. Notably, the lone pairs on the nitrogen atom can delocalise into the ring system, enhancing the aromatic character and stabilising the resulting hydrogen bonded complexes. Additionally, the strong H-bond donating ability of the NH moieties further contributes to the efficacy of squaramides in self-assembly and molecular recognition. Conformationally, squaramides favour an *anti/anti* arrangement with respect to their R substituents, in which the two N-H groups are orientated in the same direction - particularly favourable for bidentate hydrogen bonding. This conformational has been confirmed by both NMR and X-ray crystallographic studies, notably by Costa and co-workers.[128] However, it should be noted that an *anti/syn* conformation has also been observed, indicating some level of conformational flexibility depending on substituents/environment.

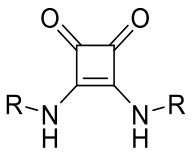

Figure 1.31: General structure of a squaramide, showing *anti/anti*-conformation

A key advantage of squaramides is their relative ease of synthesis. Symmetric bis-squaramides can be readily prepared from the ethyl ester derivative of squaric acid via simple aminolysis. More importantly, squarates can form squaramide esters: nucleophilic attack by an amine on the ester, followed by elimination of ethanol, leads to amidation at a single reactive site. The resulting amido-squarate is less electrophilic

than its parent di-squarate, yet further amidation can be carried out to produce asymmetric bis-squaramides (**Figure 1.32**). This synthetic accessibility allows for extensive structural variation and functional group incorporation, enabling fine-tuning of anion-binding properties.

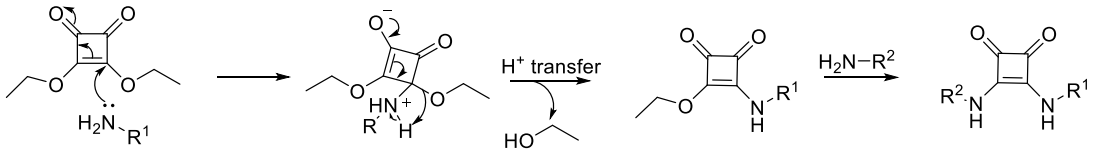

Figure 1.32: General mechanism for the formation of an asymmetric bis-squaramide.

Squaramides have predominately been used as isosteres for ureas, thioureas and guanidine, but also for carboxylic acids, amino acids and phosphates. The ability of squaramides to act as isosteres for ureas has been extensively studied in terms of their anion binding capabilities. Early work by Fabbrizzi *et al.* directly compared a series of urea binders with their analogous squaramide derivatives in a series of publications.[129] These works showed that the squaramide **1.17** showed a 1:1 anion/receptor complex with Cl^- with a higher binding affinity than the urea derivatives. (log*K* = 6.05 for compound **1.17**, and 4.55 for its urea counterpart). The same group also showed similar results when comparing compound **1.18** with the corresponding urea and sulfonamide derivates (**Figure 1.33**).[130]

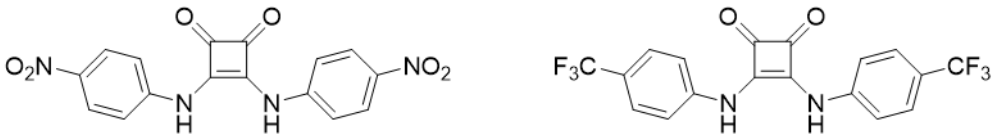

1.17 **1.18**

Figure 1.33: Structure of squaramide based receptors developed by Fabbrizzi *et al.*

The ease with which functional R-substituents can be introduced to the squaric acid core enables modulation of both the geometry and strength of anion binding. As anion binding affinity is closely related to the p*K*a of the NH groups,[131] the ability to modulate this value with different R-groups makes squaramides highly tuneable.[132] Furthermore, this modulation of R-groups also allows for additional binding sites to be introduced. For instance, Li *et al.* developed a family of N-*tert*-butyl sulfinyl squaramide receptors and found that the symmetrical bis-derivatives exhibited enhanced Cl^- affinity when compared to the asymmetric variants (**Figure 1.34**).[133] This

enhancement was attributed to weak C -H - anion interactions involving the *tert*-butyl group. This interaction was then absent when the sulfinyl substituent was replaced by aromatic groups.

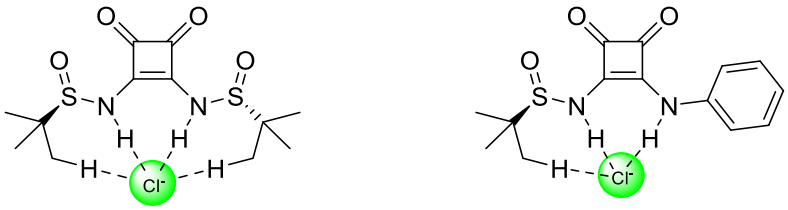

Figure 1.34: Receptors developed by Li *et al* showing C-H assisted hydrogen bonding.

While initial research focused on simple anion binders, this chemical flexibility of squaramides has rapidly expanded their use in the development in fluorescent sensors for use in anion sensing. As with much of the early pioneering work into squaramides as anion binders, it was again the work of Costa and co-workers that began the chemical space of anion sensing using squaramides. Their early work was based on host-guest complexes whereby there is an intermolecular competition between the indicator and target analyte for interaction with the receptor, leading to a measurable response.[134–136] Their family of squaramide-ammonium charge-assisted receptors which targeted oxyanions in aqueous media, leading to both fluorescent changes and colorimetric changes. Indeed, the Elmes group has developed a squaramide-naphthalimide based fluorescent sensor, **1.19**, which showed a remarkable 500% increase in fluorescence intensity upon Br^- binding (**Figure 1.35**).[137] As the fluorescence of naphthalimides is sensitive to π- π stacking and aggregation,[138,139] the binding of Br^- was capable of disrupting the packing and subsequently lead to disaggregation induced emission (DIE).

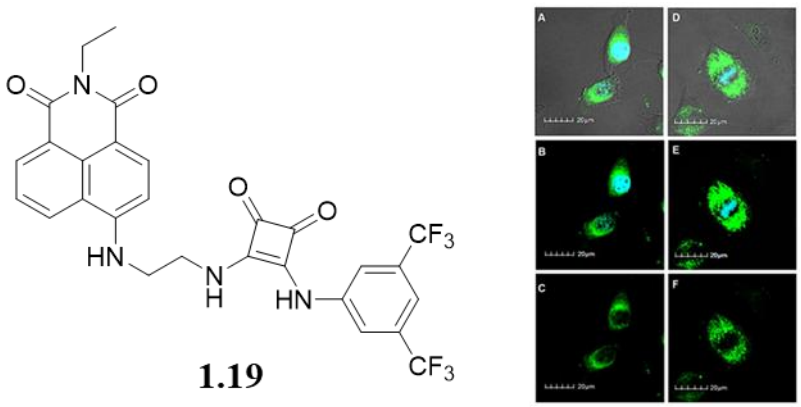

1.19

Figure 1.35: Structure of **1.19** and confocal microscopy images of **1.19** in HeLa cells.

As bioisosteres, squaramides have also been utilised in contemporary drug design. While early reports in the literature of squaramide based drugs go as far back as the 70's, uptake in their use in drug design has remained surprisingly low, especially when compared to seemingly unending research into their applications in catalysis and molecular recognition. This is made doubly surprising when you take into account their relative ease of synthesis and most importantly, their stability towards hydrolytic attack.[140] The available examples can, perhaps somewhat crudely, be described as arising from simply replacing the bioisoster with a squaramide. This led to the first squaramide containing drug candidates, developed by Smith Kline & French.[141] Of the numerous examples of squaramide based drugs however, ranging from isosteres of ureas, guanadines, amides and phosphates, to date, only 4 have entered clinical trials, with their structures shown below in **Figure 1.36**.[142–144]

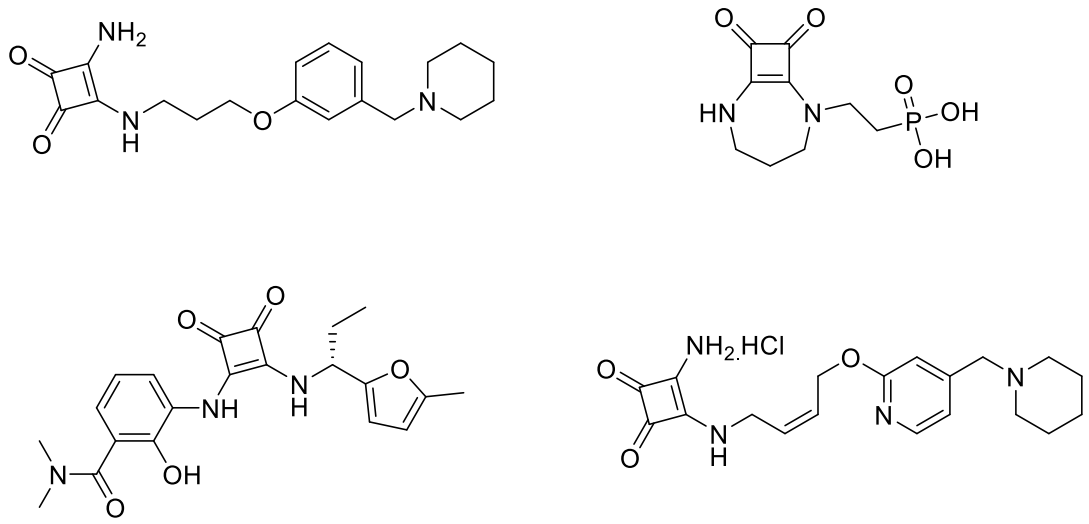

Figure 1.36: Structures of squaramide-containing drugs that have reached clinical trials

In an effort to aid the fight against antimicrobial resistance (AMR), the Elmes' group reported the design and synthesis of several squaramide-indole hybrids, titled "squindoles", which displayed potent antimicrobial activity, stemming from its chloride transport ability and subsequent induction of oxidative and osmotic stress. Compound **1.20**, shown below in **Figure 1.37**, displayed clinically relevant LC_{50} values against both *S.aureus* and MRSA (2.5 μM and 2.35 μM respectively.[145] Furthermore, more recent observations within the group have seen cyclic squaratide derivatives showing antimicrobial activity, although at the time of writing the exact mechanism is yet to be established.

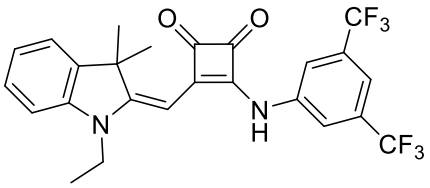

Figure 1.37: Structure of squindole **1.20**

1.3.3.1 Responsive squaramide based systems

The ease of synthesis of squaramides has also allowed them to be used as a linker to bioconjugate active compounds.[146] and very recently, squaramides have shown the potential to act as a new family of self-immolative spacers. This design and strategy were reported in 2021 by Rotger and coworkers, who developed both a proof of concept, and followed up with an NTR responsive prodrug, **1.21,** capable of delivering an Aniline Nitrogen Mustard (ANM) derivative.[147] Their design featured two self-immolative spacers, one being the classic nitrobenzyl moiety, which upon NTR reduction underwent electron cascade releasing a free N-methylated amine. This then promoted an intramolecular nucleophilic attack forming a seven-membered ring and releasing the active drug (**Figure 1.38**). Drug activity was verified in both U87-MG and LN229 glioblastoma cells. The authors also remark at the inclusion of the *N*-methyl groups in the design, which showed faster cyclisation times compared to the primary amine derivates. This was owed to the favouring of the *E,Z* conformation of the N-methylated squaramide precursor,[148] giving a favourable conformation towards cyclisation. Despite this promising and innovative result however, at the time of writing it remains the sole example of this prodrug design strategy.

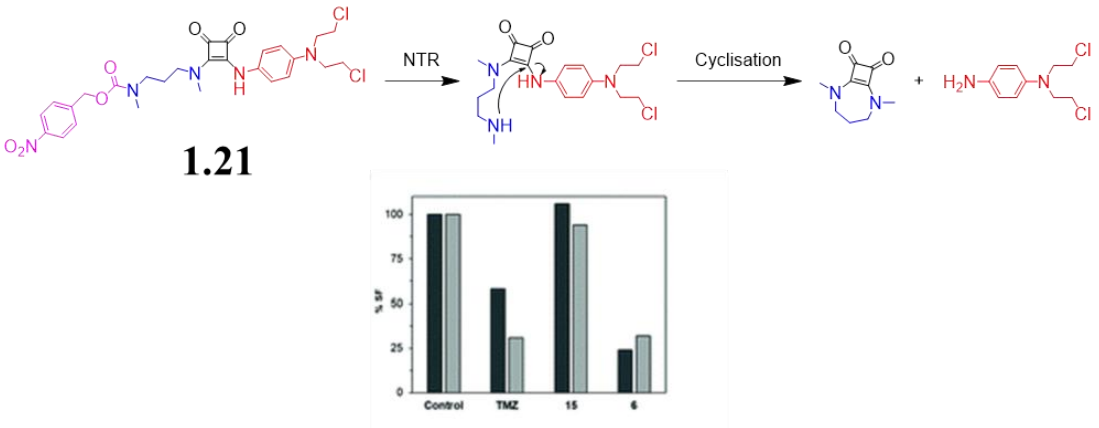

Figure 1.38: Self-immolation of compound **1.21** based on intramolecular cyclisation developed by Rotger *et al*. **(top)**, Survival Factor index for LN229 (black) and U87-MG (grey) cells as determined by the clonogenic assay. **(bottom)**

The above sections have aimed to provide an overview of the chemical space surrounding responsive molecular systems, with particular emphasis on the use of linker chemistry to mask the activity of fluorophores or therapeutics until selectively triggered. While the literature highlights rapid growth in this area, it is equally evident that the landscape continues to evolve, and there remains a persistent need for innovative methodologies to advance the development of responsive systems. This need is especially pronounced in the context of anion binding, where examples of selective and responsive binders are still relatively scarce. This thesis aims not only to build upon existing approaches but also to introduce a new strategy for designing and constructing responsive molecular scaffolds. The following section outlines the specific aims of this work and provides a summary of the research presented in each chapter.

1.4 Aims

The field of stimuli-responsive molecular systems has become a vital area of research across a multitude of use cases, from material science to medicinal applications. The aim of the above introduction was to highlight the triggers and spacers used in their design, focusing particular attention on the use of self-immolative spacers. Their use has seen success in the development of profluorophores and prodrugs and are now beginning to become a mainstay in theranostic design. However, despite this, their use in the newly developed responsive anion binding motifs is few and far between

The work carried out in this thesis builds upon the current knowledge of self-immolative spacers in theranostic design, while also introducing them into the chemical space of responsive anion binding systems. The three primary objectives of this thesis are as follows:

The first objective of this thesis is to develop a ROS-responsive self immolative dendrimer capable of being activated by Cold Atmospheric Plasma (CAP) treatment (**Chapter 2**). The design will consist of 4 distinct motifs: an arylboronic ester triggering group, a cresol core, a naphthalimide fluorophore and amonafide drug. It is hypothesised that under CAP treatment, the induced ROS would cleave the trigger, releasing the fluorophore and drug. This would have a two-fold advantage of not only increasing the selectivity of the treatment, also allowing for real time monitoring of drug release. This selectivity will be even further enhanced by the incorporation of CAP, giving a high degree of spatiotemporal control over the ROS production (**Figure 1.39**).

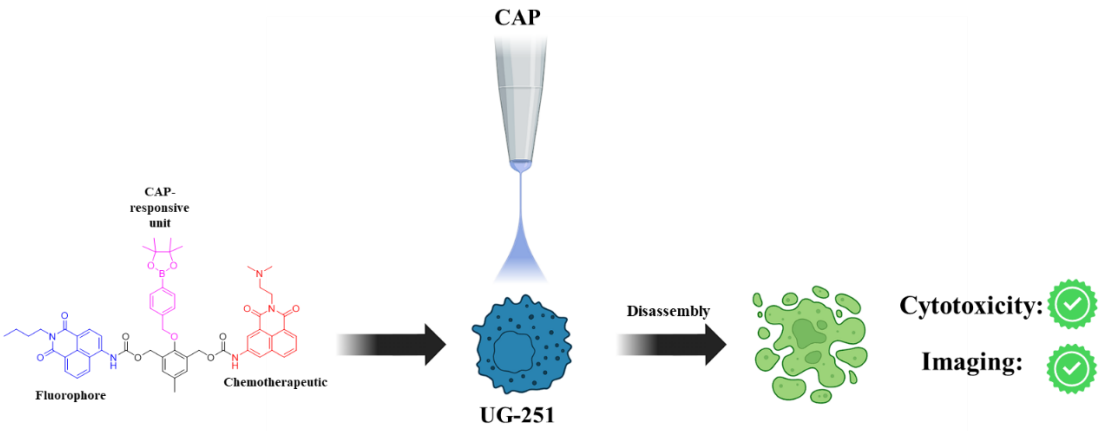

Figure 1.39: Graphical representation of a CAP-activated theranostic.

The second objective is to develop a small ring-closed squaramide scaffold about which to build a responsive anion binder that will undergo a skeletal rearrangement and subsequent ring-expansion (**Chapter 3**). This will in turn result in a "switch-on" in anion binding, depicted graphically in **Figure 1.40**. The parameters about which the rearrangement occurs will be investigated, along with the ability to introduce orthogonal triggers to further increase the use cases and selectivity of the binders. Successful candidates will then be screened to assess their anion binding capabilities.

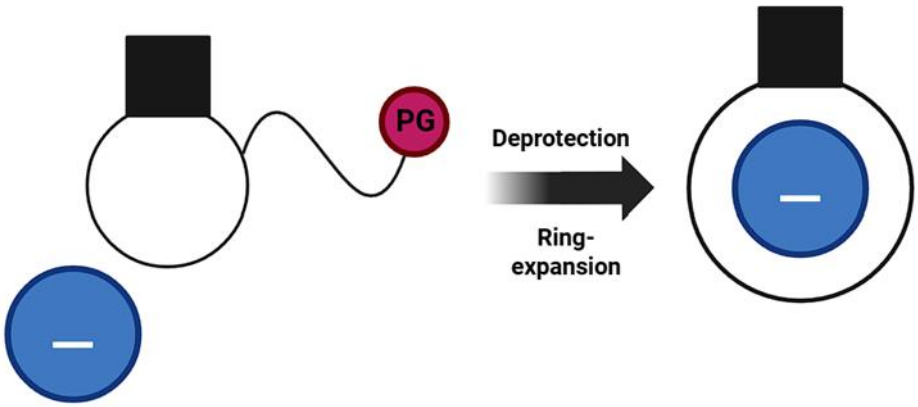

Figure 1.40: Graphical representation a ring expansion strategy towards selective ring expansion

The final objective (**Chapter 4**) is to build upon the aforementioned responsive binders, with an emphasis on biologically relevant stimuli as the targets (**Figure 1.41**). The 'switch-on' on rearrangement will be achieved *via* peroxide mediated hydrolysis and NTR-mediated reduction. The design will also be expanded upon to include a profluorophore, with the aim of developing a responsive anion sensor.

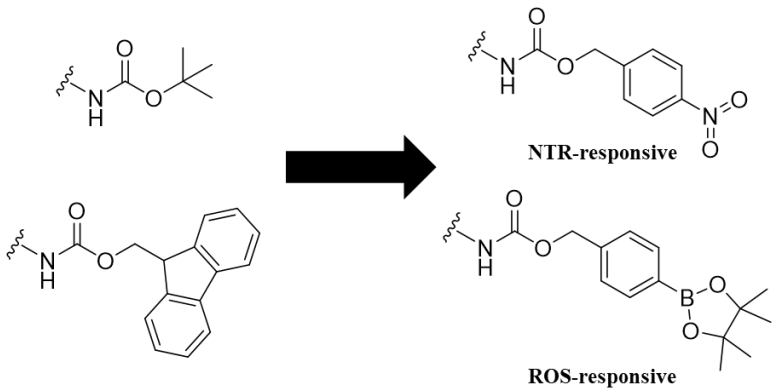

Figure 1.41: Modulation of *N*-terminus protecting groups to allow for the targeting of biologically relevant stimuli.

Chapter 2

Towards the Synthesis of Cold Atmospheric Plasma Activated Theranostics

2. Towards the Synthesis of Cold Atmospheric Plasma Activated Theranostics

2.1 Introduction

Reactive Oxygen Species play a pivotal role in cancer cells and can often be described as a "double-edged sword". Typically, cancer cells display elevated levels of ROS when compared to normal cells, which contributes to their growth, cell proliferation and metastasis.[149] However, sufficiently high concentrations of ROS lead to cell death and, most importantly, makes cells more sensitive to treatment.[150] Glioblastoma Multiforme is particularly relevant given its aggressive nature as a malignant primary brain tumour where long term survival is rare. Gliomas are typically graded I-IV in terms of severity, with GBM being a grade IV and having a survival rate of only 10 months following traditional treatment of adjuvant temozolomide treatment.[151] GBM cells appear to be especially sensitive to ROS levels, with cell death occurring when ROS concentrations rise above or fall below a critical threshold.[152,153] Therefore, a treatment which can manipulate the finely tuned ROS concentration of GBM cells would represent a promising strategy to selectively induce tumour cell death while sparing healthy tissue, potentially enhancing therapeutic efficacy.

Building on the concept of leveraging oxidative stress for therapeutic benefit, Cold Atmospheric Plasma (CAP) emerges as a promising tool that induces ROS to target cancer cells with a high degree of precision.[154] Cold Atmospheric Plasma, as the name suggests, is a partially ionised gas consisting of electrons, ions and neutral particles, which can be generated at standard temperature and pressure. It is classified as a nonthermal plasma, characterised by high electron temperatures while the bulk heavy particles remain near ambient temperature. This unique property facilitates the generation of CAP at relatively low power, making it a versatile tool for various applications. Most importantly, however, as CAP is generated under atmospheric conditions, air can diffuse into the discharge region resulting in the generation of reactive oxygen species (ROS) and reactive nitrogen species (RNS), such as H_2O_2, O_3, O_2^- and NO to name just a few. It is the generation of these biologically important analytes that have made CAP a tool of expanding interest for medicinal research, most recently in cancer research.[155] Initially CAP was investigated and implanted for wound healing[156] and sterilisation,[157] however recent advancements have shown promising

results for CAP anticancer efficacy, driven by its ability to locally induce cytotoxic levels of RONS within a cancer cell. A study published in 2020 by Shokri *et al.* showed CAPs ability to trigger apoptosis within Hela and MDA-MB-231 cell lines, via both direct CAP and plasma activated medium treatments.[158] Likewise, CAP was demonstrated to have anticancer abilities in both colorectal adenocarcinoma and lung adenocarcinoma cells, with CAP treatment leading to an expression of apoptosis related markers such as a Cyt c, caspase-3 and Bax, both *in vitro* and *in-vivo.*[159]

Recently, research into the anti-cancer capabilities of CAP have moved to include to use of prodrugs in combination to CAP treatment to enhance treatment efficacy. Stephens *et al.* demonstrated that in U-251MG cells, a select number of pyrazolopyrimidinones, showed between a 5–15-fold increase in reactive species dependant cytotoxicity when used synergistically with CAP. This result was demonstrated for both direct and indirect CAP treatment.[160] Although the exact activated forms of these compounds, along with the mechanism of action, was not explored within the study, it was determined that the CAP-generated ROS was a key player in the activation process.

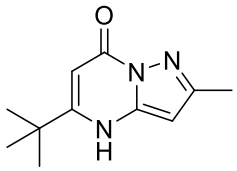

Figure 2.1: Structure of pyrazolopyrimidinone **2.1**.

Despite being published in 2021, this remains the only study to the best of our knowledge that probes the ability of CAP, not only as a cancer therapy of its own, but also as a tool for activating latent prodrugs and enhancing the efficacy of treatment. The induction of ROS species within cells via CAP treatment makes it an immensely attractive means by which to "switch-on" ROS-responsive theranostics with extremely high spatiotemporal control of drug activation.

The use of self-immolative dendrimers has emerged in recent years as an innovative new ideology around which to build compounds for applications in fluorescence imaging, and even more recently, theranostics. Since the near-simultaneous reports by Shabat, Scheeren, and McGrath in 2003, significant advances have been made in dendritic design, enabling more complex functionalities and a broader range of

applications.[161–163] The core concept behind self-immolative dendrimers involves a "trigger" that masks the compound's activity. When this trigger is activated by an analyte, it is cleaved, causing the dendrimer to fragment into its core components and release its tail units (**Figure 2.2**). This release activates the compound, leading to effects such as increased fluorescence (as seen with profluorophores), enhanced cytotoxicity (in prodrugs), or both (in theranostics).

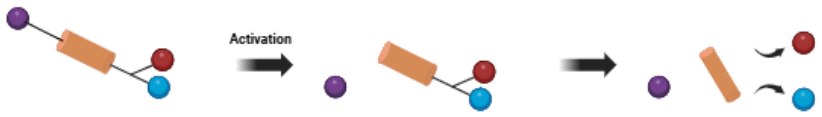

Figure 2.2: Schematic of the activation and disassembly of self-immolative dendrimers

Building on the scaffold initially developed by Shabat in 2004, Gao and colleagues synthesized compound **2.2**; a doxorubicin-based theranostic incorporating tetraphenylethene with aggregation-induced emission properties (**Figure 2.3**). Their studies demonstrated a remarkable 142-fold increase in fluorescence intensity in the presence of in situ-generated H_2O_2. Furthermore, cytotoxicity assays revealed that **2.2** exhibited no significant cytotoxic effects in the absence of H_2O_2; however, the introduction of H_2O_2 resulted in a concentration-dependent increase in cytotoxicity, with higher prodrug concentrations leading to greater reductions in cell viability.[164]

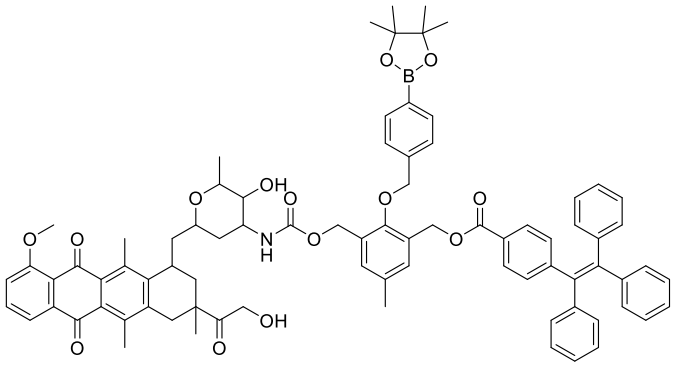

Figure 2.3: Structure of compound **2.2.**

Together, the precise ROS delivery offered by CAP and the selective activation of self-immolative dendrimers suggest strong potential for a combined therapeutic approach. However, this integration has received little attention to date, representing a clear gap in the current research. This chapter aims to address this gap through the design, synthesis and evaluation of two novel self-immolative dendrimers capable of releasing either a pro-fluorophore or pro-fluorophore and a pro-drug through CAP activation

2.2 Chapter Objectives

The aim of this chapter is to synthesise two novel CAP-activated self-immolative dendrimers. This design of these compounds is graphically portrayed in **Figure 2.4**, where three moieties are linked together by a central core. In our instance, the 3 moieties consist of a trigger, a profluorophore and a cytotoxic agent.

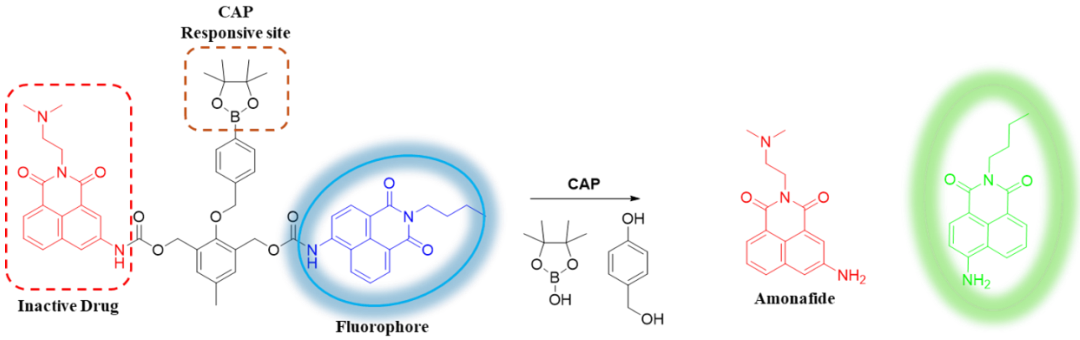

Figure 2.4: Graphical representation for the design of CAP activated prodrugs

The dendritic release of our cargo is expected to proceed as shown in **Figure 2.5.** Following exposure to ROS, the boronic ester is oxidised and converted to a phenol intermediate. This intermediate then undergoes a dendritic collapse by way of quinone methide elimination, which releases the phenol of the cresol unit. 1,4-elimination then releases the fluorescent reporter, corresponding in a modulation in fluorescence output from blue to green emission. The newly formed ortho quinone methide-type intermediate then acts as a Michael acceptor, where it is quenched by water to restore the aromaticity of the ring. Consequently, this is then followed by a second 1,4-elimination, releasing a dormant cytotoxic agent in its active form.

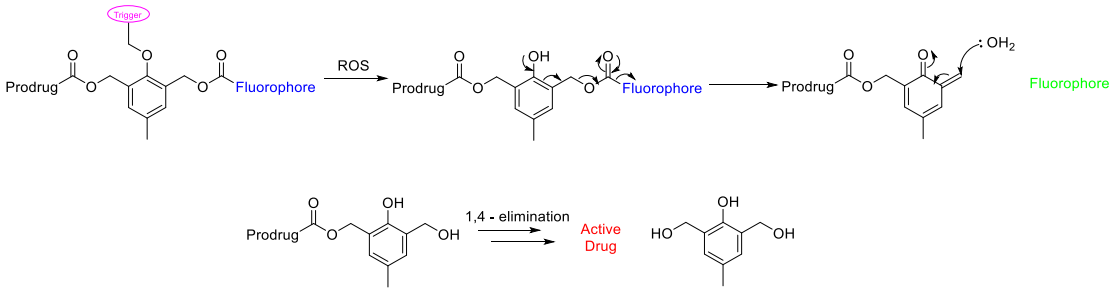

Figure 2.5: Self-immolation of a ROS-responsive dendrimer

Once the overall design and release mechanism had been finalised, compounds **2.3** and **2.4** were chosen as the target compounds. Compound **2.3**, depicted in **Figure 2.6**, features a phenylboronic ester linked to the central cresol core, with two n-butyl-4-

amino-1,8-naphthalimides appended to the core via a carbamate linkage. Naphthalimides were selected due to their fluorescent properties being highly sensitive to the nature of their substituents, allowing precise tuning of the intramolecular charge transfer (ICT) excited state.[165] They are also highly resistant to photobleaching and have a considerable Stokes' shift. The alteration in ICT behaviour, accompanied by a corresponding shift in emission characteristics, is also well-documented in the context of converting a carbamate into a free amine.[166] Both compounds **2.3** and **2.4** utilise this transformation to achieve their functionality.

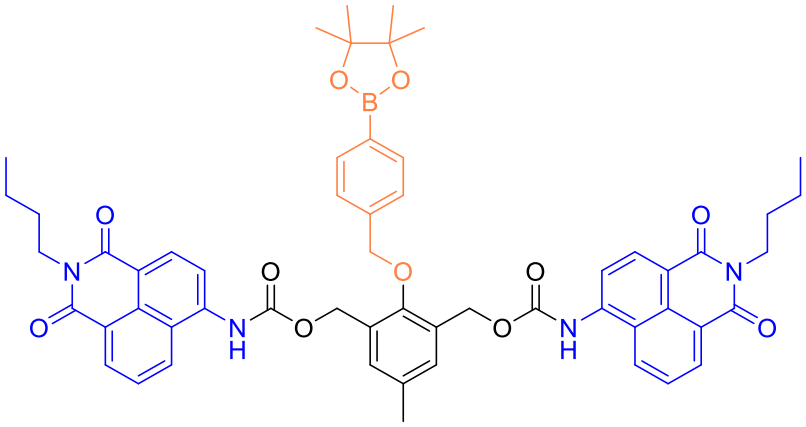

2.3

Figure 2.6: Structure of compound **2.3**. Phenylboronic ester (orange) and naphthalimides (blue)

Compound **2.4** in **Figure 2.7** builds on the structure shown above, and follows a theranostic approach, where **2.4** is comprised of a phenylboronic ester linked to the central cresol core, n-butyl-4-amino-1,8-naphthalimide conjugated via a carbamate bond to the core and amonafide conjugated via a carbamate bond to the core. Amonafide was chosen in the design as it is a known topoisomerase inhibitor and DNA intercalator that showed activity against breast and prostate cancer.[167,168] However, amonafide is no longer undergoing clinical trials due to the toxicity of *N*-acetyl-amonafide, one of its metabolites.[169] The design of **2.4** has the potential to overcome some of the toxicity associated with amonafide as it will limit its release in a spatiotemporally controlled manner. Examples of amonafide based prodrugs strategies, which target ROS as the stimuli, have appeared in the literature, in efforts to reintroduce amonafide as a relevant chemotherapeutic.[170]

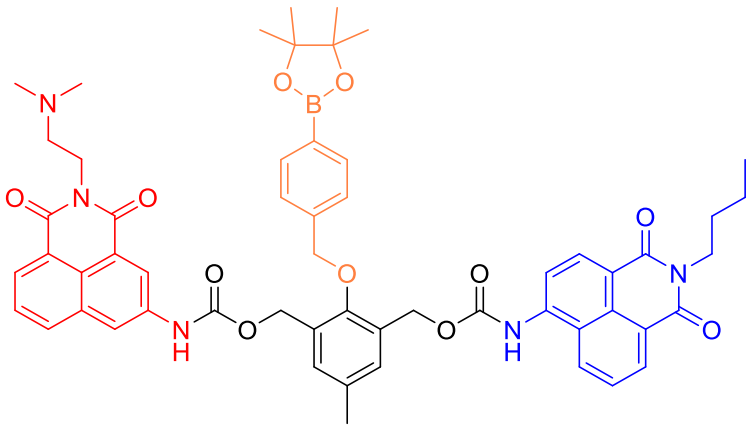

2.4

Figure 2.7: Structure of compound **2.4**. Phenylboronic ester (orange), naphthalimide (blue) and amonafide (red)

The synthetic pathways to reach the proposed target structures are shown in **figures 2.8** and **2.9**. The primary goal was to first synthesise an hydroxymethyl derivative of the central core, via ether linkage to the ROS responsive trigger, and then react with the carbamoyl chloride derivatives of the naphthalimides forming a carbamate linkage. These carbamoyl chlorides can be accessed by reaction of the aromatic amines with triphosgene. In **Figure 2.8**, the aim is to react the core with an excess of the carbamoyl chloride derivative of the fluorophore with the aim of obtaining two fluorophores on each side of the dendrimer. This will allow for the proof of concept to be investigated fluorometrically.

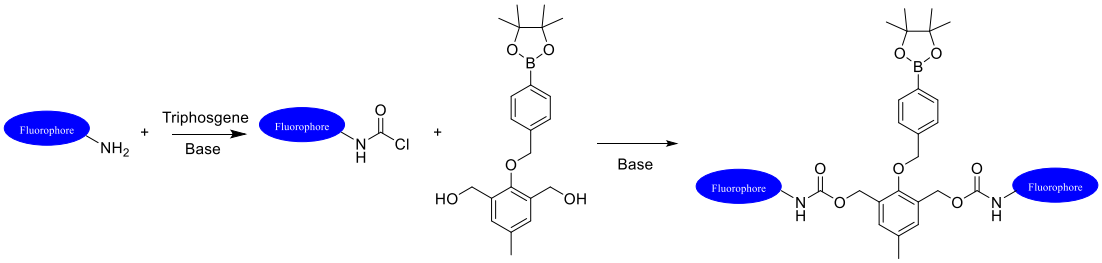

Figure 2. 8: Proposed synthetic pathway of compound **2.3**

In **Figure 2.9** on the other hand, it would be required that firstly an intermediate of amonafide would be conjugated to the core, with one hydroxyl arm remaining free. Following this, the fluorophore could be reacted with this intermediate giving the target compound.

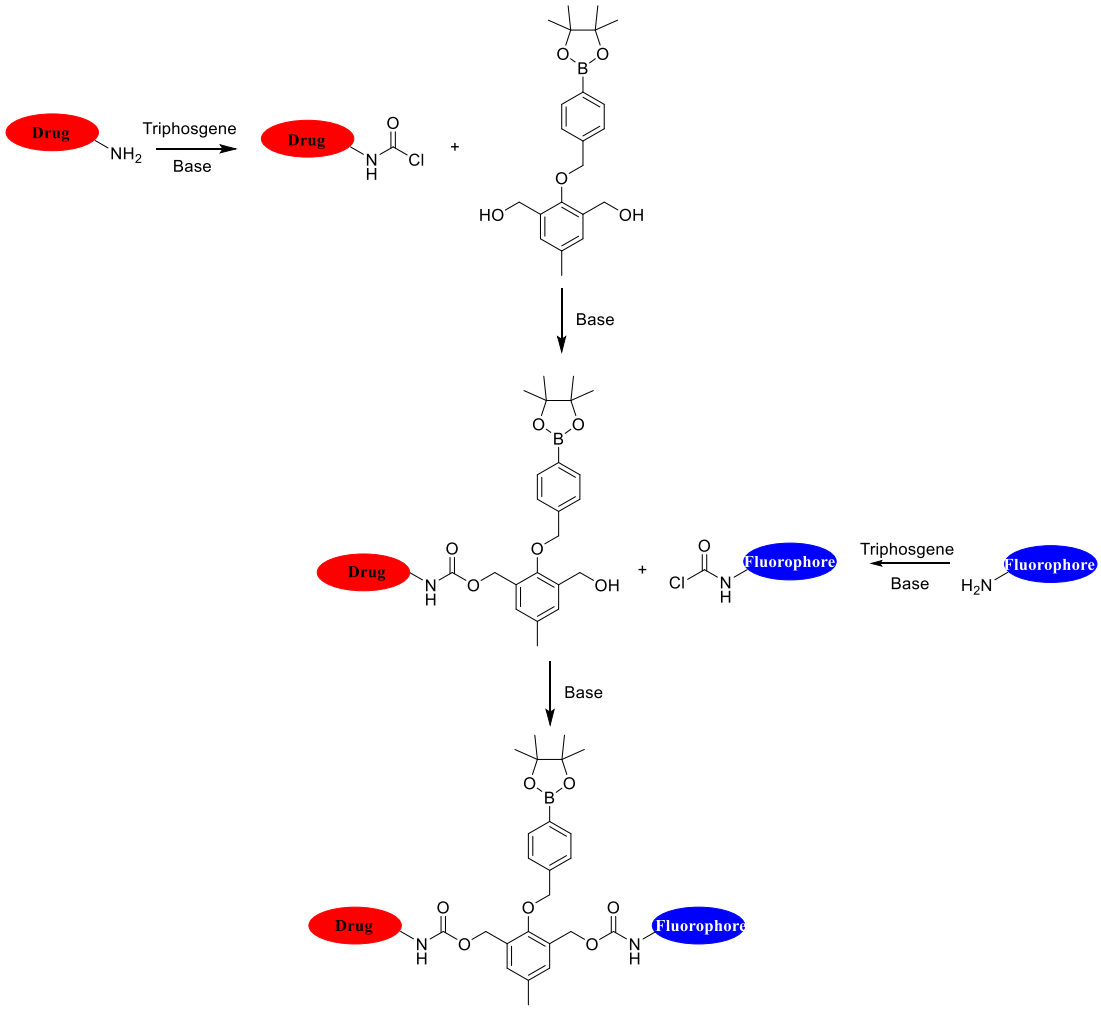

Figure 2.9: Proposed synthetic pathway of compound **2.4**

2.3 Synthesis and Characterisation of 2.3 and 2.4

2.3.1 Synthesis of **2.5**, **2.6**, **2.7**.

Before synthesising **2.3** and **2.4,** the syntheses of **2.5, 2.6** and **2.7** were required for the proposed synthesis to be completed successfully. **2.5** was synthesised via silyl ether protection of the hydroxyl groups, shown in **Figure 2.1** below. This was achieved by reacting 2,6-bis-hydroxymethyl-p-cresol with *tert*-butyldimethylsilyl chloride in the presence of imidazole. Compound **2.1** was obtained in an 75% yield following column purification.

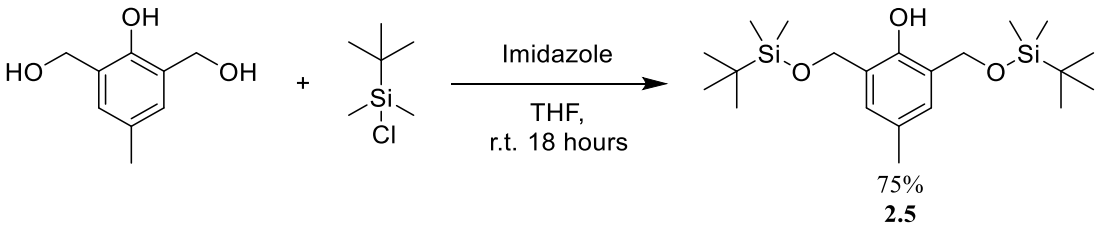

Scheme 2.1: Synthesis of compound **2.5**

As seen from the below ^{1}H NMR in **Figure 2.10,** the key characteristic peaks of **2.5** are the two peaks in the aliphatic region. The singlets at 0.12 and 0.94 ppm being the protons of the dimethyl groups and the *tert*-butyl groups of the silyl ether respectively, with the former integrating for 12H and the latter 18H. This double integration value, along with the presence of the singlet at 4.82 ppm, integrating for 4H, confirms the protection of both hydroxyl groups. The singlet peak at 8.02 ppm, integrating for 1H, shows the presence of the phenol OH.

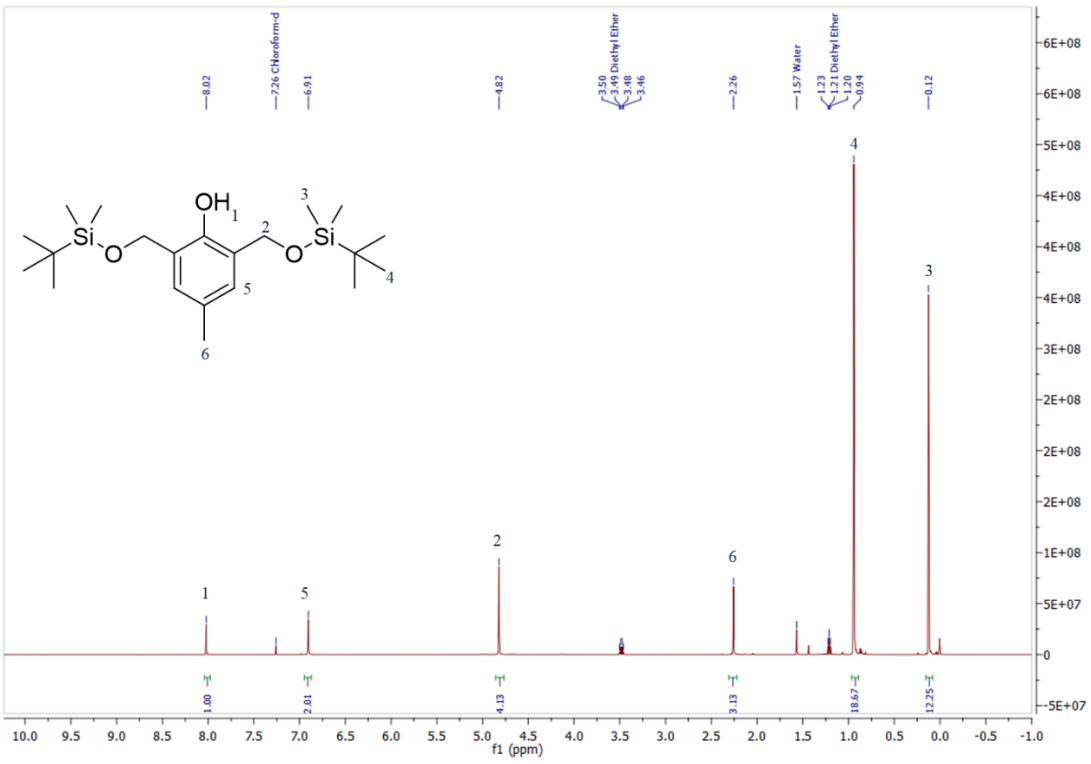

Figure 2.10: ^{1}H NMR of **2.5** in $CDCl_3$.

2.6 was synthesised via Williamson ether synthesis, as shown in **Scheme 2.2**. This involved the reaction of **2.5** and 2-(4-(bromomethyl)penyl)-4,4,5,5-tertamethyl-1,3,2-dioxaborolane in the presence of potassium carbonate as the base to yield the target compound in a 71% yield after column chromatography

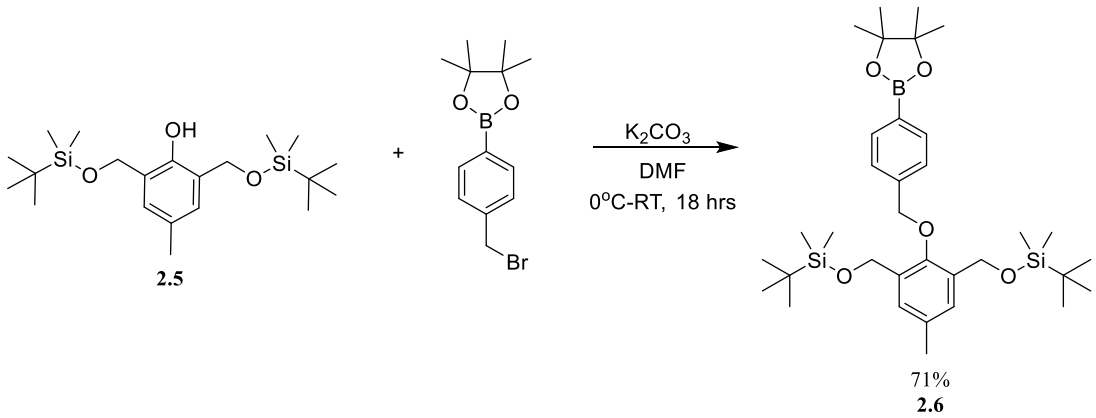

Scheme 2.2: Synthesis of **2.6**

Figure 2.11 below shows the ^{1}H NMR spectra of **2.6**. From this figure, the two sets of doublets at 7.85-7.83 and 7.43-7.42 ppm are characteristic of the two sets of aromatic protons of the phenyl ring of the arylboronic ester. This is further indicated by the appearance of the peak at 1.36 ppm, integrating for 12H, corresponding to the methylene protons of the boronic ester. Finally, the peak at 4.89 ppm, integrating for two, indicates successful ether linkage. Also, it is noted the disappearance of the singlet peak at 8.08 ppm, indicating functionalisation of the phenol.

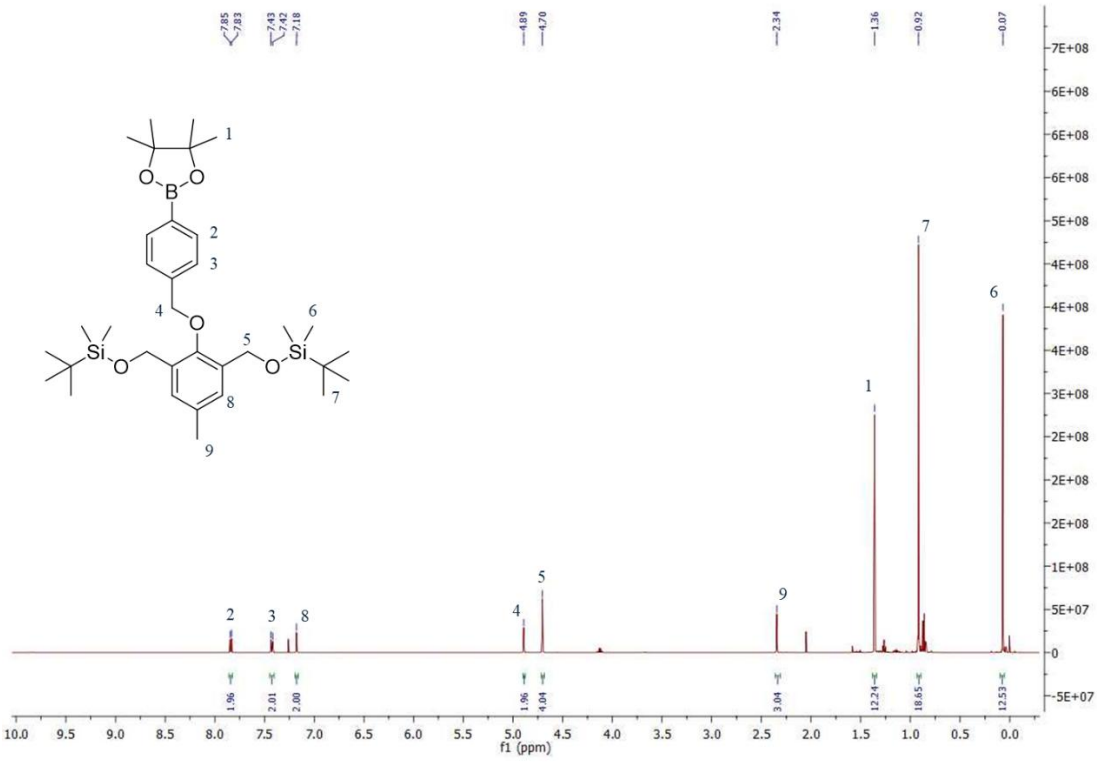

Figure 2.11: ^{1}H NMR of **2.6** in $CDCl_3$.

The synthesis of **2.7** is depicted below in **Scheme 2.3**. Silyl ether deprotection was achieved by stirring **2.6** in MeOH with a catalytic amount of p-toluenesulfonic acid to yield the deprotected product in a 66% yield.

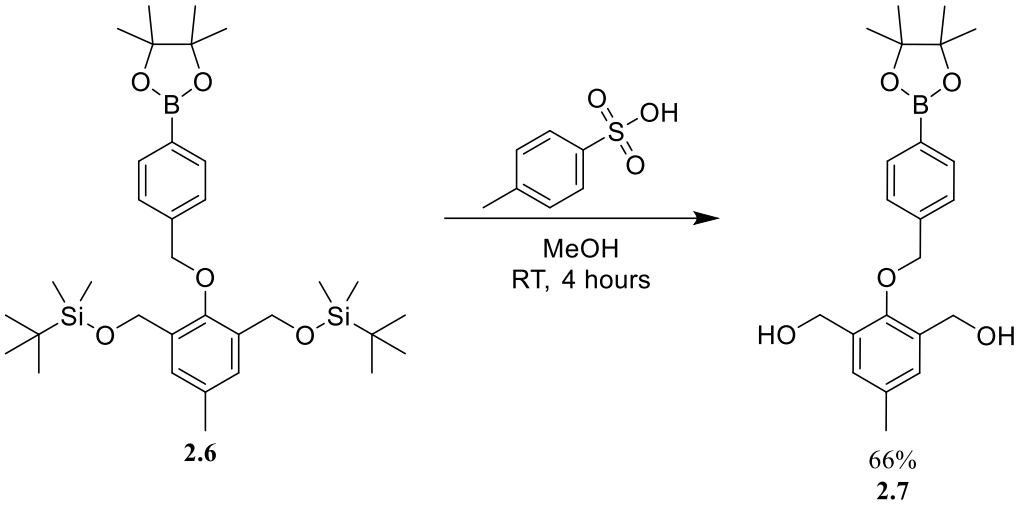

2.6 **2.7**

Scheme 2.3: Synthesis of **2.7.**

Figure 2.12 shows the ^{1}H NMR spectrum with the key evidence being the disappearance of the signals corresponding to the silyl ether groups at approx. 0.25 and 0.92 ppm. There is also restoration of the hydroxy OH protons at 1.92 ppm.

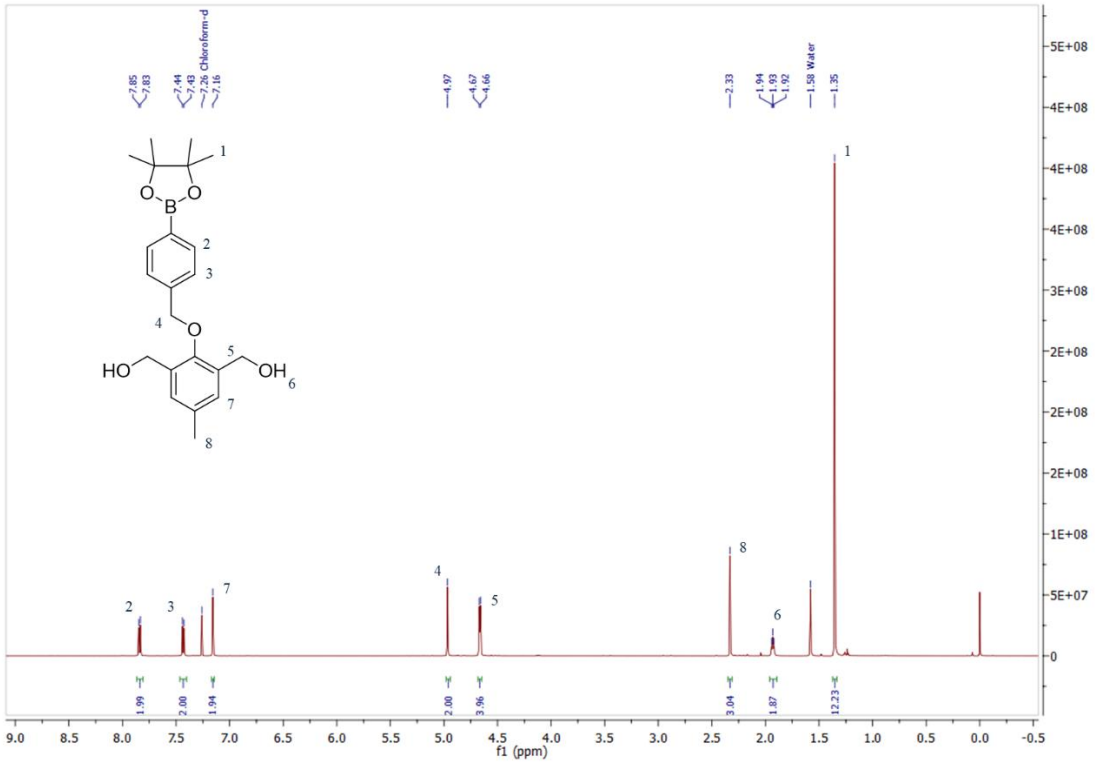

Figure 2.12: ^{1}H NMR of compound **2.7** in $CDCl_3$

2.3.2 Synthesis of **2.8**, **2.9**

With the above central scaffold in hand, it was next required to synthesise both the fluorophore and the chemotherapeutic agent. Compound **2.8** was synthesised via **Scheme 2.4**. Firstly, condensation of n-butylamine with 4-nitro-1,8-naphthalic anhydride gave **2.10** in 75% yield. Reduction of **2.10** in the presence of catalytic amounts of Pd/C and H_2 gave the amino derivative **2.8** in 93% yield.

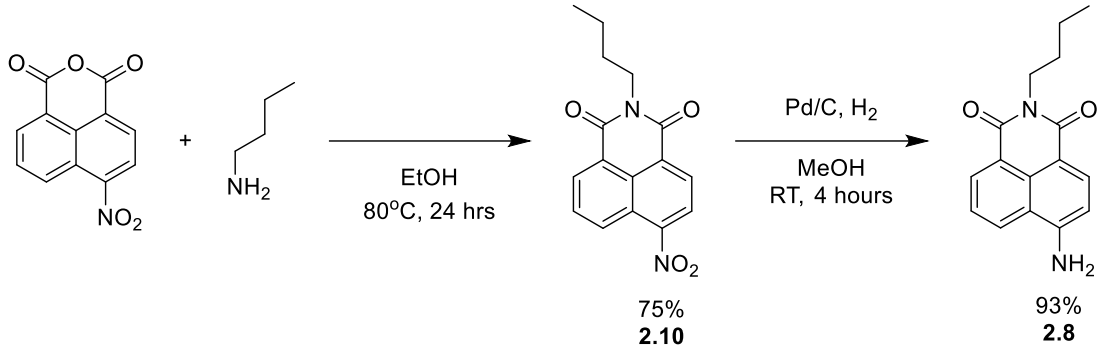

Scheme 2.4: Synthesis of **2.8**

Observing the ^{1}H NMR below, the characteristic NH_2 protons of **2.8** are seen as a singlet at 4.94 ppm. Also seen are the two doublets each integrating for 1H at 8.42 and 6.88 ppm, corresponding to the protons in the 2 and 3 position of the naphthalimide moiety. The butyl protons are also observed at 4.16, 1.71, 1.43 and 0.97 ppm, all showing the correct integration and splitting patterns.

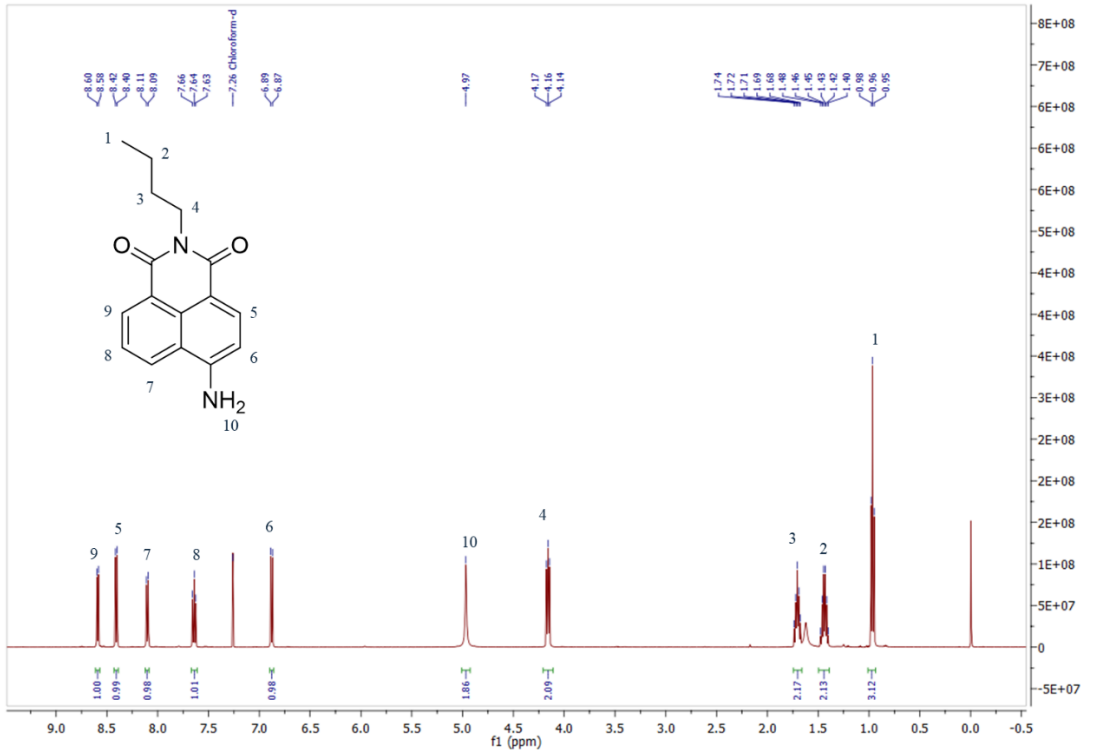

Figure 2.13: ^{1}H NMR of **2.8** in $CDCl_3$.

Compound **2.9** was synthesised as outlined in Scheme **2.5**, using a synthetic route analogous to that of compound **2.8**. N,N-dimethylethylenediamine was condensed with 3-nitro-1,8-naphthalic anhydride to give **2.11** in a 78% yield. Following condensation, **2.11** was reduced in the presence of catalytic amounts of Pd/C and H_2 gave amonafide, **2.9,** in 91% yield.

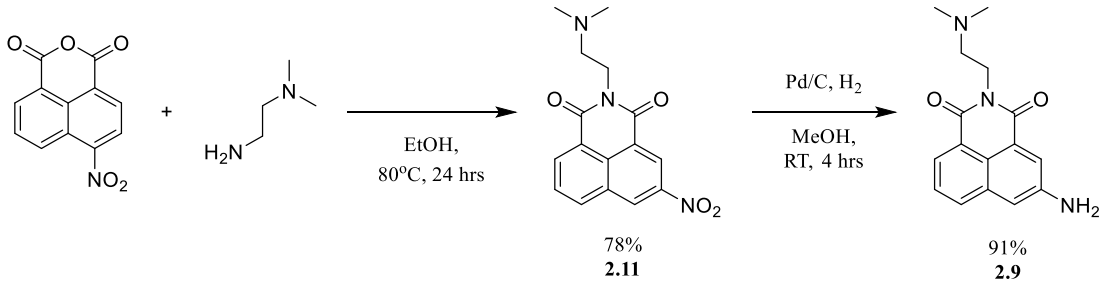

Scheme 2.5: Synthesis of **2.9**

Figure 2.14 shows the ^{13}C NMR of **2.9.** the signature carbonyls of the naphthalimide moiety can be seen at 164.7 and 164.4 ppm, as well as the carbons of the dimethyl amino moiety at 45.91 ppm. In the ^{1}H NMR, (see **Fig S2.20**), characteristic signals are seen at 4.85 ppm integrating for 2H which is corresponding to the NH_2 group in the 3-position of the naphthalimide. Also seen are the two singlets at 8.01 and 7.29 ppm,

both integrating for 1H, and correspond to the protons in the 2- and 4- position of the naphthalimide moiety respectively. Finally, the singlet at 2.35 ppm integrating for 6H is indicative of the protons of the dimethylamino group.

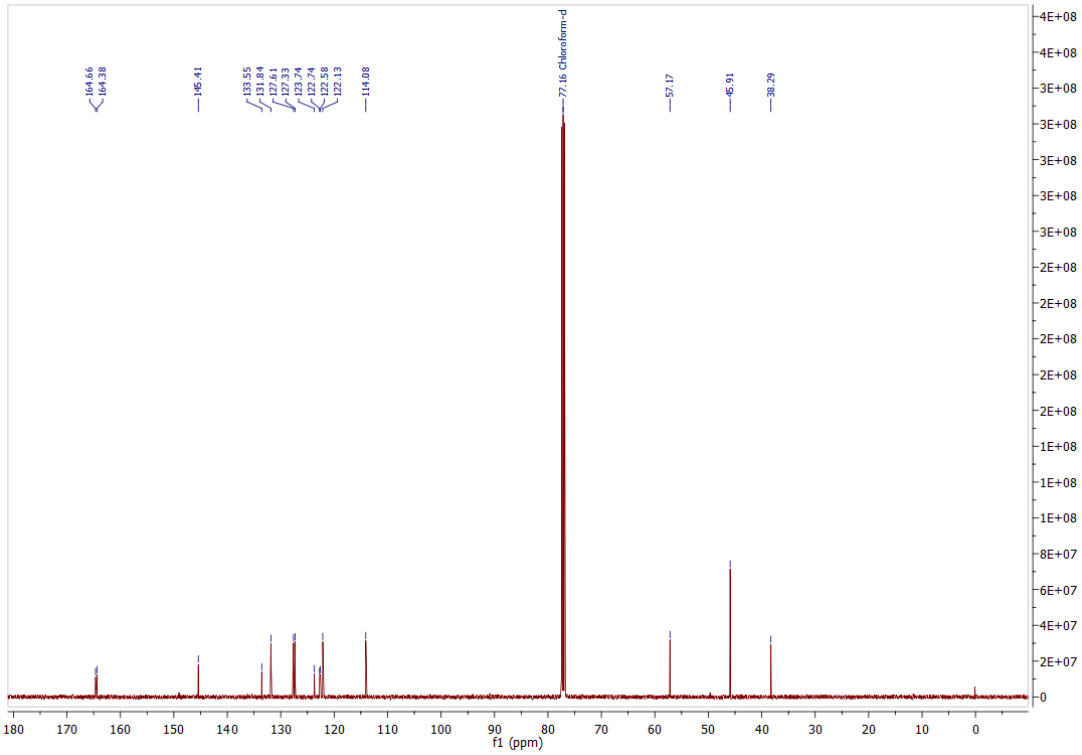

Figure 2.14: ^{13}C NMR of **2.9** in $CDCl_3$.

2.3.3 Synthesis of **2.3.**

The synthesis of **2.3** proceeded as shown in **Scheme 2.6.** Firstly, **2.7** was reacted with triphosgene in the presence of TEA as the base. This reaction led to the formation of the highly reactive carbamoyl chloride intermediate **2.12**. This was reaction was carried out in a one-pot fashion, with **2.7** being added to the reaction mixture, ensuring that **2.12** remained in excess (approx. 3:1 **2.12** to **2.7**) to promote carbamate formation at both hydroxymethyl sites. Purification of **2.3** was carried out by precipitation from ethyl acetate, followed by washing of the precipitate with cold methanol, removing any **2.8** remaining in the crude mixture, and giving **2.3** in a 73% yield.

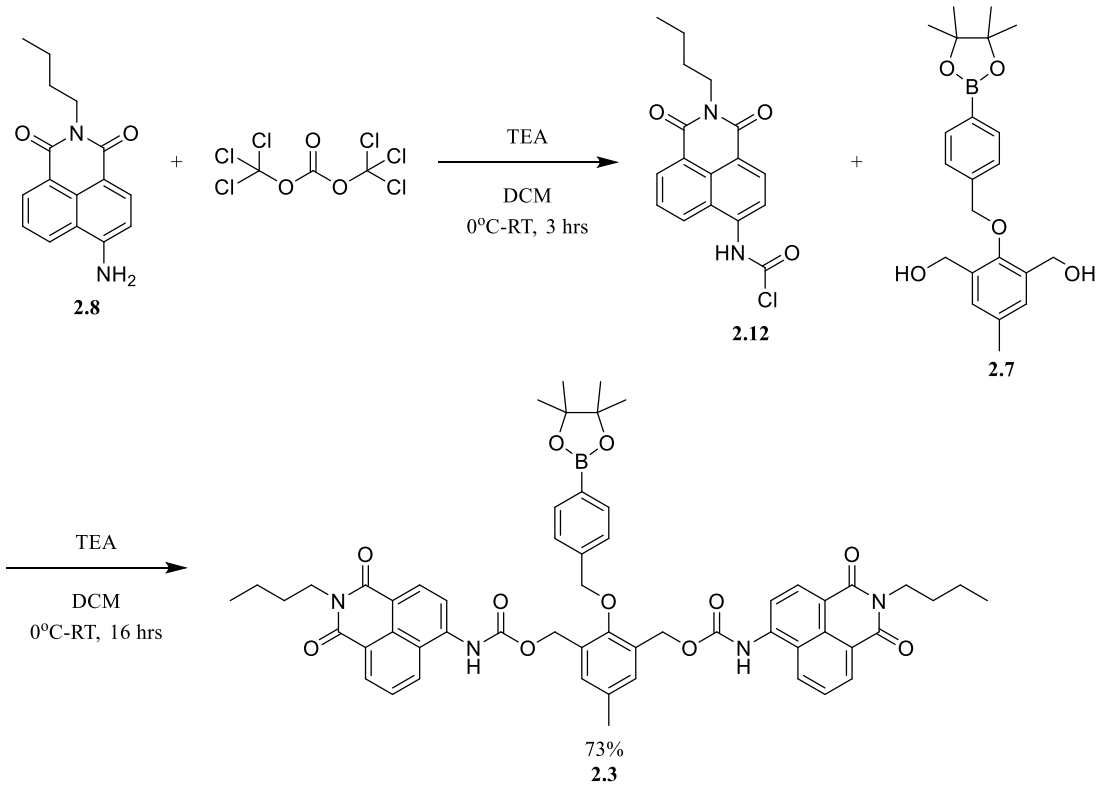

Scheme 2.6: Synthesis of **2.3.**

As seen in **Figure 2.15**, there is strong evidence confirming the formation of **2.3.** The singlet peak at 7.50 ppm integrating for 2H, corresponds to the two NH protons of the carbamate bond formed between the aromatic NH_2 of the naphthalimide moiety and the hydroxymethyl groups of **2.3.** Furthermore, the singlet at 5.34 ppm, integrating for 4H corresponds to the methylene protons adjacent to the carbamate bonds, and the integration value shows the desired di-substitution of **2.18** to the core due to the centre of symmetry of compound **2.3**. Finally, further confirmation is observed through the n-butyl protons of the fluorophore at 4.15, 1.70, 1.43 and 0.96 ppm, which all integrate for double the number of protons expected from one substituent, certifying di-substitution has occurred.

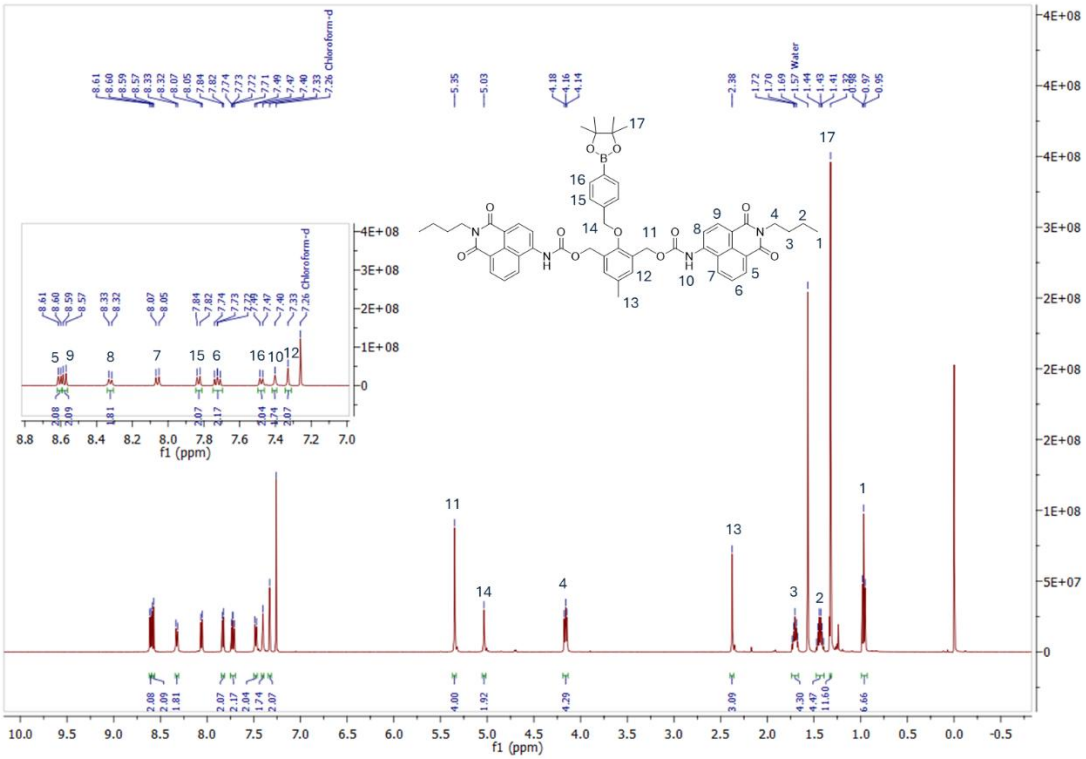

Figure 2.15: ^{1}H NMR of **2.3** in $CDCl_3$. **(inset)** zoom of aromatic region.

Formation of **2.3** was also confirmed using HRMS, where **Figure 2.16** below shows ionisation at 995.1010, corresponding to $[M + Na]^+$ of **2.3**. Unfortunately, because of the lipophilicity of the compound, an LCMS trace was not possible, due to the compound not eluting under the given LC operational parameters. Nevertheless, NMR analysis confirms the high degree of purity of **2.3.**

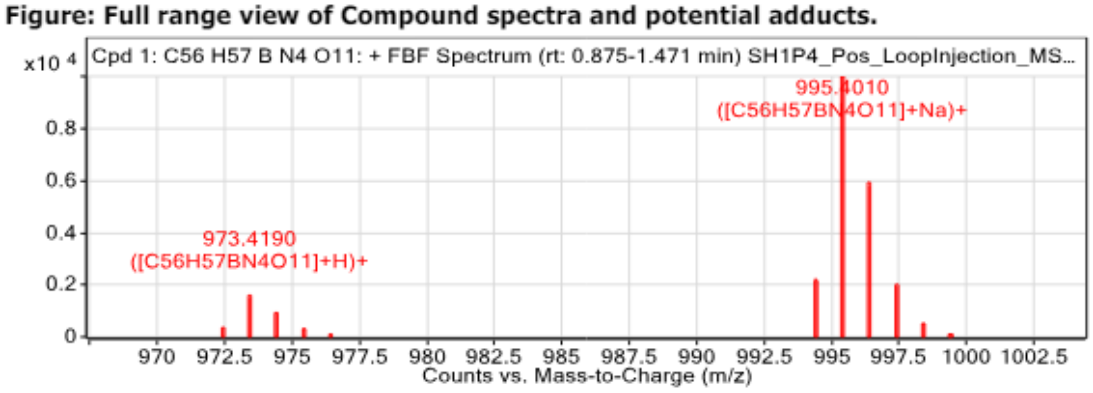

Figure 2.16: HRMS of **2.3.**

2.3.4 Synthesis of **2.4**

As compound **2.4** required two different cargo units appended to the core of the dendrimer, initially it was hoped that orthogonal protecting groups would remove the

issue of having to rely on mono-substitution of the cresol core. To this end, synthesis of a selectively protected derivative was carried out, utilising TIPS and allyl ether as the protecting groups. However, efforts to remove the allyl group using sodium borohydride led to the degradation of the compound, by way of removal of the boronic ester so ultimately this strategy was abandoned. This forced an alternative synthetic pathway which would involve mono-substitution of **2.9** to **2.7.** To this end, compound **2.13** was required as an intermediate. **2.13** was comprised of **2.9** carbamate linked to one of the hydroxymethyl arms of **2.7.** The synthesis of **2.13** was carried out as outlined in **Scheme 2.7** shown below. This reaction is closely related to that for **2.3**, however it differs in the equivalents of the starting materials used. To favour mono-functionalisation, **2.7** was used in a slight excess with respect (approx. 1.1 eq.) to **2.14** and the order of addition was changed. Instead of a one-pot reaction, **2.14** was added dropwise to a stirring solution of **2.7**, which was cooled to 0°C. This led to formation of the mono-substituted **2.13** in an isolated 25% yield after column chromatography. This low yield was presumed to be due to the formation of side products such as the double O-alkylated derivative, and the possible formation of a bis-urea derivative of **2,9**.

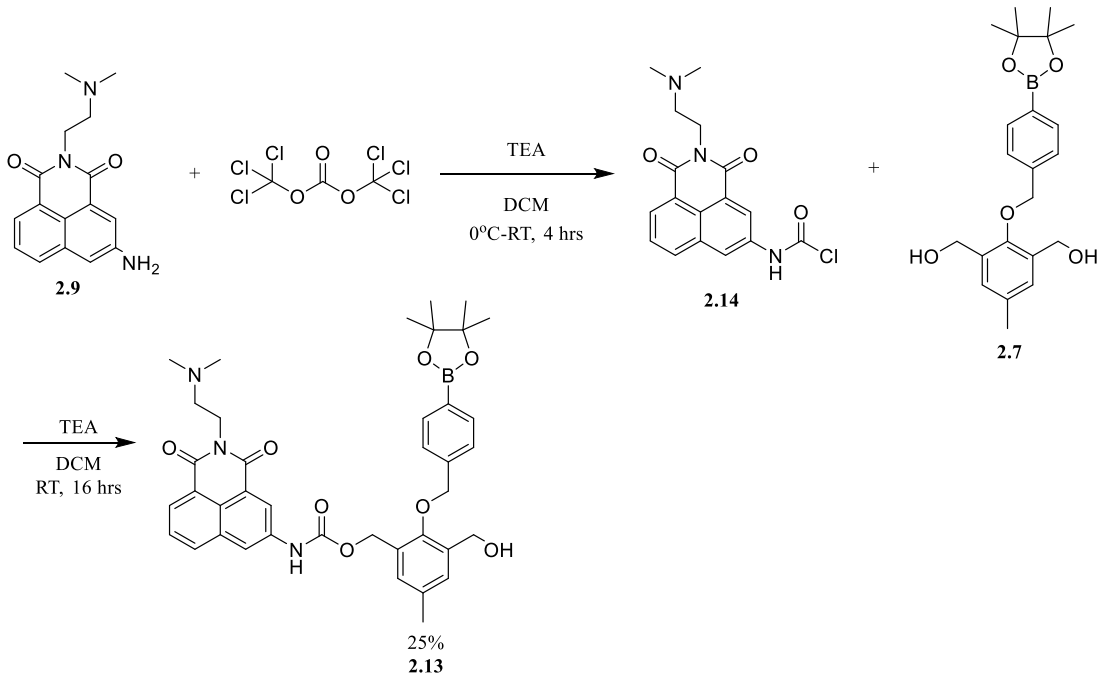

Scheme 2.7: Synthesis of **2.13**

Figure 2.17 shows the ^{1}H NMR spectrum of **2.13.** From this spectrum, the splitting of the two CH_2 signals of the central cresol unit can be observed at 5.30ppm and

4.96ppm, with both signals integrating for 2H, with the former correlating to the CH_2 adjacent to the carbamate linker. This splitting is indicative of mono-substitution of the amonafide moiety and resulting in the desymmetrisation of the compound. Further confirmation is the disappearance of the NH_2 signal seen in compound **2.9** (**Figure S2.20**) as it is converted to a carbamate NH, which was not observed on the ^{1}H NMR of **2.13.**

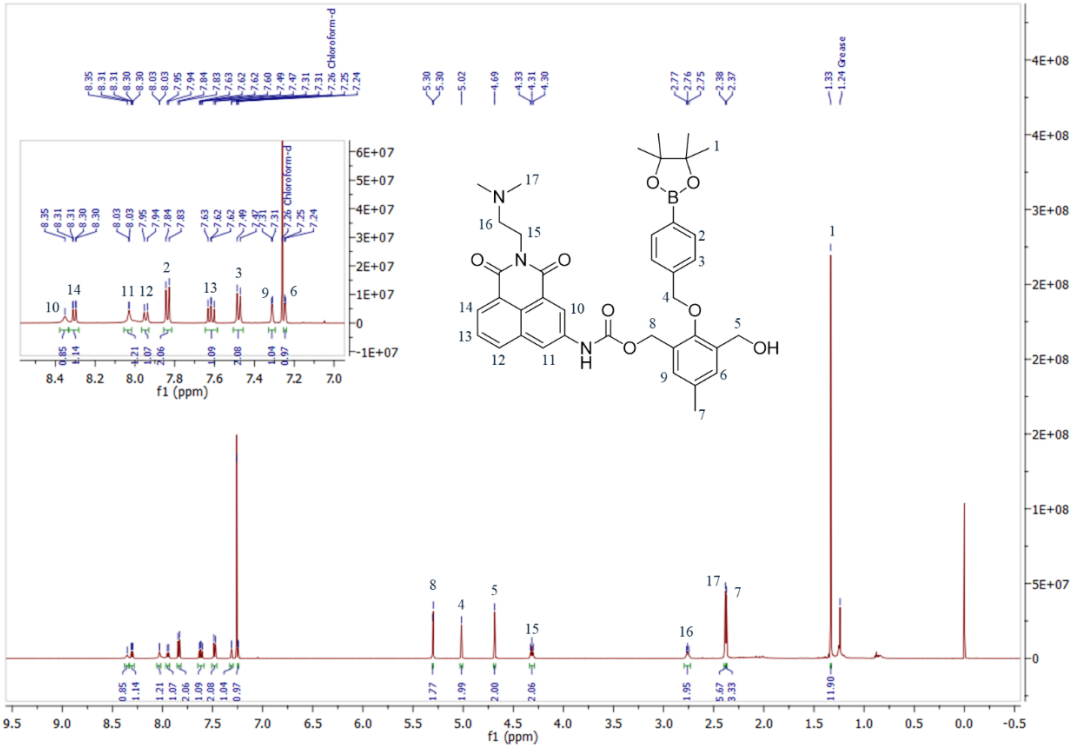

Figure 2.17: ^{1}H NMR of **2.13** in $CDCl_3$. **(inset)** zoom of aromatic region.

Formation of **2.13** was also confirmed using LCMS analysis, shown below in **Figure 2.18.** Under the mobile phase conditions used to carry out LC-MS analysis of **2.13,** which includes 1% formic acid in water, two peaks are observed on the UV chromatogram. The peak with retention time at approx 29 minutes with ionisation corresponding to that of $[M+H]^+$ of **2.13** at 694 is of the boronic ester derivative of **2.13**. However, under acidic aquous conditions, boronic esters have a propensity to undergo hydrolysis, converting to the diboronic acid.[171] This phenomenom was observed on the UV trace, with the appearance of a second peak, with retention time of approx 26 minutes, showing ionisation mass of 612, corresponding to $[M+H]^+$ of the diboronic acid derivative of **2.13**. Additional proof of compound formation **2.13**

was also achieved via HRMS with observed ionisation at 694.33, which corresponds to $[M+H]^+$ for compound **2.13.**

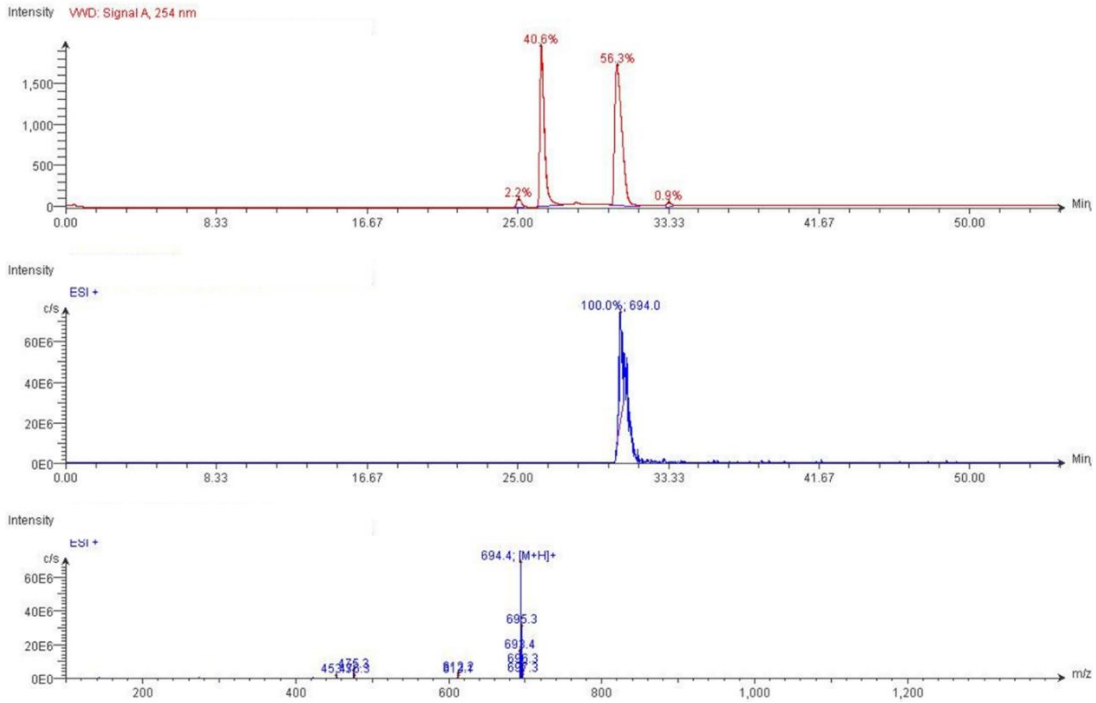

Figure 2.18: LCMS of **2.13.**

Compound **2.4** was then prepared according to **Scheme 2.8**. Compound **2.8** was reacted with triphosgene and TEA to form **2.12**, the carbamoyl chloride derivative of the fluorophore, which was subsequently reacted with **2.13** in a 2:1 excess, in a one pot reaction to result in **2.4**, and was then purified using column chromatography to give a final yield of 49%.

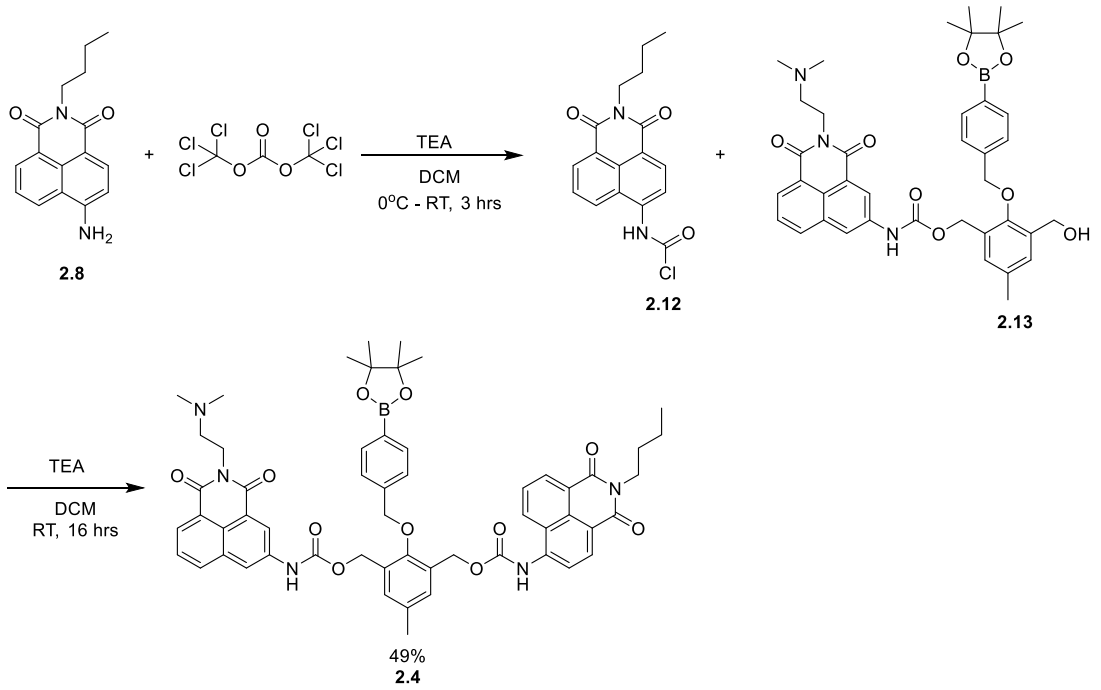

Scheme 2.8: synthesis of **2.4**.

2.4 was fully characterised using ^{1}H NMR, ^{13}C NMR, IR and HRMS. ^{1}H-^{1}H COSY, HSQC and HMBC were used to assign ^{1}H NMR peaks. The ^{1}H NMR spectrum is shown below in **Figure 2.19.** Similarly to **2.13**, following the chemical shifts of the CH_2 protons on the cresol core, we can now see two peaks integrating for 2 protons at 5.34ppm and 5.33ppm. This is strongly indicative that we have functionalised **2.12** to the core via a carbamate. The almost identical chemical shifts of the CH_2 are to be expected as both are adjacent to the carbamate bonds of the naphthalimide moieties. It is also observed in the aromatic region the singlets of the amonafide moiety at 8.52 and 8.21 ppm. Interestingly however, is the apparent broadening of the peaks correlating to the amonafide portion of the compound. This is most noticeable at peaks at the head of the dimethylamino moiety, at 2.72 and 2.39ppm. For the purpose of characterising the singlet at 2.39 ppm, HSQC analysis was used and confirmed that the peak corresponded to two signals, the 6 protons of the dimethylamino groups, and the methyl group in the 4-position of the central benzyl core.

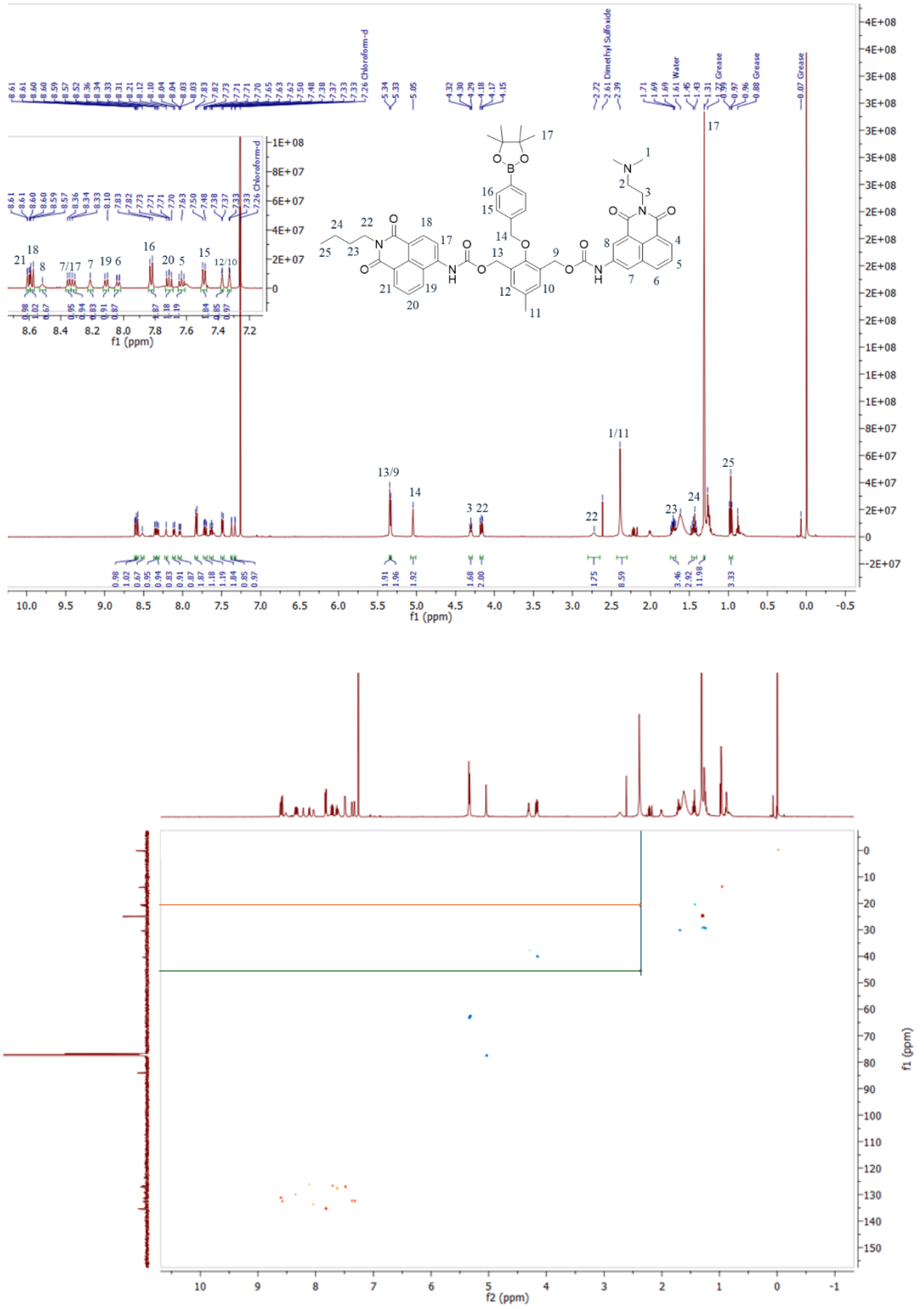

Figure 2.19: ^{1}H NMR **(top)** and HSQC **(bottom)** of **2.4** in $CDCl_3$. **Top inset**: zoom of aromatic region. (lines on HSQC show peak at 2.39 ppm coupling to two carbon signals).

Further confirmation of the formation of **2.4** was also achieved via HRMS, where **figure 2.20** below showing ionisation at 988.33, which corresponds to $[M+H]^+$ for compound **2.4.**

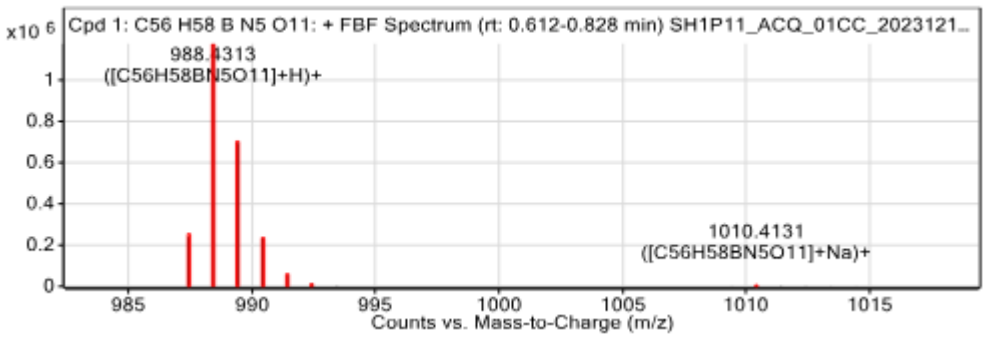

Figure 2.20: HRMS of **2.4**

It is also worth noting the LC-MS trace of **2.4,** shown in **Figure 2.21,** which shows the same hydrolysis pattern seen with **2.13.** The observed hydrolysis may also be attributed to the use of DMSO as the sample diluent, as residual water in DMSO could promote hydrolytic degradation. The observed masses of 988 and 906 correspond to $[M + H]^+$ of both **2.4** and its corresponding boronic acid respectively, confirming this degredation. This was similarly reflected in the NMR spectra of compound **2.4**, where the use of DMSO-d_6 as the solvent resulted in the appearance of multiple additional peaks, likely corresponding to degradation products. In contrast, spectra acquired in $CDCl_3$, which contains substantially less water, showed significantly cleaner profiles. Nonetheless, using this LC-MS analysis in conjunction with ^1H NMR spectra in chloroform and HRMS, it can be confirmed **2.4** was synthesised to a high degree of purity.

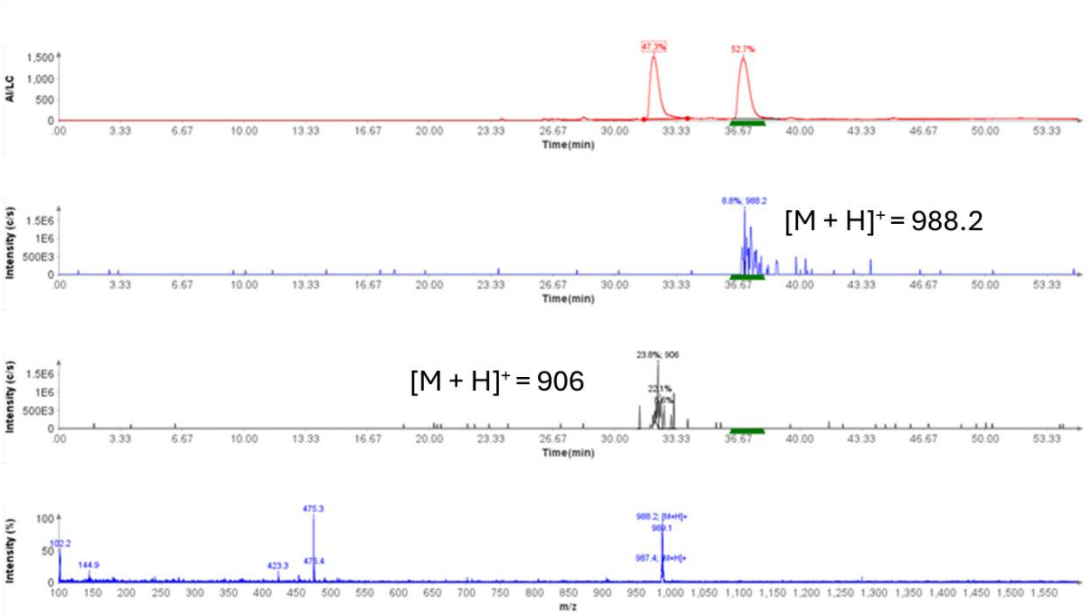

Figure 2.21: LC-MS trace of **2.4,** showing hydrolysis of compound.

2.4 Spectroscopic Response of 2.3 and 2.4 to Peroxide

With compounds **2.3** and **2.4** in hand, we next wished to evaluate the spectroscopic response of both compounds upon exposure to ROS using both UV/Vis and fluorescence spectroscopy. Hydrogen peroxide (H_2O_2) was used as a model for the ROS induced via CAP owing to it being one of the most abundant and long lived ROS induced by CAP,[172] and also its oxidation reaction with boronic esters is well established,[173] with the mechanism shown in **Figure 1.10**. Due to the relative quantaties of **2.3** available it was decided that it would be used to carry out the initial studies and these parametres would then be used to guide similar experiments using **2.4.** Firstly the changes in the UV/Vis spectrum of compound **2.3** were investigated upon addition of H_2O_2, where, as seen in **Figure 2.22**, this resulted in a decrease in the absorbance of the parent compound at 375 nm. However this was anticipated to be matched with a subsequnt increase in absorbance at 440 nm, which would be emblamatic of release of **2.8**. Instead, there was no significant increase in absorbance at this wavelength, which brought into question the solvent system used. Due to the inclusion of n-butyl moieties at the head of the naphthalmide fluorophore, it was postulated that upon release from the dendritic core, the fluorophore was precipitating from solution due to hydrophobicity, thus affecting its absorbance. Importantly, this was not believed to be affecting the mechanism of action, as the decrease in

absorbance of the parent compound still suggested that some form of self-immolation was occuring.

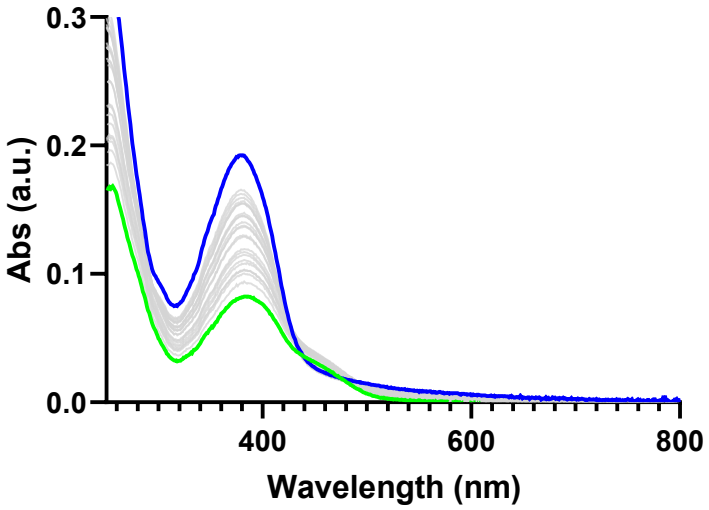

Figure 2.22: The UV/Vis spectra of **2.3** (10μM) following treatment with 1 mM H_2O_2 in PBS pH 7.4 over the course of 24 hours.

In order to investigate this, DMSO was added to the solvent system and at 50% DMSO concentration, there is a clear increase in absorbance at 440 nm, thus giving validation to the claim that a highly aqueous enviroment is compromising the spectroscopic studies due to the poor solubility of **2.8** under these conditions.

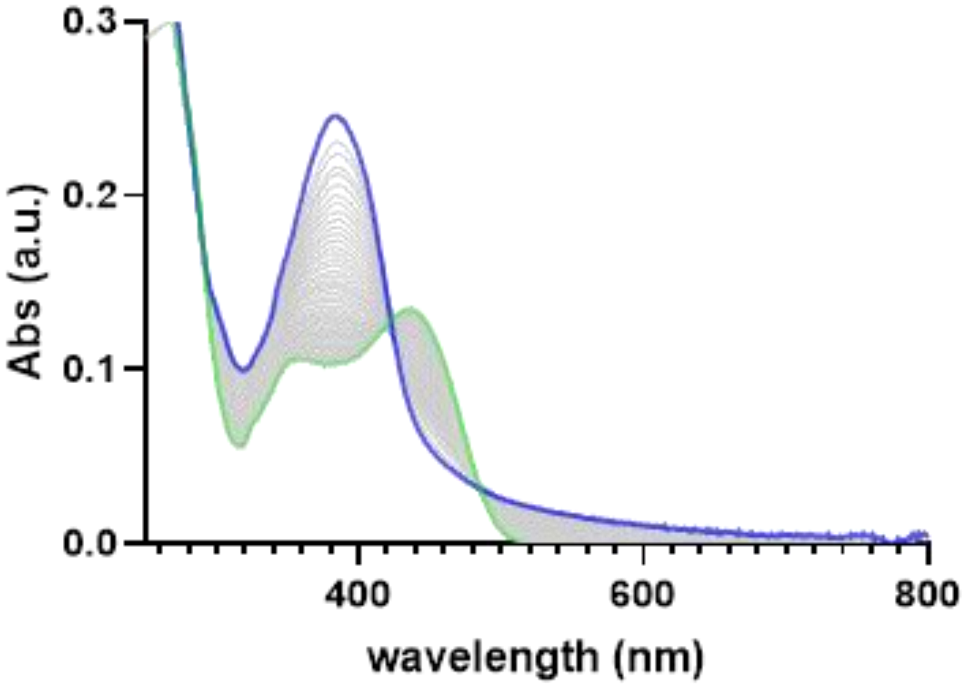

Figure 2.23: The UV/Vis spectra of **2.3** (10 μM) following treatment with 1 mM H_2O_2 in PBS:DMSO (50:50) over the course of 24 hours.

Using the isosbestic point of 420 nm as the excitation wavelength, **2.3** displayed an emission maximum at 489 nm. Upon addition of 1 mM peroxide (100 eq.), emission at 489 nm was diminished significantly after 24 hours, with a new emission maximum present at 535 nm: indicative of free naphthalimide release. This emission continued to increase beyond 24 hours. To investigate further, the experiments were extended to 72 hours. The results showed a plateau in intensity around the 60-hour mark, consistent with literature reports indicating that immolation can take up to 72 hours due to the slow hydrolysis of the benzyl ether.[174] The ratiometric fluorescence signal had also displayed a 5.1-fold increase in emission output. As with the UV/Vis experiments, a concentration of 50% DMSO was required, where the fluorescence output of the naphthalimide in aqueous solution was quenched. Fluorescence experiments in PBS buffer displayed a similar decrease in fluorescence emission at 489 nm, but this was met with a much smaller increase in output at 535 nm, due to this quenching effect, as well as the aforementioned solubility issues.

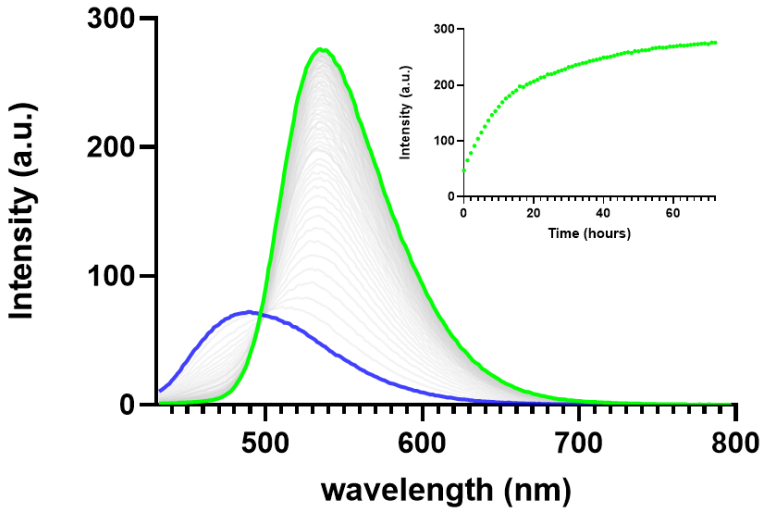

Figure 2.24: Fluorescence spectrum of **2.3** (10μM) following the addition of H_2O_2 (1 mM) in 50% DMSO in PBS over the course of 72 hours. λ_{exc} = 420 nm. **(inset)** changes in fluorescence intensity at 535 nm as a function of time.

As it was postulated that without the initial hydrolysis of the boronic ester to the corresponding phenol via peroxide coordination, the immolation process would not occur and would not lead to an increase in emission at 535 nm. it was necessary to investigate the role of this ROS oxidation. To this end, a solution of 100 μM H_2O_2 in DMSO:PBS (50%) was pretreated with 4 mM N-acetyl cysteine (NAC), a known ROS scavenger,[175] for 6 hours. Following incubation, **2.3** (10 μM) was added and the reaction was further incubated for 18 hours. As seen in **Figure 2.25**, the NAC pretreated sample showed minimal increase in emission at 535 nm following 18 hours incubation, comparing favourably to a solution of **2.3** with no H_2O_2 present. This is in stark contrast to a solution containing H_2O_2, which displayed an approx. 3.9-fold increase in emission at 535 nm.

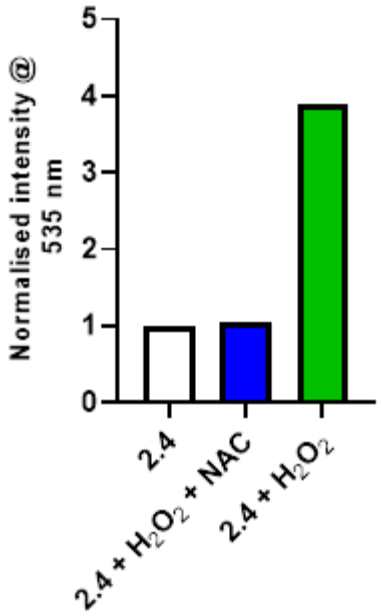

Figure 2.25: Inhibition of the fluorescence response of **2.3** to H_2O_2 via N-acetyl cysteine. **2.3** concentration was 10μM and H_2O_2 concentration was 100 μM in all cases. Reaction time was 18 hours and λ_{exc} was 420 nm.

Finally, in order to probe the sensitivity of **2.3** towards ROS and evaluate it efficacy as a ROS responsive probe, a limit of detection (LOD) analysis was carried out, whereby a calibration curve was generated showing the relative intensity of fluorescence output for **2.3** (10 μM) at λ_{max} = 535 nm, at known concentrations of peroxide (1 – 100 μM) following incubation for 24 hours. Using the formula LOD = 3.33(σ/K), where σ is the standard deviation of the blank measurement, and K is the slope of the line between fluorescence intensity and peroxide concentration, the LOD was calculated to be 0.58 μM. This LOD value is slightly higher compared with other reported LOD values for ROS-responsive boronic esters reported in the literature.[176] It is also important to note that the R^2-value is above the 0.990 threshold,[177] so this result can be extrapolated to a good degree of confidence.

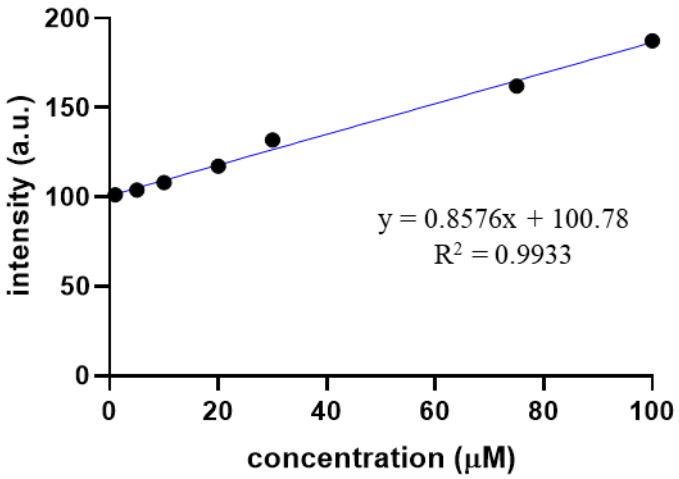

Figure 2.26: Calibration curve of fluorescence intensity of **2.3** (λ_{max} = 535) at known conc. of H_2O_2 (1 – 100 μM). Reaction was incubated for 24 hours.

With the above information in hand, it was next investigated whether **2.4** would display similar results upon exposure to peroxide. Under analogous conditions, the changes in the UV/Vis spectrum of **2.4** matched closely the behaviour seen for **2.3**, with a decrease in the parent compound absorption at 375 nm, and a subsequent increase at 440 nm.

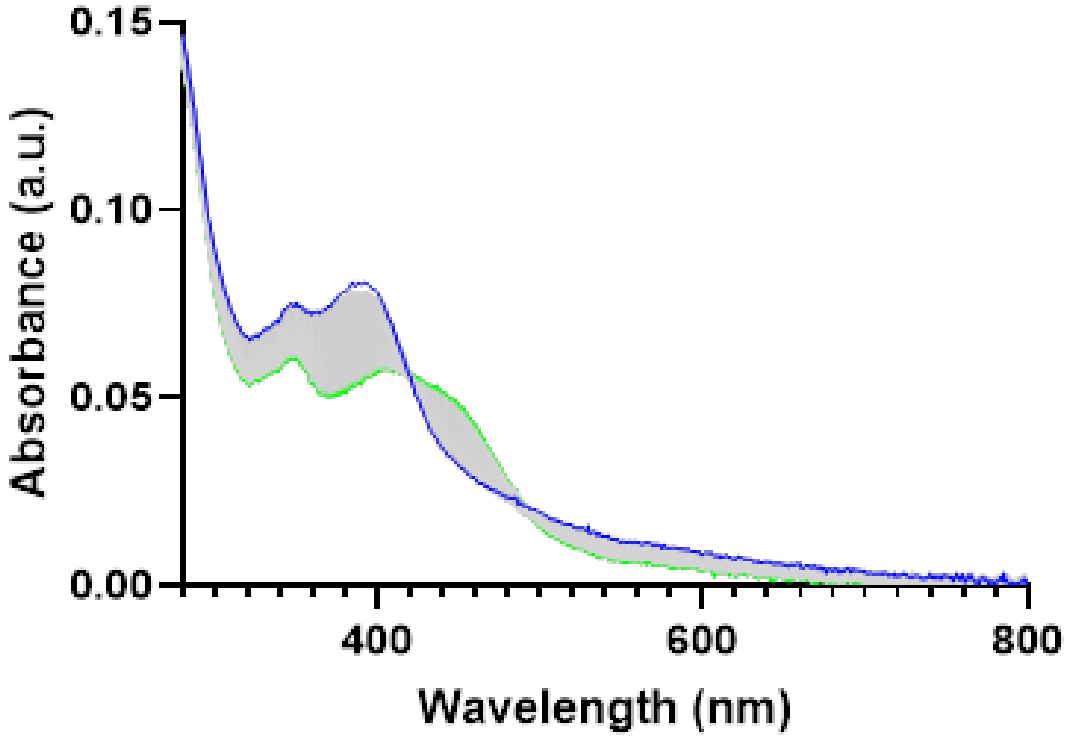

Figure 2.27: The UV/Vis spectra of **2.4** (5 μM) following treatment with 1 mM H_2O_2 in PBS:DMSO (50:50) over the course of 24 hours.

Similarly, the fluorescence emission response was investigated and, in this case, had a much smaller red shift in emission when excited at 420 nm of only 9 nm. As previously noted, the fluorescence characteristics of naphthalimides are highly solvent dependant, with aqueous environments leading to red shifts in emission. It has been reported than 3-substituted naphthalimides are more greatly red-shifted than their 4-substituted counterparts.[58] It is therefore plausible that the inclusion of the amonafide (**2.9**) moiety may have an impact on the emission maxima observed in **2.4**. Possible FRET interactions between both naphthalimide moieties also cannot be discounted. Despite this, a clear increase in emission at 535 nm was observed, with a 3.3-fold increase in fluorescence intensity. It should also be noted that although **2.9** displays an emission maximum at 595 nm which would result in a much larger red shift in emission, its intensity relative to **2.8** is substantially less. This reduced intensity is likely due to the poor ICT efficiency of 3-amino-naphthalimides, which typically exhibit significantly lower quantum yields than their 4 amino counterparts.[178]

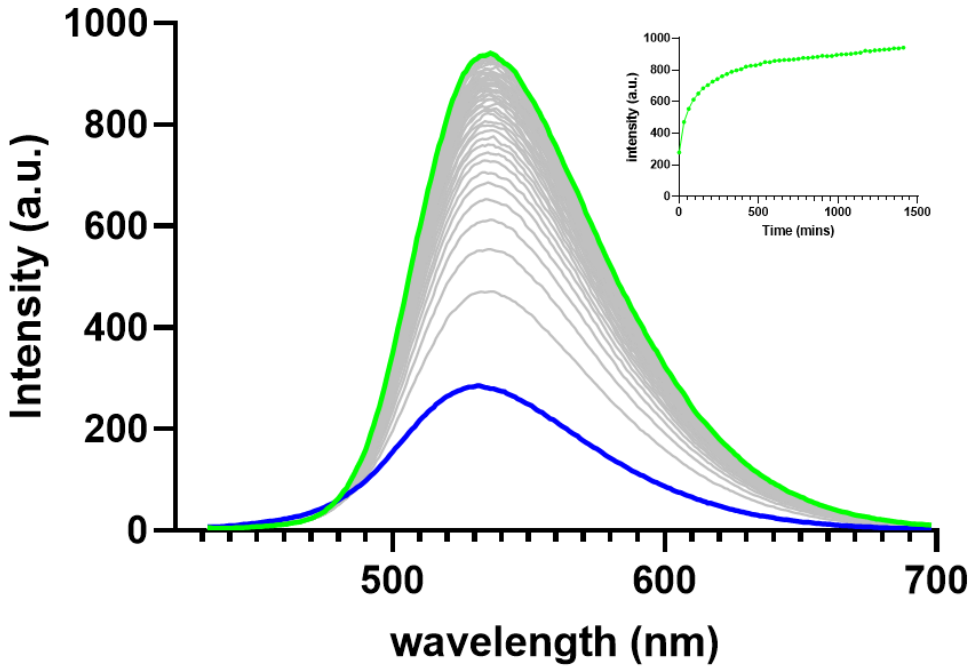

Figure 2.28: Fluorescence spectrum of **2.4** (10μM) following the addition of H_2O_2 (1 mM) in 50% DMSO in PBS over the course of 24 hours. λ_{exc} = 420 nm. **(inset)** changes in fluorescence intensity at 535 nm as a function of time.

2.5 LC-MS study of 2.4 towards peroxide

The above changes in both UV/Vis and fluorescence behaviour of both dendrimers were strong evidence that the conversion of the boronic ester to the corresponding phenol, via coordination of the peroxide anion, followed by self-immolation was releasing compounds **2.8** and **2.9.** To further confirm this hypothesis, an LC-MS analysis was conducted, where changes in mass and retention time in the UV trace at 254 nm were tracked to show release of both cargo units. In this study, a reaction of **2.4** (2.5 mM) and H_2O_2 (25 mM) was prepared in DMSO/PBS (80/20). As can be seen in **Figure 2.29**, the parent compound has a retention time of approximately 37 minutes. Following peroxide addition, there was the appearance of two peaks; one at 23.58 minutes, which is in agreement with LCMS analysis of free **2.9**, and shows ionisation for 239, which corresponds to that of $[M + H]^+$ of **2.9**, and the other at 36.17 minutes shows ionisation for 269, again, matching that of free **2.8** and corresponds to that of $[M + H]^+$ of **2.8**. Importantly, there was no evidence of the peak for **2.4**, indicating that it had fully reacted with the peroxide present and completely fragmented. The large

cluster of peaks at approximately 27 minutes may correspond to numerous degradation products, with no discernible masses found.

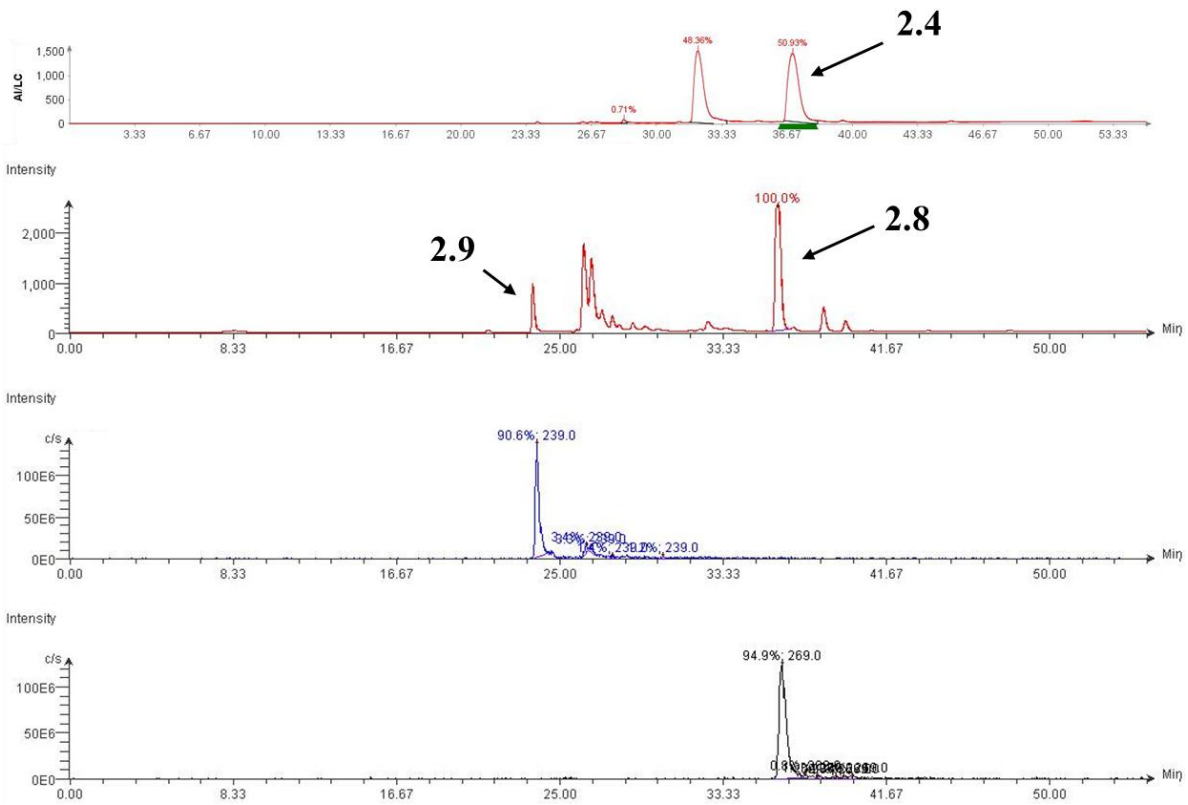

Figure 2.29: TIC trace of **2.4** after 18-hour treatment with H_2O_2 (10 eq.). a) Compound **2.4**, b) trace following peroxide treatment, c) ESI+ trace for peak at 36.17 mins, d) ESI+ trace for peak at 23.58 mins

The above LCMS study confirms that upon reaction with H_2O_2, compound **2.4** undergoes a self-immolation mechanism, releasing both **2.8** and **2.9**. This result then allowed for subsequent cytotoxic evaluations to be undertaken.

2.6 Cytotoxicity Analysis of 2.4

To validate the ability of **2.4** to act as a CAP-activated theranostic, cell viability assays were carried on the U-251 MG cell line derived from human glioblastoma cells by Dr. Janith Wanigasekara of the Curtin group in Technological University Dublin, Ireland. Cells were plated in 96-well plates and treated with **2.4** at various concentrations in the culture medium. Cells were then exposed to 20 seconds of CAP treatment and incubated for 24 hours. 20 seconds of CAP treatment was chosen as the treatment duration due to CAP's ability to induce cytotoxicity in a dose-dependent manner. 20 seconds of treatment would allow for induction of ROS into the cell but not to the

extent that CAP treatment itself is inducing a killing effect on the cells, with the LC_{50} for a single CAP treatment reported to be 164s for U-251 MG 2D cells.[179] This would ensure that any cytotoxicity measured would be as a result of prodrug activation. Cytotoxicity was determined using the Almar Blue Cell Viability Reagent. Fluorescence was measured using the Varioskan Lux multi-plate reader and results were described as cell viability percentage. As shown in **Figure 2.30** below, 20 seconds of CAP treatment did not cause a significant increase in cytotoxicity, with only marginal increases even at high concentrations of **2.4**.

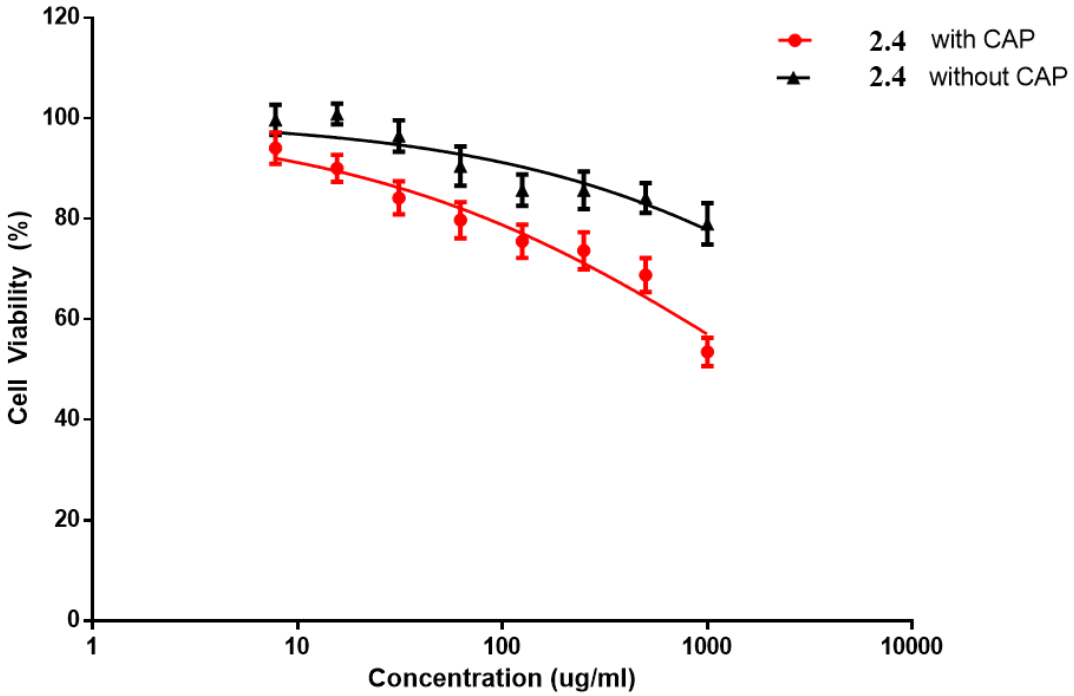

Figure 2.30: Cell viability of U-251 cells upon treatment with **2.4,** followed by 20 seconds of CAP treatment and 24 hours incubation

This result brought into question whether the lack of cytotoxicity demonstrated was a result of incubation time, as 24 hours may not have been long enough to allow for complete immolation and subsequent drug release, or a ROS concentration dependency. To examine the latter, cells pretreated with **2.4** were exposed to three repetitions of 20s CAP exposure. This extended treatment allowed for a higher concentration of ROS to be generated within the cells, while remaining well below the tolerated threshold. After treatment, the cells were again incubated for 24 hours. As seen in **Figure 2.31**, this resulted in a substantial increase in the cytotoxicity observed, with a moderate LC_{50} of 84 µM after multiple CAP treatments. To further examine

whether this cytotoxicity was as a result of amonafide release or CAP-mediated cytotoxicity analogous experiments were carried out with **2.3**, which was expected to not show a similar cytotoxic ability due to the design lacking the amonafide moiety. Indeed, multiple CAP treatments of cells pretreated with **2.3** showed much greater cell viability than those treated with **2.4**. (See **Appendix**)

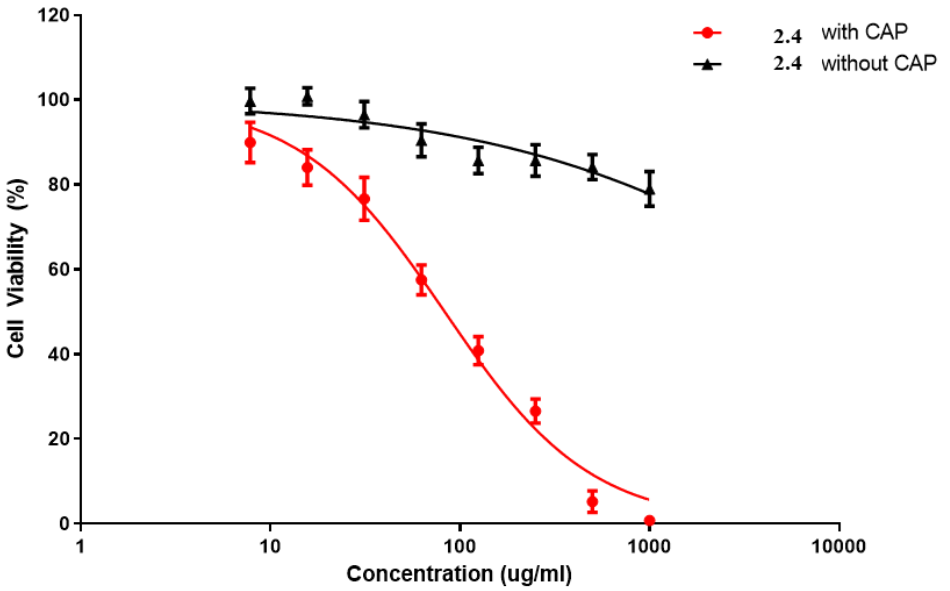

Figure 2.31: Cell viability of U-251 cells upon treatment with **2.4,** followed by 20 seconds of CAP treatment (x3) and 24 hours incubation

It should also be noted that single 20s CAP treatments left to incubate for 96 hours also showed a marginal increase in cytotoxicity compared to 24 hours incubation, so it's plausible that a greater incubation time coupled with increased CAP treatment times would have an even more drastic effect on cytotoxicity. Nevertheless, the cytotoxicity results clearly showed a 'turn on' of cytotoxicity as a function of CAP treatment, indicating the successful release of **2.9**.

2.7 Confocal Microscopy of 2.3 and 2.4

Finally, to observe the ratiometric change in fluorescence following CAP treatment, confocal imaging was carried out by Dr. Abhik Mallick in RSCI, Dublin. Both **2.3** and **2.4** were added to U-251 MG cells, treated with 20s of CAP and allowed to incubate for 24 hours. As can be seen in **Figure 2.32** below, prior to CAP treatment, the merged image of the blue and green channels showed predominately blue fluorescence output

as anticipated. CAP treated cells however clearly display more intense green fluorescence, likely due to the CAP initiated immolation of **2.3,** releasing **2.8**

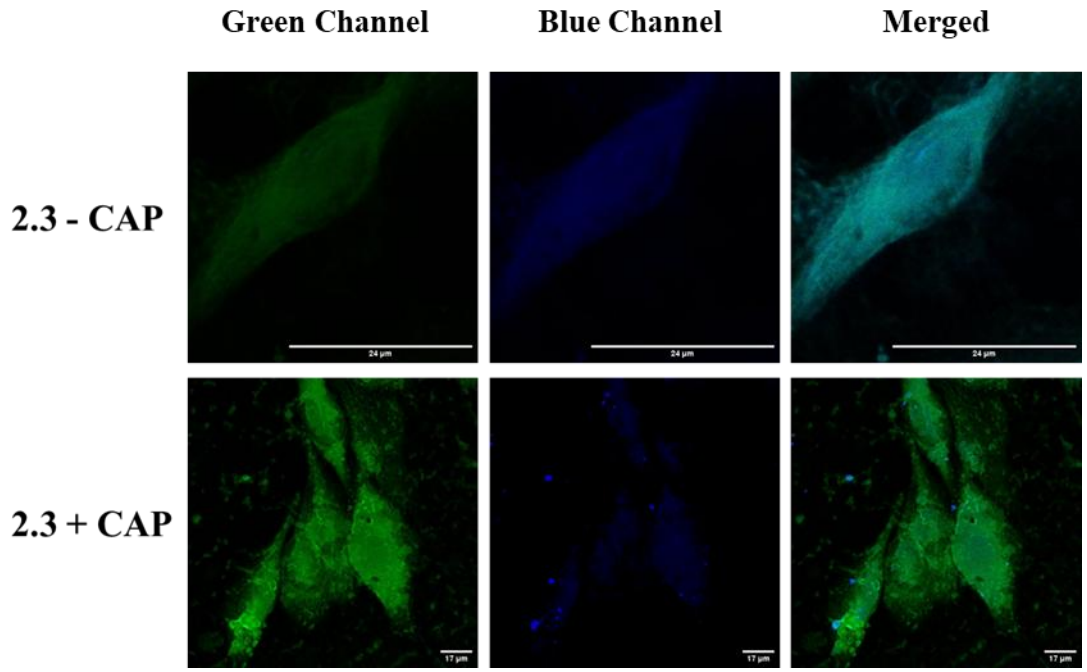

Figure 2.32: Confocal microscope images of U-251 MG GBM cells pretreated with **2.3** before and after CAP treatment. The images on the left show the fluorescence output through the green filter. The images in the middle show fluorescence through the blue filter. The images on the left show the merged images

A similar result was seen for **2.4**, with the absence of CAP treatment resulting in predominantly blue fluorescence output, which contrasted with the CAP exposed cells, which displayed strong green fluorescence. In order to quantify the change in emission, the ratio of relative intensities from both channels was measured. CAP treated cells displayed a 7:1 ratio of green:blue (512:421 nm) intensity following CAP treatment (**Figure 2.33**(b)). While the below ratiometric change in fluorescence is much more pronounced than in the spectroscopic studies shown previously, it may be caused by the naphthalimide fluorophores entering hydrophobic pockets within the cells, behaviour which has been demonstrated with other naphthalimide derivatives in cancer cell lines.[180] This may have the effect of reducing the red-shift caused by the highly aqueous environment demonstrated in **Figure 2.28**, and lead to a much more dramatic ratiometric change in fluorescence *in vitro*.

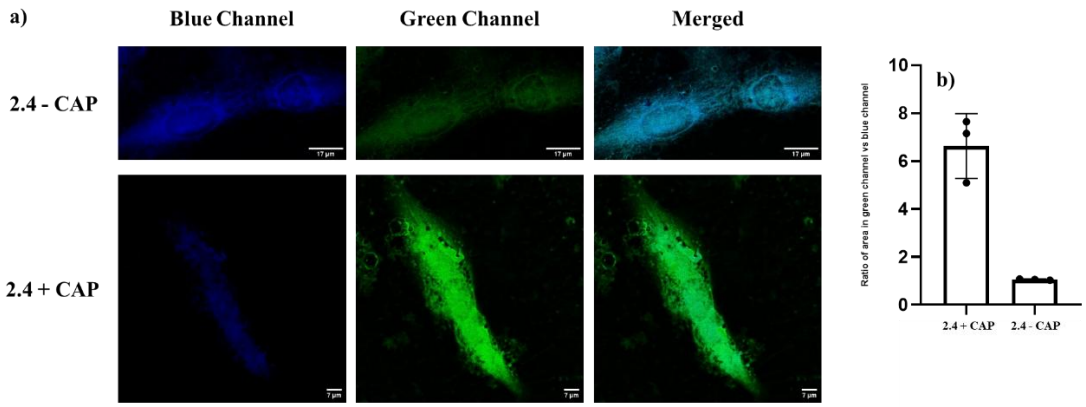

Figure 2.33: a) Confocal microscope images of U-251 MG GBM cells pretreated with **2.4** before and after CAP treatment. b) ratio of intensity in green vs blue channels before and after CAP

2.8 Conclusions and Future Work

In conclusion, two novel ROS-responsive self immolative dendrimers **2.3** and **2.4** were synthesised. These compounds were both achieved through a common intermediate scaffold utilising an aryl-boronic ester as the ROS-responsive triggering group. This was then followed by carbamate linkages of two instances of the fluorescent reporter in the case of **2.3**, and carbamate linkages between the core and a chemotherapeutic and a fluorescent reporter in the case of **2.4**.

The anticipated ratiometric changes in spectroscopic characteristics were observed for both **2.3** and **2.4**, with the expected increase in absorbance at 440 nm exhibited for both compounds upon peroxide exposure suggesting release of **2.8** in both cases. This was matched with a fluorescence wavelength modulation with a red shift in emission to 535 nm also in both cases. These results were then coupled with an LCMS study of the release of both compounds **2.8** and **2.9**, confirming that the self-immolation of **2.4** proceeds as expected.

The CAP studies added further validation to the potential of **2.4** as a CAP-activated theranostic. Cells treated with **2.4** and subjected to multiple CAP treatments exhibited a pronounced increase in cytotoxicity attributed to the release of **2.9**, whereas cells not exposed to CAP showed no cytotoxic effects. This provides compelling evidence that CAP-generated reactive oxygen species directly activates **2.4**, triggering the release of the cytotoxic agent and thereby mediating the observed cell death with a moderate LC_{50} of 84 μM calculated for **2.4** following multiple CAP treatments. Furthermore, confocal microscopy experiments showed a clear ratiometric change in fluorescence from blue to green upon treatment with CAP. Both of these results provide clear evidence that CAP treatment can be used to active a latent theranostic and may provide an exciting new therapy against cancer.

With regards future work, since the immolation of the compound is proposed to rely on the oxidation of the boronic ester to initiate the process, it would be valuable to synthesize a control compound in which an unsubstituted benzyl group is ether-linked to the scaffold. Exposing this control to various oxidative and biologically relevant species would not only reinforce the critical role of reactive oxygen species - and thus CAP - in the activation mechanism but also serve to validate the overall stability of the molecule, particularly the carbamate linkages.

Due to clear solubility issues demonstrated by the fluorophore used, efforts could be made to help increase the solubility of **2.7** upon release from the central core. This can be done by modulation of the head of the naphthalimides, by incorporating a PEG-like chain instead of the simple alkyl chain used in this chapter, a strategy that has been previously demonstrated to enhance the solubility of naphthalimides.[181] Furthermore, the fluorescent characteristics of the fluorophore could also be modulated by changing the substituent at the 4-position of the naphthalimide (**Figure 2.35**). Changing the amino group in the 4-position to a styrene moiety for example, would red-shift the fluorescence of both the bound and free fluorophore, with the free derivative emitting red light, making it more attractive from an imaging perspective. This could be easily incorporated into the design shown in this chapter, by carbamate linkage to the core using the same synthetic pathway as described in this chapter.

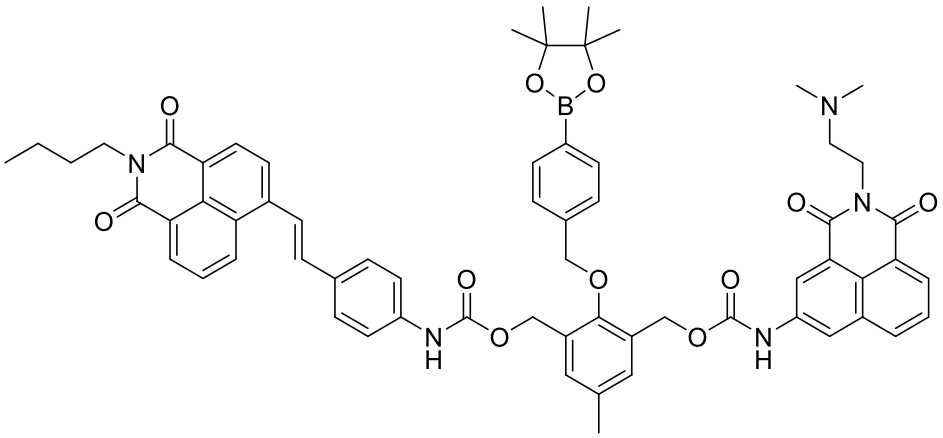

Figure 2.35: Possible modulation to **2.4** to allow for red emission upon immolation.

Chapter 3

Ring-expansion as a Strategy Towards Responsive Anion Binders

3. Ring-expansion as a Strategy Towards Responsive Anion Binders

3.1 Introduction

In recent decades, squaramides have begun to be employed in macrocyclic receptor design. Hydrogen bond macrocycles consist of a cyclic array of hydrogen bond doners in a specific geometry to create a pocket for the anionic guest. These macrocyclic receptors contain numerous key features which make then highly effective for anion recognition, premium of which is the preorganised conformation which minimise the entropic cost of binding.[182] The control over the binding cavity size also is advantageous as it allows for the receptor to be tailored to the desired anion, increasing sensitivity and selectivity.[183] Some of the earliest examples of squaramide based macrocyclic receptors was carried out by Jolliffe *et al.* where they synthesised a series of macrocycles (**3.1** and **3.2**) comprised of alternating squaramide and benzylic groups.[184] Both compounds demonstrated a 1:1 binding fit and showed strong binding affinity towards SO_4^{2-}, with $K_a > 10^4\ M^{-1}$ in DMSO-d_6 (0.5% water) in both instances, while additionally **3.2** showed a similar affinity towards $H_2PO_4^-$ ($K_a > 10^4\ M^{-1}$) and AcO^- ($K_a = 7530\ M^{-1}$) (**Figure 3.1**).

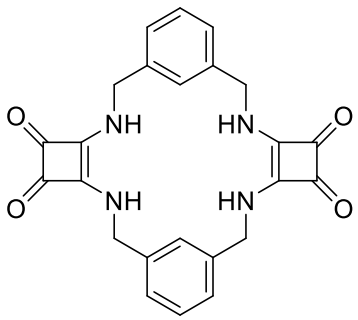

3.1

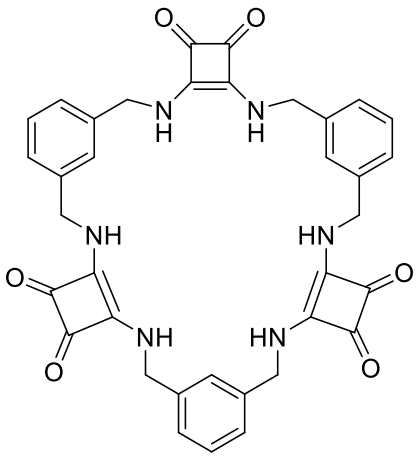

3.2

Figure 3.1: Structures of compounds **3.1 and 3.2**

Building on this work, Romanski *et al.* developed a fluorescent sensor with selectivity towards SO_4^{2-} based on a macrocyclic squaramide core, appended to which was a benzo-18-crown-6 and a naphthalene fluorophore (**Figure 3.2**).[185] This compound,

3.3, showed a change in fluorescent output upon addition of TBA sulphate, with a bathochromic shift in the absorbance maximum from 291 nm to 296 nm. Consequently, this led to an increase in emission intensity and an appearance of a new band at 420 nm.

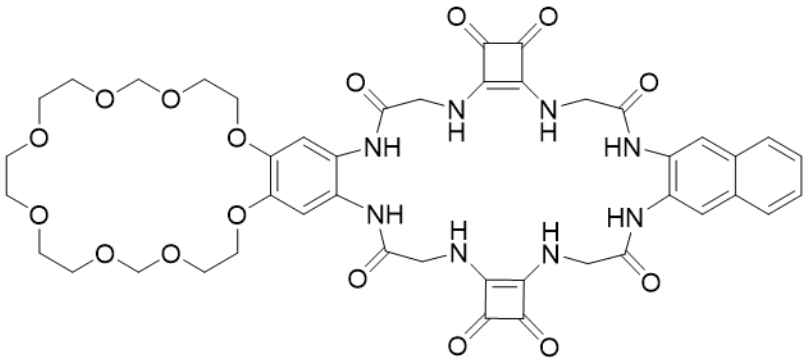

3.3

Figure 3.2: Structure of anion sensor **3.3**

One of the most crucial aspects of anion recognition using macrocycles is matching the cavity size of the receptor to the size of the anion.[183] The term "large ring" is usually used to describe a ring size greater than twelve atoms, while cyclic compounds of 8-11 atoms are termed "medium rings", and small rings being anything below seven atoms. While small rings experience ring strain, making their synthesis more nuanced than they would appear,[186] large rings suffer from a loss of entropy, requiring typical end-to-end cyclisation to be carried out under high dilution to avoid intermolecular interactions.[187] Medium rings, however, fall between these two extremes, and their synthesis is hampered by both high levels of transannular strain and the loss of entropy, making them incredibly difficult to access.[188]

A popular means by which to access medium sized rings is via "ring expansions." This method attempts to avoid the barriers faced with medium sized ring formation, by "growing" the ring size from a smaller ring. This ensures that the cyclisation step involves the formation of ring sizes of 4-6 atoms, which are much more favourable to form. One way of achieving this ring expansion is via "side-chain insertion"; that is, a side chain with a reactive handle is appended to a small ring which under certain conditions will rearrange via nucleophilic attack, expanding the ring size. The scope of this work is broad, with side-chain activation achieved through various strategies,

such as a simple deprotonation,[189] protecting group cleavage,[190] or functional group conversion.[191] Furthermore, an often key mechanistic step is the cleavage of a C-X bond, with X commonly being a nitrogen atom.[192] Although the early pioneering work for this field was carried out by Hesse and co-workers, who developed a method for ring expansions based on the use of *N*-containing side chains,[189] the group of Will Unsworth continue to move the needle and expand the scope of what they have coined Successive Ring Expansions (SuRE).[193] They have demonstrated that following C-acylation of a 12-membered β-keto ester with an acid chloride, fmoc deprotection yielded a ring expansion intermediate which spontaneously rearranged forming the 16-membered ring expanded product (**Scheme 3.1**).[194]

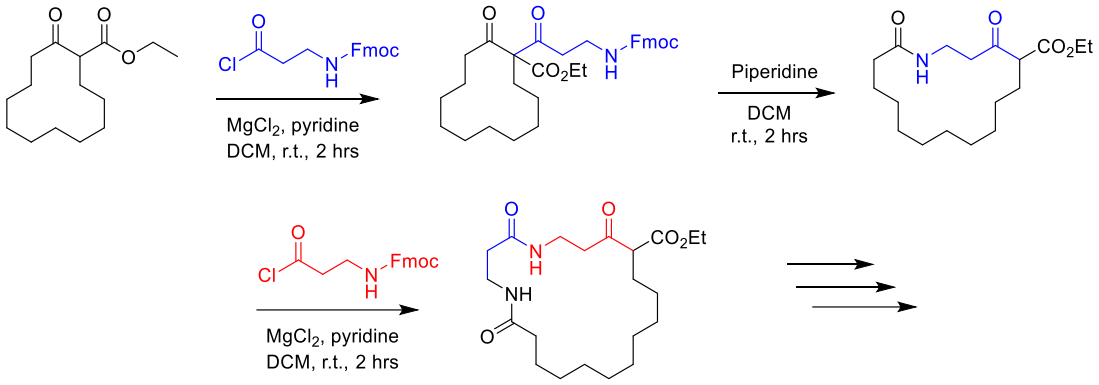

Scheme 3.1: Work carried out by the Unsworth group in the synthesis of medium-sized lactams via the SuRE method.

This methodology for ring expansion is particularly compelling, as squaramides and their cyclic derivatives are known for their effective anion binding capability but their lack of selectivity and control over binding behaviour remains underexplored. When applied to SuRE methodology, squaramides offer a promising scaffold for constructing ring-expansion motifs. They not only contain the requisite C-N bond but are also easily modified to introduce a reactive handle. Indeed, previous work within the group have shown that squaramides are capable of undergoing amide bond formation between the NH of the squaramide and a carboxylic acid to form a new class of squaramides named "amidosquaramides"[195]. Building on this, one could envision inserting an amino acid side chain into a ring-closed squaramide, triggering a similar ring-expansion mechanism. This approach could enable precise control over the binding site and allow for 'switch-on' anion binding in response to a specific analyte. This chapter will aim to apply this theoretical framework to develop a new family of reactive anion binders

that respond to external stimulation. By leveraging ring expansion in squaramide-based systems, this approach could open new avenues for designing functional molecular architectures with potential applications in sensing and transport.

3.2 Chapter Objectives

The aim of this chapter is to synthesise a series of expanding anion receptors which, upon reaction with an analyte will remove a 'triggering' group from the compound and lead to an intramolecular cyclisation reaction, culminating in a ring expansion and a "turn-on" in anion binding. This concept is graphically portrayed in **Figure 3.3**, whereby the proposed receptors will feature an initial small ring, consisting of a ring-closed amidosquaramide with *N*-terminus protection. These medium ring macrocycles will lack the cavity space size to allow for anion binding, while also containing one 'tertiary squaramide" which will lack the hydrogen bond doner group necessary for anion binding. The side chain amino acids will be of varying chain length to allow for a variety of cavity sizes upon rearrangement and will be protected in the first instance by simple *N*-boc-protection, to allow for a proof of concept to be established.

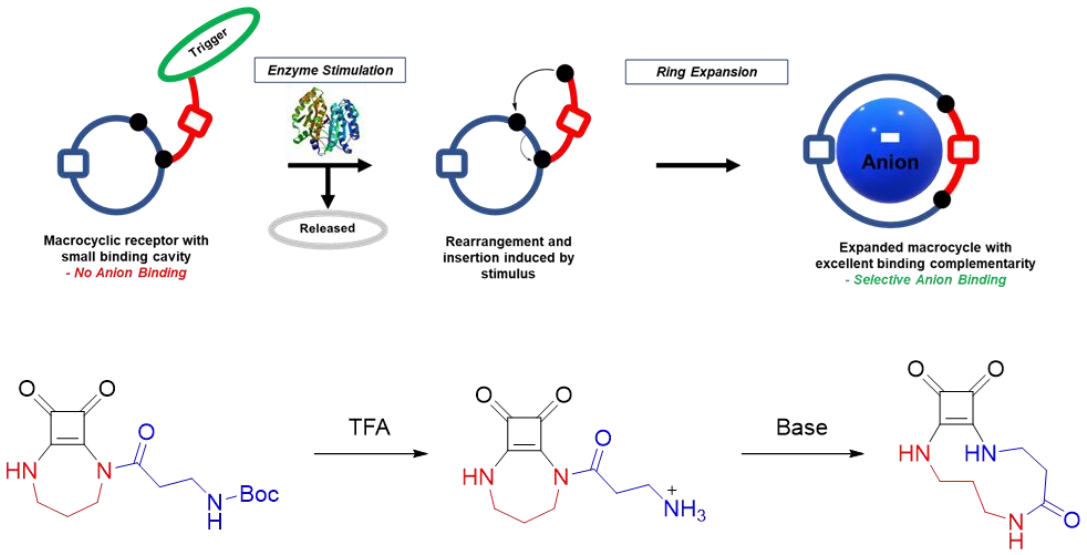

Figure 3.3: Schematic representation of the principal behind expanding anion receptors. **(top)**, proposed chemical structures and general scheme towards spontaneous ring expansion **(bottom).**

This idea builds upon a serendipitous discovery within the group, whereby attempts to Boc-deprotect the squaratide structure shown below in **Scheme 3.2** showed a skeletal rearrangement in which the newly liberated N-terminus formed a C-N bond with the cyclobutadione ring, releasing a terminal amide. It can be envisioned therefore, that upon N-terminus deprotection, this skeletal rearrangement could result in ring expansion, increasing the cavity size of a cyclic squaramide, and subsequently switch on anion binding behaviour.

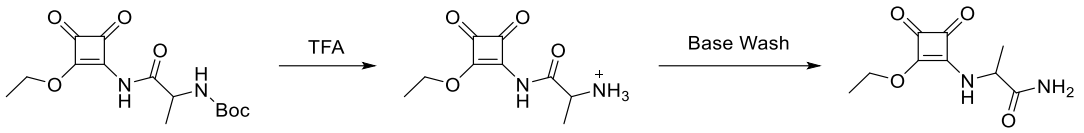

Scheme 3.2: Previous work within the group displaying the skeletal rearrangement of a simple squaratide upon n-terminus deprotection.

In the first instance, the 'ideal' medium ring sized will be assessed by reaction of various diamines with diethyl squarate. Following this, the optimal 'arm' length will be identified by way of reaction with various amino acids of varying chain lengths. Upon the synthesis of a family of lead compounds, all will be subjected to *N*-terminus deprotection to assess their ability to undergo spontaneous ring expansion. If successful, the possibility of a double rearrangement will be assessed by including a second reactive handle to the unexpanded scaffold. (pathway **A** in **Figure 3.4** below). Finally, the ability to incorporate orthogonal triggers will be assessed by introducing an fmoc group to the scaffold. Sequential rearrangements will then be investigated. (pathway **B** below). Once all expansions are complete, the expanded macrocycles will be probed for their anion binding capabilities and compared with the unexpanded derivatives to verify the claim that they can act as responsive anion binders.

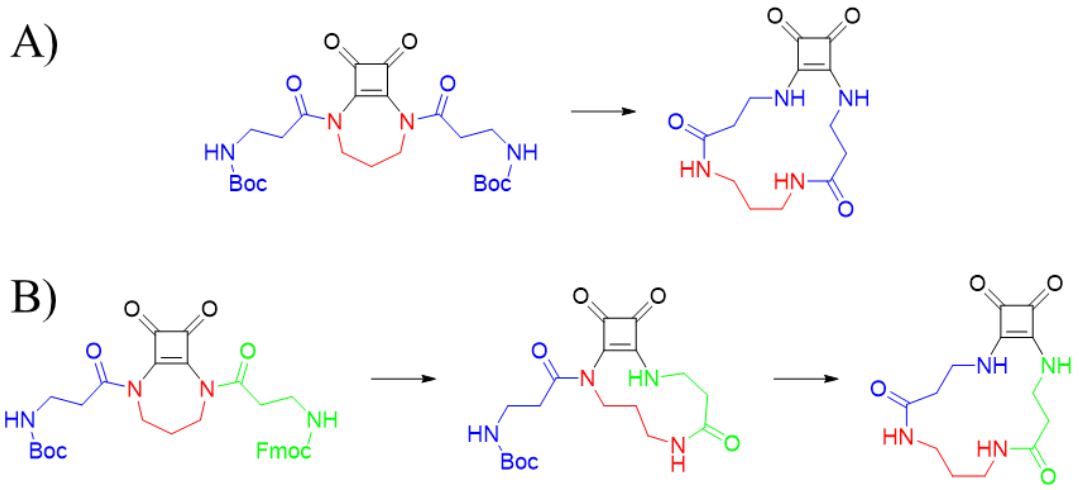

Figure 3.4: Proposed proof of concept to show the feasibility of **(A)** a double ring expansion approach to responsive anion binding and **(B)** orthogonal protecting groups for further selectivity of ring expansion

In the following sections, the synthesis of the protected squaramides will be discussed along with the discussion as to any failed synthetic derivatives, as the ideal starting macrocycle size and amino acid chain length were investigated.

3.3 Synthesis and Characterisation of Protected Medium Sized Macrocycles

The first step towards synthesising the expanded macrocycles was to first investigate the scope of the starting macrocycle size. This was to be done according to **Scheme 3.3**, whereby conversion from squaric acid to diethyl squarate (**3.4**) was carried out followed by reaction with 1,3-diaminopropane to give the cyclised product, **3.5**. In order to promote cyclisation over dimerisation, the reaction was carried out using syringe pumps, in which the starting materials were each dissolved in 5 mL of ethanol, and added at a flow rate of 5 mL/hr to a reseviour of ethanol, leading to isolated yields of 78% after filtration of the precipitate.

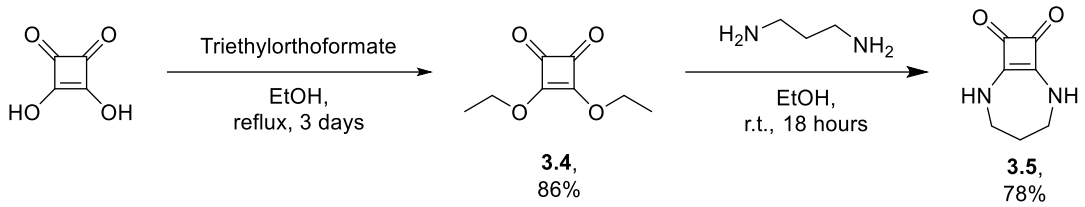

Scheme 3.3. General synthetic pathway of **3.5**.

Upon successful synthesis of **3.5**, the same protocol was applied to a range of derivatives to asses whether different diamine lengths could yield a family of medium sized squaramide rings. Under similar conditions however, in the case of both 1,2 and 1,4 diamines, the desired product was not isolated, with LCMS analysis suggesting the favourable formation of dimers and trimers. This was not entirely unexpected, with derivatives using a 2-carbon chain also showing poor cyclisation in the literature, attributed to the ring strain about the cyclobutadione ring.[196] LCMS analysis of both reactions did show formation of the desired macrocycles, however due to the highly insoluble nature of both, and the apparent low yields, it was decided not to optimise this step.

With the above cyclic squaramide in hand, the neccesary side chains were assessed to optimise rearrangement. In this reaction, succinimide-*N*-boc-amino acids were coupled to the squaramides, forming amide bonds. This reaction was successful for each of glycine, β-alanine and γ-amino-β-alanine, to varying yields, with each instance only showing amide bond formation at one of the squaramide NHs. The *N*-hydroxysuccinimide ester derivative of *γ*-(Boc-amino)butyric acid was not commercially available and its synthesis is described in **Section 6.3** (**Compound**

3.16). In the first instance, amino acids derivatives without side chains were selected to maintain consistency in the synthesis and eliminate any variables that side chains might introduce. As shown in **Scheme 3.4** below, this reaction involved reaction between in **3.5** and various activated-amino acid derivates in DMSO under basic conditions, yielding the desired responsive scaffolds to various yields following column chromatography.

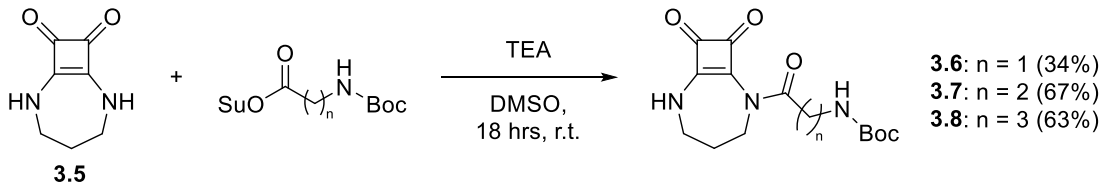

Scheme 3.4. General synthetic pathway of responsive anion binders

Below is the ^{1}H NMR for compound **3.7**, the β-Alanine derivative (**Figure 3.5**). The spectra shows the characteristic NH signal of the squaramide at 9.31 ppm, along with the Boc-NH triplet at 6.76 ppm. Signals corresponding to the β-Alanine spine are seen at 3.17 and 3.2 ppm, both integrating for 2 protons. Finally, 3 CH_2 signals at 3.84, 3.39 and 1.98 ppm were obsereved which correspond to the CH_2 groups of the propylene portion of the ring.

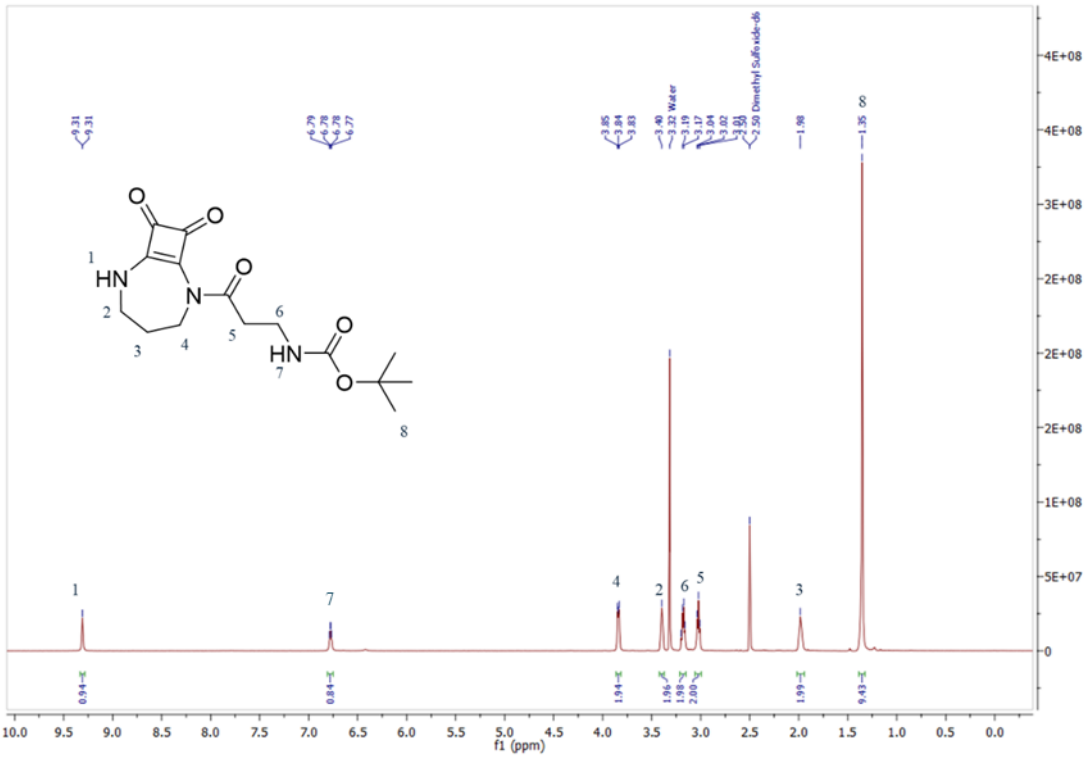

Figure 3.5: ^{1}H NMR of **3.7** in DMSO-d_6.

In order to identify the amide carbonyl carbon conjugated to the squaramide, HMBC analysis was used. As can be seen in **Figure 3.6** below, both the beta alanine methylene protons (labelled 5 and 6 above) and the methylene protons of the squaramide (labelled 4) show coupling to the carbon signal at 172 ppm.

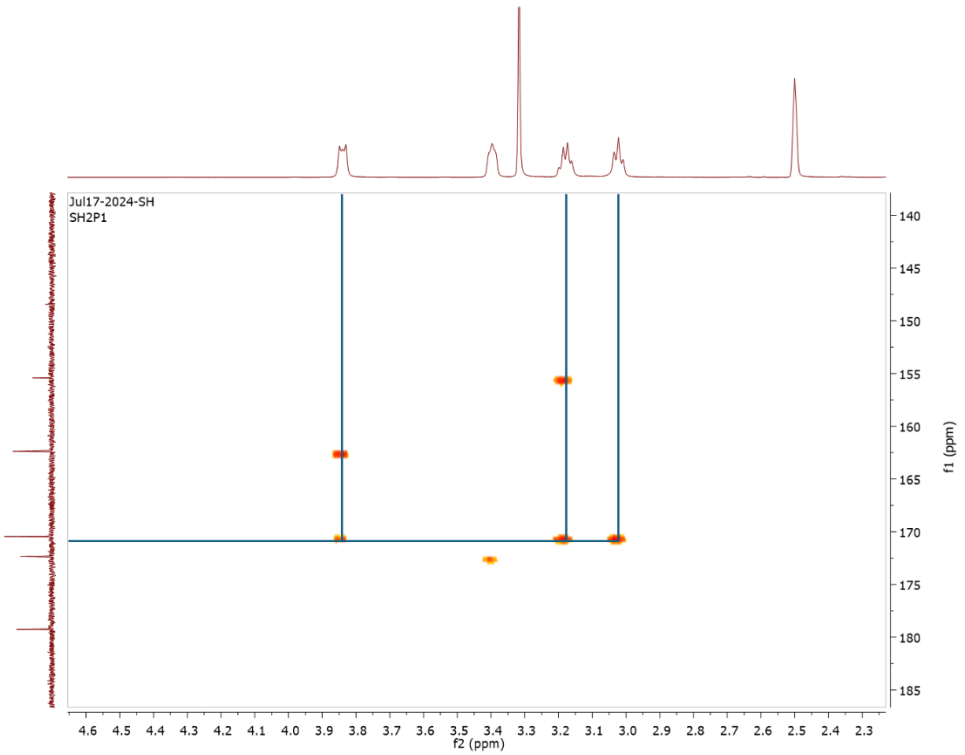

Figure 3.6: zoom of HMBC spectrum of **3.7** showing coupling between the amide carbonyl and methylene protons, labelled 4,5 and 6 in **Figure 3.4**.

A crystal structure of the compound was also obtained from the slow evaporation of DMSO. Analysis of the crystals were carried out by Dr. Brendan Twamley in Trinity College Dublin. X-ray analysis found the structure existed in two conformers shown in in **Figure 3.7** below, in a 74:26% majority of the A conformer. **3.7** was also found to engage in intermolecular H-bonding between the carbonyls and the squaramide NH of a neighbouring molecule.

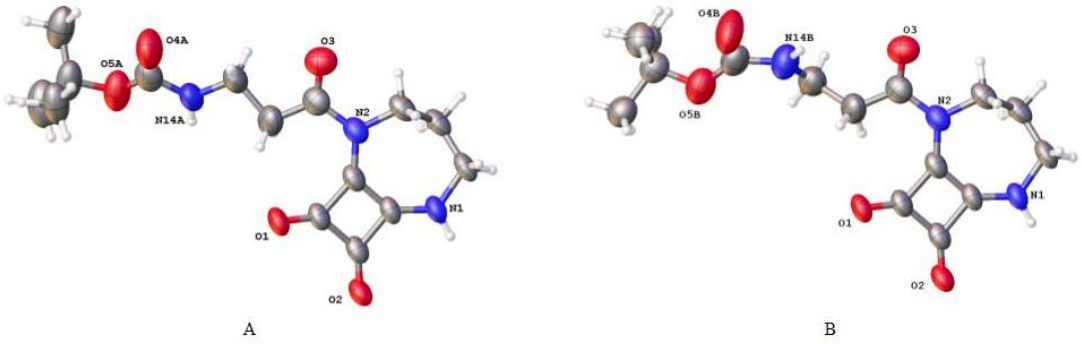

Figure 3.7: Individual representations of each disordered moiety in **3.7**.

While not discussed in this section, the synthesis of both **3.6** and **3.8** were successful to isolated yields of 34 and 63% respectively and the characterisation data for each can be found in the appendix.

3.4 Ring expansion of 3.7

With the target unexpanded macrocycles successfully synthesised, the next step was to investigate their ability to undergo the intended rearrangement. The rearrangement is postulated to occur via a pseudo-Smiles rearrangement mechanism. Firstly, base deprotonates the NH_3^+ to form a primary amine. This nucleophilic amine then attacks the alkene carbon of the squaramide moiety, forming an enolate-like intermediate. Re-establishment of the carbonyl and squaramide alkene breaks the C-N bond and subsequent proton transfer releases the secondary amide and results in the ring expansion from 7-atoms to 11-atoms.

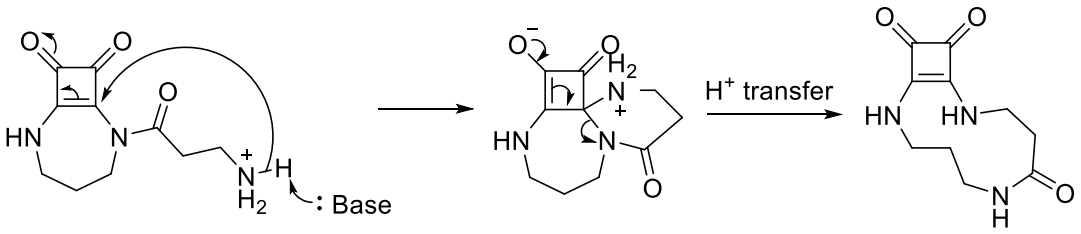

Scheme 3.5: Proposed mechanism for the spontaneous ring expansion following *boc*-deprotection of **3.7**

This was done via **Scheme 3.6**, which focuses on **3.7.** Boc-deprotecion was carried out using TFA:DCM, with the intermediate salt being isolated via precipitation from ice-cold ether. The isolated deprotected macroycle was then redissolved in ethanol and reacted with 4 equivalents of TEA. This reaction led to the formation of a precipitate

after approximately 30 minutes, however LCMS analysis indicated the presence of some starting material still remaining. The reaction was then left to stir overnight until there was no apparent conversion to **3.10**, which was approximately after 16 hours. Isolation of the precipate led to yields of 55-65%. This range of yields may be due to fluctuations in reaction efficiency, but also the slight solubility of **3.10** in ethanol, with some of the compound remaining in solution and being removed in the isolation step. A similar result was seen when the ring expansion step was carried out in MeCN.

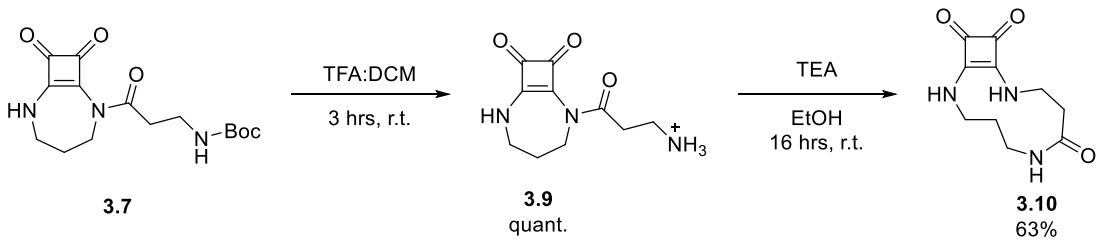

Scheme 3.6. Synthesis of **3.10** via boc-deprotection and spontaneous ring expansion

When analysing the ^{1}H NMR of **3.10**, a stark broadening of the signals was observed (**Figure 3.8**). This was not unexpected with squaramides often undergoing a self-assembly processes due to intermolecular H-bonding between the carbonyls and NHs, resulting in stacking and broadening the signals in ^{1}H NMR spectra.[197] However, what could be indentified was three broad signals in the aromatic region, all approximately integrating for 1 proton, indicating the successful rearrangement and re-establishment of a squaramide NH and liberation of a secondary amide.

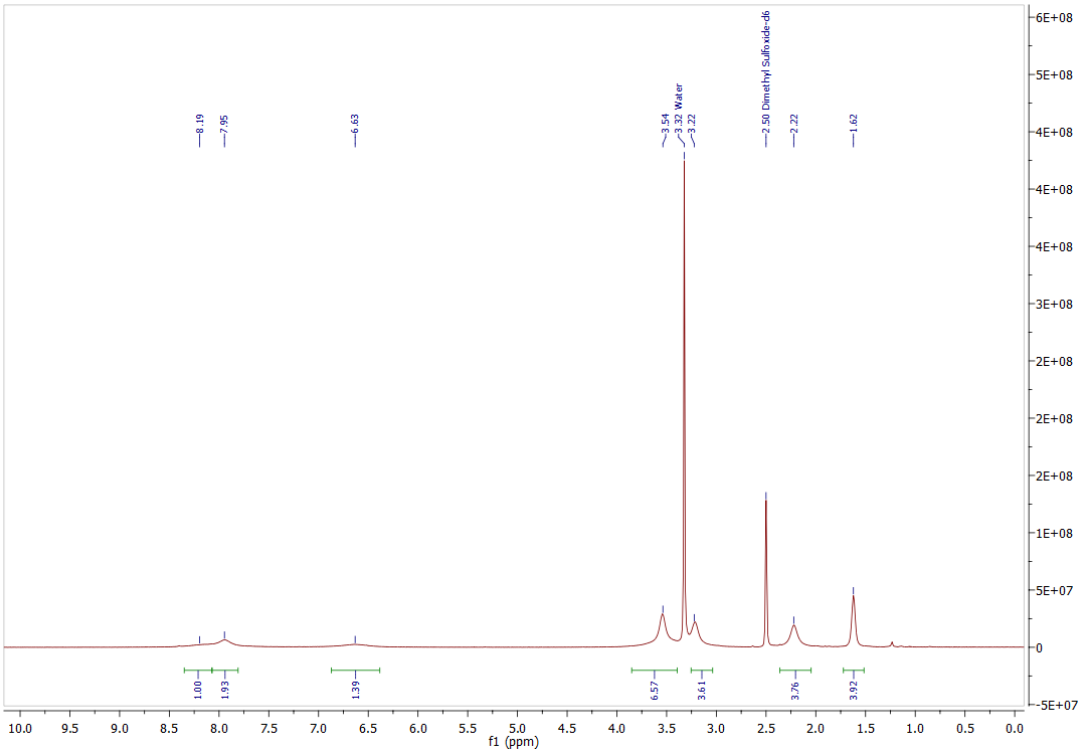

Figure 3.8: ^{1}H NMR of **3.10** in DMSO-d_6.

To try and disrupt the aggregation of **3.10** and obtain a clearer NMR spectra, VT NMR was run at 60ºC. This led to a dramatic sharpening of signals in the ^{1}H NMR spectra upon heating. Observing the spectra below in **Figure 3.9**, the squaramide NHs show as one broad peak at 7.84 ppm, with the amide NH at 6.64 ppm.

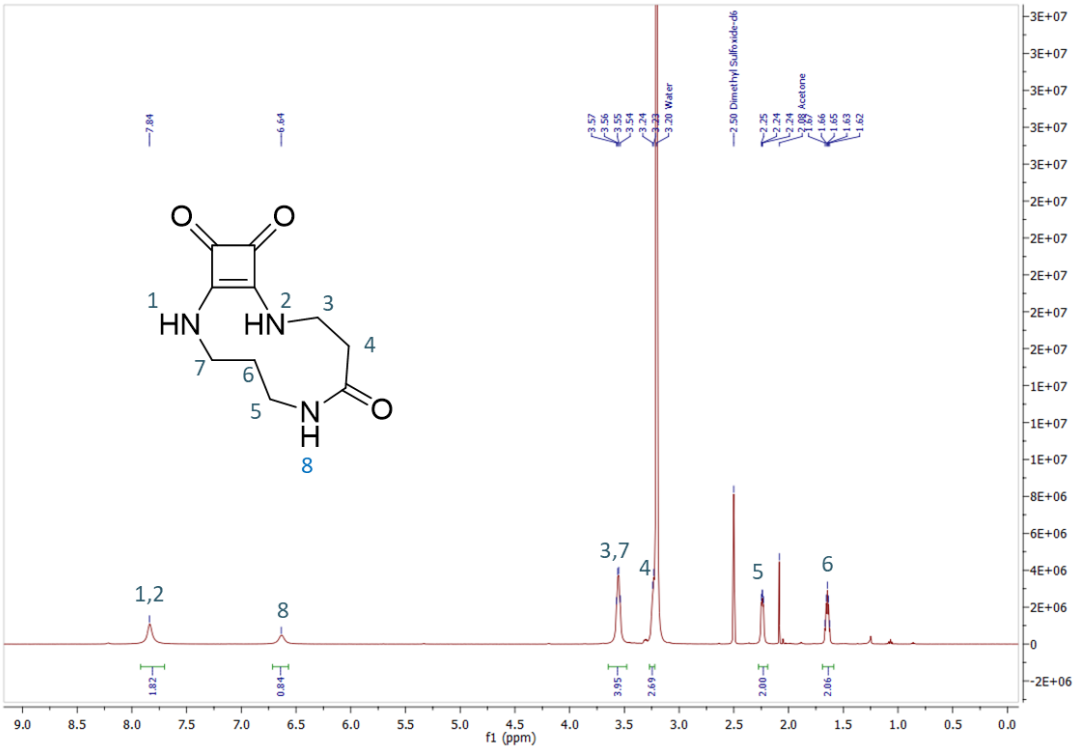

Figure 3.9: ^{1}H NMR of **3.10** in DMSO-d_6 at 333 K.

Stacked ^{1}H NMR spectra shown in **Figure 3.10** below tracks the changes in the NMR spectra from **3.7** through the intermediate **3.9** and the ring expanded **3.10.**

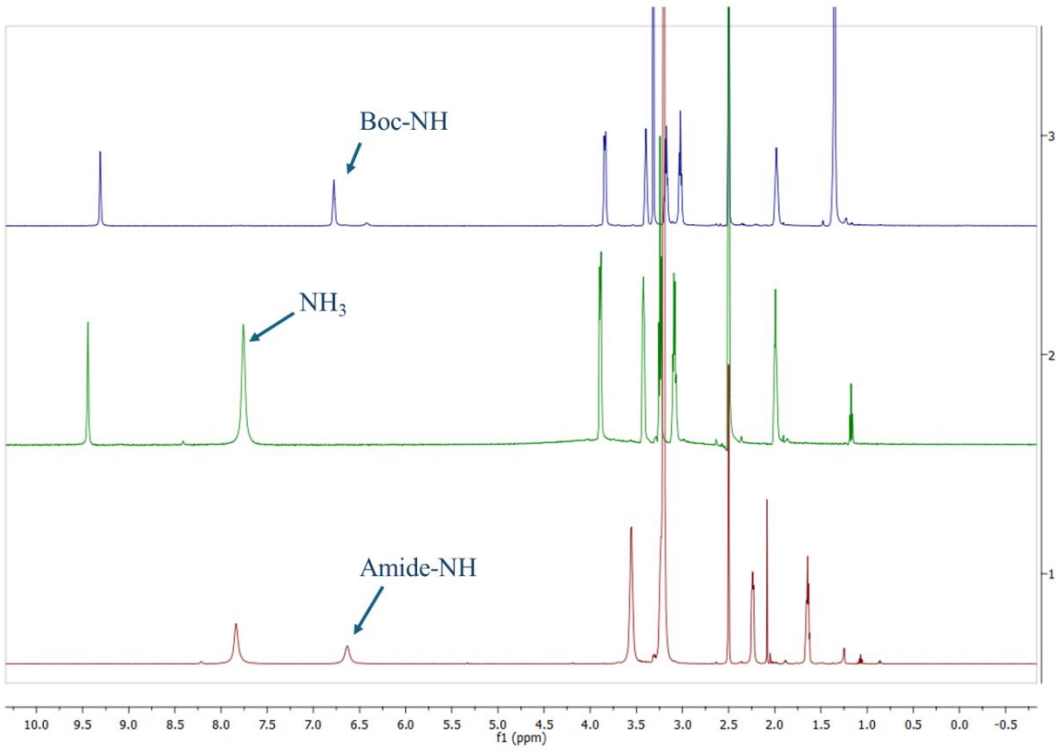

Figure 3.10: Stacked ^{1}H NMR of **3.7 (top), 3.9 (middle)** and **3.10 (bottom)** in DMSO-d_6.

This deprotection and rearrangement could also be tracked using LC analysis, with distinct retention times shown for each compound. This is shown in **Figure 3.11** below.

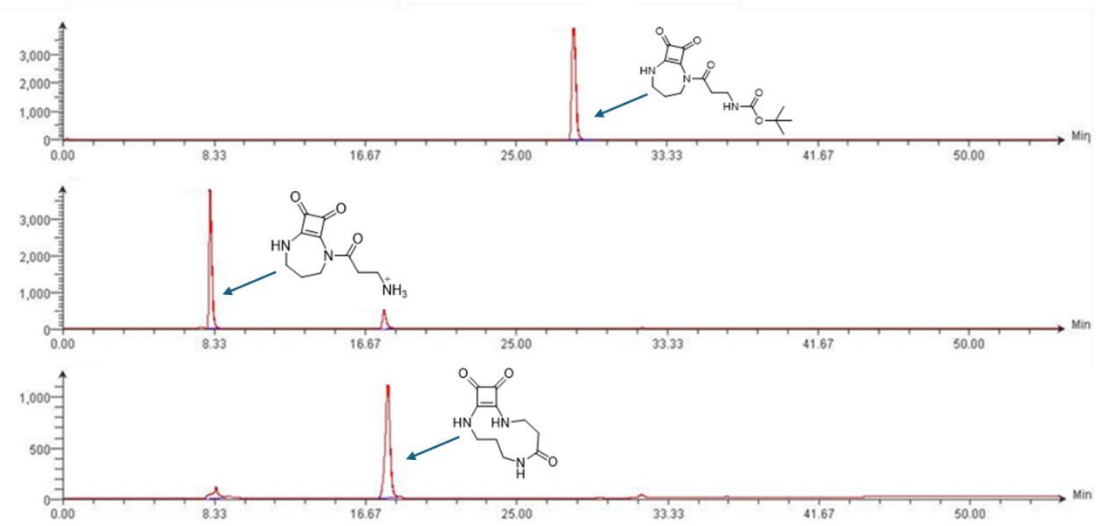

Figure 3.11: Stacked LC spectra tracking the ring expansion of **3.7** to **3.10,** through the intermediate **3.9**.

Formation of **3.10** was also confirmed *via* HRMS with observed ionisation at 224.1031, which corresponds to $[M+H]^+$ for **3.10** as well as ionisation at 246.0849, which corresponds to $[M+Na]^+$(**Figure 3.12**).

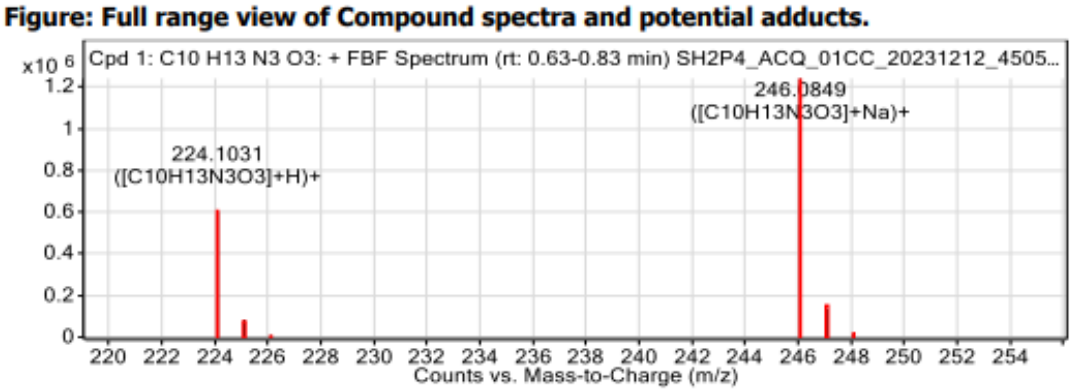

Figure 3.12: HRMS of **3.10**

Crystals of **3.10** were obtained through the slow evaporation of a DMSO solution. X-ray analysis, performed by Dr Brendan Twamley, Trinity College Dublin, revealed the orientation of the NHs of the molecule. The amide NH and squaramide NH in closest proximity align themselves perpendicular to the cavity, whereas the remaining squaramide NH is orientated in a *anti/syn* manner with respect to its counterpart

(**Figure 3.13**). This orientation would have implications in the binding behaviour of the molecule and will be broached in a later section.

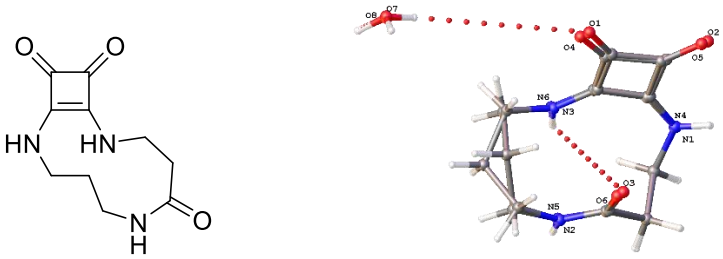

Figure 3.13: Structure of the theoretical unit of **3.10** (left) and overlay view of **3.10** showing the different conformations of each ring

Futhermore, the X-ray analysis displayed packing interactions due to the squaramide NH forming an intermolecular hydrogen bonds with the carbonyl of the cyclobutadione ring of a neighbouring molecule as well as an intermolecular H-bond between the amide carbonyl and amide NH. Moreover, the cyclobutadione carbonyl H-bonds with a neighbouring water molecule (**Figure 3.14**).

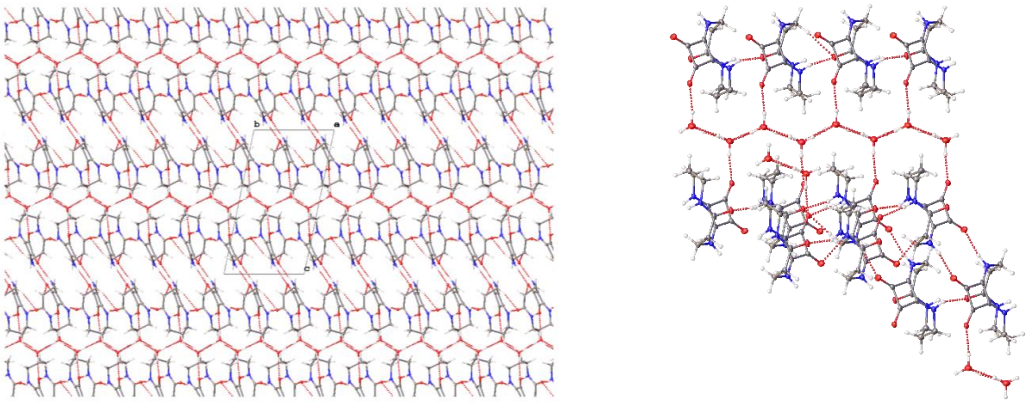

Figure 3.14: Schematic packing diagram and detail of the hydrogen bond pattern seen in **3.10.** Displacement paramaters shown at 50% displacement.

Having succesfully demonstrated the rearrangment of **3.7** upon *N*-terminus deprotection, it was next decided to apply this methodology towards the rearrangements of **3.6** and **3.8**.

3.5 Attempted ring expansions of 3.6 and 3.8

The expansion of both compounds **3.6** and **3.8** were investigated in the same manner as **3.7**, with *N*-Boc deprotection followed by reaction with 4 equivalents of TEA. In

the case of **3.6**, LCMS analysis showed primarily returned starting material upon treatment with triethylamine. There was evidence of a possible rearranged structure with a new peak with retention time similar to **3.10**, however there was no descernable ionisation mass found so it made identification difficult (**Figure 3.16**). The lack of efficacy in converting from the free amine to the 10-membered macrocycle could be postulated to be due to the mechanism proceeding *via* a constrained 5-membered ring transition state. 5 membered rings suffer higher angular distortion and tortional strain, making their formation difficult and thermodymically unfavourable (**Figure 3.15**). As is well established, the strain energies for methylene based rings are lowest for 6 membered rings (1.43 kcal/mole) whereas they are slightly higher for 5-membered rings (7.28 kcal/mol).[198] This small discrepency in angle strain may explain the lower conversion to the desired macrocycle when compared to **3.7**.

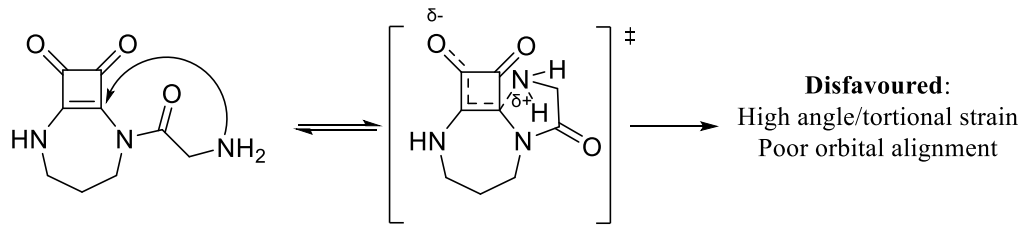

Figure 3.15: Cyclisation mechanism showing the 5-membered TS state.

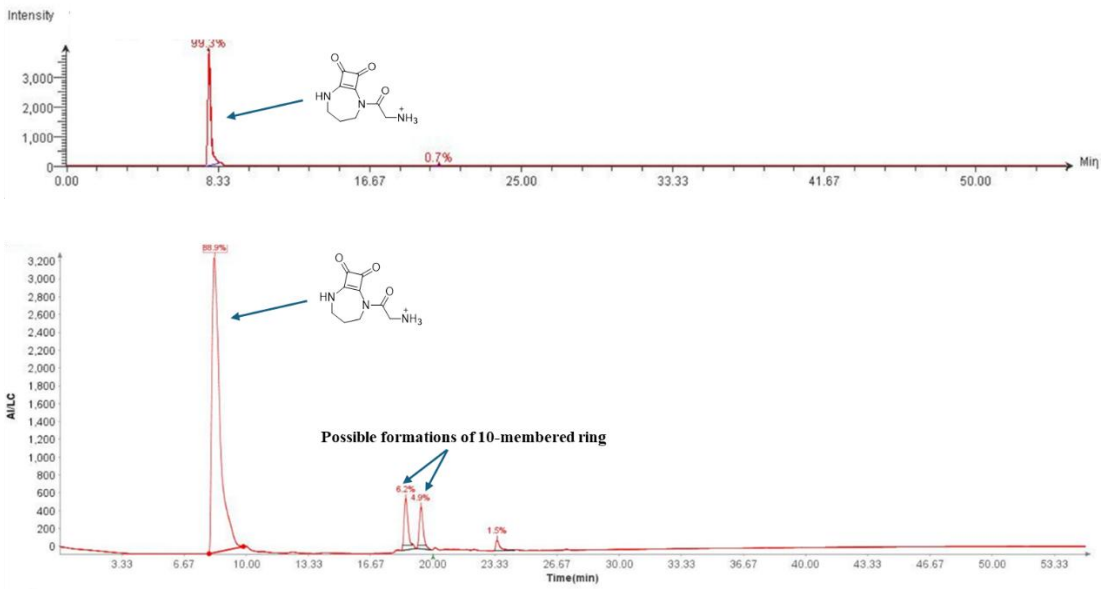

Figure 3.16: LCMS analysis of **3.6** before (**top**) and after reaction with TEA (**bottom**)

A similar lack of rearrangement was seen for **3.8**, where attempts to rearrange resulted in the fragmentation of the compound, removing the amino acid portion from the

scaffold and yielding the starting macrocyclic squaramide, **3.5**. This may again be attributed to the fact that, to undergo the desired ring expansion, it would involve the formation of a 7-membered ring intermediate. Like with the 5-membered ring intermediate, the angle strain for this 7-membered intermediate could be expected to be higher than the 6-membered transition state of **3.10**, thus making it somewhat unfavourable to form. Clearly there is a competition between forming the 5-membered intermediate via the blue pathway shown in **Scheme 3.7** below, and the 7-membered ring intermediate, shown in the red pathway. It could be postulated that the red pathway suffers both from the ring strain explained above, but also an increased distance between the two reaction sites, thus favouring the blue pathway. A similar observation was made by Ivanov *et al.* in their work synthesising cyclic dipeptides *via* ring expansion.[192] The resulting rearrangement was confirmed by ^{1}H NMR of the precipitate formed upon reaction of the deprotected intermediate of **3.8** with TEA, shown in **Figure 3.17.** Observed here was one signal integrating for 2 protons at 8.41 ppm, indicating the presence of two squaramide NHs. Also observed were two signals integrating for 2 and 4 protons, which correlated to the methylene protons of the 7-membered ring.

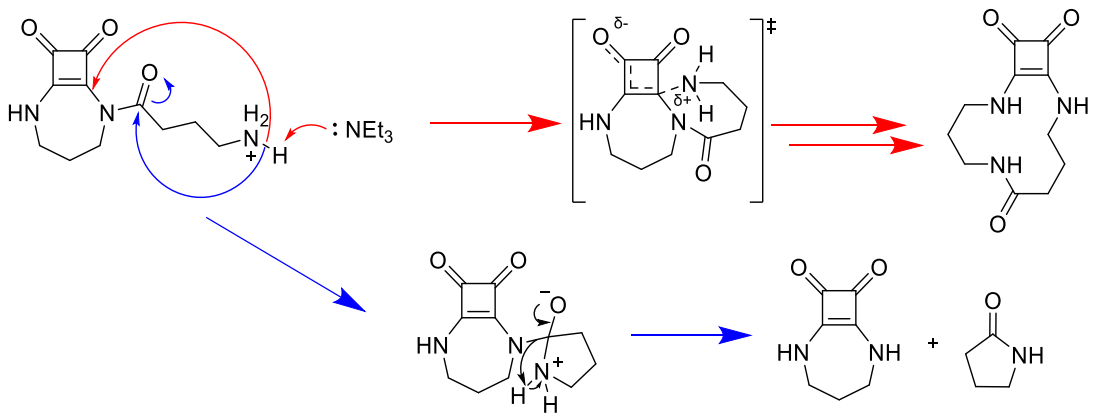

Scheme 3.7: Desired intramolecular rearrangement of **3.8** (red) and observed fragmentation (blue)

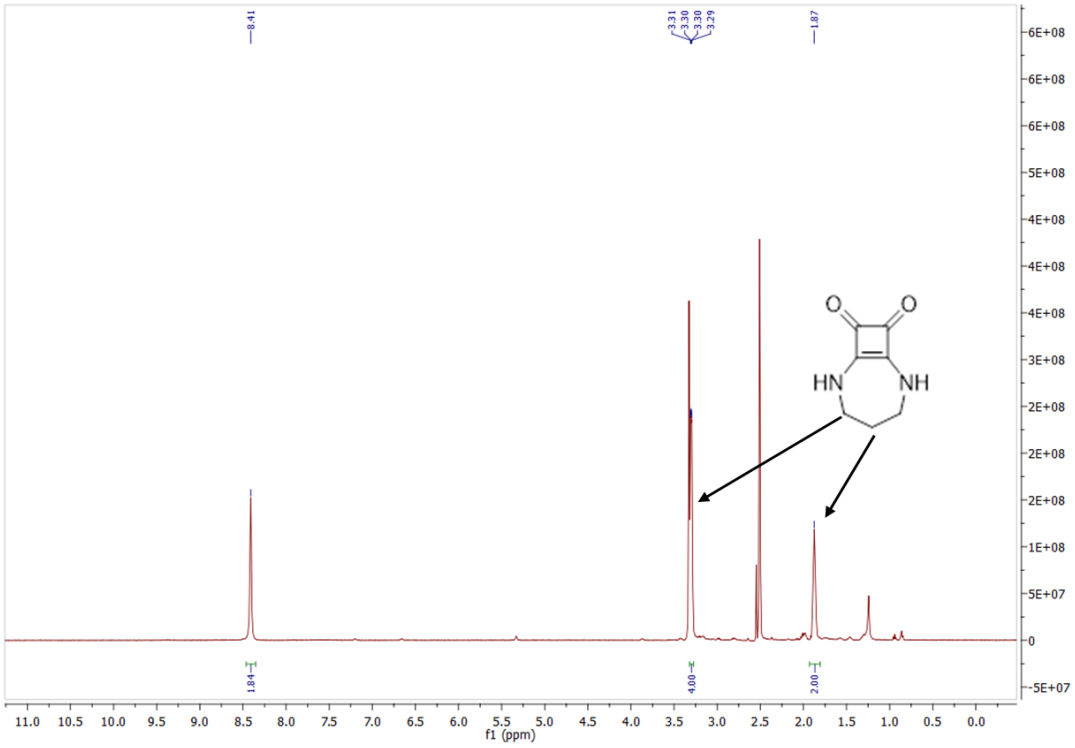

Figure 3.17: ^{1}H NMR of the isolated product of the reaction between **3.10** and TEA, showing the formation of **3.5** in DMSO-d_6.

With the above experimental data in hand, it was next decided to expand the scope of this ring expansion strategy, and to investigate whether a double rearrangement was possible.

3.6 Expanding the scope of receptor design.

Building on the observation that this family of compounds can undergo triggered ring expansion, it was hypothesised that a double rearrangement would generate a larger cavity with the potential for enhanced binding properties. A larger cavity could allow the squaramide NHs to adopt a *syn/syn* orientation, strengthening hydrogen-bonding interactions, while the introduction of a second amide through rearrangement would provide additional binding sites. Together, these features were expected to increase the overall binding affinity of the resulting macrocycle.

This was assessed by first attempting to synthesise an unexpanded macrocycle with two *N*-Boc-β-Alanine side chains. This was initially attempted by reacting **3.7** with another equivalent of *N*-Boc-β-Ala-OSu. However, LCMS analysis of the reaction mixture after 24 hours showed only returned starting material with no evidence of di-substitution. The temperature was subsequently increased daily in increments of 10°C,

but unfortunately this resulted in degradation of the starting material, back to the central scaffold **3.5**, at temperatures exceeding 50ºC. This result led to a new synthetic pathway, utilising peptide coupling chemistry (**Scheme 3.8**).

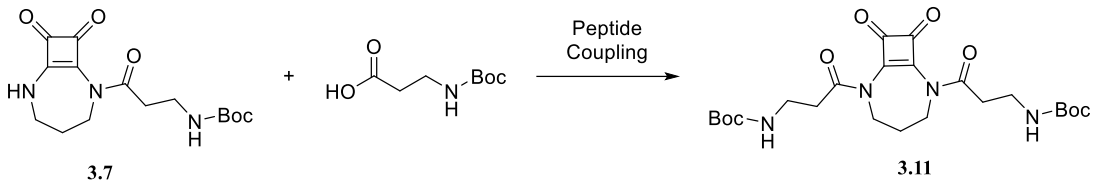

Scheme 3.8: Alternative synthetic pathway to achieve di-substitution via traditional peptide coupling

In the first instance, PyBOP was reacted with *N*-Boc-β-Alanine to form the activated ester, followed by addition of **3.7.** It was hoped that the activated ester would be sufficiently electrophilic to allow for attack by the squaramide NH. Allowing the reaction to stir for 24 hours did indeed lead to the formation of the desired product, however, attempts to isolate the target product proved challenging. Normal-phase flash chromatography returned primarily the free boc-β-alanine and **3.7**, bringing into question the stability of the newly formed C-N bond on silica gel. Furthermore, moving to reverse-phase chromatography resulted in co-elution of the PyBOP, **3.7** and the desired product under all tested mobile-phase conditions.

Upon seeing this result with PyBOP, it was decided to screen several coupling reagents in the hope that one would give full conversion to the product, thus removing the need to utilise column chromatography to remove **3.7**. Firstly to tackle the lack of efficacy observed with PyBOP coupling, the more reactive HATU was used.[199] HATU/DIPEA clearly showed an increase in coupling efficacy in comparison to PyBOP, with little to no starting material remaining after 5 hours. Unfortunately, however, HATU byproducts are not water soluble, and it was hoped these impurities would be removed *via* trituration but attempts to do so with a range of solvents were unsuccessful. It was next decided to use water soluble coupling reagents, with the hope being that any impurities could be washed away during an aqueous workup. Both EDCI and DMTMM showed little to no conversion to the product (< 5%), however COMU showed excellent coupling efficacy. **Table 3.1** summarises the coupling conditions attempted for the synthesis of **3.11**.

Reagent	Base	Rxn time (hrs)	Conversion to 3.11
PyBOP	DIPEA	16	~50%
HATU	DIPEA	5	>95%
EDCI	DIPEA	16	< 5%
DMTMM	DIPEA	16	< 5%
COMU	DIPEA	5	>95%

Table 3.1: Summary of coupling conditions in the aim of synthesising **3.11**

The efficacy of COMU in this reaction may be due to its increased reactivity when compared to several benzotriazole derivates[200] and also the presence of the morpholino group in the carbon skeleton has implication in terms of both solubility of the reagent itself and of its by-products. Moreover, the coupling reaction can be tracked colourimetrically, with a change from pale yellow to deep orange upon successful coupling. As shown in **Scheme 3.9**, the first step in the proposed mechanism is deprotonation of the carboxylic acid by DIPEA, followed by nucleophilic attack from the carboxylate with the imine of COMU, forming an unstable isuronium salt. The newly liberated OxymaPure derivative then attacks the salt, forming an Oxyma activated ester, and a water-soluble dimethyl morpholino urea by-product. Finally, the amine reacts with the activated ester to form the desired peptide bond.

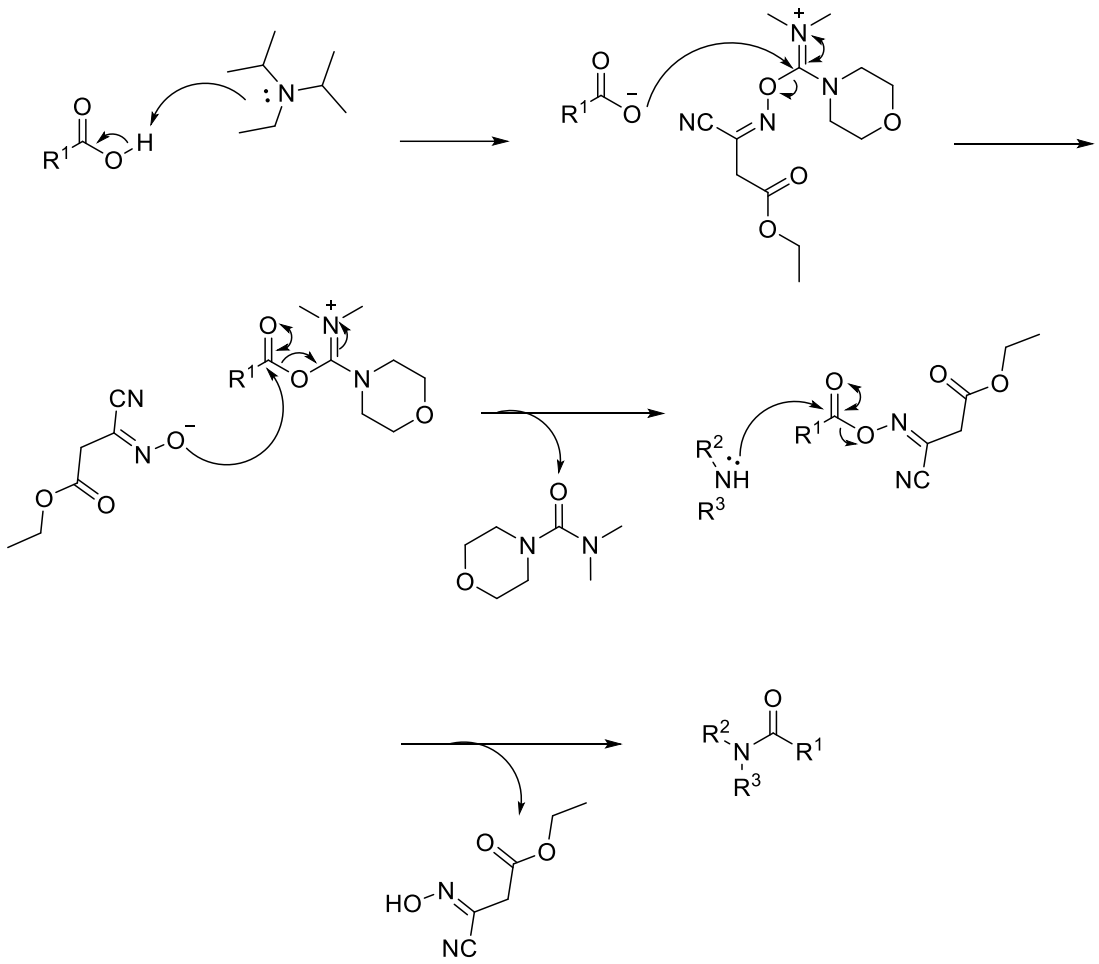

Scheme 3.9: Proposed mechanism for the COMU/DIPEA mediated peptide bond formation.

Using COMU as the preferred coupling reagent, the synthesis of **3.11** was carried via the synthetic scheme shown in **Scheme 3.10**. Here, **3.7**, boc-β-alanine was stirred in DMF along with DIPEA, followed by addition **3.7** and COMU. The reaction was left to stir for 5 hours, and subsequent aqueous workup yielded the crude product in a 67% yield.

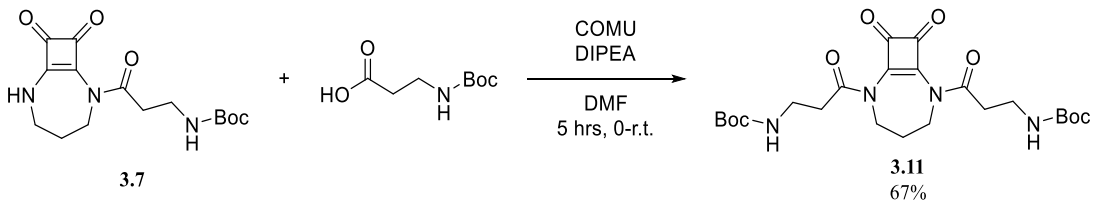

Scheme 3.10. Synthesis of **3.11** via COMU-mediated coupling

As seen from the ^{1}H NMR below in **Figure 3.18**, there was clear evidence that COMU coupling was successful in the formation of **3.11**. The disappearance of the NH signal at approx. 9.4 ppm shows reaction at the squaramide NH, with the amide NH signal at

6.86 ppm now integrating for 2 protons. Due to the symmetrical nature of the molecule, there are three signals integrating for 4 protons, with the peaks at 3.21 and 2.94 ppm corresponding to the methylene protons of the beta-alanine moiety. Finally, the methylene protons of the 7-membered ring can be seen at 3.93 and 2.39 ppm, with the former integrating for 4 protons due to the line of symmetry within the molecule.

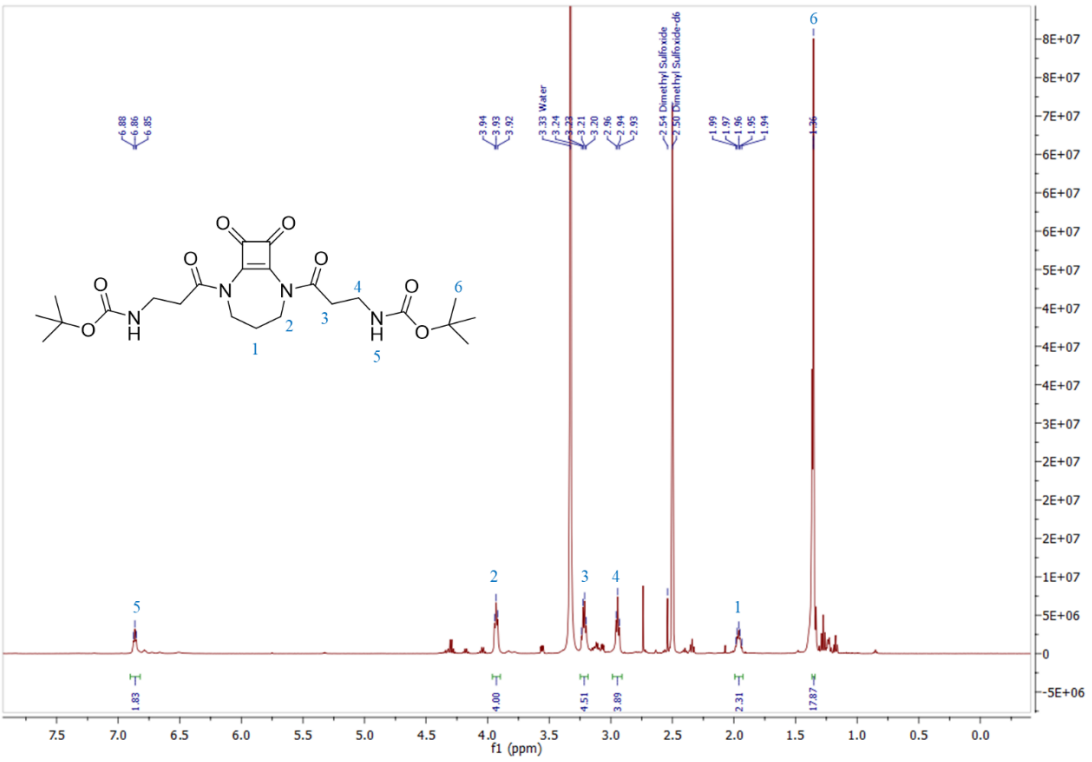

Figure 3.18: ^{1}H NMR of **3.11** in DMSO-d_6 **(bottom).**

As can be seen in the ^{1}H NMR however, there are several baseline impurities, with LCMS analysis showing the sample is at approximately 86% purity (**Figure 3.19**). The remaining impurities were identified to be a small amount of unreacted **3.7**, as well as some remaining dimethyl-morpholine byproduct that was not removed in the aqueous workup. Due to the previous chromatography issues and the risk of losing the product in further purification steps, it was decided to proceed with ring expansion studies with these impurities present.

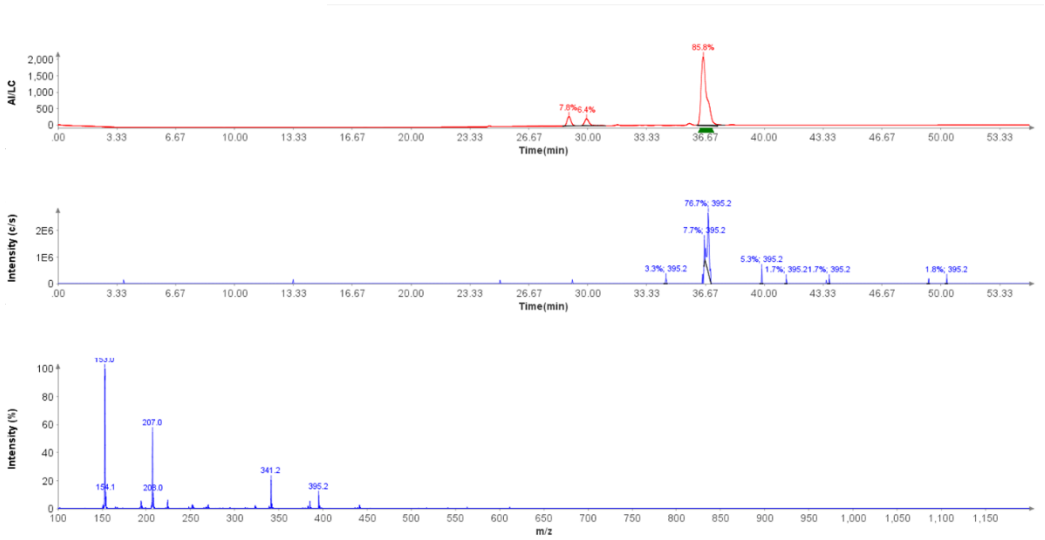

Figure 3.19: LCMS analysis of **3.11.**

3.7 Ring-expansion of 3.11.

3.11 was deprotected using TFA:DCM as with previous derivatives and the deprotected intermediate was isolated *via* ether precipitation. This was then redissolved in EtOH reacted with 4 equiv. of TEA and allowed to stir at room temperature, leading to the formation of a precipitate, which was isolated via centrifugation in an isolated 49% yield (**Scheme 3.11**). While this yield is comparatively low compared to the single ring expansion, its plausible the reaction is just as efficient, but impurities present in the starting material may be affecting the yield calculations. Furthermore, as seen with **3.10**, **3.12** is also slightly soluble in EtOH so it may not completely precipitate out of solution, causing loss of yield in the isolation steps.

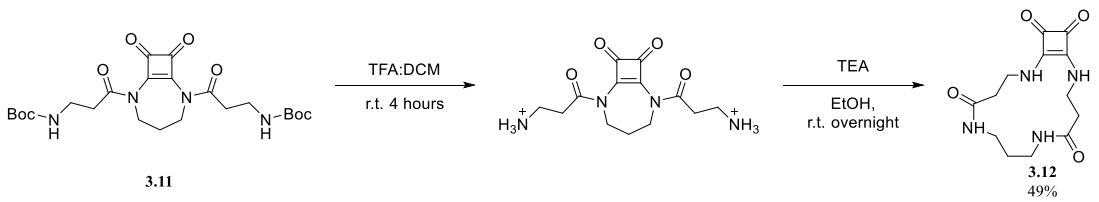

Scheme 3.11: Synthetic scheme for the deprotection and subsequent ring-expansion of **3.11**

Analysis of the isolated precipitate confirmed formation of the desired macrocycle with the ^{1}H NMR shown below in **Figure 3.20**. As can be seen, akin to **3.10**, there is a stark broadening of the signals, presumably due to similar H-bonding interactions. However, despite the broadening, there is clear evidence of formation of the expanded

macrocycle. The signals at 7.75 ppm and 7.22 ppm correspond to the squaramide NHs and the amide NHs respectfully, with both signals integrating for approximately 2 protons due to the line of symmetry within the molecule. Moreover, there are three signals integrating for approx. 4 protons, with the signals at 3.11 and 2.25 ppm corresponding to the CH_2 of the beta-alanine moiety, and the methylene protons of the propylene chain are seen at 3.64 and 1.63 ppm.

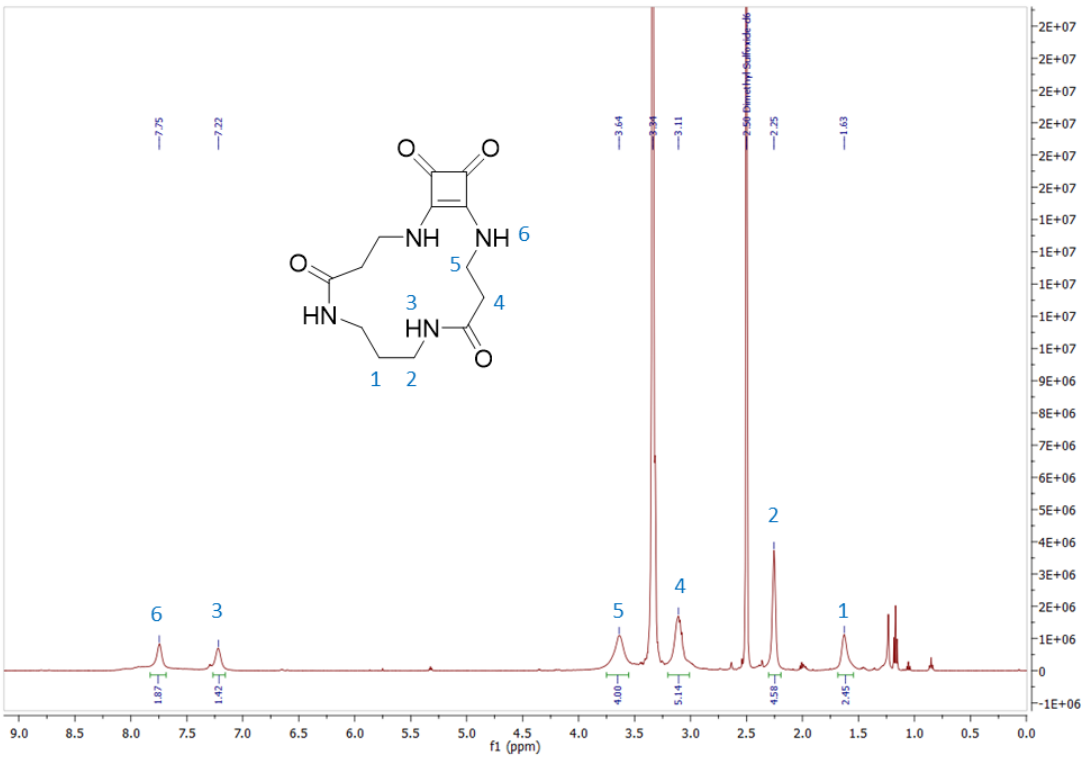

Figure 3.20. ^{1}H NMR of **3.12** in DMSO-d_6.

Like with **3.7** previously, the rearrangement of **3.12** could be tracked via LC analysis, with a retention time shift from 36 minutes to 18 minutes upon rearrangement. LCMS analysis of the rearranged product also showed ionisation for $[M + H]^+$ at 295. It is also worth noting that the impurities present in **3.11** were removed in the ring expansion step, evidenced by the pure LCMS shown in **Figure 3.21**.

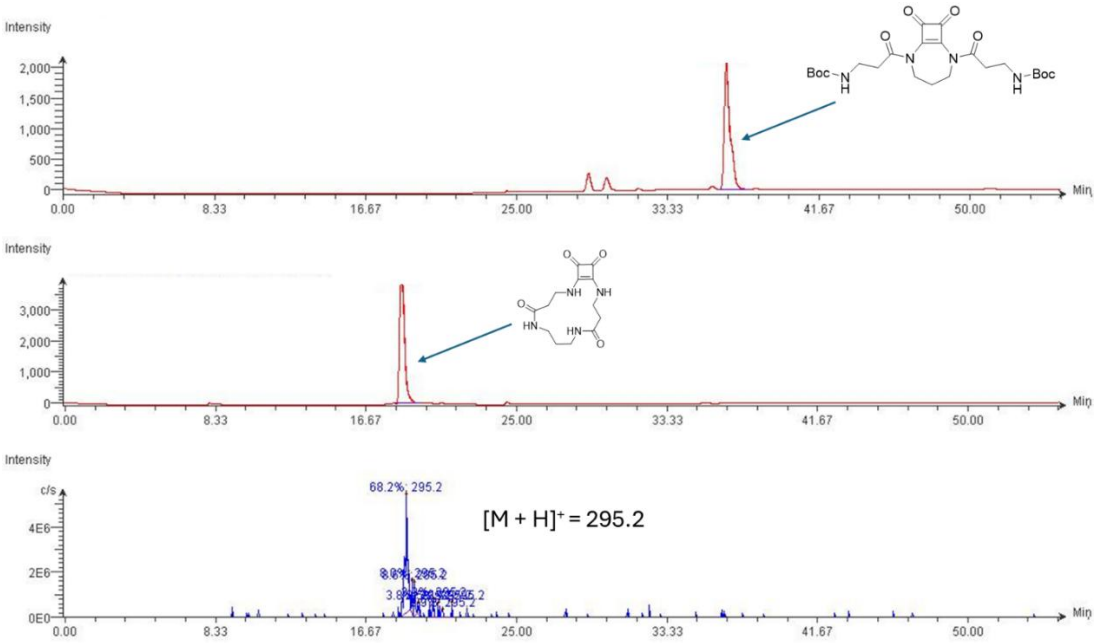

Figure 3.21: Stacked LC spectra tracking the ring expansion of **3.11** to **3.12**

The above section details the successful synthesis of di-substituted cyclic squaramide, by functionalisation of two β-alanine derivatives at both squaramide NHs. Furthermore, global deprotection of both N-termini was shown to lead a double ring expansion, resulting in a 15-membered ring.

3.8 Orthogonal Protecting groups.

Having confirmed the feasibility of the double rearrangement, the next step was to explore the use of orthogonal protecting groups as a strategy to gain greater control over cavity size and to selectively regulate the conditions that trigger anion binding. To probe this, an Fmoc protecting group was used in place instead of one of the boc-groups. The inclusion of an Fmoc group would allow for the first ring expansion to be initiated under basic conditions, leading to an 11-membered ring, while leaving the boc-protected handle intact. Then, exposure to acidic conditions would initiate a second ring expansion, giving a 15-membered ring. The synthesis of the target compound **3.13** is shown below in **Scheme 3.12**. This reaction is analogous to the previous derivative with fmoc-β-alanine being coupled to **3.7** using COMU in the presence of DIPEA with the desired product being isolated in 65% yield after aqueous workup.

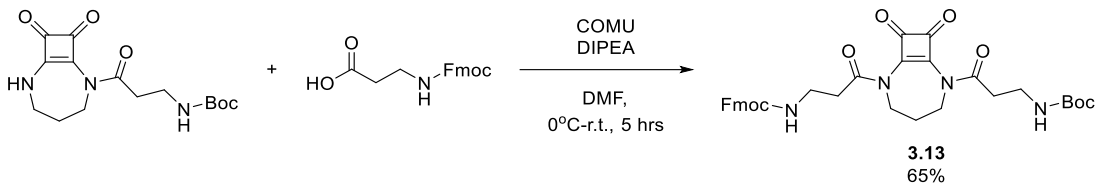

Scheme 3.12. Synthesis of **3.13**

Observing the ^{1}H NMR of **3.13** below, (**Figure 3.22**), there is clear evidence for the formation of the desired product. The squaramide NH at 9.33 ppm is no longer visible and the four signals in the aromatic region are indicative of the fmoc-protecting group as well as the multiplet at 4.20 ppm integrating for 1 proton, which corresponds to the methine proton of the fmoc group. Further characteristic peaks are evident at 4.28 ppm, which is a doublet integrating for two and corresponds to the methylene proton of the fmoc group. The newly added beta-alanine skeleton is evident by the peaks at 3.29 and 2.96 ppm. Finally, the peaks at 3.92, 3.89 and 1.95 ppm, all integrating for 2 protons, correspond to the methylene protons of the squaramide scaffold, and the boc-protons are still visible at 1.35 ppm. As with compound **3.11**, there remains minor impurities in the sample (approx. 85% purity by LCMS), but it was again decided to continue the synthesis without further purification.

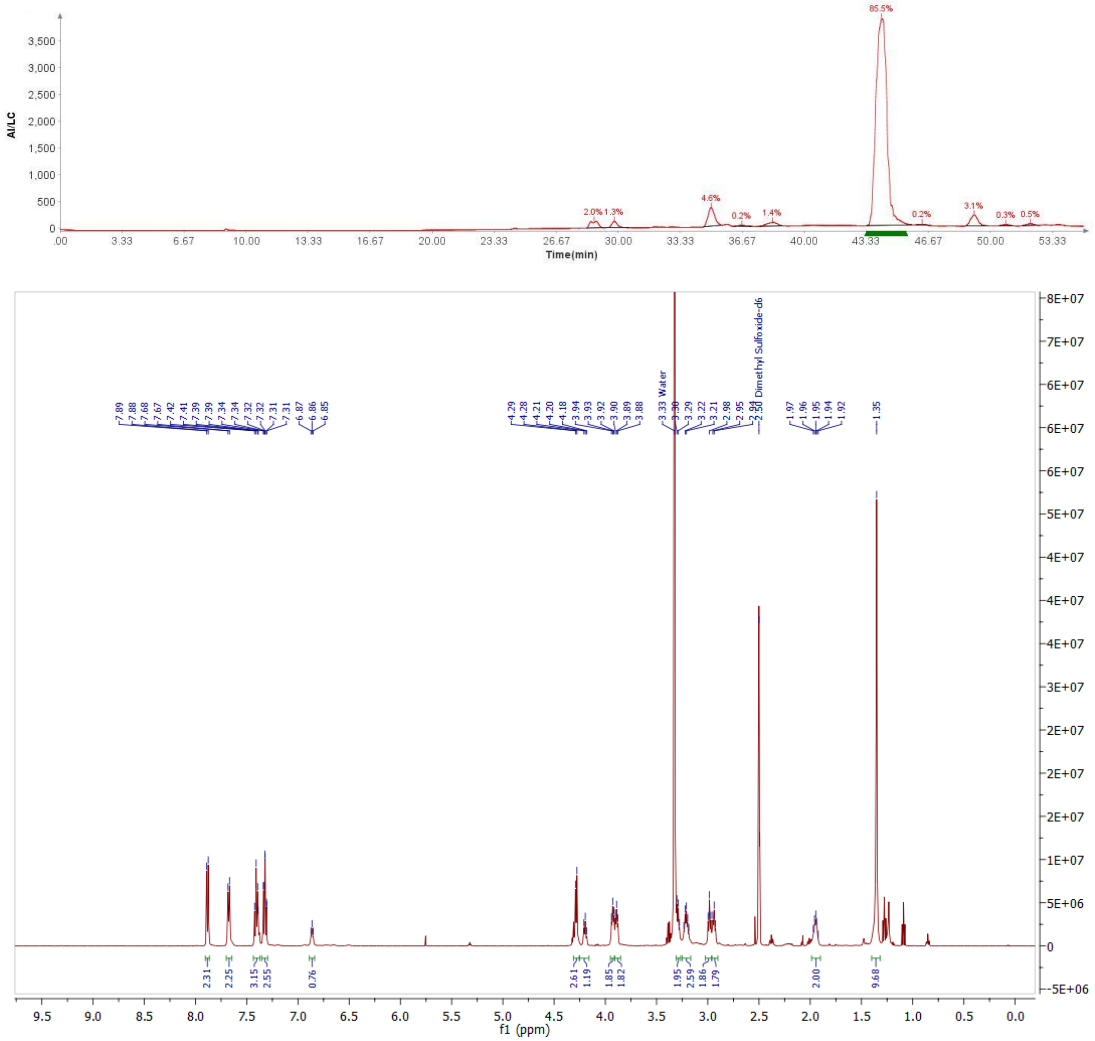

Figure 3.22. LC trace of **3.13 (top)** and ^{1}H NMR of **3.13** in DMSO-d_6 **(Bottom).**

3.8.1 LCMS analysis of sequential rearrangements of **3.14**

Given the previous success of tracking the intramolecular rearrangements of compounds **3.7** and **3.**10 via LMCS, it was decided in the first instance to use it to track sequential rearrangements of **3.13**. To probe the ability of **3.13** to undergo a single rearrangement, Fmoc-deprotection was carried out according to **Scheme 3.13**. DBU was chosen as the base due to its application in similar ring expansion methods,[201] but also its higher reactivity leads to faster reaction times and less likelihood of incomplete Fmoc-removal when compared to piperidine deprotection. Furthermore, Fmoc deprotection would yield the rearranged intermediate in the same step as the deprotection, so both steps would be carried out in a one pot fashion. The product was precipitated from cold diethyl-ether and purified using reverse-phase column chromatography.

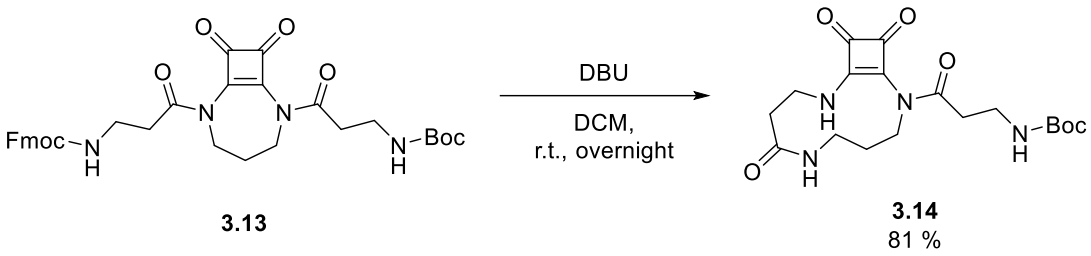

3.13 **3.14**
81 %

Scheme 3.13. Synthesis of **3.14**

LCMS analysis of the isolated product showed a retention time shift from 41 minutes to 27 minutes with the dominant peak showing ionisation of 395 attributed to the $[M + H]^+$ ion of **3.14** (**Figure 3.23**).

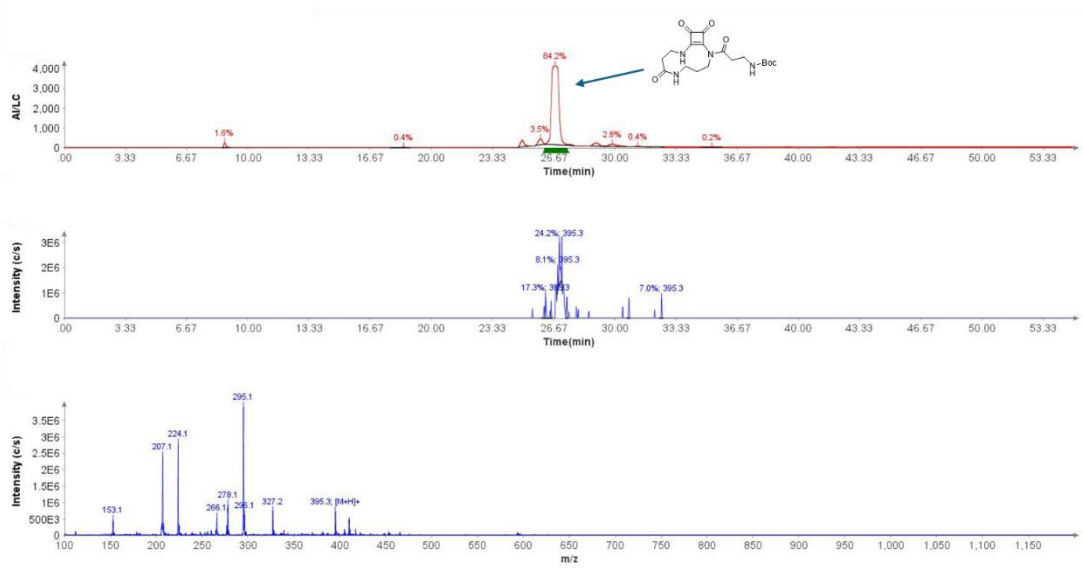

Figure 3.23: LCMS analysis of **3.14**

^{1}H NMR spectra, shown below in **Figure 3.24**, further suggested the desired rearrangement with the appearance of three signals in the aromatic region, all integrating for approximately one and possibly corresponding to the 3 NH signals. Despite the impurities present, this ^{1}H NMR coupled with the LCMS data, was good evidence that the mono-rearrangement occurred.

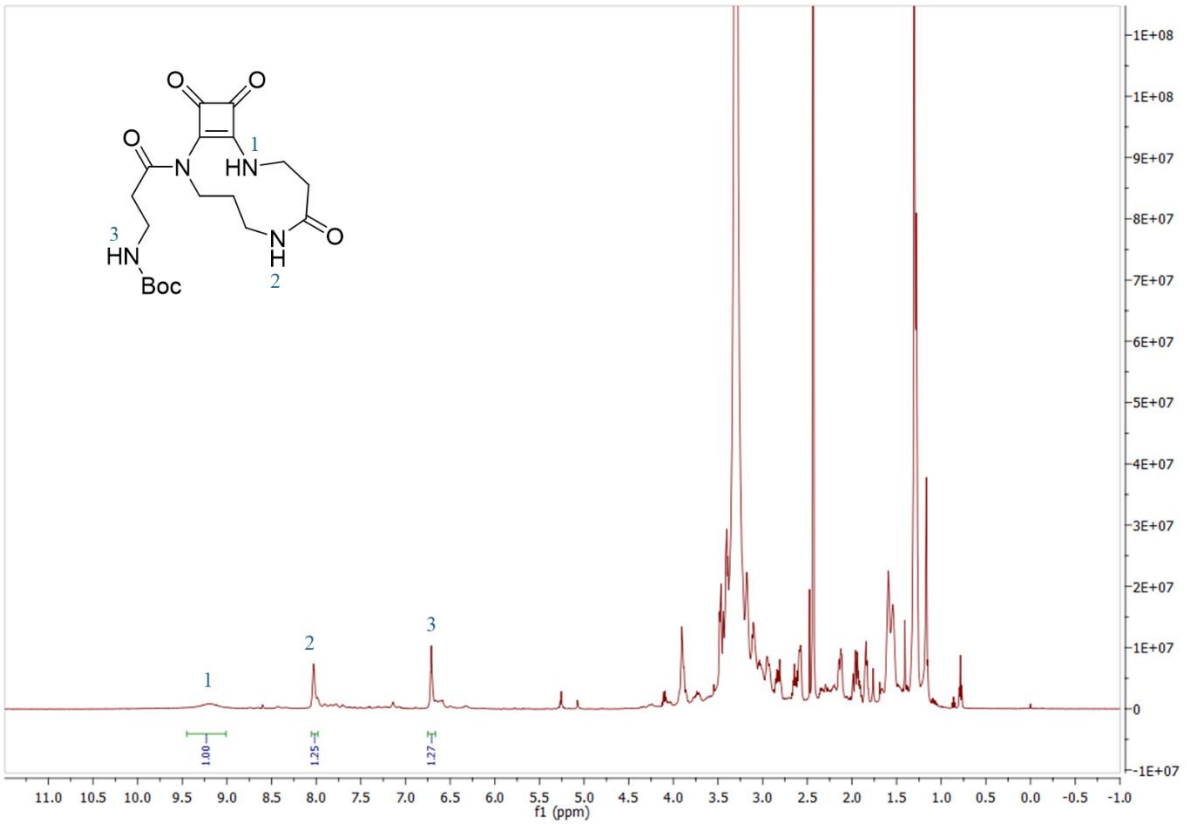

Figure 3.24. ^{1}H NMR of **3.14** in DMSO-d_6

Finally to probe if the second rearrangement could result in the formation of **3.12**, **3.14** was deprotected using TFA:DCM for four hours, with the intermediate isolated using ether precipitation, and subsequently treated with TEA. Due to the highly insoluble nature of the deprotected intermediate, this reaction was carried out in DMSO. Analysis of the reaction after 18 hours suggested the conversion from **3.14** to **3.12,** with the extracted ion chromatogram (XIC) showing ionisation at 295.4 corresponding to $[M + H]^+$ of **3.12** at a retention time of approx. 18 minutes (**Figure 3.25**). This observation matches the expectation from the LCMS analysis shown in **Figure 3.21** above.

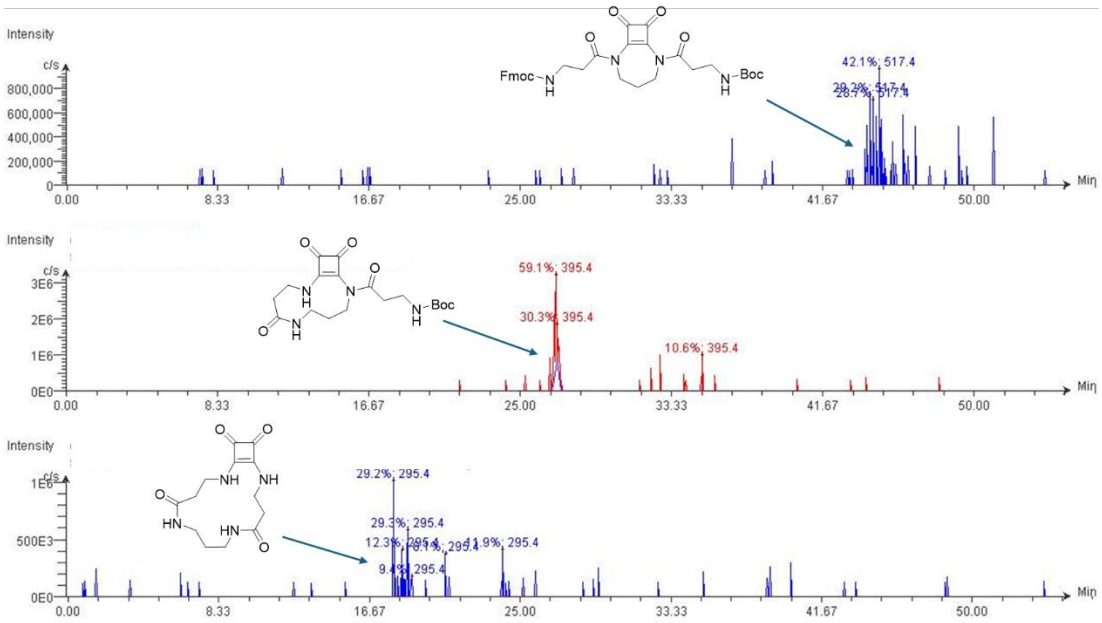

Figure 3.25: XIC of **3.13 (top) 3.14 (middle)** and **3.12 (bottom).**

The above section highlights the versatility of the expansion strategy employed to access macrocyclic squaramide receptors by employing orthogonal protecting groups. Sequential rearrangements were demonstrated first by removal of an fmoc group initiating a ring expansion to the 11-membered ring **3.14**. The remaining boc group was then deprotected and the intermediate subsequently rearranged giving the 16-membered ring **3.12**. Although it would be worthwhile to optimise the second rearrangement from **3.14** to **3.12,** as synthesising **3.14** was challenging, efforts were not directed toward preparing additional material but instead focused on investigating the anion binding properties of **3.10** and **3.12**.

3.9 Anion Binding Studies of 3.10 and 3.12

3.9.1 Anion binding studies of **3.10**

To investigate the claim that the above family of protected cyclic squaramides could behave as responsive anion binders, it was necessary to probe the anion binding behaviour before and after ring expansion. It was hoped that the unexpanded derivative **3.**7 would demonstrate no anion binding behaviour towards selected anions, whereas upon rearrangement there would be a clear 'turn-on' in anion recognition behaviour. To first assess the anion binding behaviour of **3.10**, it was subjected to an anion screen with various TBA salts of halides and oxyanions. This was done via ^{1}H NMR

spectroscopic anion screening in DMSO-d_6 by tracking the changes in the chemical shifts of the NH protons upon addition of 10 equivalents of each anion (**Figure 3.26**)

When treated with F^-, **3.10** underwent deprotonation, indicated by the formation of H_2F^-, with the characteristic triplet peak appearing at 16.25 ppm. In the case of Br^-, HSO_4^- and NO_3^- there was very little to no observed changes in the NMR spectrum, suggesting there was very weak interactions between these anions and the receptor. Both Cl^- and I^- and led to very minor changes in the chemical shift of the NH signals, suggesting some level of H-bonding with **3.10**. For AcO^- however, there was a large downfield shift of the squaramide NH proton and amide proton of 1.9 and 2 ppm respectively, indicating H-bonding. Moreover, there was an even more pronounced downfield shift upon addition of $PhCOO^-$ of 1.9 ppm. Both these observations suggest some level of selectivity towards carboxylates.

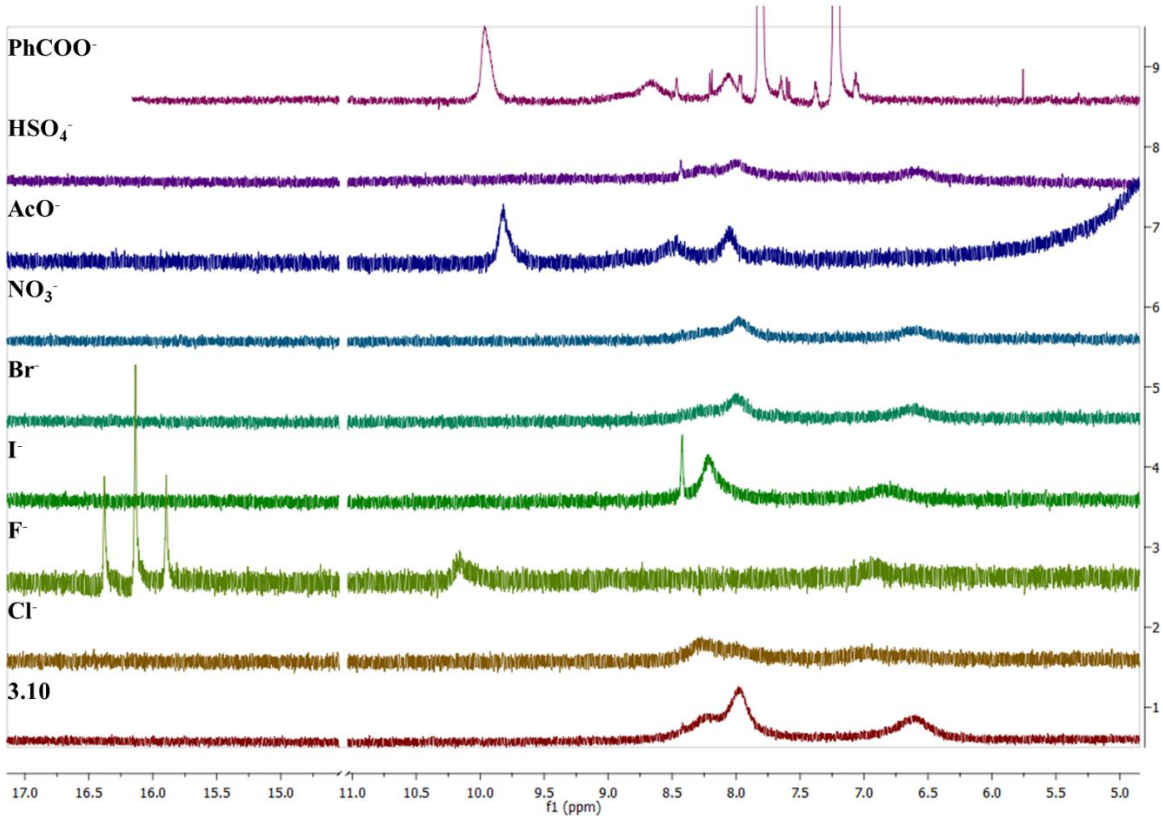

Figure 3.26: ^{1}H NMR stack plot of **3.10** (5 mM) in DMSO-d_6 treated with TBA salts of various anions (10 equiv.).

Taking the above observations into account, a more detailed ^{1}H NMR spectroscopic titration was carried out in DMSO-d_6 at 298 K to determine the binding mode and binding constants in the presence of AcO^-. As seen in **Figure 3.27**, sequential additions

of TBA AcO^- (0.2 – 20 eq.) resulted in the downfield shift of one of the squaramide NH protons as well as a downfield shift of the amide NH. Also observed was a slight up field shift for the second squaramide NH.

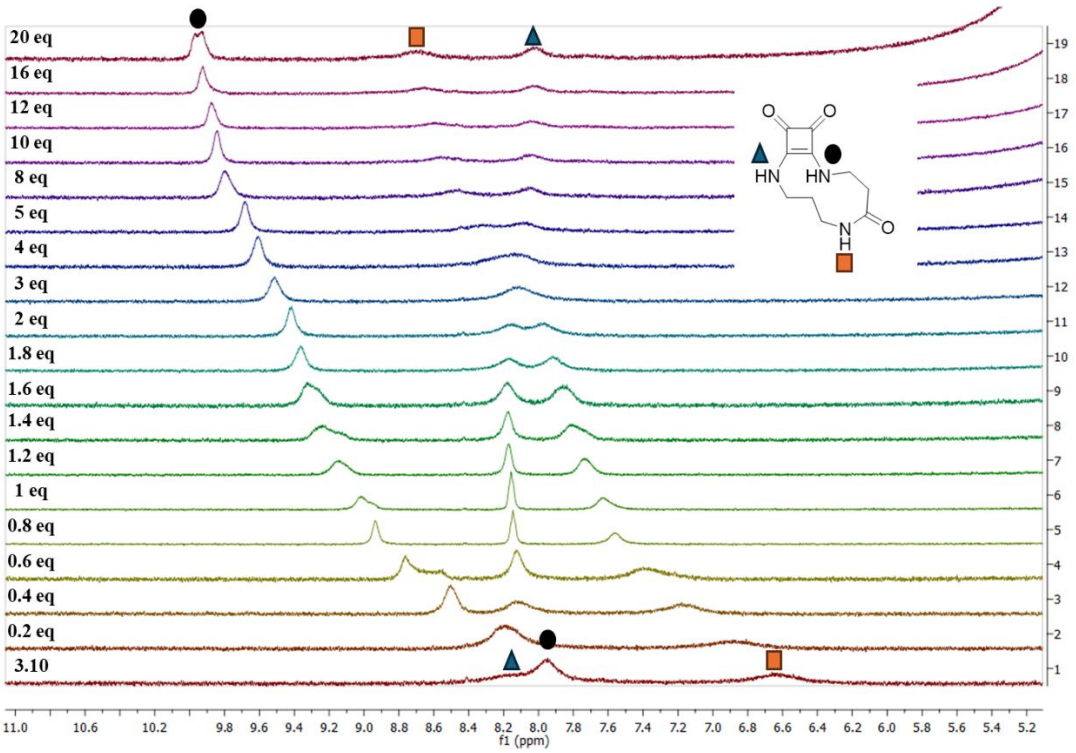

Figure 3.27: ^{1}H NMR stack plot of **3.10** (2.5 mM) and 0.0 – 20 eq. of TBA AcO^- in DMSO-d_6.

It was initially assumed that the expanded macrocycle would bind to anions via both the squaramide NHs, however observing using the above NMR, it appeared that the anion binds to the squaramide via H-bonding to one of the squaramide NHs and the amide NH. This was postulated to be due to the arrangement of the squaramide NHs in the crystal structure, with the compound forming an *anti/syn* arrangement, with one NH orientated away from the cavity, and the other pointing downwards, aligning with the orientation of the amide NH (**Figure 3.28**). It would therefore be reasonable to suggest that these two NH sites were active in the bidentate binding of AcO^-.

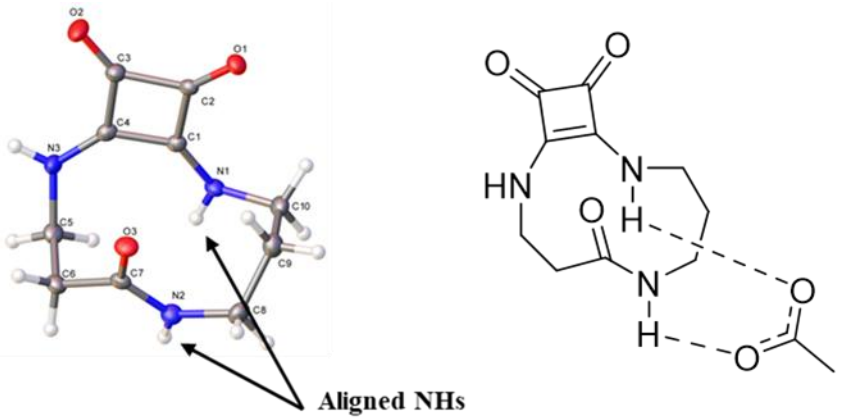

Figure 3.28: Crystal structure of **3.10** showing arrangement of the NHs (**left**) and possible 1:1 complex formed between **3.10** and AcO^- (**right**).

Binding constants were then determined by plotting the changes in the chemical shifts of the NH peaks against anion concentration and the resulting plots were analysed using the open access software BindFit (**Figure 3.29**) and were then fitted to a 1:1 binding model giving a binding affinity of 761 M^{-1} (± 9%) in DMSO-d_6. The 1:1 binding model was supported via Jobs Plot analysis, by plotting the mole fraction of **3.10** against the mole fraction*(δppm).

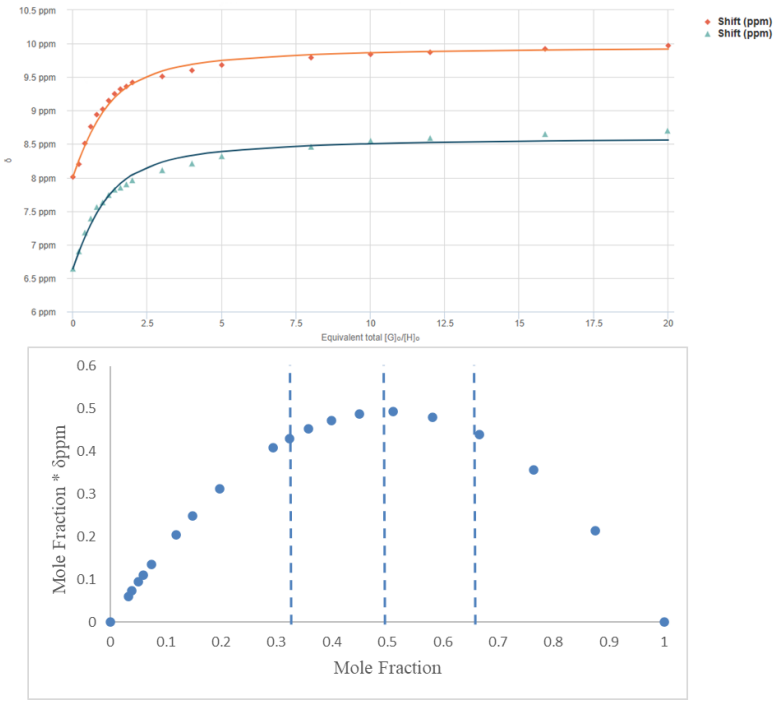

Figure 3.29: Fitted binding isotherm for the titration of **3.10** (2.5mM) in the presence of increasing concentrations of AcO^- in DMSO-d_6. The data is fitted to 1:1 binding mode and shows the chemical shifts of the NH signals throughout the titration. **(left)** Jobs Plot analysis for **3.12.AcO$^-$** complex supporting the 1:1 binding of **3.10** to AcO^-. **(right)**

To probe the anion binding behaviour of **3.10** towards $PhCOO^-$, a similar titration was carried out, with increasing concentration of anion leading again to a downfield shift of both the squaramide NH and amide NH (**Figure 3.30** (**a**)). Using Bindfit, the binding constant was found to be 278 M^{-1} (±8 %) in DMSO-d_6 when fit to a 1:1 binding mode and Jobs plot analysis supports this binding mode.

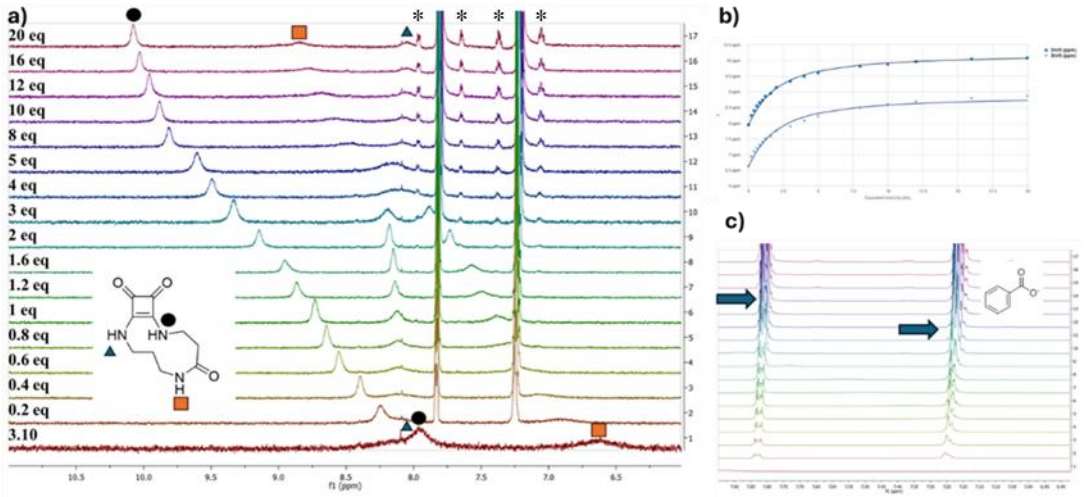

Figure 3.30: a) ^{1}H NMR stack plot of **3.10** (2.5 mM) and 0.0 – 20 eq. of TBA $PhCOO^-$ in DMSO-d_6. ($PhCOO^-$ satellite peaks notated with *) **b)** Fitted binding isotherm for the titration of **3.10** (2.5mM) in the presence of increasing concentrations of $PhCOO^-$ in DMSO-d_6. The data is fitted to 1:1 binding mode and shows the chemical shifts of the NH signals throughout the titration. **c)** zoom of the aromatic region showing the upfield shift of the phenyl protons of $PhCOO^-$

Having confirmed that the expanded macrocycle was an effective anion receptor, it was next decided to investigate the claim that **3.7** would act as a responsive anion receptor and thus would exhibit no binding in its unexpanded form. To explore this, a similar anion binding titration was conducted using **3.7** and AcO^-. Excitingly, as seen below in **Figure 3.31**, there was no apparent binding observed towards AcO^- instead displaying a slight downfield shift and ultimate disappearance of the squaramide NH signal, suggesting a possible deprotonation event. Similar minor chemical shifts and significant peak broadening were also observed for the squaramide NH upon addition of $PhCOO^-$ (See **Figure S3.103**).

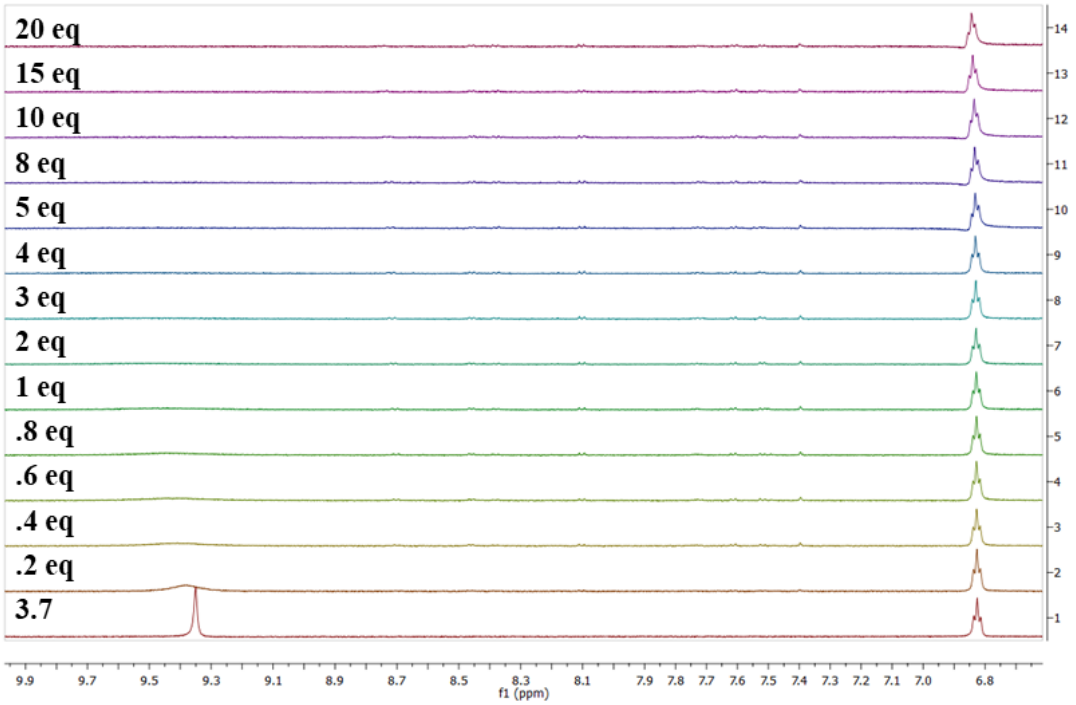

Figure 3.31: ^{1}H NMR stack plot of **3.7** (5 mM) and 0.0 – 20 eq. of TBA AcO^{-} in DMSO-d_6.

3.9.2 Anion binding studies of **3.12**

Following the promising results shown above, it was next necessary to evaluate the hypothesis that the larger cavity size, and postulated *syn/syn* alignment of the squaramide NHs would allow for a larger array of anions to bind to the receptor. To this end, a similar anion screen was run using **3.12** (See **Figure S3.104** in **Appendix**). Upon addition of 10 eq. of different anions there appeared to be little or no interaction between halides (slight ppm shifts for chloride) or with nitrate. However, once again it showed clear binding affinity towards AcO^{-} and PhCOO^{-}.

To investigate the changes in binding affinity of **3.12** towards AcO^{-} compared to **3.10**, a detailed AcO^{-} titration was carried out and the stack plot of the ^{1}H NMR spectra is shown below in **Figure 3.32**.

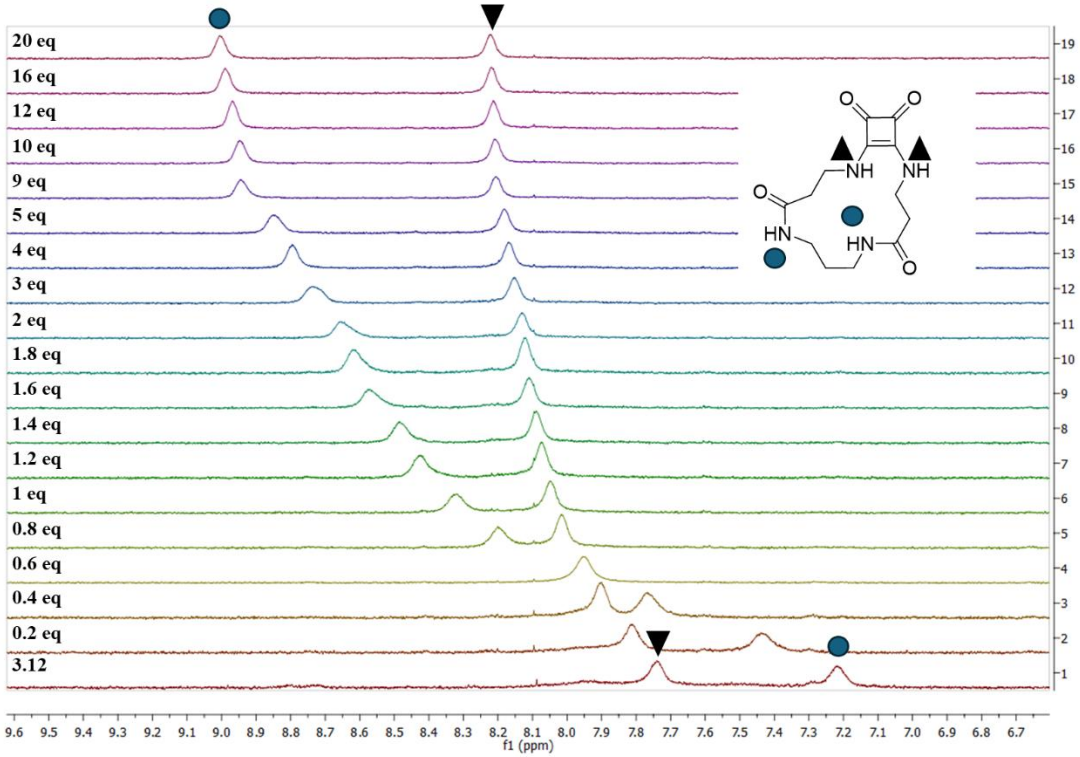

Figure 3.32: ^{1}H NMR stack plot of **3.12** (2.5 mM) and 0.0 – 20 eq. of TBA AcO^- in DMSO-d_6.

The result of the AcO^- titration showed a change in the binding mode with respect to **3.10**. The best fit for the binding of **3.12** to AcO^- was found to be a 1:2 host:guest binding mode, with K_{11} = 7313 M^{-1} (±10%) and K_{21} = 112 M^{-1} (±10%) in DMSO-d_6. This switch from 1:1 binding to 1:2 binding with AcO^- when going from **3.10** to **3.12** was not largely unexpected. With respect to **3.10**, upon ring expansion there is now four NH bond donors (two squaramide NHs and two amide NHs). This may allow for the bidentate binding of two AcO^- anions simultaneously. Observing the speciation plot below, at low concentrations there is a clear preference for the 1:1 binding mode. However, after approximately 5 eq. of anion there is a switch in binding mode, favouring a 1:2 complex (**Figure 3.33 (B)**).

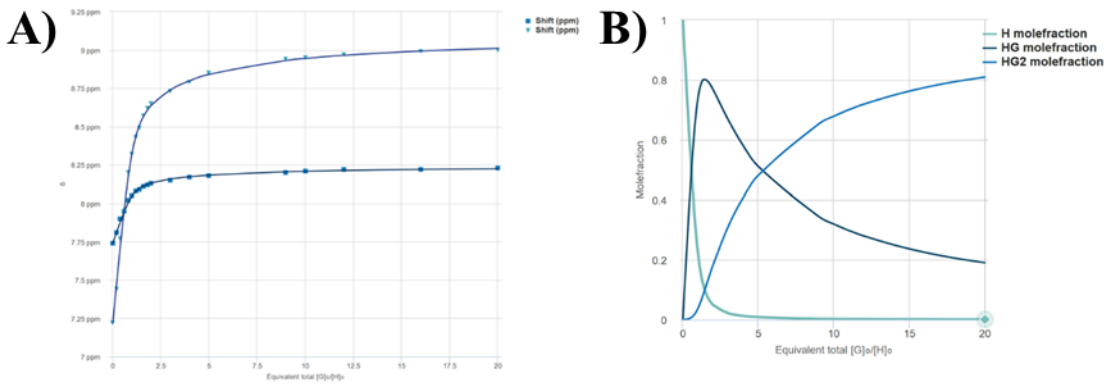

Figure 3.33: A) Fitted binding isotherm for the titration of **3.12** (2.5mM) in the presence of increasing concentrations of AcO^- in DMSO-d_6. The data is fitted to 2:1 binding mode and shows the chemicals shifts of the NH signals throughout the titration. **B)** Speciation plot for the titration of **3.12** and AcO^-.

To investigate whether this change in binding mode was consistent for other anions, a similar titration was carried out using $PhCOO^-$, with increasing concentrations of anion resulting in the downfield shifts of both the squaramide and amide NHs (**Figure 3.34**). Again, the best fit for this titration was found to be a 1:2 host:guest model, with K_{11} = 6287 M^{-1} (±9%) and K_{12} = 125 M^{-1} (±2%) in DMSO-d_6. This 1:2 stoichiometry was supported by Jobs plot analysis (**Figure 3.35**), plotting the mole fraction of the host against the mole fraction*δppm.

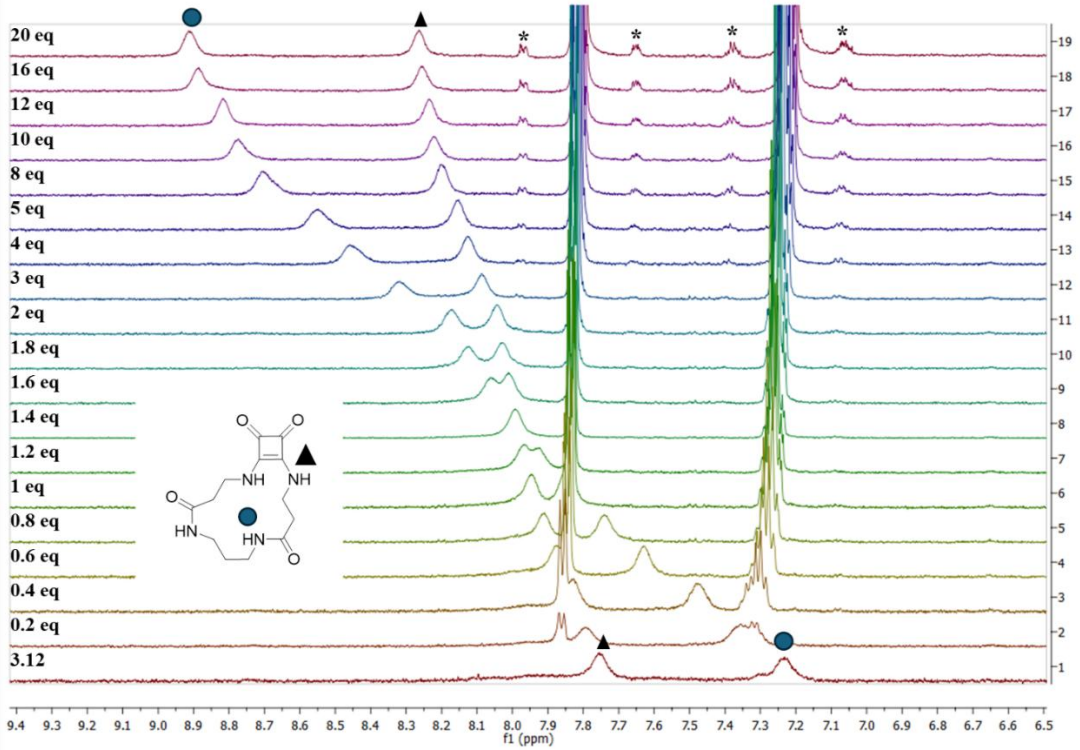

Figure 3.34: ^{1}H NMR stack plot of **3.12** (2.5 mM) and 0.0 – 20 eq. of TBA PhCOO^{-} in DMSO-d_6. PhCOO satellite peaks are labelled with ***.**

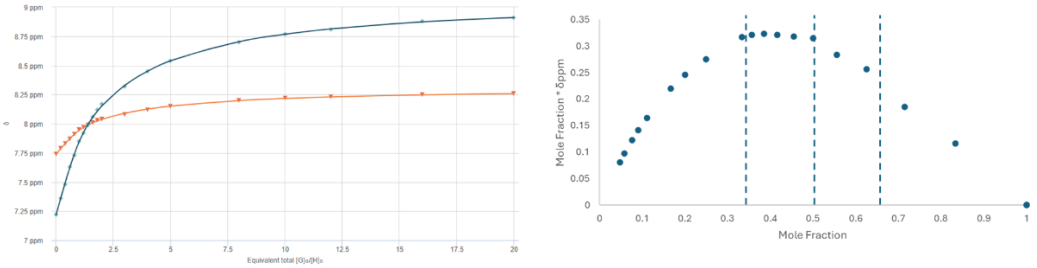

Figure 3.35: Fitted binding isotherm for the titration of **3.12** (2.5mM) in the presence of increasing concentrations of PhCOO^{-} in DMSO-d_6. The data is fitted to 1:2 binding mode and shows the chemical shifts of the NH signals throughout the titration. **(left)** Jobs Plot of supporting the 1:2 binding of **3.12** to PhCOO^{-}. **(right)**

As with the binding of AcO^{-}, it could be presumed that all four NH donors are involved in the bidentate binding of PhCOO^{-}. Observing the speciation plot below, it matches that of **Figure 3.33** almost exactly. Also observed was the upfield shift in the phenyl protons of the benzoate anion, suggesting some level of π-π interaction upon binding **(Figure 3.36)**.

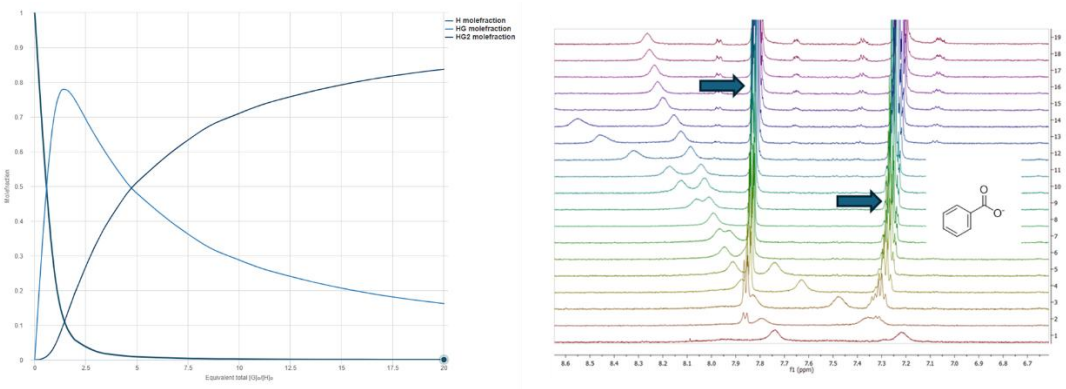

Figure 3.36: Speciation plot for the titration of **3.12** and PhCOO. **(left)** zoom of the aromatic region showing the upfield shift of the phenyl protons of $PhCOO^-$.

Although the binding studies provide strong evidence for the 1:2 complexation of receptor **3.12** with carboxylates, the precise binding conformation remains unresolved with numerous possible binding conformations possible. One possibility is that the enlarged cavity permits formation of an internal binding pocket, with the NH groups oriented inward toward the guest. Alternatively, the NH groups may adopt a perpendicular alignment with respect to the cavity, as observed with receptor **3.10**, resulting in the anion residing below rather than within the cavity (**Figure 3.37**). Moreover, the carboxylate may not bind via both oxygen atoms and instead be involved in monodentate binding through one oxygen to two NHs. However, due to the absence of suitable crystals of both the free and bound receptor, definitive structural analysis was not achieved within the timeframe of this work.

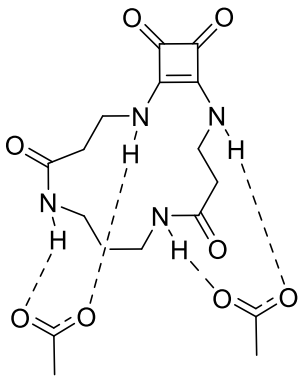

Figure 3.37: Possible 1:2 binding conformation formed between **3.12** and acetate

The results of the anion binding studies confirmed that the expanded macrocycles are effective carboxylate receptors and display an 'activation' in anion binding behaviour via chemically stimulated ring expansion. Unfortunately, crystals of both **3.10** and **3.12**

bound complexes were not obtained before the conclusion of the project, and these crystals would have given vital information as to the nature of the binding in both cases.

3.10 Conclusions and Future Work

In conclusion, a new strategy for the development of responsive anion binding was developed based on ring expansion. In the first instance, the ideal starting cyclic squaramide size was investigated and was found to be a 7-membered ring, with attempts to form 6 and 8-membered rings unsuccessful. Following this, the side chain length was investigated for its ability to undergo a ring expansion upon deprotection. This was found to proceed via a 2-carbon β-alanine moiety, with glycine and GABA derivatives not proceeding via the desired intramolecular mechanism. Having determined both the ideal cyclic squaramide and side-chain length, a novel family of responsive anion receptors, **3.7**, **3.11** and **3.13**, featuring *N*-amide linkages to an *N*-terminus protected β-alanine were synthesised. These squaramide-amino acid conjugates were accessed through the common 7-membered squaramide ring, utilising peptide coupling chemistry with moderate isolated yields of between 30 and 70%.

The anticipated rearrangement of compound **3.7** was indeed successful, with *N*-Boc-deprotection and subsequent treatment with triethylamine leading to the formation of **3.10**. X-ray analysis showed the packing of **3.10** due to intermolecular H-bonding interactions, and the orientation of the NH groups, which had implication in the binding behaviour. **3.11** also underwent a similar rearrangement, yielding the larger 15-membered macrocycle **3.12**. LCMS analysis of compound **3.13** suggested that it could undergo controlled and selective ring expansion via orthogonally stimulated expansions.

The anion binding behaviour of both **3.10** and **3.12** showed that they were selective towards carboxylates, with both receptors showing an affinity for both AcO^- and $PhCOO^-$. Importantly however, the unexpanded derivative **3.**7 showed little to no anion binding behaviour upon addition of either AcO^- or $PhCOO^-$. These observations validate the claim that this cyclic squaramide scaffold could provide a new moiety towards responsive anion binders. Interestingly, the binding mode changed from **3.10** to **3.12**, with the smaller **3.10** adopting a 1:1 complex with both AcO and $PhCOO^-$.

Conversely, **3.12** bound to both AcO^- and $PhCOO^-$ in a 1:2 host:guest complex, with a higher binding affinity for both anions with respect to **3.10**.

In terms of future work, it would be worthwhile to revise the sequential ring expansions from **3.13** to **3.12**. Isolation of the final rearrangement could provide details of the conformational changes seen upon rearrangement, and anion binding experiments could be run on **3.14**, to determine if it differs from the original mono-expanded product, **3.10**. Furthermore, obtaining crystals of the macrocycle-anion complexes would provide vital details into their binding modes. Moreover, introduction of sidechains to the β-alanine backbone could be investigated as to their possible roles in modulating the anion binding properties of the macrocycle.

Finally, investigation into whether this strategy could be modified to follow a SuRE method would be worthwhile as theoretically it could provide a synthetic pathway towards macrocyclic squaramides that would otherwise be unattainable via traditional cyclisation means (**Figure 3.38**).

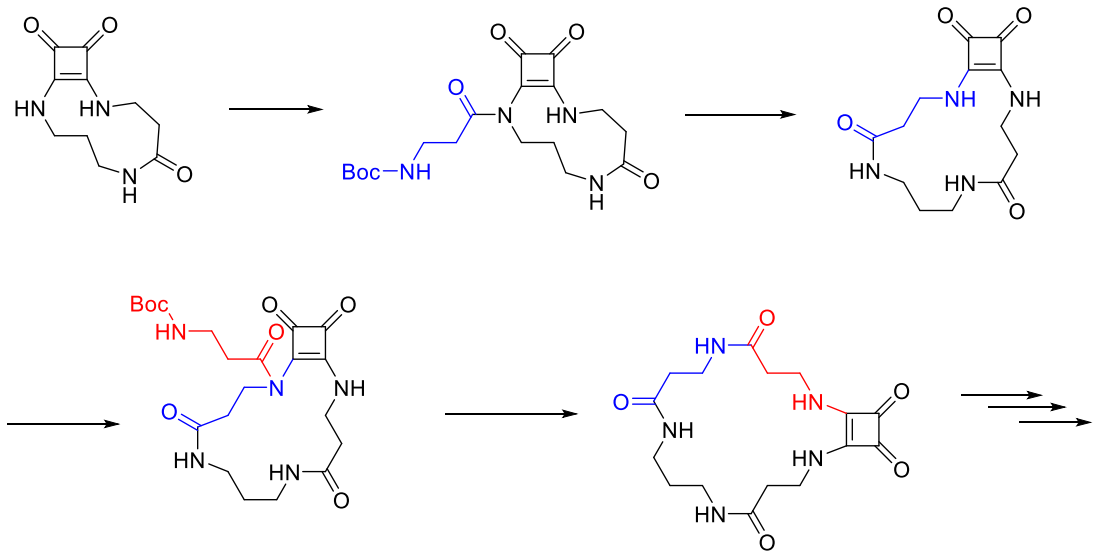

Figure 3.38: General synthetic scheme for the synthesis of macrocyclic squaramides using the SuRE method.

Chapter 4

Bio-Responsive Squaramides for the Selective Binding and Sensing of Carboxylates

4. Bio-Responsive Squaramides for the Selective Binding and Sensing of Carboxylates

4.1 Introduction

Carboxylic acids and carboxylates are fundamental in biological processes. Take the short chain fatty acids (SCFA) for example (**Figure 4.1**). SCFAs play a key role in regulating the composition and function of the intestinal microbiota[202] and are increasingly recognised for their importance to human health. Indeed, SCFAs have been shown to exert anti-inflammatory, anti-obesity, anticancer, and cardioprotective effects.[203–205] Conversely, dysregulation of SCFA levels has been associated with pathological conditions; altered SCFA profiles are emerging as biomarkers in neurodegenerative and neurodevelopmental disorders such as depression and autism,[206,207] while reduced SCFA concentrations have been observed in patients with ulcerative colitis.[208]

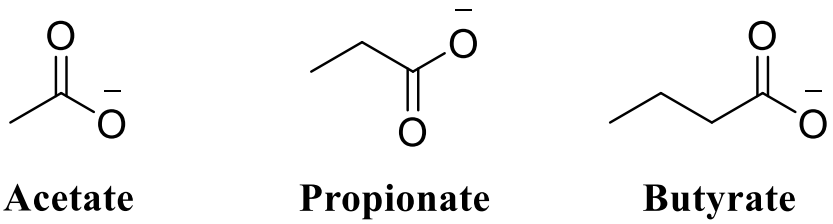

Figure 4.1: Chemical structure of the three most common SCFAs in their anionic form

Among the short-chain fatty acids, acetate is by far the most abundant, typically accounting for 60% of the total SCFA pool in the gut, with concentrations in the mM ranges.[209] Once internalised, acetate is converted into acetyl-CoA,[210] a vital metabolite that fuels the tricarboxylic acid cycle,[211] supports cholesterol biosynthesis[212] and regulates protein acetylation,[213] all of which contribute directly to cellular growth. Given its diverse roles, acetate concentration is increasingly recognised as a sensitive biomarker of physiological state. Altered levels of acetate have been reported in metabolic syndrome[214] and obesity,[215] Moreover, acetate is recently becoming more implicate in cancer metabolism, where tumour cells can exploit acetate as an alternative carbon source under hypoxic conditions. To this end, DeBerardinis and co-workers demonstrated that acetate serves as a critical fuel in glioblastoma and hepatocellular carcinoma.[216]

Beyond SCFAs, dicarboxylic acids and their derivatives occupy an equally critical position in cellular metabolism. Glutamate, for instance, is a non-essential amino acid that functions as the principal excitatory neurotransmitter in the central nervous system.[217] Dysregulation of glutamate handling has been strongly linked to excitotoxicity,[218] a process implicated in neurodegenerative disorders such as Alzheimer's disease.[219] Similarly, succinate represents a pivotal intermediate of the tricarboxylic acid cycle and perturbations in succinate levels have been associated with chronic inflammation[220] and tumour progression,[221] underscoring its emerging role as both a metabolic fuel and a signalling molecule in disease states.

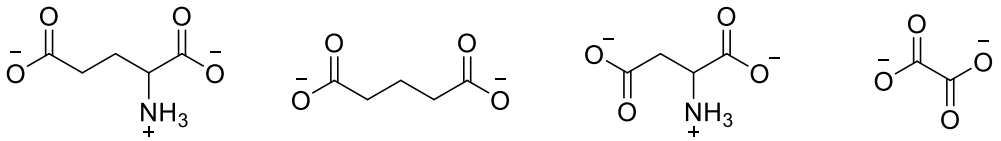

Figure 4.2: Chemical structure of common dicarboxylates in their anionic form

In bacteria, C_4-dicarboxylates are metabolised through both anaerobic and aerobic processes and are essential for bacterial growth.[222] *E. Coli* for example, contains two of these Dcu proteins, DcuA and DcuB, and function as antiporters to any combination of pairs between aspartate, fumarate, malate and succinate.[223] Since the early 2010s, increasing attention has been given to the role of C4-dicarboxylate transport (Dct) systems in bacterial physiology, with more recent efforts directed toward exploiting their inhibition as a strategy for antimicrobial intervention. Work published in 2011 by Lapouge and co-workers identified that inhibition of the *dct*A gene in *pseudomonas aeruginosa* caused a growth defect of the strain when supplemented with a number of dicarboxylates.[224]

Given their central roles in biology, strategies for the selective recognition of carboxylates have become a focal point in supramolecular chemistry. Among the motifs explored, squaramide-based receptors stand out for their well-established ability to engage carboxylates through strong hydrogen-bonding interactions. Indeed, some of the earliest examples of squaramide based anion receptors developed by Costa *et al.* showed moderate binding affinities (200 - 10000+ M^{-1}) for acetate in DMSO-d_6.[225] These receptors all demonstrated bidentate binding via both the squaramide NHs and adopted a 1:1 stoichiometry. Jolliffe and coworkers have reported numerous

examples of squaramide based amino acids capable of binding to acetate. **4.1** below features a lysine derivative whereby the side chain has been functionalised to a squaramide moiety (**Figure 4.3**).[226] This showed good affinity towards acetate with a binding constant of 1724 M^{-1} in DMSO-d_6 (0.5% H_2O) when fit to a 1:1 binding model. Conversion to the linear dimer maintained the acetate recognition properties, albeit to a lower efficacy (421 M^{-1} in DMSO-d_6 (0.5% H_2O)). In a subsequent report, modulation of the C- and N-terminus protecting groups to increase the lipophilicity of the receptor led to drastic changes in binding affinity towards acetate.[227] It should be noted however, the receptor was not selective for acetate, with much higher binding affinities measured for sulphate, while also showing binding to benzoate and chloride.

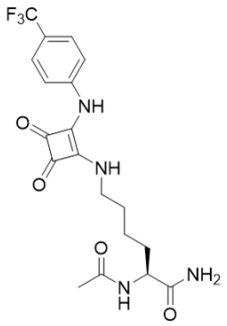

4.1

Figure 4.3: Chemical structure of compound **4.1**

Our group has reported the selective binding of acetate through a disaggregation-induced approach, by way of squaramide-naphthalimide conjugates.[228] Compound **4.2** below experiences self-aggregation in DMSO, while also quenching the emission of the naphthalimide moiety, through either the self-aggregation or the inclusion of the squaramide, with the removal of the squaramide in the scaffold resulting in emission at 450 nm. However, ^{1}H NMR experiments of different TBA anions showed that **4.2** has an affinity for AcO^-, with increasing concentrations of anion leading to significantly improved resolution of the peaks, as well as a downfield shift of the squaramide NHs (**Figure 4.4**). This binding was fit to a 1:1 binding model and gave an affinity of 422 M^{-1} in DMSO-d_6. This low affinity was attributed to the competing self-assembly behaviour. Unfortunately, however, this disaggregation did not lead to an increase in fluorescence intensity, perhaps due to the use of unsubstituted naphthalimides which are inherently weakly fluorescent. However, although **4.3** does not have the desired "switch-on" in fluorescence upon AcO^- binding, it does provide

an interesting platform about which to develop a biological responsive AcO^- probe via disaggregation induced emission.

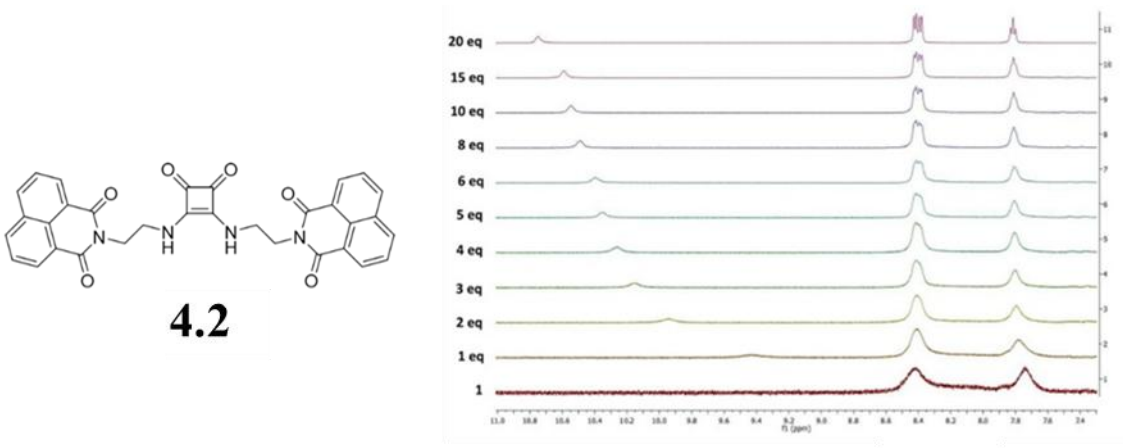

Figure 4.4: Chemical structure of **4.2** (**left**) and the changes in the ^{1}H NMR spectrum upon the addition 0–20 equivalents of TBA OAc^- in DMSO-d_6.

Squaramides have also seen utilisation in the area of dicarboxylate binding, with Costa *et al* developing a family of squaramide-ammonium based receptors capable of forming 1:1 complexes with oxalate, with compound **4.3** below having a binding constant of 30000 ± 10000 M^{-1} in MeOH.[229] In 2006, Anslyn and coworkers synthesised a tripodal squaramide-ammonium based receptor **4.4 (Figure 4.5)** for the recognition of tricarboxylates, with the inclusion of the triethyl phenyl moiety allowing for the preorganisation of the binding entities. Receptor **4.4** also demonstrated good to moderate binding affinities for dicarboxylates glutarate and succinate. (2200 and 280 M^{-1} respectively) in H_2O:EtOH 1:3 v/v.[230]

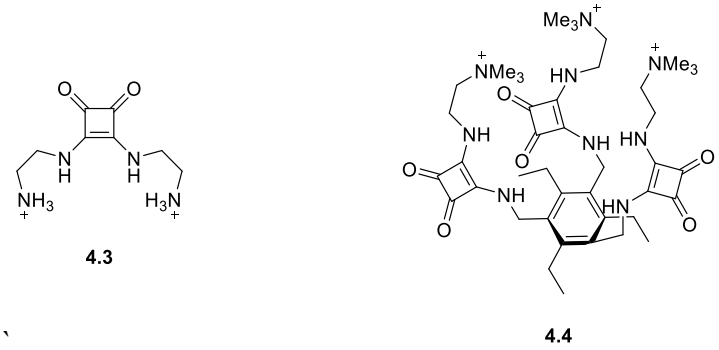

Figure 4.5: Chemical structures of compounds **4.3** and **4.4**

The preceding discussion has aimed to outline the central importance of carboxylates in biological systems and summarised key examples of squaramide-based receptors

reported in the literature. However, these receptors largely belong to the category of ‘always on’ systems, lacking the ability to be activated under specific conditions. Developing conditionally responsive carboxylate probes therefore represents a promising approach to overcome this limitation. This chapter builds on the foundations laid in the previous chapter, by taking the proof of concept to a biologically relevant application.

4.2 Chapter Objectives

The first objective of this chapter is to build upon the findings presented in **Chapter 3** by developing a series of bio-activated carboxylate receptors. This will be accomplished by replacing the previously employed *tert*-butyloxycarbonyl (Boc) and fluorenylmethyloxycarbonyl (Fmoc) protecting groups with stimuli-responsive moieties that are sensitive to biologically relevant species. Specifically, nitroreductase (NTR), a naturally occurring enzyme, and reactive oxygen species (ROS), known to be prevalent as a cellular stress response. These stimuli will be targeted using *para*-nitrobenzyl and phenylboronic ester derivatives, respectively. To enable conjugation of these triggers to the parent macrocycle, each will first be linked to the *N*-terminus β-alanine via carbamate linkage as outlined in **Figure 4.6**.

4.5 **4.6**

Figure 4.6: Chemical structures of NTR-responsive anion receptor **4.5,** and ROS-responsive anion receptor **4.6**.

In the case of compound **4.5**, it was proposed that the reduction of the aryl nitro group to the corresponding amine would lead to a quinone methide type elimination and subsequent rearrangement to yield the expanded macrocycle, outlined schematically in **Scheme 4.1**.

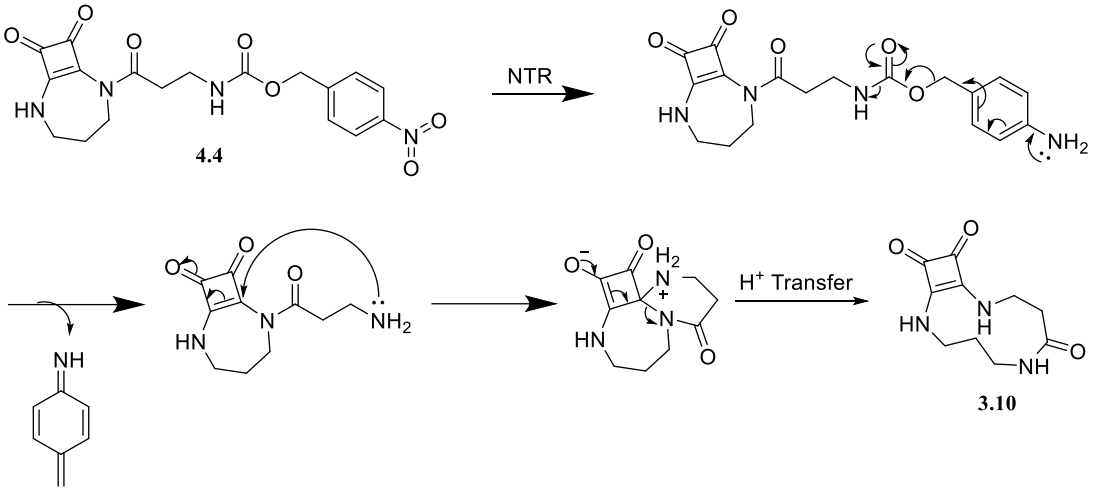

Scheme 4.1: Proposed mechanism for the NTR-mediated rearrangement of compound

The second objective is to build upon this design further, where a profluorophore will be incorporated into the central scaffold to provide a fluorescent response to the stimuli while simultaneously releasing an active carboxylate receptor. As previously discussed in **Chapter 3**, the anion-binding behaviour observed for the liberated, expanded macrocycle suggests that one of the squaramide NH protons does not participate in binding. From a design perspective, this observation supports the rationale for functionalisation at this site with a fluorophore, without effecting the anion binding behaviour. Ideally, the chosen fluorophore would not only be amenable to conjugation with the macrocyclic core but also exhibit a simultaneous fluorescence modulation in response to an analyte, thereby forming the basis for a responsive sensing system. As previously demonstrated in **Chapter 2**, 1,8-naphthalimides are particularly well-suited, as their fluorescence properties are strongly influenced by substitution at the 4-position but also, importantly for this design, their anhydride functionality readily accommodates condensation with a broad range of primary amines. This allows for the introduction of an amino acid derivative at the anhydride site via its *N*-terminus, leaving the C-terminus available for conjugation to the non-binding squaramide NH. The proposed design of this scaffold is shown in **Scheme 4.2** (compound **4.7**). To realise this design, the naphthalimide fluorophore would first need to be synthesised. This will involve initial condensation of a carboxylic acid handle onto the anhydride site, providing a point of attachment for subsequent conjugation to the squaramide NH. The *para*-nitrobenzyl group could then be introduced via triphosgene-mediated carbamate formation at the naphthalimide's amino group, in a manner analogous to the synthetic approach described in Chapter 2. This would allow

for conjugation to **4.5** via COMU-coupling conditions, yielding **4.7**. The proposed synthetic approach to compound **4.7** is shown below. Firstly, a γ-amino-butyric acid derivative will be condensed into the naphthalimide. This 4-carbon derivative will aim to reduce any possible steric hinderance that may limit the coupling step further into the synthesis. Also, it is necessary to protect the C-terminus as to avoid competing side reaction when functionalising the NTR-responsive unit. Once synthesised, the nitro group will reduce to the corresponding amine, which would then be carbamate linked to a *para*-nitrobenzyl group. Finally, the free carboxylic acid will be deprotected *via* *tert*-butyl deprotection to allow for functionalisation to compound **4.5**

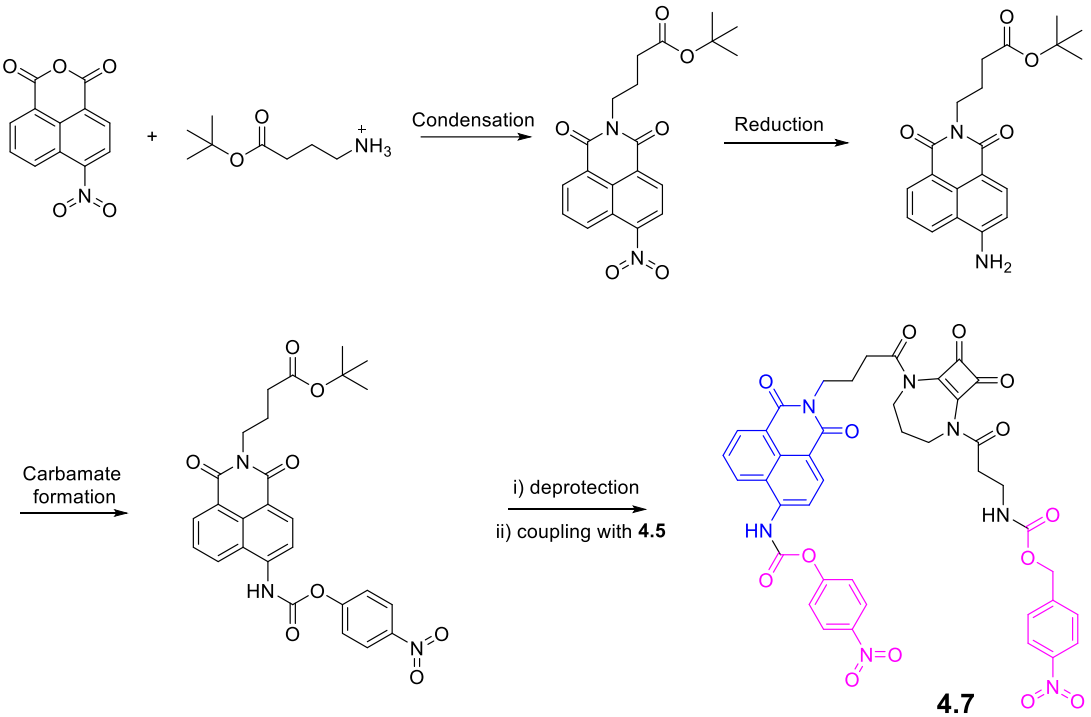

Scheme 4.2: Synthetic outline for the synthesis of compound **4.7**.

Furthermore, as is noted in **Chapter 3**, upon rearrangement the receptor may undergo self-aggregation. This behaviour has been observed with previous squaramide-naphthalimide conjugates,[137,228] and this results in the fluorescence of the naphthalimide moiety being substantially quenched. However, this fluorescence may also be "switched-on" through Disaggregation Induced Emission (DIE), so it is reasonable to expect similar behaviour in this instance. Reduction of the nitro groups of **4.7** would have two effects: (a) release of the free amine of the β-alanine arm resulting in the rearrangement and subsequent aggregation of the receptor, and (b) the release of the free amine of the 4-position of the naphthalimide. While this would be

expected to result in a ratiometric change in emission from blue to green, the self-aggregation behaviour of the sensor may perturb this expected behaviour. If this was the case, it could be expected that green fluorescence would then be "switched on" by binding with AcO^-, allowing the design to act as a dual NTR and AcO^- sensor (**Figure 1.6**). This dual modality may allow for a strategy towards investigating possible correlations between carboxylate concentrations and other chemical species within cancer cells.

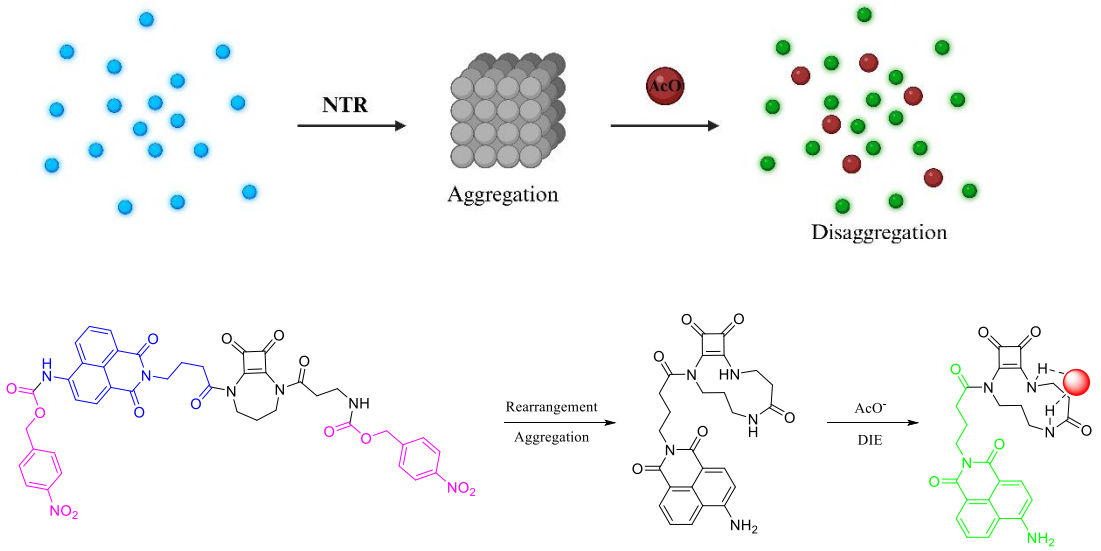

Figure 4.7: Graphical representation of the proposed mode of action of **4.7 (top)** Proposed chemical structures and fluorescence modulation following rearrangement (**Bottom**).

In the following sections, the synthesis of two novel bio-responsive receptors will be discussed along with discussion of any synthetic issues encountered as the bio-responsive trigger was modulated to allow for the targeting of different analytes.

4.3 Synthesis of NTR-responsive Anion Binder.

The synthesis of compound **4.5** involved a multistep synthesis which firstly involves the synthesis of compound **4.8**. This involved carbamate linking the *para*-nitrobenzyl responsive group to the *N*-terminus of the β-alanine. This reaction was carried out according to **Scheme 4.3** below where β-alanine was stirred in the presence of 4-nitrobenzylchlorofomate under basic conditions in 1,4-dioxane:water resulting in the successful formation of **4.8** in 55% yield after purification by column chromatography.

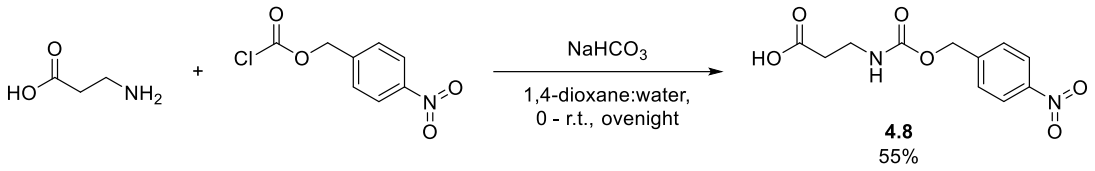

Scheme 4.3: Synthetic scheme for the synthesis of **4.7**

^{1}H NMR analysis confirmed the formation of the product with the characteristic carboxylic acid OH appearing at 12.22 ppm, as well as the amide NH at 7.45 ppm as shown in **Figure 4.8** below, along with the LC trace suggesting the high degree of purity.

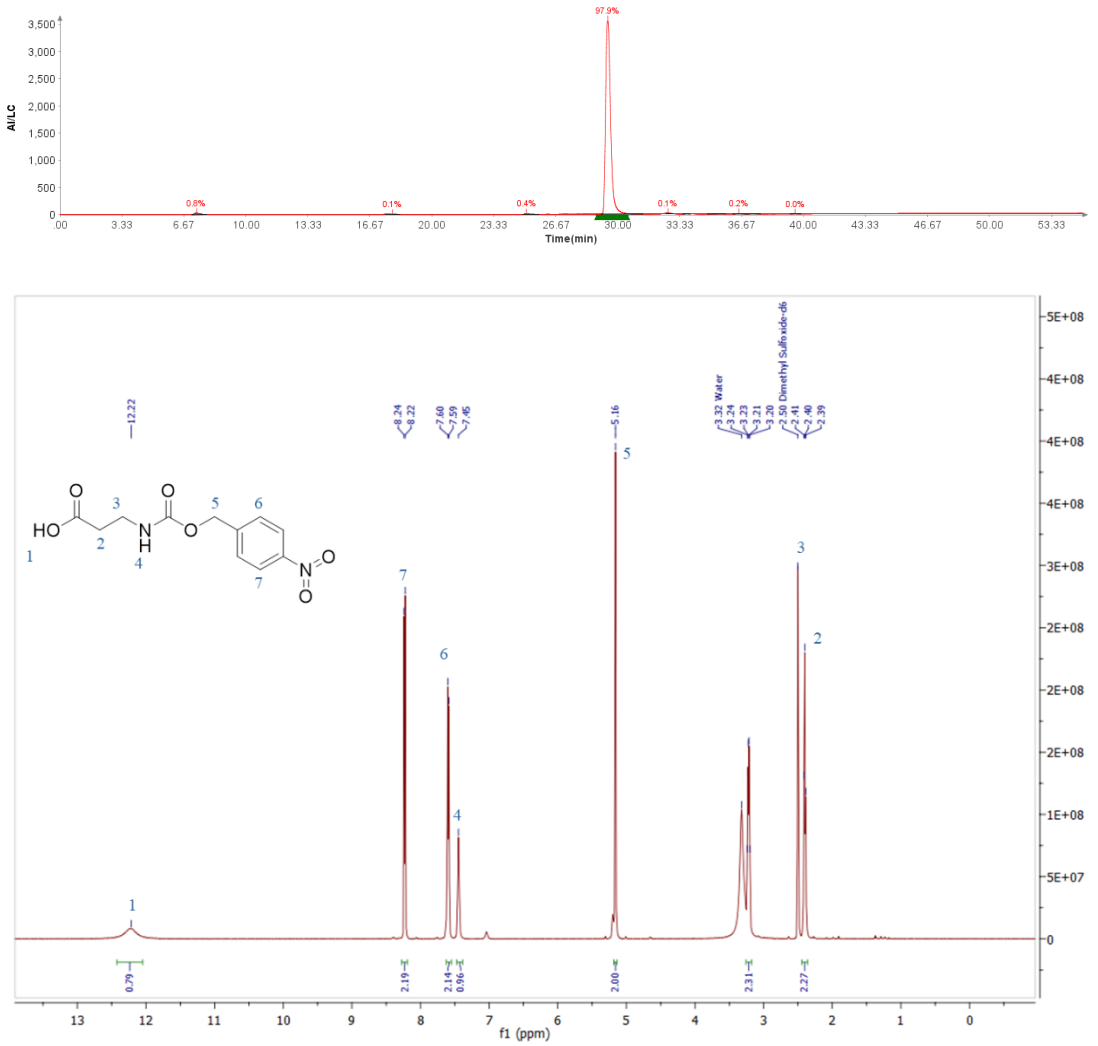

Figure 4.8: LCMS of **4.8 (top)** and ^{1}H NMR of **4.7** in DMSO-d_6 **(bottom).**

The next step of the synthesis was to convert the carboxylic acid of compound **4.8** to the succinimide ester, to allow for functionalisation to the squaramide scaffold. This

was done using N-hydroxysuccimide and the coupling reagent EDCI. This synthetic scheme is shown below in **Scheme 4.4** whereby **4.8** was stirred in DCM along with EDCI.HCl, followed by addition of NHS. After allowing to stir at r.t. overnight, aqueous workup yielded **4.9** in an 85% yield and was used without further purification.

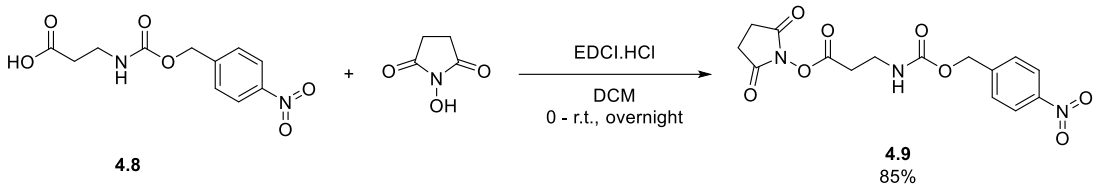

4.8 **4.9** 85%

Scheme 4.4: Synthetic scheme of **4.8**

Confirmation of the successful conversion to **4.9** can be clearly seen in the ^{1}H NMR (See appendix **Figure S4.9**). The disappearance of the carboxylic acid OH is matched with the appearance of a new signal at 2.82, integrating for 4 protons. This signal is characteristic of the 4 methylene protons of the succinimide portion of the molecule. Similarly, observing the ^{13}C below, (**Figure 4.9**), the carbonyl carbons of the succinimide were observed at 170.1 ppm, further suggesting the successful formation of **4.9**.

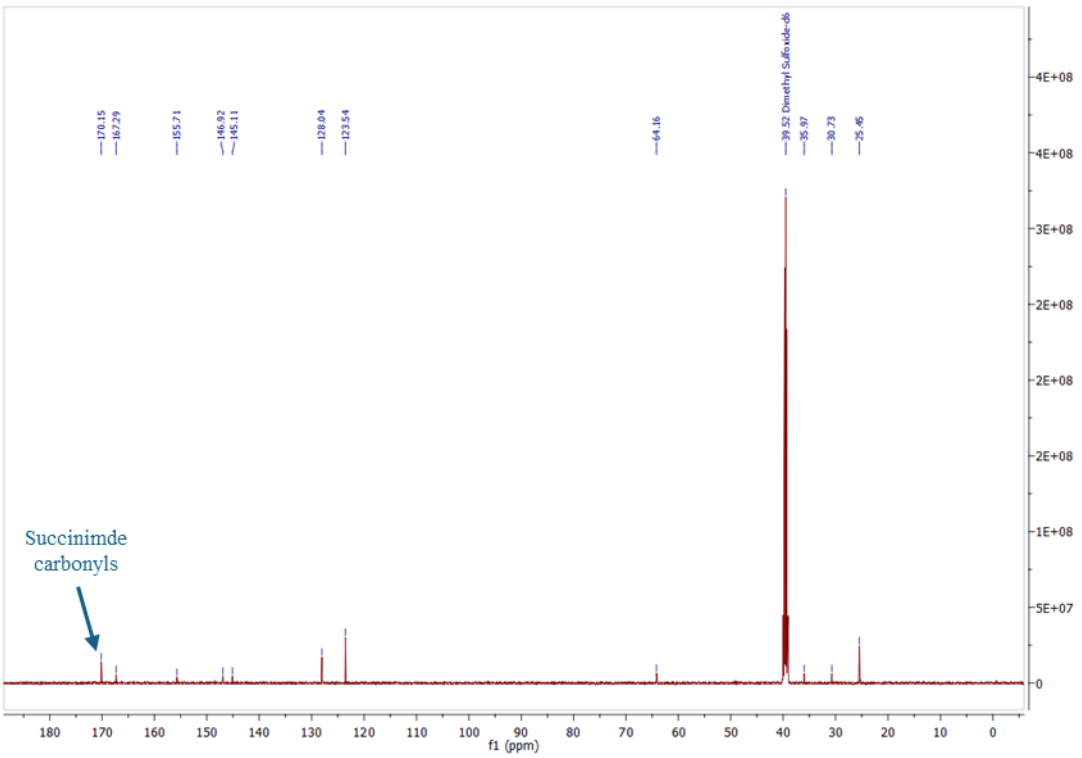

Figure 4.9: ^{13}C NMR of compound **4.9** DMSO-d_6.

With **4.9** in hand, the final step was to functionalise to the squaramide scaffold. This was done via **Scheme 4.5** below and follows an analogous pathway as the synthesis developed in Chapter 3. Briefly, **4.9** was stirred under basic conditions along with compound **3.5** to yield the bio responsive receptor **4.5** in a 32% yield following column purification. This low yield could be due to the use of DMSO as the reaction solvent, with aqueous workup to remove DMSO possibly causing losses of the product also.

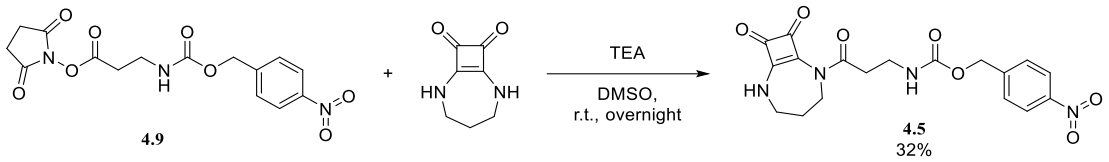

Scheme 4.5: Synthetic pathway of **4.5**

As seen below in the ^{1}H NMR in **Figure 4.10**, the formation of compound **4.5** is evident by the appearance of the squaramide NH signal as a broad singlet 9.33 ppm. The benzyl protons can be clearly seen as doublets integrating for two protons at 8.22 and 7.58 ppm, as well as the carbamate NH, appearing as a triplet at 7.44 ppm/ moving further downfield, the methylene protons of the nitrobenzyl portion of the molecule are still seen at 5.16 ppm. Finally, the methylene protons of the squaramide scaffold can be seen at 3.84, 3.39 and 1.96 ppm. Moreover, the ^{13}C NMR shows the characteristic squaramide carbonyls at 188 and 179 ppm.

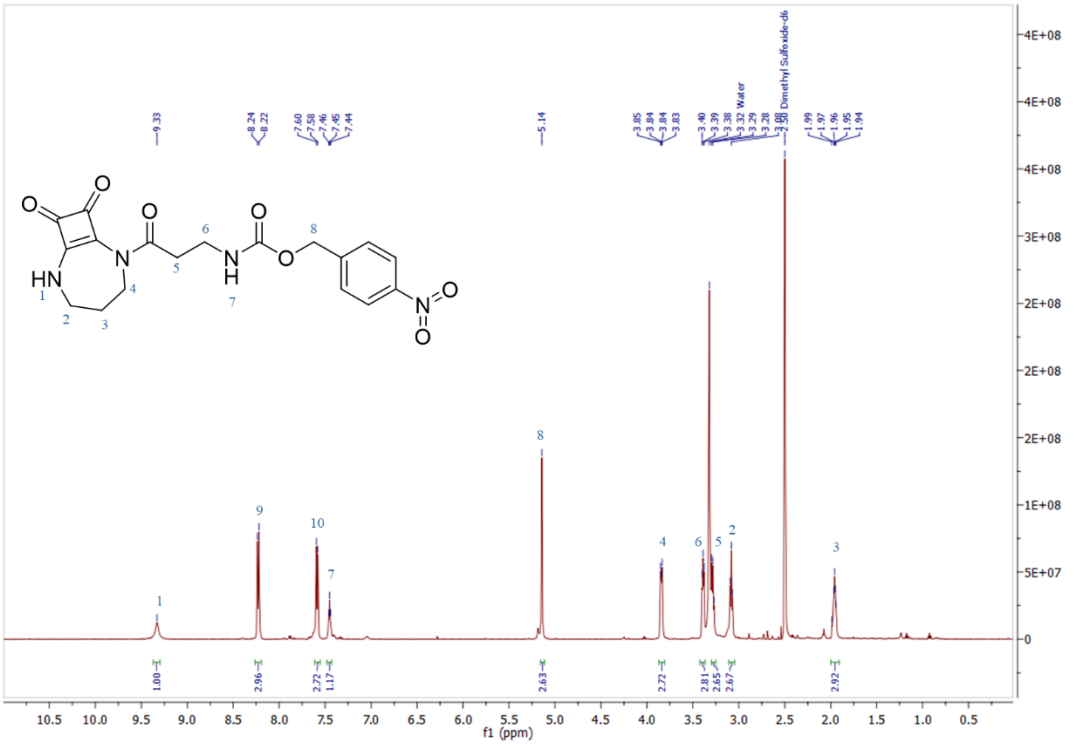

Figure 4.10: ^{1}H NMR of **4.5** in DMSO-d_6.

The purity of the compound was then confirmed via LCMS, with the chromatogram in **Figure 4.11** showing one peak at approx. 30 mins, with ionisation at 403 and 425, corresponding to $[M+H]^+$ and $[M+Na]^+$ of **4.5** respectively.

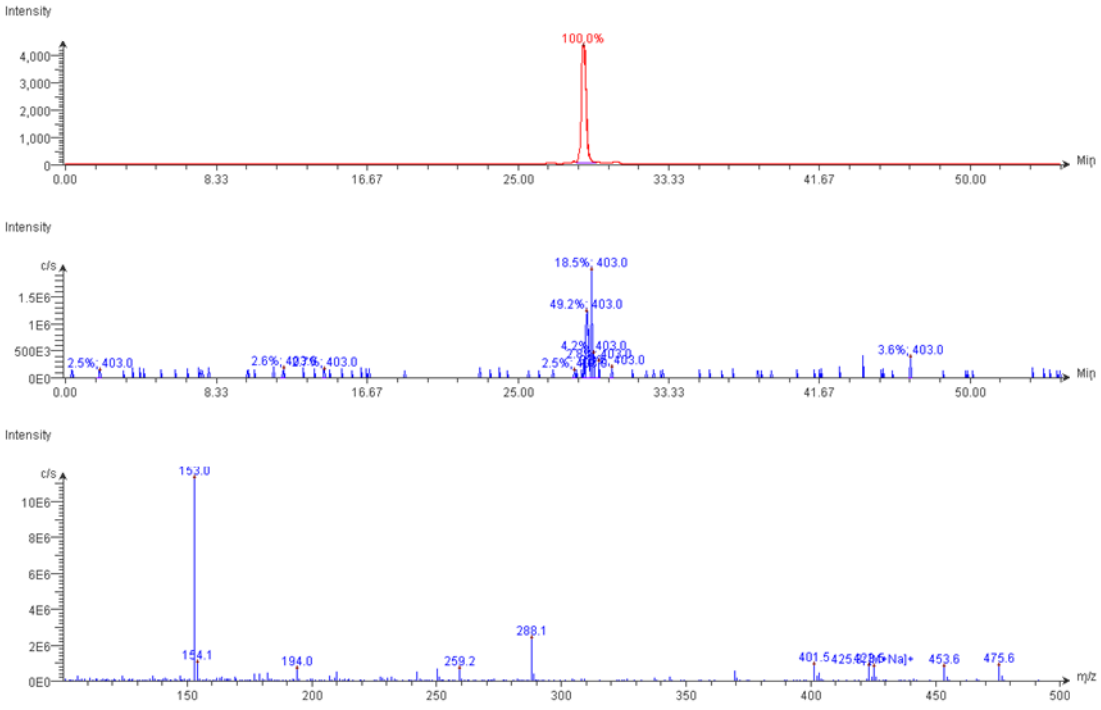

Figure 4.11: LCMS analysis of **4.5**

Finally, further confirmation of the successful synthesis of **4.5** was also confirmed *via* HRMS analysis with observed ionisation at 403.1253 and 425.1069, which correspond to the $[M+H]^+$ and $[M+Na]^+$ ions of **4.5 (Figure 4.12).**

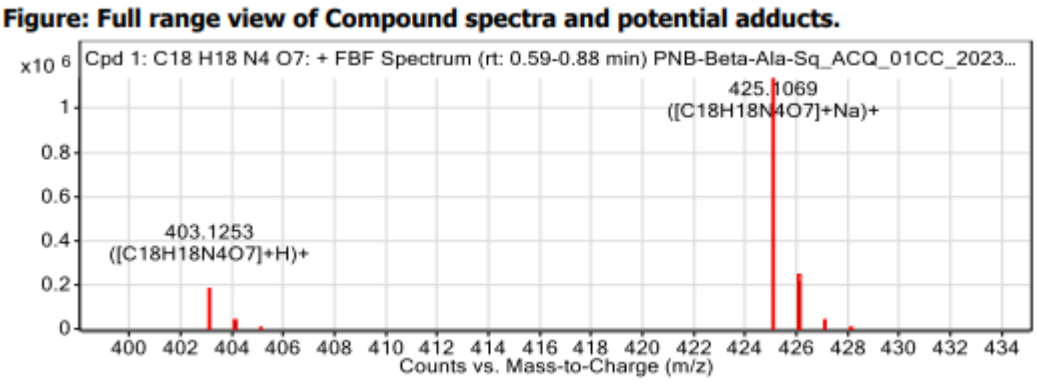

Figure 4.12: HRMS of **4.5**

4.4 Synthesis of ROS-responsive Anion Binder.

Using the above synthetic route, it was next decided to develop a ROS responsive derivative using a phenylboronic ester as the cleavable linker. As the chloroformate was not readily available, it was first generated *in situ* under triphosgene conditions prior to addition of β-alanine (**Scheme 4.6**). However, after reaction of the phenylboronic ester protected benzyl alcohol with phosgene to form the reactive chloroformate intermediate, LCMS analysis showed no reaction between β-alanine and the chloroformate intermediate.

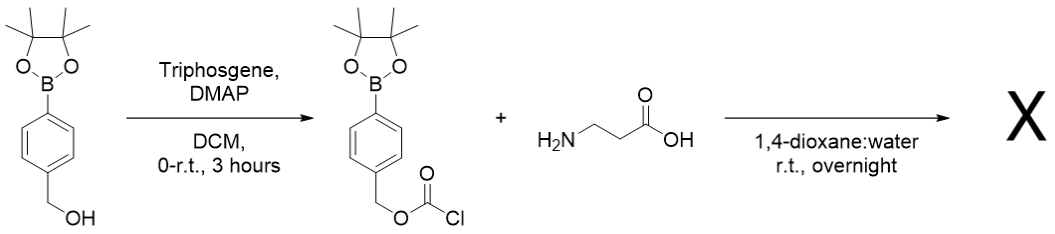

Scheme 4.6: Attempted synthesis of ROS-responsive handle using triphosgene conditions

This observation brought into question the efficacy of the reaction with triphosgene to form the intermediate. To investigate this, a secondary pathway was derived which first involved the synthesis of compound of an *N*-acyl imidazole, **4.10**, following the scheme below in **Scheme 4.7**. It was hoped that, although the activated acid would be less reactive than the chloroformate derivative, it would at least be stable enough to analyse and confirm that activation of the alcohol was possible.

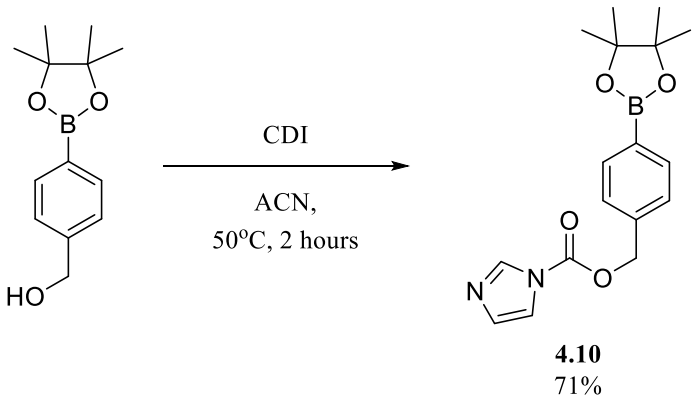

Scheme 4.7: Synthesis of compound **4.10**

Formation of the activated acid was confirmed using NMR and HRMS analysis (See **Appendix**). Following this it was again decided to react **4.10** with β-alanine in 1:1 dioxane:water but this showed no formation of the desired product. In an effort to remove the biphasic nature of the reaction, the *tert*-butyl protected hydrochloride salt of β-alanine was used to allow the reaction to be carried out in DCM (**Scheme 4.8**). However once again there was no indication of reaction between the activated acid and the amine as measured by LCMS.

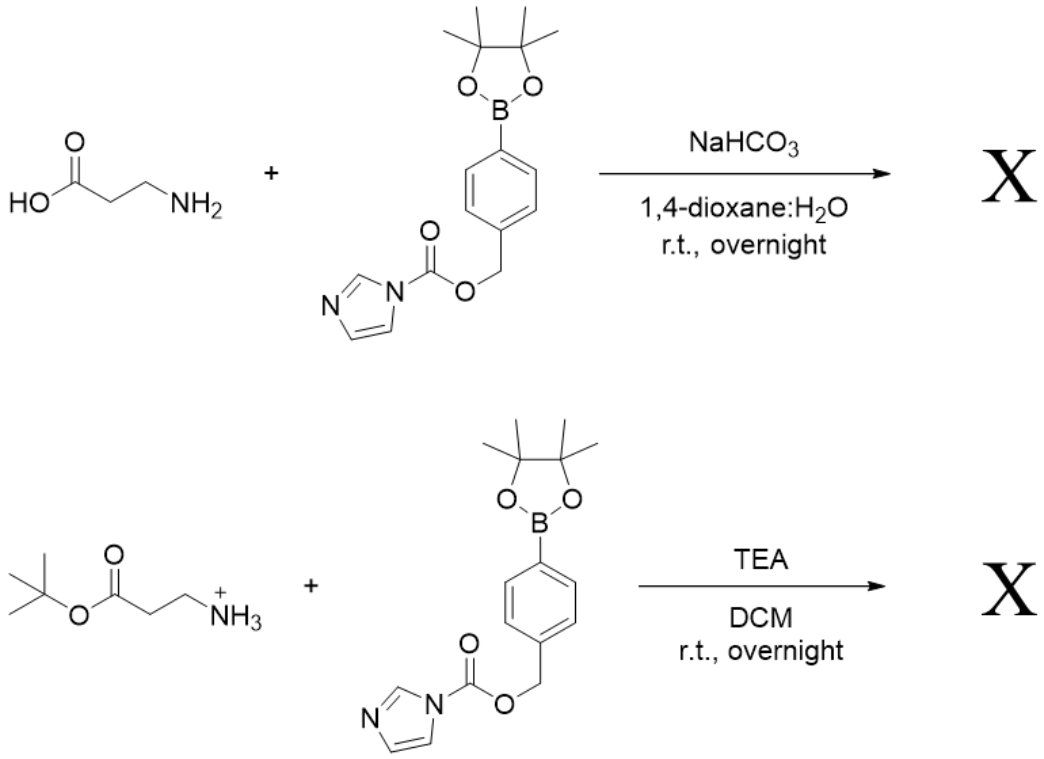

Scheme 4.8: Attempted synthesis of ROS-responsive handle via **4.10**

4.4.1 Alternative Design Strategy

Upon encountering the above synthetic challenges, it was decided that it would be worthwhile to review the literature to find other ROS-responsive units that would be suitable for functionalisation with β-alanine. To this end, the α-keto acid moiety was of particular interest, due to its ability to undergo rapid oxidative decarboxylation.[231] Indeed, this reaction has been utilised for the release of benzoic acid *via* H_2O_2 mediated decarboxylation of benzoylformic acid.[232] Furthermore, this strategy has also been employed for the oxidation of benzil, a 1,2-diketone, in the development of fluorescein and BODIPY peroxide probes.[233,234] Excitingly, α-ketoacetamides have also been reported in probe design, showing rapid oxidative decarboxylation in the presence of H_2O_2 releasing a free amine.[235] Its proposed mechanism of action is described below (**Scheme 4.9**). Firstly, the α-ketoamide undergoes nucleophilic attack by the hydroperoxide anion, followed by a Baeyer-Villiger type rearrangement. This is then followed by hydrolysis to a carboxylic acid, releasing CO_2 and a free amine.[236]

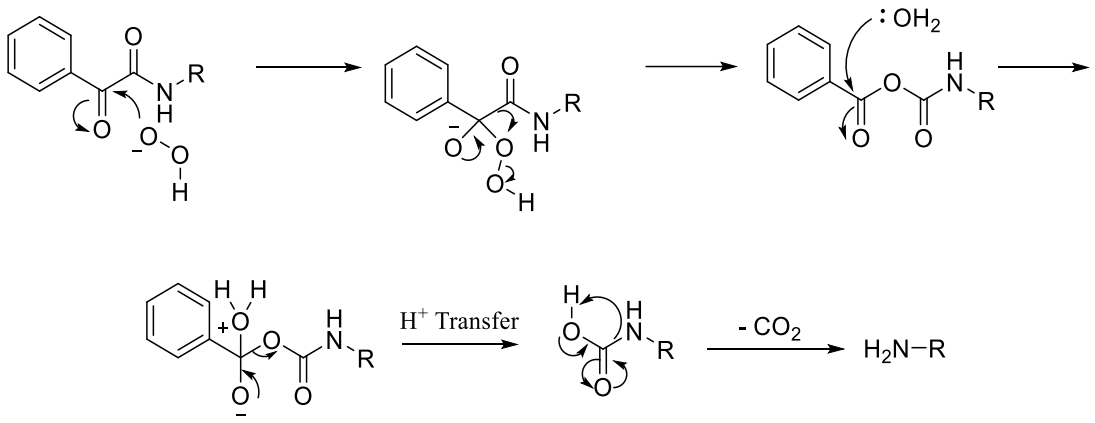

Scheme 4.9: Proposed reaction mechanism for the release of tail unit upon reaction with peroxide.

This mechanism shows clear applicability with the ring expansion strategy described thus far, with coupling of phenylglycoxalic acid to the *N*-terminus of β-alanine forming the ROS-responsive unit. This would then be conjugated to **3.5**, to give the responsive scaffold **4.11**. Exposure to H_2O_2 would then release the free amine via the mechanism in **Scheme 4.9** and allow for the spontaneous ring expansion to occur (**Scheme 4.10**).

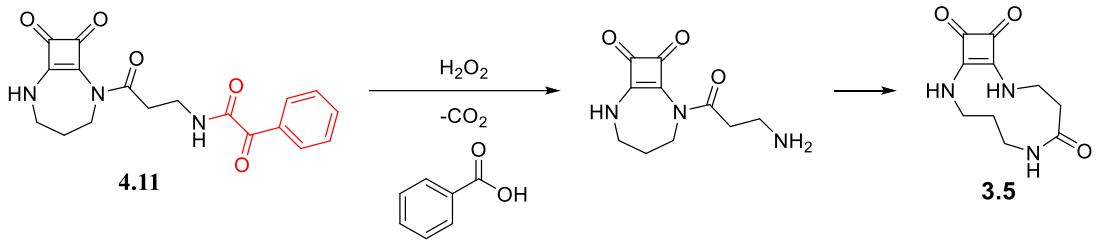

Scheme 4.10: Proposed H_2O_2-mediated ring expansion of **4.11** to give **3.5.**

The first step of synthesising **4.11** was to couple the acid to the *N*-terminus of β-alanine. This was carried out using standard PyBOP coupling conditions shown in **Scheme 4.11** below, giving the title compound in a 52% yield following purification.

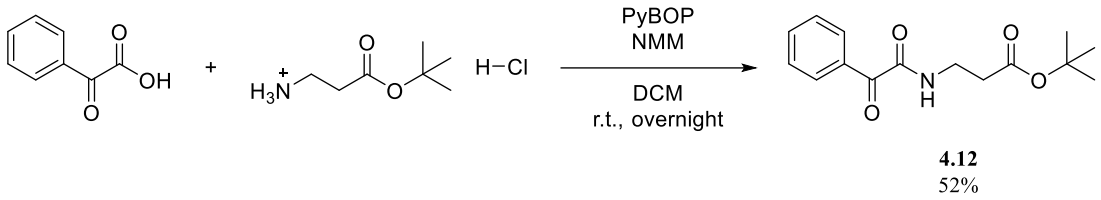

Scheme 4.11: Synthesis of compound **4.12**

Confirmation of the formation of the *tert*-butyl protected derivative can be seen in the ^{1}H NMR of **Figure 4.13**. The three sets of signals for the phenyl portion of the compound are visible at 7.96, 7.72 and 7.56 ppm as well as the newly formed amide NH at 8.97 ppm showing successful coupling. Finally, the protons of the *tert*-butyl group can be seen at 1.41 ppm.

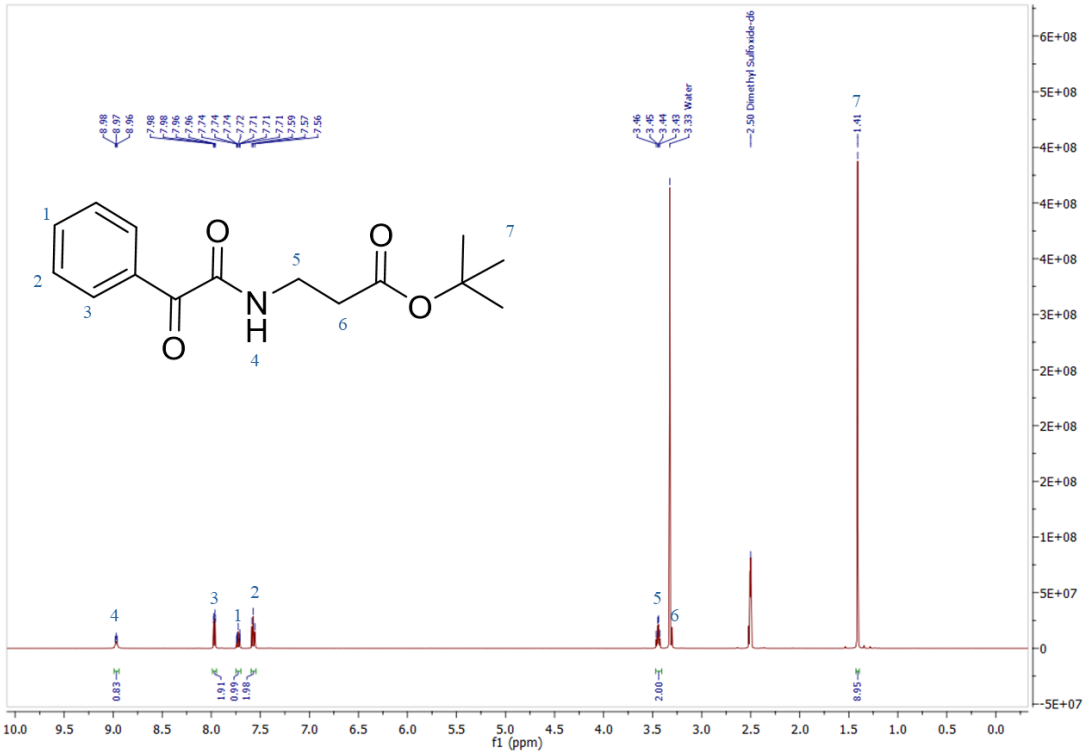

Figure 4.13: ^{1}H NMR of compound **4.12**

Moreover, observing the ^{13}C NMR the three carbonyls can be seen at 190, 170 and 164 ppm, as well as the four aromatic carbons between 128 and 134 ppm (**Figure 4.14**).

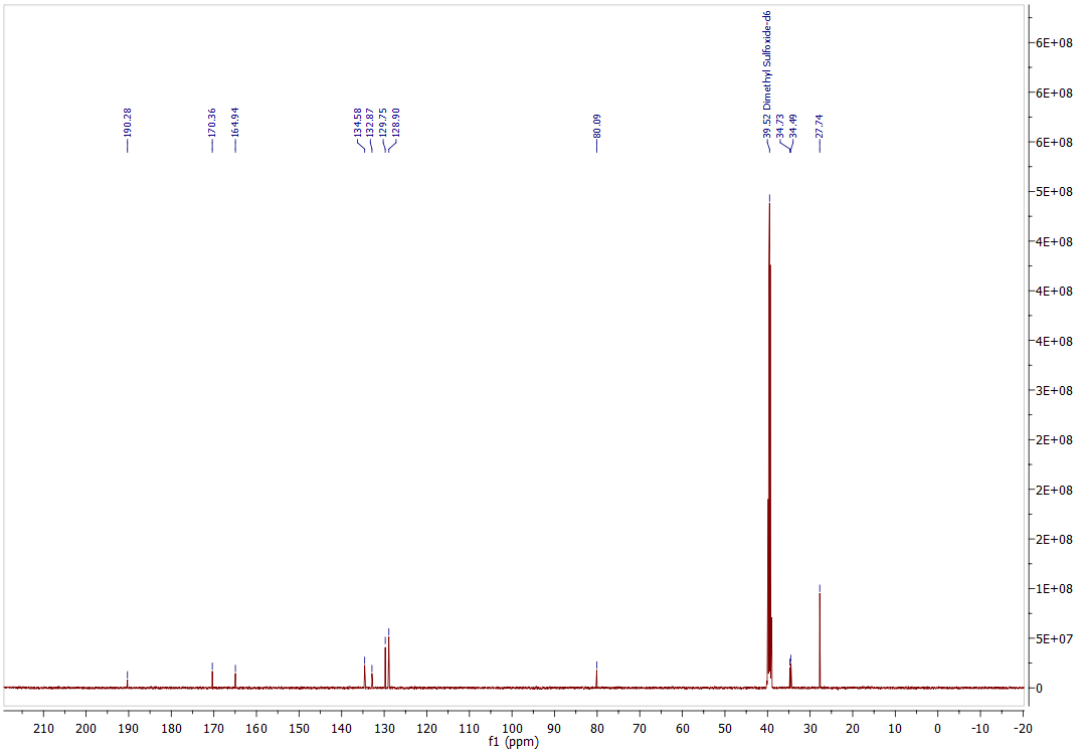

Figure 4.14: ^{13}C NMR of compound **4.12**

The next portion of the synthetic pathway was carried out over two steps, with the first using TFA:DCM to remove the *tert*-butyl group to liberate the acid, and then reaction of the acid with NHS to form the succinimide, using EDCI as the coupling reagent. The free carboxylic acid was not isolated and was instead used directly into the next step. The below reaction scheme (**Scheme 4.12**) outlines the synthesis which yielded the target compound in an overall isolated yield of 47% following aqueous workup.

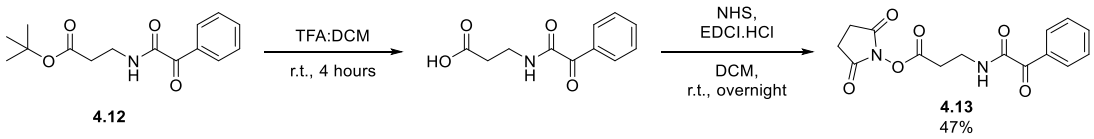

4.12 → **4.13** 47%

Scheme 4.12: Synthesis of compound **4.13**

Analysis of the ^{1}H NMR below, it can be clearly seen that conversion to the NHS-ester was successful, with the disappearance of the *tert*-butyl signal and the appearance of the signal at 2.82 ppm, integrating for 4 protons, which corresponds to the 4 methylene protons of the succinimide moiety (**Figure 4.15**).

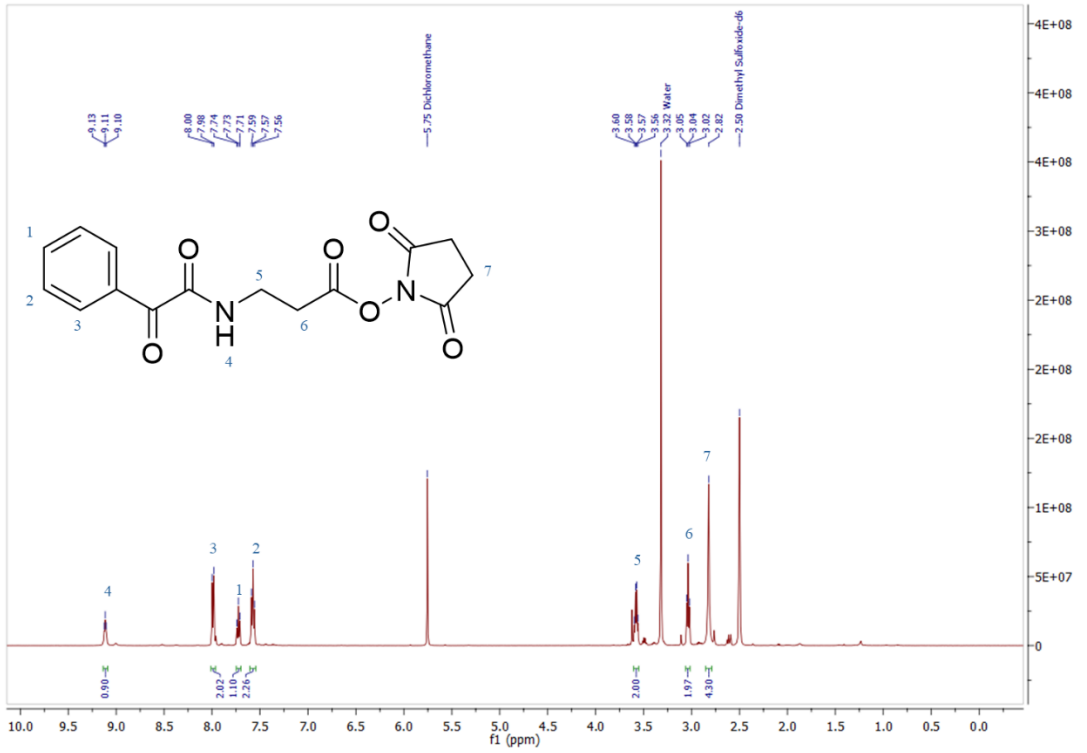

Figure 4.15: ^{1}H NMR of compound **4.13**

The final step was then to conjugate the ROS-responsive β-alanine derivative to the central squaramide core. This again was done using similar methods as before and is shown in **Scheme 4.13** below.

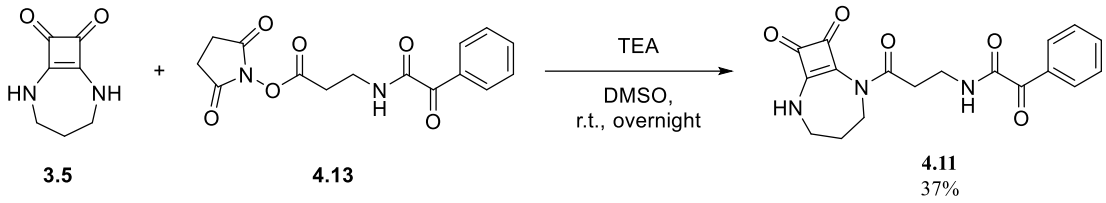

Scheme 4.13: Synthetic pathway for compound **4.11**

Observing the ^{1}H NMR below in **Figure 4.16**, it can be clearly seen that the above reaction was successful with the appearance of the squaramide NH peak at 9.34 ppm. Furthermore, the methylene protons of the 7-membered squaramide ring can also be seen at 3.88, 3.4 and 1.98 ppm. LCMS analysis of compound **4.11** also showed a high degree of purity, with [M + H+] of 356.1 observed under the peak at 29 mins. Finally, HRMS analysis confirmed the formation of the product with analysis showing ionisation at 356.1243 and 378.1060, corresponding to $[M+H]^{+}$ and $[M + Na]^{+}$ respectively of compound **4.11 (Figure 4.17).**

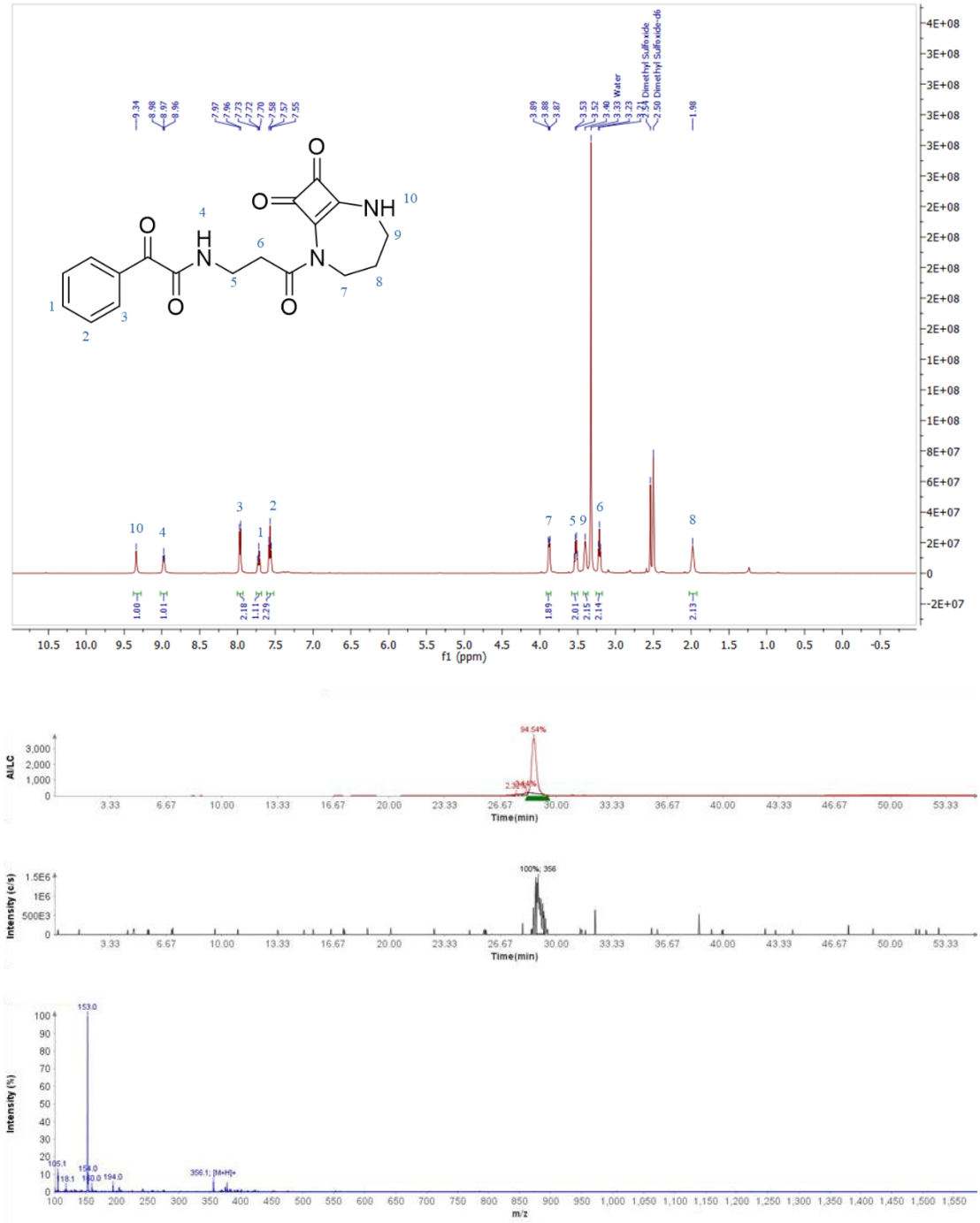

Figure 4.16: ^{1}H NMR of compound **4.11 (top)** and LCMS chromatogram **(bottom).**

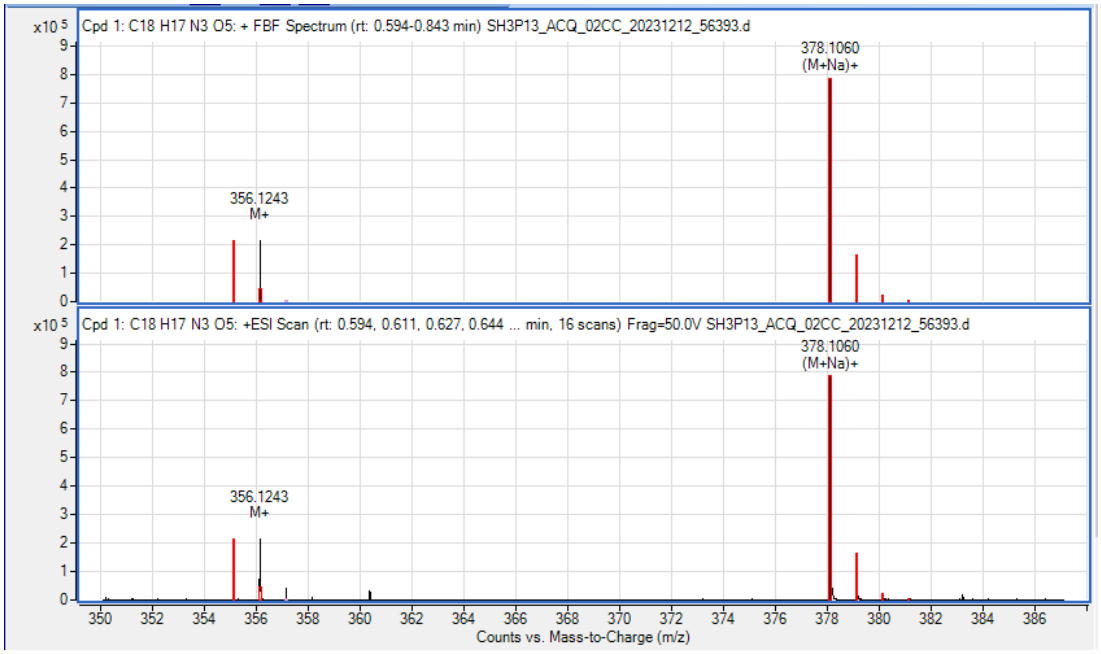

Figure 4.17: HRMS of **4.11.**

With both **4.5** and **4.11** in hand, the next phase of the project was to address the 2nd objective and synthesise the dual responsive sensor molecule **4.7**. The synthesis of this target will be outlined in the sections below.

4.4 Attempted Synthesis of NTR-Responsive Anion Sensor

4.4.1 Synthesis of Naphthalimide Fluorophore

The synthesis of compound **4.15** is shown below in **Scheme 4.14**. Here, the *tert*-butyl γ-amino-butyric acid hydrochloride was condensed into 4-nitro-1,8-naphthalic anhydride via reflux under basic conditions to yield the nitro-naphthalimide in an isolated 78% yield following recrystallisation from EtOH. This was then converted to the corresponding amino derivative via hydrogenation with Pd/C and H_2 to give **4.15** in near quantitative yields.

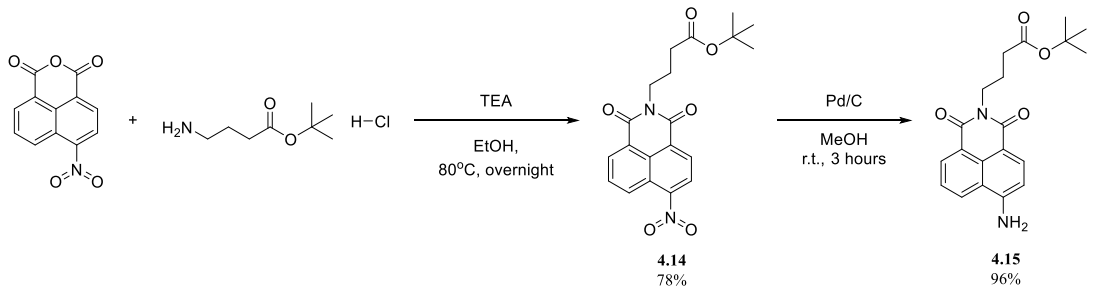

Scheme 4.14: Synthetic scheme for the synthesis of compound **4.15**

Observing the ^{1}H NMR below in **Figure 4.18**, the successful synthesis of compound **4.15** is evident by the appearance of the peak corresponding to the amine in the 4-position at 4.99 ppm. Furthermore, the *tert*-butyl protons can be found at 1.42 ppm, with the methylene protons of the γ-amino-butyric acid moiety at 4.21, 2.35 and 2.05 ppm. LCMS analysis also confirmed the high degree of purity of the compound.

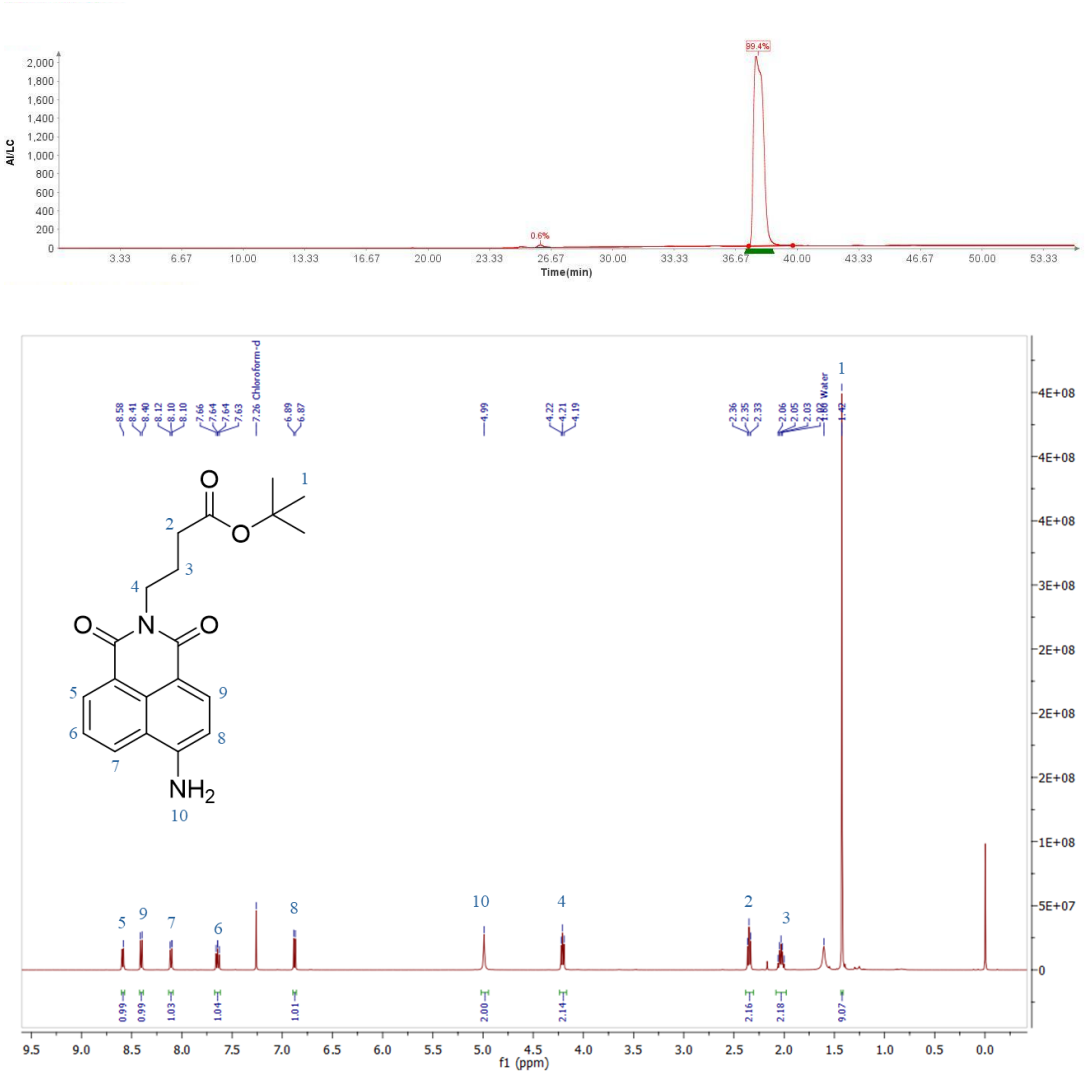

Figure 4.18: LC chromatogram of **4.15 (top)** and ^{1}H NMR of **4.15** in DMSO-d_6 **(bottom).**

The next step was to carbamate link the *para*-nitrobenzyl moiety to the amino group of the naphthalimide. This was carried out via **Scheme 4.15**, which utilised triphosgene conditions to first access the carbamoyl chloride derivative of compound **4.15**, which was then reacted with *para*-nitrobenzyl alcohol to yield the carbamate. The conversion to the carbamoyl chloride could be tracked via UV illumination, with the fluorescence output changing from green to blue over the course of 4 hours. Following isolation of compound **4.16** via column chromatography, the next step was

to the deprotect the C-terminus to release the free carboxylic acid. This was carried out under standard deprotection conditions using TFA:DCM and the deprotected derivative was precipitated out of cold diethyl ether and isolated *via* centrifugation in a 94% yield.

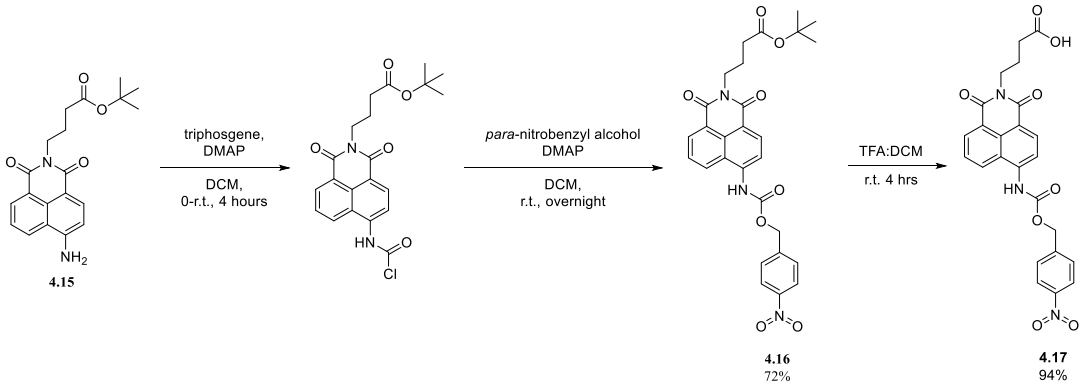

Scheme 4.15: Synthetic scheme of compound **4.17**

^{1}H NMR analysis confirmed the successful synthesis of compound **4.17**, with the appearance of a singlet peak at 10.49 ppm, which was confirmed to be the carbamate NH using HSQC analysis, showing no correlation to a carbon peak. The appearance of the two aromatic protons of the nitrobenzyl moiety can be seen at 8.49 and 7.78 ppm, with both signals integrating for 2 protons. Finally, the CH_2 protons of the benzyl moiety are seen at 5.43 ppm (**Figure 4.19**).

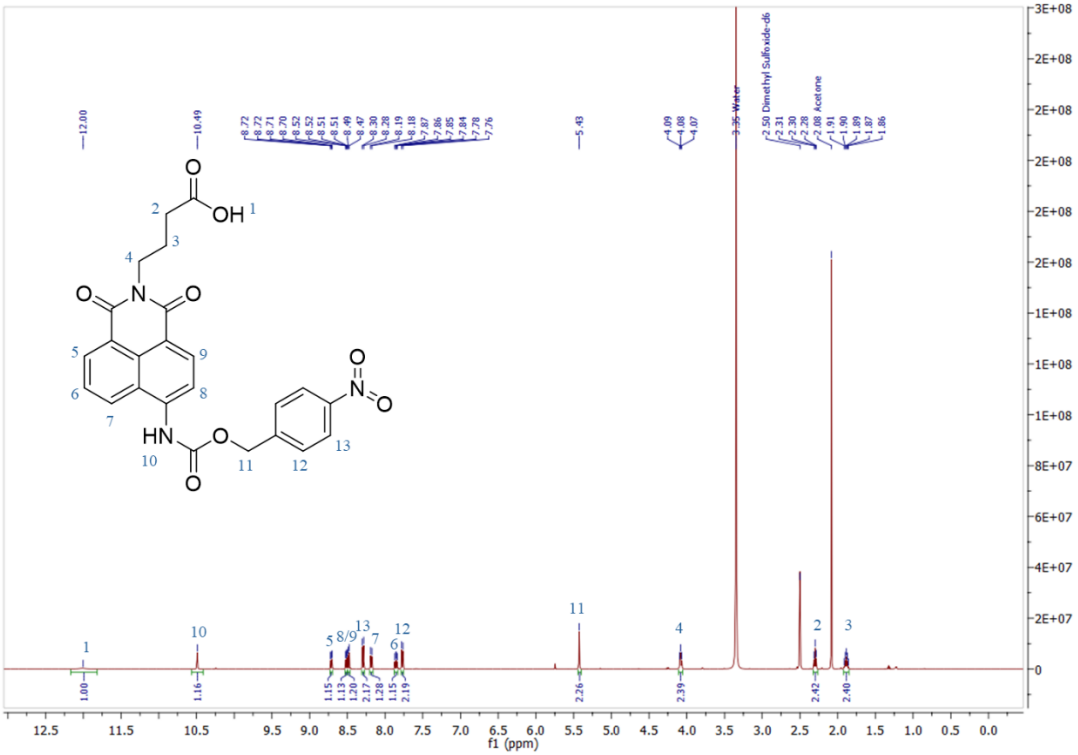

Figure 4.19: ^{1}H NMR of compound **4.17**.

Also observed in the ^{13}C in **Figure 4.20** is the carbamate carbonyl at 154.5 ppm. This was confirmed using HMBC analysis, with CH_2 of the nitro-benzyl moiety coupling to this carbon signal.

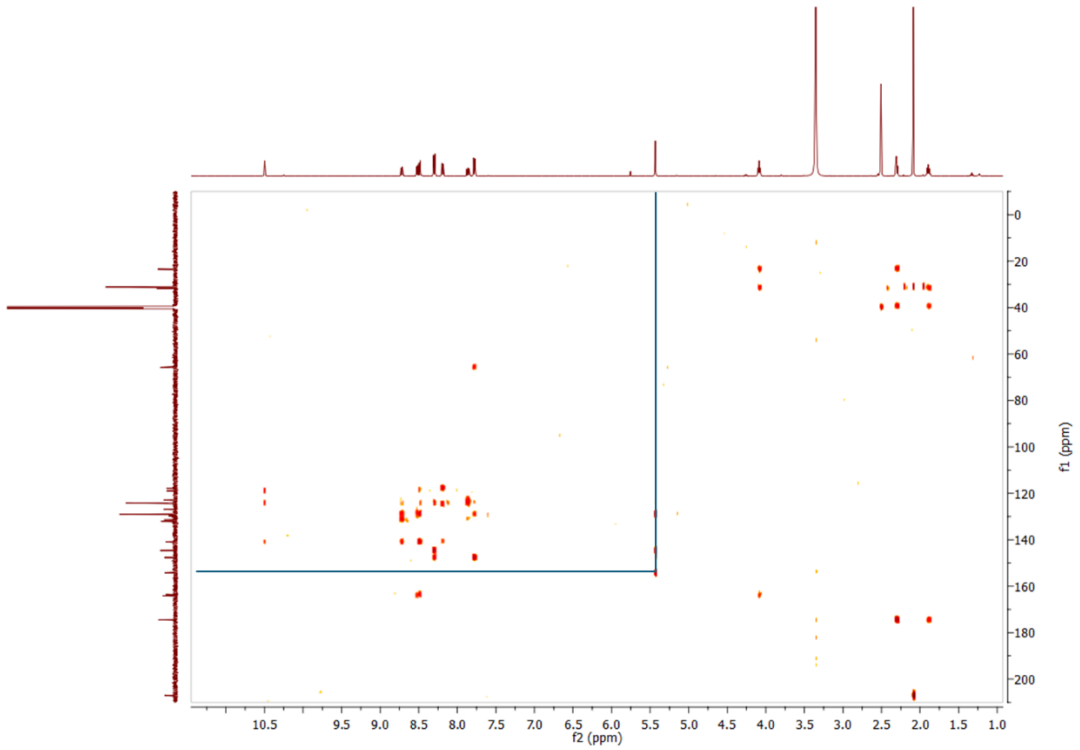

Figure 4.20: HMBC spectrum of **4.17** in DMSO-*d*

4.4.2 Attempted Coupling of **4.16** to **4.4**

To then access the desired final compound, **4.17** was reacted with **4.4** under coupling conditions using COMU as the coupling reagent. This scheme is shown below in **Scheme 4.16**.

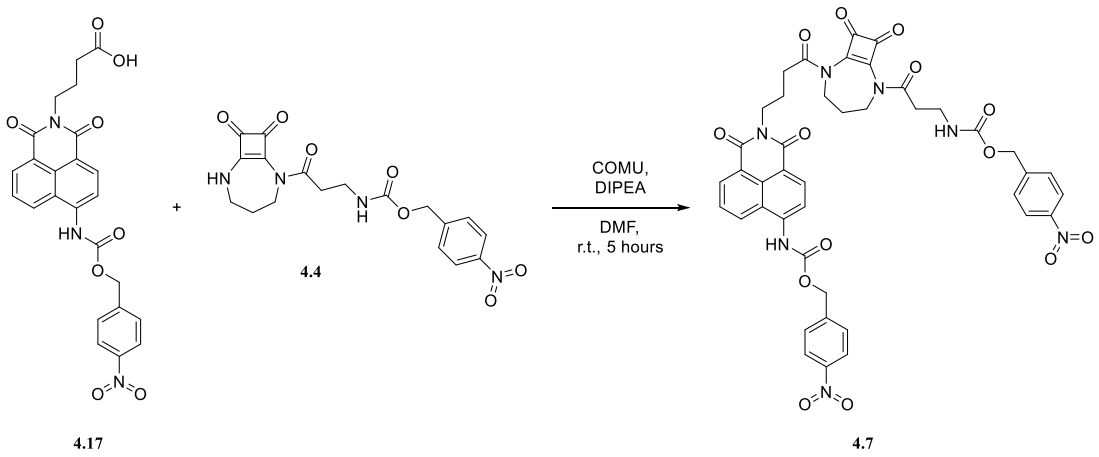

Scheme 4.16: Proposed synthetic scheme of compound **4.7**

Despite the best efforts however, the above reaction did not lead to the formation of the desired compound. LCMS analysis of the reaction mixture below in **Figure 4.21** showed a large quantity of starting material remaining after 5 hours, but it was hoped

that the peak at 41 minutes may correspond to **4.7**, with similar retention times seen for other disubstituted derivates in **Chapter 3**. However, ^{1}H NMR of the crude product following aqueous workup showed no indication of a successful reaction, with no characteristic peaks to suggest the formation of **4.7**.

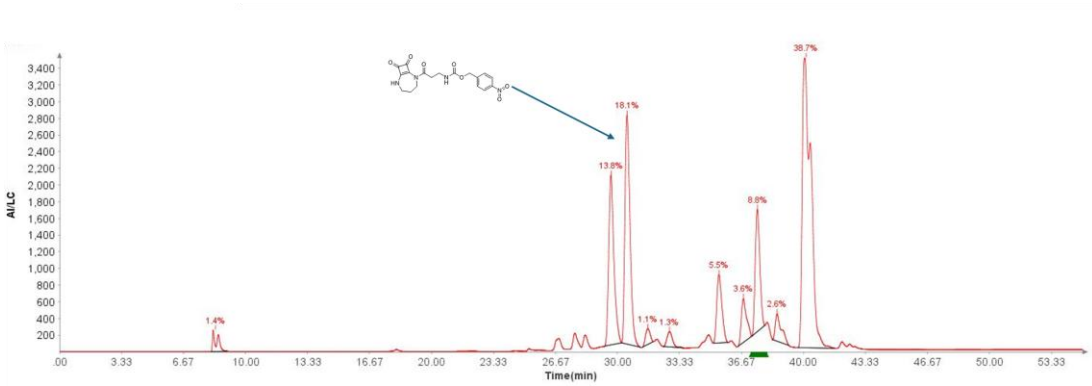

Figure 4.21: LC trace of reaction mixture after 5 hours showing large quantities of starting material remaining

While it would have been worthwhile to screen several coupling reagents, due to the lack of quantities of both compounds available and the multistep syntheses of both **4.4** and **4.16**, it was decided against optimising the synthesis of **4.7** and instead to evaluate the responses of **4.5** and **4.11** to their respective analytes.

4.5 Response of 4.5 and 4.11 to Stimuli

4.4.1 Response of **4.5** to $Na_2S_2O_4$ and NTR

Despite the disappointing result described in the previous section, the synthesis of two biologically relevant responsive anion binders was successful, and it was worthwhile to investigate whether exposure to their chosen stimuli would lead to the desired rearrangement. In the case of compound **4.5**, it was proposed that the reduction of the aryl nitro group to the corresponding amine would lead to a quinone methide type elimination and subsequent rearrangement to yield the expanded macrocycle, outlined schematically in **Scheme 4.1**.

To probe the above hypothesis, **4.5** was treated with sodium dithionite ($Na_2S_2O_4$) for 72 hours. $Na_2S_2O_4$ was chosen in the first instance as a biologically relevant reductant, given its ability to reduce aryl nitro-groups to the corresponding amines.[237] This was done by first dissolving compound **4.5** in a 90/10 DMSO/Water mix to give a solution concentration of 3 mM, followed by addition of 10 eq. of $Na_2S_2O_4$ and the solution

was left to shake in an Eppendorf tube for 72 hours. LCMS analysis after 72 hours, (**Figure 4.22**) showed the appearance of a peak at 17 minutes, with a peak for mass 245.9 which corresponds to $[M + Na]^+$ of **3.10**. The broad peak at 23 mins showed a mass hit of 106, corresponding to $[M + H]^+$ of the aza-quionone methide released as part of the fragmentation. This result is good evidence that the immolation and subsequent rearrangement proceeded as anticipated and confirms the viability of this as a general approach to ring expansion under biologically relevant conditions.

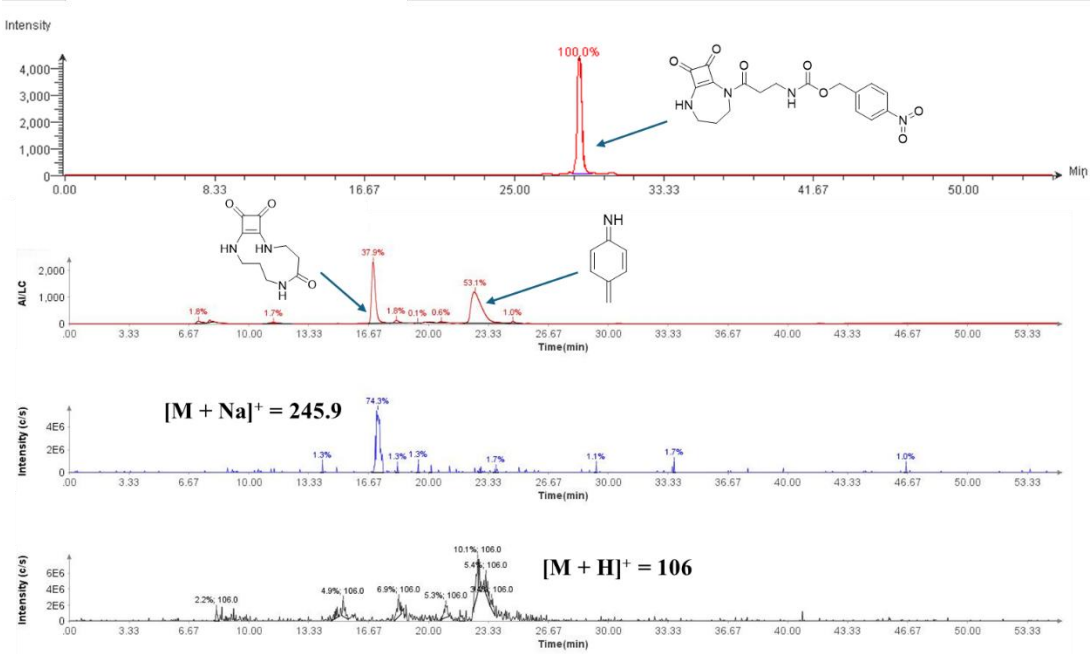

Figure 4.22: LC trace of compound **4.5** before $Na_2S_2O_4$ (**top**), LC trace and ESI+ after $Na_2S_2O_4$ (10 eq.) **(bottom)**.

Confident in the conclusions drawn from the dithionite study, NTR was then investigated as to whether it could elicit a similar result. To do this, compound **4.5** was dissolved in DMSO to give a stock solution with concentration 3mM and subsequently added to 1 mL of PBS to give a final concentration of 50 µM. To this was added 8µg mL^{-1} of NTR and 500 µM of NADH and the resulting solution was shaken for 72 hours to allow time to ensure complete immolation of the quinone methide and subsequent rearrangement. This was then followed by lyophilisation and resulting solids were then redissolved in 250 µL of DMSO to ensure suitable peak intensity. As can be seen in **Figure 4.23** below, although there is no evidence of compound **4.5** remaining, there was no appearance of a peak at 17 minutes to suggest the formation of desired 11-

membered ring. While there is a broad peak with a similar retention time, there was no observed mass to suggest that this peak is indicative of the desired macrocycle.

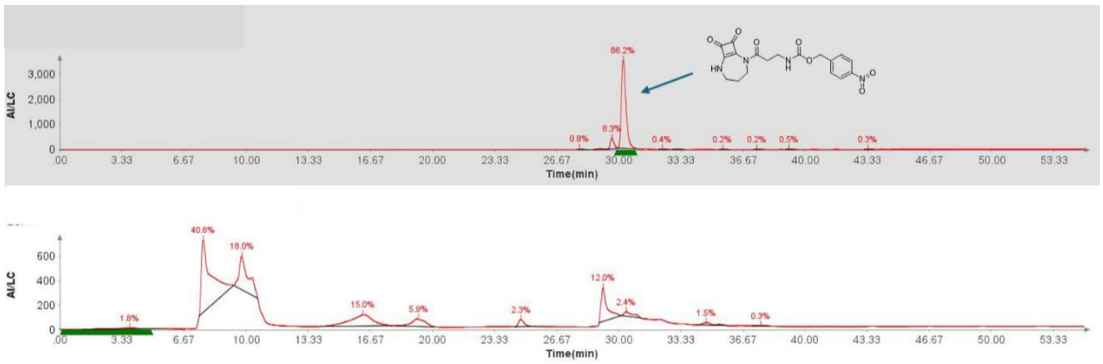

Figure 4.23: LC chromatogram of **4.5** before (top) and after addition of NTR (8µg mL^{-1}) and NADH (500 µM) in PBS.

As **4.5** is very sparingly soluble in PBS, it was decided a second experiment using 10% DMSO in PBS was worthwhile to address any possible solubility issues that may be hampering the reaction with NTR. In this case, the reaction conditions were kept constant as before, except for the addition of 10% DMSO to the solvent mixture. LCMS analysis of the lyophilised residue revealed a strong peak at approximately 17 minutes, consistent with the expected retention time of the expanded macrocycle **3.10** (**Figure 4.24**). Although no definitive ionisation corresponding to **3.10** was detected, the disappearance of the starting material **4.5** following reaction with NTR indicates full consumption of the parent compound. Previous NTR reduction studies conducted by other group members have also shown a strong peak at around 17 minutes, attributed to NADH, suggesting that any signal from the product may be obscured by co-elution. Nonetheless, these findings suggest that the NTR-mediated reduction and subsequent rearrangement may have occurred as intended, but further experimental work will be required to confirm formation of the ring-expanded product.

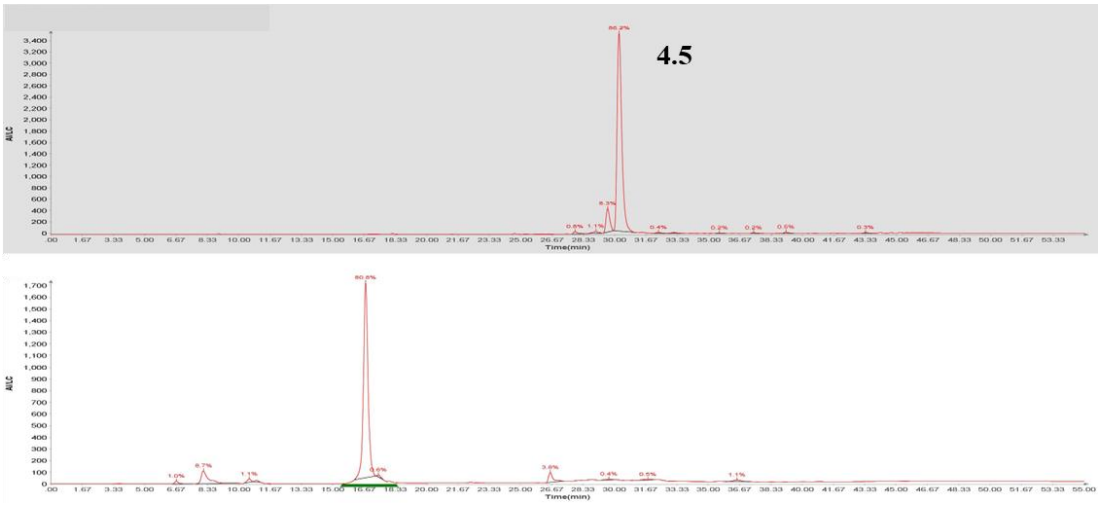

Figure 4.24: LC chromatogram of **4.5** before **(top)** and after addition of NTR (8μg mL^{-1}) and NADH (500 μM) in 90:10 PBS:DMSO. **(bottom)**

4.4.2 Response of **4.11** to H2O2

In a similar fashion to above, **4.11** was dissolved in a 90/10 PBS/DMSO mix to give a concentration of 3 mM and was treated with 10 eq. of H_2O_2, left to shake for 24 hours followed by LCMS analysis. Interestingly however, although there is a clear consumption of **4.11**, it appears that the H_2O_2 resulted in a cleavage of the N-C linkage between the squaramide and β-alanine. Examining the peak at approximately 17 minutes showed strong ionisation at 153 which is corresponds to [M + H]+ of compound **3.5**. Moreover, it also showed no ionisation at 245.9 which corresponds to $[M + Na]^+$ of **3.10**. This observation suggested there may have been a competing degradation event.

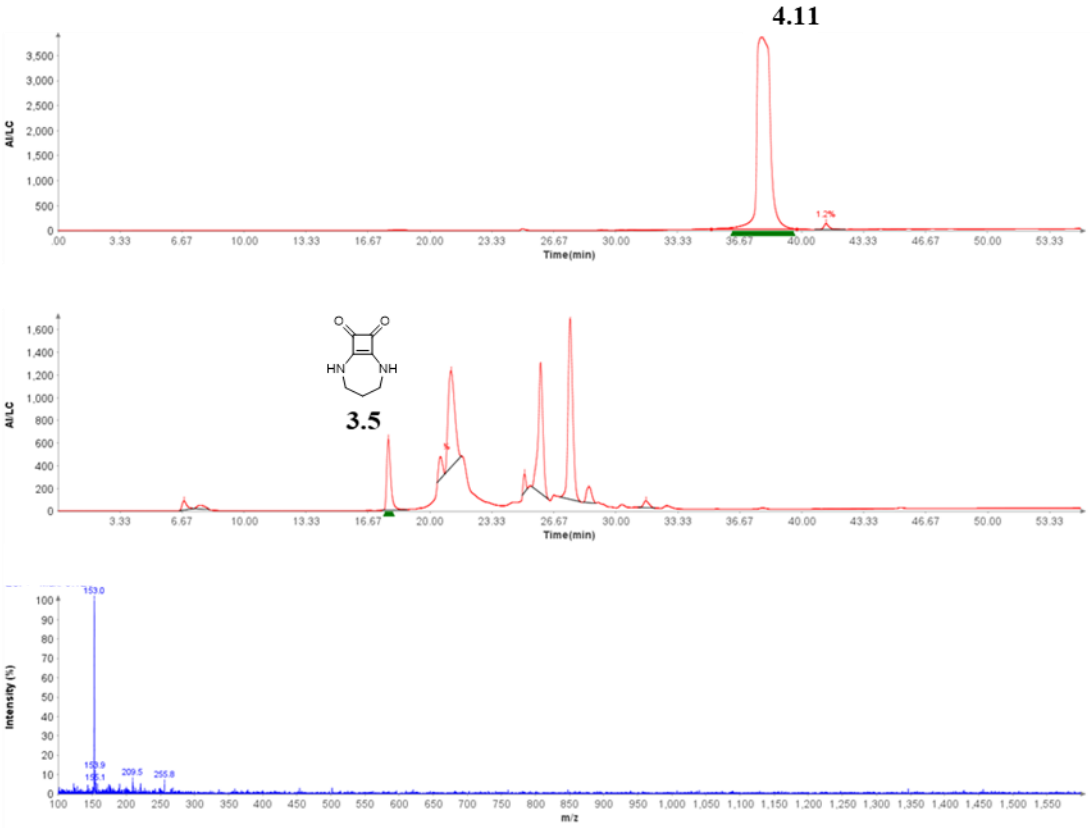

Figure 4.25: LC trace of compound **4.11** before H_2O_2 **(top)**, LC trace and ESI+ after H_2O_2 (10 eq) **(bottom).**

The observed degradation may be attributed to differences in electrophilicity between the carbonyl groups within the molecule. Under the proposed mechanism for the Baeyer-Villiger-type rearrangement shown in **Scheme 4.8** the nucleophilic peroxide anion is expected to attack the electrophilic benzoyl ketone carbonyl, leading to decarboxylation, release of the free amine and subsequent ring expansion. However, in this instance it appears the electrophilic carbonyl of the amidosquaramide moiety was favoured in this instance for attack (**Figure 4.26**). This mechanism of degradation could follow a similar pathway to that followed by reaction of H_2O_2 and thiazolidinones, proposed by Cohen *et al*.[29]

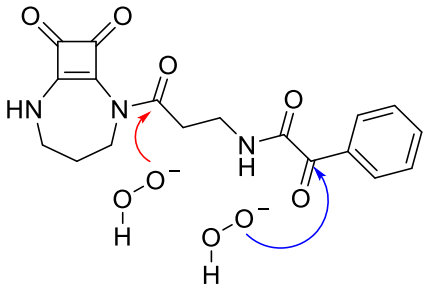

Figure 4.26: Graphic depicting nucleophilic attack of the peroxide anion on **4.11** The blue arrow shows the desired nucleophilic attack, while the red arrow shows the proposed observed reaction.

This observed difference in reaction mechanism may be due in part to the squaramide moiety adjacent to the carbonyl carbon in question. Typically, amide carbonyls exhibit reduced electrophilicity due to resonance stabilisation from the nitrogen lone pair, which donates electron density into the carbonyl π-system. This has the overall result of decreasing susceptibility to nucleophilic attack. In this case, the nitrogen lone pair is also delocalised into the conjugated cyclobutadione system, which competes with the resonance donation into the amide carbonyl. This competing resonance would be expected to diminish the electron density on the amide carbonyl carbon, increasing its electrophilicity (**Figure 4.27**). Consequently, nucleophilic attack could occur this amide carbonyl, ultimately releasing compound **3.5**.

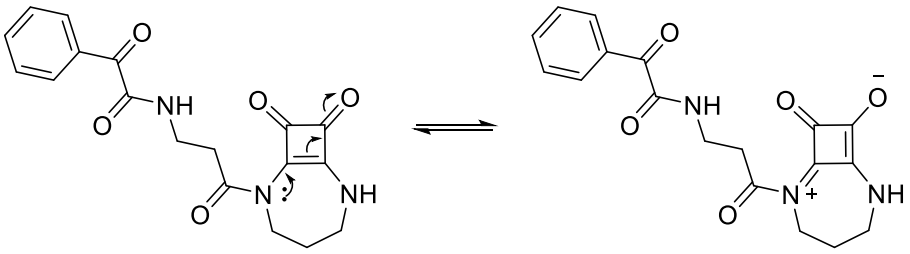

Figure 4.27: Delocalisation of N lone pair into the cyclobutadione ring, enhancing electronegativity of the adjacent carbonyl carbon.

While the above result was disappointing, there remains scope to make structural changes to allow for preferential reaction at the benzoyl ketone carbonyl. This could include the incorporation of an electron withdrawing group *para*- to the ketone functional group (**Figure 4.28**). Such derivatives have successfully increased reaction kinetics with both a nitro- and cyano- employed as EWGs.[234]

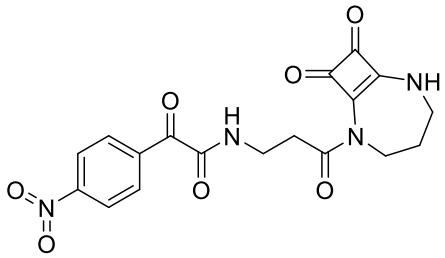

Figure 4.28: Structural modification of **4.11** utilising a 4-nitro group

The previous sections provide positive results as to the efficacy of the above squaramide scaffolds to act as bio-responsive binders. **4.5** showed complete conversion to the desired expanded macrocycle upon reaction with $Na_2S_2O_4$, and subsequent reactions with NTR also showed good LCMS evidence that the desired fragmentation and expansion pathway may have occurred. A lack of material prevented further analysis however, the above data is very promising in the context of bio-responsive ring expansion for molecular recognition. Unfortunately, **4.11** did not proceed as expected upon exposure to H_2O_2 due to a competing side reaction, however, it is anticipated that minor structural changes may yield a more favourable result. Further results will be required to fully probe the potential of this approach.

4.5 Spectroscopic Response of 4.5 to $Na_2S_2O_4$

Given the difficulties outlined in **Section 4.5.1** in determining the rearrangement of 4.5 in response to NTR, UV/Vis experiments were carried out using $Na_2S_2O_4$ to assess whether this technique could serve as a viable alternative to track the rearrangement process. UV/Vis spectroscopy was selected due to its sensitivity to changes in electronic conjugation and chromophore environment, which were expected to differ between the parent compound **4.5** and the ring-expanded product **3.10**. It was anticipated that upon chemical reduction with $Na_2S_2O_4$, any conversion of **4.5** to **3.10** would be reflected by characteristic shifts in the absorbance maxima and overall spectral profile. To evaluate this, absorbance spectra of both **4.5** and **3.10** were first recorded independently under identical solvent and concentration conditions to establish baseline profiles, as shown in **Figure 4.29**. The spectrum of 4.5 displayed two distinct absorbance maxima at 266 and 303 nm, whereas **3.10** exhibited a single absorbance maximum at 295 nm.

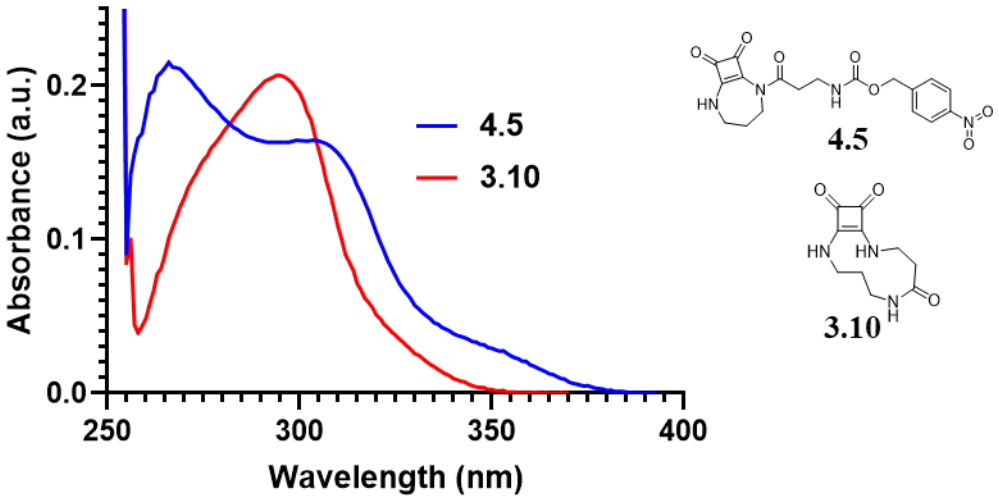

Figure 4.29: Absorbance spectra of **4.5** and **3.10** in 10% DMSO in 10 mM PBS pH 7.4. Both compound concentrations are 10 μM.

To observe the changes in the UV/Vis spectra of **4.5** upon reaction with Na2S2O4 a time study was conducted, whereby Na2S2O4 (10 mM) was added to **4.5** and the UV/Vis spectra were measured over the course of 24 hours. As seen in **Figure 4.30** below this resulted in a bathochromic shift in absorbance from 266 nm to 275 nm, as well as a decrease in absorbance at 303 nm. Although this result does not provide clear evidence of the formation of **3.10**, the changes observed suggest that a change in the molecular structure is occurring. This is a promising preliminary result towards the validity of UV/Vis to track the rearrangement of **4.5**, however, further analysis is required to fully validate this approach.

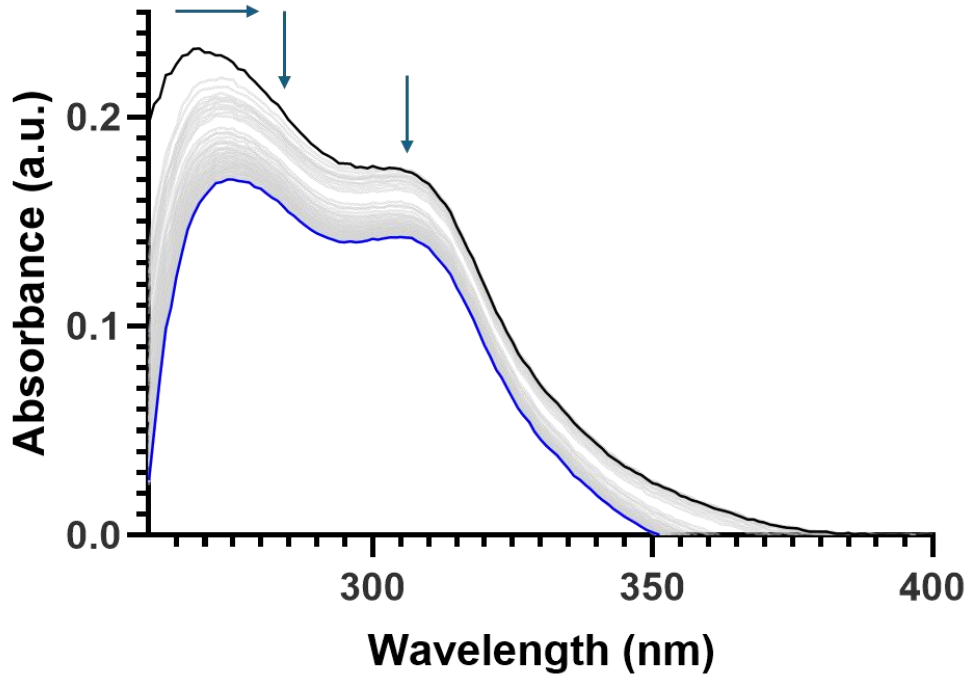

Fig 4.30: Changes in the UV/Vis absorbance over the course of 24 hours of **4.5** (10 μM) in response to $Na_2S_2O_4$ (1mM) in 10% DMSO:Water solution.

4.6 Binding Abilities of 3.10 in Aqueous Environments

To assess the ability of the expanded macrocycle, and thus **4.5,** to act as an efficient carboxylate binder in competitive aqueous environments, a series of UV/Vis titrations were carried out. Here, a stock solution of **3.10** in DMSO was diluted to 20 μM in three solvent systems; DMSO, 10% water and 20% water in DMSO. This was followed by additions of TBA AcO^- up to 10 equivalents and the change in absorbance was measured. **Figure 4.31** below shows the change in absorbance in 100 % DMSO, where addition of AcO^- results in an overall increase in absorbance as well as a hypsochromic shift in the λ_{max}, from 295 nm to 291 nm.

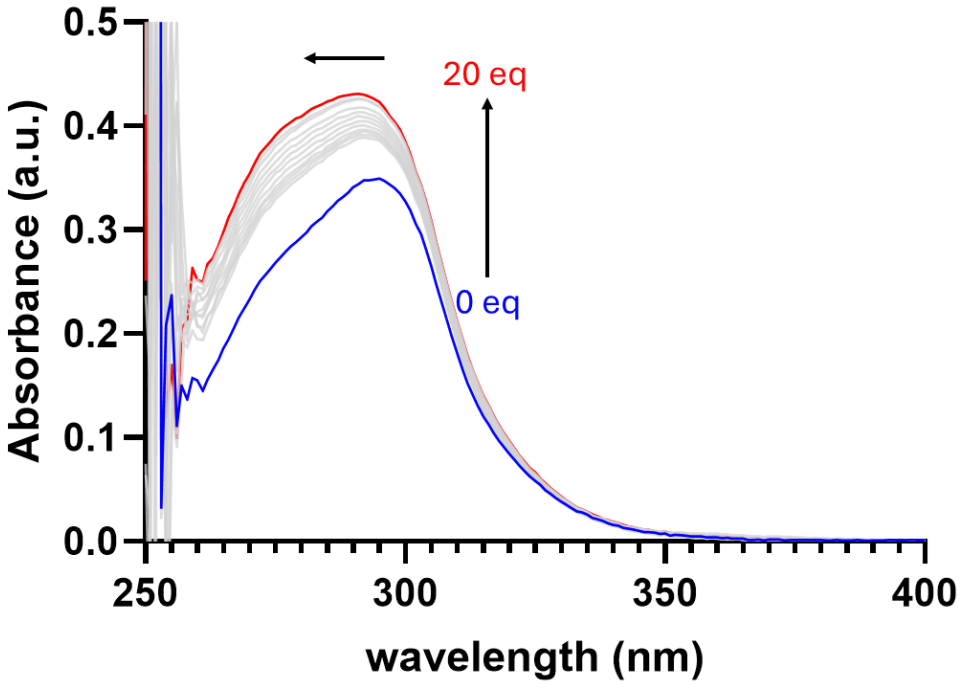

Figure 4.31: changes in the UV spectra of **3.10** (20 μM) upon addition of TBA AcO^- in DMSO

These titrations were then repeated in solvents systems with 10% and 20% water and as can be seen in **Figure 4.32**, even at 20% water concentration, additions of acetate induced a similar increase in absorbance of **3.10**, albeit to a lesser extent (16% and 7% respectively), and displayed a similar hypsochromic shift in absorbance maxima. These results suggest a decrease in binding affinity in more aqueous environments. But importantly, the changes observed suggest that **3.10** still maintains some recognition capabilities for AcO^- in aqueous systems.

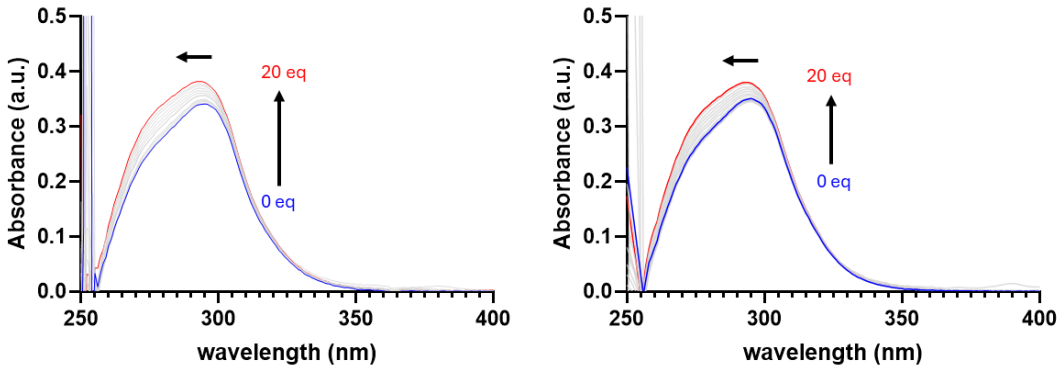

Figure 4.32: changes in the UV spectra of **3.10** (20 μM) upon addition of TBA AcO^- in DMSO (10% water) **(left)** and DMSO (20% water) **(right).**

4.7 Conclusions

In conclusion, a second generation of responsive anion binders was developed, designed to exploit biomarker triggers (NTR and ROS) to initiate spontaneous ring expansion and a subsequent 'switch-on' in anion binding. The NTR-responsive derivative **4.5** was successfully synthesised via carbamate linkage of β-alanine to a 4-nitrobenzyl group. In contrast, preparation of the ROS-responsive derivative proved more challenging, with attempts to incorporate a boronic ester unsuccessful. Both triphosgene-mediated conditions and carbamate formation via an N-acyl imidazole intermediate failed, necessitating a revised strategy. Ultimately, amide coupling of phenylglyoxylic acid to β-alanine (PyBOP-mediated) followed by conjugation to the squaramide scaffold yielded **4.11**.

Attempts to further expand the design with an activatable fluorophore met with limited success. Although the naphthalimide derivative was obtained, COMU-mediated coupling to **4.5** failed to produce the desired conjugate, and the length and complexity of the synthetic route precluded development of an alternative pathway.

Preliminary evaluation of the ring-expansion behaviour revealed that **4.5** responded effectively to NTR-mimicking conditions, with LCMS analysis showing complete conversion to the ring-expanded product upon treatment with $Na_2S_2O_4$. Subsequent experiments with NTR gave good evidence that NTR-mediated reduction of **4.5** did lead to a skeletal rearrangement, however the presence of NADH obscured the target peak in LCMS studies. UV/Vis experiments probing tracking the changes in absorbance of **4.5** upon reaction with $Na_2S_2O_4$ did result in the modulation of absorbance characteristics, however further analysis are required to fully validate this analytical approach to observing ring expansion and anion binding. With regards the exposure of **4.11** to H_2O_2, this did not result in rearrangement; instead, LCMS analysis suggested degradation, most likely due to Baeyer-Villiger oxidation at an alternative electrophilic site, leading to cleavage of the squaramide-β-alanine amide bond.

Looking forward, further optimisation of synthetic methodology is warranted, particularly screening alternative coupling reagents to facilitate preparation of **4.7**. In addition, incorporation of a pro-fluorophore could be pursued using coumarin scaffolds. Notably, 7-nitro-3-hydroxyethyl-coumarin offers direct carbamate linkage to β-alanine and could promote the electron cascade necessary to release the terminal

amine, enabling both fluorescence 'switch-on' and ring expansion (**Scheme 4.18**). A possible synthetic pathway is shown in **Scheme 4.17**.

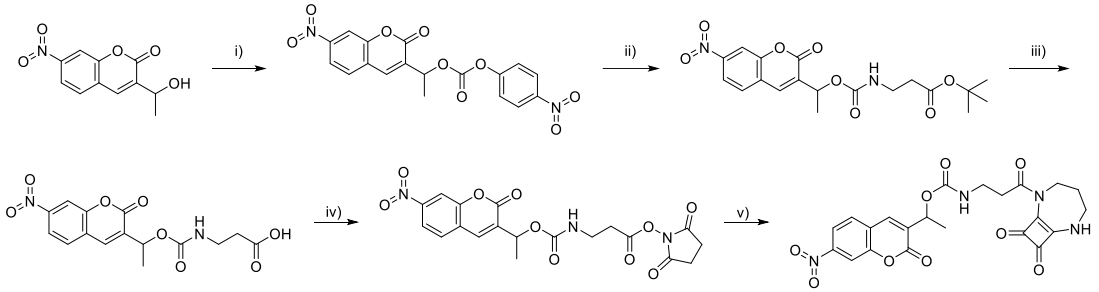

Scheme 4.17: Alternative synthesis of NTR-responsive acetate sensor. i) 4-nitrobenzyl orthochloroformate, ii) β-alanine t-butyl ester hydrochloride, TEA, iii) TFA:DCM, iv) NHS, EDCI.HCl, v) **3.5**.

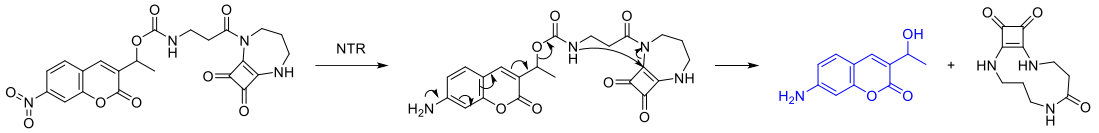

Scheme 4.18: Proposed mechanism of NTR-mediated spontaneous ring-expansion leading to a "switch-on" in coumarin fluorescence and AcO^- binding.

Chapter 5

Thesis Summary and Future Work

5 Thesis Summary and Future Work

Responsive molecular systems are increasingly important in biological contexts, from theranostics that enable more selective and effective cancer treatments to sensors that provide insight into the cellular microenvironment. This thesis aimed to develop a synergistic approach to theranostic strategies, exploiting the ROS-generating properties of cold atmospheric plasma (CAP), while also exploring a new methodology for responsive anion binding and sensing.

Chapter 2 focused on the design and synthesis of a cold atmospheric plasma (CAP)-activated theranostic agent (**2.4**). Upon reaction with CAP-generated reactive oxygen species (ROS), **2.4** underwent a controlled self-immolation process. Oxidisation of the boronic ester to a phenol initiated a cascade of quinone-methide eliminations, ultimately releasing both a free naphthalimide fluorophore and the chemotherapeutic agent amonafide. Release of the naphthalimide was first confirmed through ratiometric photophysical changes following exposure to hydrogen peroxide (H_2O_2). Compound **2.4** displayed an absorbance maximum at 375 nm prior to treatment, which shifted to 440 nm after H_2O_2 exposure, consistent with fluorophore release. This was accompanied by a minimal red shift in emission wavelength (524 to 535 nm) and a 3.3-fold increase in emission intensity. Limit of detection (LOD) analysis with an analogous derivative demonstrated good sensitivity, with a measured LOD of 0.58 μM. LCMS analysis further confirmed release of both products, with H_2O_2 exposure yielding two distinct peaks corresponding to free naphthalimide and amonafide.

The theranostic activity of **2.4** was evaluated in U-251 MG cells. Cytotoxicity assays showed no intrinsic toxicity at concentrations up to the millimolar range. However, CAP treatment activated cytotoxicity, yielding an LC_{50} of 84 μM. Confocal microscopy confirmed that this activation could be tracked *in vitro*, as CAP-treated U-251 MG cells displayed a ratiometric fluorescence shift from blue to green. Future work in this chapter focuses on the modulation of the naphthalimide fluorophore to improve solubility and modulate the fluorescence behaviour

Chapter 3 shifted the focus towards the supramolecular field, while retaining the underlying principle of a responsive molecular system, and explored a novel strategy for the development of adaptive anion binders. This approach sought to exploit an intramolecular rearrangement that would induce ring expansion of a cyclic

squaramide. The resulting increase in cavity size would create a binding pocket capable of accommodating an anion. To establish proof of concept, this rearrangement was initially blocked through protection of a nucleophilic amine with a Boc group. As a first step, the size of the starting macrocycle was varied, allowing identification of an optimal cavity dimension. The reactive handle was then modified through conjugation with amino acids of differing chain lengths. This robust synthetic methodology afforded glycine, β-alanine, and GABA derivatives of the scaffold (compounds **3.6, 3.7**, and **3.8**). Each was assessed for its ability to undergo the desired rearrangement. Compounds **3.6** and **3.8** did not react as anticipated; however, compound **3.7** underwent spontaneous ring expansion upon Boc deprotection, yielding an 11-membered macrocycle **3.10**. X-ray crystallography of the product revealed both the compound's self-aggregation pattern and the alignment of the NH groups relative to the binding cavity.

Building on this design, a second iteration introduced a Boc-protected reactive handle at the central scaffold, enabling the possibility of a double rearrangement. This yielded compound **3.11**, designed to undergo expansion to an even larger binding cavity and thereby modulate receptor binding properties. Indeed, deprotection and rearrangement experiments confirmed that 3.11 underwent the anticipated double expansion to a 15-membered ring (**3.12**). Finally, orthogonal protecting groups were employed to investigate the feasibility of sequential rearrangements. To this end, compound **3.13** was synthesised, bearing both Fmoc and Boc protecting groups. LCMS analysis following Fmoc deprotection and column chromatography suggested successful formation the mono-expanded 11-membered ring, while subsequent Boc deprotection, confirmed by LC-MS analysis, successfully triggered the second rearrangement, yielding the 15-membered ring.

Anion binding studies of compound **3.10** demonstrated that the receptor exhibited selectivity towards carboxylate, with binding affinities of 760 M^{-1} and 278 M^{-1}. Analysis using the open-source software Bindfit indicated that a 1:1 binding model provided the best fit, with acetate interacting with one squaramide NH and the amide NH. In contrast, the unexpanded boc-protected derivative showed no measurable anion binding, confirming the validity of this novel strategy for responsive anion recognition. Further studies of compound **3.12** revealed that, while it retained the ability to bind acetate and benzoate there was a change in the binding mode observed.

3.12 adopted a 1:2 binding stoichiometry with both acetate and benzoate, indicating a distinct change in binding behaviour relative to **3.10.** This was accompanied by an increased affinity for AcO^- (K_{11} = 7313 M^{-1}) and $PhCOO^-$ (K_{11} = 6287 M^{-1}). The observed shift in binding mode is postulated to arise from the introduction of a fourth NH H-bond donor site, as well as the larger cavity size allowing for the fitting of multiple anions. Future work in the first instance would be to attempt to obtain crystals of both **3.10** and **3.12** bound complexes to gain insight into the binding conformations for both. Furthermore, it would be worthwhile to isolate larger quantities of **3.13** to fully characterise the sequential rearrangements, and to evaluate the SuRE methodology to access a larger family of macrocyclic squaramides.

Chapter 4 aimed to build on the proof of concept developed in chapter 3 and employ biologically relevant triggering systems to selective acetate binding. To this end, a *para*-nitro benzyl group was conjugated to β-alanine via carbamate linkage to form the reactive handle, which was then appended to the cyclic squaramide scaffold to yield an NTR-responsive binder (**4.5**). While it was initially hoped a boronic ester could be employed as a ROS-initiator, synthetic difficulties led to a pivot to a α-ketoamide as the ROS-responsive group (**4.11**). Attempts were made to further expand the design by incorporating a naphthalimide fluorophore, allowing this family of anion binder to become anion sensors. However, these synthetic difficulties were again encountered when attempting to couple the fluorophore to **4.5** using COMU-mediated conditions. Unfortunately, the low yielding multistep pathway towards the starting materials required meant there was not enough time to investigate alternative pathways.

Attempts to deprotect and induce rearrangement of **4.11** using H_2O_2 were unsuccessful. LC–MS analysis indicated that the compound underwent unintended degradation, resulting in the release of the core cyclic squaramide 3.5. Encouragingly, treatment of **4.5** with $Na_2S_2O_4$ successfully triggered the desired rearrangement, with LC–MS analysis showing a peak corresponding to $[M + Na]^+$ for **3.10**, alongside a peak for the azo-quinone methide generated during the elimination process. Attempts to effect rearrangement of **4.5** using NTR were, however, inconclusive. Nevertheless, the positive outcome with $Na_2S_2O_4$ highlights a promising avenue for the development of enzyme-responsive anion binders. Future work would focus on the coupling of the

fluorophore to **4.4**, including possible incorporation of a coumarin moiety within the reactive handle itself, to negate the synthetic issues with the second coupling step.

5.1 Publications

A. Abogunrin, **S. A. Healy,** O. Fenelon and R.B.P. Elmes, 'Head vs Tail Squaramide – Naphthalimide Conjugates: Self Assembly and Anion Binding Behaviour, 2022, Chemistry (MDPI), Advance Article

A. Grundzi, **S. A. Healy**, O. Fenelon and R.B.P. Elmes, 'Squaramide-Naphthalimide Conjugates – Exploiting Self Aggregation Effects in Acetate Recognition', 2022, Results in Chemistry, Advance Article.

Chapter 6
Experimental Procedures

6. Experimental Procedures

6.1 General Procedures and Instrumentations

All reagents were purchased from commercial suppliers and used without further purification. DCM and MeCN were dried over 3 Å molecular sieves. Anhydrous DMF was purchased from Sigma Adrich. Analytical TLC was performed using Merck Silica Gel 60 F_{254} plates. Flash chromatography was performed using silica gel 60. Compounds were lyophilised using a Labconco Freezone 1 Dry system. LC-MS analysis was carried out using an Agilent Technologies 1200 series coupled to a Advion Expression L Compact Mass Spectrometry (ESI) operating in both positive and negative mode, using an Agilent XDB-C18 (5µm, 4.6 x 150 mm) column at 40ºC, eluting with a flow rate at 0.2 ml/min and a gradient of 0.1% formic acid in MeCN and 0.1% formic acid in H_2O. NMR spectra were recorded using a Bruker Ascend 500 spectrometer, operating at 500 MHz for ^{1}H NMR and 126 MHz for ^{13}C, both at 273 K unless stated otherwise. The residual solvent peak was used as the internal standard for DMSO-d_6 and TMS for $CDCl_3$. NMR spectra were processed and stack plots produced using MestreNova 6.0.2 software. Assignments of NMR spectra were carried out with the aid of 2D NMR experiments (COSY, HSQC, HMBC). Multiplicity is given as s = singlet, bs = broad singlet, d = doublet, brd = broad singlet, dd = doublet of doublets, ddd = doublet of doublet of doublets, t = triplet, q = quartet, m = multiplet as appropriate and *J* values given in Hz. Infrared (IR) spectra were obtained using ATR as a solid on a zinc selenide crystal in the of 4000 – 400 CM^{-1} using a Perkin Elmer Spectrum 100 FT-IR spectrophotometer. High Resolution Mass Spectrometry (HRMS) were recorded – courtesy of Bath University – on an Agilent 6200 series TOF/6500 series Q-TOF instrument with an ESI source. UV/Vis spectroscopy measurements were made at 25ºC on a Lambda 365 Perkin Elmer UV-vis spectrophotometer. Fluorescence emission spectra were performed at 25ºC on an Agilent Spectrofluorometer equipped with a 450 W xenon lamp for excitation.

6.2 Synthetic Procedures for Chapter 2

2,6-bis(((*tert*-butyldimethylsilyl)oxy)methyl)-4-methylphenol (2.5)

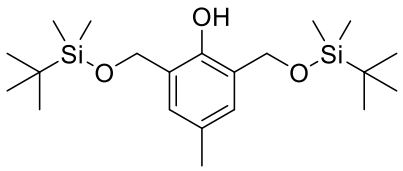

2,6-is-(hydroxymethyl-*p*-cresol (4.00 g, 23.8 mmol) and imidazole (3.24 g, 47.6 mmol) were dissolved in THF, purged with N_2 and cooled to 0° C. TBDMSCl (10.71 g, 71.4 mmol) dissolved in THF was added slowly and the reaction mixture was allowed to stir at r.t. overnight. After reaction, the solution was reduced *in vacuo*, diluted with diethyl ether and washed with water and brine. The organic layer was dried over sodium sulphate and concentrated *in vacuo*. The crude product was purified using flash column chromatography eluting with 95/5 pet. ether/ethyl acetate to yield the title compound as a yellow oil. (7.1g, 75%). **^{1}H NMR** (500 MHz, $CDCl_3$) δ 8.08 (s, 1H), 6.98 (s, 2H), 4.89 (s, 4H), 2.33 (s, 3H), 1.02 (s, 18H), 0.2 (s, 12H). **^{13}C NMR** (126 MHz, $CDCl_3$**)** 151.0, 128.4, 126.3, 125.9, 63.2, 26.0, 20.8, 18.5, -5.3**. IR** (ATR): ν_{max} (cm^{-1}) = 2928, 2952, 2891, 2856, 1613, 1460, 1399, 1358, 1321, 1252, 1143, 1111, 1003, 982, 928, 833, 773, 725, 669, 656, 577.

(((5-methyl-2-((4-(4,4,5,5-tetramethyl-1,3,2-dioxaborolan-2-yl)benzyl)oxy)-1,3-phenylene)bis(methylene))bis(oxy))bis(*tert*-butyldimethylsilane) (2.6)

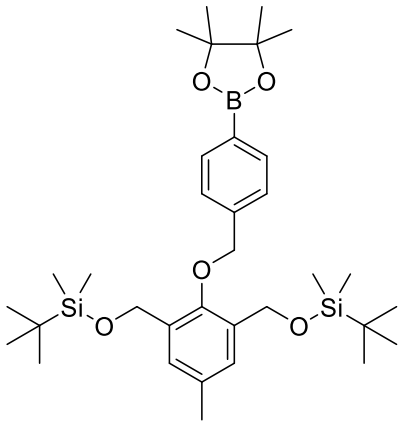

2.5 (1.00 g, 2.5 mmol) and K_2CO_3 (1.04 g, 7.5 mmol) were dissolved in DMF and flask was purged with N_2, cooled to 0° C and stirred for 10 mins. 2-(4-(bromomethyl)phenyl)-4,4,5,5-tetramethyl-1,3,2-dioxaborolane (742 mg, 2.5 mmol) was added and reaction was stirred at r.t. overnight. The solution was concentrated *in*

vacuo, diluted with ether, washed with saturated ammonium chloride, water and brine, dried over sodium sulphate and concentrated *in vacuo*. The crude product was purified using flash column chromatography eluting with 95/5 pet. ether/ethyl acetate to yield the title compound as a clear oil (1.10 g, 71%). **^{1}H NMR** (500 MHz, $CDCl_3$) δ 7.84 (d, *J* = 8.1 Hz, 2H), 7.43 (d, *J* = 8.1 Hz, 2H), 7.18 (s, 2H), 4.89 (s, 2H), 4.70 (s, 4H), 2.34 (s, 3H), 1.36 (s, 12H), 0.92 (s, 18H), 0.07 (s, 12H). **^{13}C NMR** (126 MHz, $CDCl_3$**)** 151.2, 140.9, 135.1, 133.9, 133.8, 128.0, 127.1, 84.0, 76.2, 60.5, 26.1, 25.0, 21.3, 18.6, -5.1. **IR** (ATR): ν_{max} (cm^{-1}) = 2928, 2894, 2858, 1614, 1495, 1400, 1358, 1321, 1252, 1201, 1144, 1112, 1089, 1003, 963, 928, 834, 772, 725, 658, 578, 409.

(5-methyl-2-((4-(4,4,5,5-tetramethyl-1,3,2-dioxaborolan-2-yl)benzyl)oxy)-1,3-phenylene)dimethanol (2.7)

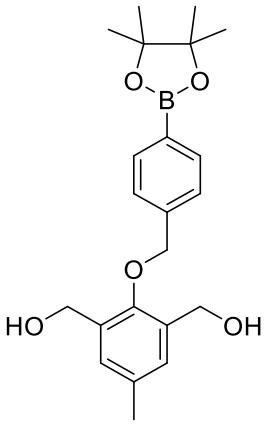

2.6 (1.00 g 1.6 mmol) was suspended in MeOH and a catalytic amount of *p*-TSOH was added. The reaction was stirred for 4 hours at r.t. and then concentrated *in vacuo*. The crude product was purified using flash column chromatography eluting with 50/50 pet ether/ethyl acetate to yield the title compound as a clear oil (415 mg, 66%). **^{1}H NMR** (500 MHz, $CDCl_3$) δ 7.83 (d, *J* = 8.1 Hz, 2H), 7.42 (d, *J* = 8.1 Hz, 2H), 7.15 (s, 2H), 4.95 (s, 2H), 4.65 (s, 4H), 2.32 (s, 3H), 1.35 (s, 12H). **^{13}C NMR** (126 MHz, $CDCl_3$**)** 152.9, 140.0, 135.3, 134.6, 134.0, 129.8, 127.3, 84.1, 77.0, 61.3, 25.0, 20.9.

5-Amino-2-[2-(dimethylamino)ethyl]-1H-benz[de]isoquinoline-1,3(2H)-dione (2.9)

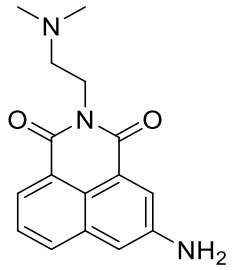

3-nitro-1,8-naphthalic anhydride (500 mg, 2.0 mmol) and *N,N*-dimethylethylenediamine (181 mg, 2.0 mmol) were dissolved in EtOH and then refluxed overnight. The reaction was cooled on ice, and the precipitate was filtered and washed with cold EtOH, yielding the nitro-intermediate, which was used without further purification. The resulting solid was dissolved in MeOH without further purification or characterisation before 10% mol Pd/C was added and the reaction mixture was stirred under H_2 for 3 hours. The solution was filtered through celite and the filtrate was concentrated *in vacuo* to yield the title compound as a yellow solid (441 mg, 78%) **^{1}H NMR** (500 MHz, $CDCl_3$) δ 8.30 (dd, *J* = 7.2, 0.6 Hz, 1H), 7.98 (d, *J* = 2.3 Hz, 1H), 7.90 (d, *J* = 8.1 Hz, 1H), 7.65 – 7.53 (m, 1H), 7.25 (d, *J* = 2.3 Hz, 1H), 4.33 – 4.28 (m, 2H), 4.17 (s, 2H), 2.67 – 2.62 (m, 2H), 2.35 (s, 6H).**^{13}C NMR** (126 MHz, $CDCl_3$) δ 164.7, 164.3, 154.4, 133.6, 131.8, 127.6, 127.3, 123.7, 122.7, 122.6, 122.1, 144.1, 57.2, 45.9, 38.3**. IR** (ATR): ν_{max} (cm^{-1}) = 3441, 3345, 3227, 2968, 2821, 2761, 1695, 1651, 1618, 1581, 1517, 1447, 1393, 1354, 1291, 1238, 1212, 1175, 1149, 1101, 1067, 1029, 985, 912, 860, 119, 746, 676, 642, 610, 550, 529, 479, 403.

***N*-Butyl-4-amino-1,8-naphthalimide (2.8)**

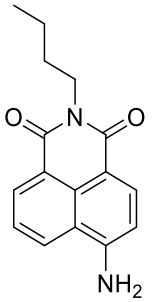

4-nitro-1,8-naphthalic anhydride (500 mg, 2 mmol) and *N*-butylamine (146 mg, 2 mmol) were dissolved in EtOH and refluxed overnight. The reaction was reduced *in vacuo* and the crude was purified using flash column chromatography eluting with

DCM to yield the nitro- intermediate as a beige solid. The resulting solid was dissolved in MeOH without further purification or characterisation before 10% mol Pd/C was added and the reaction mixture was stirred under H_2 for 3 hours. The solution was filtered through celite and the filtrate was concentrated *in vacuo* to yield the title compound as an orange solid (400 mg, 75%) **^{1}H NMR** (500 MHz, $CDCl_3$) δ 8.59 (d, *J* = 7.3 Hz, 1H), 8.41 (d, *J* = 8.1 Hz, 1H), 8.10 (d, *J* = 8.4 Hz, 1H), 7.68 – 7.59 (m, 1H), 6.88 (d, *J* = 8.1 Hz, 1H), 4.97 (s, 2H), 4.23 – 4.11 (m, 2H), 1.75 – 1.67 (m, 2H), 1.49 – 1.38 (m, 2H), 0.96 (t, *J* = 7.4 Hz, 3H).**^{13}C NMR** (126 MHz, $CDCl_3$) δ164.7, 164.2, 149.1, 149.0, 133.9, 131.6, 129.9, 126.9, 125.2, 123.4, 120.3, 112.5, 109.7, 40.2, 30.4, 20.6, 14.0**. IR** (ATR): ν_{max} (cm^{-1}) = 3419, 3353, 3254, 2956, 2925, 2861, 1671, 1635, 1571, 1527, 1479, 1431, 1374, 1347, 1303, 1238, 1186, 1153, 1113, 1077, 959, 940, 888, 839, 770, 662, 628, 581, 486, 410.

3-((((2-butyl-1,3-dioxo-2,3-dihydro-1*H*-benzo[de]isoquinoline-6-yl)carbamoyl)oxy)methyl)-5-methyl-2((4-(4,4,5,5-tetramethyl-1,3,2-dioxaborolan-2-yl)benzyl)oxy)benzyl(2-(2-(dimethylamino)ethyl)-1,3-dioxo-2,3-dihydro-1*H*-benzo[de]iosquinolin-5-yl)carbamate (2.3)

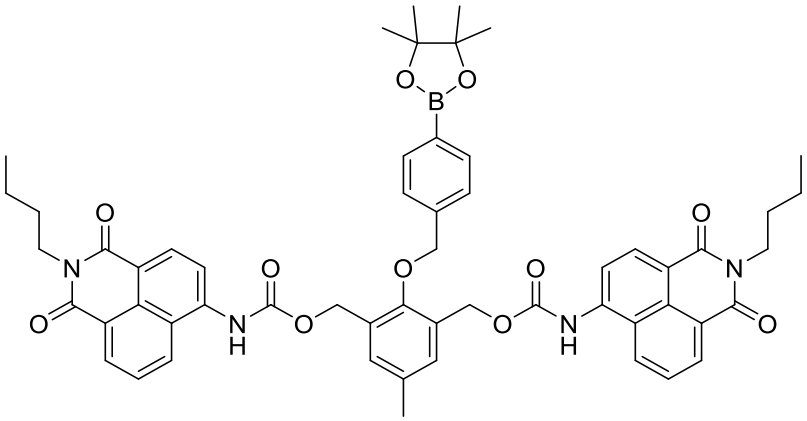

2.8 (46 mg, 0.17 mmol) was dissolved in DCM and cooled to 0ºC, after which triphosgene (51 mg, 0.17 mmol) and TEA (34 mg, 0.33 mmol) were added, and the reaction was allowed to come up to room temperature and then stirred for 3 hours. Excess triphosgene was removed using pressurised N_2 and the residue was redissolved in DCM and added slowly to a stirring solution of **2.7** (22 mg, 0.057 mmol) in DCM at 0ºC. the reaction was allowed to come to room temperature and then stirred overnight. The reaction was concentrated *in vacuo,* and the resulting residue was dissolved in ethyl acetate. The resulting precipitate was filtered, washed with MeOH,

and lyophilised to yield the title compound as a yellow solid. (41 mg, 73%). **^{1}H NMR** (500 MHz, $CDCl_3$) δ 8.62 – 8.59 (m, 2H), 8.58 (d, *J* = 8.2 Hz, 2H), 8.32 (d, *J* = 8.2 Hz, 2H), 8.06 (d, *J* = 8.5 Hz, 2H), 7.83 (d, *J* = 7.9 Hz, 2H), 7.72 (dd, *J* = 8.4, 7.4 Hz, 2H), 7.48 (d, *J* = 7.8 Hz, 2H), 7.40 (s, 2H), 7.33 (s, 2H), 5.35 (s, 4H), 5.03 (s, 4H), 4.20 – 4.13 (m, 4H), 2.38 (s, 3H), 1.71 (dq, *J* = 15.2, 7.6 Hz, 4H), 1.48 – 1.39 (m, 4H), 1.32 (s, 12H), 0.97 (t, *J* = 7.4 Hz, 6H). **^{13}C NMR** (126 MHz, $CDCl_3$) δ 164.3, 163.8, 154.4, 152.1, 139.8, 138.8, 135.4, 134.9, 132.58, 132.4, 131.4, 129.3, 129.1, 127.0, 126.8, 126.0, 132.7, 128.2, 117.1, 84.1, 77.6, 63.3, 40.4, 30.4, 25.0, 21.0, 20.5, 14.0. **IR** (ATR): ν_{max} (cm^{-1}) = 3277, 2957, 1697, 1651, 1620, 1592, 1537, 1509, 1447, 1390, 1380, 1223, 1146, 1061, 1001, 967, 878, 857, 817, 780, 758, 730, 658, 634, 579, 501. **HRMS** (ESI+) *m/z* calcd. for $C_{56}H_{57}BN_4O_{11}$ $[M+Na]^+$ 995.4145, found 995.4010 (-0.68 ppm).

3-(hydroxymethyl)-5-methyl-2-((4-(4,4,5,5-tetramethyl-1,3,2-dioxaborolan-2-yl)oxy)benzyl(2-(2-dimethylamino)ethyl)-1,3-dioxo-2,3-dihydro-1*H*-benzo[de]isoquinolin-5-yl)carbamate (2.13)

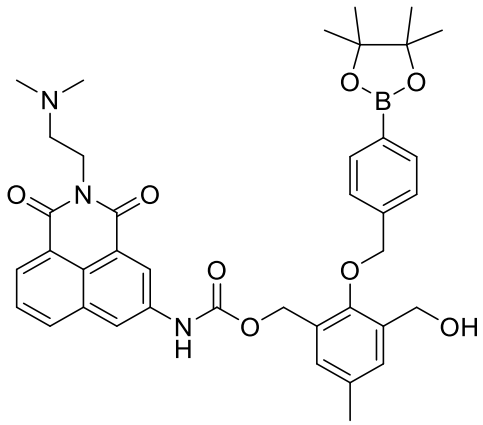

2.9 (38 mg, 0.14 mmol) was dissolved in DCM and cooled to 0° C, after which triphosgene (42 mg, 0.14 mmol) and TEA (43 mg, 0.42 mmol) were added, and the reaction was allowed to warm to room temperature and stirred for 3 hours. Excess triphosgene was removed using pressurised N_2 and the residue was redissolved in DCM and added slowly to a stirring solution of **2.7** (59 mg, 0.15 mmol) in DCM at 0° C. The reaction was allowed to come to room temperature and was stirred overnight. The reaction was concentrated *in vacuo,* and the resulting residue was purified using flash column chromatography eluting with $CHCl_3$/MeOH (96/4) to yield the title compound as a yellow solid. (24 mg, 25%). **^{1}H NMR** (500 MHz, $CDCl_3$) δ 8.35 (s,

1H), 8.30 (dd, *J* = 7.2, 0.8 Hz, 1H), 8.03 (s, 1H), 7.95 (d, *J* = 8.2 Hz, 1H), 7.84 (d, *J* = 8.1 Hz, 2H), 7.62 (dd, *J* = 8.2, 7.3 Hz, 1H), 7.48 (d, *J* = 8.0 Hz, 2H), 7.31 (d, *J* = 1.9 Hz, 1H), 7.25 (d, *J* = 1.9 Hz, 1H), 5.30 (s, 2H), 5.02 (s, 2H), 4.69 (s, 2H), 4.31 (t, *J* = 6.4 Hz, 2H), 2.76 (t, *J* = 6.0 Hz, 2H), 2.38 (s, 6H), 2.37 (s, 3H), 1.33 (s, 12H). **^{13}C NMR** (126 MHz, $CDCl_3$) 164.4, 163.9, 153.4, 140.0, 135.3, 134.6, 134.4, 133.6, 133.5, 131.0, 130.9, 130.7, 129.6, 129.2, 127.6, 127.3, 124.5, 123.3, 122.4, 120.7, 119.9, 84.0, 77.3, 62.7, 61.2, 57.5, 45.7, 37.9, 29.9, 25.0, 21.0. **IR** (ATR): ν_{max} (cm^{-1}) = 3322, 2922, 2158, 2037, 1974, 1699, 2658, 1554, 1512, 1465, 1431, 1357, 1232, 1174, 1143, 1058, 1015, 981, 860, 819, 783, 746, 731, 658, 576, 543, 517, 488. **HRMS** (ESI+) *m/z* calcd. for $C_{39}H_{44}BN_3O_8$ $[M+H]^+$ 694.3258, found 694.3322 (+ 2.95 ppm).

(5-methyl-2-((4-(4,4,5,5-tetramethyl-1,3,2-dioxaborolan-2-yl)benzyl)oxy)-1,3-phenylene)bis(methylene) bis((2-butyl-1,3-dioxo-2,3-dihydro-1H-benzo[de]isoquinolin-6-yl)carbamate) (2.4)

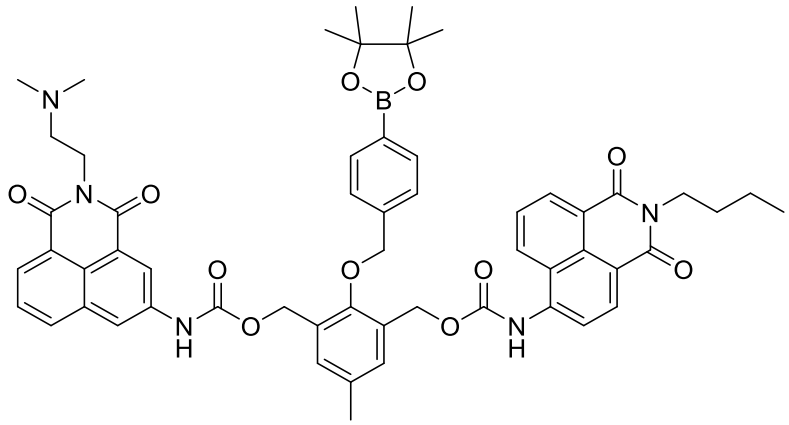

2.8 (23 mg, 0.085 mmol) was dissolved in DCM and cooled to 0ºC, after which triphosgene (25 mg, 0.085 mmol) and TEA (17 mg, 0.17 mmol) were added, and reaction was allowed to come up to room temperature and was stirred for 3 hours. Excess triphosgene was removed using pressurised N_2 and the residue was redissolved in DCM and added slowly to a stirring solution of **2.13** (29 mg, 0.042 mmol) in DCM and was stirred at r.t. overnight. The reaction was concentrated *in vacuo,* and the resulting residue was purified using flash column chromatography, eluting with $CHCl_3$/MeOH (96/4) to yield the title compound as a yellow solid. (20 mg, 49%). **^{1}H NMR** (500 MHz, $CDCl_3$) δ 8.60 (dd, *J* = 7.3, 0.8 Hz, 1H), 8.58 (d, *J* = 8.2 Hz, 1H), 8.52 (br s, 1H), 8.35 (d, *J* = 7.3 Hz, 1H), 8.32 (d, *J* = 8.2 Hz, 1H), 8.21 (br s, 1H), 8.11 (d, *J* = 8.3 Hz, 1H), 8.06 – 8.02 (m, 1H), 7.82 (d, *J* = 8.0 Hz, 2H), 7.71 (dd, *J* = 8.4,

7.4 Hz, 1H), 7.65 – 7.61 (m, 1H), 7.49 (d, *J* = 7.9 Hz, 2H), 7.37 (d, *J* = 1.7 Hz, 1H), 7.33 (d, *J* = 1.9 Hz, 1H), 5.34 (s, 2H), 5.33 (s, 2H), 5.05 (s, 2H), 4.30 (t, *J* = 6.4 Hz, 2H), 4.19 – 4.15 (m, 2H), 2.72 (br s, 2H), 2.39 (s, 9H), 1.74 – 1.67 (m, 2H), 1.44 (dd, *J* = 15.7, 7.0 Hz, 3H), 1.31 (s, 12H), 0.97 (t, *J* = 7.4 Hz, 3H). **^{13}C NMR** (126 MHz, $CDCl_3$) δ 164.3, 164.0, 163.8, 154.9, 154.4, 153.4, 153.2, 139.8, 138.8, 135.4, 135.2, 133.7, 132.7, 132.6, 132.5, 131.4, 131.2, 129.9, 129.6, 129.2, 129.1, 127.6, 127.1, 126.8, 126.5, 126.3, 126.0, 123.6, 122.1, 84.1, 77.7, 63.4, 62.7, 45.3, 40.4, 38.0, 30.4, 25.0, 21.0, 20.5, 14.0. **IR** (ATR): ν_{max} (cm^{-1}) = 2920, 2860, 1996, 1666, 1609, 1545, 1511, 1467, 1430, 1387, 1368, 1235, 1202, 1175, 1142, 1076, 962, 828, 780, 721, 655, 578, 501. **HRMS** (ESI+) *m/z* calcd. for $C_{56}H_{58}BN_5O_{11}$ $[M+H]^+$ 988.4268, found 988.4313 (+ 0.62 ppm).

6.3 Synthetic Procedures for Chapter 3

3,4-diethoxycyclobut-3-ene-1,2-dione (3.4)

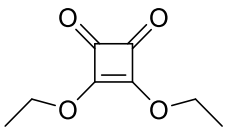

3,4-dihydroxy-3-cyclobutene-1,2-dione (10 g, 87 mmol) was suspended in EtOH Triethyl orthoformate (40 mL, 241 mmol) was added and the reaction was refluxed for 72 hours. Solvent was removed *in vacuo* and resulting residue was purified via column chromatography eluting with DCM to yield the title compound as a yellow oil. (13.2 g, 86%) All spectral data is in agreement with the literature.[195] **^{1}H NMR** (500 MHz, DMSO-d_6) δ 4.65 (q, J = 7.1 Hz, 4H), 1.37 (t, J = 7.1 Hz, 6H). **^{13}C NMR** (126 MHz, DMSO-d_6) δ 189.1, 183.7, 70.2, 15.3.

2,6-diazabicyclo[5.2.0]non-1(7)-ene-8,9-dione (3.5)

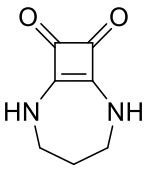

A solution of **3.4** (1.00 g, 5.88 mmol) in 5ml of EtOH and a solution of propylene diamine (435 mg, 5.88 mmol) in 5ml of EtOH were added to two separate 5ml syringes. Both solutions were added to 150ml of EtOH at a flow rate of 1 ml/hour and left to stir for 16 hrs. the resulting precipitate was filtered, washed with EtOH and diethyl ether and lyophilised to yield the title compound as an off-white powder. (700 mg, 78%) **^{1}H NMR** (500 MHz, DMSO-d_6) δ 8.41 (s, 2H), 3.31 – 3.27 (m, 4H), 1.89 – 1.83 (m, 2H). **^{13}C NMR** (126 MHz, DMSO-d_6) δ 181.4, 169.0, 46.4, 30.9. **IR** (ATR): ν_{max} (cm^{-1}) = 3286, 3188, 3145, 3045, 2965, 2912, 2862, 1645, 1552, 1437, 1363, 1323, 1272, 1207, 1117, 1004, 953, 890, 840, 720, 625, 554, 474, 450. **HRMS** (ESI+) *m/z* calcd. for $C_7H_8N_2O_2$ $[M+Na]^+$ 175.0586, found 175.0477 (- 0.41 ppm).

***tert*-butyl (3-(8,9-dioxo-2,6-diazabicyclo[5.2.0]non-1(7)-en-2-yl)-3-oxopropyl)carbamate (3.7)**

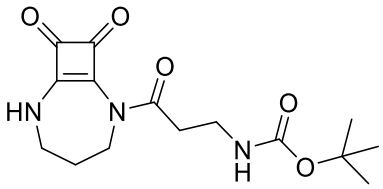

3.5 (100 mg, 0.66 mmol) was dissolved in DMSO and boc-β-Ala-Osu (566 mg, 1.98mmol) and TEA (400 mg, 3.9mmol) were added and the reaction was stirred at room temperature overnight. DMSO was removed via lyophilisation and water was added to the residue. The crude product was extracted with DCM, and the organic layers were combined, washed with water, brine and dried over sodium sulphate. The solvent was removed *in vacuo,* and the crude product was purified *via* reverse-phase column chromatography (MeCN:H_2O, 0 – 50% MeCN) to yield the title compound as a white solid. (143 mg, 67%) **^{1}H NMR** (500 MHz, DMSO-d_6) δ 9.31 (s, 1H), 6.79-6.77 (t, J = 5.3 Hz, 1H), 3.85-3.83 (dd, J = 5.5, 3.5 Hz, 2H), 3.42 – 3.38 (m, 2H), 3.18 (dd, J = 12.3, 6.3 Hz, 2H), 3.02 (t, J = 6.6 Hz, 2H), 1.99 (br s, 2H), 1.35 (s, 9H). **^{13}C NMR** (126 MHz, DMSO-d_6) δ 188.3, 179.3, 172.4, 170.5, 162.4, 155.4, 77.6, 46.0, 45.7, 36.4, 36.0, 28.4, 28.2. **IR** (ATR): ν_{max} (cm^{-1}) =3260, 2979, 2932, 1802, 1693, 1620, 1523, 1474, 1410, 1366, 1321, 1251, 1217, 1166, 1066, 1006, 984, 873, 826, 779, 722, 644, 599, 552, 492, 429. **HRMS** (ESI+) *m/z* calcd. for $C_{15}H_{21}N_3O_5$ $[M+Na]^+$ 346.1480, found 346.1372 (- 0.33 ppm).

***tert*-butyl (2-(8,9-dioxo-2,6-diazabicyclo[5.2.0]non-1(7)-en-2-yl)-2-oxoethyl)carbamate (3.6)**

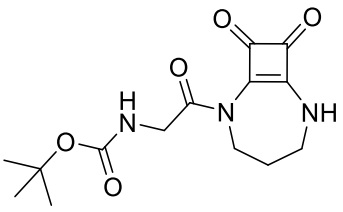

3.5 (100 mg, 0.66 mmol) was dissolved in DMSO and boc-Gly-Osu (359mg, 1.32mmol) and TEA (200mg, 1.98mmol) was added and the reaction was stirred at room temperature overnight. DMSO was removed via lyophilisation and water was added to the residue. The crude product was extracted with DCM, and the organic layers were combined, washed with water, brine and dried over sodium sulphate. The

solvent was removed *in vacuo,* and the crude product was purified *via* reverse-phase column chromatography (MeCN:H_2O, 0 – 50% MeCN) to yield the title compound as a brown solid. (68 mg, 34%) **^{1}H NMR** (500 MHz, DMSO-d_6) δ 9.35 (s, 1H), 7.05 (t, J = 5.9 Hz, 1H), 4.31 (d, J = 6.0 Hz, 2H), 3.90 – 3.83 (m, 2H), 3.46 – 3.38 (m, 2H), 1.96 (br t, J = 4.3 Hz, 2H), 1.39 (s, 9H).**^{13}C NMR** (126 MHz, DMSO-d_6) δ 188.3, 179.2, 172.4, 169.1, 161.6, 155.9, 78.0, 46.2, 45.71, 44.2, 28.6, 28.2. **IR** (ATR): ν_{max} (cm^{-1}) = 3380, 3253, 2980, 2922, 1798, 1700, 1673, 1610, 1504, 1449, 1363, 1504, 1449, 1353, 1325, 1227, 1158, 1074, 1048, 1023, 998, 872, 823, 758, 635, 599. **HRMS** (ESI+) *m/z* calcd. for $C_{14}H_{19}N_3O_5$ $[M+Na]^+$ 332.1325, found 332.1216 (- 4.16 ppm).

2-glycyl-2,6-diazabicyclo[5.2.0]non-1(7)-ene-8,9-dione

2,5-dioxopyrrolidin-1-yl 4-((tert-butoxycarbonyl)amino)butanoate (3.16)

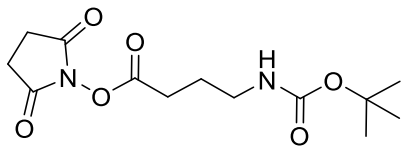

Boc-GABA-OH (500 mg, 2.46 mmol) and *N*-hydroxysuccinamide (424 mg, 3.69 mmol) were dissolved in MeCN and cooled to 0°C. EDC.HCl (705mg, 3.69mmol) was then added and the reaction was stirred on ice for 1 hour before heating to room temperature and left to stir for a further 16 hours. The solvent was removed *in vacuo* and the resulting residue was redissolved in DCM and was washed with water and brine. The organic layer was concentrated to yield the title compound as a white solid, which was used without further purification. **^{1}H NMR** (500 MHz, DMSO-d_6) δ 6.91 (d, J = 4.4 Hz, 1H), 2.99 (q, J = 6.6 Hz, 2H), 2.81 (s, 4H), 2.66 (t, J = 7.5 Hz, 2H), 1.72 (p, J = 7.2 Hz, 2H), 1.38 (s, 9H). **^{13}C NMR** (126 MHz, DMSO-d_6) δ 170.2, 168.8, 155.6, 77.6, 38.9, 28.2, 27.3, 25.4, 24.7. **IR** (ATR): ν_{max} (cm^{-1}) = 3332, 2985, 2934, 1791, 1732, 1682, 1537, 1451, 1367, 1319, 1292, 1252, 1200, 1170, 1066, 1003, 945, 891, 857, 816, 782, 748, 642, 581, 557, 461, 430.

tert-butyl (4-(8,9-dioxo-2,6-diazabicyclo[5.2.0]non-1(7)-en-2-yl)-4-oxobutyl)carbamate (3.8)

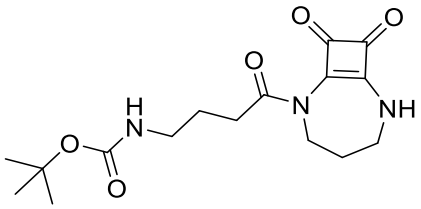

3.5 (100 mg, 0.66 mmol) was dissolved in DMSO. **3.16** (394 mg, 1.32 mmol) and TEA (200 mg, 1.98 mmol) were added, and the reaction was stirred at room temperature overnight. DMSO was removed via lyophilisation, water was added to the residue, and the crude product was extracted with DCM. The organic layers were combined, washed with water and brine, dried over sodium sulphate and the solvent was removed *in vacuo*. The residue was purified *via* reverse-phase column chromatography (MeCN:H_2O, 0 – 50% MeCN) to yield the title compound as a white solid (140 mg, 63%). **^{1}H NMR** (500 MHz, DMSO-d_6) δ 9.29 (s, 1H), 6.77 (s, 1H), 3.89 – 3.82 (m, 2H), 3.40 (dd, J = 6.4, 2.8 Hz, 2H), 2.91 (dd, J = 12.6, 6.4 Hz, 2H), 2.82 (t, J = 6.7 Hz, 2H), 1.98 (s, 2H), 1.65 (p, J = 6.9 Hz, 2H), 1.34 (s, 9H). **^{13}C NMR** (126 MHz, DMSO-d_6) δ 188.4, 179.3, 172.4, 171.5, 162.6, 155.6, 77.4, 46.0, 45.7, 38.9, 32.2, 28.5, 29.0, 25.1. **IR** (ATR): ν_{max} (cm^{-1}) = 3379, 3334, 3180, 2968, 2931, 2875, 1799, 1707, 1681, 1629, 1589, 1517, 1462, 1417, 1360, 1320, 1251, 1222, 1159, 1069, 991, 968, 880, 828, 783, 712, 633, 596, 488, 458, 408. **HRMS** (ESI+) *m/z* calcd. for $C_{15}H_{21}N_3O_5$ $[M+Na]^+$ 360.1628, found 360.1530 (+ 0.22 ppm).

2-(3-aminopropanoyl)-2,6-diazabicyclo[5.2.0]non-1(7)-ene-8,9-dione (3.9)

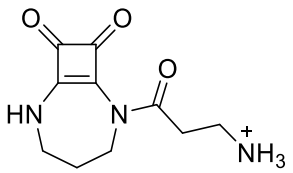

3.7 (50 mg, 0.015 mmol) was dissolved in DCM:TFA (1:1) and left to stir for 3 hrs. The solvent was removed *in vacuo,* and the resulting oil was redissolved in a minimum amount of MeOH and precipitated out of ice-cold diethyl ether. The precipitate was isolated *via* centrifugation to yield the product as a white solid, which was used without further purification. (31 mg, 91%) **^{1}H NMR** (500 MHz, DMSO-d_6) δ 9.48 (s, 1H), 7.77 (s, 3H), 3.93 – 3.87 (m, 2H), 3.46 – 3.40 (m, 2H), 3.25 (t, J = 6.5 Hz, 2H), 3.13 – 3.05 (m, 2H), 2.03 – 1.96 (m, 2H). **^{13}C NMR** (126 MHz, DMSO-d_6) δ 188.4,

179.2, 172.6, 169.4, 161.6, 46.0, 45.7, 35.0, 33.1, 28.3. **IR** (ATR): ν_{max} (cm^{-1}) = 3090, 2957, 2919, 1800, 1671, 1608, 1537, 1470, 1404, 1369, 1332, 1284, 1197, 1130, 1110, 1066, 953, 892, 830, 796, 719, 637, 600, 568, 543, 517, 448, 403. **HRMS** (ESI+) *m/z* calcd. for $C_{10}H_{13}N_3O_3$ $[M+Na]^+$ 246.0958, found 246.0849 (+ 0.42).

2,6,10-triazabicyclo[9.2.0]tridec-1(11)-ene-5,12,13-trione (3.10)

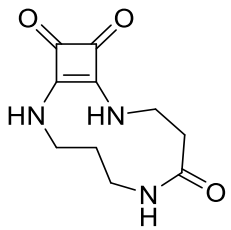

3.9 (22 mg, 0.01 mmol) was dissolved in EtOH along with TEA (40 mg, 0.04 mmol) and allowed to stir at room temperature for 16 hours. The resulting precipitate was isolated *via* centrifugation to yield the title product as a white solid (14 mg, 63%) **^{1}H NMR** (500 MHz, DMSO-d_6, 333 K) δ 7.84 (s, 2H), 6.64 (s, 1H), 3.56 (dd, *J* = 10.6, 6.2 Hz, 4H), 3.24 (d, *J* = 4.8 Hz, 2H, under H_2O peak), 2.24 (dd, *J* = 6.0, 4.3 Hz, 2H), 1.65 (dt, *J* = 10.9, 5.5 Hz, 2H). **^{13}C NMR** (126 MHz, DMSO-d_6, 333 K) δ 185.1, 184.3, 171.0, 169.1, 43.2, 40.6, 38.8, 37.3, 28.6. **IR** (ATR): ν_{max} (cm^{-1}) = 3299, 3277, 3236, 1638, 1570, 1484, 1463, 1442, 1368, 1341, 1202, 1167, 1108, 742, 705, 636, 589, 499, 465, 434. **HRMS** (ESI+) *m/z* calcd. for $C_{10}H_{13}N_3O_3$ $[M+Na]^+$ 246.0957, found 246.0849 (0.19 ppm).

di-tert-butyl ((8,9-dioxo-2,6-diazabicyclo[5.2.0]non-1(7)-ene-2,6-diyl)bis(3-oxopropane-3,1-diyl))dicarbamate (3.11)

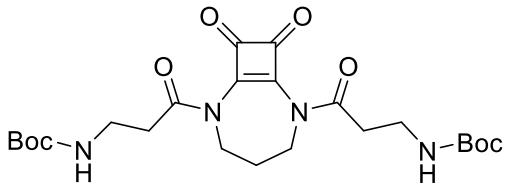

3.7 (85 mg, 0.27 mmol), boc-β-alanine (55 mg, 0.29 mmol) and DIPEA (75 mg, 0.58 mmol) were dissolved in DMF and allowed to stir at 0°C, followed by the addition of COMU (125 mg, 0.29 mmol). The solution was allowed to stir at 0°C, allowed to warm to room temperature and stirred for 5 hours. DMF was removed *in vacuo*, and the residue was redissolved in DCM, washed with 1M HCl, sodium bicarb., water and brine, dried over sodium sulphate and concentrated *in vacuo* yielding the title compound as a white solid, which was used without further purification. (87 mg, 67%)

^{1}H NMR (500 MHz, DMSO-d_6) δ 6.86 (t, J = 5.5 Hz, 2H), 3.93 (t, J = 6.0 Hz, 4H), 3.22 (dd, J = 12.5, 6.4 Hz, 4H), 2.94 (t, J = 6.7 Hz, 4H), 1.96 (dt, J = 12.3, 6.3 Hz, 2H), 1.36 (s, 18H). **^{13}C NMR** (126 MHz, DMSO-d_6) δ 175.1, 170.6, 155.5, 77.8, 36.2, 35.2, 28.2, 23.7. **IR** (ATR): ν_{max} (cm^{-1}) = 3372, 2976, 1795, 1740, 1688, 1563, 1509, 1414, 1365, 1340, 1248, 1274, 1159, 1036, 965, 858, 781, 566, 460. **HRMS** (ESI+) *m/z* calcd. for $C_{23}H_{34}N_4O_8$ $[M+Na]^+$ 517.2377, found 517.2266 (- 2.13 ppm).

2,6,10,14-tetraazabicyclo[13.2.0]heptadec-1(15)-ene-5,11,16,17-tetraone (3.12)

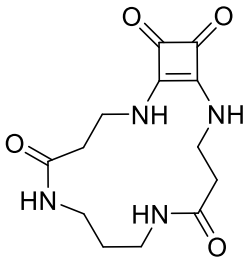

3.11 (40 mg, 0.08 mmol) was dissolved in TFA:DCM (1:1) and allowed to stir at room temperature for 4 hours. DCM:TFA was removed *in vacuo,* and the crude product was redissolved in a minimum amount of MeOH and subsequently added dropwise to ice cold diethyl ether. The resulting precipitate was isolated *via* centrifugation to yield the deprotected intermediate as a white solid, which was used without further purification or characterisation. The deprotected amine was dissolved in EtOH along with TEA (55 mg, 0.31 mmol) and allowed to stir at room temperature overnight. The resulting precipitate was isolated *via* centrifugation and lyophilised to yield the title compound as a white solid. (11 mg, 49%) **^{1}H NMR** (500 MHz, DMSO-d_6) δ 7.75 (br s, 2H), 7.22 (br s, 2H), 3.64 (br s, 4H), 3.11 (br s, 4H), 2.25 (br s, 4H), 1.63 (br s, 2H). ^{13}C NMR could not be characterised due to the aggregation of the compound resulting in low peak intensity. **IR** (ATR): ν_{max} (cm^{-1}) = 3230, 1797, 1639, 1564, 1484, 1461, 1439, 1364, 1325, 1202, 1166, 1102, 1006, 873, 833, 705, 625, 587, 499, 466, 430. **HRMS** (ESI+) *m/z* calcd. for $C_{13}H_{18}N_4O_4$ $[M+H]^+$ 295.1317, found 295.1402 (- 3.64 ppm).

tert-butyl (3-(6-(3-((((9H-fluoren-9-yl)methoxy)carbonyl)amino)propanoyl)-8,9-dioxo-2,6-diazabicyclo[5.2.0]non-1(7)-en-2-yl)-3-oxopropyl)carbamate (3.13)

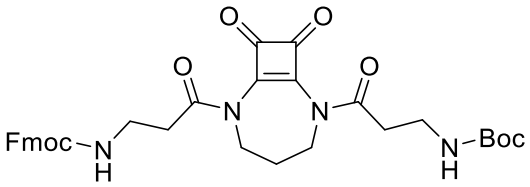

3.7 (50 mg, 0.15 mmol), fmoc-β-alanine (53 mg, 0.17 mmol) and DIPEA (44mg, 0.34 mmol) were dissolved in DMF and allowed to stir at 0ºC, followed by the addition of COMU (72 mg, 0.17 mmol). The solution was allowed to stir at 0ºC, allowed to warm to room temperature and stirred for 5 hours. DMF was removed in *vacuo*, and the residue was redissolved in DCM, washed with 1M HCl, sodium bicarb., water and brine, dried over sodium sulphate and concentrated, yielding the title compound as a white solid, which was used without further purification. (61 mg, 65%) **^{1}H NMR** (500 MHz, DMSO-d_6) δ 7.88 (d, J = 7.5 Hz, 2H), 7.68 (d, J = 7.4 Hz, 2H), 7.40 (dd, J = 12.5, 5.0 Hz, 3H), 7.32 (td, J = 7.4, 1.0 Hz, 2H), 6.86 (t, J = 5.3 Hz, 1H), 4.28 (d, J = 6.9 Hz, 2H), 4.20 (t, J = 6.7 Hz, 1H), 3.95 – 3.91 (m, 2H), 3.91 – 3.85 (m, 2H), 3.31 – 3.26 (m, 2H), 3.21 (dt, J = 11.7, 6.0 Hz, 2H), 2.98 (t, J = 6.7 Hz, 2H), 2.94 (t, J = 6.6 Hz, 2H), 1.99 – 1.90 (m, 2H), 1.35 (s, 9H).**^{13}C NMR** (126 MHz, DMSO-d_6) δ 185.8, 175.0, 175.0, 170.5, 170.4, 156.0, 155.5, 143.9, 140.7, 127.6, 127.1, 125.1, 120.1, 77.7, 65.9, 65.4, 46.9, 46.7, 44.8, 36.4, 35.1, 28.2, 23.7, 13.9. **IR** (ATR): ν_{max} (cm^{-1}) = 3355, 2976, 1794, 1694, 1562, 1514, 1449, 1414, 1366, 1340, 1245, 1164, 1039, 1007, 857, 760, 740, 644, 564, 461, 426. **HRMS** (ESI+) *m/z* calcd. for $C_{33}H_{36}N_4O_8$ $[M+Na]^+$ 639.2532, found 639.2427 (- 0.12 ppm).

tert-butyl (3-oxo-3-(7,12,13-trioxo-2,6,10-triazabicyclo[9.2.0]tridec-1(11)-en-2-yl)propyl)carbamate (3.14)

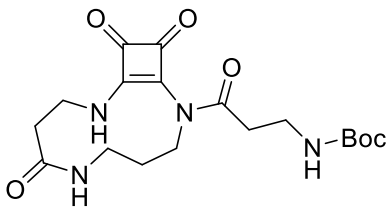

3.13 (40 mg, 0.064 mmol) was dissolved in DCM along with DBU (49 mg, 0.32 mmol) and left to stir at room temperature overnight. Solvent was removed *in vacuo,* and the crude product was precipitated from ice-cold diethyl ether. The crude product was then

purified *via* reverse-phase column chromatography (MeCN:H_2O, 0 – 50% MeCN) to yield the product as a pale-yellow solid, which was used without further purification. (20 mg, 81%).

6.4 Synthetic Procedures for Chapter 4

3-((((4-nitrobenzyl)oxy)carbonyl)amino)propanoic acid (4.8)

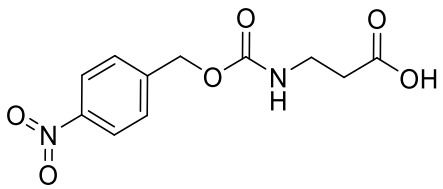

β-alanine (250 mg, 2.8 mmol) was dissolved in 1:1 dioxane:water along with Na_2HCO_3 (471 mg, 5.61 mmol) and allowed to stir at 0°C for 5 mins. *Para*-nitrobenzyl chloroformate (787 mg, 3.7 mmol) was then added and the reaction was stirred at room temperature overnight. Solution was then washed with diethyl ether, and the aqueous layer was acidified to pH 1 with 1M HCl. Crude was extracted with ethyl acetate, organic layers were combined and washed with water, brine and dried over sodium sulphate. The crude product was reduced *in vacuo* and purified using column chromatography eluting with 5% MeOH in DCM, yielding the title compound as a white solid. (400 mg, 55%). **^{1}H NMR** (500 MHz, DMSO--d_6) δ 12.23 (s, 1H), 8.23 (d, J = 8.7 Hz, 2H), 7.59 (d, J = 8.4 Hz, 2H), 7.45 (s, 1H), 5.16 (s, 2H), 3.22 (d, J = 6.1 Hz, 2H), 2.40 (t, J = 6.9 Hz, 2H). **^{13}C NMR** (126 MHz, DMSO-d_6) δ 172.7, 155.7, 146.9, 145.2, 128.1, 123.5, 64.0, 36.6, 34.1. **IR** (ATR): ν_{max} (cm^{-1}) = 3342, 2949, 1728, 1684, 1606, 1541, 1512, 1437, 1408, 1345, 1270, 1221, 1135, 1109, 1076, 1010, 934, 901, 849, 778, 738, 688, 598, 544, 465. HRMS (ESI+) calcd. for $C_{11}H_{12}N_2O_6$ $[M+H]^+$ 269.0770, found 269.0770.

2,5-dioxopyrrolidin-1-yl 3-((((4-nitrobenzyl)oxy)carbonyl)amino)propanoate (4.9)

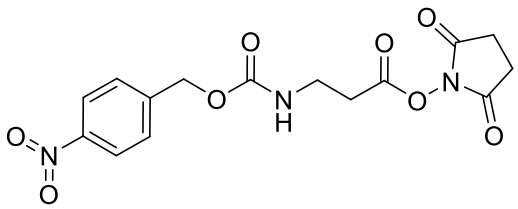

4.8 (50 mg, 0.19 mmol) and N-hydroxysuccinimide (32 mg, 0.28 mmol) were dissolved in DCM and stirred at 0°C for 5 mins, after which EDCI.HCl (53 mg, 0.28 mmol) was added, and the solution was allowed to stir for overnight. The solution was washed with water and brine, and the organic layer was concentrated to yield the title

compound as a white solid, which was used without further purification. (59 mg, 85%) **^{1}H NMR (**500 MHz, DMSO-d_6**)** δ 8.23 (d, *J* = 8.6 Hz, 2H), 7.60 (d, *J* = 8.2 Hz, 3H), 5.18 (s, 2H), 3.37 – 3.32 (m, 2H), 2.88 (t, *J* = 6.7 Hz, 2H), 2.82 (s, 4H). **^{13}C NMR (126 MHz, DMSO-d_6)** δ 170.2, 167.3, 155.7, 146.9, 1451, 128.0, 123.5, 64.2, 36.0, 30.7, 25. 5, 25.2. **IR** (ATR): ν_{max} (cm^{-1}) = 3357, 2940, 1808, 1783, 1738, 1696, 1605, 1534, 1505, 1436, 1414, 1342, 1290, 1264, 1201, 1160, 1096, 1068, 1028, 996, 970, 922, 890, 861, 839, 796, 737, 699, 646, 607, 464, 427. **HRMS** (ESI+) *m/z* calcd. for $C_{15}H_{15}N_3O_8$ $[M+Na]^+$ 388.0861, found 388.0752 (+ 0.47 ppm).

4-nitrobenzyl (3-(8,9-dioxo-2,6-diazabicyclo[5.2.0]non-1(7)-en-2-yl)-3-oxopropyl)carbamate (4.5)

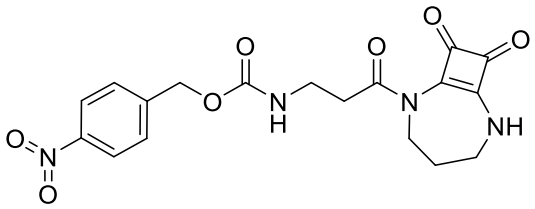

3.5 (22 mg, 0.14 mmol) was dissolved in DMSO. **4.9** (75 mg, .22mmol) and TEA (44mg, 0.43 mmol) were added and the reaction was stirred at room temperature overnight. DMSO was removed *via* lyophilisation, water was added to the residue, and the crude product was extracted with DCM. The organic layers were combined, washed with water, brine, dried over sodium sulphate and concentrated *in vacuo*. The resulting residue was purified *via* reverse-phase column chromatography (MeCN:H_2O, 0 – 50% MeCN) to yield the title compound as a white solid. (19 mg, 32%) **^{1}H NMR (**500 MHz, DMSO-d_6**)** δ 9.33 (s, 1H), 8.23 (d, *J* = 8.5 Hz, 2H), 7.59 (d, *J* = 8.4 Hz, 2H), 7.45 (t, *J* = 5.6 Hz, 1H), 5.14 (s, 2H), 3.87 – 3.81 (m, 2H), 3.42 – 3.37 (m, 2H), 3.30 – 3.25 (m, 2H), 3.08 (t, *J* = 6.6 Hz, 2H), 2.00 – 1.91 (m, 2H). **^{13}C NMR (**126 MHz, DMSO-d_6**)** δ 188.4, 179.3, 172.4, 170.2, 162.3, 155.7, 146.9, 145.2, 128.1, 123.5, 64.0, 46.0, 45.7, 36.8, 35.8, 28.4. **IR** (ATR): ν_{max} (cm^{-1}) = 3389, 3253, 2919, 2849, 1799, 1697, 1618, 1511, 1463, 1410, 1341, 1318, 1246, 1215, 1166, 1133, 1097, 1054, 1012, 894, 825, 773, 734, 645, 597, 521, 489, 454, 411. **HRMS** (ESI+) *m/z* calcd. for $C_{18}H_{18}N_4O_7$ $[M+H]^+$ 403.1177, found 403.1253 (+ 0.48 ppm).

4-(4,4,5,5-tetramethyl-1,3,2-dioxaborolan-2-yl)benzyl 1H-imidazole-1-carboxylate (4.10)

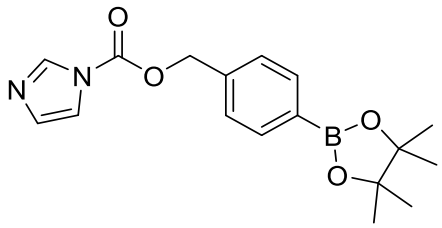

Carbonyldiimidazole (750 mg, 3.2 mmol) was dissolved in dry MeCN and purged with N_2. (4-(4,4,5,5-tetramethyl-1,3,2-dioxaborolan-2-yl)phenyl)methanol (519 mg, 3.2 mmol) was then added and the reaction was stirred at 50° C for 2 hours. The reaction was cooled to room temperature, concentrated and purified using column chromatography eluting with 60:40 pet. ether:ethyl acetate, to yield the title compound as a white solid. (698 mg, 66%). **^{1}H NMR** (500 MHz, DMSO-d_6) δ 8.30 (s, 1H), 7.71 (d, J = 7.9 Hz, 2H), 7.62 (s, 1H), 7.51 (d, J = 7.8 Hz, 2H), 7.09 (s, 1H), 5.47 (s, 2H), 1.29 (s, 12H). **^{13}C NMR** (126MHz, DMSO-d_6) δ 148.2, 137.9, 137.3, 134.6, 130.4, 127.4, 127.2, 117.6, 83.7, 68.9, 24.6. **IR** (ATR): ν_{max} (cm^{-1}) = 2980, 1745, 1615, 1518, 1448, 1360, 1325, 1258, 1233, 1142, 1086, 1021, 964, 937, 898, 859, 822, 794, 731, 655, 618, 580, 508, 449, 401

tert-butyl 3-(2-oxo-2-phenylacetamido)propanoate (4.12)

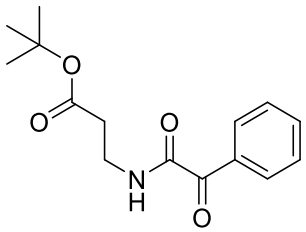

2-oxo-2-phenylacetic acid (413 mg, 2.75 mmol) and PyBop (1.43 g, 2.75 mmol) were allowed to stir in DCM for 30 mins after which β-alanine *tert*-butyl methyl ester hydrochloride (500 mg, 2.75 mmol) and NMM (556 mg, 5.5 mmol) were added, and the solution was allowed to stir at r.t. overnight. The solution was washed with aq. sodium bicarb., water and brine and dried over sodium sulphate. The organic layer was concentrated *in vacuo,* and the crude product was purified using flash chromatography eluting with DCM:MeOH (95:5) to yield the title compound as a clear oil. (400 mg, 52%) **^{1}H NMR** (500 MHz, DMSO-d_6) δ 8.97 (t, J = 5.2 Hz, 1H), 7.97 (dd, J = 8.3, 1.2 Hz, 2H), 7.75 – 7.69 (m, 1H), 7.57 (dd, J = 11.0, 4.6 Hz, 2H), 3.44 (dd, J = 12.6, 6.7

Hz, 2H), 2.5 (2H) 1.41 (s, 9H). **^{13}C NMR (**126 MHz, DMSO-d_6**)** δ 190.3, 170.4, 164.9, 134.6, 132.9, 129.8, 128.9, 80.1, 34.7, 34.5, 27.7. **IR** (ATR): ν_{max} (cm^{-1}) = 3270, 1799, 1663, 1611, 1516, 1448, 1409, 1362, 1325, 1225, 1165, 1097, 1071, 1001, 826, 749, 690, 672, 594, 516, 453. **HRMS** (ESI+) *m/z* calcd. for $C_{15}H_{19}NO_4$ $[M+Na]^+$ 300.1314, found 300.1206 (+ 0.11 ppm).

2,5-dioxopyrrolidin-1-yl 3-(2-oxo-2-phenylacetamido)propanoate (4.13)

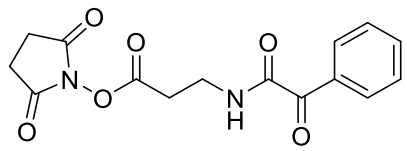

4.12 (200 mg, 0.721 mmol) was dissolved in DCM:TFA (1:1) and allowed to stir at room temperature for 4 hours. Solvent was removed in vacuo and residue was redissolved in DCM along with N-hydroxysuccinimide (124 mg, 1.08 mmol) and EDCI.HCl (206 mg, 1.08 mmol). Reaction was allowed to stir overnight and was washed with water and brine, dried over sodium sulphate and concentrated *in vacuo*, to yield the title compound as a clear oil. (105 mg, 47%) **^{1}H NMR** (500 MHz, DMSO-d_6) δ 9.11 (t, *J* = 5.1 Hz, 1H), 7.99 (d, *J* = 7.4 Hz, 2H), 7.73 (t, *J* = 7.4 Hz, 1H), 7.57 (t, *J* = 7.7 Hz, 2H), 3.58 (q, *J* = 6.5 Hz, 2H), 3.04 (t, *J* = 6.7 Hz, 2H), 2.82 (s, 4H). **^{13}C NMR (**126 MHz, DMSO-d_6**)** δ 189.9, 170.1, 167.3, 164.8, 134.6, 132.9, 129.9, 128.9, 34.0, 30.0, 25.5.

N-(3-(8,9-dioxo-2,6-diazabicyclo[5.2.0]non-1(7)-en-2-yl)-3-oxopropyl)-2-oxo-2-phenylacetamide (4.11)

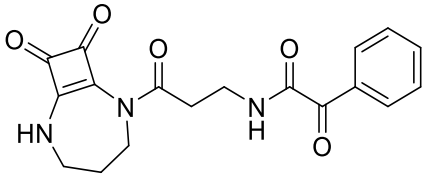

3.5 (15 mg, 0.098 mmol) and TEA (60 mg, 0.59 mmol) were dissolved in DMSO, followed by **4.13** (94 mg, 0.295 mmol) and allowed stir at room temperature overnight. DMSO was removed *via* lyophilisation, and the resulting residue was suspended in water and extracted with DCM. The organic layers were combined and washed with water and brine, dried over sodium sulphate and concentrated *in vacuo*. The crude product was purified *via* reverse-phase column chromatography (MeCN:H_2O, 0 – 50%

MeCN) to yield the title compound as an orange solid. (13mg, 37**%) ^{1}H NMR** (500 MHz, DMSO-d_6) δ 9.34 (s, 1H), 8.97 (t, J = 4.9 Hz, 1H), 7.97 (d, J = 7.6 Hz, 2H), 7.72 (t, J = 7.3 Hz, 1H), 7.57 (t, J = 7.6 Hz, 2H), 3.92 – 3.86 (m, 2H), 3.52 (dd, J = 12.3, 6.2 Hz, 2H), 3.40 (br s, 2H), 3.21 (t, J = 6.5 Hz, 2H), 1.98 (br s, 2H). **^{13}C NMR** (126 MHz, DMSO-d_6) δ 190.3, 188.4, 179.3, 172.5, 170.1, 165.0, 162.2, 134.5, 132.9, 129.8, 128.9, 46.0, 45.7, 35.17, 34.8, 28.4. **IR** (ATR): ν_{max} (cm^{-1}) = 3270, 1799, 1633, 1511, 1516, 1448, 1409, 1362, 1325, 1225, 1165, 1097, 1071, 1001, 826, 759, 690, 672, 594, 516. **HRMS** (ESI+) *m/z* calcd. for $C_{18}H_{17}N_3O_5$ $[M+Na]^+$ 378.1168, found 378.1060 (+ 2.52 ppm).

tert-butyl 4-(6-nitro-1,3-dioxo-1H-benzo[de]isoquinolin-2(3H)-yl)butanoate (4.14)

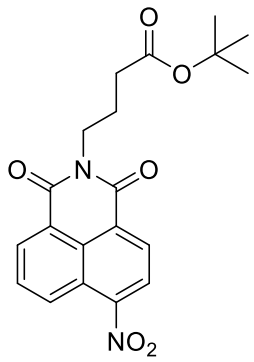

4-nitro-1,8-naphthalic anhydride (250 mg, 1.03 mmol), *tert*-butyl-4-aminobutanoate hydrochloride (201 mg, 1.03 mmol) and TEA (208 mg, 2.06 mmol) were dissolved in EtOH and refluxed overnight. The solution was cooled to r.t. and the resulting precipitate was filtered and washed with ice-cold EtOH. The crude product was then recrystallised from EtOH to yield the target compound as a beige solid (310 mg, 78%) **^{1}H NMR (**500 MHz, $CDCl_3$**)** δ 8.84 (d, J = 8.6 Hz, 1H), 8.74 (d, J = 7.1 Hz, 1H), 8.69 (d, J = 7.9 Hz, 1H), 8.40 (d, J = 7.8 Hz, 1H), 7.98 (t, J = 7.9 Hz, 1H), 4.25 (t, J = 6.9 Hz, 2H), 2.37 (t, J = 7.2 Hz, 2H), 2.12 – 2.02 (m, 2H), 1.42 (s, 9H). **^{13}C NMR (**126 MHz, $CDCl_3$**)** δ 172.2, 163.5, 162.6, 149.7, 132.6, 130.7, 130.0, 129.5, 129.3, 127.1, 124.0, 123.8, 123.1, 80.6, 40.2, 33.26, 28.2, 23.5. **IR** (ATR): ν_{max} (cm^{-1}) = 3076, 2976, 1724, 1702, 1659, 1621, 1582, 1530, 1437, 1410, 1381, 1363, 1339, 1312, 1230, 1153, 1128, 1054, 967, 879, 849, 822, 785, 759, 712, 624, 584, 550. **HRMS** (ESI+) *m/z* calcd. for $C_{20}H_{20}N_2O_6$ $[M+Na]^+$ 407.1322, found 407.1214 (+ 0.29 ppm).

tert-butyl 4-(6-amino-1,3-dioxo-1H-benzo[de]isoquinolin-2(3H)-yl)butanoate (4.15)

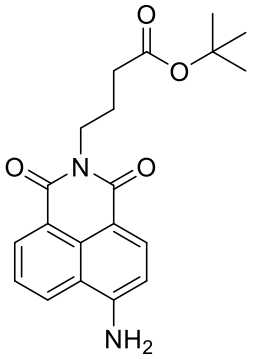

4.14 (250 mg, 0.65 mmol) was suspended in MeOH, along 10% mol. Pd/C, placed under a H_2 atmosphere and allowed to stir for 3 hours. The Pd/C was removed by filtering through celite, and the filtrate was concentrated *in vacuo* to yield the title compound as an orange solid. (220 mg, 96%). **^{1}H NMR (**500 MHz, $CDCl_3$**)** δ 8.58 (s, 1H), 8.40 (d, *J* = 8.1 Hz, 1H), 8.13 – 8.09 (m, 1H), 7.64 (dd, *J* = 8.2, 7.5 Hz, 1H), 6.88 (d, *J* = 8.2 Hz, 1H), 4.99 (s, 2H), 4.24 – 4.17 (m, 2H), 2.35 (t, *J* = 7.7 Hz, 2H), 2.08 – 1.98 (m, 2H), 1.42 (s, 9H). **^{13}C NMR (**126 MHz, $CDCl_3$**)** δ 172.6, 164.7, 164.2, 149.2, 134.0, 131.7, 130.0, 127.0, 125.2, 123.3, 120.3, 112.4, 109.7, 80.4, 39.6, 33.5, 28.2, 23.9. **IR** (ATR): ν_{max} (cm^{-1}) = 3443, 3354, 3257, 2969, 1707, 1680, 1642, 1613, 1576, 1525, 1480, 1457, 1430, 1381, 1354, 1339, 1305, 1284, 1247, 1158, 1101, 1054, 974, 945, 900, 880, 788, 671, 627, 589, 505. **HRMS** (ESI+) *m/z* calcd. for $C_{20}H_{22}N_2O_4$ $[M+Na]^+$ 377.1582, found 377.1473 (+ 0.57 ppm).

tert-butyl 4-(6-((((4-nitrobenzyl)oxy)carbonyl)amino)-1,3-dioxo-1H-benzo[de]isoquinolin-2(3H)-yl)butanoate (4.16)

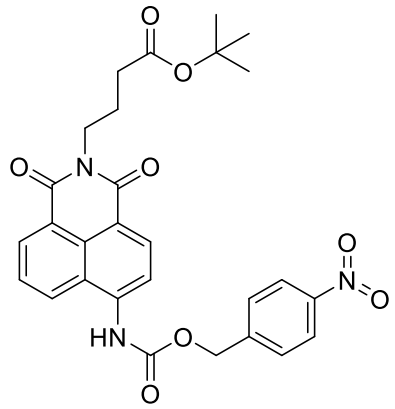

4.15 (45 mg, 0.13 mmol), DMAP (15 mg, 0.13 mmol) and triphosgene (38 mg, 0.13 mmol) were dissolved in DCM, purged with N_2, and allowed to stir at 0°C for three hours. Excess triphosgene was removed using pressurised N_2 and the resulting residue was redissolved in DCM. 4-nitrobenzyl alcohol (49 mg, 0.32 mmol) was added and solution was allowed to stir at r.t. overnight. The reaction was quenched with water, and the crude was extracted with DCM. The organic layers were combined washed with water, brine, dried over sodium sulphate, and concentrated *in vacuo*. The crude product was purified using flash column chromatography eluting with DCM/MeOH (0 – 5%) to yield the target compound as a yellow solid (48 mg, 72%) **^{1}H NMR (**500 MHz, $CDCl_3$) δ 8.63 (d, *J* = 7.2 Hz, 1H), 8.60 (d, *J* = 8.2 Hz, 1H), 8.35 (d, *J* = 8.2 Hz, 1H), 8.26 (d, *J* = 8.7 Hz, 2H), 8.20 (d, *J* = 8.2 Hz, 1H), 7.80 – 7.75 (dd, 1H), 7.61 (d, *J* = 8.6 Hz, 2H), 7.57 (s, 1H), 5.40 (s, 2H), 4.22 (t, *J* = 7.2 Hz, 2H), 2.35 (t, *J* = 7.6 Hz, 2H), 2.09 – 1.99 (m, 2H), 1.42 (s, 9H). **^{13}C NMR (**126 MHz, $CDCl_3$**)** δ 172.4, 164.2, 163.7, 152.8, 148.1, 142.7, 138.54, 132.6, 131.6, 129.1, 128.9, 127.0, 125.9, 124.1, 118.4, 117.3, 80.5, 66.5, 39.8, 33.4, 28.2, 23.7. **IR** (ATR): ν_{max} (cm^{-1}) = 3308, 2973, 1696, 1660, 1621, 1592, 1544, 1515, 1447, 1391, 1343, 1283, 1152, 1126, 1091, 1067, 1017, 899, 842, 782, 764, 734, 581, 463. **HRMS** (ESI+) *m/z* calcd. for $C_{28}H_{27}N_3O_8$ $[M+Na]^+$ 556.1795, found 556.1687 (- 0.62 ppm).

4-(6-((((4-nitrobenzyl)oxy)carbonyl)amino)-1,3-dioxo-1H-benzo[de]isoquinolin-2(3H)-yl)butanoic acid (4.17)

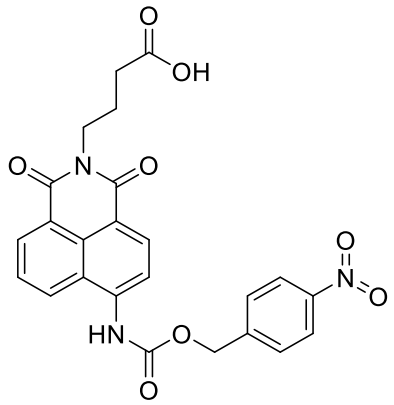

4.16 (20 mg, 0.037 mmol) was dissolved in TFA:DCM (1:1) and allowed to stir at r.t. for 4 hours. The reaction was concentrated, and the resulting residue was redissolved in MeOH and precipitated in ice-cold diethyl ether. The precipitate was isolated *via* centrifugation to yield the title compound as a pale yellow solid (17 mg, 94%) **^{1}H NMR (**500 MHz, DMSO-d_6**-)** δ δ 12.00 (s, 1H), 10.49 (s, 1H), 8.71 (dd, J = 8.6, 0.8 Hz, 1H), 8.51 (dd, J = 7.2, 0.8 Hz, 1H), 8.48 (d, J = 8.2 Hz, 1H), 8.29 (d, J = 8.8 Hz, 2H), 8.18 (d, J = 8.2 Hz, 1H), 7.85 (dd, J = 8.5, 7.3 Hz, 1H), 7.77 (d, J = 8.8 Hz, 2H), 5.43 (s, 2H), 4.08 (t, J = 6.9 Hz, 2H), 2.30 (t, J = 7.3 Hz, 2H), 1.89 (p, J = 7.1 Hz, 2H). **^{13}C NMR (**126 MHz, DMSO-d_6**)** δ 206.6, 174.0, 163.6, 163.1, 153.8, 147.2, 144.2, 140.4, 1331.6, 131.0, 129.2, 128.6, 128.4, 126.5, 123.7, 122.4, 118.5, 117.5, 65.3, 31.3, 30.7, 23.0. **IR** (ATR): ν_{max} (cm^{-1}) = 3290, 2976, 1723, 1695, 1660, 1621, 1592, 1554, 1516, 1447, 1391, 1346, 1237, 1155, 1123, 1091, 1053, 963, 901, 855, 781, 735, 658, 455. **HRMS** (ESI+) *m/z* calcd. for $C_{24}H_{19}N_3O_8$ $[M+Na]^+$ 500.1081, found 500.1081.

6.5 Peroxide Experiments

6.5.1 Uv/Vis and fluorescence titrations

Peroxide UV/Vis titrations were carried out using Lambda 365 Perkin Elmer UV-Vis spectrophotometer and fluorescence titrations were carried out using an Agilent Spectrofluorometer equipped with a 450 W xenon lamp for excitation. A stock solution of compound of (1 mM) was prepared in DMSO and was subsequently diluted to a final volume of 2.5 mL in a UV cuvette to result in a final concentration of 10 µM (unless stated otherwise) in 10 mM PBS (50% DMSO). A stock solution of H_2O_2 of 100 mM was prepared daily in 10 mM PBS and diluted to a concentration of 1 mM in the final volume of 2.5 mL. Upon addition of peroxide to the final volume, absorbance was measured between 250 – 800 nm at time intervals of 60 minutes, and emission wavelengths were selected and slit widths adjusted. Emission spectra were generated from a chosen range from 350 – 800 nm over chosen time periods with intervals of 60 mins.

6.5.2 N-acetyl cysteine Study

NAC inhibition studies were carried out using an Agilent Spectrofluorometer equipped with a 450 W xenon lamp for excitation. A stock solution of NAC of 500 mM was prepared in 10 mM PBS and diluted to a final volume of 2.5 mM in a fluorescent cuvette containing 100 µM H_2O_2, to result in a final concentration of 4 mM and left to incubate for 6 hours. 10 µM of **2.3** was then added to the cuvette and solution was left to incubate for 18 hours. An excitation wavelength was chosen, and the emission spectra was generated from an emission wavelength range ranging from 430 – 700 nm.

6.5.3 LCMS study

LCMS studies were conducted on an Agilent Technologies 1200 series setup, utilising an Agilent Eclipse XDB-C18 (5 µm, 4.6 x 150 mm) column at 40° C. A flow rate of 0.2 ml min^{-1} and gradient of 0.1% of formic acid in CH_3CN (solvent A) in 0.1% of formic acid in H_2O (solvent B) was used as mobile phase. Electrospray in positive mode was used for ionisation. Each sample was prepared in DMSO (20% PBS) to give a final concentration of 2.5 mM of compound and 25 mM peroxide. Solutions were allowed to incubate for 18 hours before injection onto the LCMS.

6.6 CAP Studies

6.6.1 2D Cell Culture

Carried out by Dr. Janith Wanigasekara in TUD. The human glioblastoma cell line (U-251 MG, formerly known as U-373 MG-CD14) was purchased from an ATCC European distributor (LGC Standards). The absence of mycoplasma was checked by using a MycoAlert PLUS mycoplasma detection kit (Lonza). Cells were maintained in Dulbecco's modified Eagle medium (DMEM) - high glucose supplemented with 10% fetal bovine serum (FBS) and 1% penicillin/streptomycin. Cells were maintained in a humidified incubator containing 5% CO_2 atmosphere at 37°C in a TC flask T25, standard for adherent cells (Sarstedt). Cells were routinely sub-cultured when 80% confluence was reached using 0.25% w/v Trypsin-EDTA solution. Cells were seeded at a density of 2.5×10^3 cells/well (6 days treatment) (100 µL culture medium per well), in triplicate in 96-well plates (Sarstedt, Ireland). Plates were incubated overnight at 37 ◦C with 5 % CO2 to allow proper adherence. Existing media was removed from each well and cells were then treated with compounds and serially diluted from 1000 µg/ml to 7.81 µg/ml; 20 % dimethyl sulfoxide (DMSO) was used as a positive control and media was used as a negative control.

6.6.2 Pin-to-Plate System

Carried out by Dr. Janith Wanigasekara in TUD. A pin to plate electrode design was employed to generate a large volume atmospheric discharge. The reactor consisted of 88 slightly convex pins attached stainless steel electrode (150 mm x 200 mm), paired with a flat stainless steel ground plate (200 mm x 250 mm) powered by an AC power supply (Leap100, PlasmaLeap Technologies, Ireland). This Leap100 power supply has a discharge voltage up to 80 kV (p-p), resonance frequency from 30 kHz to 125 kHz, discharge frequency from 100 Hz to 3000 Hz and power from 50 W to 700 W. The air gap between the pin electrodes and the ground plate serves as the sample treatment area, with all samples in this study being placed in the centre. All the samples were treated at a resonant frequency of 55.51 kHz, with a discharge frequency of 1000 Hz and duty cycle of 73 µs while, the discharge gap was kept at 40 mm. Cells were treated for 20 s. The electrodes / sample treatment area was covered in a fitted container to minimize escape of CAP generated reactive species into the general environment.

6.6.3 AlamarBlue Cell Viability Assay

Carried out by Dr. Janith Wanigasekara in TUD. Cell viability was analysed using AlamarBlue cell viability reagent (Thermo Fisher Scientific). After the post treatment incubation, cells were incubated for 3 h at 37 °C with a 10% AlamarBlue solution. Fluorescence was measured using an excitation wavelength of 530 nm and an emission wavelength of 590 nm with a Varioskan Lux multi-plate reader (Thermo Scientific). All experiments consisted of at least three independent tests with a minimum of 3 replicates per experiment and are presented as mean ± S.E.M.

6.7 Anion Binding Studies

6.7.1. ^{1}H NMR anion studies

Tetrabutylammonium salts and receptors were subjected to lyophilisation before use. Solutions of the TBA salts were made up using DMSO-d_6, which was dried using 3Å molecular sieves to a concentration of 250 mM. A stock solution of receptor in DMSO-d_6 was made up to 1 mL and an aliquot of stock solution was diluted to 600 µL to give a final concentration of 2.5 mM in an NMR tube (unless stated otherwise) and ^{1}H NMR was recorded. Subsequent additions of the TBA salts were added and the tube was shaken to allow for homogenisation. This process was repeated until 20 equivalents of anion were added such that the total volume added was 120 µL. ^{1}H NMR spectra were analysed and processed, and stackplots generated using MestreNova 6.0.2 software. A global fitting analysis was employed to provide a binding constant (K_a/M^{-1}), by fitting the chemical shifts of the NH signal as a function of anion concentration using the open access software BindFit.

6.7.2 UV/Vis anion studies

Tetrabutylammonium salts, sodium salts and receptors were subjected to lyophilisation before use. Solutions of the TBA salts were made up using DMSO, which was dried using 3Å molecular sieves to a concentration of 10 mM and sodium salts were made up using Milli-Q water to a concentration of 10 mM. An aliquot of stock solution of receptor in DMSO was diluted to 2.5 mL in a UV cuvette and UV/Vis spectra was recorded. Subsequent additions of the anions were added, and the solution was mixed to allow for homogenisation. This process was repeated until 10 equivalents of anion were added. UV/Vis spectra were analysed and plotted using

GraphPad Prism 8.0 software. A global fitting analysis was employed to provide a binding constant (K_a/M^{-1}), by fitting the changes in absorbance as a function of anion concentration using the open access software BindFit.

Chapter 7

Bibliography

7. Bibliography

(1) Catalano, A.; Iacopetta, D.; Ceramella, J.; Scumaci, D.; Giuzio, F.; Saturnino, C.; Aquaro, S.; Rosano, C.; Sinicropi, M. S. Multidrug Resistance (MDR): A Widespread Phenomenon in Pharmacological Therapies. *Mol. Basel Switz.* **2022**, *27* (3), 616. https://doi.org/10.3390/molecules27030616.

(2) Craig, M.; Jernigan, D.; Laserson, K.; McBride, S.; Fairbanks, J.; Sievert, D.; Armstrong, P. A.; Ewing Ogle, H.; Zucker, H. Antimicrobial Resistance at a Crossroads: The Cost of Inaction. *Lancet Lond. Engl.* **2024**, *404* (10458), 1083–1085. https://doi.org/10.1016/S0140-6736(24)01705-7.

(3) Duan, C.; Yu, M.; Xu, J.; Li, B.-Y.; Zhao, Y.; Kankala, R. K. Overcoming Cancer Multi-Drug Resistance (MDR): Reasons, Mechanisms, Nanotherapeutic Solutions, and Challenges. *Biomed. Pharmacother.* **2023**, *162*, 114643. https://doi.org/10.1016/j.biopha.2023.114643.

(4) Alouane, A.; Labruère, R.; Le Saux, T.; Schmidt, F.; Jullien, L. Self-Immolative Spacers: Kinetic Aspects, Structure–Property Relationships, and Applications. *Angew. Chem. Int. Ed.* **2015**, *54* (26), 7492–7509. https://doi.org/10.1002/anie.201500088.

(5) De Souza, M. M.; Gini, A. L. R.; Moura, J. A.; Scarim, C. B.; Chin, C. M.; Dos Santos, J. L. Prodrug Approach as a Strategy to Enhance Drug Permeability. *Pharmaceuticals* **2025**, *18* (3), 297. https://doi.org/10.3390/ph18030297.

(6) Tsuchiya, K.; Masunaga, H.; Numata, K. Chemoenzymatic Polymerization/Depolymerization of Semiaromatic Polyamides for Chemical Recycling. *ACS Sustain. Chem. Eng.* **2025**, *13* (10), 3994–4004. https://doi.org/10.1021/acssuschemeng.4c09489.

(7) Blencowe, C. A.; Russell, A. T.; Greco, F.; Hayes, W.; Thornthwaite, D. W. Self-Immolative Linkers in Polymeric Delivery Systems. *Polym Chem* **2011**, *2* (4), 773–790. https://doi.org/10.1039/C0PY00324G.

(8) Gnaim, S.; Shabat, D. Quinone-Methide Species, A Gateway to Functional Molecular Systems: From Self-Immolative Dendrimers to Long-Wavelength Fluorescent Dyes. *Acc. Chem. Res.* **2014**, *47* (10), 2970–2984. https://doi.org/10.1021/ar500179y.

(9) Alouane, A.; Labruère, R.; Le Saux, T.; Aujard, I.; Dubruille, S.; Schmidt, F.; Jullien, L. Light Activation for the Versatile and Accurate Kinetic Analysis of Disassembly of Self-Immolative Spacers. *Chem. – Eur. J.* **2013**, *19* (35), 11717–11724. https://doi.org/10.1002/chem.201301298.

(10) Lee, H. Y.; Jiang, X.; Lee, D. Kinetics of Self-Immolation: Faster Signal Relay over a Longer Linear Distance? *Org. Lett.* **2009**, *11* (10), 2065–2068. https://doi.org/10.1021/ol900433g.

(11) Alouane, A.; Labruère, R.; Le Saux, T.; Aujard, I.; Dubruille, S.; Schmidt, F.; Jullien, L. Light Activation for the Versatile and Accurate Kinetic Analysis of Disassembly of Self-Immolative Spacers. *Chem. – Eur. J.* **2013**, *19* (35), 11717–11724. https://doi.org/10.1002/chem.201301298.

(12) Mosey, R. A.; Floreancig, P. E. Versatile Approach to α-Alkoxy Carbamate Synthesis and Stimulus-Responsive Alcohol Release. *Org. Biomol. Chem.* **2012**, *10* (39), 7980. https://doi.org/10.1039/c2ob26571k.

(13) Chakravarty, P. K.; Carl, P. L.; Weber, M. J.; Katzenellenbogen, J. A. Plasmin-Activated Prodrugs for Cancer Chemotherapy. 2. Synthesis and Biological

Activity of Peptidyl Derivatives of Doxorubicin. *J. Med. Chem.* **1983**, *26* (5), 638–644. https://doi.org/10.1021/jm00359a004.

(14) De Groot, F. M. H.; Loos, W. J.; Koekkoek, R.; Van Berkom, L. W. A.; Busscher, G. F.; Seelen, A. E.; Albrecht, C.; De Bruijn, P.; Scheeren, H. W. Elongated Multiple Electronic Cascade and Cyclization Spacer Systems in Activatible Anticancer Prodrugs for Enhanced Drug Release. *J. Org. Chem.* **2001**, *66* (26), 8815–8830. https://doi.org/10.1021/jo0158884.

(15) Liu, G.; Lovell, J. F.; Zhang, L.; Zhang, Y. Stimulus-Responsive Nanomedicines for Disease Diagnosis and Treatment. *Int. J. Mol. Sci.* **2020**, *21* (17), 6380. https://doi.org/10.3390/ijms21176380.

(16) Wieczorkiewicz, P. A.; Krygowski, T. M.; Szatylowicz, H. Substituent Effects and Electron Delocalization in Five-Membered N-Heterocycles. *Phys. Chem. Chem. Phys.* **2024**, *26* (28), 19398–19410. https://doi.org/10.1039/D4CP01709A.

(17) Robbins, J. S.; Schmid, K. M.; Phillips, S. T. Effects of Electronics, Aromaticity, and Solvent Polarity on the Rate of Azaquinone–Methide-Mediated Depolymerization of Aromatic Carbamate Oligomers. *J. Org. Chem.* **2013**, *78* (7), 3159–3169. https://doi.org/10.1021/jo400105m.

(18) Ermini, E.; Brai, A.; Cini, E.; Finetti, F.; Giannini, G.; Padula, D.; Paradisi, L.; Poggialini, F.; Trabalzini, L.; Tolu, P.; Taddei, M. A Novel Bioresponsive Self-Immolative Spacer Based on Aza-Quinone Methide Reactivity for the Controlled Release of Thiols, Phenols, Amines, Sulfonamides or Amides. *Chem. Sci.* **2024**, *15* (16), 6168–6177. https://doi.org/10.1039/D4SC01576B.

(19) De Gracia Lux, C.; McFearin, C. L.; Joshi-Barr, S.; Sankaranarayanan, J.; Fomina, N.; Almutairi, A. Single UV or Near IR Triggering Event Leads to Polymer Degradation into Small Molecules. *ACS Macro Lett.* **2012**, *1* (7), 922–926. https://doi.org/10.1021/mz3002403.

(20) Chen, E. K. Y.; McBride, R. A.; Gillies, E. R. Self-Immolative Polymers Containing Rapidly Cyclizing Spacers: Toward Rapid Depolymerization Rates. *Macromolecules* **2012**, *45* (18), 7364–7374. https://doi.org/10.1021/ma301667c.

(21) Milstien, S.; Cohen, L. A. Rate Acceleration by Stereopopulation Control: Models for Enzyme Action. *Proc. Natl. Acad. Sci.* **1970**, *67* (3), 1143–1147. https://doi.org/10.1073/pnas.67.3.1143.

(22) Levine, M. N.; Raines, R. T. Trimethyl Lock: A Trigger for Molecular Release in Chemistry, Biology, and Pharmacology. *Chem. Sci.* **2012**, *3* (8), 2412. https://doi.org/10.1039/c2sc20536j.

(23) Liu, J.; Jia, B.; Li, Z.; Li, W. Reactive Oxygen Species-Responsive Polymer Drug Delivery Systems. *Front. Bioeng. Biotechnol.* **2023**, *11*. https://doi.org/10.3389/fbioe.2023.1115603.

(24) Shah, M. A.; Rogoff, H. A. Implications of Reactive Oxygen Species on Cancer Formation and Its Treatment. *Semin. Oncol.* **2021**, *48* (3), 238–245. https://doi.org/10.1053/j.seminoncol.2021.05.002.

(25) Jian, J.; Hammink, R.; McKenzie, C. J.; Bickelhaupt, F. M.; Poater, J.; Mecinović, J. Probing the Lewis Acidity of Boronic Acids through Interactions with Arene Substituents. *Chem. – Eur. J.* **2022**, *28* (9). https://doi.org/10.1002/chem.202104044.

(26) Ishiyama, T.; Murata, M.; Miyaura, N. Palladium(0)-Catalyzed Cross-Coupling Reaction of Alkoxydiboron with Haloarenes: A Direct Procedure for

Arylboronic Esters. *J. Org. Chem.* **1995**, *60* (23), 7508–7510. https://doi.org/10.1021/jo00128a024.

(27) Xu, L.; Dong, Z.; Zhang, Q.; Deng, N.; Li, S.-Y.; Xu, H.-J. Protoboration of Alkynes and Miyaura Borylation Catalyzed by Low Loadings of Palladium. *J. Org. Chem.* **2022**, *87* (21), 14879–14888. https://doi.org/10.1021/acs.joc.2c01649.

(28) Thompson, C. L. S.; Kabalka, G. W.; Akula, M. R.; Huffman, J. W. The Conversion of Phenols to the Corresponding Aryl Halides Under Mild Conditions. *N. Y.* **2005**, No. 4.

(29) Perez, C.; Monserrat, J.-P.; Chen, Y.; Cohen, S. M. Exploring Hydrogen Peroxide Responsive Thiazolidinone-Based Prodrugs. *Chem. Commun.* **2015**, *51* (33), 7116–7119. https://doi.org/10.1039/C4CC09921D.

(30) Lu, M.; Zhang, X.; Zhao, J.; You, Q.; Jiang, Z. A Hydrogen Peroxide Responsive Prodrug of Keap1-Nrf2 Inhibitor for Improving Oral Absorption and Selective Activation in Inflammatory Conditions. *Redox Biol.* **2020**, *34*, 101565. https://doi.org/10.1016/j.redox.2020.101565.

(31) Mathew, J.; Ru-Hung; Le, T.-N.; Pham, H.-P.; Kumar, P.; Lee, C.-K.; Shunmugam, R.; Rao, N. V. ROS-Responsive Camptothecin-Linked Thioketal Drug Delivery System Based on Ring-Closing Polymerization. *Eur. Polym. J.* **2024**, *202*, 112646. https://doi.org/10.1016/j.eurpolymj.2023.112646.

(32) Muz, B.; De La Puente, P.; Azab, F.; Azab, A. K. The Role of Hypoxia in Cancer Progression, Angiogenesis, Metastasis, and Resistance to Therapy. *Hypoxia* **2015**, 83. https://doi.org/10.2147/hp.s93413.

(33) Chen, Z.; Han, F.; Du, Y.; Shi, H.; Zhou, W. Hypoxic Microenvironment in Cancer: Molecular Mechanisms and Therapeutic Interventions. *Signal Transduct. Target. Ther.* **2023**, *8* (1). https://doi.org/10.1038/s41392-023-01332-8.

(34) Wu, Y.; Wei, C. Dual-Functional Fluorescent Probe for Imaging ROS and Hypoxia Dynamic in Cancer Cells. *Sens. Actuators B Chem.* **2024**, *419*, 136417. https://doi.org/10.1016/j.snb.2024.136417.

(35) Chen, J.; Dai, R. J.; Tong, B.; Xiao, S. Y.; Meng, W. Reduction of 4-Nitrophenol Catalyzed by Nitroreductase. *Chin. Chem. Lett.* **2007**, *18* (1), 10–12. https://doi.org/10.1016/j.cclet.2006.11.009.

(36) Lippert, A. R.; New, E. J.; Chang, C. J. Reaction-Based Fluorescent Probes for Selective Imaging of Hydrogen Sulfide in Living Cells. *J. Am. Chem. Soc.* **2011**, *133* (26), 10078–10080. https://doi.org/10.1021/ja203661j.

(37) Romano, B.; Pagano, E.; Iannotti, F. A.; Piscitelli, F.; Brancaleone, V.; Lucariello, G.; Nanì, M. F.; Fiorino, F.; Sparaco, R.; Vanacore, G.; Di Tella, F.; Cicia, D.; Lionetti, R.; Makriyannis, A.; Malamas, M.; De Luca, M.; Aprea, G.; D'Armiento, M.; Capasso, R.; Sbarro, B.; Venneri, T.; Di Marzo, V.; Borrelli, F.; Izzo, A. A. *N*-Acylethanolamine Acid Amidase (NAAA) Is Dysregulated in Colorectal Cancer Patients and Its Inhibition Reduces Experimental Cancer Growth. *Br. J. Pharmacol.* **2022**, *179* (8), 1679–1694. https://doi.org/10.1111/bph.15737.

(38) Kumari, R.; Majumder, M. M.; Lievonen, J.; Silvennoinen, R.; Anttila, P.; Nupponen, N. N.; Lehmann, F.; Heckman, C. A. Prognostic Significance of Esterase Gene Expression in Multiple Myeloma. *Br. J. Cancer* **2021**, *124* (8), 1428–1436. https://doi.org/10.1038/s41416-020-01237-1.

(39) Ghosh, A. K.; Brindisi, M. Organic Carbamates in Drug Design and Medicinal Chemistry. *J. Med. Chem.* **2015**, *58* (7), 2895–2940. https://doi.org/10.1021/jm501371s.
(40) Ramiah, D.; Mmereki, D. Synthesizing Efficiency Tools in Radiotherapy to Increase Patient Flow: A Comprehensive Literature Review. *Clin. Med. Insights Oncol.* **2024**, *18*, 11795549241303606. https://doi.org/10.1177/11795549241303606.
(41) Baskar, R.; Lee, K. A.; Yeo, R.; Yeoh, K.-W. Cancer and Radiation Therapy: Current Advances and Future Directions. *Int. J. Med. Sci.* **2012**, *9* (3), 193–199. https://doi.org/10.7150/ijms.3635.
(42) Mee, T.; Kirkby, N. F.; Defourny, N. N.; Kirkby, K. J.; Burnet, N. G. The Use of Radiotherapy, Surgery and Chemotherapy in the Curative Treatment of Cancer: Results from the FORTY (Favourable Outcomes from RadioTherapY) Project. *Br. J. Radiol.* **2023**, *96* (1152), 20230334. https://doi.org/10.1259/bjr.20230334.
(43) Cancer Multidrug Resistance. *Nat. Biotechnol.* **2000**, *18* (S10), IT18–IT20. https://doi.org/10.1038/80051.
(44) Khan, S. U.; Fatima, K.; Aisha, S.; Malik, F. Unveiling the Mechanisms and Challenges of Cancer Drug Resistance. *Cell Commun. Signal.* **2024**, *22* (1). https://doi.org/10.1186/s12964-023-01302-1.
(45) Whitaker, K. Earlier Diagnosis: The Importance of Cancer Symptoms. *Lancet Oncol.* **2020**, *21* (1), 6–8. https://doi.org/10.1016/s1470-2045(19)30658-8.
(46) Attia, M. F.; Anton, N.; Wallyn, J.; Omran, Z.; Vandamme, T. F. An Overview of Active and Passive Targeting Strategies to Improve the Nanocarriers Efficiency to Tumour Sites. *J. Pharm. Pharmacol.* **2019**, *71* (8), 1185–1198. https://doi.org/10.1111/jphp.13098.
(47) Hoyt, K. Super-Resolution Ultrasound Imaging for Monitoring the Therapeutic Efficacy of a Vascular Disrupting Agent in an Animal Model of Breast Cancer. *J. Ultrasound Med.* **2024**, *43* (6), 1099–1107. https://doi.org/10.1002/jum.16438.
(48) Mendive-Tapia, L.; Vendrell, M. Activatable Fluorophores for Imaging Immune Cell Function. *Acc. Chem. Res.* **2022**, *55* (8), 1183–1193. https://doi.org/10.1021/acs.accounts.2c00070.
(49) The Huy, B.; Thangadurai, D. T.; Sharipov, M.; Ngoc Nghia, N.; Van Cuong, N.; Lee, Y.-I. Recent Advances in Turn Off-on Fluorescence Sensing Strategies for Sensitive Biochemical Analysis - A Mechanistic Approach. *Microchem. J.* **2022**, *179*, 107511. https://doi.org/10.1016/j.microc.2022.107511.
(50) Madhu, M.; Santhoshkumar, S.; Tseng, W.-B.; Tseng, W.-L. Maximizing Analytical Precision: Exploring the Advantages of Ratiometric Strategy in Fluorescence, Raman, Electrochemical, and Mass Spectrometry Detection. *Front. Anal. Sci.* **2023**, *3*. https://doi.org/10.3389/frans.2023.1258558.
(51) Mendive-Tapia, L.; Vendrell, M. Activatable Fluorophores for Imaging Immune Cell Function. *Acc. Chem. Res.* **2022**, *55* (8), 1183–1193. https://doi.org/10.1021/acs.accounts.2c00070.
(52) Michel, L.; Durand, P.; Chevalier, A. A Naphthalimide Based “Turn-ON” Probe for Wash-Free Imaging of Lipid-Droplet in Living Cells With an Excellent Selectivity. *ChemBioChem* **2024**, e202400270. https://doi.org/10.1002/cbic.202400270.

(53) Jiao, C.; Liu, Y.; Lu, W.; Zhang, P.; Ma, X.; Wang, Y. A Simple Sensor Based on 1,8-Naphthalimide with Large Stokes Shift for Detection of Hypochlorous Acid in Living Cells. *RSC Adv.* **2019**, *9* (54), 31196–31201. https://doi.org/10.1039/C9RA06174F.

(54) Chen, X.; Wang, F.; Hyun, J. Y.; Wei, T.; Qiang, J.; Ren, X.; Shin, I.; Yoon, J. Recent Progress in the Development of Fluorescent, Luminescent and Colorimetric Probes for Detection of Reactive Oxygen and Nitrogen Species. *Chem Soc Rev* **2016**, *45* (10), 2976–3016. https://doi.org/10.1039/C6CS00192K.

(55) Panchenko, P. A.; Fedorov, Y. V.; Fedorova, O. A.; Jonusauskas, G. Comparative Analysis of the PET and ICT Sensor Properties of 1,8-Naphthalimides Containing Aza-15-Crown-5 Ether Moiety. *Dyes Pigments* **2013**, *98* (3), 347–357. https://doi.org/10.1016/j.dyepig.2013.03.008.

(56) Wang, L.; Fujii, M.; Yamaji, M.; Okamoto, H. Fluorescence Behaviour of 2-, 3- and 4-Amino-1,8-Naphthalimides: Effects of the Substitution Positions of the Amino Functionality on the Photophysical Properties. *Photochem. Photobiol. Sci.* **2018**, *17* (10), 1319–1328. https://doi.org/10.1039/c8pp00302e.

(57) Geraghty, C.; Wynne, C.; Elmes, R. B. P. 1,8-Naphthalimide Based Fluorescent Sensors for Enzymes. *Coord. Chem. Rev.* **2021**, *437*, 213713. https://doi.org/10.1016/j.ccr.2020.213713.

(58) Wang, L.; Fujii, M.; Yamaji, M.; Okamoto, H. Fluorescence Behaviour of 2-, 3- and 4-Amino-1,8-Naphthalimides: Effects of the Substitution Positions of the Amino Functionality on the Photophysical Properties. *Photochem. Photobiol. Sci.* **2018**, *17* (10), 1319–1328. https://doi.org/10.1039/c8pp00302e.

(59) Xu, A.; Tang, Y.; Lin, W. Endoplasmic Reticulum-Targeted Two-Photon Turn-on Fluorescent Probe for Nitroreductase in Tumor Cells and Tissues. *Spectrochim. Acta. A. Mol. Biomol. Spectrosc.* **2018**, *204*, 770–776. https://doi.org/10.1016/j.saa.2018.05.092.

(60) Liu, X.; Gu, F.; Zhou, X.; Zhou, W.; Zhang, S.; Cui, L.; Guo, T. A Naphthalimide-Based Turn-on Fluorescence Probe for Peroxynitrite Detection and Imaging in Living Cells. *RSC Adv.* **2020**, *10* (63), 38281–38286. https://doi.org/10.1039/D0RA06564A.

(61) Ao, X.; Bright, S. A.; Taylor, N. C.; Elmes, R. B. P. 2-Nitroimidazole Based Fluorescent Probes for Nitroreductase; Monitoring Reductive Stress in Cellulo. *Org. Biomol. Chem.* **2017**, *15* (29), 6104–6108. https://doi.org/10.1039/C7OB01406F.

(62) Wynne, C.; Elmes, R. B. P. Utilising a 1,8-Naphthalimide Probe for the Ratiometric Fluorescent Visualisation of Caspase-3. *Front. Chem.* **2024**, *12*, 1418378. https://doi.org/10.3389/fchem.2024.1418378.

(63) Du, F.; Qu, Y.; Li, M.; Tan, X. Mitochondria-Targetable Ratiometric Fluorescence Probe for Carbon Monoxide Based on Naphthalimide Derivatives. *Anal. Bioanal. Chem.* **2021**, *413* (5), 1395–1403. https://doi.org/10.1007/s00216-020-03103-8.

(64) Markovic, M.; Ben-Shabat, S.; Dahan, A. Prodrugs for Improved Drug Delivery: Lessons Learned from Recently Developed and Marketed Products. *Pharmaceutics* **2020**, *12* (11), 1031. https://doi.org/10.3390/pharmaceutics12111031.

(65) Albert, A. Chemical Aspects of Selective Toxicity. *Nature* **1958**, *182* (4633), 421–422. https://doi.org/10.1038/182421a0.
(66) Testa, B. Prodrug Research: Futile or Fertile? *Biochem. Pharmacol.* **2004**, *68* (11), 2097–2106. https://doi.org/10.1016/j.bcp.2004.07.005.
(67) Dagogo-Jack, I.; Shaw, A. T. Tumour Heterogeneity and Resistance to Cancer Therapies. *Nat. Rev. Clin. Oncol.* **2018**, *15* (2), 81–94. https://doi.org/10.1038/nrclinonc.2017.166.
(68) Khageh Hosseini, S.; Kolterer, S.; Steiner, M.; Von Manstein, V.; Gerlach, K.; Trojan, J.; Waidmann, O.; Zeuzem, S.; Schulze, J. O.; Hahn, S.; Steinhilber, D.; Gatterdam, V.; Tampé, R.; Biondi, R. M.; Proschak, E.; Zörnig, M. Camptothecin and Its Analog SN-38, the Active Metabolite of Irinotecan, Inhibit Binding of the Transcriptional Regulator and Oncoprotein FUBP1 to Its DNA Target Sequence FUSE. *Biochem. Pharmacol.* **2017**, *146*, 53–62. https://doi.org/10.1016/j.bcp.2017.10.003.
(69) Wang, L.; Xie, S.; Ma, L.; Chen, Y.; Lu, W. 10-Boronic Acid Substituted Camptothecin as Prodrug of SN-38. *Eur. J. Med. Chem.* **2016**, *116*, 84–89. https://doi.org/10.1016/j.ejmech.2016.03.063.
(70) Chatterjee, K.; Zhang, J.; Honbo, N.; Karliner, J. S. Doxorubicin Cardiomyopathy. *Cardiology* **2010**, *115* (2), 155–162. https://doi.org/10.1159/000265166.
(71) Skarbek, C.; Serra, S.; Maslah, H.; Rascol, E.; Labruère, R. Arylboronate Prodrugs of Doxorubicin as Promising Chemotherapy for Pancreatic Cancer. *Bioorganic Chem.* **2019**, *91*, 103158. https://doi.org/10.1016/j.bioorg.2019.103158.
(72) Ye, M.; Han, Y.; Tang, J.; Piao, Y.; Liu, X.; Zhou, Z.; Gao, J.; Rao, J.; Shen, Y. A Tumor-Specific Cascade Amplification Drug Release Nanoparticle for Overcoming Multidrug Resistance in Cancers. *Adv. Mater.* **2017**, *29* (38), 1702342. https://doi.org/10.1002/adma.201702342.
(73) Park, E. J.; Choi, K. S.; Kwon, T. K. β-Lapachone-Induced Reactive Oxygen Species (ROS) Generation Mediates Autophagic Cell Death in Glioma U87 MG Cells. *Chem. Biol. Interact.* **2011**, *189* (1–2), 37–44. https://doi.org/10.1016/j.cbi.2010.10.013.
(74) Kennedy, L.; Sandhu, J. K.; Harper, M.-E.; Cuperlovic-Culf, M. Role of Glutathione in Cancer: From Mechanisms to Therapies. *Biomolecules* **2020**, *10* (10), 1429. https://doi.org/10.3390/biom10101429.
(75) Liu, G.; Jiang, Z.; Lovell, J. F.; Zhang, L.; Zhang, Y. Design of a Thiol-Responsive, Traceless Prodrug with Rapid Self-Immolation for Cancer Chemotherapy. *ACS Appl. Bio Mater.* **2021**, *4* (6), 4982–4989. https://doi.org/10.1021/acsabm.1c00247.
(76) Janczy-Cempa, E.; Mazuryk, O.; Kania, A.; Brindell, M. Significance of Specific Oxidoreductases in the Design of Hypoxia-Activated Prodrugs and Fluorescent Turn off-on Probes for Hypoxia Imaging. *Cancers* **2022**, *14* (11), 2686. https://doi.org/10.3390/cancers14112686.
(77) Huang, Y.; Jin, C.; Yu, J.; Wang, L.; Lu, W. A Novel Multifunctional 2-Nitroimidazole-Based Bioreductive Linker and Its Application in Hypoxia-Activated Prodrugs. *Bioorganic Chem.* **2020**, *101*, 103975. https://doi.org/10.1016/j.bioorg.2020.103975.
(78) Winn, B. A.; Shi, Z.; Carlson, G. J.; Wang, Y.; Nguyen, B. L.; Kelly, E. M.; Ross, R. D.; Hamel, E.; Chaplin, D. J.; Trawick, M. L.; Pinney, K. G. Bioreductively Activatable Prodrug Conjugates of Phenstatin Designed to

Target Tumor Hypoxia. *Bioorg. Med. Chem. Lett.* **2017**, *27* (3), 636–641. https://doi.org/10.1016/j.bmcl.2016.11.093.

(79) Borch, R. F.; Liu, J.; Schmidt, J. P.; Marakovits, J. T.; Joswig, C.; Gipp, J. J.; Mulcahy, R. T. Synthesis and Evaluation of Nitroheterocyclic Phosphoramidates as Hypoxia-Selective Alkylating Agents. *J. Med. Chem.* **2000**, *43* (11), 2258–2265. https://doi.org/10.1021/jm0001020.

(80) Dal Corso, A.; Borlandelli, V.; Corno, C.; Perego, P.; Belvisi, L.; Pignataro, L.; Gennari, C. Fast Cyclization of a Proline-Derived Self-Immolative Spacer Improves the Efficacy of Carbamate Prodrugs. *Angew. Chem. Int. Ed.* **2020**, *59* (10), 4176–4181. https://doi.org/10.1002/anie.201916394.

(81) Jiang, X.; Zhu, L.; Wei, Q.; Lu, W.; Yu, J.; Zhu, S. Enhancing SN38 Prodrug Delivery Using a Self-Immolative Linker and Endogenous Albumin Transport. *J. Controlled Release* **2024**, *369*, 622–629. https://doi.org/10.1016/j.jconrel.2024.04.019.

(82) Peng, Y.; Shi, Z.; Liang, Y.; Ding, K.; Wang, Y. Targeting the Tumor Microenvironment by an Enzyme-Responsive Prodrug of Tubulin Destabilizer for Triple-Negative Breast Cancer Therapy with High Safety. *Eur. J. Med. Chem.* **2022**, *236*, 114344. https://doi.org/10.1016/j.ejmech.2022.114344.

(83) Dunsmore, L.; Navo, C. D.; Becher, J.; De Montes, E. G.; Guerreiro, A.; Hoyt, E.; Brown, L.; Zelenay, V.; Mikutis, S.; Cooper, J.; Barbieri, I.; Lawrinowitz, S.; Siouve, E.; Martin, E.; Ruivo, P. R.; Rodrigues, T.; Da Cruz, F. P.; Werz, O.; Vassiliou, G.; Ravn, P.; Jiménez-Osés, G.; Bernardes, G. J. L. Controlled Masking and Targeted Release of Redox-Cycling Ortho-Quinones via a C–C Bond-Cleaving 1,6-Elimination. *Nat. Chem.* **2022**, *14* (7), 754–765. https://doi.org/10.1038/s41557-022-00964-7.

(84) Mozafari, M. R. Editorial to the Special Issue “Theranostic Drug Delivery: Prospects and Problems.” *Biomedicines* **2024**, *12* (7), 1533. https://doi.org/10.3390/biomedicines12071533.

(85) Yordanova, A.; Eppard, E.; Kürpig, S.; Bundschuh, R.; Schönberger, S.; Gonzalez-Carmona, M.; Feldmann, G.; Ahmadzadehfar, H.; Essler, M. Theranostics in Nuclear Medicine Practice. *OncoTargets Ther.* **2017**, *Volume 10*, 4821–4828. https://doi.org/10.2147/OTT.S140671.

(86) Kim, E.-J.; Bhuniya, S.; Lee, H.; Kim, H. M.; Cheong, C.; Maiti, S.; Hong, K. S.; Kim, J. S. An Activatable Prodrug for the Treatment of Metastatic Tumors. *J. Am. Chem. Soc.* **2014**, *136* (39), 13888–13894. https://doi.org/10.1021/ja5077684.

(87) Setsukinai, K.; Urano, Y.; Kikuchi, K.; Higuchi, T.; Nagano, T. Fluorescence Switching by O-Dearylation of 7-Aryloxycoumarins. Development of Novel Fluorescence Probes to Detect Reactive Oxygen Species with High Selectivity. *J. Chem. Soc. Perkin Trans. 2* **2000**, No. 12, 2453–2457. https://doi.org/10.1039/b006449l.

(88) Ravikumar, G.; Bagheri, M.; Saini, D. K.; Chakrapani, H. A Small Molecule for theraNOstic Targeting of Cancer Cells. *Chem. Commun.* **2017**, *53* (100), 13352–13355. https://doi.org/10.1039/C7CC08526E.

(89) Liu, J.; Cao, C. A Simple and Effective “Elimination” Approach for Selective Cancer Therapy to Reveal the Role of H_2O_2. *ACS Omega* **2020**, *5* (35), 22157–22162. https://doi.org/10.1021/acsomega.0c02240.

(90) Feng, W.; Gao, C.; Liu, W.; Ren, H.; Wang, C.; Ge, K.; Li, S.; Zhou, G.; Li, H.; Wang, S.; Jia, G.; Li, Z.; Zhang, J. A Novel Anticancer Theranostic Pro-

Prodrug Based on Hypoxia and Photo Sequential Control. *Chem Commun* **2016**, *52* (60), 9434–9437. https://doi.org/10.1039/C6CC02932A.
(91) Li, K.; Sun, Y.; Ma, Z.; Chen, Y.; Li, X.; Dong, G.; Liu, D.; Sheng, C.; Wu, S. Evodiamine-Based Nitroreductase Responsive Theranostic Agents for Treatment of Colon Cancer. *J. Med. Chem.* **2025**, *68* (12), 12402–12413. https://doi.org/10.1021/acs.jmedchem.4c02822.
(92) Liu, P.; Xu, J.; Yan, D.; Zhang, P.; Zeng, F.; Li, B.; Wu, S. A DT-Diaphorase Responsive Theranostic Prodrug for Diagnosis, Drug Release Monitoring and Therapy. *Chem. Commun.* **2015**, *51* (46), 9567–9570. https://doi.org/10.1039/C5CC02149A.
(93) Hettiarachchi, S. U.; Prasai, B.; McCarley, R. L. Detection and Cellular Imaging of Human Cancer Enzyme Using a Turn-On, Wavelength-Shiftable, Self-Immolative Profluorophore. *J. Am. Chem. Soc.* **2014**, *136* (21), 7575–7578. https://doi.org/10.1021/ja5030707.
(94) Deshayes, E.; Fersing, C.; Thibault, C.; Roumiguie, M.; Pourquier, P.; Houédé, N. Innovation in Radionuclide Therapy for the Treatment of Prostate Cancers: Radiochemical Perspective and Recent Therapeutic Practices. *Cancers* **2023**, *15* (12), 3133. https://doi.org/10.3390/cancers15123133.
(95) Barca, C.; Griessinger, C. M.; Faust, A.; Depke, D.; Essler, M.; Windhorst, A. D.; Devoogdt, N.; Brindle, K. M.; Schäfers, M.; Zinnhardt, B.; Jacobs, A. H. Expanding Theranostic Radiopharmaceuticals for Tumor Diagnosis and Therapy. *Pharm. Basel Switz.* **2021**, *15* (1), 13. https://doi.org/10.3390/ph15010013.
(96) Wang, S.-J. Recent Advances in Clinical Trial Design Considerations in Thera“Nostics.” *Contemp. Clin. Trials* **2020**, *96*, 106100. https://doi.org/10.1016/j.cct.2020.106100.
(97) Williams, G. T.; Haynes, C. J. E.; Fares, M.; Caltagirone, C.; Hiscock, J. R.; Gale, P. A. Advances in Applied Supramolecular Technologies. *Chem. Soc. Rev.* **2021**, *50* (4), 2737–2763. https://doi.org/10.1039/D0CS00948B.
(98) Lehn, J. Supramolecular Chemistry—Scope and Perspectives Molecules, Supermolecules, and Molecular Devices (Nobel Lecture). *Angew. Chem. Int. Ed. Engl.* **1988**, *27* (1), 89–112. https://doi.org/10.1002/anie.198800891.
(99) Cooper, G. M. *The Cell: A Molecular Approach*, 2nd ed.; 2000.
(100) Zhang, Q.; Jian, L.; Yao, D.; Rao, B.; Xia, Y.; Hu, K.; Li, S.; Shen, Y.; Cao, M.; Qin, A.; Zhao, J.; Cao, Y. The Structural Basis of the pH-Homeostasis Mediated by the Cl−/HCO3− Exchanger, AE2. *Nat. Commun.* **2023**, *14* (1), 1812. https://doi.org/10.1038/s41467-023-37557-y.
(101) Chen, D.; Yu, S. P.; Wei, L. Ion Channels in Regulation of Neuronal Regenerative Activities. *Transl. Stroke Res.* **2014**, *5* (1), 156–162. https://doi.org/10.1007/s12975-013-0320-z.
(102) Linsdell, P. Mechanism of Chloride Permeation in the Cystic Fibrosis Transmembrane Conductance Regulator Chloride Channel. *Exp. Physiol.* **2006**, *91* (1), 123–129. https://doi.org/10.1113/expphysiol.2005.031757.
(103) Lowe, A. J.; Dyson, G. A.; Pfeffer, F. M. Factors Influencing Anion Binding Stoichiometry: The Subtle Influence of Electronic Effects. *Eur. J. Org. Chem.* **2008**, *2008* (9), 1559–1567. https://doi.org/10.1002/ejoc.200701015.
(104) Beer, P. D.; Gale, P. A. Anion Recognition and Sensing: The State of the Art and Future Perspectives. *Angew. Chem. Int. Ed Engl.* **2001**, *40* (3), 486–516.

(105) Smith, P. J.; Reddington, M. V.; Wilcox, C. S. Ion Pair Binding by a Urea in Chloroform Solution. *Tetrahedron Lett.* **1992**, *33* (41), 6085–6088. https://doi.org/10.1016/S0040-4039(00)60012-6.
(106) Gale, P. A. Anion and Ion-Pair Receptor Chemistry: Highlights from 2000 and 2001. *Coord. Chem. Rev.* **2003**, *240* (1–2), 191–221. https://doi.org/10.1016/S0010-8545(02)00258-8.
(107) Gale, P. A.; García-Garrido, S. E.; Garric, J. Anion Receptors Based on Organic Frameworks: Highlights from 2005 and 2006. *Chem Soc Rev* **2008**, *37* (1), 151–190. https://doi.org/10.1039/B715825D.
(108) Caltagirone, C.; Gale, P. A. Anion Receptor Chemistry: Highlights from 2007. *Chem Soc Rev* **2009**, *38* (2), 520–563. https://doi.org/10.1039/B806422A.
(109) Gale, P. A. Anion Receptor Chemistry: Highlights from 2008 and 2009. *Chem. Soc. Rev.* **2010**, *39* (10), 3746. https://doi.org/10.1039/c001871f.
(110) Wenzel, M.; Hiscock, J. R.; Gale, P. A. Anion Receptor Chemistry: Highlights from 2010. *Chem Soc Rev* **2012**, *41* (1), 480–520. https://doi.org/10.1039/C1CS15257B.
(111) Mohammed, F. A.; Xiao, T.; Wang, L.; Elmes, R. B. P. Macrocyclic Receptors for Anion Recognition. *Chem. Commun.* **2024**, *60* (83), 11812–11836. https://doi.org/10.1039/D4CC04521A.
(112) Debnath, S.; Sengupta, A.; Jose, K. V. J.; Raghavachari, K. Fragment-Based Approaches for Supramolecular Interaction Energies: Applications to Foldamers and Their Complexes with Anions. *J. Chem. Theory Comput.* **2018**, *14* (12), 6226–6239. https://doi.org/10.1021/acs.jctc.8b00525.
(113) Paul, R. L.; Bell, Z. R.; Fleming, J. S.; Jeffery, J. C.; McCleverty, J. A.; Ward, M. D. Self-assembly of Anion-binding Supramolecular Cage Complexes. *Heteroat. Chem.* **2002**, *13* (6), 567–573. https://doi.org/10.1002/hc.10101.
(114) Li, H.; Valkenier, H.; Thorne, A. G.; Dias, C. M.; Cooper, J. A.; Kieffer, M.; Busschaert, N.; Gale, P. A.; Sheppard, D. N.; Davis, A. P. Anion Carriers as Potential Treatments for Cystic Fibrosis: Transport in Cystic Fibrosis Cells, and Additivity to Channel-Targeting Drugs. *Chem. Sci.* **2019**, *10* (42), 9663–9672. https://doi.org/10.1039/C9SC04242C.
(115) Bai, H.; Lv, F.; Liu, L.; Wang, S. Supramolecular Antibiotic Switches: A Potential Strategy for Combating Drug Resistance. *Chem. – Eur. J.* **2016**, *22* (32), 11114–11121. https://doi.org/10.1002/chem.201600877.
(116) Broichhagen, J.; Frank, J. A.; Trauner, D. A Roadmap to Success in Photopharmacology. *Acc. Chem. Res.* **2015**, *48* (7), 1947–1960. https://doi.org/10.1021/acs.accounts.5b00129.
(117) Velema, W. A.; Szymanski, W.; Feringa, B. L. Photopharmacology: Beyond Proof of Principle. *J. Am. Chem. Soc.* **2014**, *136* (6), 2178–2191. https://doi.org/10.1021/ja413063e.
(118) Kovbasyuk, L.; Krämer, R. Allosteric Supramolecular Receptors and Catalysts. *Chem. Rev.* **2004**, *104* (6), 3161–3188. https://doi.org/10.1021/cr030673a.
(119) Beer, P. D.; Stokes, S. E. Potassium Cations Allosterically Switch off the Halide Anion Recognition Properties of a New Cobalticinium Bis Benzo Crown Ether Receptor. *Polyhedron* **1995**, *14* (19), 2631–2635. https://doi.org/10.1016/0277-5387(95)00129-G.
(120) Chen, C. W.; Whitlock, H. W. Molecular Tweezers: A Simple Model of Bifunctional Intercalation. *J. Am. Chem. Soc.* **1978**, *100* (15), 4921–4922. https://doi.org/10.1021/ja00483a063.

(121) Shimasaki, T.; Kato, S.; Ideta, K.; Goto, K.; Shinmyozu, T. Synthesis and Structural and Photoswitchable Properties of Novel Chiral Host Molecules: Axis Chiral 2,2‘-Dihydroxy-1,1‘-Binaphthyl-Appended *Stiff* -Stilbene[1]. *J. Org. Chem.* **2007**, *72* (4), 1073–1087. https://doi.org/10.1021/jo061127v.
(122) Wezenberg, S. J.; Feringa, B. L. Photocontrol of Anion Binding Affinity to a Bis-Urea Receptor Derived from Stiff-Stilbene. *Org. Lett.* **2017**, *19* (2), 324–327. https://doi.org/10.1021/acs.orglett.6b03423.
(123) Danowski, W.; Van Leeuwen, T.; Browne, W. R.; Feringa, B. L. Photoresponsive Porous Materials. *Nanoscale Adv.* **2021**, *3* (1), 24–40. https://doi.org/10.1039/D0NA00647E.
(124) Dąbrowa, K.; Niedbała, P.; Jurczak, J. Anion-Tunable Control of Thermal Z→E Isomerisation in Basic Azobenzene Receptors. *Chem Commun* **2014**, *50* (99), 15748–15751. https://doi.org/10.1039/C4CC07798A.
(125) Rananaware, A.; Samanta, M.; Bhosale, R. S.; Kobaisi, M. A.; Roy, B.; Bheemireddy, V.; Bhosale, S. V.; Bandyopadhyay, S.; Bhosale, S. V. Photomodulation of Fluoride Ion Binding through Anion-π Interactions Using a Photoswitchable Azobenzene System. *Sci. Rep.* **2016**, *6* (1), 22928. https://doi.org/10.1038/srep22928.
(126) Taylor, A. J.; Hein, R.; Patrick, S. C.; Davis, J. J.; Beer, P. D. Redox-Modulated Fluorescent Halogen Bonding and Hydrogen Bonding Anion Sensing. Chemistry October 20, 2023. https://doi.org/10.26434/chemrxiv-2023-4nlzd.
(127) Hein, R.; Docker, A.; Davis, J. J.; Beer, P. D. Redox-Switchable Chalcogen Bonding for Anion Recognition and Sensing. *J. Am. Chem. Soc.* **2022**, *144* (19), 8827–8836. https://doi.org/10.1021/jacs.2c02924.
(128) Rotger, M. C.; Piña, M. N.; Frontera, A.; Martorell, G.; Ballester, P.; Deyà, P. M.; Costa, A. Conformational Preferences and Self-Template Macrocyclization of Squaramide-Based Foldable Modules. *J. Org. Chem.* **2004**, *69* (7), 2302–2308. https://doi.org/10.1021/jo035546t.
(129) Amendola, V.; Bergamaschi, G.; Boiocchi, M.; Fabbrizzi, L.; Milani, M. The Squaramide versus Urea Contest for Anion Recognition. *Chem. – Eur. J.* **2010**, *16* (14), 4368–4380. https://doi.org/10.1002/chem.200903190.
(130) Amendola, V.; Fabbrizzi, L.; Mosca, L.; Schmidtchen, F. Urea-, Squaramide-, and Sulfonamide-Based Anion Receptors: A Thermodynamic Study. *Chem. – Eur. J.* **2011**, *17* (21), 5972–5981. https://doi.org/10.1002/chem.201003411.
(131) Macreadie, L. K.; Gilchrist, A. M.; McNaughton, D. A.; Ryder, W. G.; Fares, M.; Gale, P. A. Progress in Anion Receptor Chemistry. *Chem* **2022**, *8* (1), 46–118. https://doi.org/10.1016/j.chempr.2021.10.029.
(132) Marchetti, L. A.; Krämer, T.; Elmes, R. B. P. Amidosquaramides – a New Anion Binding Motif with pH Sensitive Anion Transport Properties. *Org. Biomol. Chem.* **2022**, *20* (35), 7056–7066. https://doi.org/10.1039/D2OB01176J.
(133) Li, Y.; Yang, G.-H.; Shen, Y.-Y.; Xue, X.-S.; Li, X.; Cheng, J.-P. *N* - *Tert* -Butyl Sulfinyl Squaramide Receptors for Anion Recognition through Assisted *Tert* -Butyl C–H Hydrogen Bonding. *J. Org. Chem.* **2017**, *82* (16), 8662–8667. https://doi.org/10.1021/acs.joc.7b01634.
(134) Prohens, R.; Martorell, G.; Ballester, P.; Costa, A. A Squaramide Fluorescent Ensemble for Monitoring Sulfate in Water. *Chem. Commun.* **2001**, No. 16, 1456–1457. https://doi.org/10.1039/b104172j.

(135) Piña, M. N.; Soberats, B.; Rotger, C.; Ballester, P.; Deyà, P. M.; Costa, A. Selective Sensing of Competitive Anions by Non-Selective Hosts: The Case of Sulfate and Phosphate in Water. *New J. Chem.* **2008**, *32* (11), 1919. https://doi.org/10.1039/b809454c.

(136) Neus Piña, M.; Carmen Rotger, M.; Costa, A.; Ballester, P.; Deyà, P. M. Evaluation of Anion Selectivity in Protic Media by Squaramide–Cresol Red Ensembles. *Tetrahedron Lett.* **2004**, *45* (19), 3749–3752. https://doi.org/10.1016/j.tetlet.2004.03.094.

(137) Kumawat, L. K.; Abogunrin, A. A.; Kickham, M.; Pardeshi, J.; Fenelon, O.; Schroeder, M.; Elmes, R. B. P. Squaramide—Naphthalimide Conjugates as "Turn-On" Fluorescent Sensors for Bromide Through an Aggregation-Disaggregation Approach. *Front. Chem.* **2019**, *7*, 354. https://doi.org/10.3389/fchem.2019.00354.

(138) Ryan, G. J.; Elmes, R. B. P.; Quinn, S. J.; Gunnlaugsson, T. Synthesis and Photophysical Evaluations of Fluorescent Quaternary Bipyridyl-1,8-Naphthalimide Conjugates as Nucleic Acid Targeting Agents. *Supramol. Chem.* **2012**, *24* (3), 175–188. https://doi.org/10.1080/10610278.2011.638381.

(139) Ryan, G. J.; Poynton, F. E.; Elmes, R. B. P.; Erby, M.; Williams, D. C.; Quinn, S. J.; Gunnlaugsson, T. Unexpected DNA Binding Properties with Correlated Downstream Biological Applications in Mono vs. Bis-1,8-Naphthalimide Ru(II)-Polypyridyl Conjugates. *Dalton Trans.* **2015**, *44* (37), 16332–16344. https://doi.org/10.1039/C5DT00360A.

(140) Ximenis, M.; Cañellas, S.; Gomila, R. M.; Galmés, B.; Frontera, A.; Costa, A.; Rotger, C. Reaction Contest: Hydrolysis *versus* Intramolecular Cyclisation Reaction in Alkyl Squaramate Esters. *RSC Adv.* **2024**, *14* (44), 32126–32132. https://doi.org/10.1039/D4RA04362F.

(141) Cavanagh, R. L.; Buyniski, J. P. Effect of BMY-25368, a Potent and Long-acting Histamine H_2 -receptor Antagonist, on Gastric Secretion and Aspirin-induced Gastric Lesions in the Dog. *Aliment. Pharmacol. Ther.* **1989**, *3* (3), 299–313. https://doi.org/10.1111/j.1365-2036.1989.tb00217.x.

(142) Armstrong, A. J.; Geva, R.; Chung, H. C.; Lemech, C.; Miller, W. H.; Hansen, A. R.; Lee, J.-S.; Tsai, F.; Solomon, B. J.; Kim, T. M.; Rolfo, C.; Giranda, V.; Ren, Y.; Liu, F.; Kandala, B.; Freshwater, T.; Wang, J. S. CXCR2 Antagonist Navarixin in Combination with Pembrolizumab in Select Advanced Solid Tumors: A Phase 2 Randomized Trial. *Invest. New Drugs* **2024**, *42* (1), 145–159. https://doi.org/10.1007/s10637-023-01410-2.

(143) Brandt, M. R.; Cummons, T. A.; Potestio, L.; Sukoff, S. J.; Rosenzweig-Lipson, S. Effects of the N-Methyl-d-Aspartate Receptor Antagonist Perzinfotel [EAA-090; [2-(8,9-Dioxo-2,6-Diazabicyclo[5.2.0]Non-1(7)-En-2-Yl)-Ethyl]Phosphonic Acid] on Chemically Induced Thermal Hypersensitivity. *J. Pharmacol. Exp. Ther.* **2005**, *313* (3), 1379–1386. https://doi.org/10.1124/jpet.105.084467.

(144) Kijima, H.; Isobe, Y.; Muramatsu, M.; Yokomori, S.; Suzuki, M.; Higuchi, S. Structure–Activity Characterization of an H2-Receptor Antagonist, 3-Amino-4-[4-[4-(1-Piperidinomethyl)-2-Pyridyloxy]-Cis-2-Butenylamino]-3-Cyclobutene-1,2-Dione Hydrochloride (IT-066), Involved in the Insurmountable Antagonism against Histamine-Induced Positive Chronotropic Action in Guinea Pig Atria. *Biochem. Pharmacol.* **1998**, *55* (2), 151–157. https://doi.org/10.1016/S0006-2952(97)00416-4.

(145) Brennan, L. E.; Kumawat, L. K.; Piatek, M. E.; Kinross, A. J.; McNaughton, D. A.; Marchetti, L.; Geraghty, C.; Wynne, C.; Tong, H.; Kavanagh, O. N.; O'Sullivan, F.; Hawes, C. S.; Gale, P. A.; Kavanagh, K.; Elmes, R. B. P. Potent Antimicrobial Effect Induced by Disruption of Chloride Homeostasis. *Chem* **2023**, *9* (11), 3138–3158. https://doi.org/10.1016/j.chempr.2023.07.014.

(146) Arrighi, G.; Puerta, A.; Petrini, A.; Hicke, F. J.; Nocentini, A.; Fernandes, M. X.; Padrón, J. M.; Supuran, C. T.; Fernández-Bolaños, J. G.; López, Ó. Squaramide-Tethered Sulfonamides and Coumarins: Synthesis, Inhibition of Tumor-Associated CAs IX and XII and Docking Simulations. *Int. J. Mol. Sci.* **2022**, *23* (14), 7685. https://doi.org/10.3390/ijms23147685.

(147) Ximenis, M.; Sampedro, A.; Martínez-Crespo, L.; Ramis, G.; Orvay, F.; Costa, A.; Rotger, C. Introducing a Squaramide-Based Self-Immolative Spacer for Controlled Drug Release. *Chem. Commun.* **2021**, *57* (22), 2736–2739. https://doi.org/10.1039/D0CC07683J.

(148) Ximenis, M.; Pitarch-Jarque, J.; Blasco, S.; Rotger, C.; García-España, E.; Costa, A. Water-Soluble Squaramide Dihydrates: N-Methylation Modulates the Occurrence of One- and Two-Dimensional Water Clusters through Hydrogen Bonding and Dipolar Interactions. *Cryst. Growth Des.* **2018**, *18* (8), 4420–4427. https://doi.org/10.1021/acs.cgd.8b00401.

(149) Yang, Y.-C.; Zhu, Y.; Sun, S.-J.; Zhao, C.-J.; Bai, Y.; Wang, J.; Ma, L.-T. ROS Regulation in Gliomas: Implications for Treatment Strategies. *Front. Immunol.* **2023**, *14*, 1259797. https://doi.org/10.3389/fimmu.2023.1259797.

(150) Attique, I.; Haider, Z.; Khan, M.; Hassan, S.; Soliman, M. M.; Ibrahim, W. N.; Anjum, S. Reactive Oxygen Species: From Tumorigenesis to Therapeutic Strategies in Cancer. *Cancer Med.* **2025**, *14* (10). https://doi.org/10.1002/cam4.70947.

(151) Mohammed, S.; M, D.; T, A. Survival and Quality of Life Analysis in Glioblastoma Multiforme with Adjuvant Chemoradiotherapy: A Retrospective Study. *Rep. Pract. Oncol. Radiother.* **2022**, *27* (6), 1026–1036. https://doi.org/10.5603/RPOR.a2022.0113.

(152) Qin, L.; Jia, P.; Zhang, Z.; Zhang, S. ROS-P53-Cyclophilin-D Signaling Mediates Salinomycin-Induced Glioma Cell Necrosis. *J. Exp. Clin. Cancer Res.* **2015**, *34* (1). https://doi.org/10.1186/s13046-015-0174-1.

(153) Burić, S. S.; Podolski-Renić, A.; Dinić, J.; Stanković, T.; Jovanović, M.; Hadžić, S.; Ayuso, J. M.; Virumbrales-Muñoz, M.; Fernández, L. J.; Ochoa, I.; Pérez-García, V. M.; Pešić, M. Modulation of Antioxidant Potential with Coenzyme Q10 Suppressed Invasion of Temozolomide-Resistant Rat Glioma *In Vitro* and *In Vivo*. *Oxid. Med. Cell. Longev.* **2019**, *2019*, 1–14. https://doi.org/10.1155/2019/3061607.

(154) Divya Deepak, G. Review on Recent Advances in Cold Plasma Technology. *Eur. Phys. J. Appl. Phys.* **2022**, *97*, 39. https://doi.org/10.1051/epjap/2022210275.

(155) Mali, S. B. Role of Cold Atmospheric Plasma in Cancer Management. *Oral Oncol. Rep.* **2024**, *9*, 100133. https://doi.org/10.1016/j.oor.2023.100133.

(156) Haertel, B.; Woedtke, T. V.; Weltmann, K.-D.; Lindequist, U. Non-Thermal Atmospheric-Pressure Plasma Possible Application in Wound Healing. *Biomol. Ther.* **2014**, *22* (6), 477–490. https://doi.org/10.4062/biomolther.2014.105.

(157) Klämpfl, T. G.; Isbary, G.; Shimizu, T.; Li, Y.-F.; Zimmermann, J. L.; Stolz, W.; Schlegel, J.; Morfill, G. E.; Schmidt, H.-U. Cold Atmospheric Air Plasma

Sterilization against Spores and Other Microorganisms of Clinical Interest. *Appl. Environ. Microbiol.* **2012**, *78* (15), 5077–5082. https://doi.org/10.1128/AEM.00583-12.

(158) Jezeh, M. A.; Tayebi, T.; Khani, M. R.; Niknejad, H.; Shokri, B. Direct Cold Atmospheric Plasma and Plasma-activated Medium Effects on Breast and Cervix Cancer Cells. *Plasma Process. Polym.* **2020**, *17* (11), 1900241. https://doi.org/10.1002/ppap.201900241.

(159) Wang, Y.; Mang, X.; Li, X.; Cai, Z.; Tan, F. Cold Atmospheric Plasma Induces Apoptosis in Human Colon and Lung Cancer Cells through Modulating Mitochondrial Pathway. *Front. Cell Dev. Biol.* **2022**, *10*, 915785. https://doi.org/10.3389/fcell.2022.915785.

(160) He, Z.; Charleton, C.; Devine, R. W.; Kelada, M.; Walsh, J. M. D.; Conway, G. E.; Gunes, S.; Mondala, J. R. M.; Tian, F.; Tiwari, B.; Kinsella, G. K.; Malone, R.; O'Shea, D.; Devereux, M.; Wang, W.; Cullen, P. J.; Stephens, J. C.; Curtin, J. F. Enhanced Pyrazolopyrimidinones Cytotoxicity against Glioblastoma Cells Activated by ROS-Generating Cold Atmospheric Plasma. *Eur. J. Med. Chem.* **2021**, *224*, 113736. https://doi.org/10.1016/j.ejmech.2021.113736.

(161) Szalai, M. L.; Kevwitch, R. M.; McGrath, D. V. Geometric Disassembly of Dendrimers: Dendritic Amplification. *J. Am. Chem. Soc.* **2003**, *125* (51), 15688–15689. https://doi.org/10.1021/ja0386694.

(162) Sella, E.; Shabat, D. Self-Immolative Dendritic Probe for Direct Detection of Triacetone Triperoxide. *Chem. Commun.* **2008**, No. 44, 5701. https://doi.org/10.1039/b814855d.

(163) Grinda, M.; Clarhaut, J.; Renoux, B.; Tranoy-Opalinski, I.; Papot, S. A Self-Immolative Dendritic Glucuronide Prodrug of Doxorubicin. *Med Chem Commun* **2012**, *3* (1), 68–70. https://doi.org/10.1039/C1MD00193K.

(164) Gao, X.; Cao, J.; Song, Y.; Shu, X.; Liu, J.; Sun, J. Z.; Liu, B.; Tang, B. Z. A Unimolecular Theranostic System with H_2O_2 -Specific Response and AIE-Activity for Doxorubicin Releasing and Real-Time Tracking in Living Cells. *RSC Adv.* **2018**, *8* (20), 10975–10979. https://doi.org/10.1039/C8RA01185K.

(165) Duke, R. M.; Veale, E. B.; Pfeffer, F. M.; Kruger, P. E.; Gunnlaugsson, T. Colorimetric and Fluorescent Anion Sensors: An Overview of Recent Developments in the Use of 1,8-Naphthalimide-Based Chemosensors. *Chem. Soc. Rev.* **2010**, *39* (10), 3936. https://doi.org/10.1039/b910560n.

(166) Cui, L.; Zhong, Y.; Zhu, W.; Xu, Y.; Du, Q.; Wang, X.; Qian, X.; Xiao, Y. A New Prodrug-Derived Ratiometric Fluorescent Probe for Hypoxia: High Selectivity of Nitroreductase and Imaging in Tumor Cell. *Org. Lett.* **2011**, *13* (5), 928–931. https://doi.org/10.1021/ol102975t.

(167) Kornek, G.; Raderer, M.; Depisch, D.; Haider, K.; Fazeny, B.; Dittrich, C.; Scheithauer, W. Amonafide as First-Line Chemotherapy for Metastatic Breast Cancer. *Eur. J. Cancer* **1994**, *30* (3), 398–400. https://doi.org/10.1016/0959-8049(94)90264-X.

(168) Amonafide Prostate Cancer.

(169) Ratain, M. J.; Rosner, G.; Allen, S. L.; Costanza, M.; Van Echo, D. A.; Henderson, I. C.; Schilsky, R. L. Population Pharmacodynamic Study of Amonafide: A Cancer and Leukemia Group B Study. *J. Clin. Oncol.* **1995**, *13* (3), 741–747. https://doi.org/10.1200/JCO.1995.13.3.741.

(170) Yao, X.; Sun, W.; Yuan, Y.; Hu, J.; Fu, J.; Yin, J. Amonafide-Based H2O2-Responsive Theranostic Prodrugs: Exploring the Correlation between H2O2

Level and Anticancer Efficacy. *Bioorganic Chem.* **2024**, *150*, 107560. https://doi.org/10.1016/j.bioorg.2024.107560.
(171) Dai, L.; Gonzalez, J.; Zhang, K. A Simple Generic Method for Analyzing Water Sensitive Pinacol Boronate Compounds by Hydrophilic Interaction Liquid Chromatography. *J. Chromatogr. Open* **2022**, *2*, 100036. https://doi.org/10.1016/j.jcoa.2022.100036.
(172) Babajani, A.; Eftekharinasab, A.; Bekeschus, S.; Mehdian, H.; Vakhshiteh, F.; Madjd, Z. Reactive Oxygen Species from Non-Thermal Gas Plasma (CAP): Implication for Targeting Cancer Stem Cells. *Cancer Cell Int.* **2024**, *24* (1), 344. https://doi.org/10.1186/s12935-024-03523-x.
(173) Sandford, C.; Aggarwal, V. K. Stereospecific Functionalizations and Transformations of Secondary and Tertiary Boronic Esters. *Chem. Commun.* **2017**, *53* (40), 5481–5494. https://doi.org/10.1039/C7CC01254C.
(174) Yeh, C.; Chen, M.; Wu, T.; Chen, J.; Lai, C. Lectin-Triggered Aggregation of Glyco-Gold Nanoprobes for Activity-based Sensing of Hydrogen Peroxide by the Naked Eye. *Chem. – Asian J.* **2021**, *16* (21), 3462–3468. https://doi.org/10.1002/asia.202100865.
(175) Pedre, B.; Barayeu, U.; Ezeriņa, D.; Dick, T. P. The Mechanism of Action of N-Acetylcysteine (NAC): The Emerging Role of H2S and Sulfane Sulfur Species. *Pharmacol. Ther.* **2021**, *228*, 107916. https://doi.org/10.1016/j.pharmthera.2021.107916.
(176) Wang, W.-X.; Jiang, W.-L.; Mao, G.-J.; Tan, M.; Fei, J.; Li, Y.; Li, C.-Y. Monitoring the Fluctuation of Hydrogen Peroxide in Diabetes and Its Complications with a Novel Near-Infrared Fluorescent Probe. *Anal. Chem.* **2021**, *93* (6), 3301–3307. https://doi.org/10.1021/acs.analchem.0c05364.
(177) Peris-Vicente, J.; Esteve-Romero, J.; Carda-Broch, S. Validation of Analytical Methods Based on Chromatographic Techniques: An Overview. In *Analytical Separation Science*; Pino, V., Anderson, J. L., Berthod, A., Stalcup, A. M., Eds.; Wiley, 2015; pp 1757–1808. https://doi.org/10.1002/9783527678129.assep064.
(178) Johnson, A. D.; Szaciłowski, K.; Magri, D. C. Colourful 3-Amino-1,8-Naphthalimide Alkyl-Substituted Fluorescent Derivatives. *Dyes Pigments* **2024**, *231*, 112424. https://doi.org/10.1016/j.dyepig.2024.112424.
(179) Wanigasekara, J.; Barcia, C.; Cullen, P. J.; Tiwari, B.; Curtin, J. F. Plasma Induced Reactive Oxygen Species-dependent Cytotoxicity in Glioblastoma 3D Tumourspheres. *Plasma Process. Polym.* **2022**, *19* (4), 2100157. https://doi.org/10.1002/ppap.202100157.
(180) Ge, C.; Liu, L.; Wang, Y.; Di, X.; Luo, X.; Liu, H.; Qian, Y. Novel 1,8-Naphthalimide Derivatives As Antitumor Agents and Potent Demethylase Inhibitors. *ACS Med. Chem. Lett.* **2023**, *14* (11), 1551–1557. https://doi.org/10.1021/acsmedchemlett.3c00353.
(181) Choi, S.-A.; Park, C. S.; Kwon, O. S.; Giong, H.-K.; Lee, J.-S.; Ha, T. H.; Lee, C.-S. Structural Effects of Naphthalimide-Based Fluorescent Sensor for Hydrogen Sulfide and Imaging in Live Zebrafish. *Sci. Rep.* **2016**, *6* (1). https://doi.org/10.1038/srep26203.
(182) Zhang, Z.-Y.; Li, C. Biphen[*n*]Arenes: Modular Synthesis, Customizable Cavity Sizes, and Diverse Skeletons. *Acc. Chem. Res.* **2022**, *55* (6), 916–929. https://doi.org/10.1021/acs.accounts.2c00043.
(183) Qiao, B.; Anderson, Joseph. R.; Pink, M.; Flood, A. H. Size-Matched Recognition of Large Anions by Cyanostar Macrocycles Is Saved When

Solvent-Bias Is Avoided. *Chem. Commun.* **2016**, *52* (56), 8683–8686. https://doi.org/10.1039/C6CC03463B.

(184) Qin, L.; Hartley, A.; Turner, P.; Elmes, R. B. P.; Jolliffe, K. A. Macrocyclic Squaramides: Anion Receptors with High Sulfate Binding Affinity and Selectivity in Aqueous Media. *Chem. Sci.* **2016**, *7* (7), 4563–4572. https://doi.org/10.1039/C6SC01011C.

(185) Zaleskaya, M.; Jagleniec, D.; Romański, J. Macrocyclic Squaramides as Ion Pair Receptors and Fluorescent Sensors Selective towards Sulfates. *Dalton Trans.* **2021**, *50* (11), 3904–3915. https://doi.org/10.1039/D0DT04273K.

(186) Casadei, M. A.; Galli, C.; Mandolini, L. Ring-Closure Reactions. 22. Kinetics of Cyclization of Diethyl (.Omega.-Bromoalkyl)Malonates in the Range of 4- to 21-Membered Rings. Role of Ring Strain. *J. Am. Chem. Soc.* **1984**, *106* (4), 1051–1056. https://doi.org/10.1021/ja00316a039.

(187) White, C. J.; Yudin, A. K. Contemporary Strategies for Peptide Macrocyclization. *Nat. Chem.* **2011**, *3* (7), 509–524. https://doi.org/10.1038/nchem.1062.

(188) Clarke, A. K.; Unsworth, W. P. A Happy Medium: The Synthesis of Medicinally Important Medium-Sized Rings *via* Ring Expansion. *Chem. Sci.* **2020**, *11* (11), 2876–2881. https://doi.org/10.1039/D0SC00568A.

(189) Kramer, U.; Guggisberg, A.; Hesse, M.; Schmid, H. The "Zip" Reaction: A New Method for Ring Expansion; Synthesis of 17- and 21- Membered Polyaminolactams. *Angew. Chem. Int. Ed. Engl.* **1977**, *16* (12), 861–862. https://doi.org/10.1002/anie.197708611.

(190) Shang, J.; Thombare, V. J.; Charron, C. L.; Wille, U.; Hutton, C. A. Ring Expansion of Thiolactams via Imide Intermediates: An Amino Acid Insertion Strategy. *Chem. – Eur. J.* **2021**, *27* (5), 1620–1625. https://doi.org/10.1002/chem.202005035.

(191) Trost, B. M.; Vincent, J. E. A Three-Carbon Condensative Expansion. Application to Muscone. *J. Am. Chem. Soc.* **1980**, *102* (17), 5680–5683. https://doi.org/10.1021/ja00537a049.

(192) Chulin, A. N.; Rodionov, I. L.; Baidakova, L. K.; Rodionova, L. N.; Balashova, T. A.; Ivanov, V. T. Preparation and Reactivity of Aminoacyl Pyroglutamates. Facile Synthesis of 10-Membered-Ring Cyclic Dipeptides Derived from 1,4-Diaminobutyric and Glutamic Acids. *J. Pept. Sci.* **2005**, *11* (3), 175–186. https://doi.org/10.1002/psc.611.

(193) Kitsiou, C.; Hindes, J. J.; I'Anson, P.; Jackson, P.; Wilson, T. C.; Daly, E. K.; Felstead, H. R.; Hearnshaw, P.; Unsworth, W. P. The Synthesis of Structurally Diverse Macrocycles By Successive Ring Expansion. *Angew. Chem. Int. Ed.* **2015**, *54* (52), 15794–15798. https://doi.org/10.1002/anie.201509153.

(194) Baud, L. G.; Manning, M. A.; Arkless, H. L.; Stephens, T. C.; Unsworth, W. P. Ring-Expansion Approach to Medium-Sized Lactams and Analysis of Their Medicinal Lead-Like Properties. *Chem. – Eur. J.* **2017**, *23* (9), 2225–2230. https://doi.org/10.1002/chem.201605615.

(195) Marchetti, L. A.; Krämer, T.; Elmes, R. B. P. Amidosquaramides – a New Anion Binding Motif with pH Sensitive Anion Transport Properties. *Org. Biomol. Chem.* **2022**, *20* (35), 7056–7066. https://doi.org/10.1039/D2OB01176J.

(196) Ximenis, M.; Sampedro, A.; Martínez-Crespo, L.; Ramis, G.; Orvay, F.; Costa, A.; Rotger, C. Introducing a Squaramide-Based Self-Immolative Spacer for

Controlled Drug Release. *Chem. Commun.* **2021**, *57* (22), 2736–2739. https://doi.org/10.1039/D0CC07683J.

(197) Abogunrin, A. A.; Healy, S. A.; Fenelon, O.; Elmes, R. B. P. Head vs. Tail Squaramide–Naphthalimide Conjugates: Self-Assembly and Anion Binding Behaviour. *Chemistry* **2022**, *4* (4), 1288–1299. https://doi.org/10.3390/chemistry4040085.

(198) Engler, E. M.; Andose, J. D.; Schleyer, P. V. R. Critical Evaluation of Molecular Mechanics. *J. Am. Chem. Soc.* **1973**, *95* (24), 8005–8025. https://doi.org/10.1021/ja00805a012.

(199) Vrettos, E. I.; Sayyad, N.; Mavrogiannaki, E. M.; Stylos, E.; Kostagianni, A. D.; Papas, S.; Mavromoustakos, T.; Theodorou, V.; Tzakos, A. G. Unveiling and Tackling Guanidinium Peptide Coupling Reagent Side Reactions towards the Development of Peptide-Drug Conjugates. *RSC Adv* **2017**, *7* (80), 50519–50526. https://doi.org/10.1039/C7RA06655D.

(200) Albericio, F.; El-Faham, A. Choosing the Right Coupling Reagent for Peptides: A Twenty-Five-Year Journey. *Org. Process Res. Dev.* **2018**, *22* (7), 760–772. https://doi.org/10.1021/acs.oprd.8b00159.

(201) Stephens, T. C.; Lodi, M.; Steer, A. M.; Lin, Y.; Gill, M. T.; Unsworth, W. P. Synthesis of Cyclic Peptide Mimetics by the Successive Ring Expansion of Lactams. *Chem. – Eur. J.* **2017**, *23* (54), 13314–13318. https://doi.org/10.1002/chem.201703316.

(202) Fusco, W.; Lorenzo, M. B.; Cintoni, M.; Porcari, S.; Rinninella, E.; Kaitsas, F.; Lener, E.; Mele, M. C.; Gasbarrini, A.; Collado, M. C.; Cammarota, G.; Ianiro, G. Short-Chain Fatty-Acid-Producing Bacteria: Key Components of the Human Gut Microbiota. *Nutrients* **2023**, *15* (9), 2211. https://doi.org/10.3390/nu15092211.

(203) Fernández, J.; Redondo-Blanco, S.; Gutiérrez-del-Río, I.; Miguélez, E. M.; Villar, C. J.; Lombó, F. Colon Microbiota Fermentation of Dietary Prebiotics towards Short-Chain Fatty Acids and Their Roles as Anti-Inflammatory and Antitumour Agents: A Review. *J. Funct. Foods* **2016**, *25*, 511–522. https://doi.org/10.1016/j.jff.2016.06.032.

(204) Li, X.; Shimizu, Y.; Kimura, I. Gut Microbial Metabolite Short-Chain Fatty Acids and Obesity. *Biosci. Microbiota Food Health* **2017**, *36* (4), 135–140. https://doi.org/10.12938/bmfh.17-010.

(205) Chen, X.-F.; Chen, X.; Tang, X. Short-Chain Fatty Acid, Acylation and Cardiovascular Diseases. *Clin. Sci.* **2020**, *134* (6), 657–676. https://doi.org/10.1042/CS20200128.

(206) Skonieczna-Żydecka, K.; Grochans, E.; Maciejewska, D.; Szkup, M.; Schneider-Matyka, D.; Jurczak, A.; Łoniewski, I.; Kaczmarczyk, M.; Marlicz, W.; Czerwińska-Rogowska, M.; Pełka-Wysiecka, J.; Dec, K.; Stachowska, E. Faecal Short Chain Fatty Acids Profile Is Changed in Polish Depressive Women. *Nutrients* **2018**, *10* (12), 1939. https://doi.org/10.3390/nu10121939.

(207) El-Ansary, A.; Al-Salem, H. S.; Asma, A.; Al-Dbass, A. Glutamate Excitotoxicity Induced by Orally Administered Propionic Acid, a Short Chain Fatty Acid Can Be Ameliorated by Bee Pollen. *Lipids Health Dis.* **2017**, *16* (1), 96. https://doi.org/10.1186/s12944-017-0485-7.

(208) Trapecar, M.; Communal, C.; Velazquez, J.; Maass, C. A.; Huang, Y.-J.; Schneider, K.; Wright, C. W.; Butty, V.; Eng, G.; Yilmaz, O.; Trumper, D.; Griffith, L. G. Gut-Liver Physiomimetics Reveal Paradoxical Modulation of

IBD-Related Inflammation by Short-Chain Fatty Acids. *Cell Syst.* **2020**, *10* (3), 223-239.e9. https://doi.org/10.1016/j.cels.2020.02.008.

(209) Hosmer, J.; McEwan, A. G.; Kappler, U. Bacterial Acetate Metabolism and Its Influence on Human Epithelia. *Emerg. Top. Life Sci.* **2024**, *8* (1), 1–13. https://doi.org/10.1042/ETLS20220092.

(210) Moffett, J. R.; Puthillathu, N.; Vengilote, R.; Jaworski, D. M.; Namboodiri, A. M. Acetate Revisited: A Key Biomolecule at the Nexus of Metabolism, Epigenetics and Oncogenesis—Part 1: Acetyl-CoA, Acetogenesis and Acyl-CoA Short-Chain Synthetases. *Front. Physiol.* **2020**, *11*, 580167. https://doi.org/10.3389/fphys.2020.580167.

(211) Martínez-Reyes, I.; Chandel, N. S. Mitochondrial TCA Cycle Metabolites Control Physiology and Disease. *Nat. Commun.* **2020**, *11* (1), 102. https://doi.org/10.1038/s41467-019-13668-3.

(212) Shi, Q.; Chen, J.; Zou, X.; Tang, X. Intracellular Cholesterol Synthesis and Transport. *Front. Cell Dev. Biol.* **2022**, *10*, 819281. https://doi.org/10.3389/fcell.2022.819281.

(213) Shang, S.; Liu, J.; Hua, F. Protein Acylation: Mechanisms, Biological Functions and Therapeutic Targets. *Signal Transduct. Target. Ther.* **2022**, *7* (1), 396. https://doi.org/10.1038/s41392-022-01245-y.

(214) Perry, R. J.; Peng, L.; Barry, N. A.; Cline, G. W.; Zhang, D.; Cardone, R. L.; Petersen, K. F.; Kibbey, R. G.; Goodman, A. L.; Shulman, G. I. Acetate Mediates a Microbiome–Brain–β-Cell Axis to Promote Metabolic Syndrome. *Nature* **2016**, *534* (7606), 213–217. https://doi.org/10.1038/nature18309.

(215) Hernández, M. A. G.; Canfora, E. E.; Jocken, J. W. E.; Blaak, E. E. The Short-Chain Fatty Acid Acetate in Body Weight Control and Insulin Sensitivity. *Nutrients* **2019**, *11* (8), 1943. https://doi.org/10.3390/nu11081943.

(216) Mashimo, T.; Pichumani, K.; Vemireddy, V.; Hatanpaa, K. J.; Singh, D. K.; Sirasanagandla, S.; Nannepaga, S.; Piccirillo, S. G.; Kovacs, Z.; Foong, C.; Huang, Z.; Barnett, S.; Mickey, B. E.; DeBerardinis, R. J.; Tu, B. P.; Maher, E. A.; Bachoo, R. M. Acetate Is a Bioenergetic Substrate for Human Glioblastoma and Brain Metastases. *Cell* **2014**, *159* (7), 1603–1614. https://doi.org/10.1016/j.cell.2014.11.025.

(217) Meldrum, B. S. Glutamate as a Neurotransmitter in the Brain: Review of Physiology and Pathology. *J. Nutr.* **2000**, *130* (4), 1007S-1015S. https://doi.org/10.1093/jn/130.4.1007S.

(218) Zhou, Y.; Danbolt, N. C. Glutamate as a Neurotransmitter in the Healthy Brain. *J. Neural Transm. Vienna Austria 1996* **2014**, *121* (8), 799–817. https://doi.org/10.1007/s00702-014-1180-8.

(219) Esposito, Z.; Belli, L.; Toniolo, S.; Sancesario, G.; Bianconi, C.; Martorana, A. Amyloid β, Glutamate, Excitotoxicity in Alzheimer's Disease: Are We on the Right Track? *CNS Neurosci. Ther.* **2013**, *19* (8), 549–555. https://doi.org/10.1111/cns.12095.

(220) Mills, E.; O'Neill, L. A. J. Succinate: A Metabolic Signal in Inflammation. *Trends Cell Biol.* **2014**, *24* (5), 313–320. https://doi.org/10.1016/j.tcb.2013.11.008.

(221) Zhao, T.; Mu, X.; You, Q. Succinate: An Initiator in Tumorigenesis and Progression. *Oncotarget* **2017**, *8* (32), 53819–53828. https://doi.org/10.18632/oncotarget.17734.

(222) Unden, G.; Strecker, A.; Kleefeld, A.; Kim, O. B. C 4 -Dicarboxylate Utilization in Aerobic and Anaerobic Growth. *EcoSal Plus* **2016**, *7* (1). https://doi.org/10.1128/ecosalplus.esp-0021-2015.
(223) Golby, P.; Kelly, D. J.; Guest, J. R.; Andrews, S. C. Transcriptional Regulation and Organization of the *dcuA* and *dcuB* Genes, Encoding Homologous Anaerobic C 4 -Dicarboxylate Transporters in *Escherichia Coli*. *J. Bacteriol.* **1998**, *180* (24), 6586–6596. https://doi.org/10.1128/jb.180.24.6586-6596.1998.
(224) Valentini, M.; Storelli, N.; Lapouge, K. Identification of C_4 -Dicarboxylate Transport Systems in Pseudomonas aeruginosaPAO1. *J. Bacteriol.* **2011**, *193* (17), 4307–4316. https://doi.org/10.1128/JB.05074-11.
(225) Prohens, R.; Tomàs, S.; Morey, J.; Deyà, P. M.; Ballester, P.; Costa, A. Squaramido-Based Receptors: Molecular Recognition of Carboxylate Anions in Highly Competitive Media. *Tetrahedron Lett.* **1998**, *39* (9), 1063–1066. https://doi.org/10.1016/S0040-4039(97)10728-6.
(226) Elmes, R. B. P.; K. Y. Yuen, K.; Jolliffe, K. A. Sulfate-Selective Recognition by Using Neutral Dipeptide Anion Receptors in Aqueous Solution. *Chem. – Eur. J.* **2014**, *20* (24), 7373–7380. https://doi.org/10.1002/chem.201400292.
(227) Elmes, R. B. P.; Jolliffe, K. A. Amino Acid-Based Squaramides for Anion Recognition. *Supramol. Chem.* **2015**, *27* (5–6), 321–328. https://doi.org/10.1080/10610278.2014.976221.
(228) Grundzi, A.; Healy, S. A.; Fenelon, O.; Elmes, R. B. P. Squaramide-Naphthalimide Conjugates – Exploiting Self-Aggregation Effects in Acetate Recognition. *Results Chem.* **2022**, *4*, 100652. https://doi.org/10.1016/j.rechem.2022.100652.
(229) Prohens, R.; Rotger, M. C.; Piña, M. N.; Deyà, P. M.; Morey, J.; Ballester, P.; Costa, A. Thermodynamic Characterization of the Squaramide–Carboxylate Interaction in Squaramide Receptors. *Tetrahedron Lett.* **2001**, *42* (29), 4933–4936. https://doi.org/10.1016/s0040-4039(01)00880-2.
(230) Frontera, A.; Morey, J.; Oliver, A.; Piña, M. N.; Quiñonero, D.; Costa, A.; Ballester, P.; Deyà, P. M.; Anslyn, E. V. Rational Design, Synthesis, and Application of a New Receptor for the Molecular Recognition of Tricarboxylate Salts in Aqueous Media. *J. Org. Chem.* **2006**, *71* (19), 7185–7195. https://doi.org/10.1021/jo0609327.
(231) Ju, L.; Lippert, A. R.; Bode, J. W. Stereoretentive Synthesis and Chemoselective Amide-Forming Ligations of C-Terminal Peptide α-Ketoacids. *J. Am. Chem. Soc.* **2008**, *130* (13), 4253–4255. https://doi.org/10.1021/ja800053t.
(232) Lippert, A. R.; Keshari, K. R.; Kurhanewicz, J.; Chang, C. J. A Hydrogen Peroxide-Responsive Hyperpolarized^{13} C MRI Contrast Agent. *J. Am. Chem. Soc.* **2011**, *133* (11), 3776–3779. https://doi.org/10.1021/ja111589a.
(233) Wang, Y.; Liu, Y.; Liu, B.; Yuan, Y.; Wei, L.; Wang, M.; Chen, Z. A Benzil- and BODIPY-Based Turn-On Fluorescent Probe for Detection of Hydrogen Peroxide. *Molecules* **2023**, *29* (1), 229. https://doi.org/10.3390/molecules29010229.
(234) Abo, M.; Urano, Y.; Hanaoka, K.; Terai, T.; Komatsu, T.; Nagano, T. Development of a Highly Sensitive Fluorescence Probe for Hydrogen Peroxide. *J. Am. Chem. Soc.* **2011**, *133* (27), 10629–10637. https://doi.org/10.1021/ja203521e.

(235) Huang, X.; Li, Z.; Liu, Z.; Zeng, C.; Hu, L. A Near-Infrared Fluorescent Probe for Endogenous Hydrogen Peroxide Real-Time Imaging in Living Cells and Zebrafish. *Dyes Pigments* **2019**, *165*, 518–523. https://doi.org/10.1016/j.dyepig.2019.02.042.
(236) Xie, X.; Yang, X.; Wu, T.; Li, Y.; Li, M.; Tan, Q.; Wang, X.; Tang, B. Rational Design of an α-Ketoamide-Based Near-Infrared Fluorescent Probe Specific for Hydrogen Peroxide in Living Systems. *Anal. Chem.* **2016**, *88* (16), 8019–8025. https://doi.org/10.1021/acs.analchem.6b01256.
(237) Laha, J. K.; Gupta, P.; Hazra, A. Dithionite-Mediated Tandem Nitro Reduction/Imine Formation/Intramolecular Cyclization for the Synthesis of Dihydro-Benzothiadiazine-1,1-Dioxides. *J. Org. Chem.* **2024**, *89* (1), 725–730. https://doi.org/10.1021/acs.joc.3c01844.

Chapter 8

Appendix

8. Appendix

Chapter 2 – Supplementary Characterisation Data

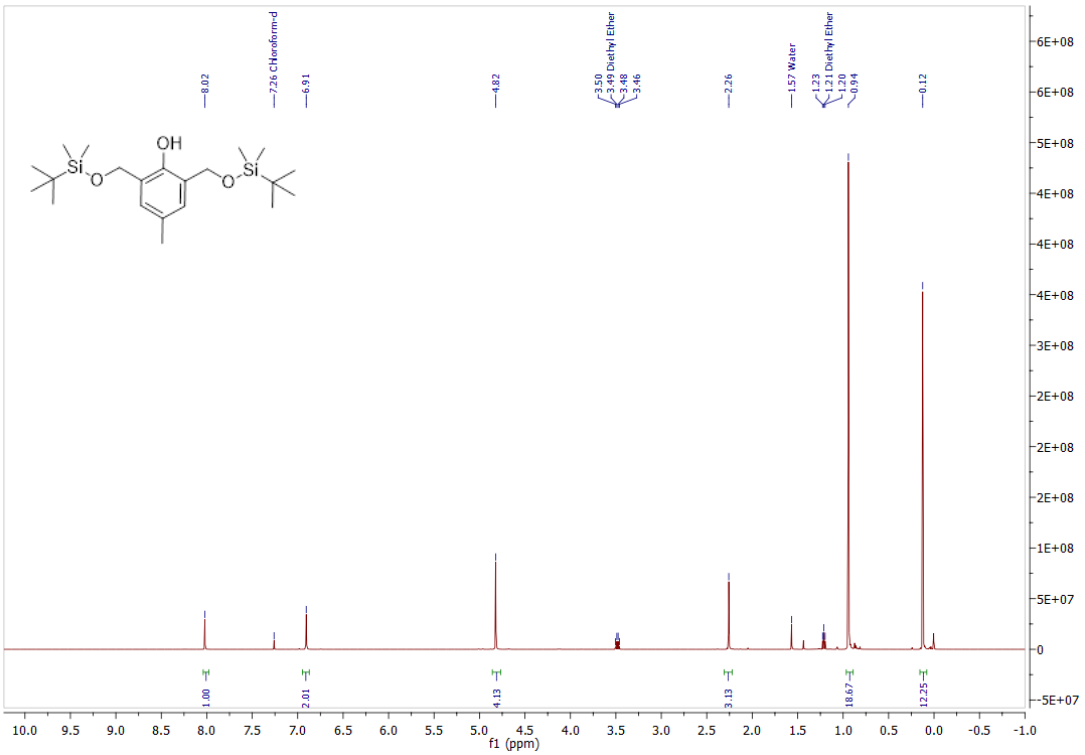

Figure S2.1: ^{1}H NMR spectrum of **2.5** in $CDCl_3$.

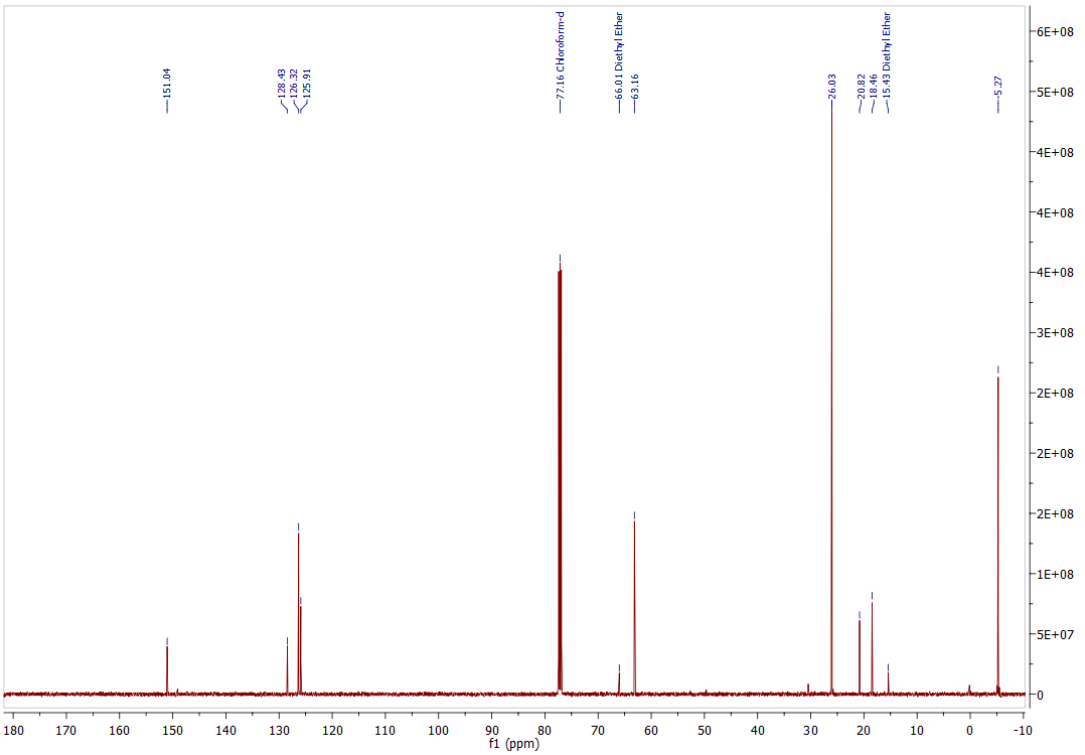

Figure S2.2: ^{13}C NMR spectrum of **2.5** in $CDCl_3$.

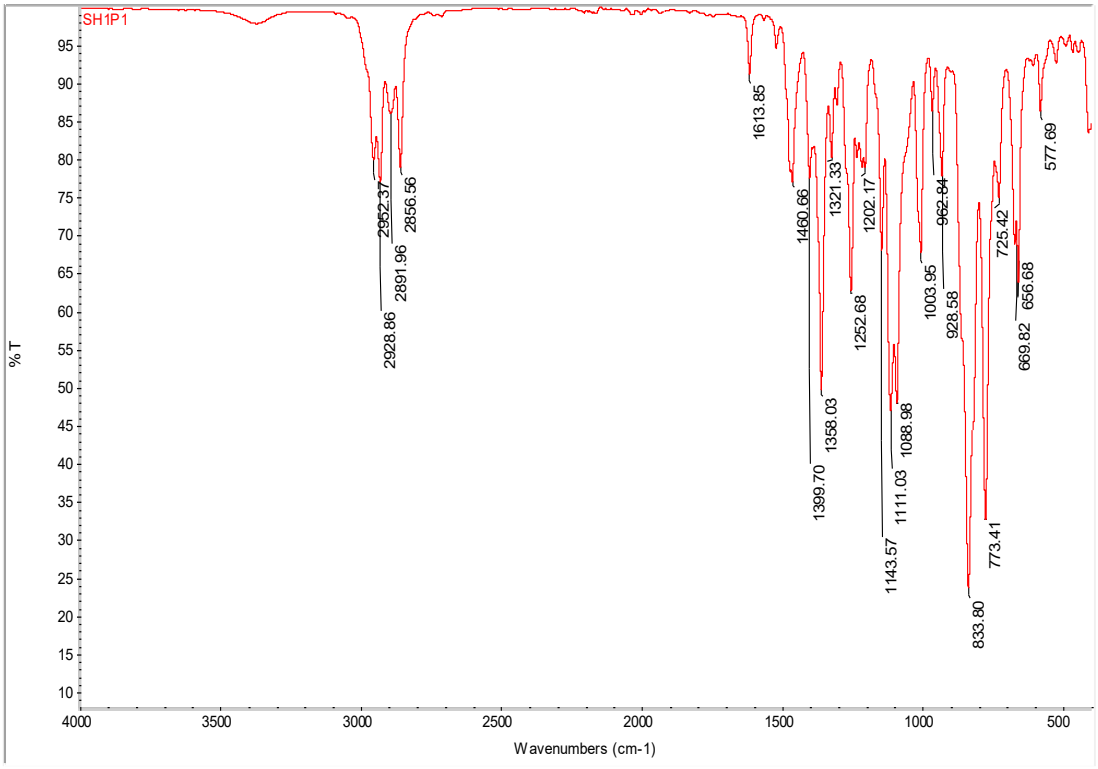

Figure S2.3: FTIR-ATR spectrum of **2.5**

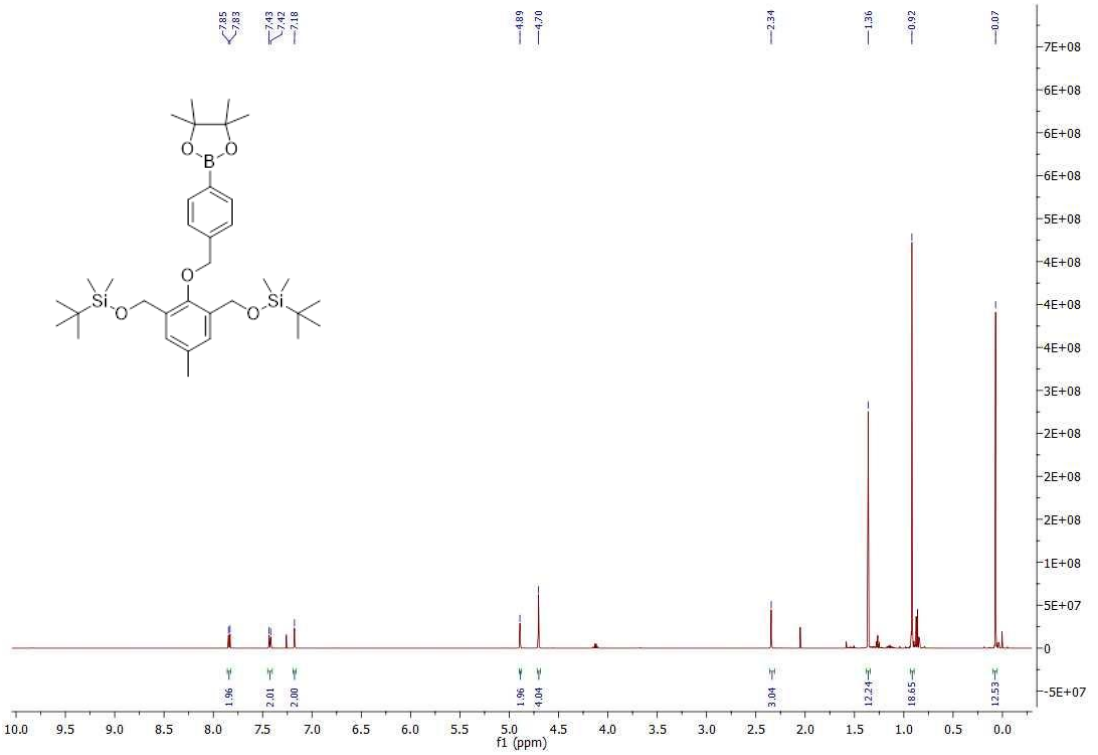

Figure S2.4: ^{1}H NMR spectrum of **2.6** in $CDCl_3$.

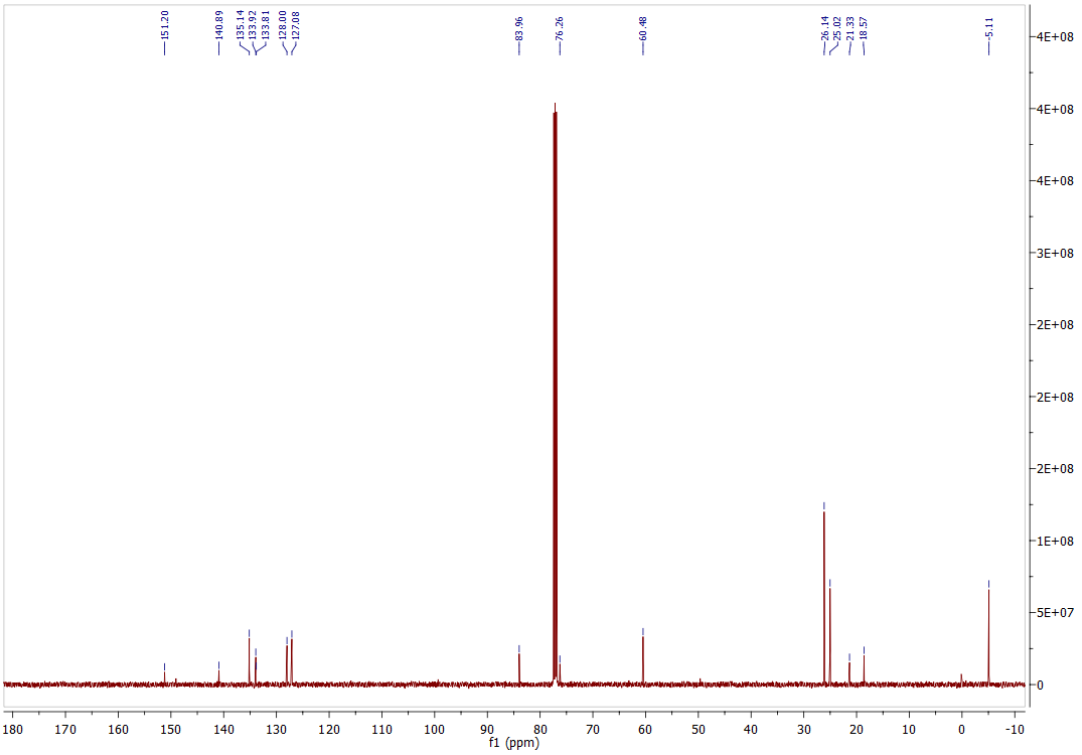

Figure S2.5: ^{13}C NMR spectrum of **2.6** in $CDCl_3$.

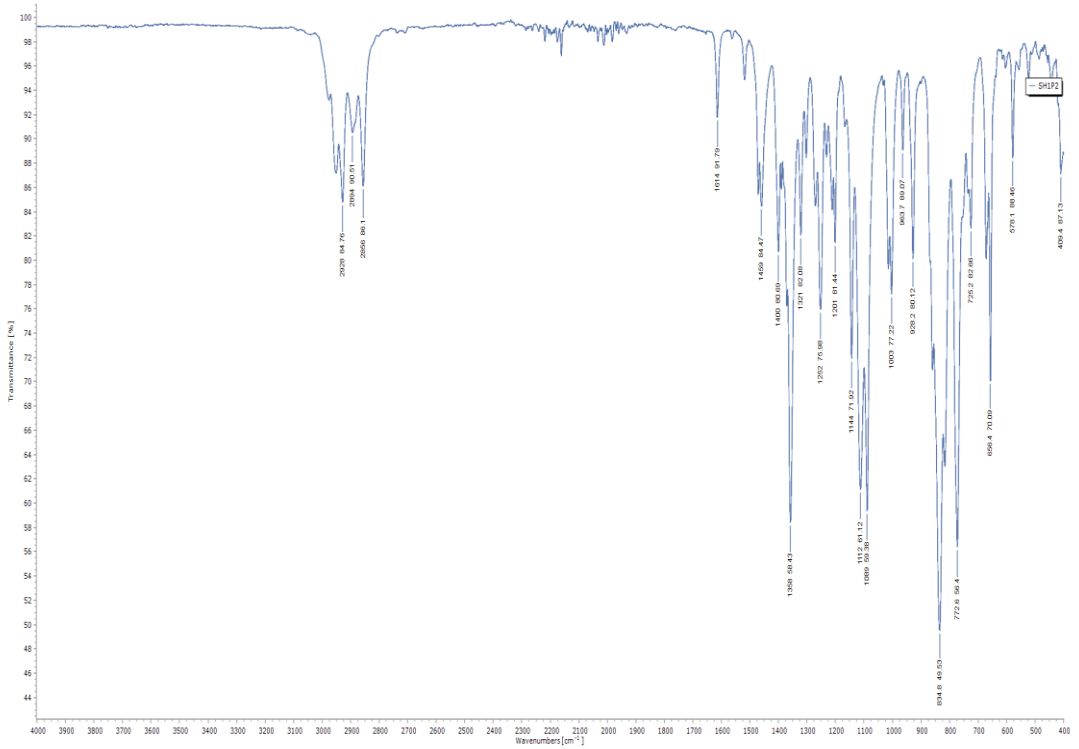

Figure 2.6: FTIR-ATR spectrum of **2.6**.

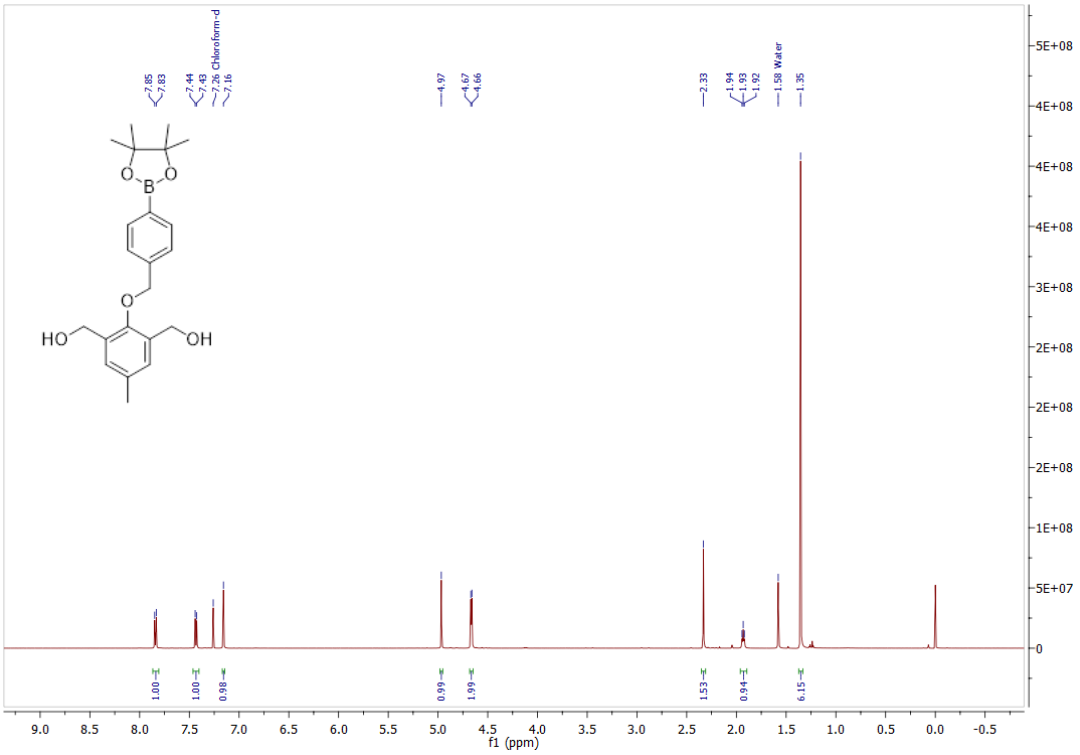

Figure S2.7: ^{1}H NMR spectrum of **2.7** in $CDCl_3$.

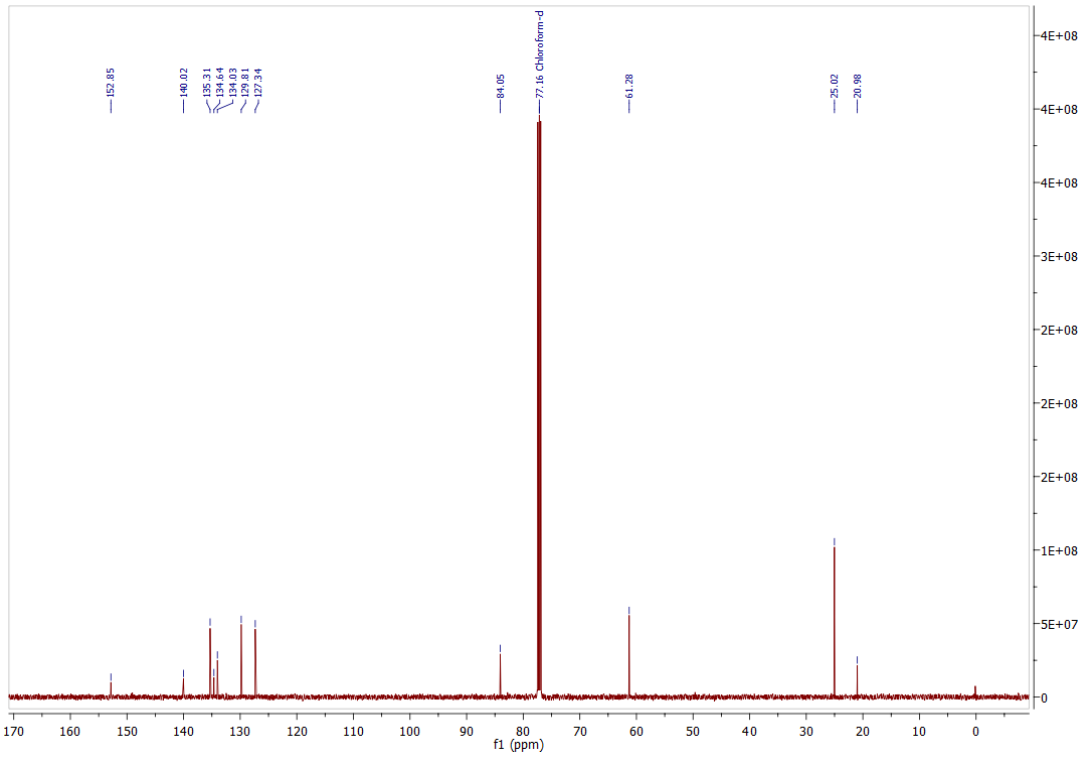

Figure S2.8: ^{13}C NMR spectrum of **2.7** in $CDCl_3$.

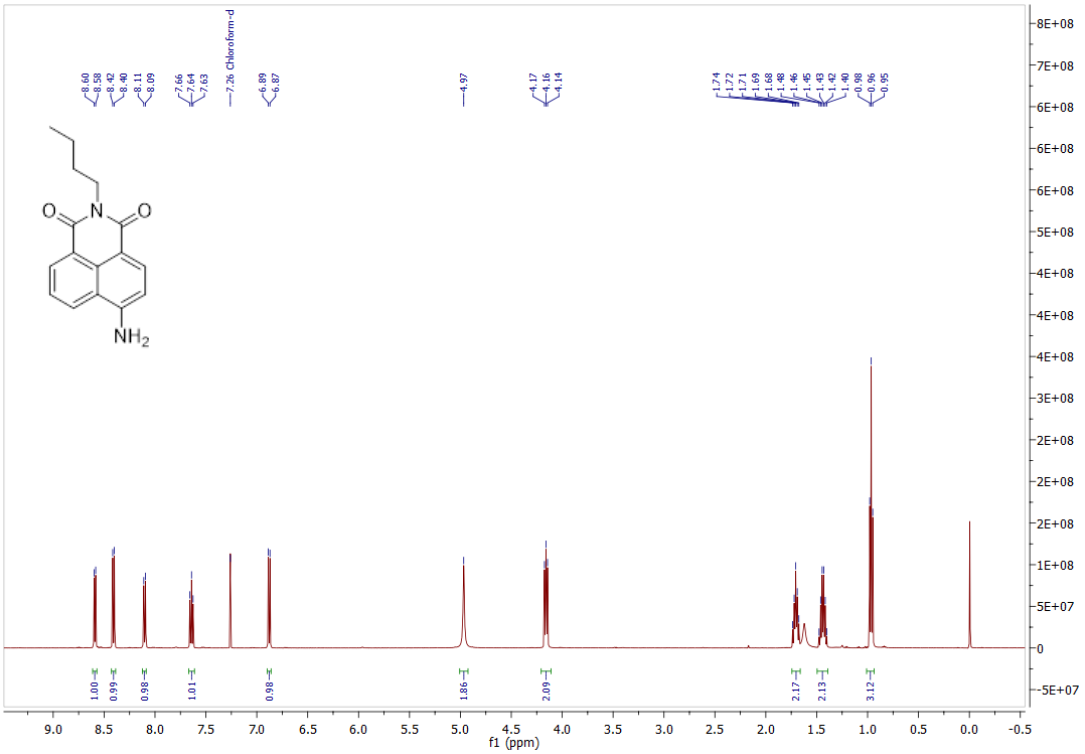

Figure S2.9: ^{1}H NMR spectrum of **2.8** in $CDCl_3$.

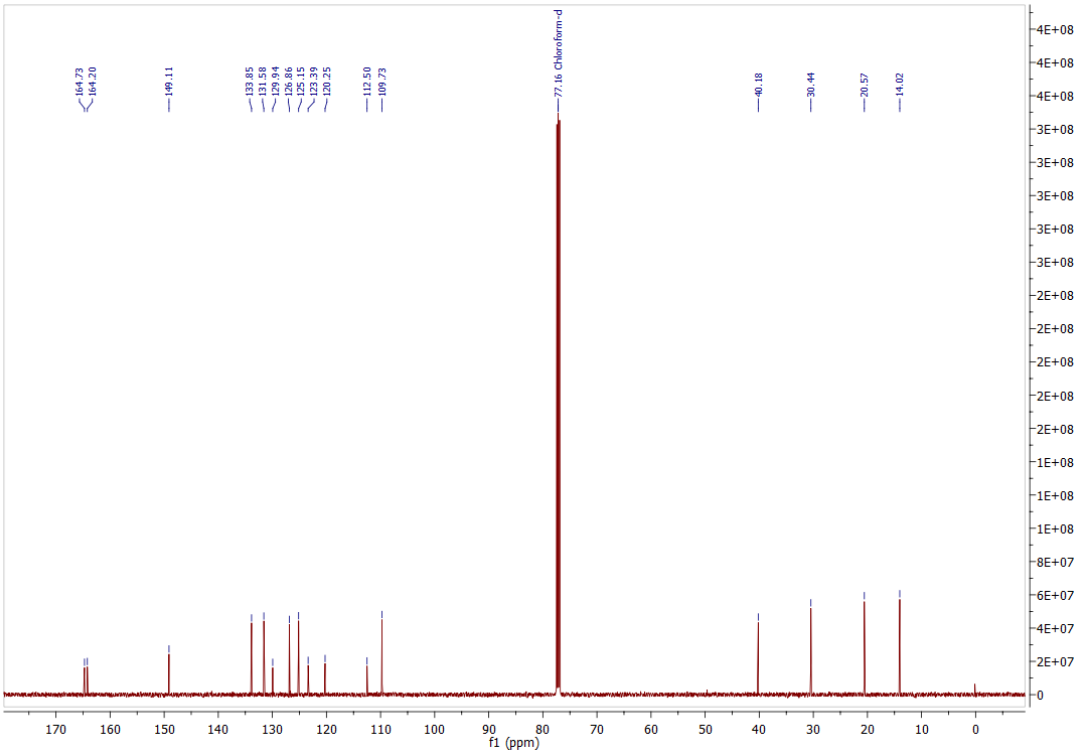

Figure S2.10: ^{13}C NMR spectrum of **2.8** in $CDCl_3$.

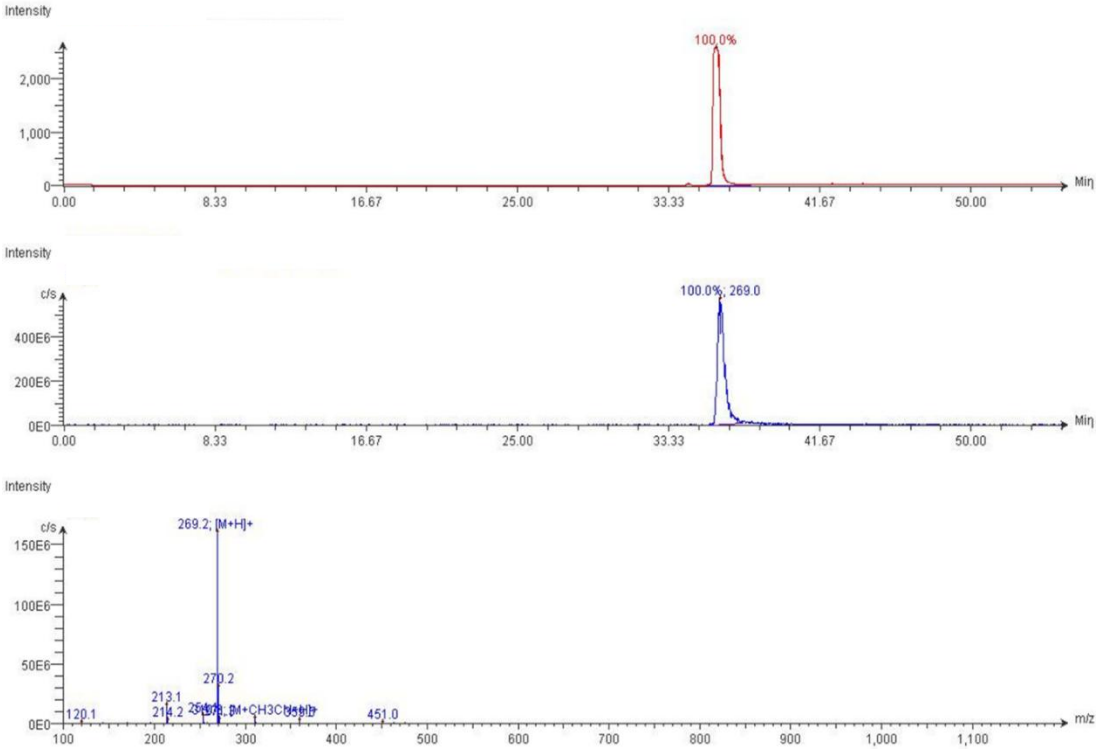

Figure S2.11: LC-MS data for **2.8.**

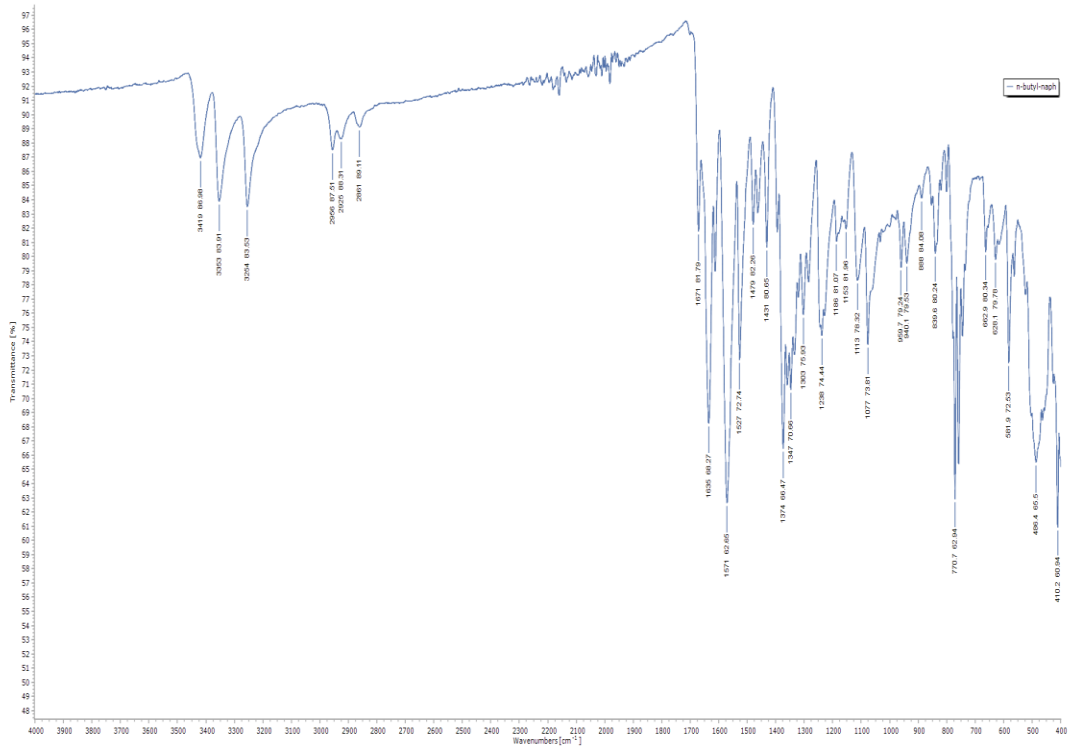

Figure S2.12: FTIR-ATR spectrum of **2.8.**

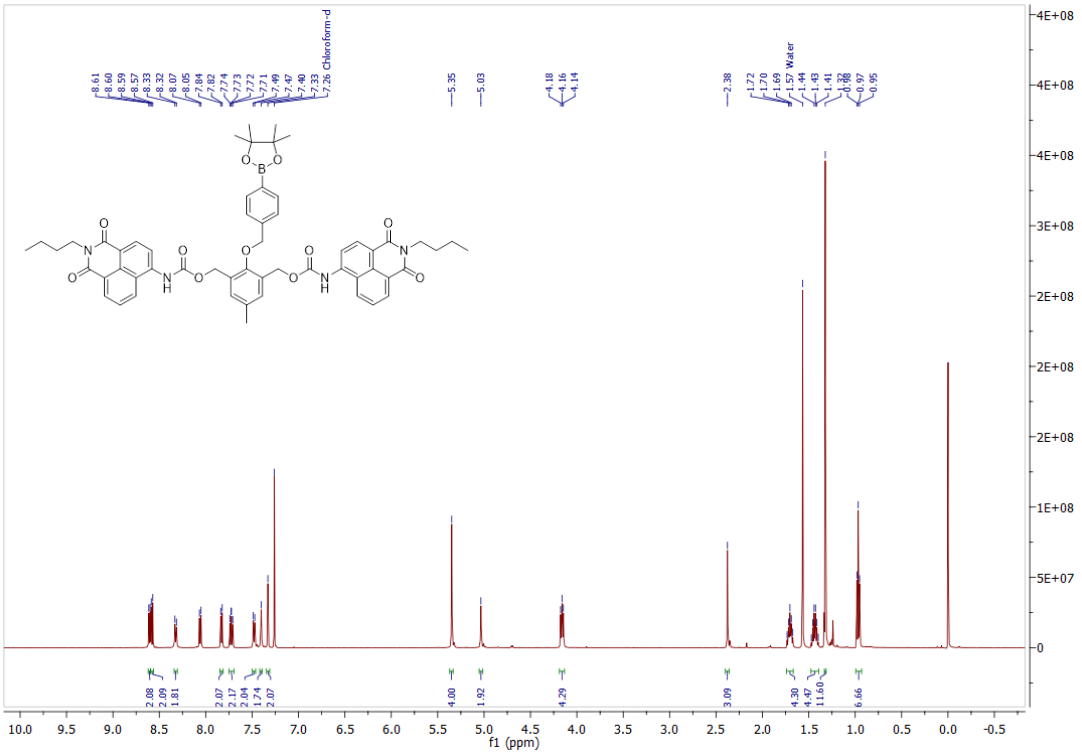

Figure S2.13: ^{1}H NMR spectrum of **2.3** in $CDCl_3$.

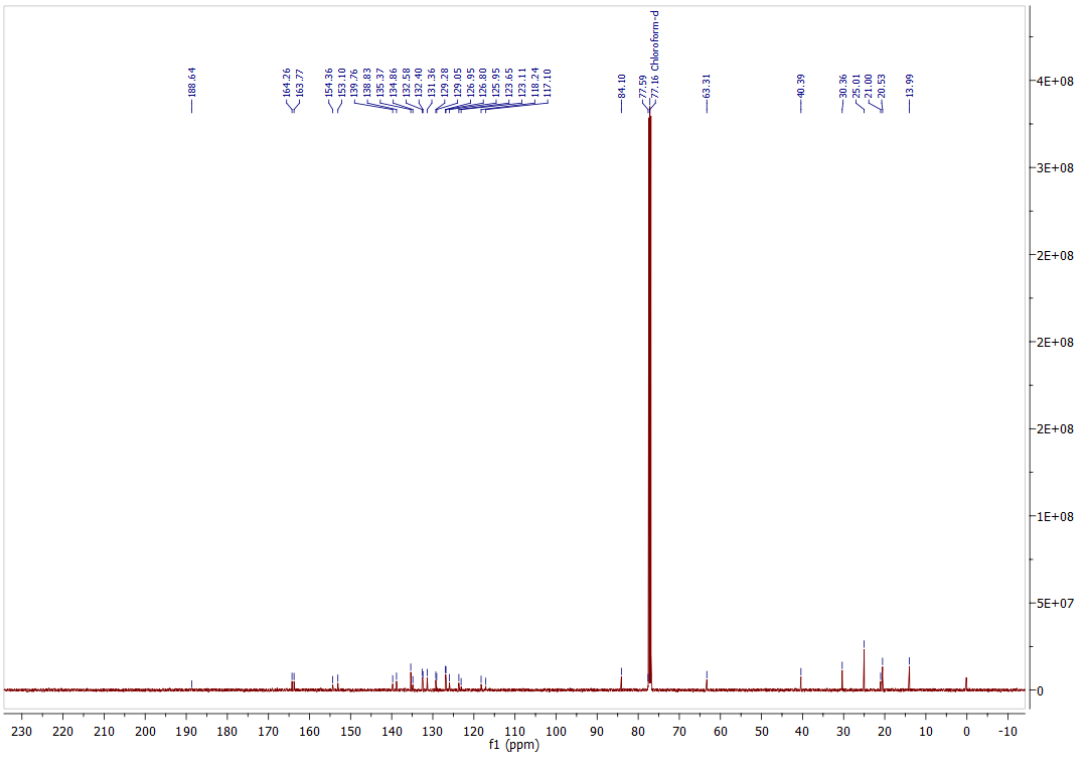

Figure S2.14: ^{13}C NMR spectrum of **2.3** in $CDCl_3$.

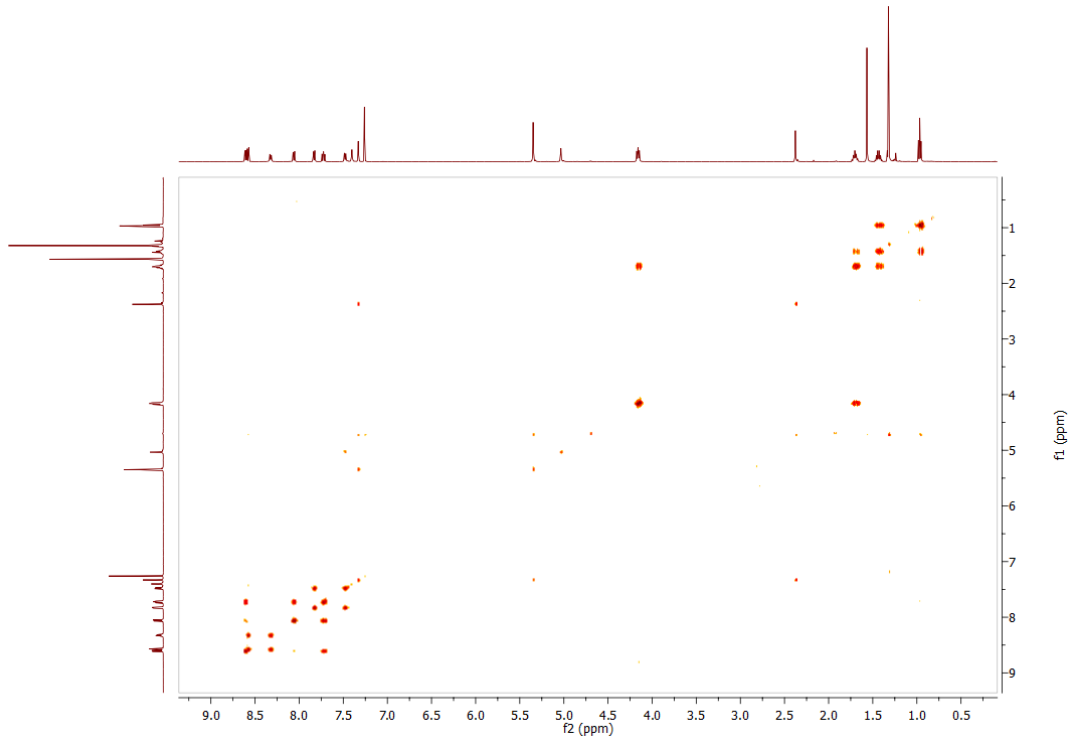

Figure S2.15: COSY spectrum of **2.3** in $CDCl_3$.

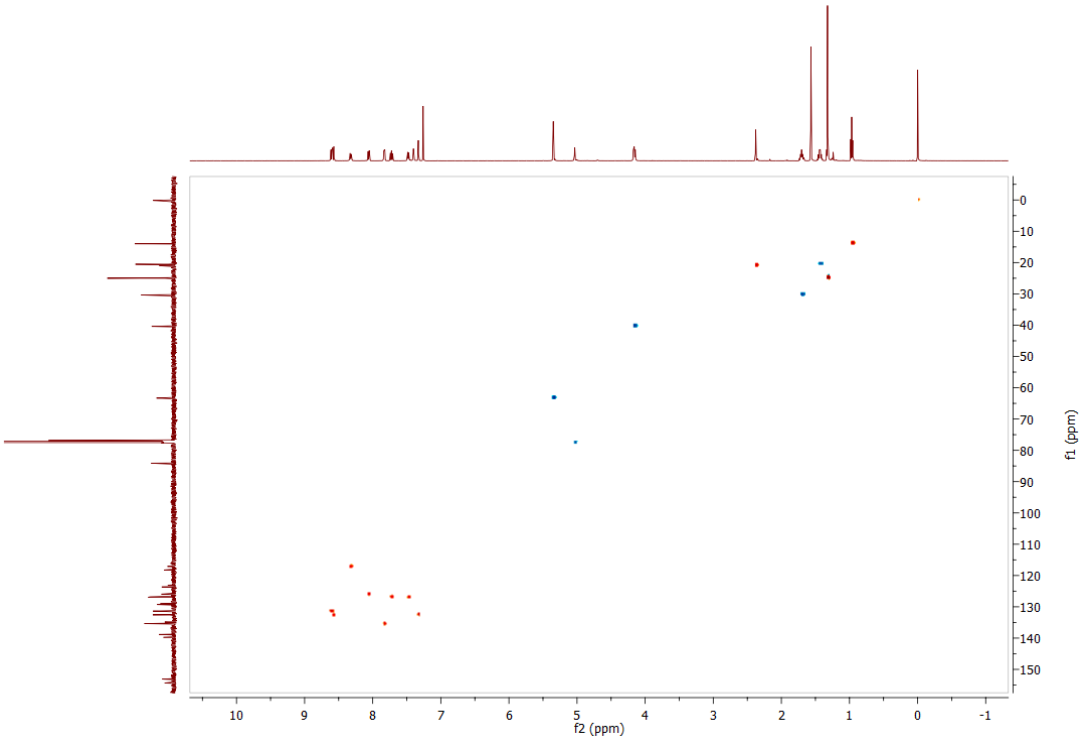

Figure S2.16: HSQC spectrum of **2.3** in $CDCl_3$.

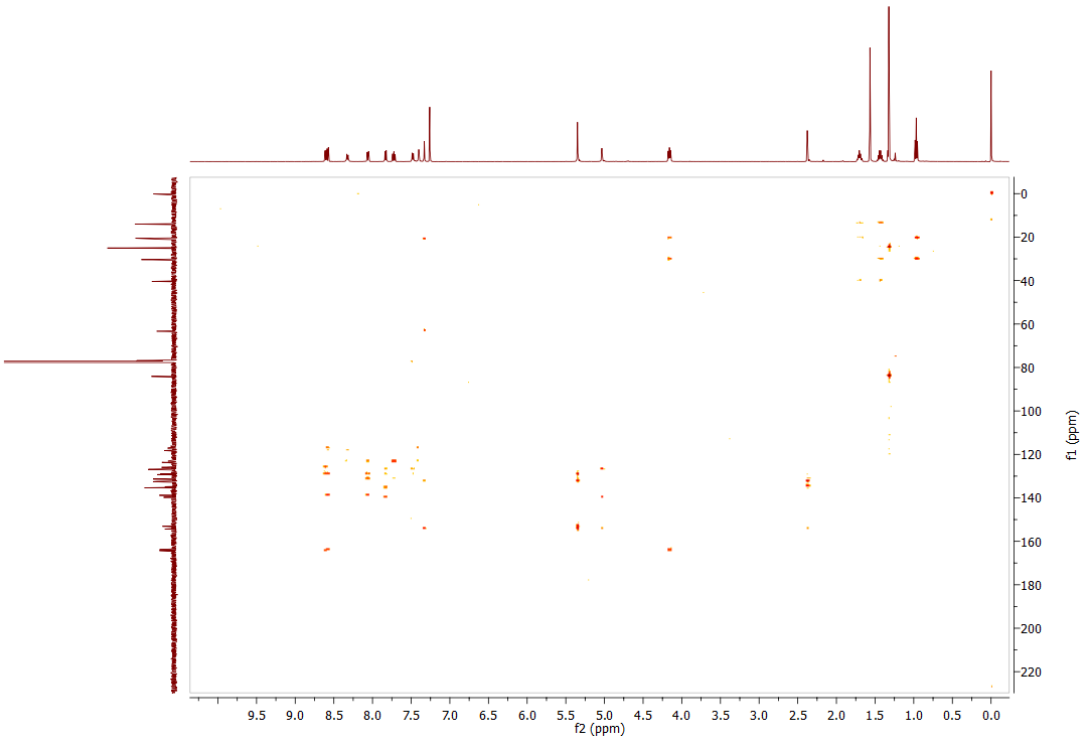

Figure S2.17: HMBC spectrum of **2.3** in $CDCl_3$.

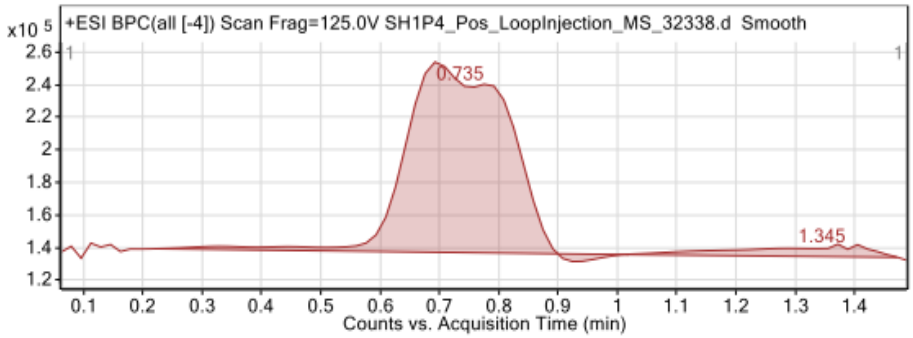

Figure 1: Base peak chromatogram

User Chromatogram Peak List

RT (min)	Area	Area %	Area Sum (%)	Base Peak (m/z)	Width (min)
0.74	1378196	100.00	93.45	141.9575	0.213
1.35	96525	7.00	6.55	149.9519	0.287

Compound Table

Compound Label	RT (min)	Observed mass (m/z)	Neutral observed mass (Da)	Theoretical mass (Da)	Mass error (ppm)	Isotope match score (%)
Cpd 1: C56 H57 B N4 O11	0.95	995.4010	971.4145	971.4153	-0.86	99.20

Mass errors of between -5.00 and 5.00 ppm with isotope match scores above 60% are considered confirmation of molecular formulae

Figure: Full range view of Compound spectra and potential adducts.

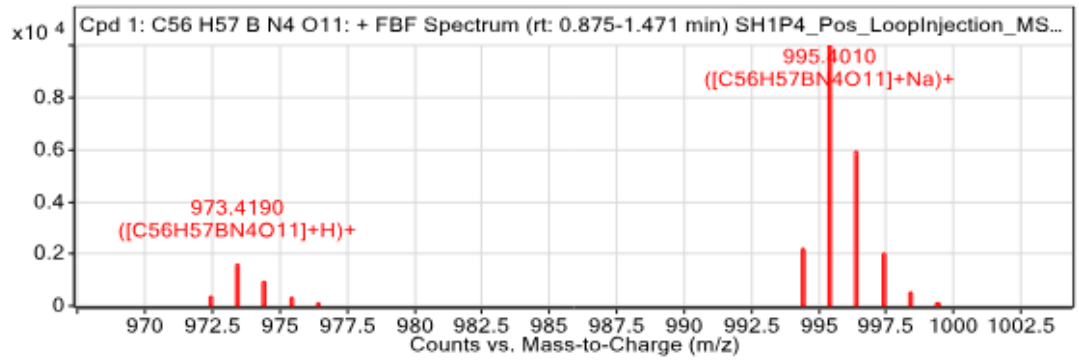

Figure 2.18: HRMS data for **2.3.**

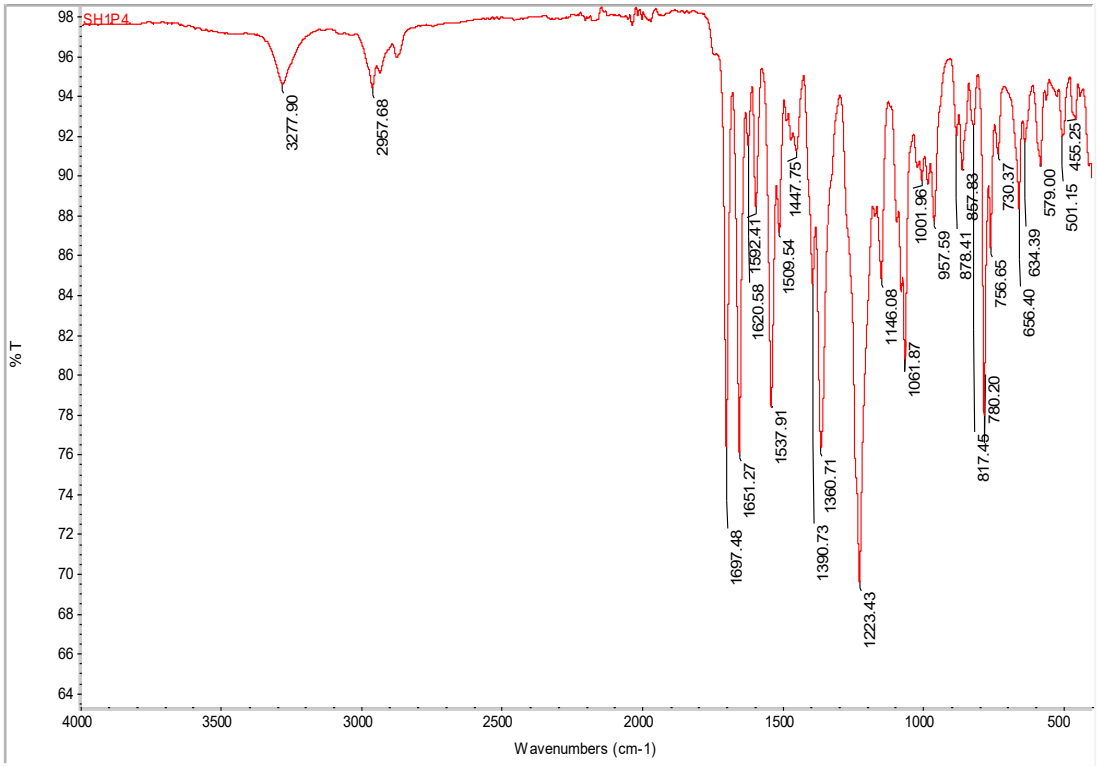

Figure 2.19: FTIR-ATR spectrum of **2.3.**

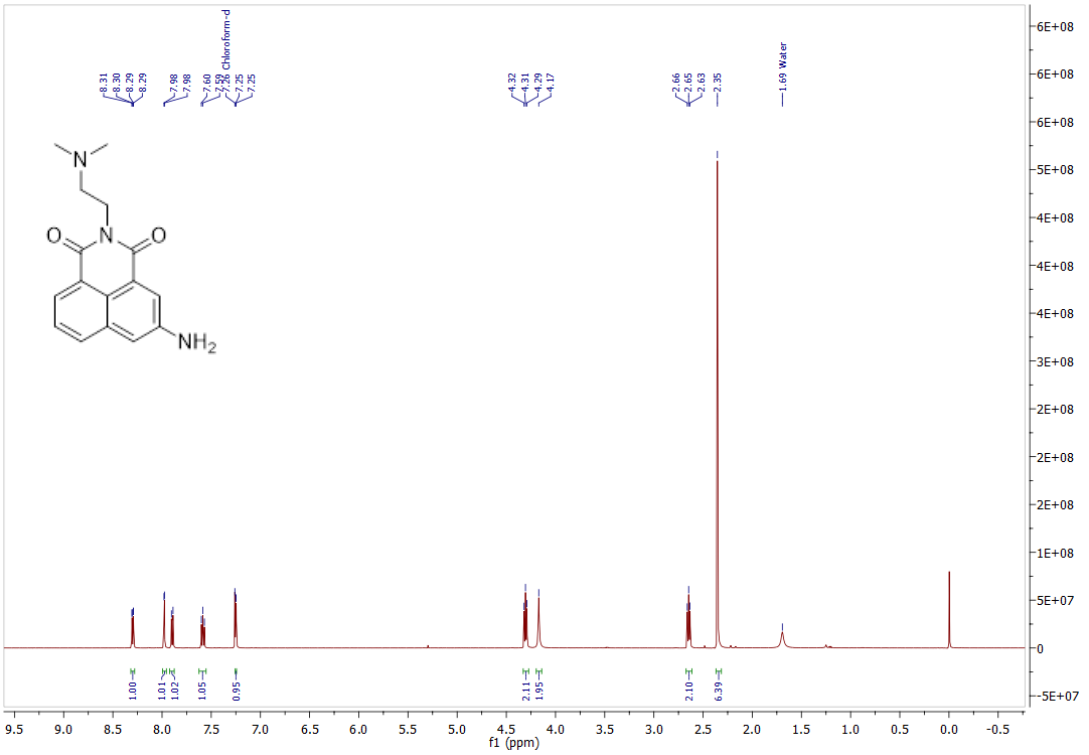

Figure S2.20: ^{1}H NMR spectrum of **2.9** in $CDCl_3$.

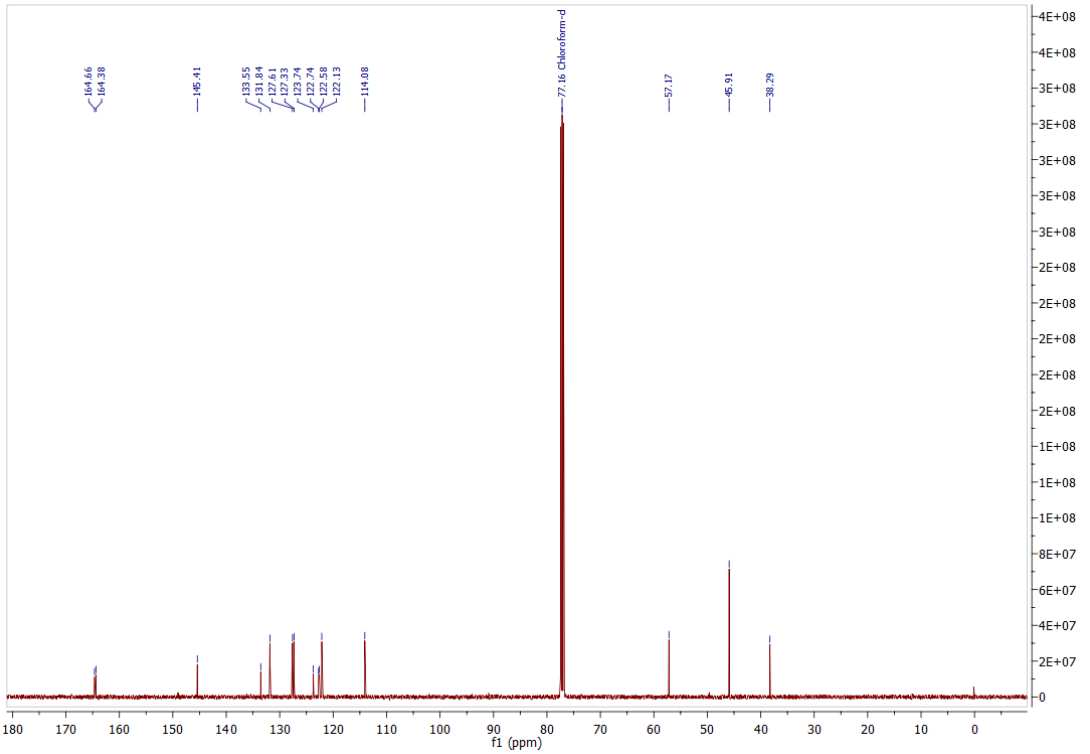

Figure S2.21: ^{13}C NMR spectrum of **2.9** in $CDCl_3$.

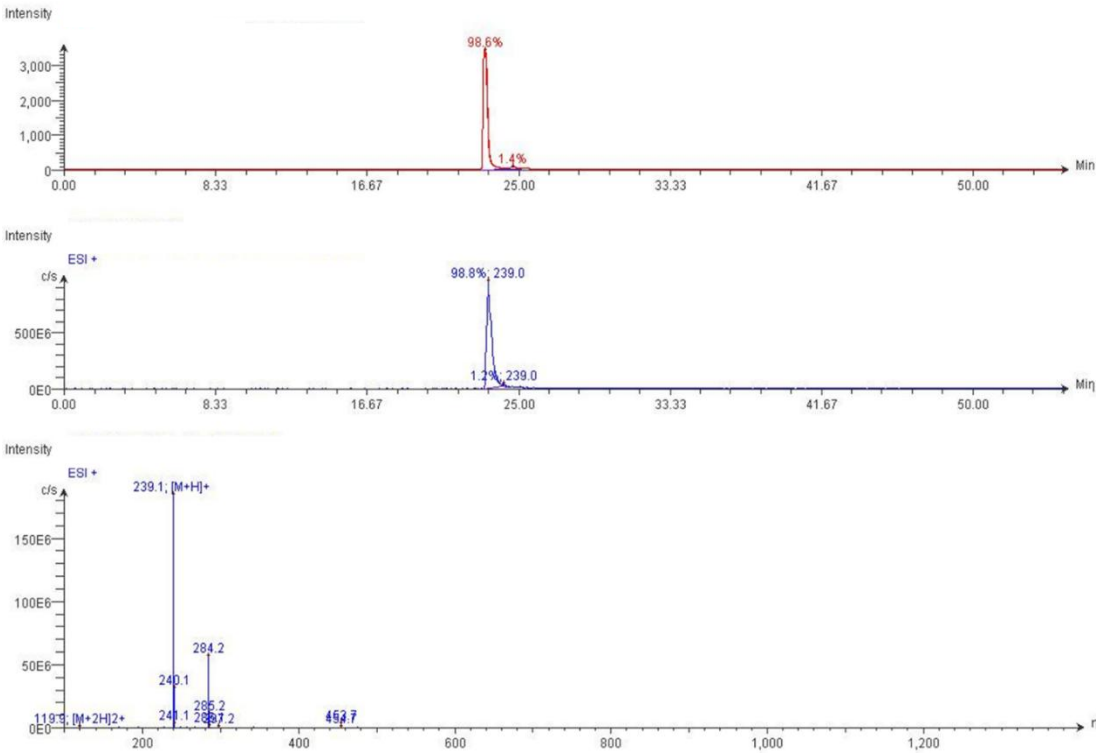

Figure S2.22: LC-MS data for **2.9.**

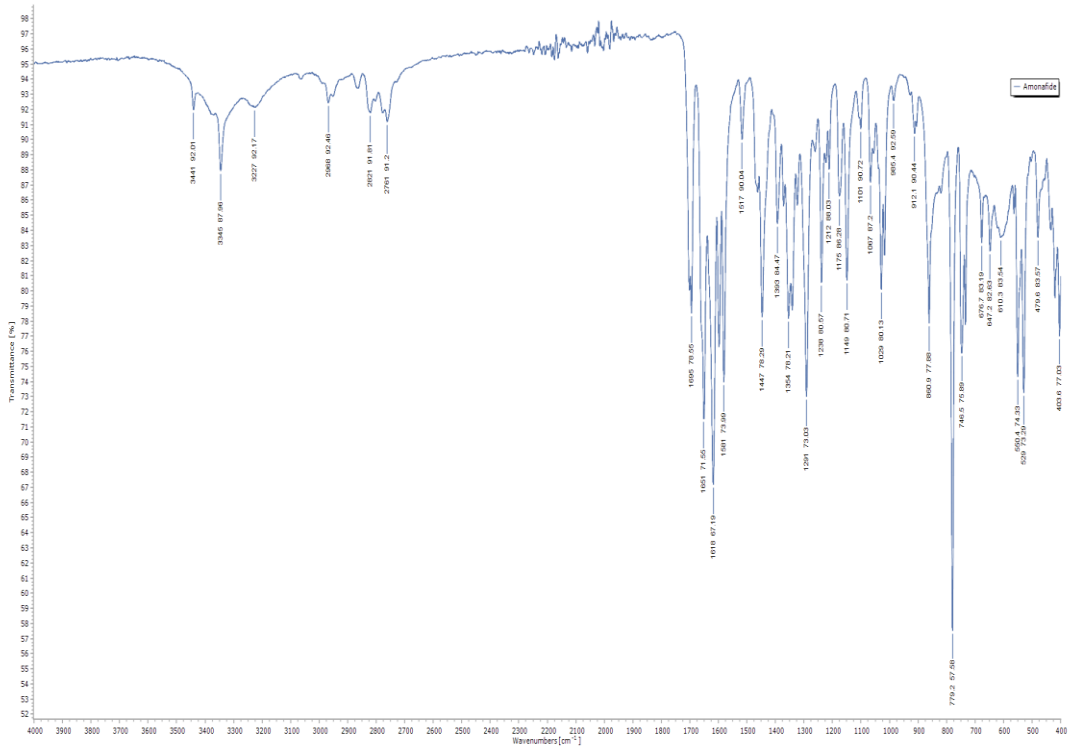

Figure 2.23: FTIR-ATR spectrum of **2.9.**

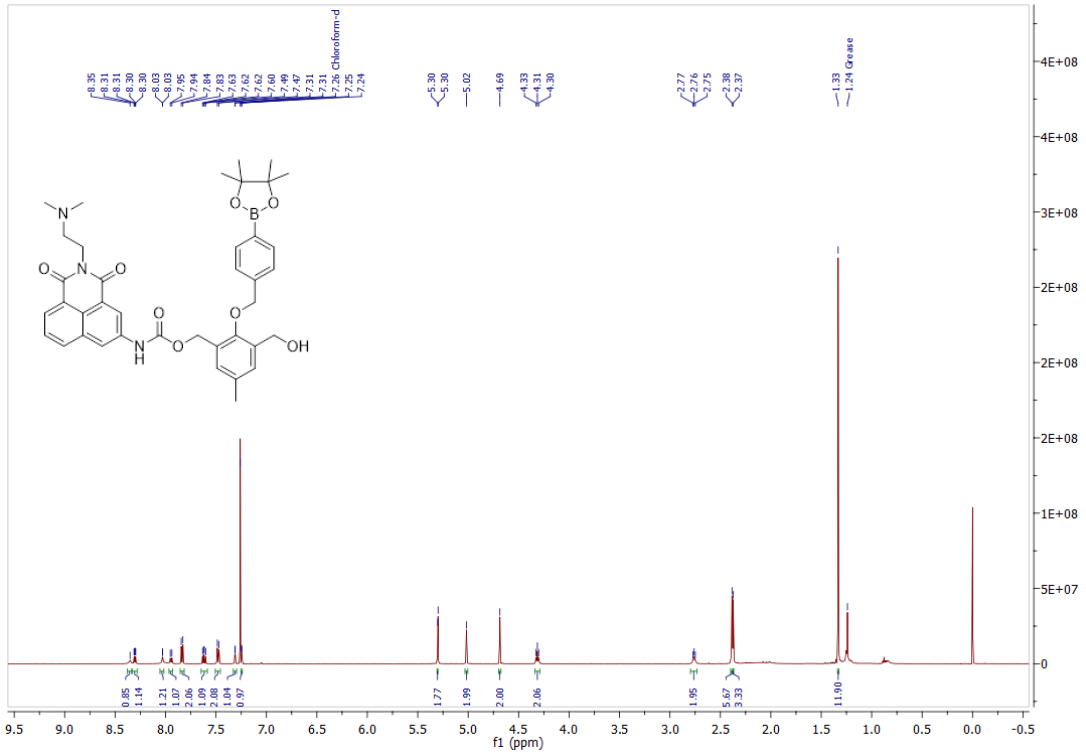

Figure S2.24: ^{1}H NMR spectrum of **2.13** in $CDCl_3$.

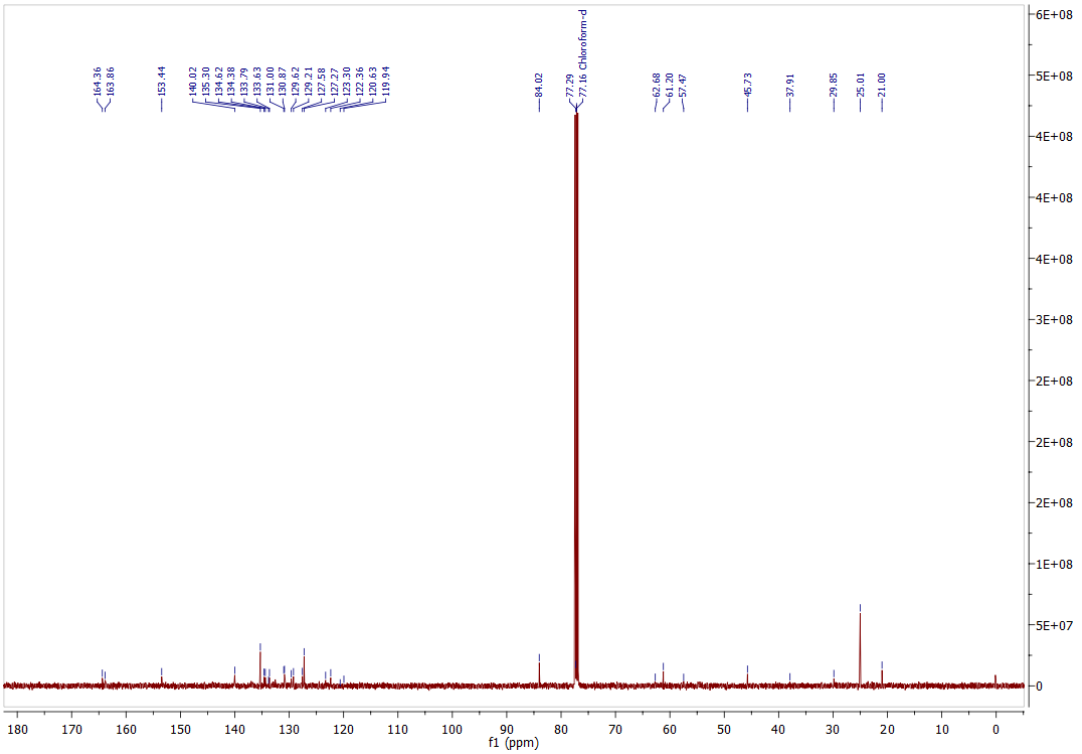

Figure S2.25: ^{13}C NMR spectrum of **2.13** in $CDCl_3$.

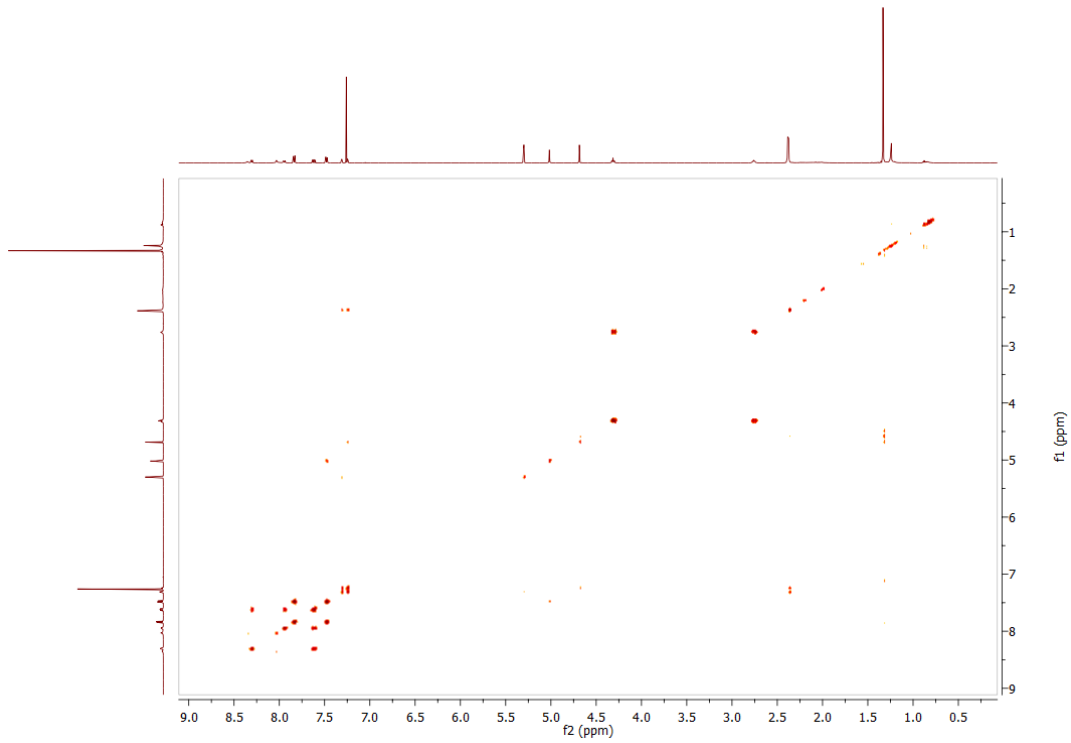

Figure S2.26: COSY spectrum of **2.13** in $CDCl_3$.

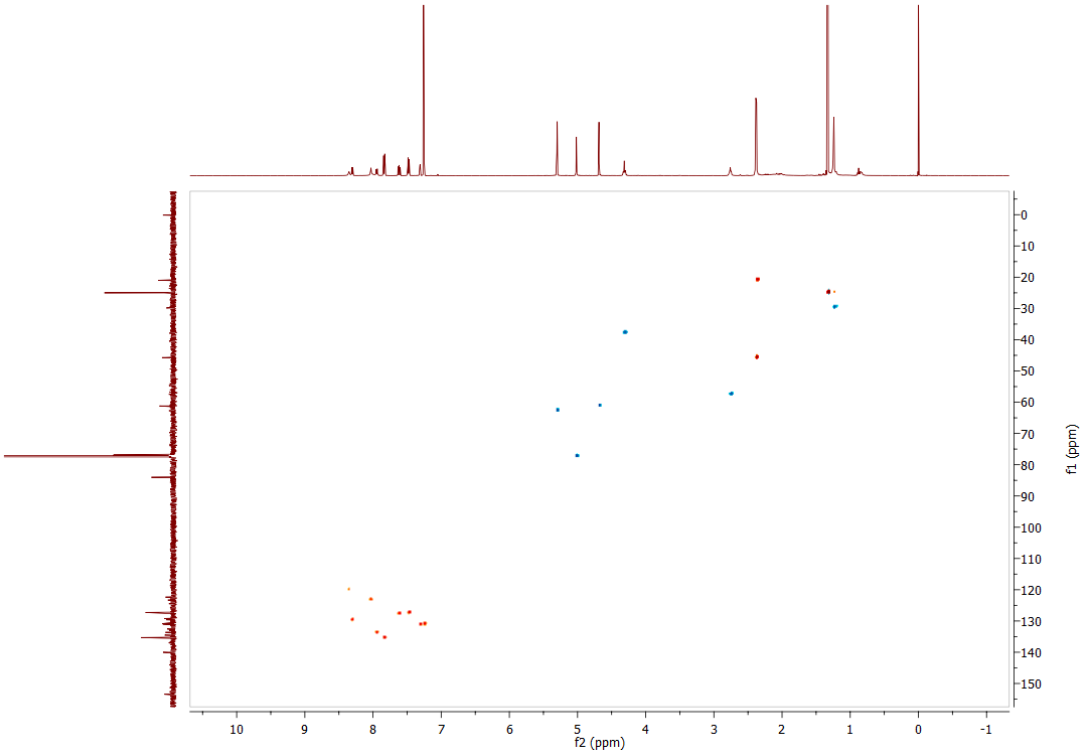

Figure S2.27: HSQC spectrum of **2.13** in $CDCl_3$.

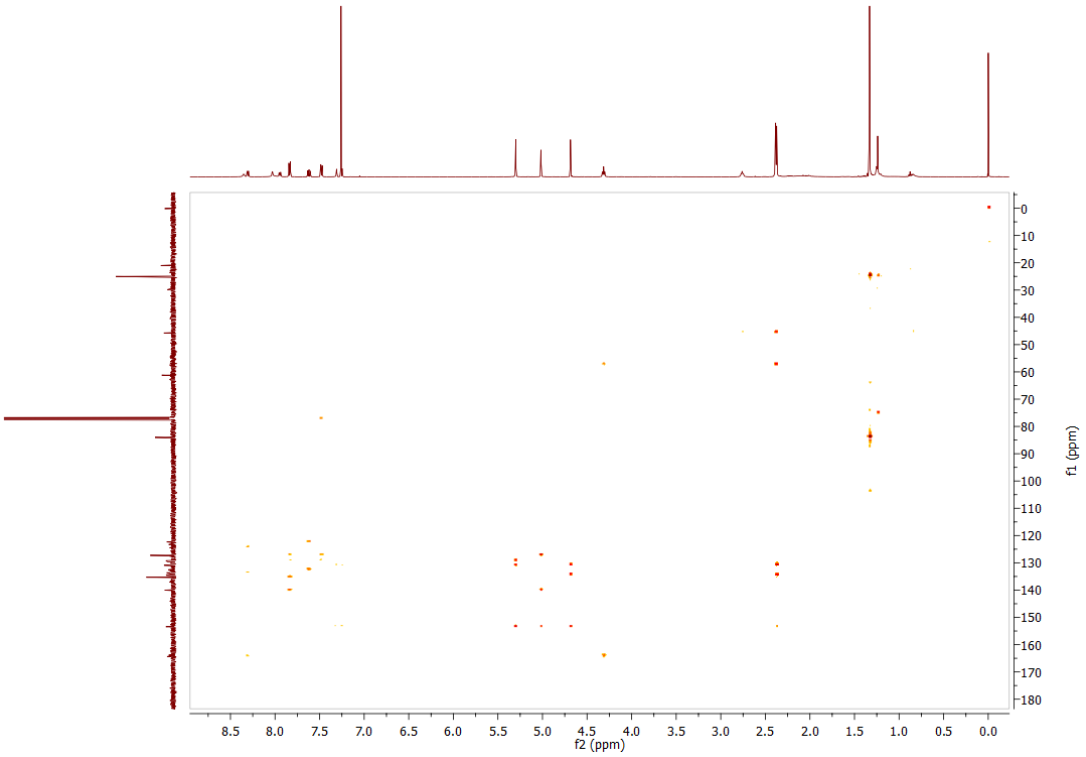

Figure S2.28: HMBC spectrum of **2.13** in $CDCl_3$.

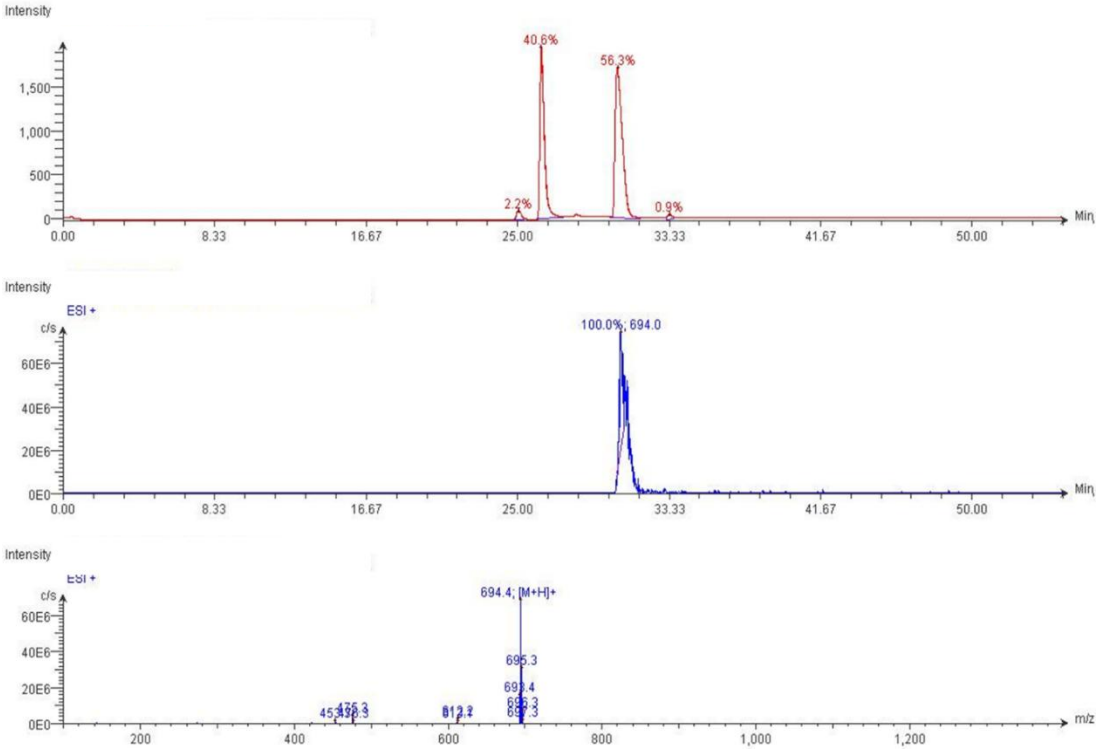

Figure S2.29: LC-MS data for **2.13.**

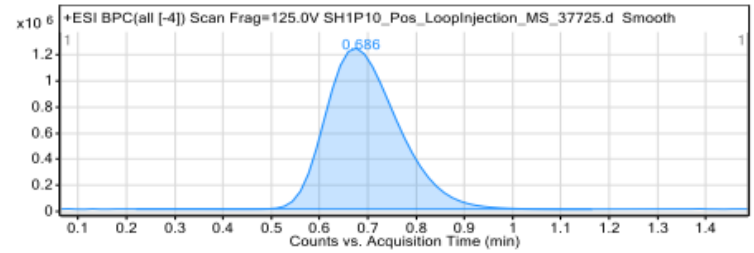

Figure 1: Base peak chromatogram

User Chromatogram Peak List

RT (min)	Area	Area %	Area Sum (%)	Base Peak (m/z)	Width (min)
0.69	12931335	100.00	100.00	694.3323	0.187

Compound Table

Compound Label	RT (min)	Observed mass (m/z)	Neutral observed mass (Da)	Theoretical mass (Da)	Mass error (ppm)	Isotope match score (%)	Error flag
Cpd 1: C40 H45 B N2 O8	0.69	716.3122	691.3255	691.3305	-7.22	5.06	low score
Cpd 2: C39 H44 B N3 O8	0.69	694.3322	692.3278	692.3258	2.95	98.46	

Mass errors of between -5.00 and 5.00 ppm with isotope match scores above 60% are considered confirmation of molecular formulae

Figure: Full range view of Compound spectra and potential adducts.

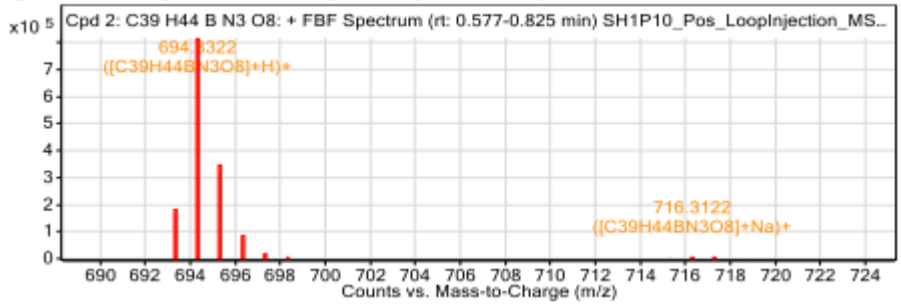

Figure S2.30: HRMS data for **2.13.**

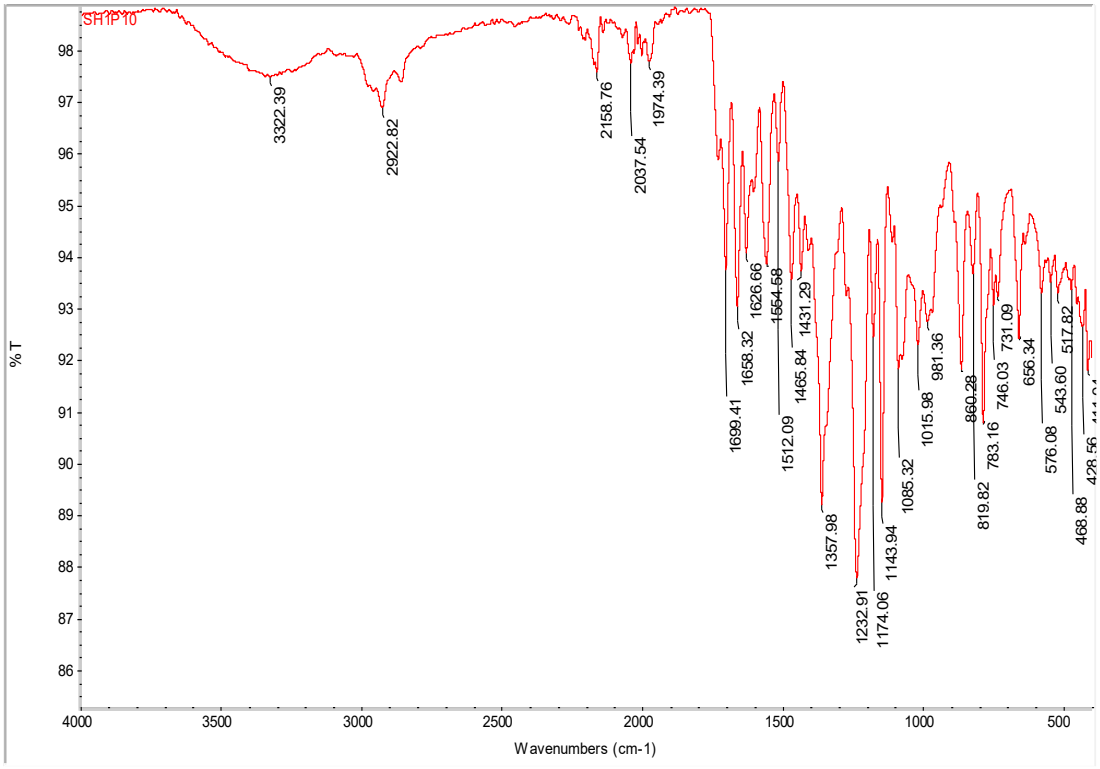

Figure S2.31: FTIR-ATR spectrum of **2.13.**

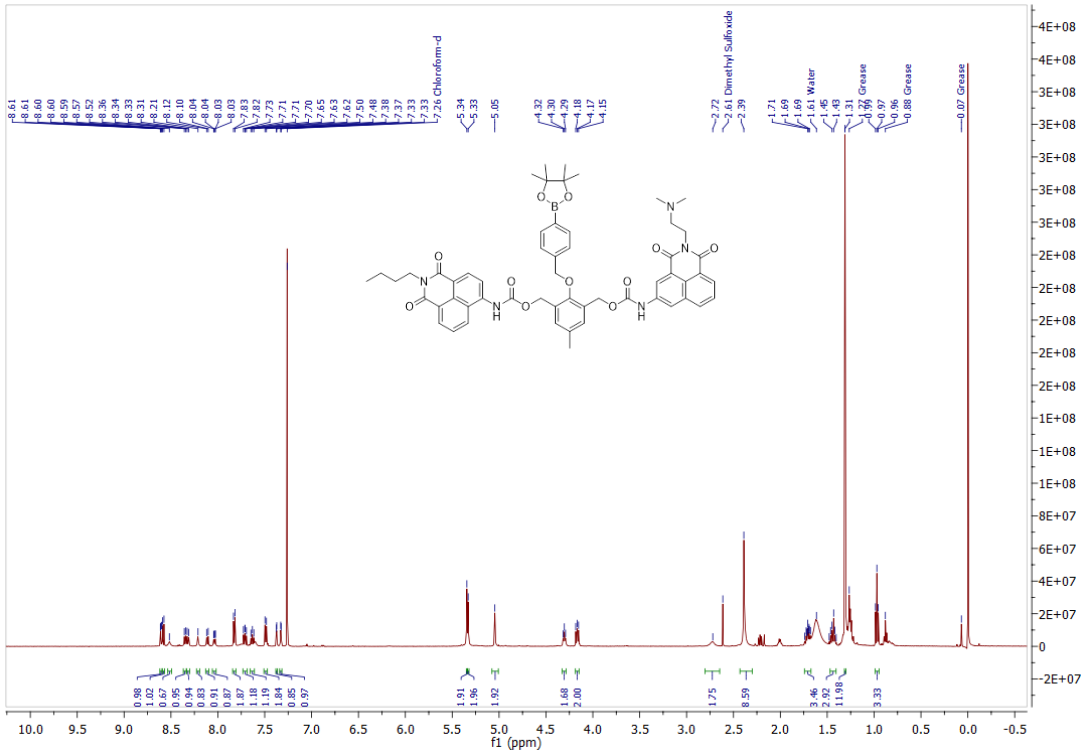

Figure S2.32: ^{1}H NMR spectrum of **2.4** in $CDCl_3$.

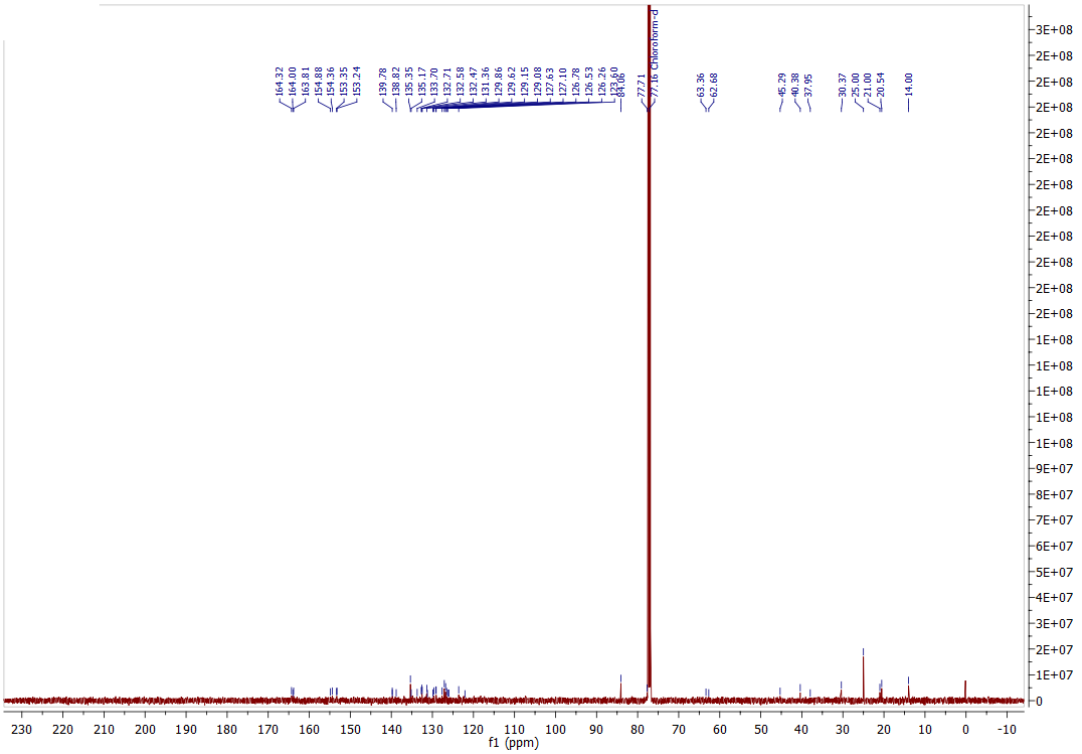

Figure S2.33: ^{13}C NMR spectrum of **2.4** in $CDCl_3$.

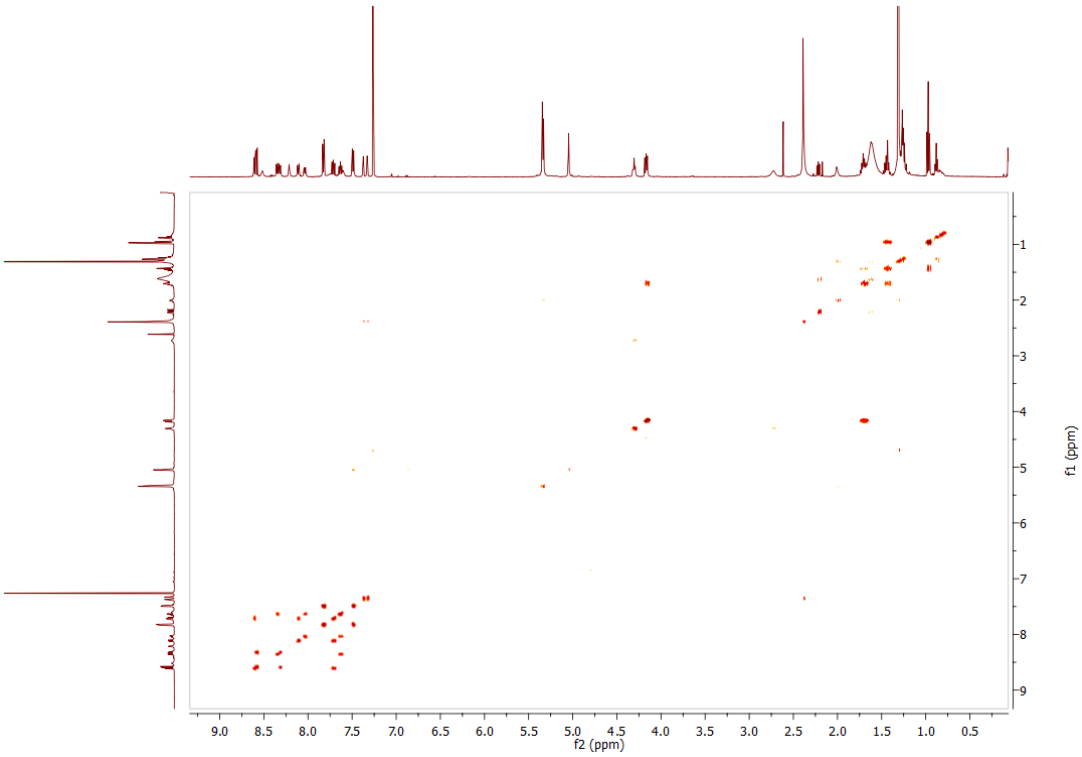

Figure S2.34: COSY NMR spectrum of **2.4** in $CDCl_3$.

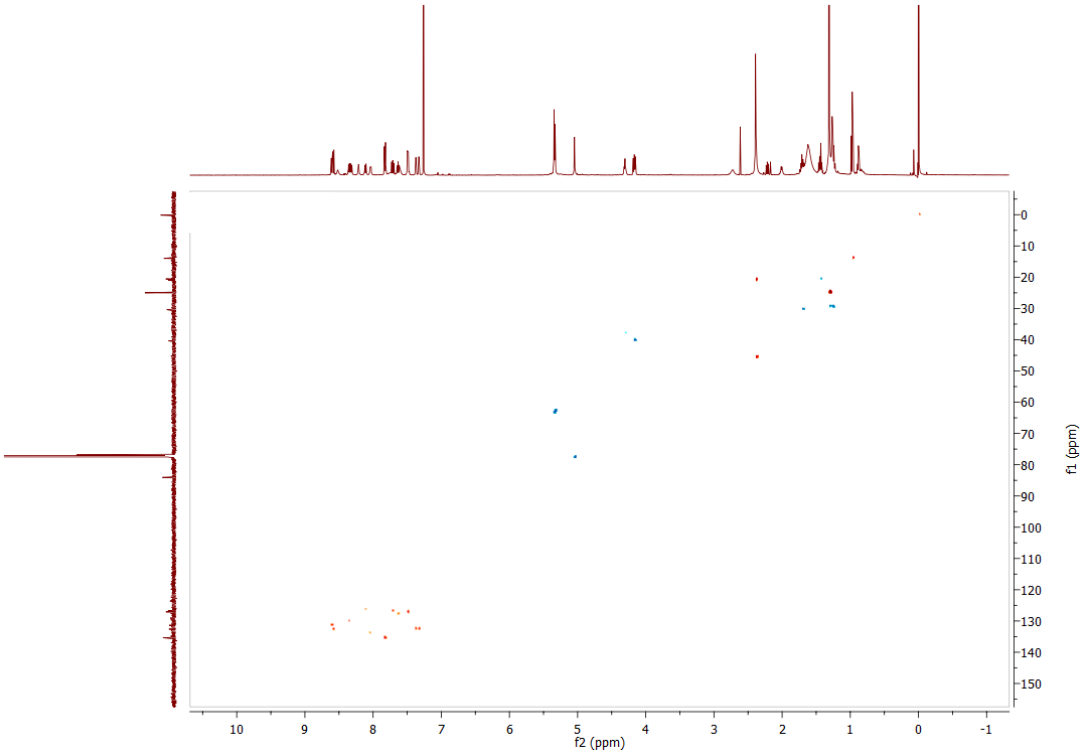

Figure S2.35: HSQC NMR spectrum of **2.4** in $CDCl_3$.

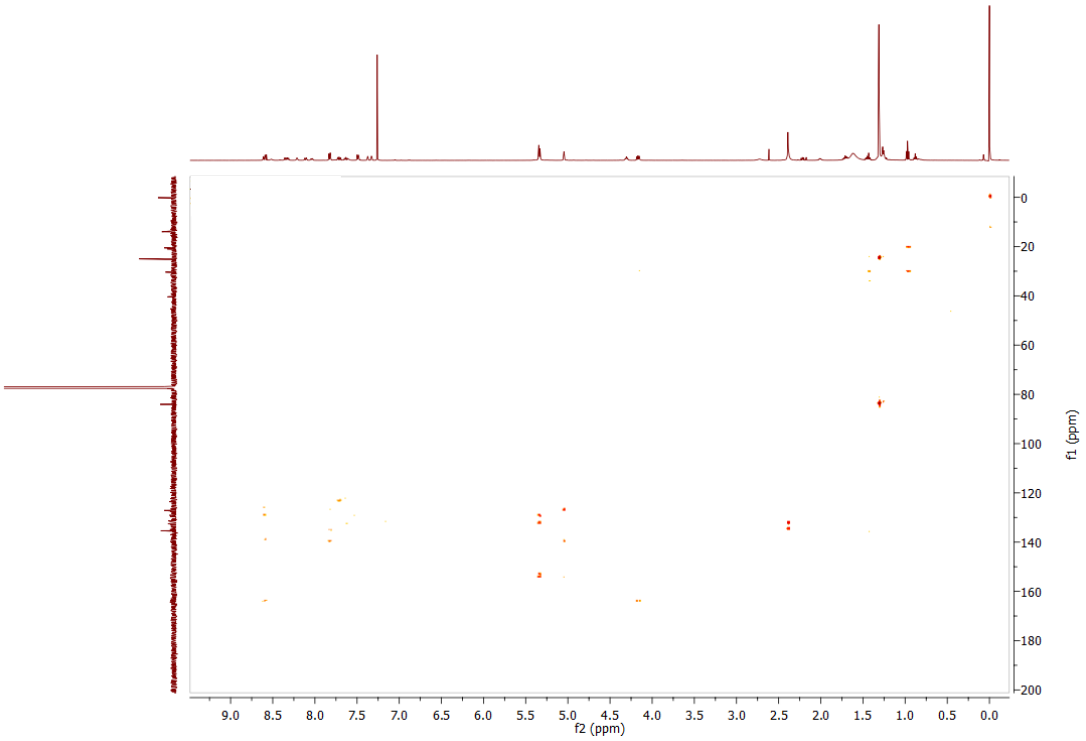

Figure S2.35: HMBC NMR spectrum of **2.4** in $CDCl_3$.

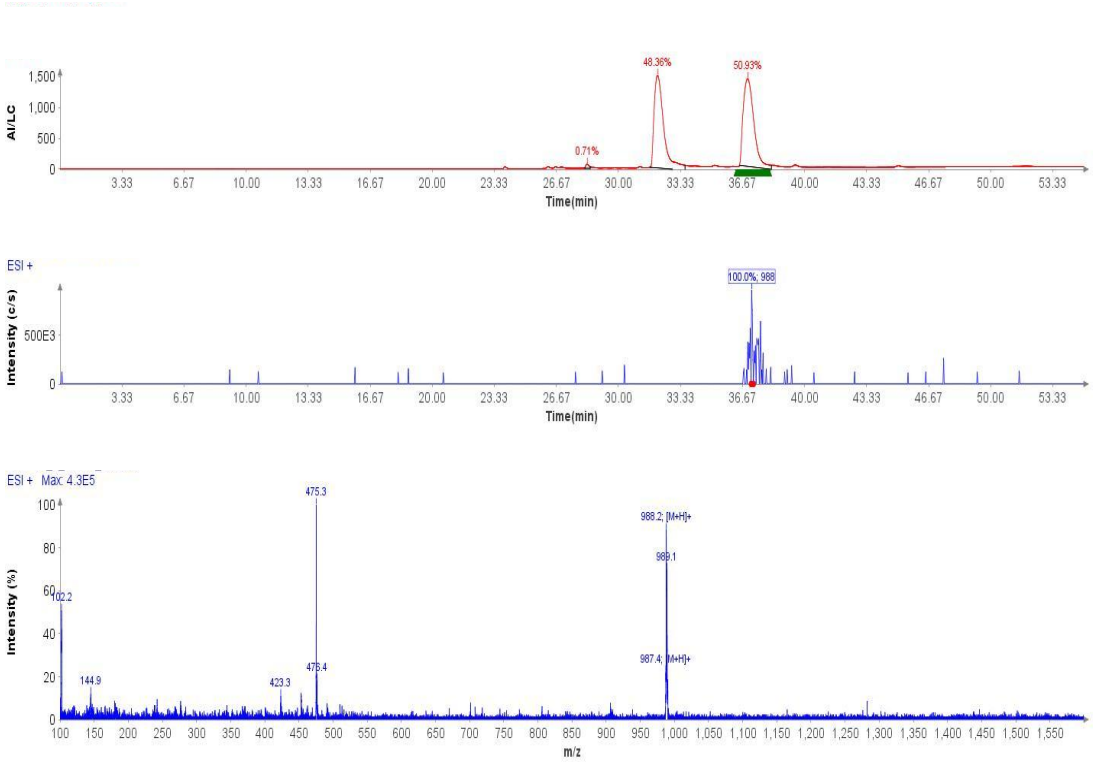

Figure S2.36: LC-MS data for **2.4.**

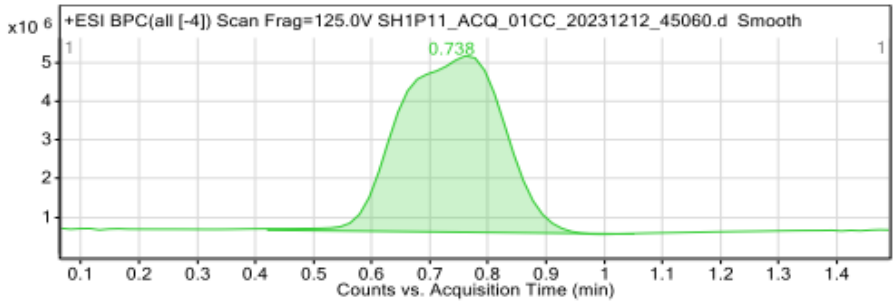

Figure 1: Base peak chromatogram

User Chromatogram Peak List

RT (min)	Area	Area %	Area Sum (%)	Base Peak (m/z)	Width (min)
0.74	58032661	100.00	100.00	144.9879	0.210

Compound Table

Compound Label	RT (min)	Observed mass (m/z)	Neutral observed mass (Da)	Theoretical mass (Da)	Mass error (ppm)	Isotope match score (%)
Cpd 1: C56 H58 B N5 O11	0.71	988.4313	986.4268	986.4262	0.62	99.80

Mass errors of between -5.00 and 5.00 ppm with isotope match scores above 60% are considered confirmation of molecular formulae

Figure: Full range view of Compound spectra and potential adducts.

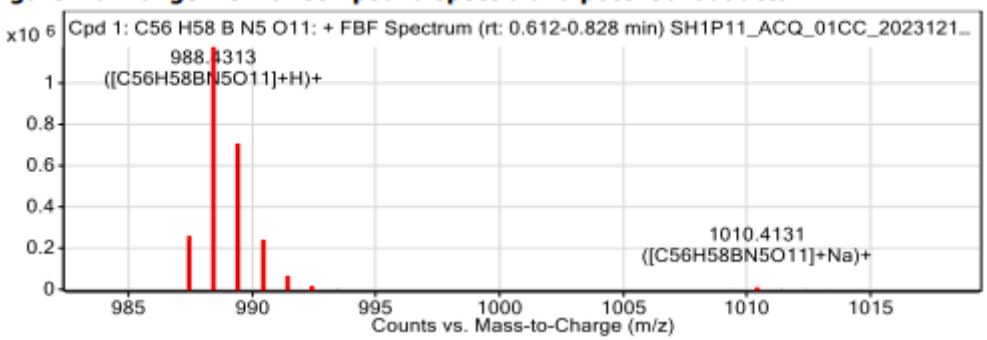

Figure S2.37: HRMS data for **2.4.**

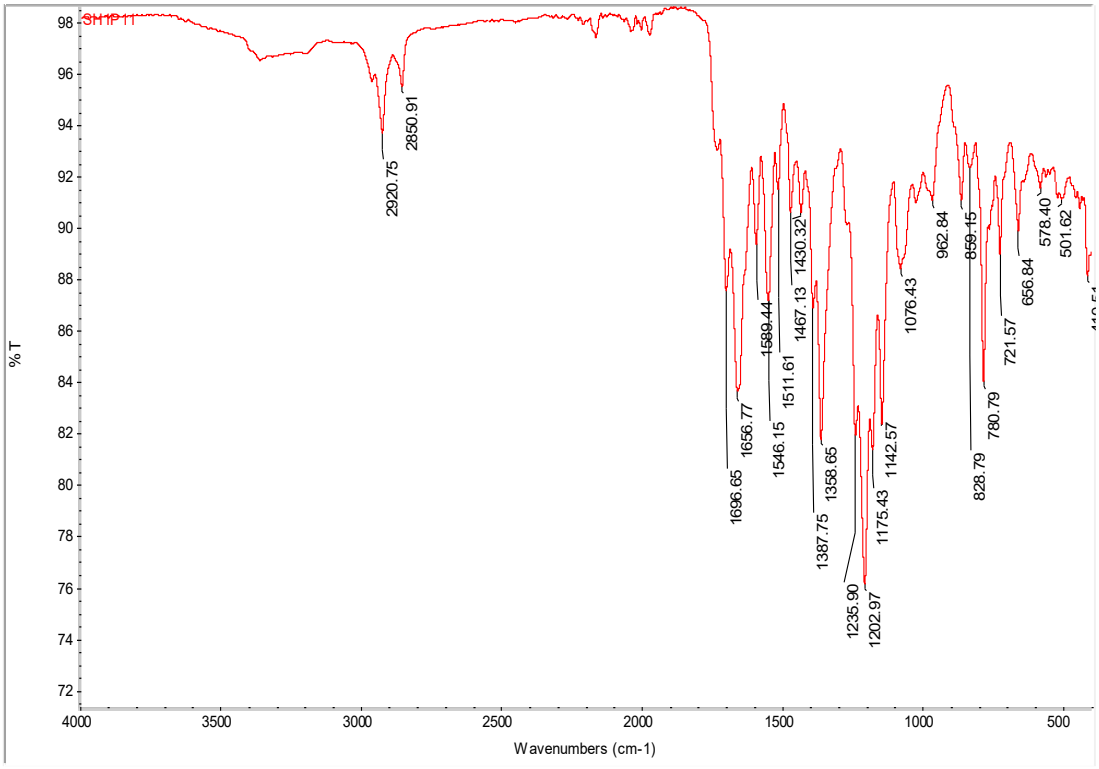

Figure S2.38: FTIR-ATR spectrum of **2.4.**

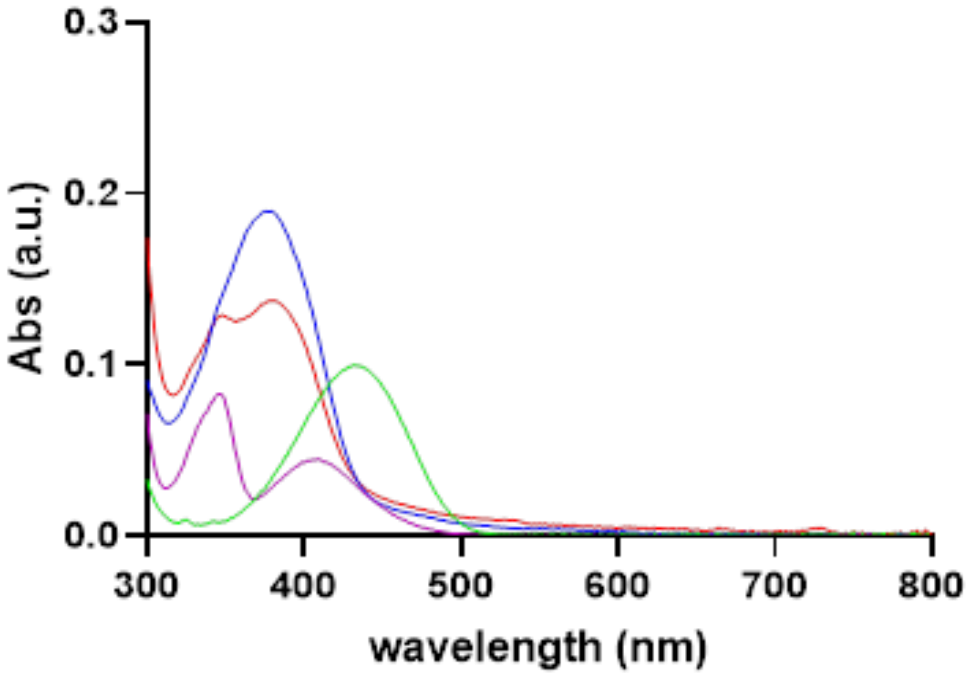

Figure S2.39: The UV/Vis spectra of **2.3** (blue), **2.4** (red), **2.8** (green) and **2.9** (purple) in 10 mM 50:50 DMSO:PBS at pH 7.4. Each concentration was 10 µM.

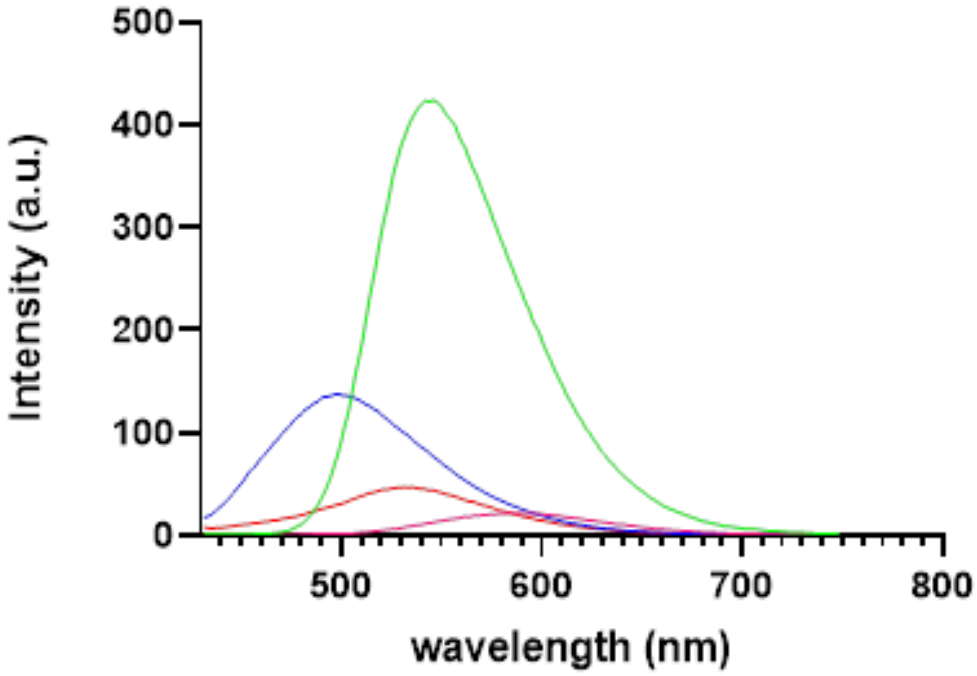

Figure S2.40: Fluorescence emission spectra of **2.3** (blue), **2.4** (red), **2.8** (green) and **2.9** (pink) in 50:50 DMSO:PBS 7.4. λ_{ex} = 420 nm. All concentrations were (10μM).

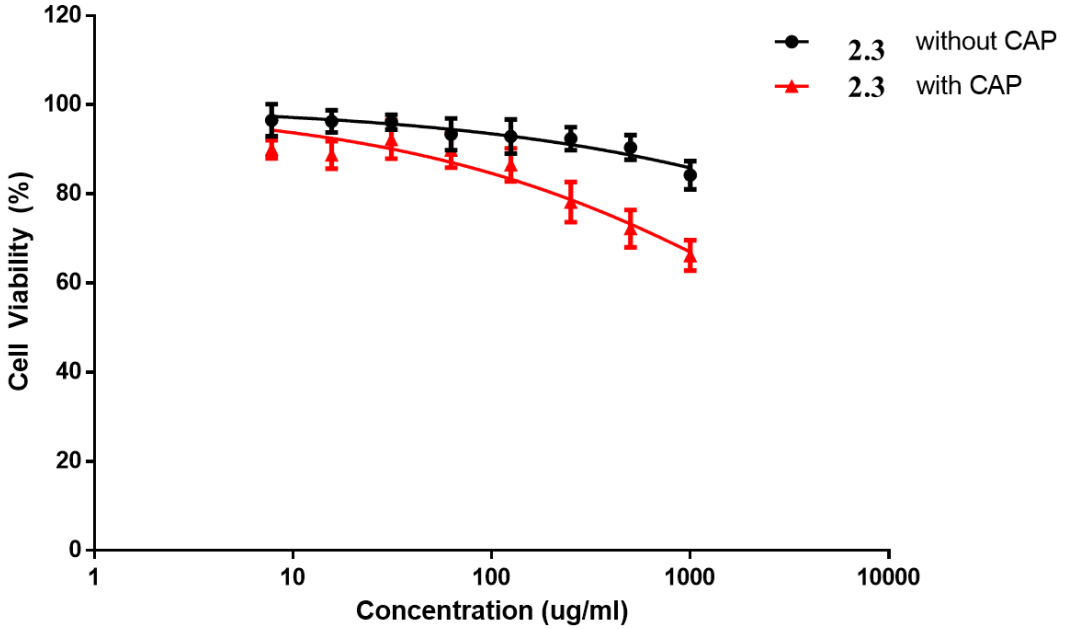

Figure S2.41: Cell viability of U-251 cells upon treatment with **2.3**, followed by 20 seconds of CAP treatment and 24 hours incubation.

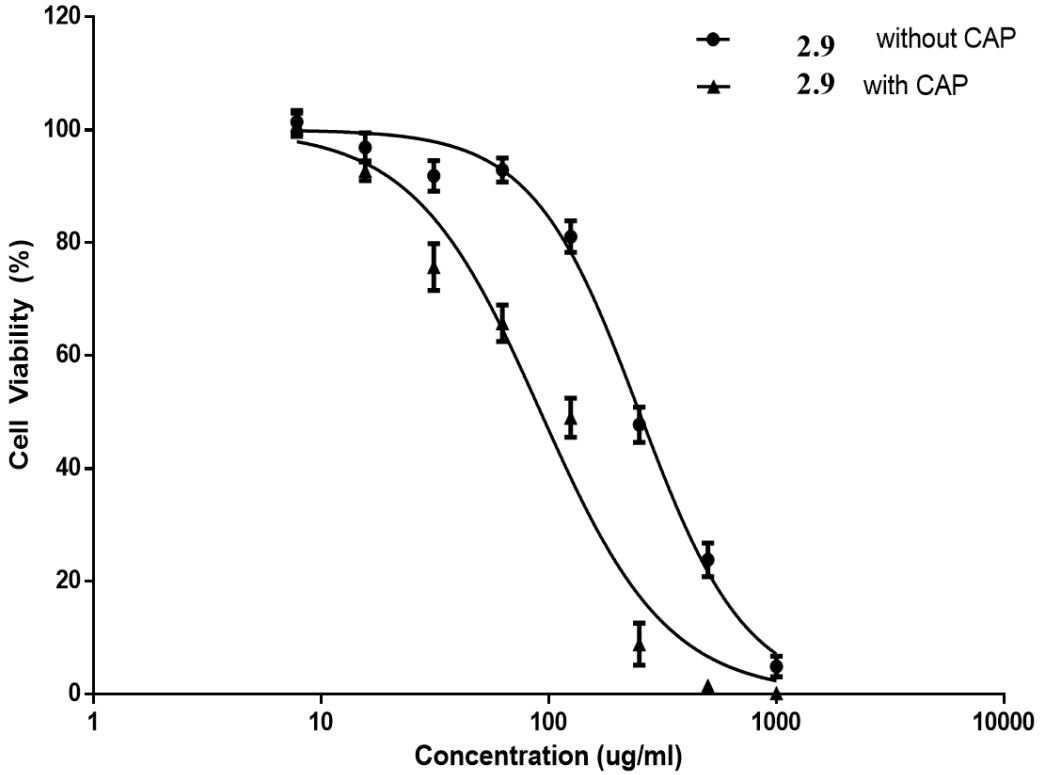

Figure S2.42: Cell viability of U-251 cells upon treatment with **2.9**, followed by 20 seconds of CAP treatment and 24 hours incubation.

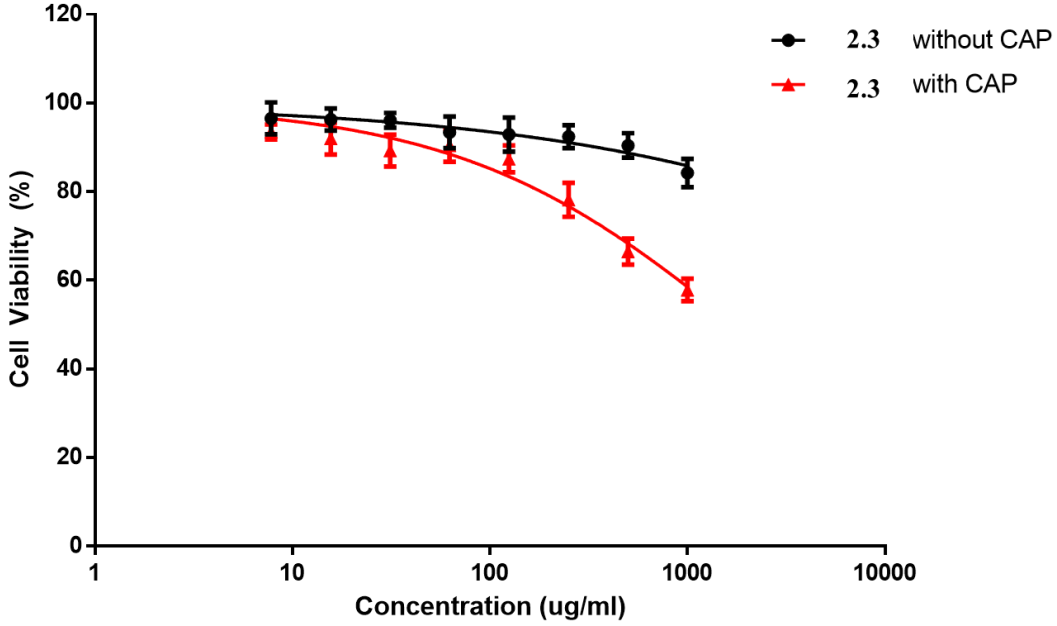

Figure S2.43: Cell viability of U-251 cells upon treatment with **2.3**, followed by 20 seconds of CAP treatment (x3) and 24 hours incubation.

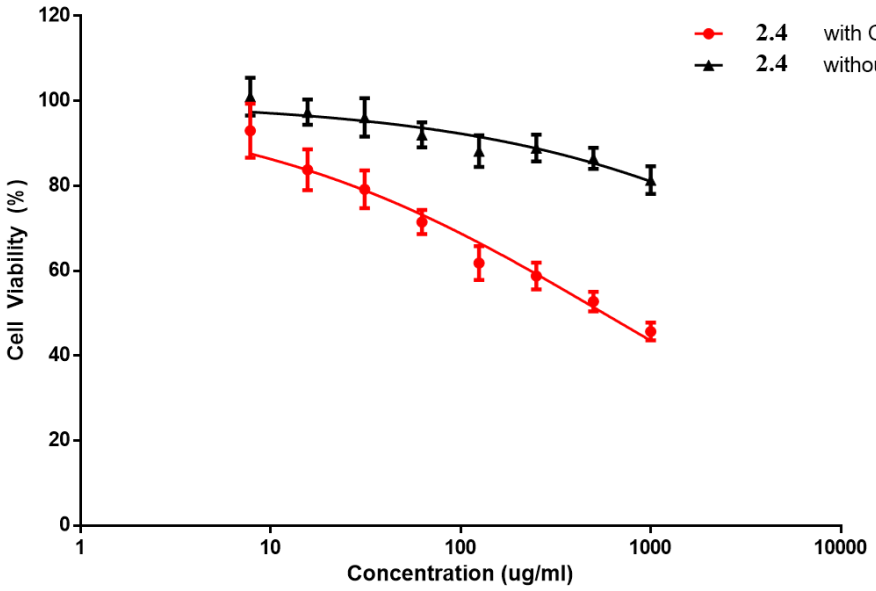

Figure S2.43: Cell viability of U-251 cells upon treatment with **2.4**, followed by 20 seconds of CAP treatment and 96 hours incubation.

Chapter 3 – Supplementary Characterisation Data

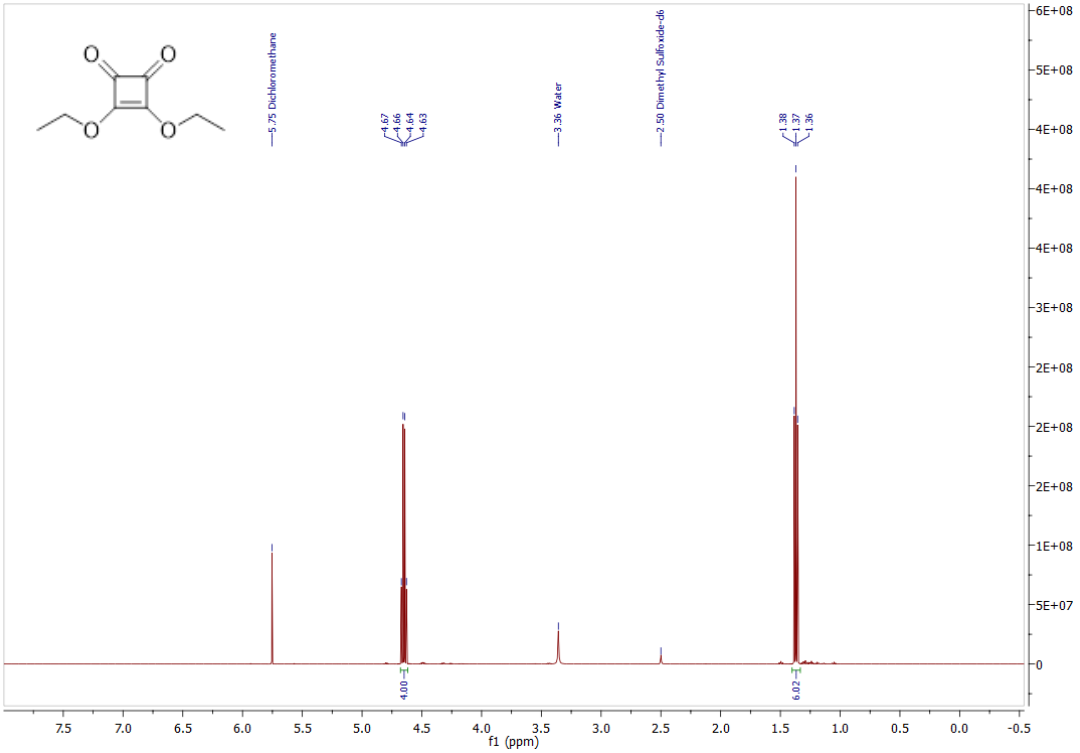

Figure S3.1: ^{1}H NMR spectrum of **3.4** in DMSO-d_6.

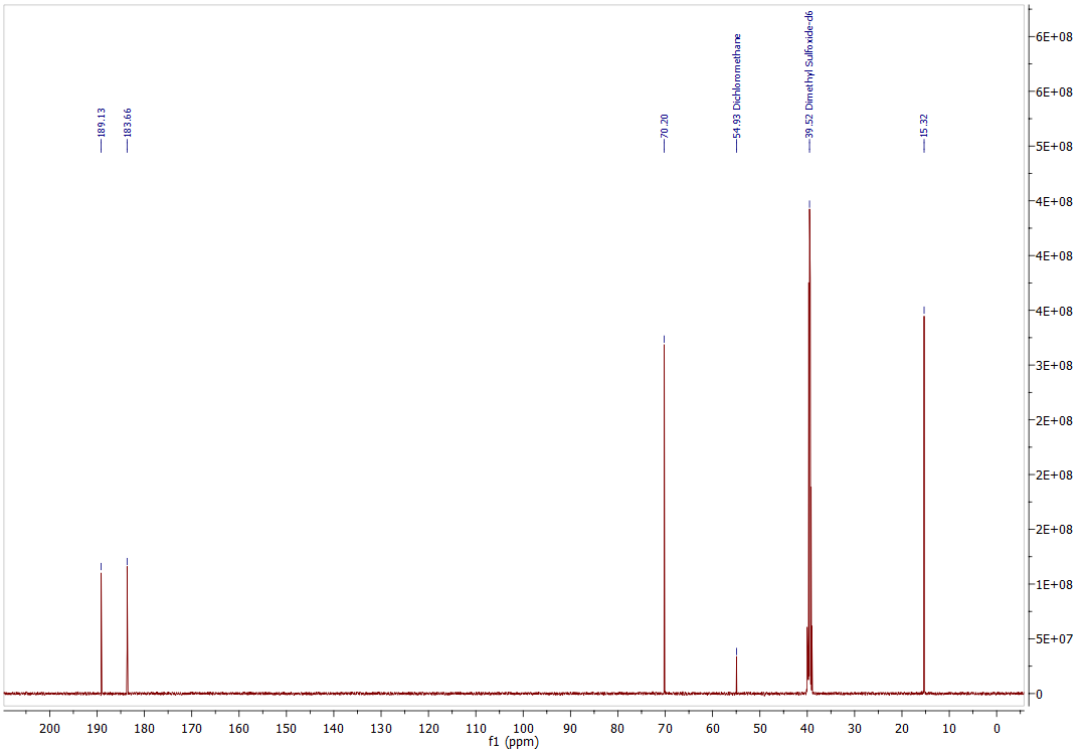

Figure S3.2: ^{13}C NMR spectrum of **3.4** in DMSO-d_6.

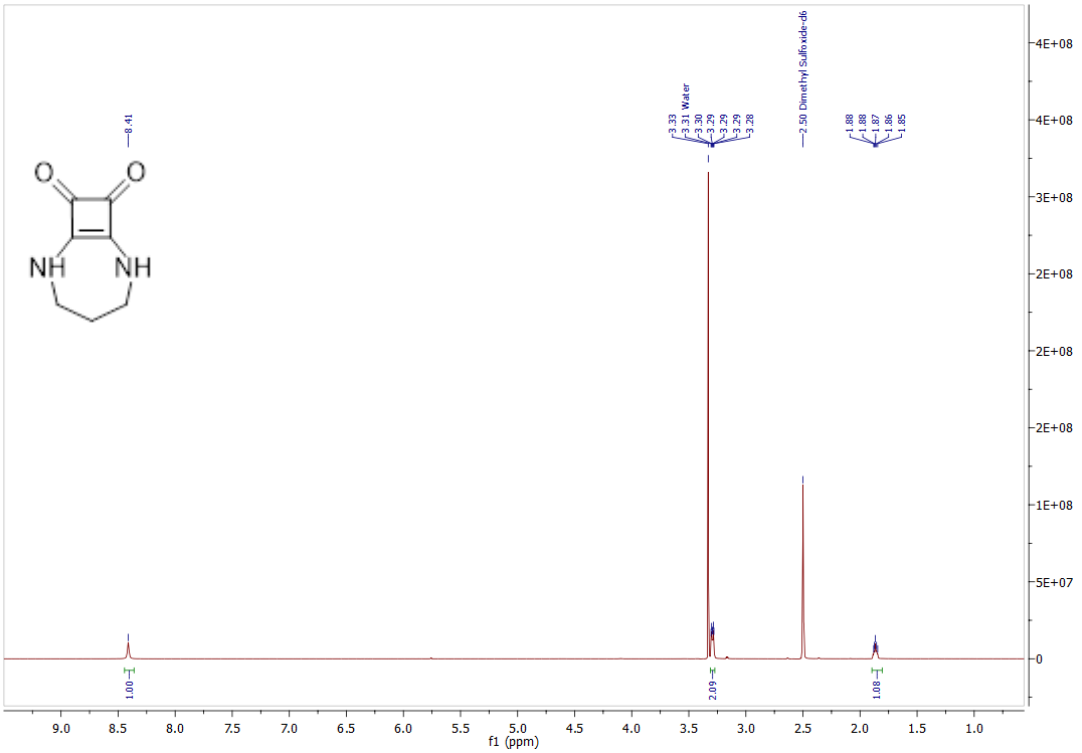

Figure S3.3: ^{1}H NMR spectrum of **3.5** in DMSO-d_6.

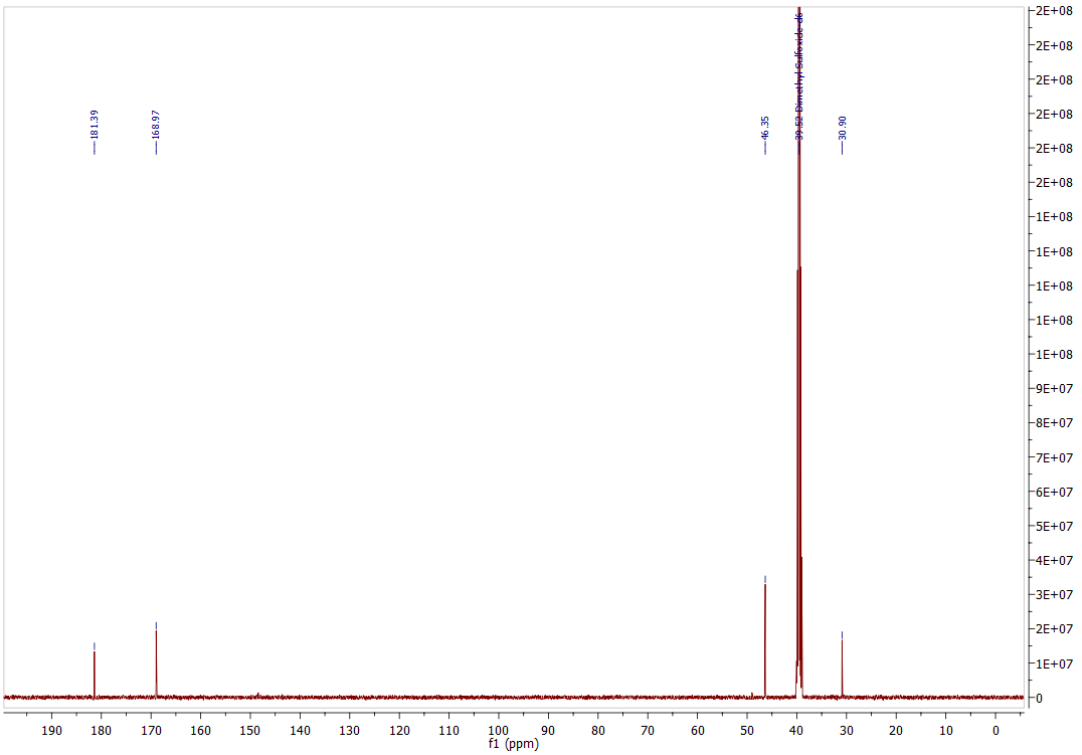

Figure S3.4: ^{13}C NMR spectrum of **3.5** in DMSO-d_6.

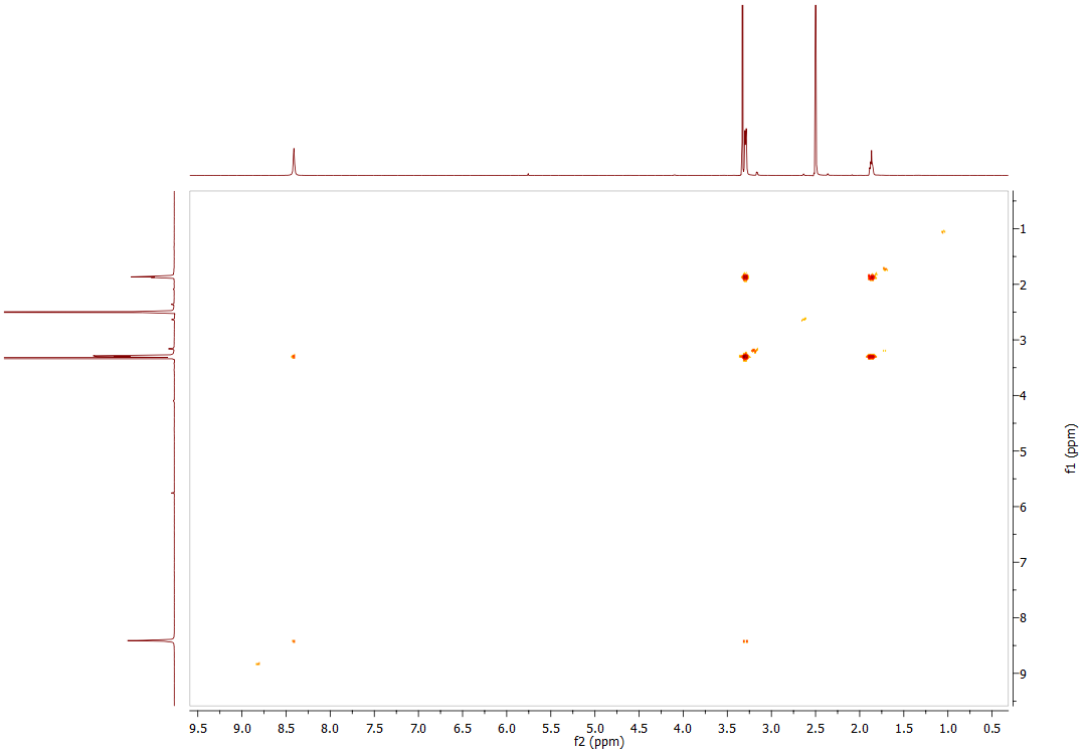

Figure S3.5: COSY spectrum of **3.5** in DMSO-d_6.

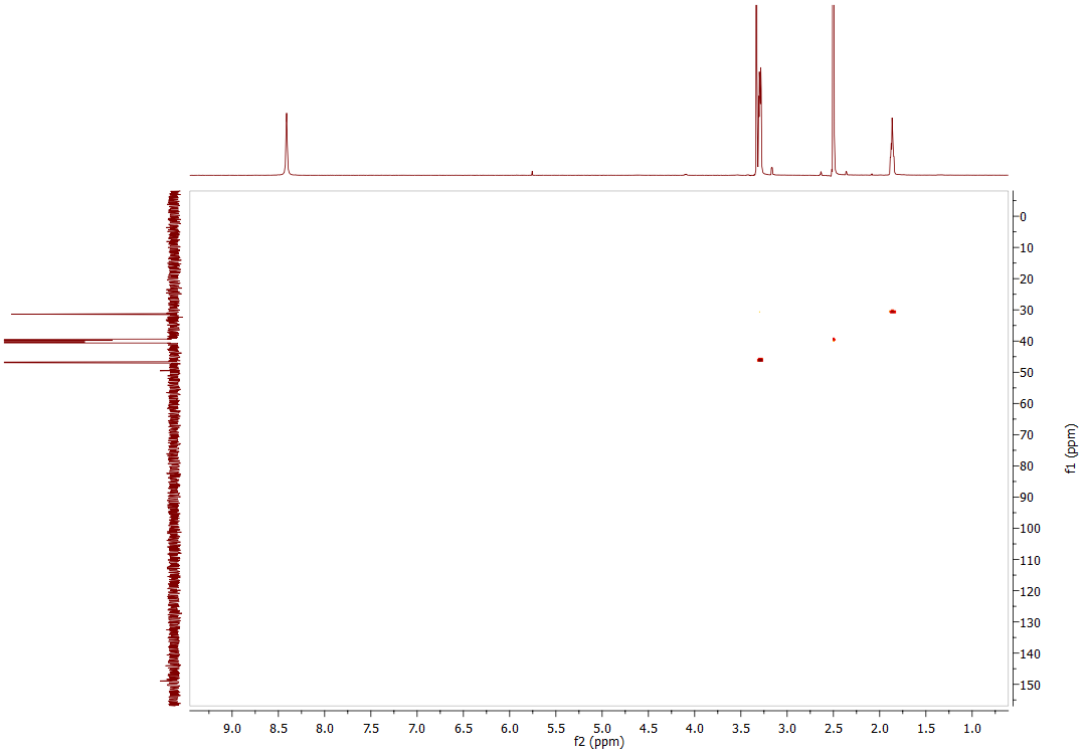

Figure S3.6: HSQC spectrum of **3.5** in DMSO-d_6.

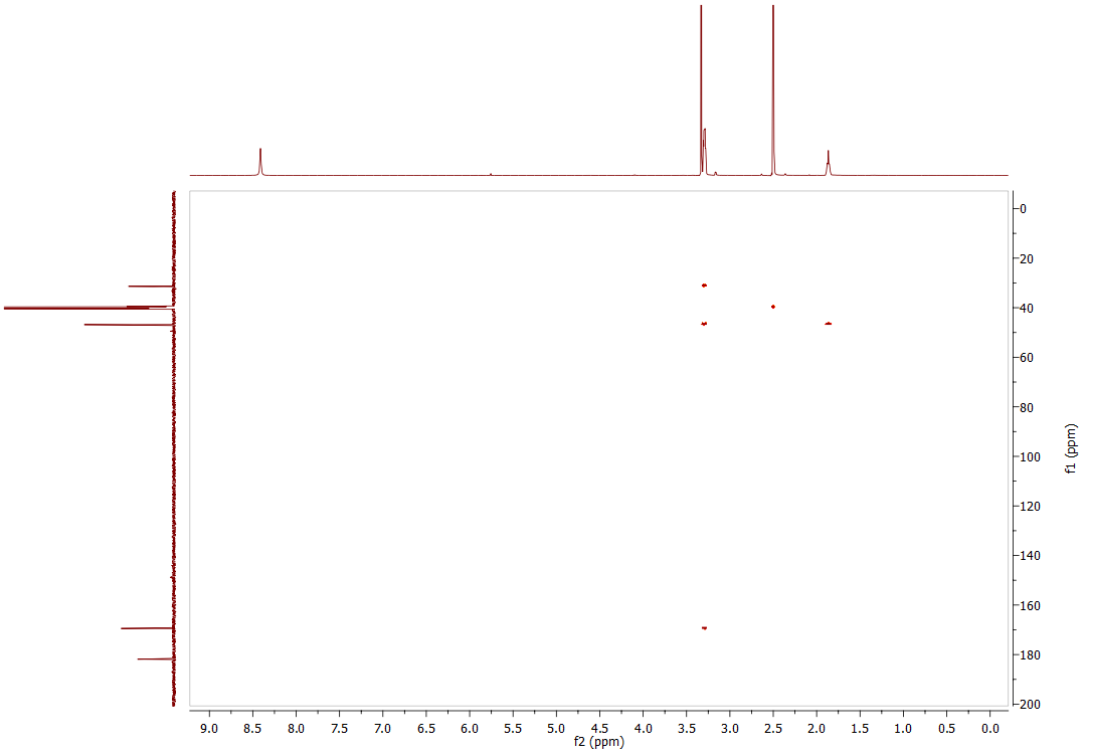

Figure S3.7: HMBC spectrum of **3.5** in DMSO-d_6.

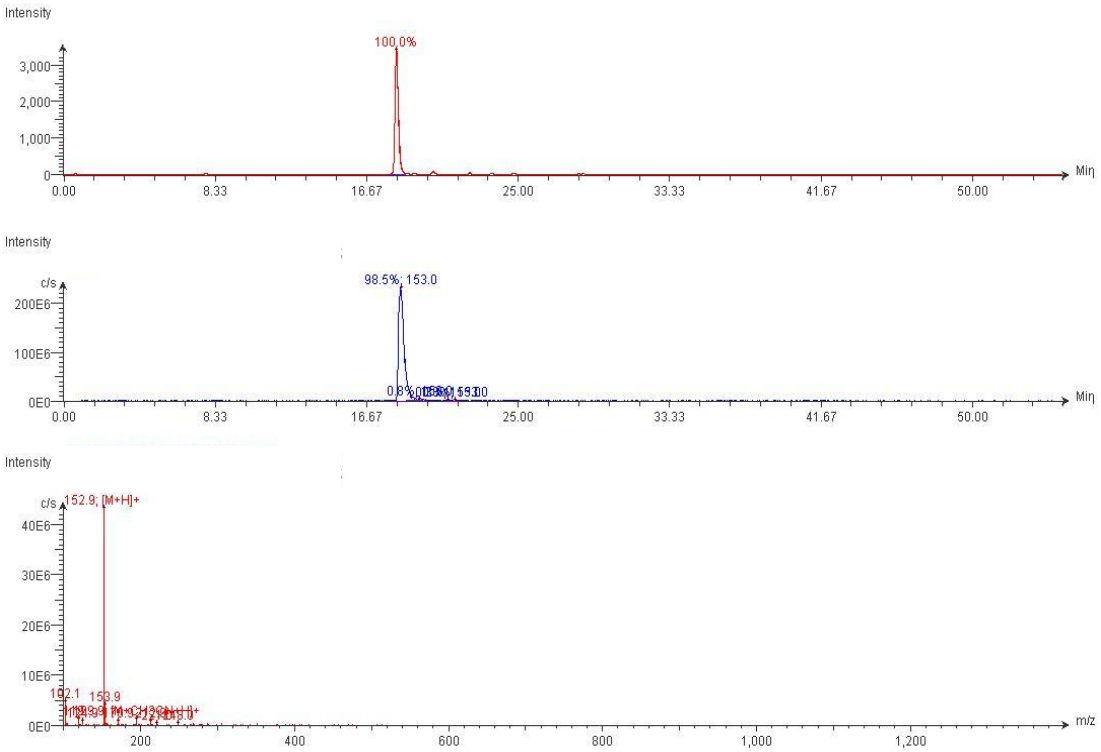

Figure S3.8: LC-MS data for **3.5.**

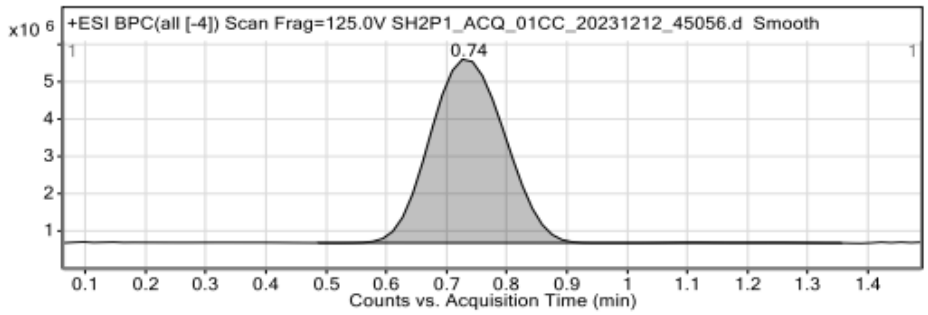

Figure 1: Base peak chromatogram

User Chromatogram Peak List

RT (min)	Area	Area %	Area Sum (%)	Base Peak (m/z)	Width (min)
0.74	42909960	100.00	100.00	175.0467	0.170

Compound Table

Compound Label	RT (min)	Observed mass (m/z)	Neutral observed mass (Da)	Theoretical mass (Da)	Mass error (ppm)	Isotope match score (%)
Cpd 1: C7 H8 N2 O2	0.74	175.0477	152.0585	152.0586	-0.41	98.51

Mass errors of between -5.00 and 5.00 ppm with isotope match scores above 60% are considered confirmation of molecular formulae

Figure: Full range view of Compound spectra and potential adducts.

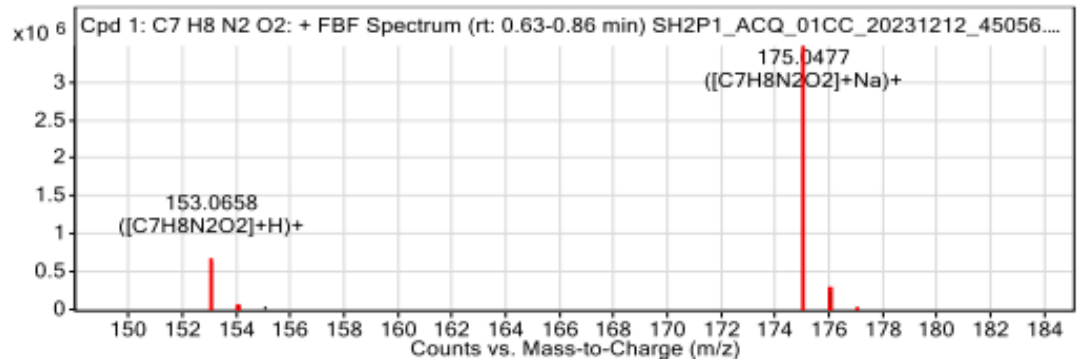

Figure S3.9: HRMS data for **3.5.**

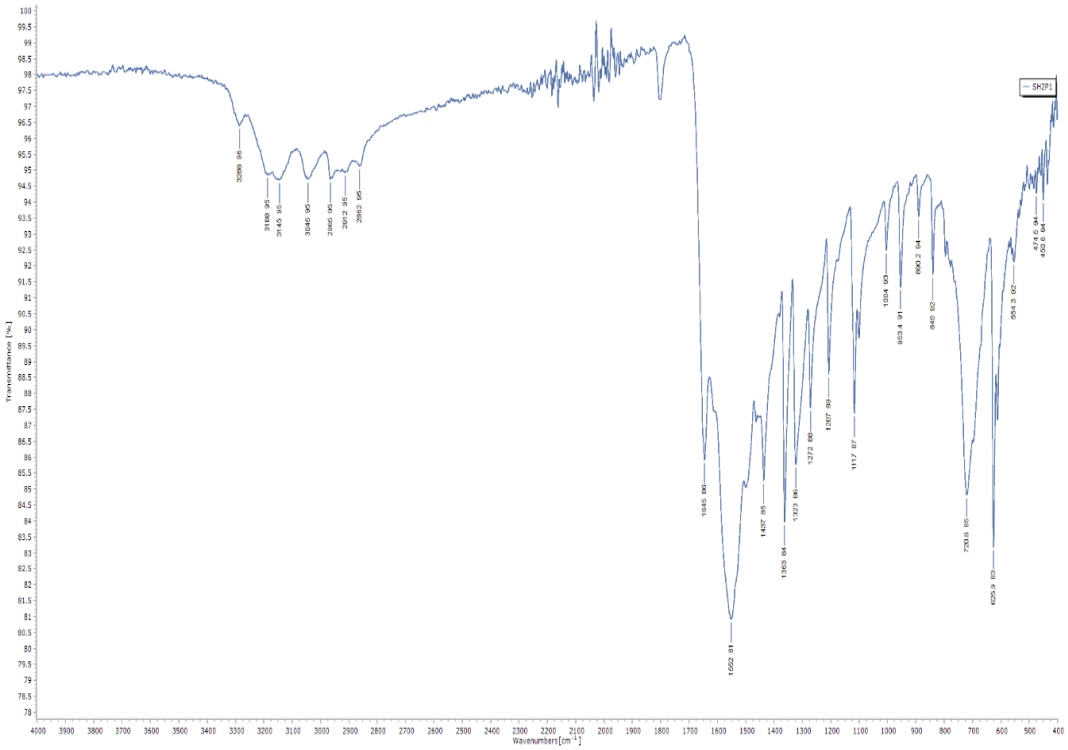

Figure S3.10: FTIR-ATR spectrum of **3.5.**

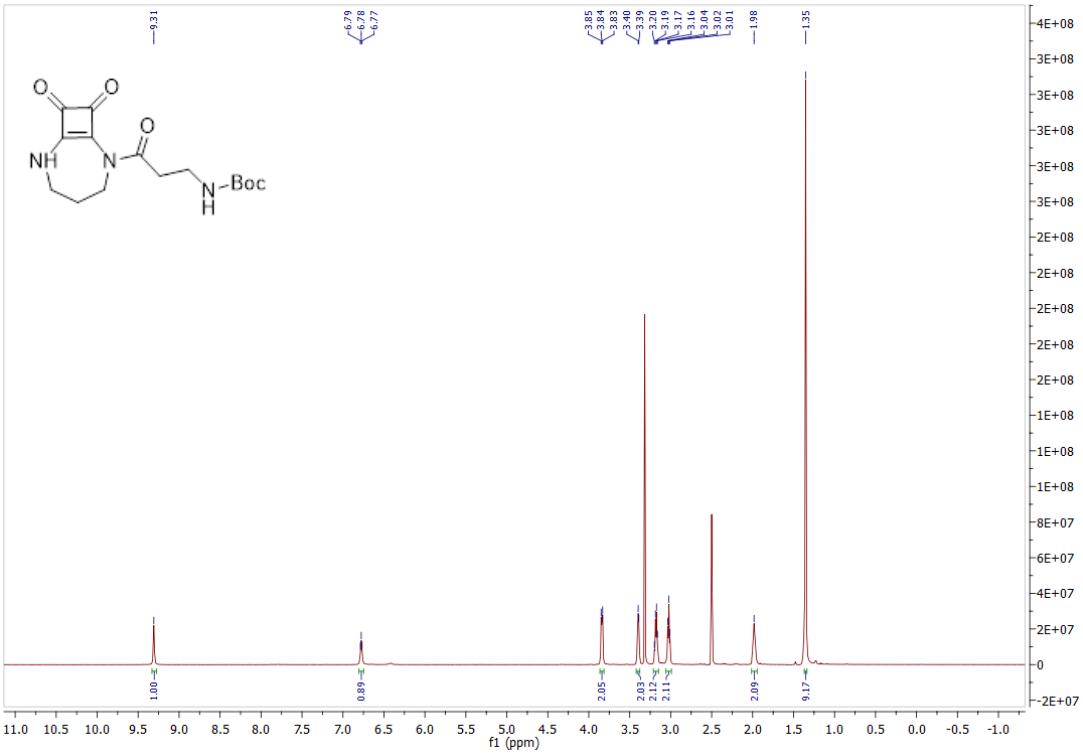

Figure S3.11: ^{1}H NMR spectrum of **3.7** in DMSO-d_6.

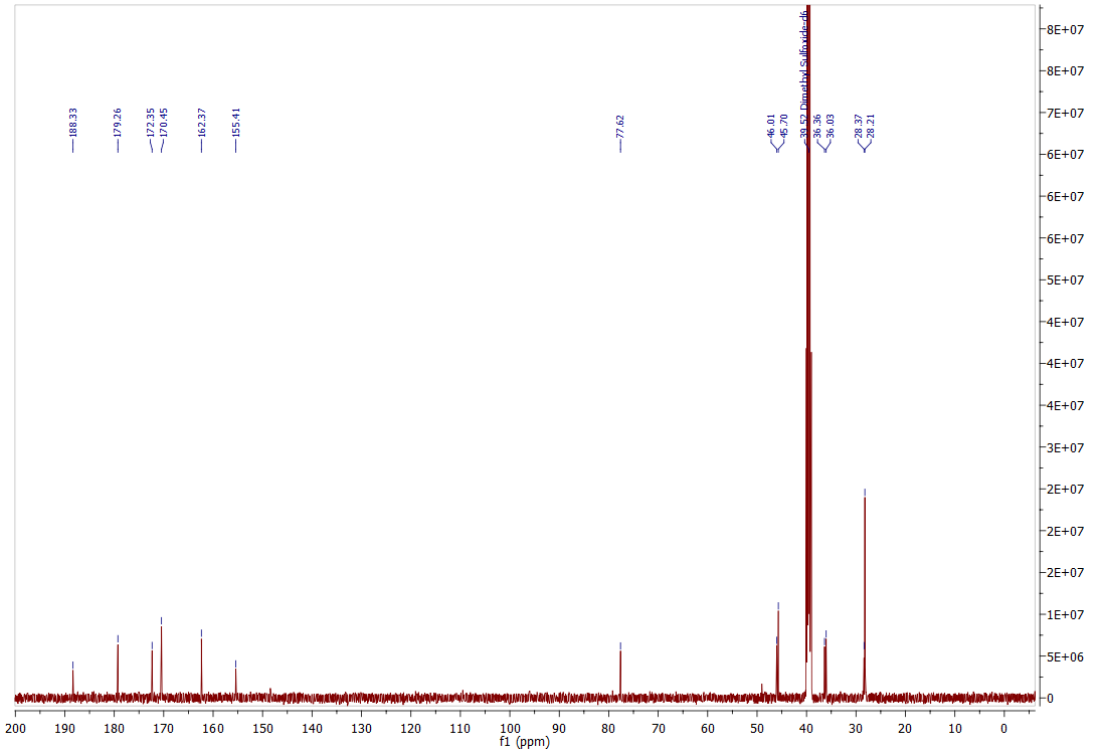

Figure S3.12: ^{13}C NMR spectrum of **3.7** in DMSO-d_6.

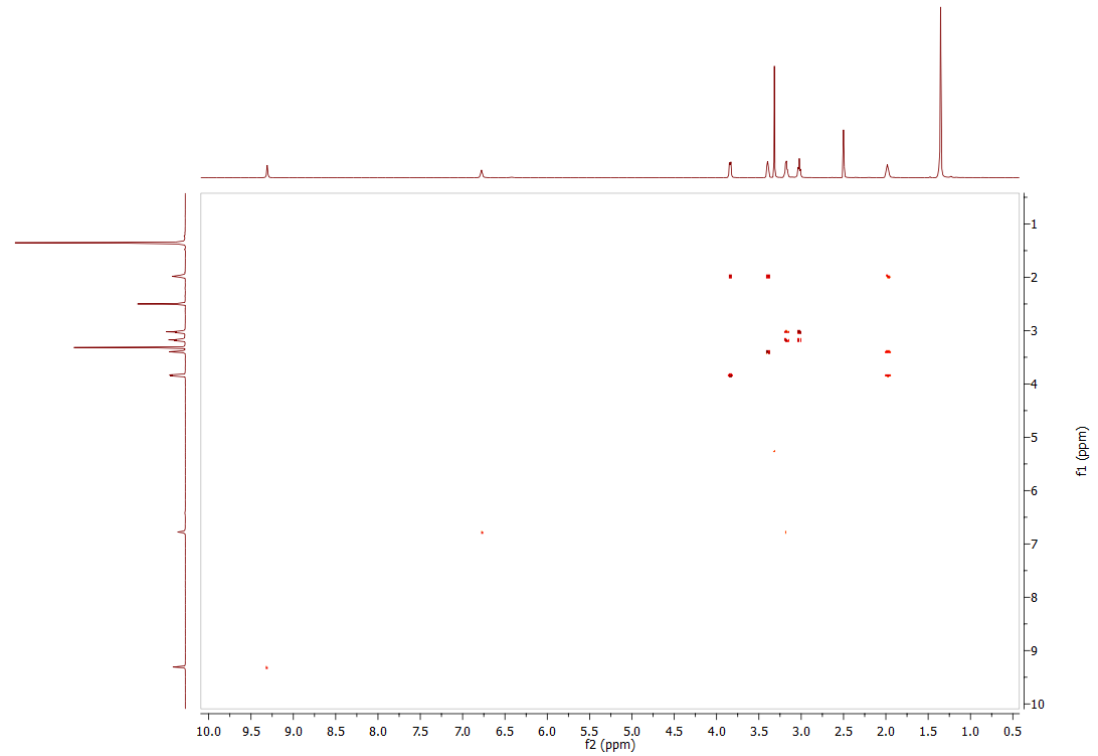

Figure S3.13: COSY spectrum of **3.7** in DMSO-d_6.

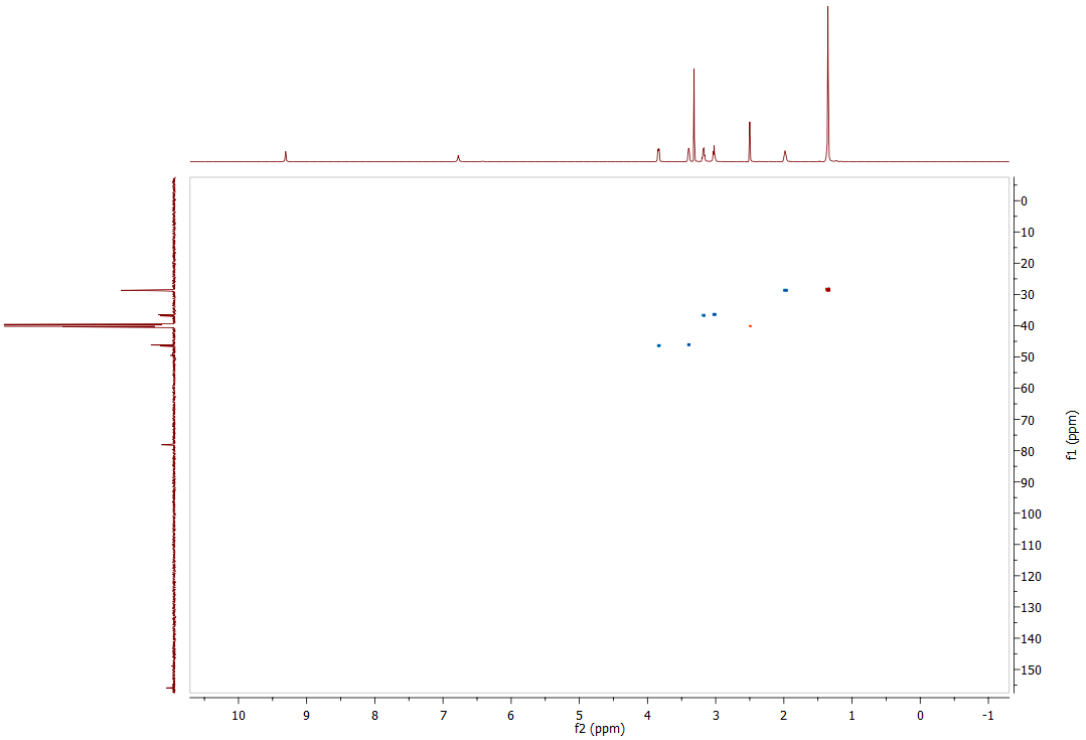

Figure S3.14: HSQC spectrum of **3.7** in DMSO-d_6.

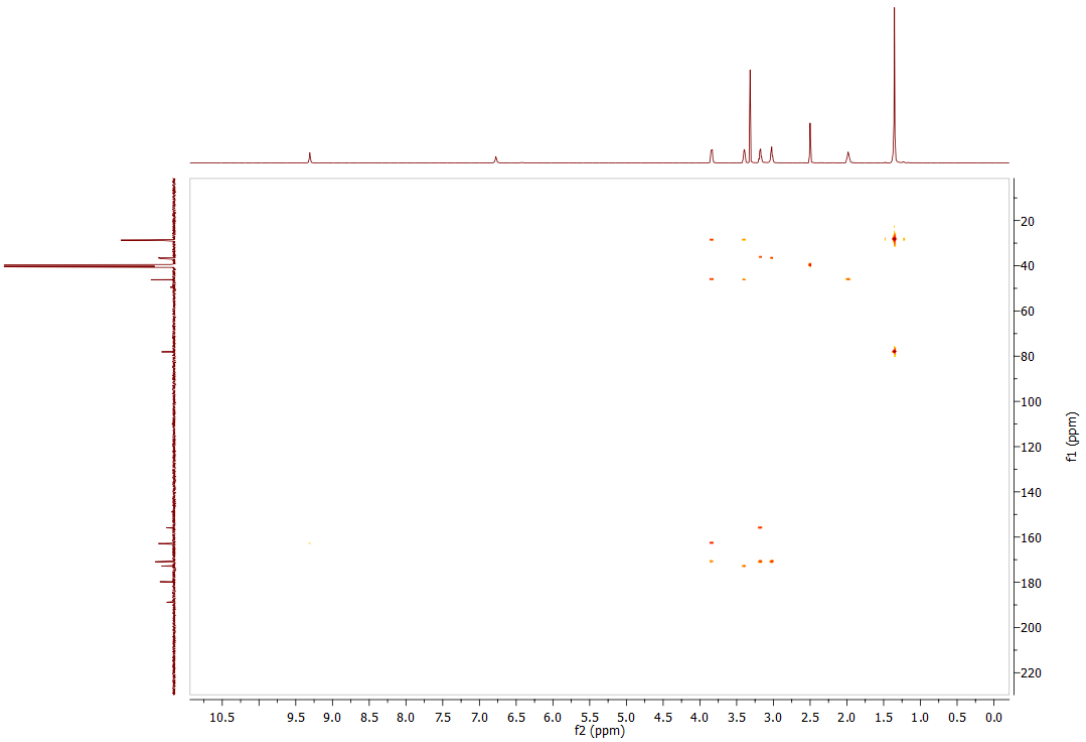

Figure S3.15: HMBC spectrum of **3.7** in DMSO-d_6.

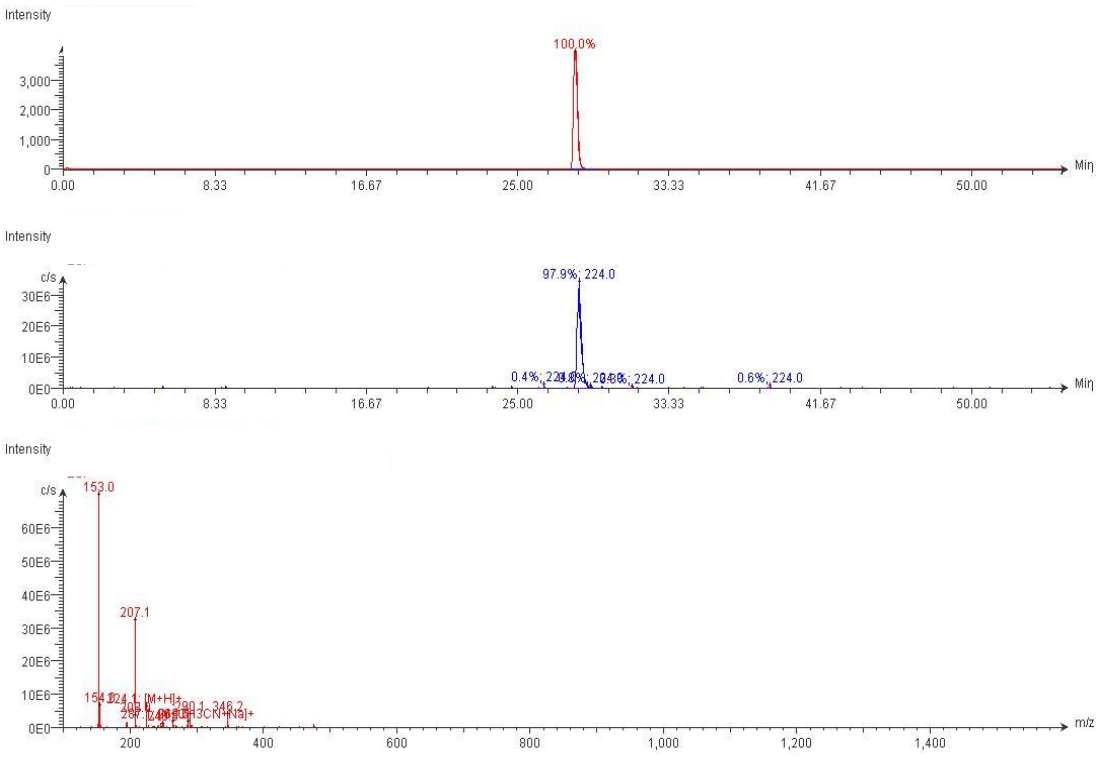

Figure S3.16: LC-MS data for **3.7.**

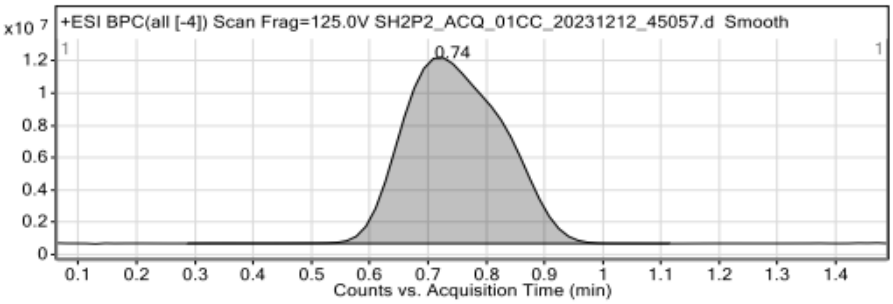

Figure 1: Base peak chromatogram

User Chromatogram Peak List

RT (min)	Area	Area %	Area Sum (%)	Base Peak (m/z)	Width (min)
0.74	142879142	100.00	100.00	346.1369	0.210

Compound Table

Compound Label	RT (min)	Observed mass (m/z)	Neutral observed mass (Da)	Theoretical mass (Da)	Mass error (ppm)	Isotope match score (%)
Cpd 1: C15 H21 N3 O5	0.74	346.1372	323.1480	323.1481	-0.33	99.64

Mass errors of between -5.00 and 5.00 ppm with isotope match scores above 60% are considered confirmation of molecular formulae

Figure: Full range view of Compound spectra and potential adducts.

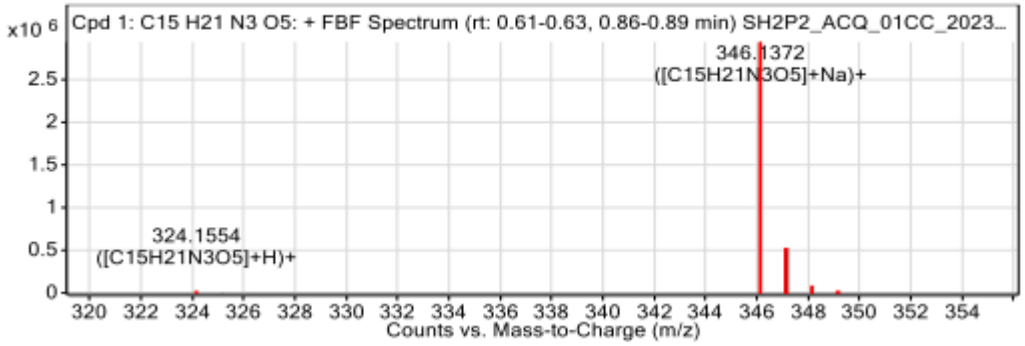

Figure S3.17: HRMS data for **3.7.**

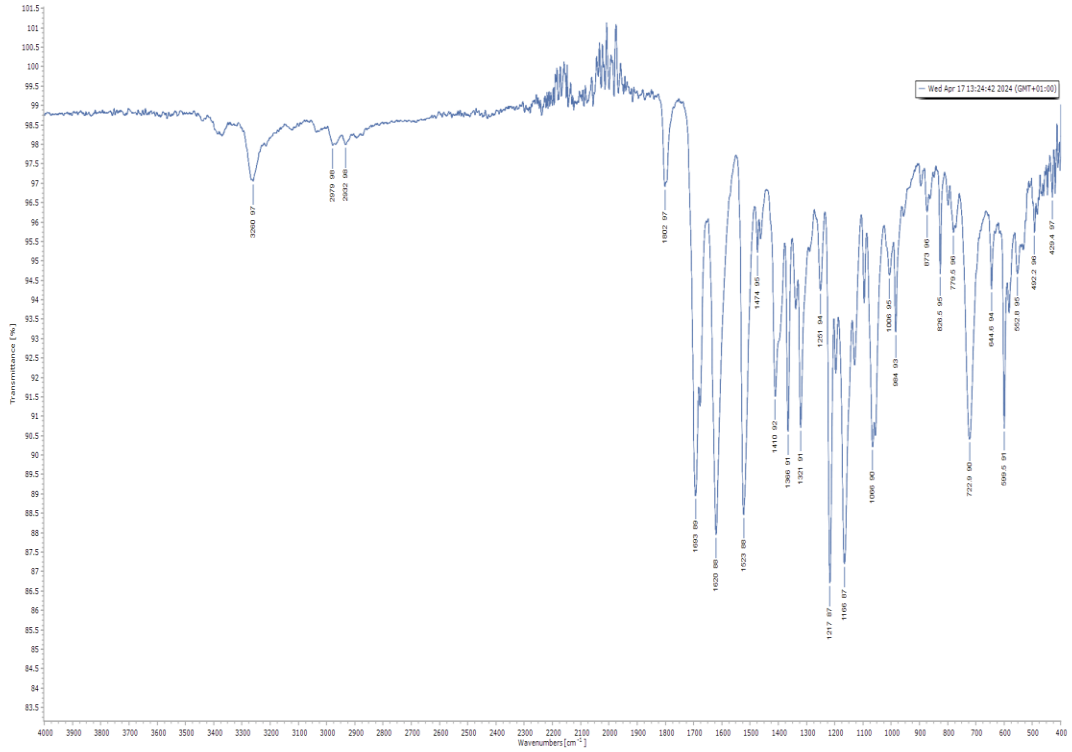

Figure S3.18: FTIR-ATR spectrum of **3.7.**

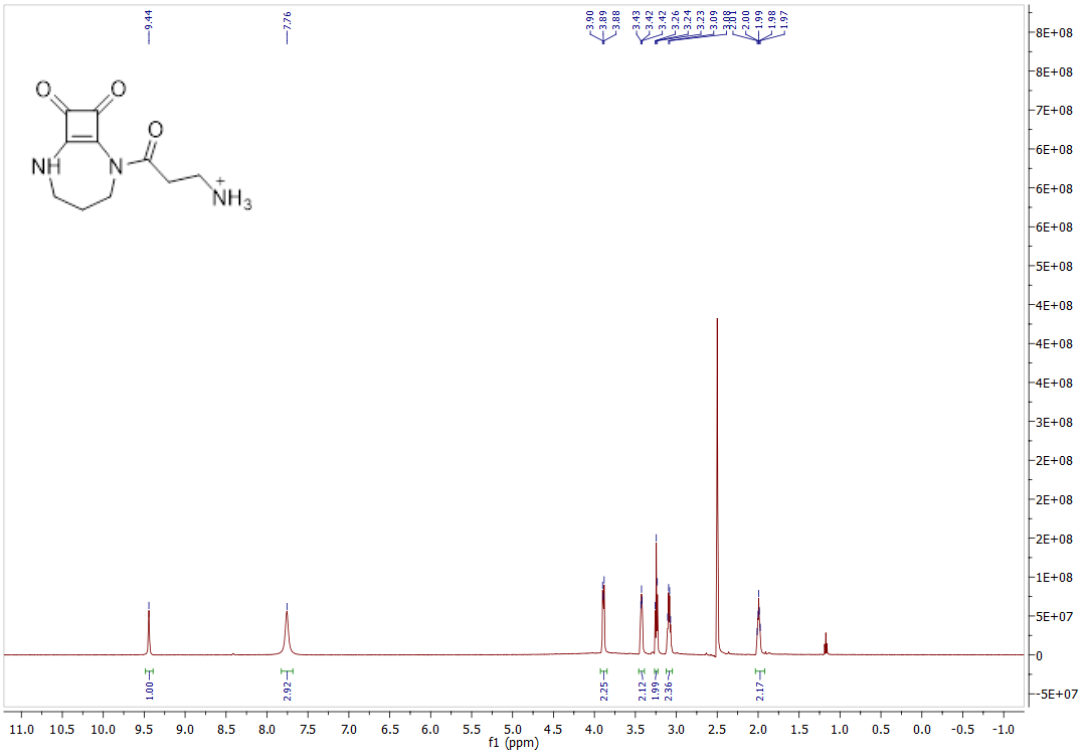

Figure S3.19: ^{1}H NMR spectrum of **3.9** in DMSO-d_6.

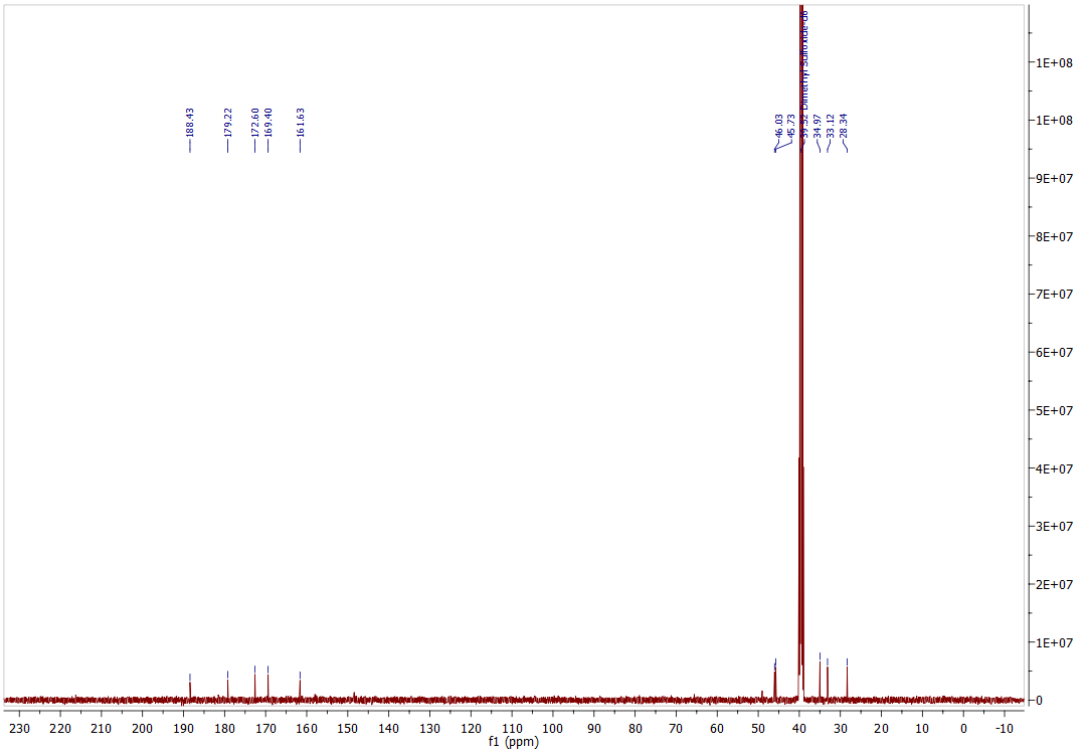

Figure S3.20: ^{13}C NMR spectrum of **3.9** in DMSO-d_6.

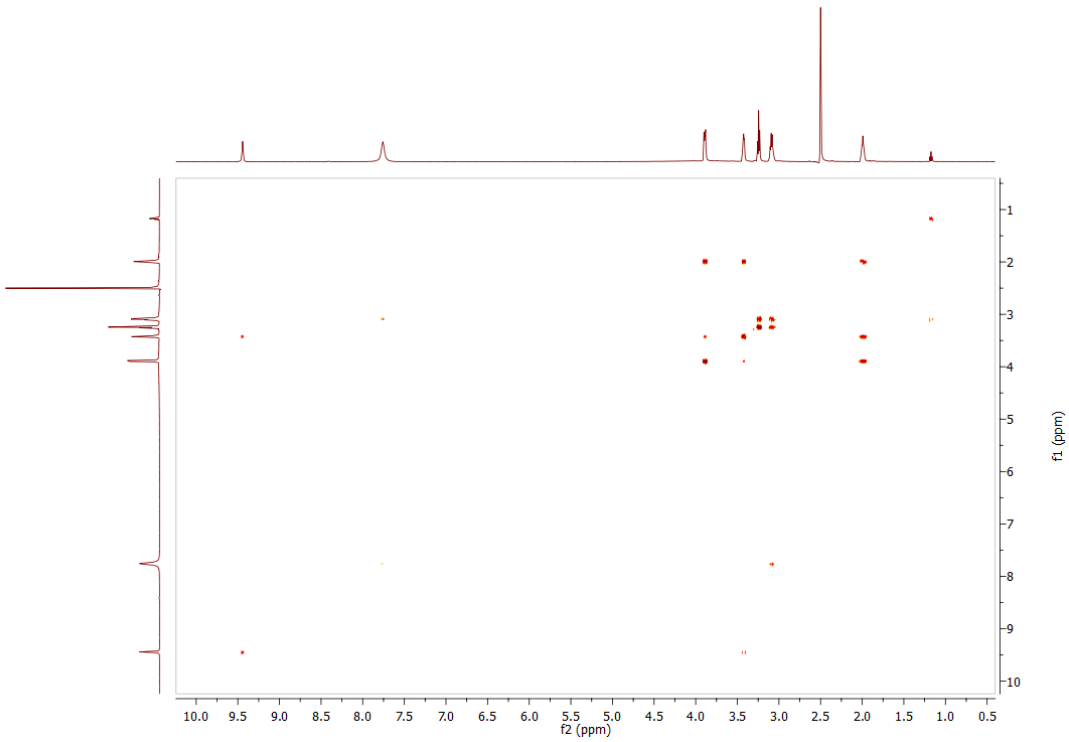

Figure S3.21: COSY spectrum of **3.9** in DMSO-d_6.

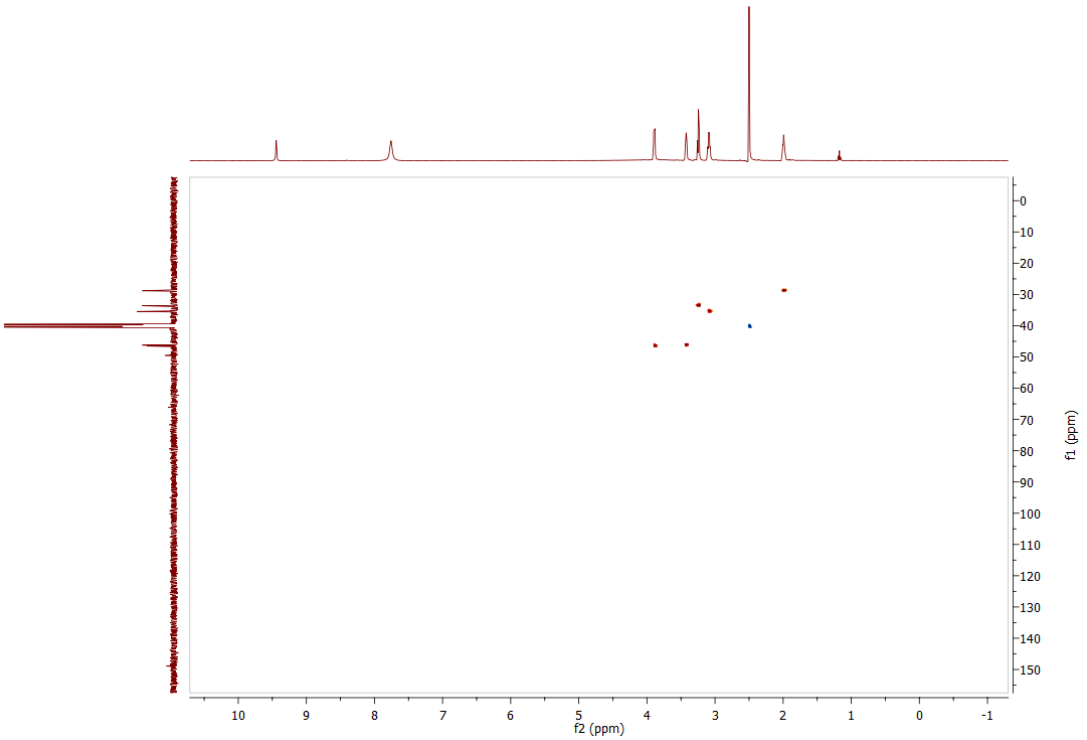

Figure S3.22: HSQC spectrum of **3.9** in DMSO-d_6.

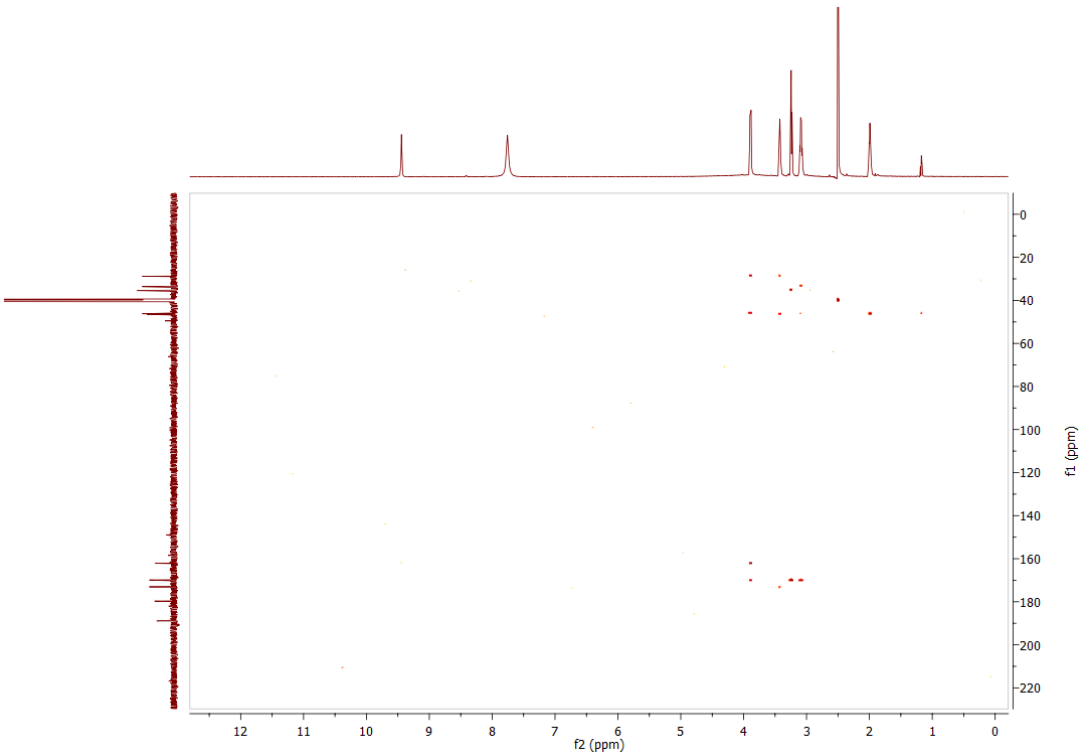

Figure S3.23: HSQC spectrum of **3.9** in DMSO-d_6.

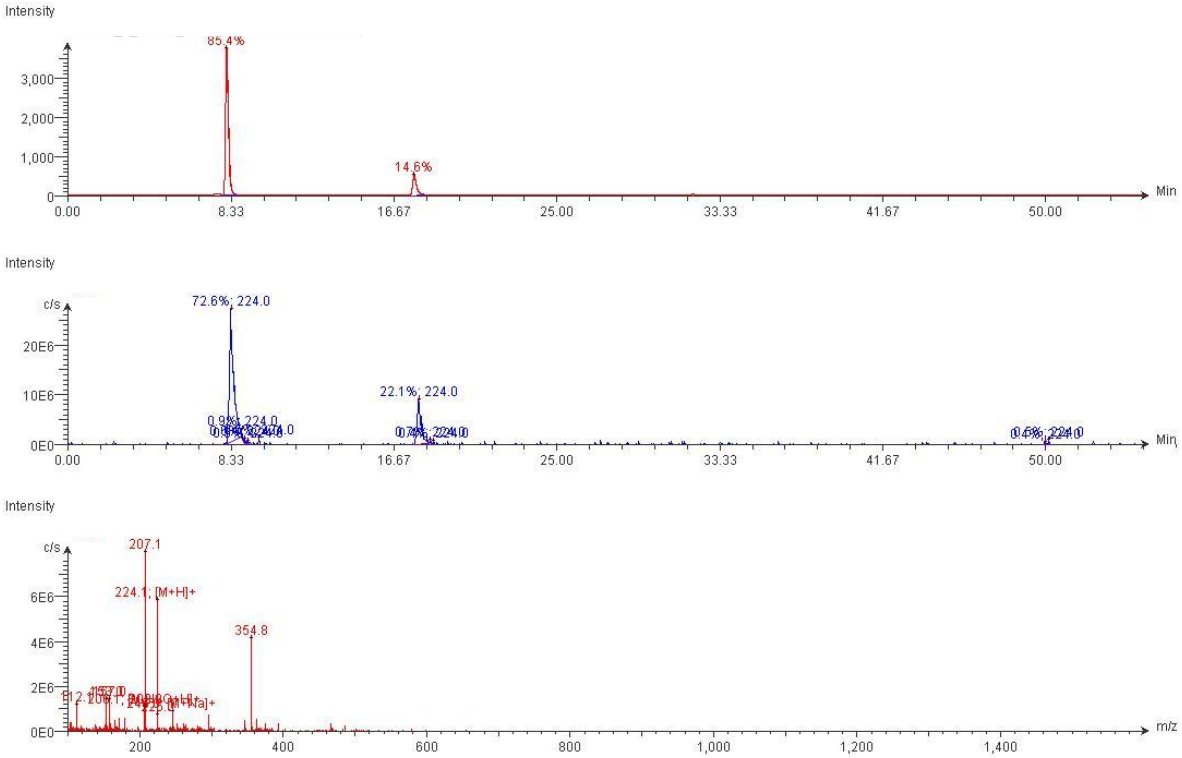

Figure S3.24: LC-MS data for **3.9.**

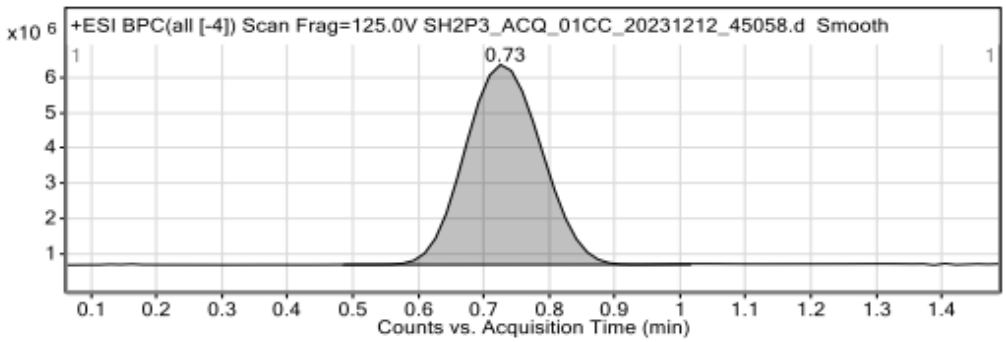

Figure 1: Base peak chromatogram

User Chromatogram Peak List

RT (min)	Area	Area %	Area Sum (%)	Base Peak (m/z)	Width (min)
0.73	46363176	100.00	100.00	104.0689	0.150

Compound Table

Compound Label	RT (min)	Observed mass (m/z)	Neutral observed mass (Da)	Theoretical mass (Da)	Mass error (ppm)	Isotope match score (%)
Cpd 1: C10 H13 N3 O3	0.74	246.0849	223.0958	223.0957	0.42	98.75

Mass errors of between -5.00 and 5.00 ppm with isotope match scores above 60% are considered confirmation of molecular formulae

Figure: Full range view of Compound spectra and potential adducts.

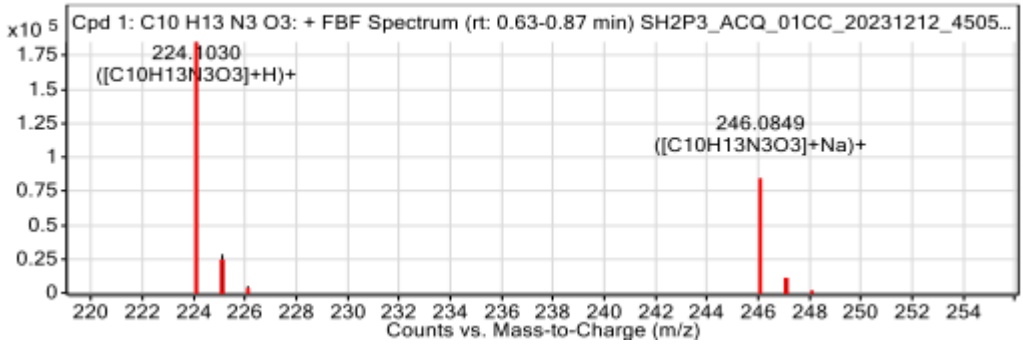

Figure S3.25: HRMS data for **3.9.**

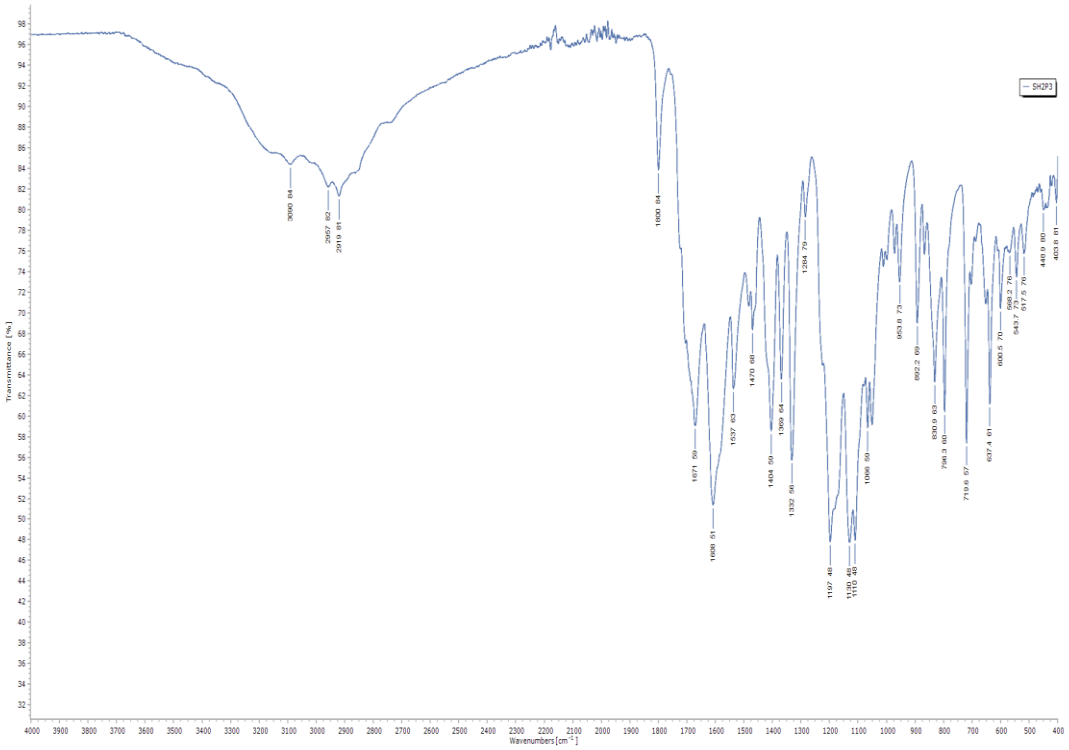

Figure S3.26: FTIR-ATR spectrum of **3.9.**

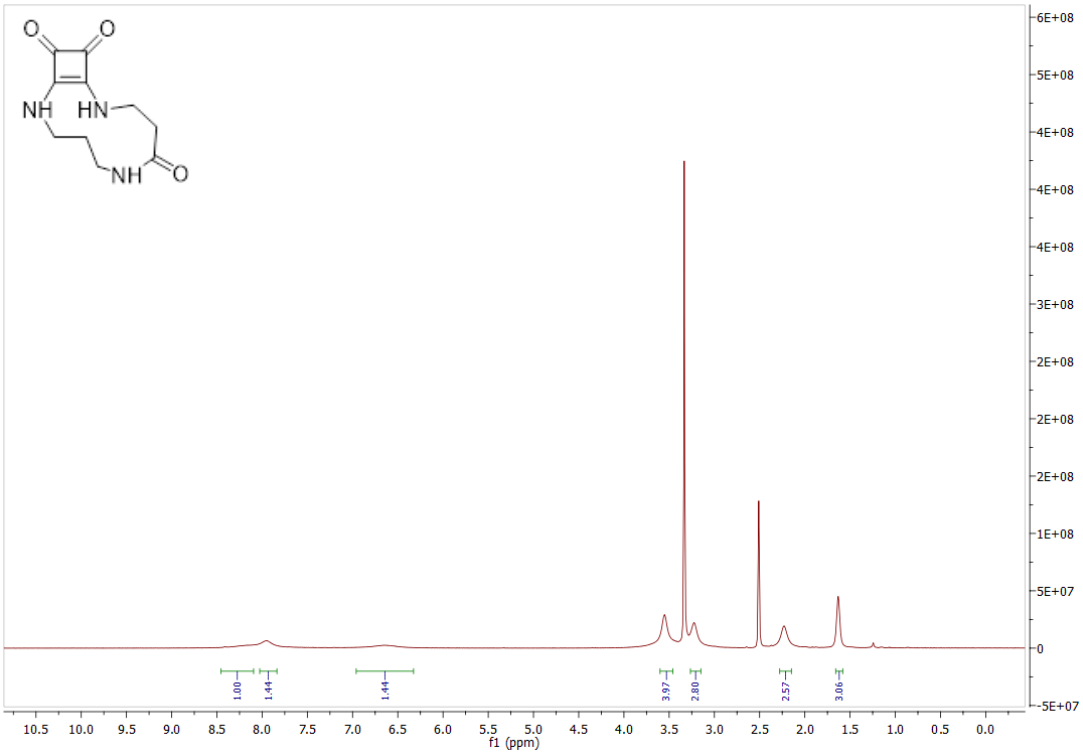

Figure S3.27: ^{1}H NMR spectrum of **3.10** in DMSO-d_6 at 273K.

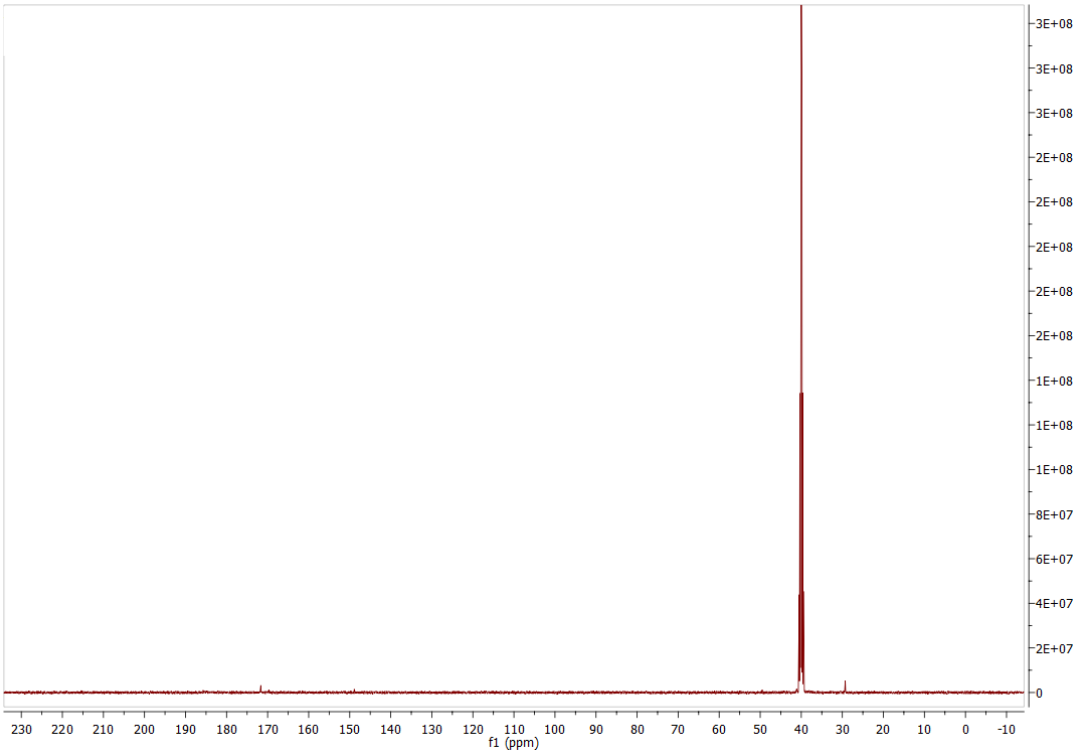

Figure S3.28: ^{13}C NMR spectrum of **3.10** in DMSO-d_6 at 273K.

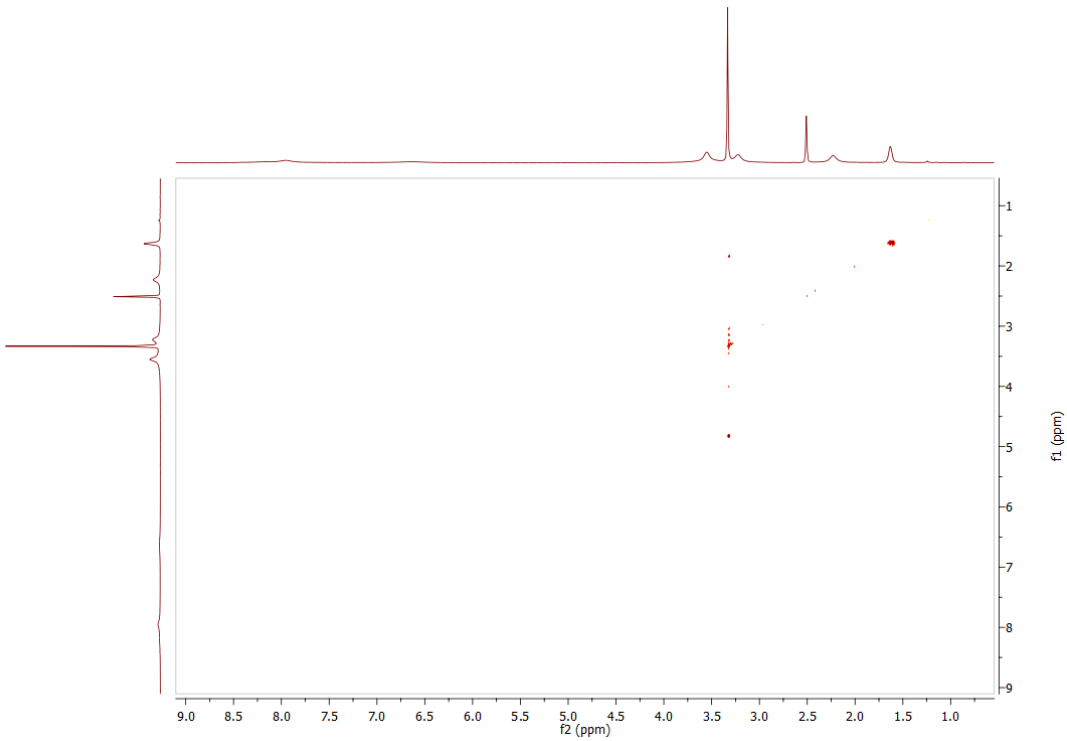

Figure S3.29: COSY spectrum of **3.10** in DMSO-d_6 at 273K.

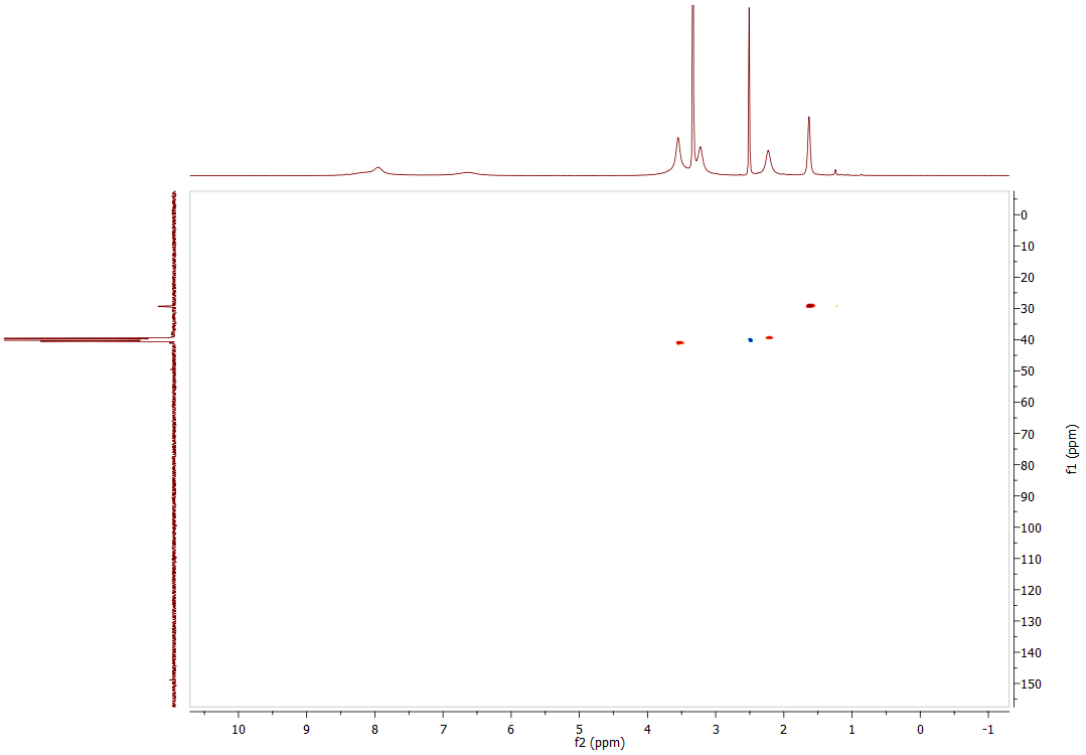

Figure S3.30: HSQC spectrum of **3.10** in DMSO-d_6 at 273K.

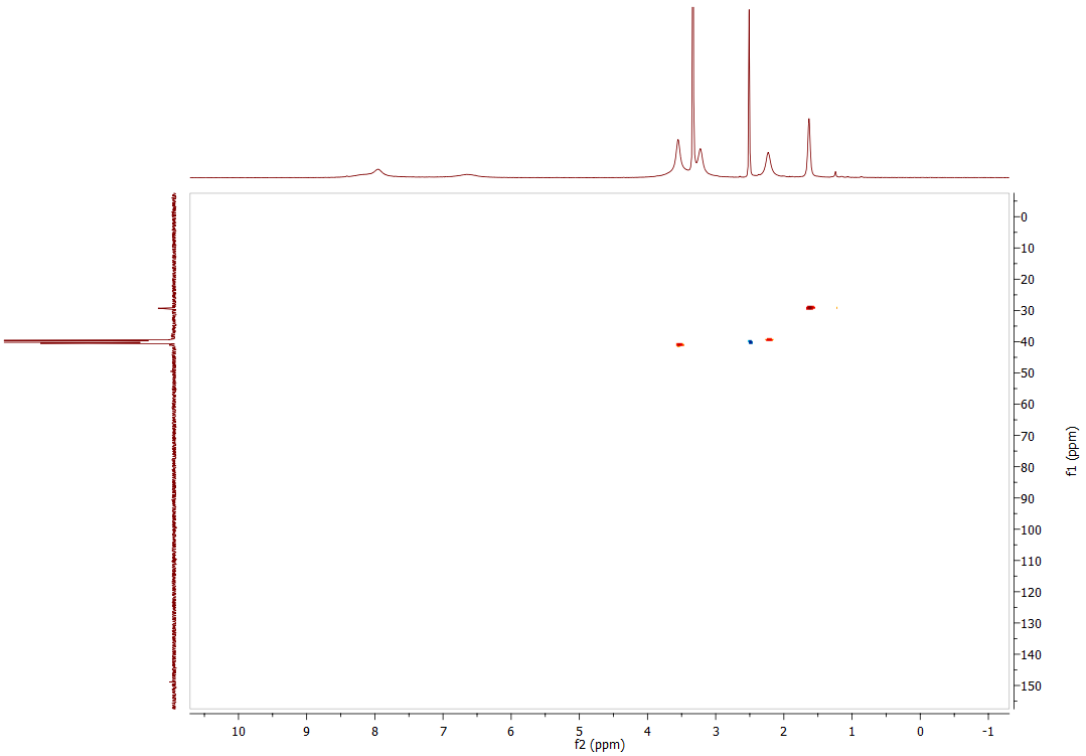

Figure S3.31: HMBC spectrum of **3.10** in DMSO-d_6 at 273K.

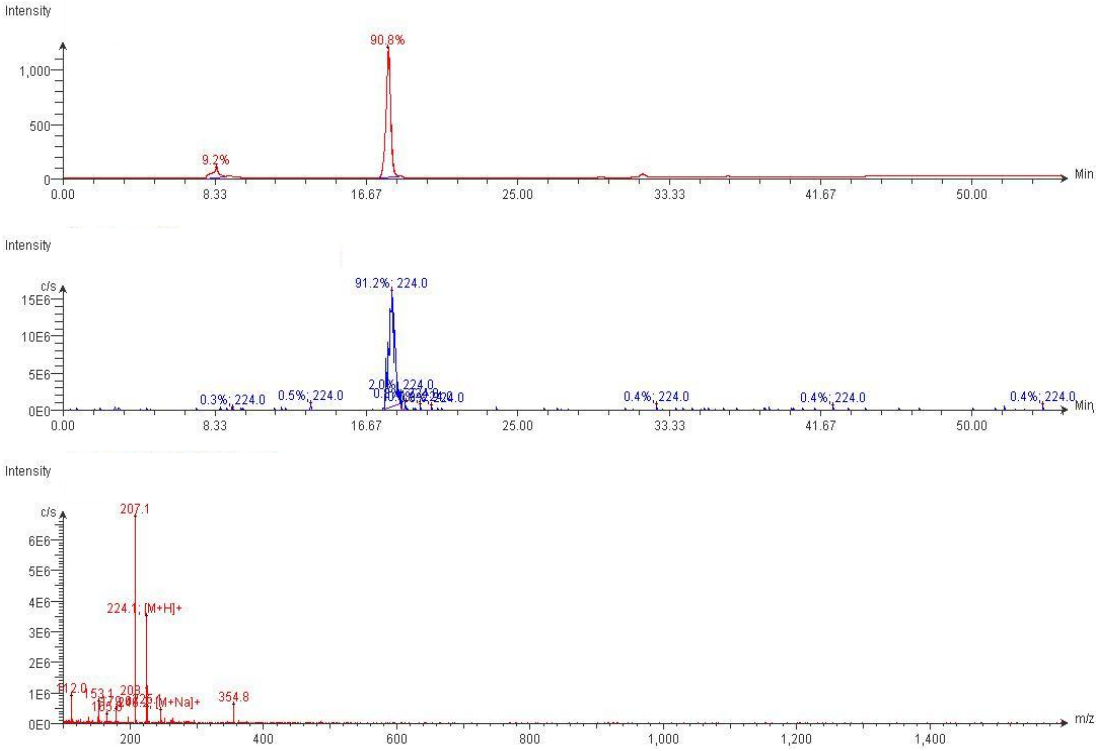

Figure S3.32: LC-MS data for **3.10.**

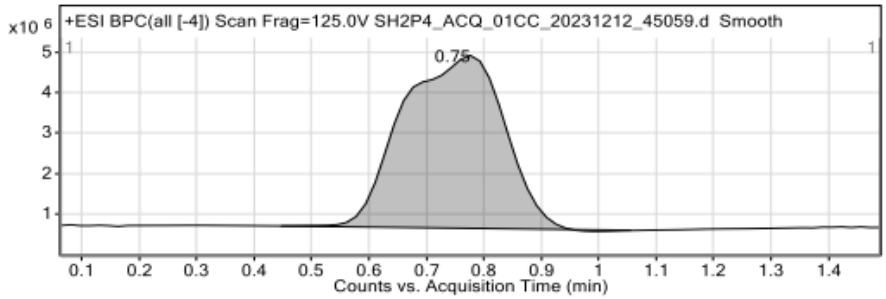

Figure 1: Base peak chromatogram

User Chromatogram Peak List

RT (min)	Area	Area %	Area Sum (%)	Base Peak (m/z)	Width (min)
0.75	53115236	100.00	100.00	144.9879	0.210

Compound Table

Compound Label	RT (min)	Observed mass (m/z)	Neutral observed mass (Da)	Theoretical mass (Da)	Mass error (ppm)	Isotope match score (%)
Cpd 1: C10 H13 N3 O3	0.72	246.0849	223.0957	223.0957	0.19	98.64

Mass errors of between -5.00 and 5.00 ppm with isotope match scores above 60% are considered confirmation of molecular formulae

Figure: Full range view of Compound spectra and potential adducts.

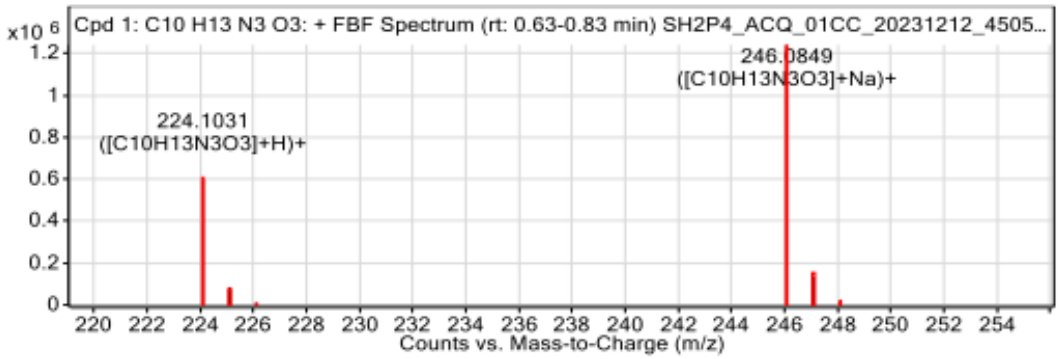

Figure S3.33: HRMS data for **3.10.**

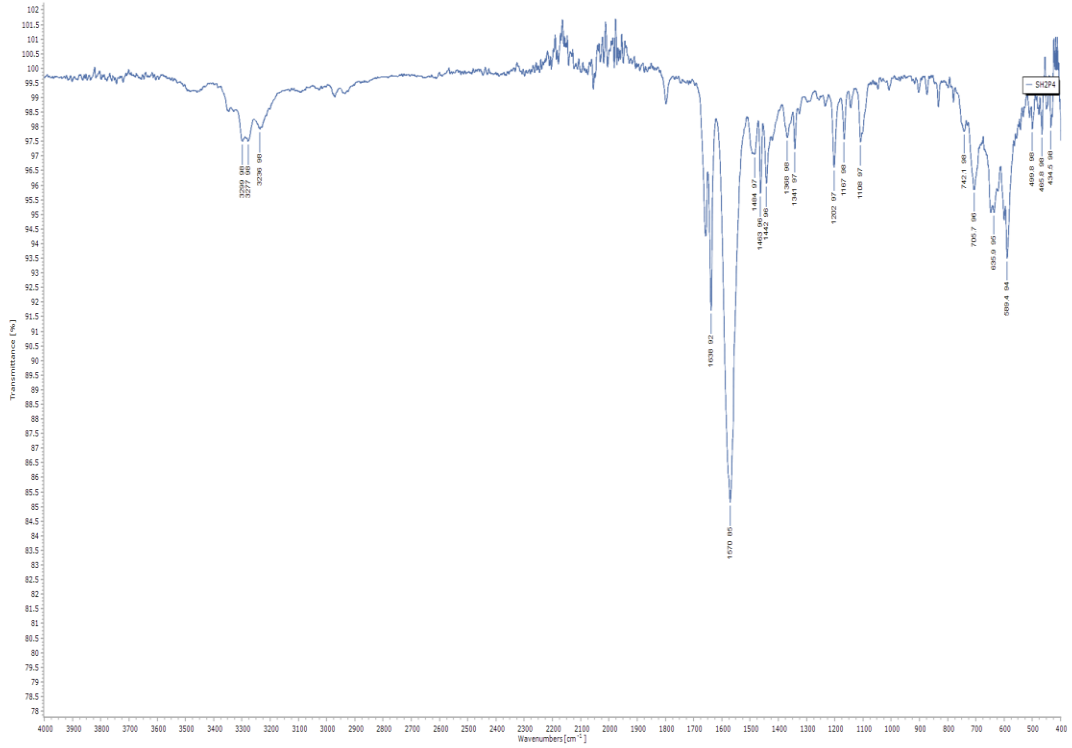

Figure S3.34: FTIR-ATR spectrum of **3.10.**

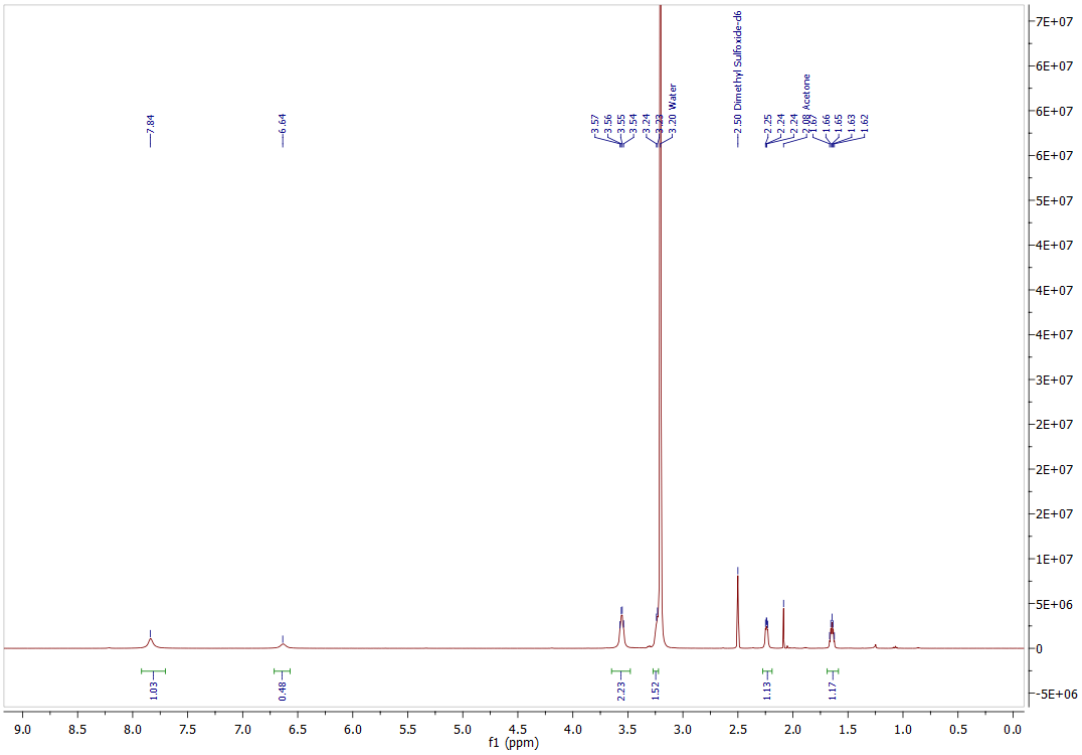

Figure S3.35: ^{1}H NMR spectrum of **3.10** in DMSO-d_6 at 333 K.

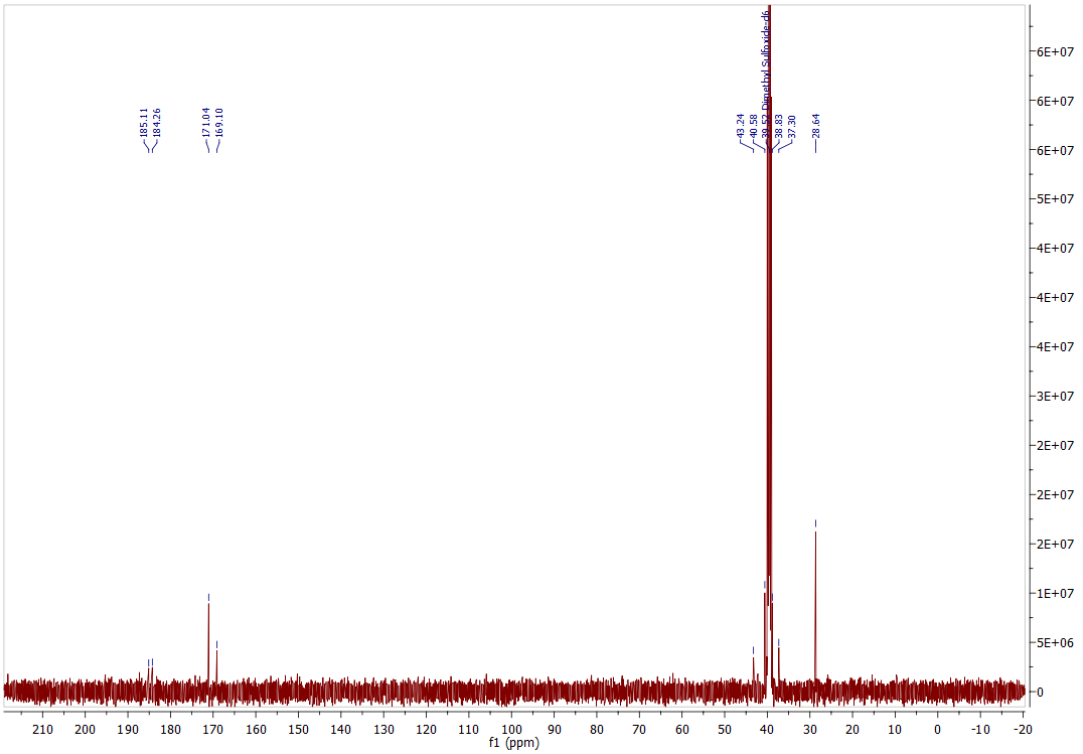

Figure S3.36: ^{13}C NMR spectrum of **3.10** in DMSO-d_6 at 333 K.

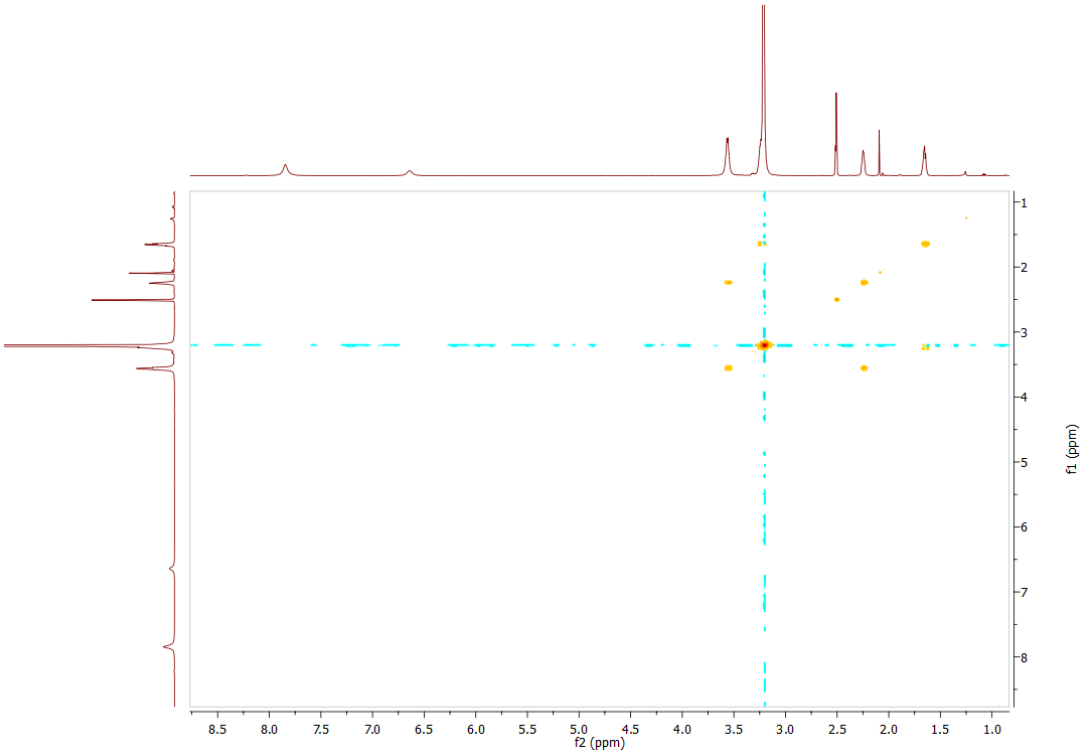

Figure S3.37: COSY spectrum of **3.10** in DMSO-d_6 at 333 K.

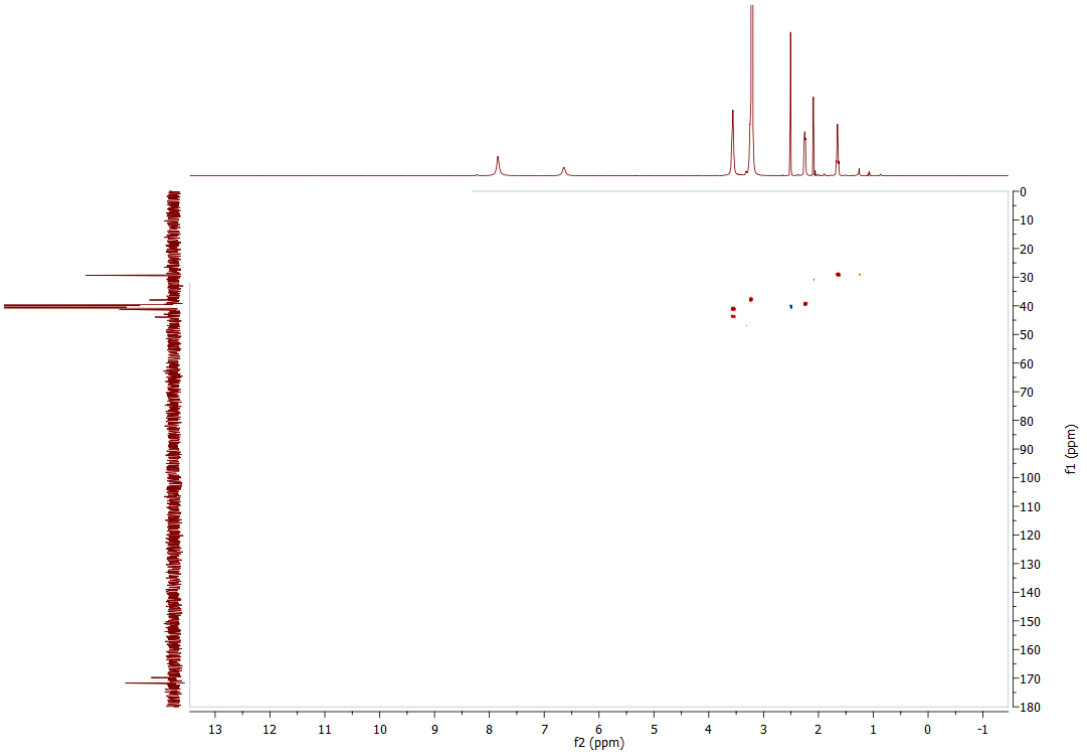

Figure S3.38: HSQC spectrum of **3.10** in DMSO-d_6 at 333 K.

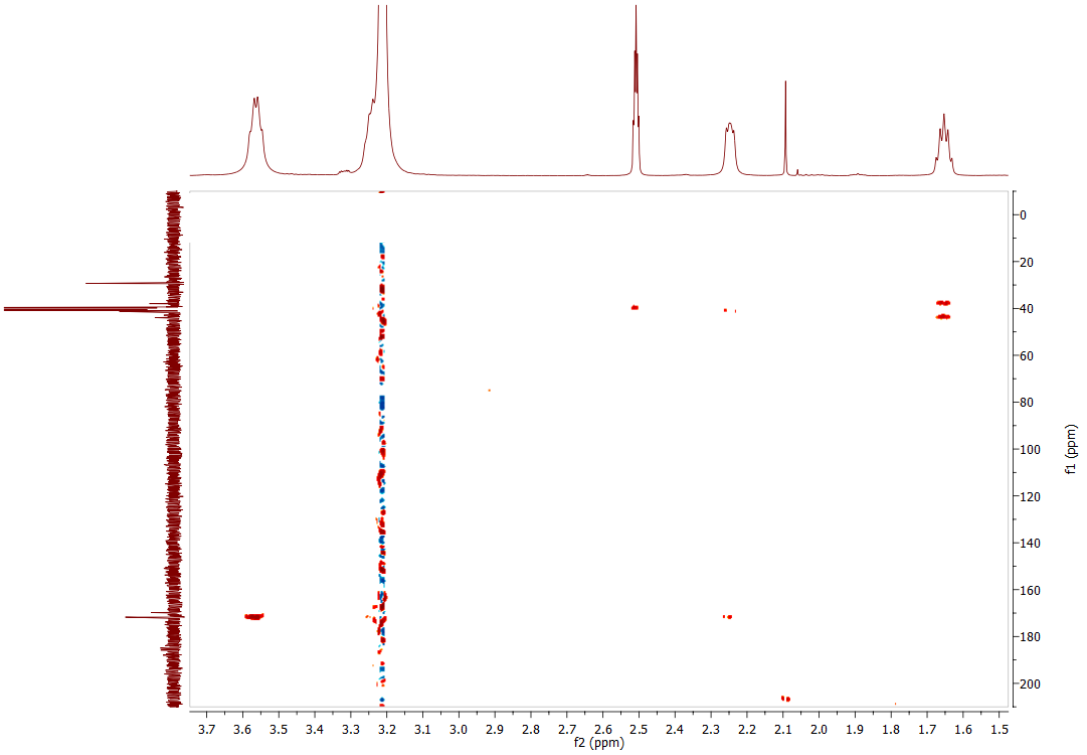

Figure S3.39: HMBC spectrum of **3.10** in DMSO-d_6 at 333 K.

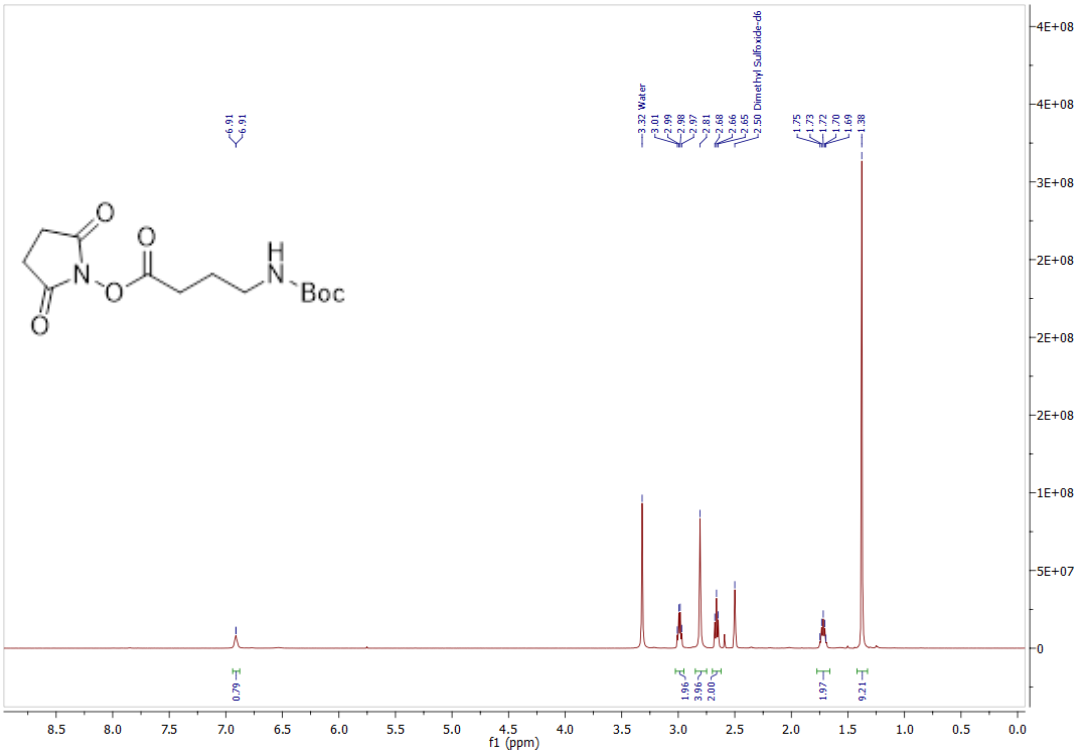

Figure S3.40: ^{1}H NMR spectrum of **3.16** in DMSO-d_6.

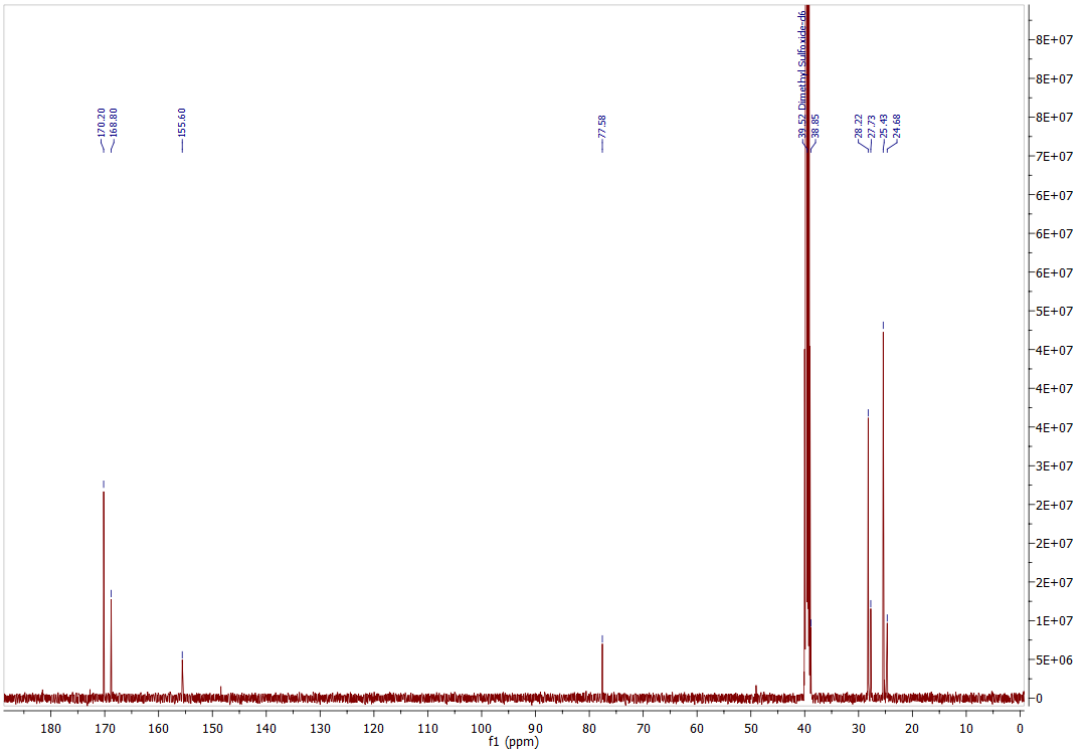

Figure S3.41: ^{13}C NMR spectrum of **3.16** in DMSO-d_6.

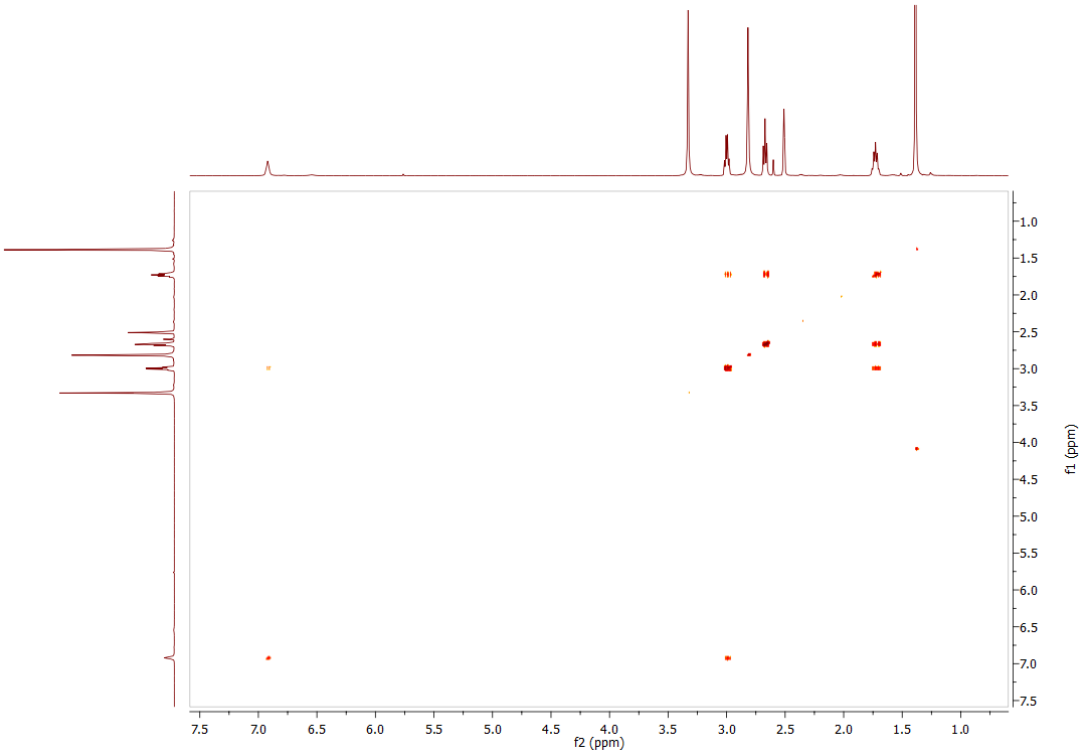

Figure S3.42: COSY spectrum of **3.16** in DMSO-d_6.

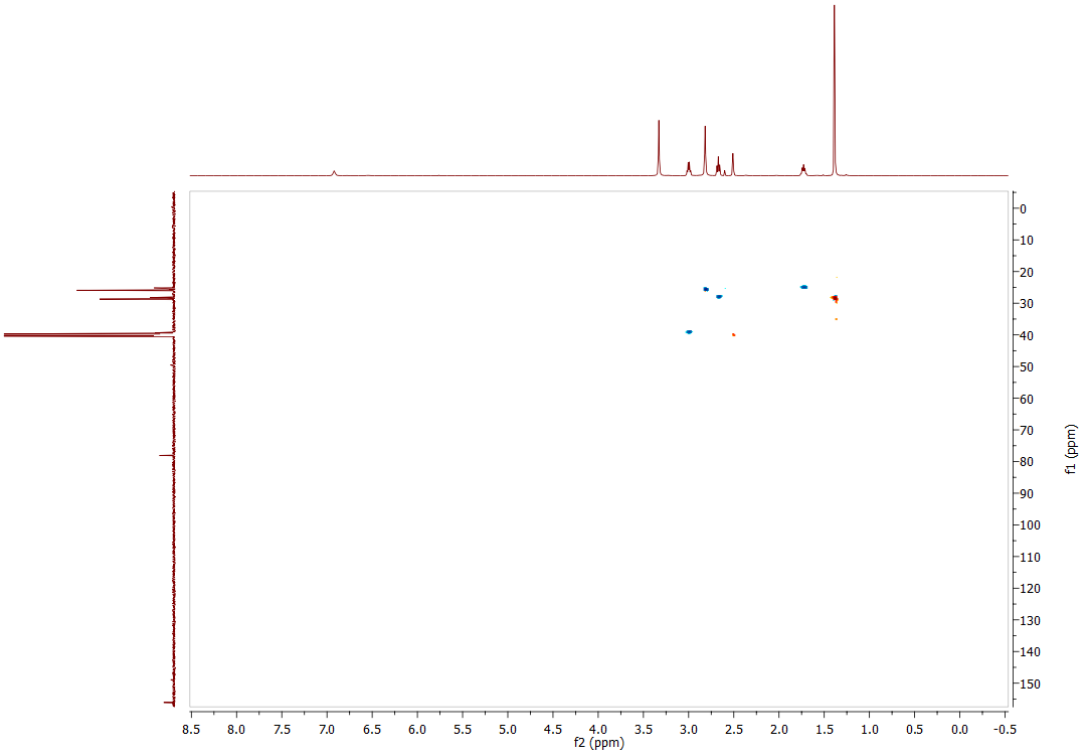

Figure S3.43: HSQC spectrum of **3.16** in DMSO-d_6.

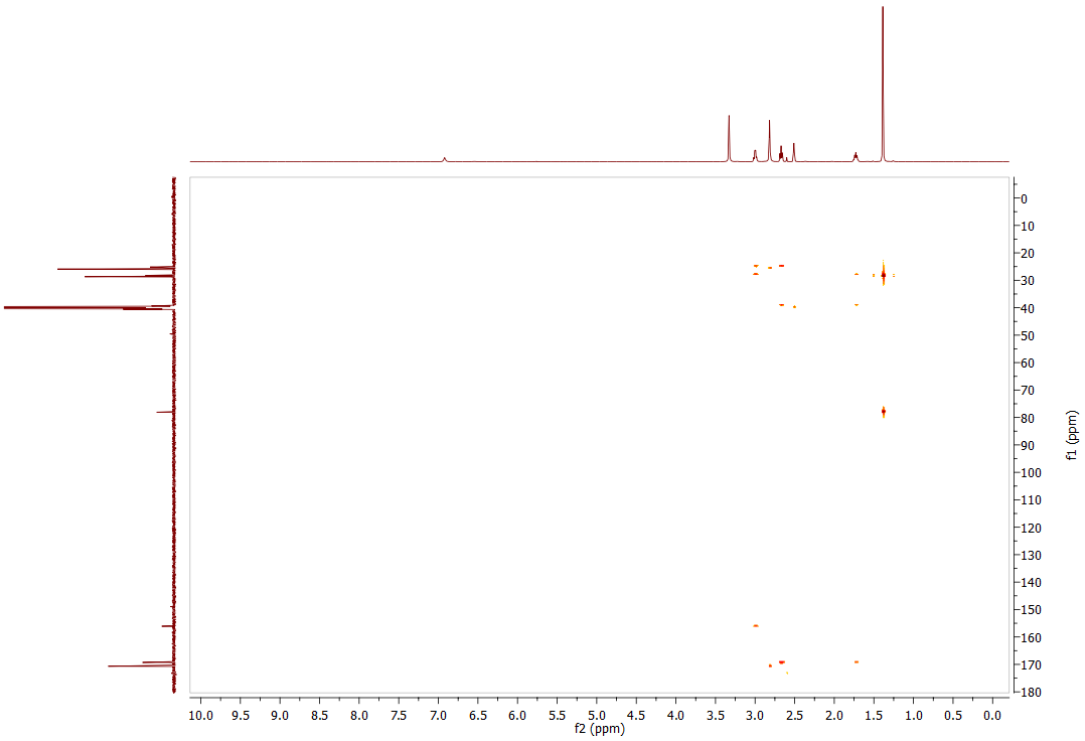

Figure S3.44: HMBC spectrum of **3.16** in DMSO-d_6.

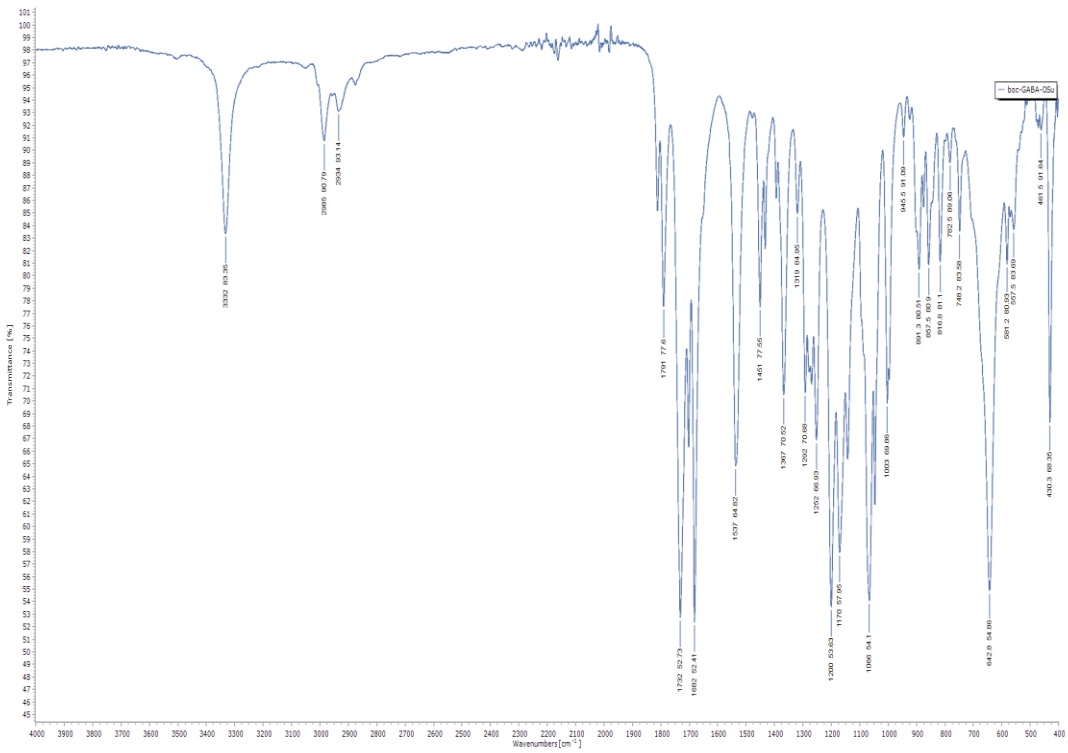

Figure S3.45: FTIR-ATR spectrum of **3.16.**

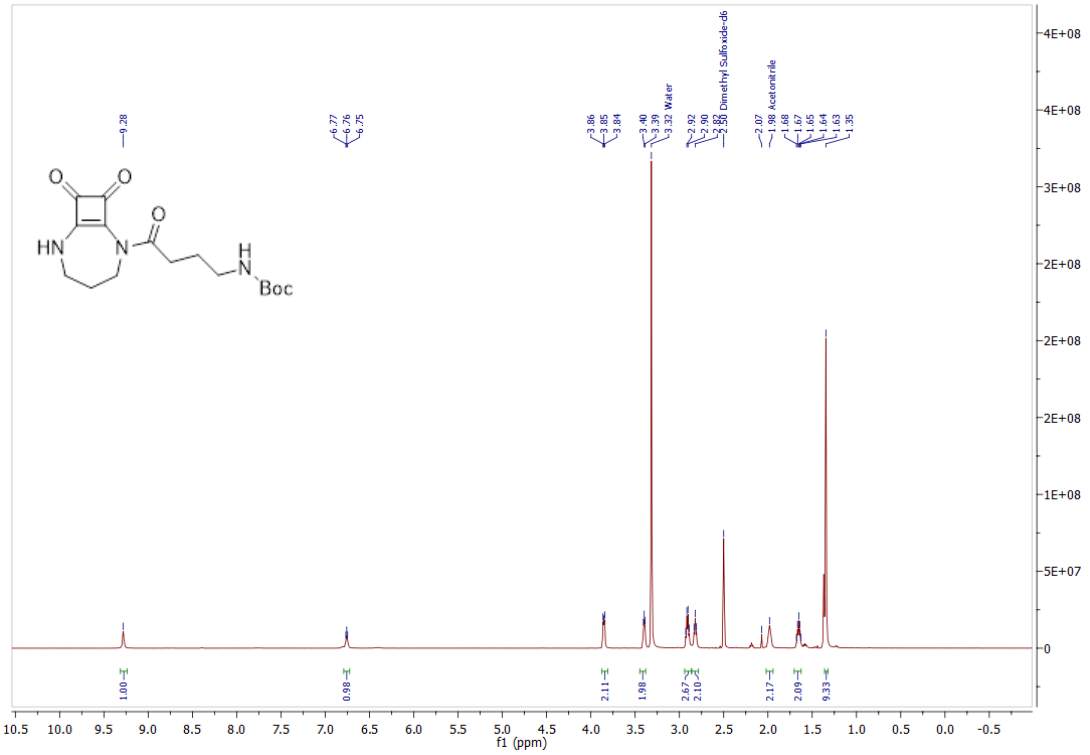

Figure S3.46: ^{1}H NMR spectrum of **3.8** in DMSO-d_6.

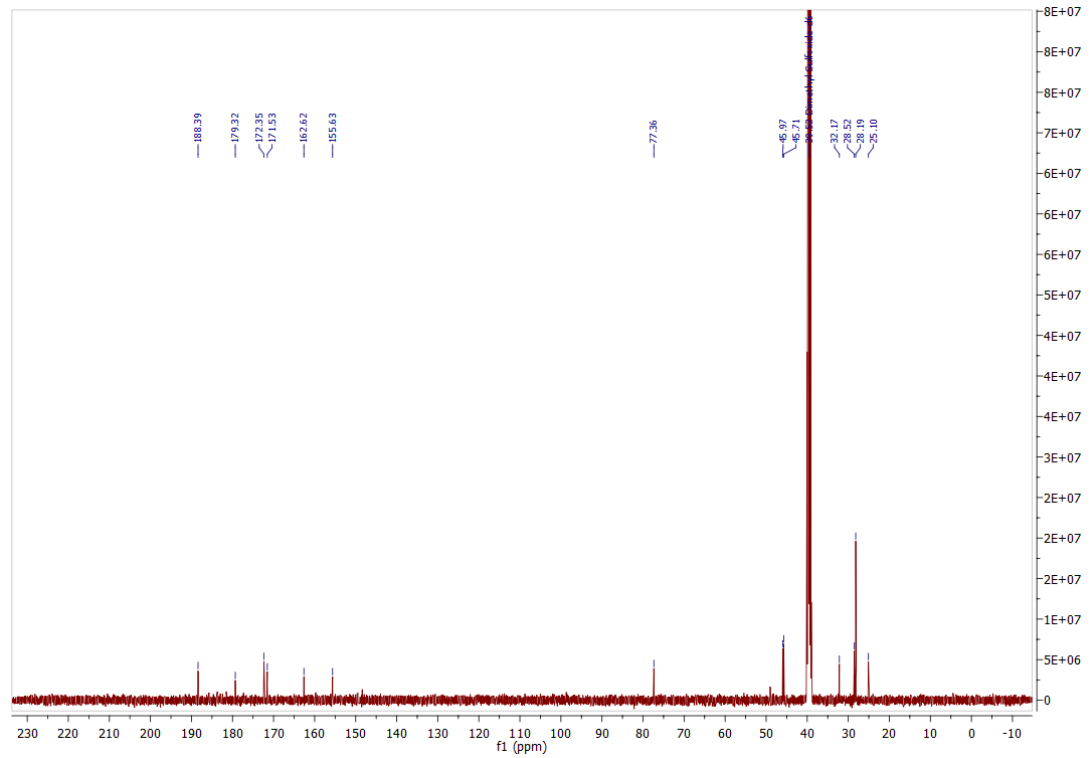

Figure S3.47: ^{13}C NMR spectrum of **3.8** in DMSO-d_6.

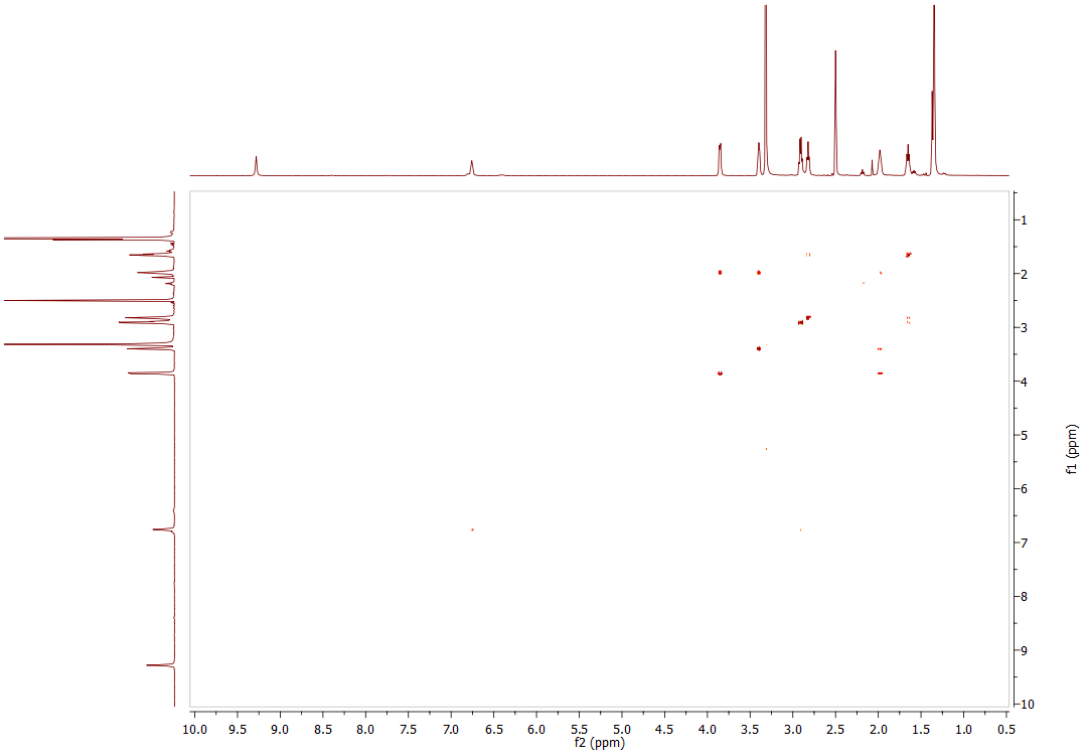

Figure S3.48: COSY spectrum of **3.8** in DMSO-d_6.

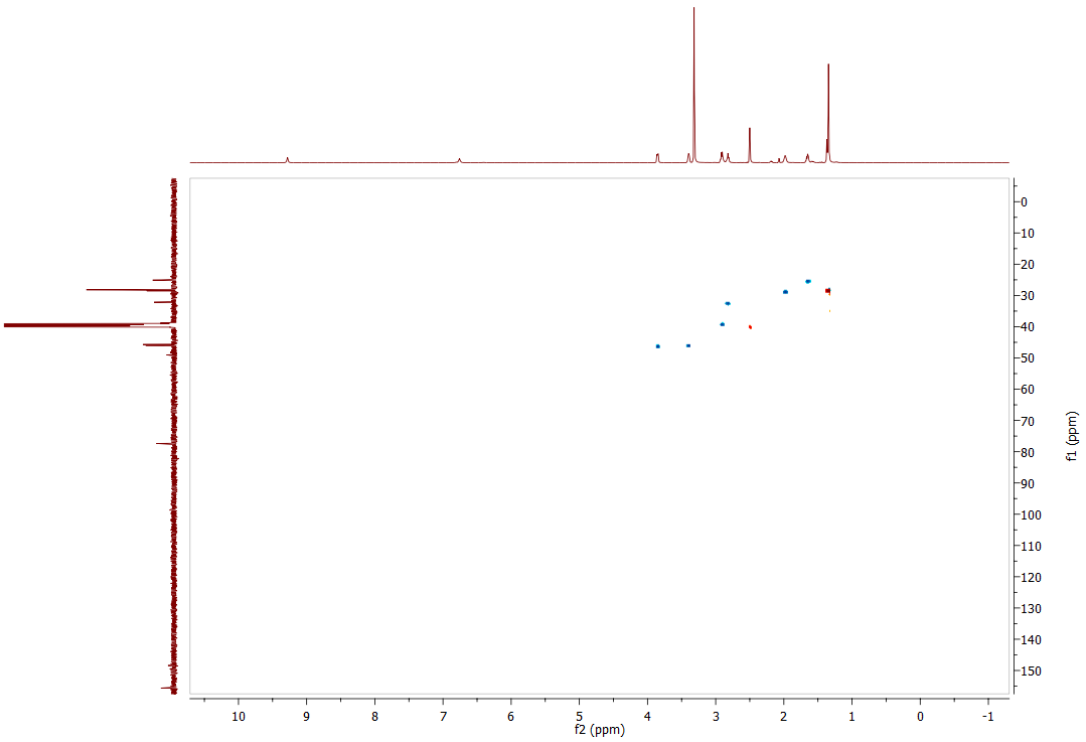

Figure S3.49: HSQC spectrum of **3.8** in DMSO-d_6.

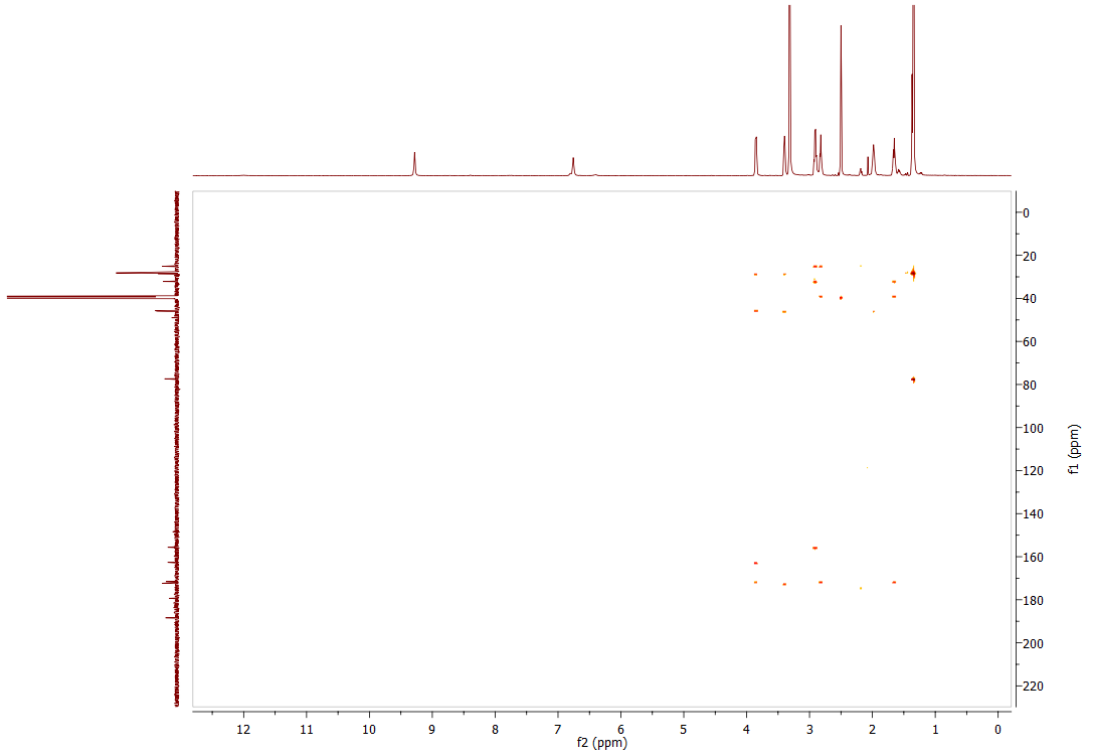

Figure S3.50: HMBC spectrum of **3.8** in DMSO-d_6.

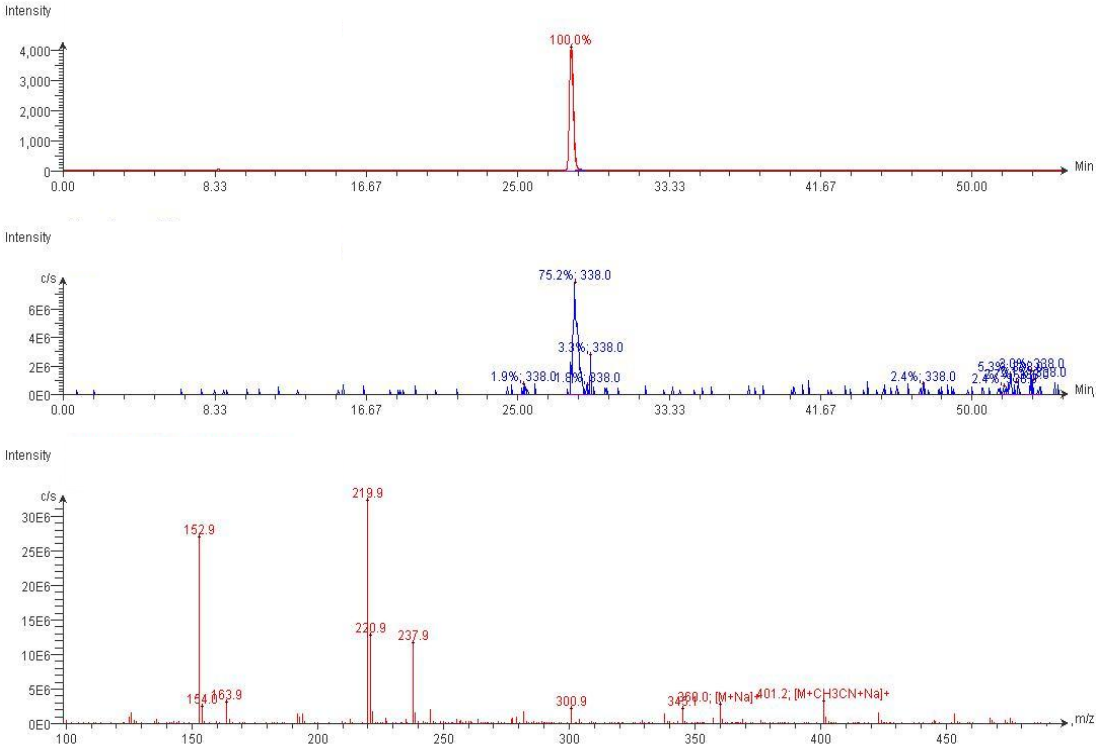

Figure S3.51: LCMS data for **3.8.**

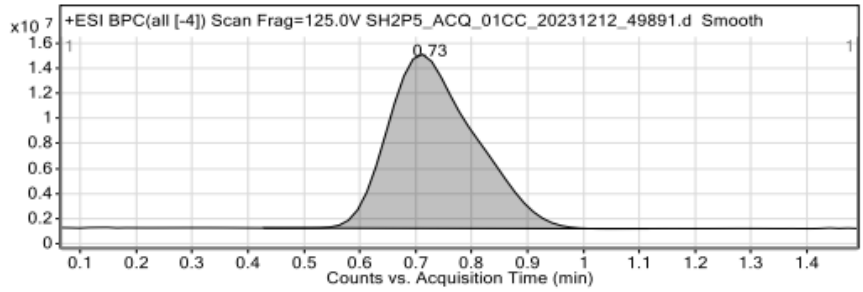

Figure 1: Base peak chromatogram

User Chromatogram Peak List

RT (min)	Area	Area %	Area Sum (%)	Base Peak (m/z)	Width (min)
0.73	149481612	100.00	100.00	376.1256	0.210

Compound Table

Compound Label	RT (min)	Observed mass (m/z)	Neutral observed mass (Da)	Theoretical mass (Da)	Mass error (ppm)	Isotope match score (%)
Cpd 1: C16 H23 N3 O5	0.75	360.1530	337.1638	337.1638	0.22	99.56

Mass errors of between -5.00 and 5.00 ppm with isotope match scores above 60% are considered confirmation of molecular formulae

Figure: Full range view of Compound spectra and potential adducts.

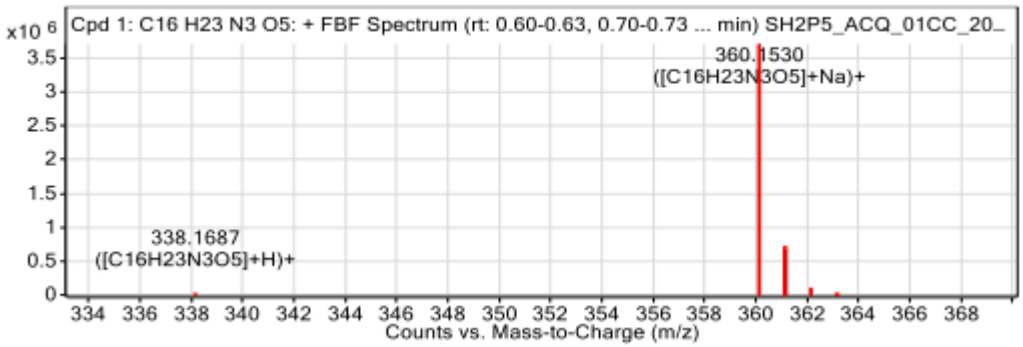

Figure S3.52: HRMS data for **3.8.**

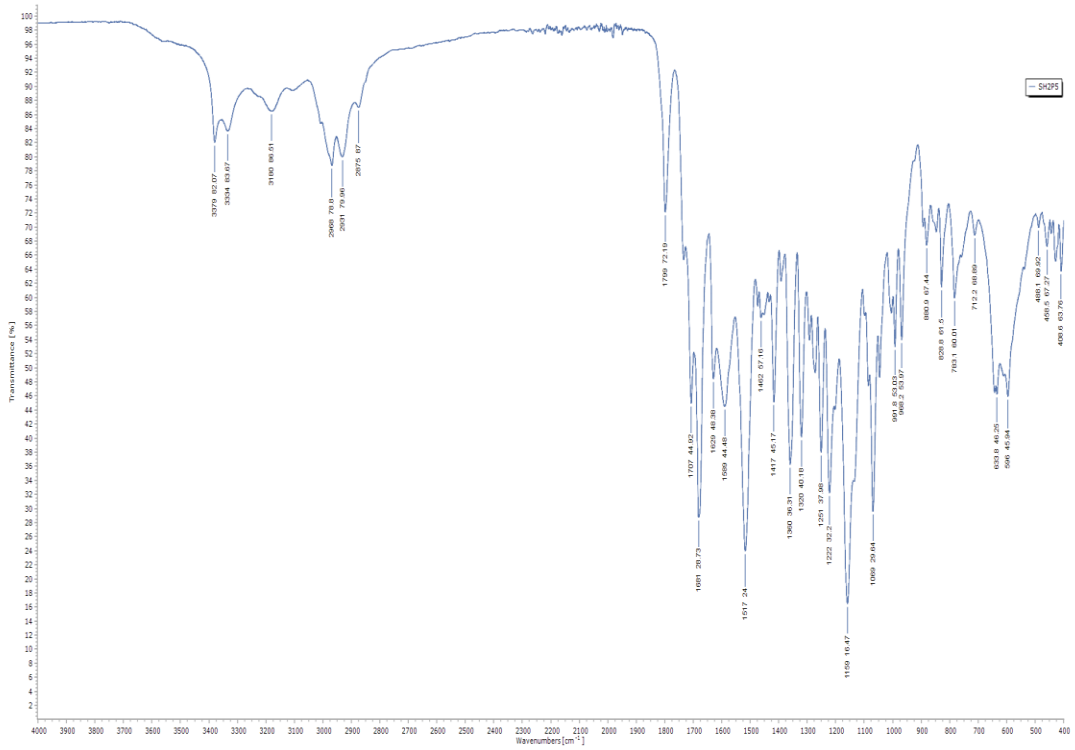

Figure S3.53: FTIR-ATR spectrum of **3.8.**

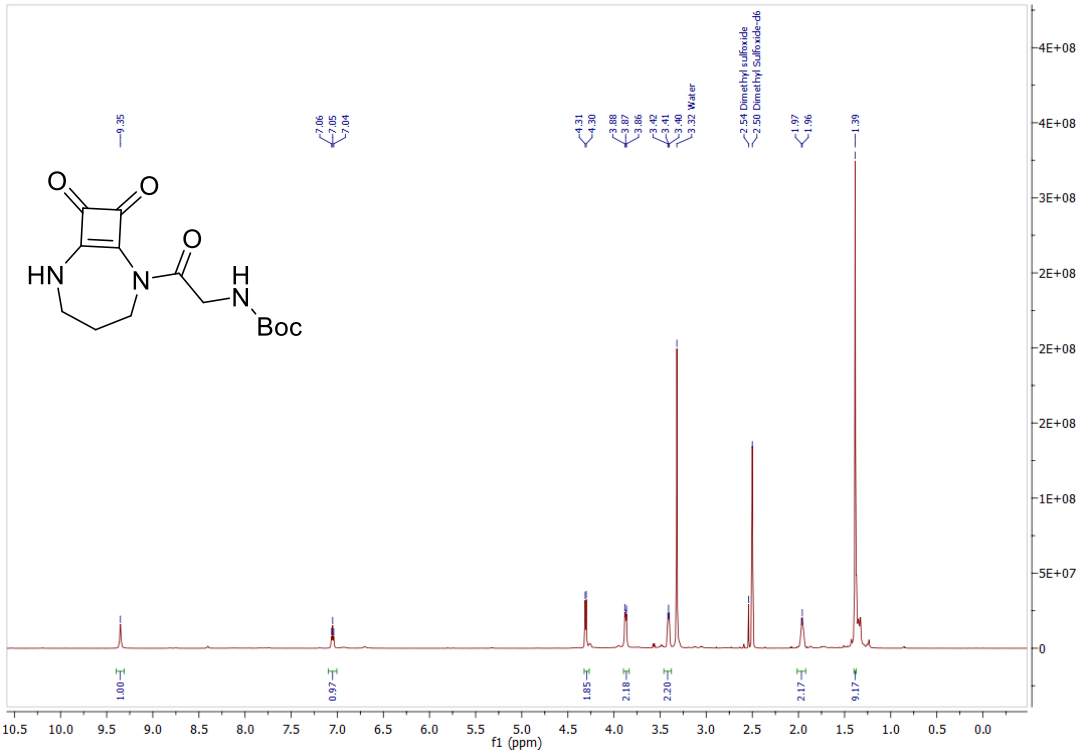

Figure S3.54: ^{1}H NMR spectrum of **3.6** in DMSO-d_6.

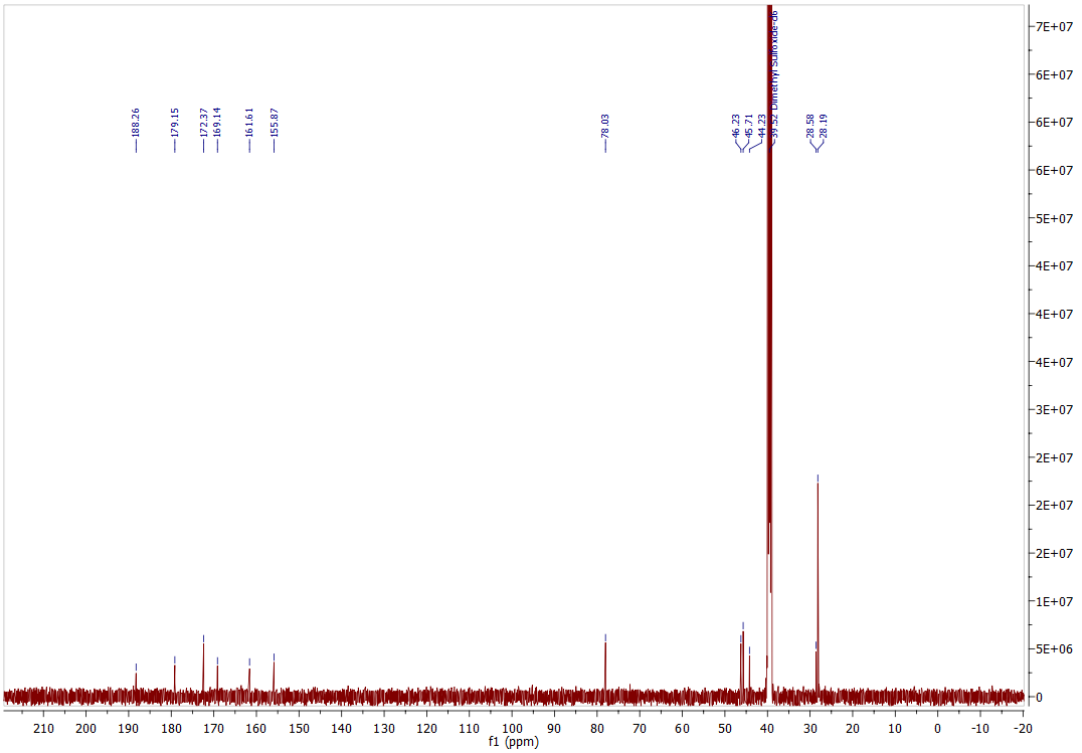

Figure S3.55: ^{13}C NMR spectrum of **3.6** in DMSO-d_6.

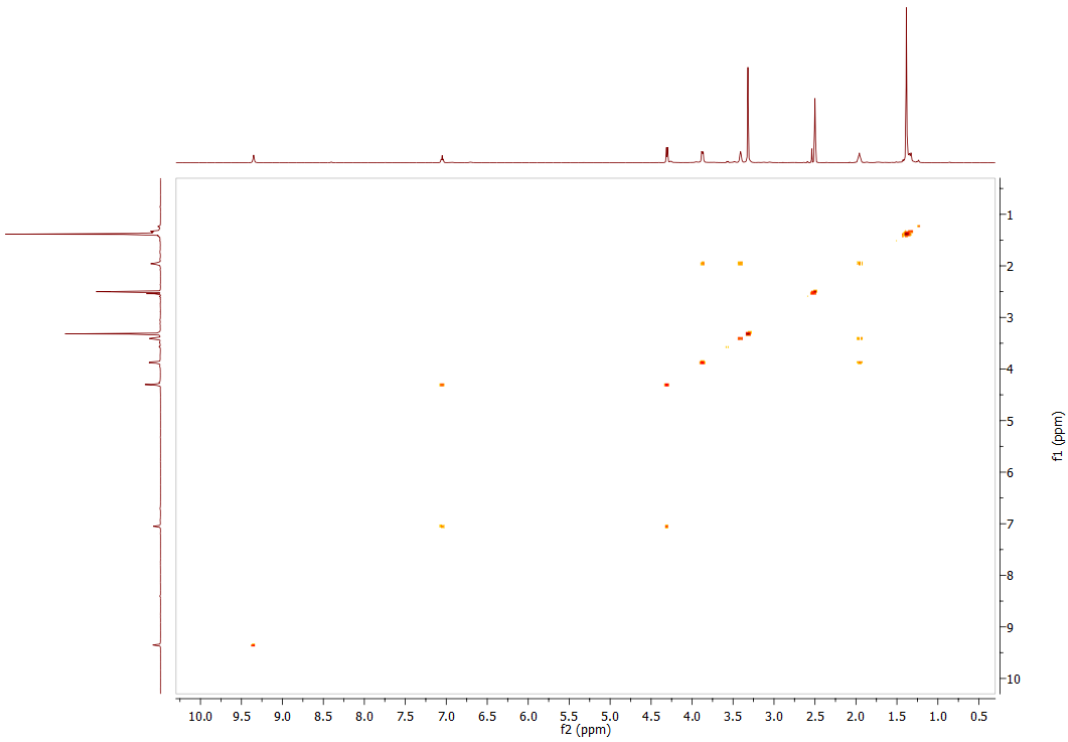

Figure S3.56: COSY spectrum of **3.6** in DMSO-d_6.

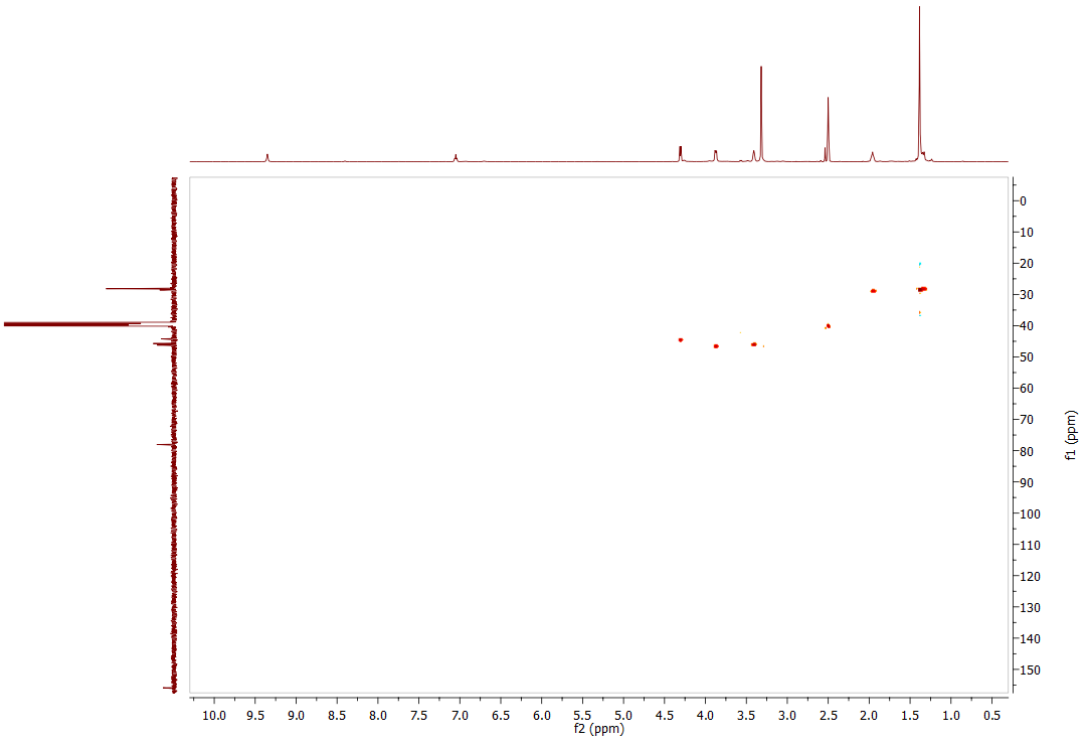

Figure S3.57: HSQC spectrum of **3.6** in DMSO-d_6.

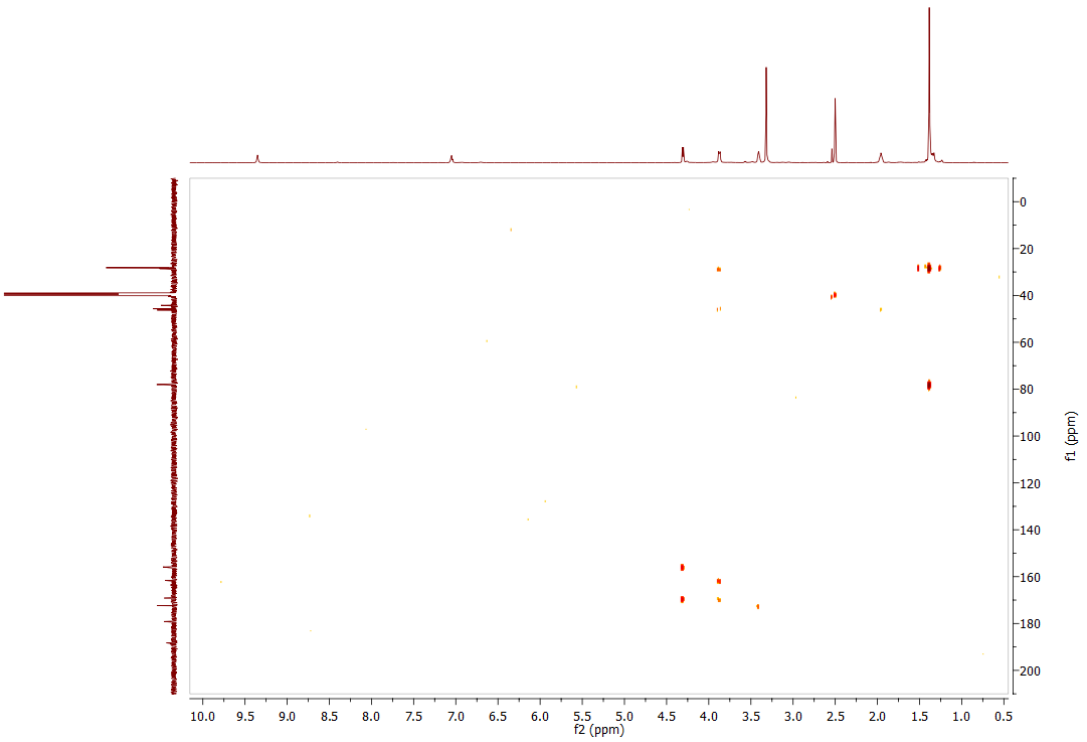

Figure S3.58: HMBC spectrum of **3.6** in DMSO-d_6.

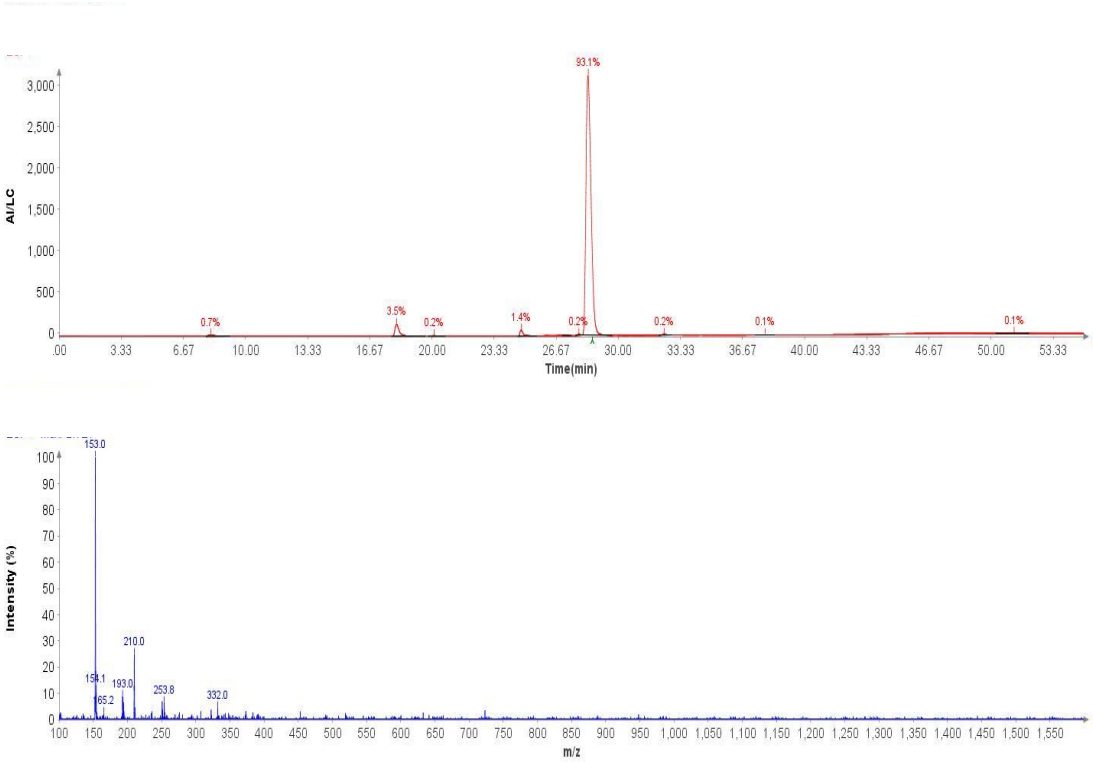

Figure S3.59: LCMS data for **3.6.**

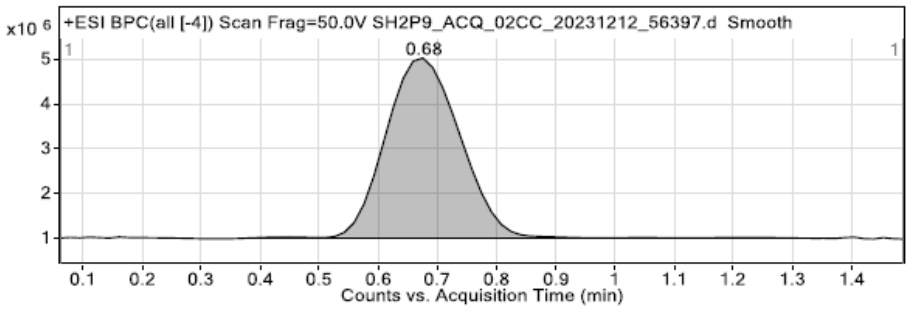

Figure 1: Base peak chromatogram

User Chromatogram Peak List

RT (min)	Area	Area %	Area Sum (%)	Base Peak (m/z)	Width (min)
0.68	36109979	100.00	100.00	641.2538	0.170

Compound Table

Compound Label	RT (min)	Observed mass (m/z)	Neutral observed mass (Da)	Theoretical mass (Da)	Mass error (ppm)	Isotope match score (%)
Cpd 1: C14 H19 N3 O5	0.68	332.1216	309.1312	309.1325	-4.26	99.02

Mass errors of between -5.00 and 5.00 ppm with isotope match scores above 60% are considered confirmation of molecular formulae

Figure: Full range view of Compound spectra and potential adducts.

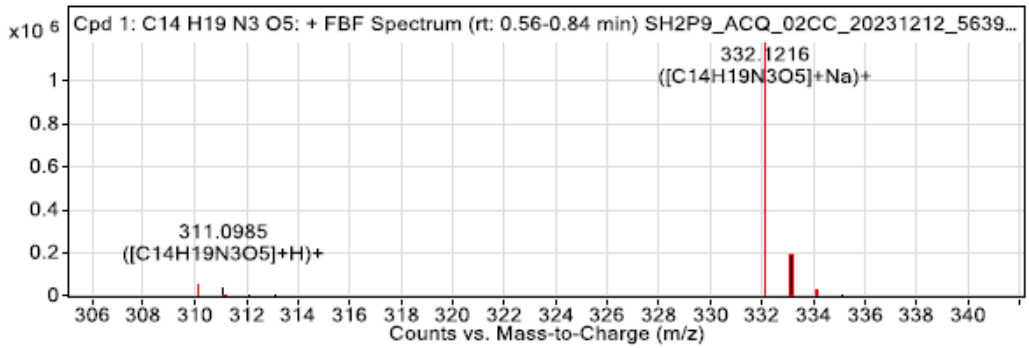

Figure S3.60: HRMS data for **3.6.**

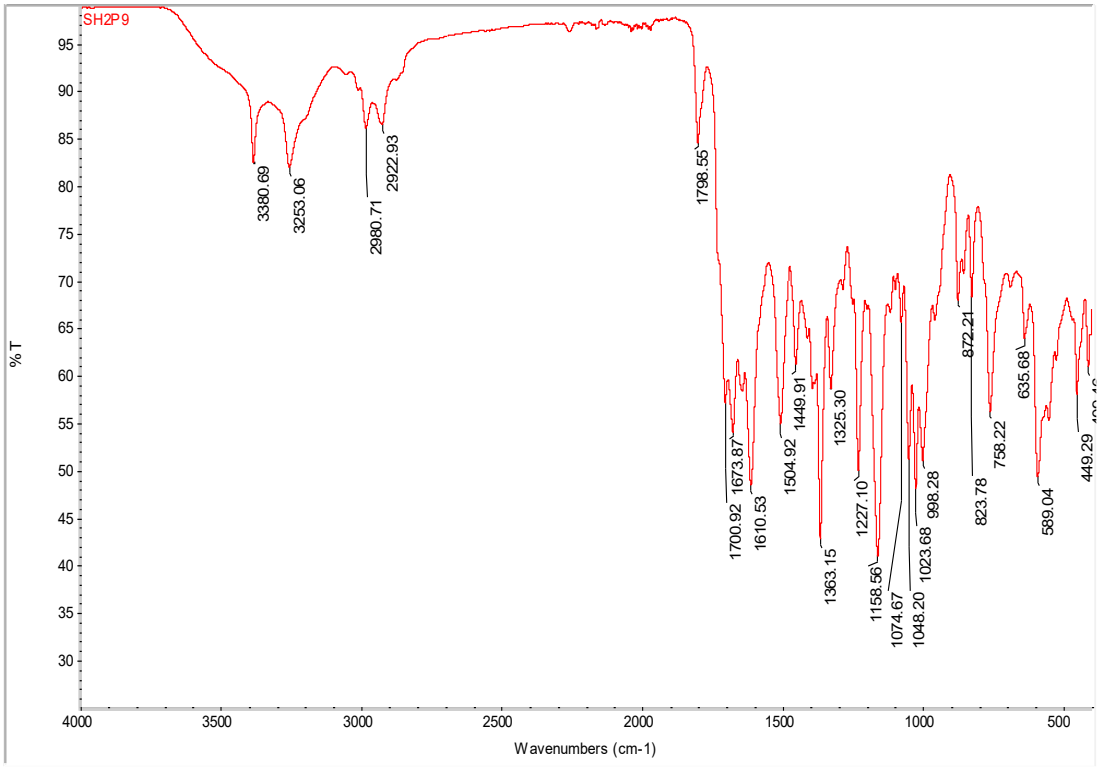

Figure S3.61: FTIR-ATR spectrum of **3.6.**

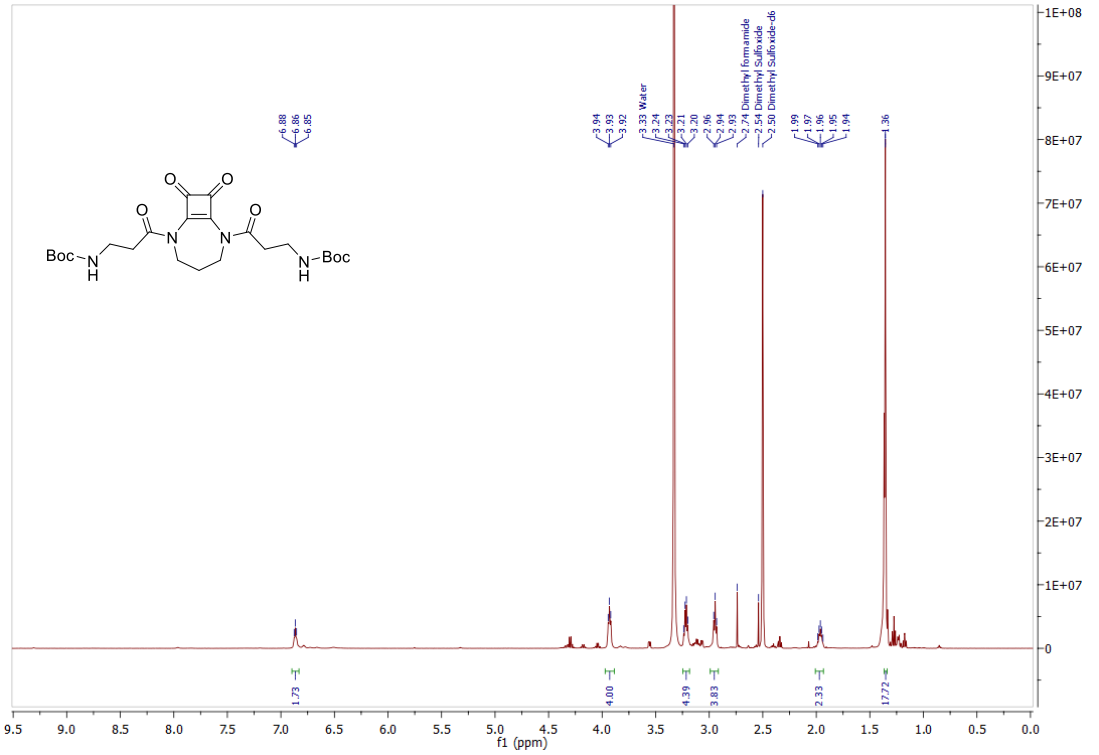

Figure S3.62: ^{1}H NMR spectrum of **3.11** in DMSO-d_6.

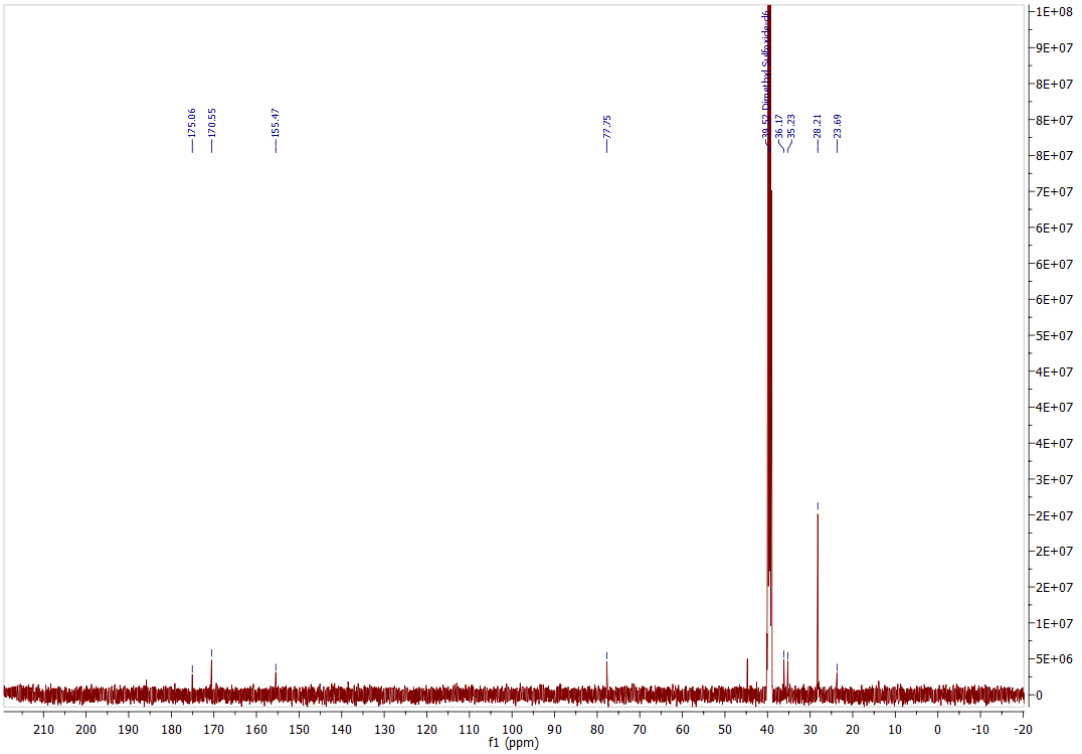

Figure S3.63: ^{13}C NMR spectrum of **3.11** in DMSO-d_6.

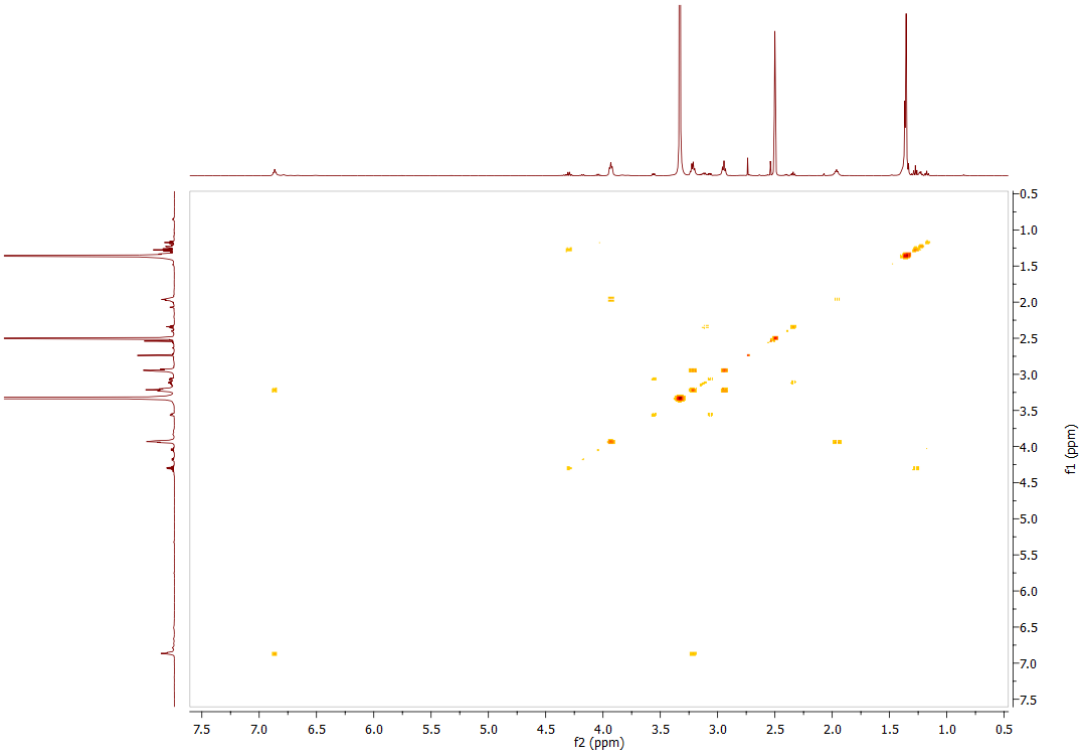

Figure S3.64: COSY spectrum of **3.11** in DMSO-d_6.

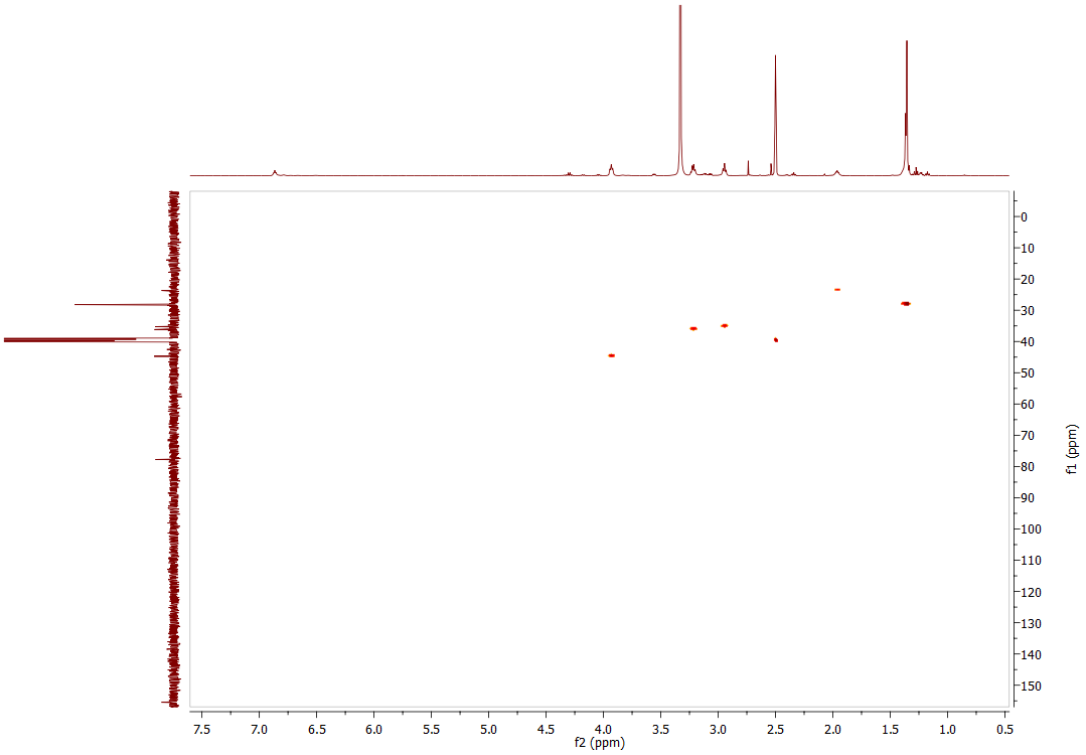

Figure S3.65: HSQC spectrum of **3.11** in DMSO-d_6.

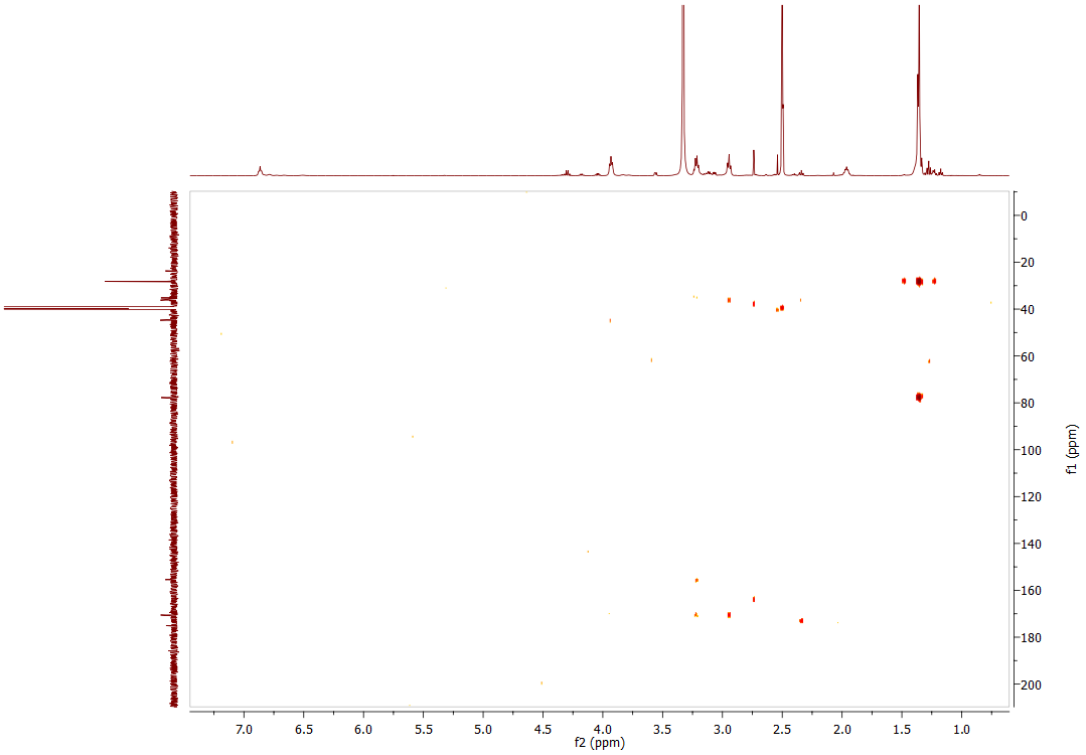

Figure S3.66: HMBC of **3.11** in DMSO-d_6.

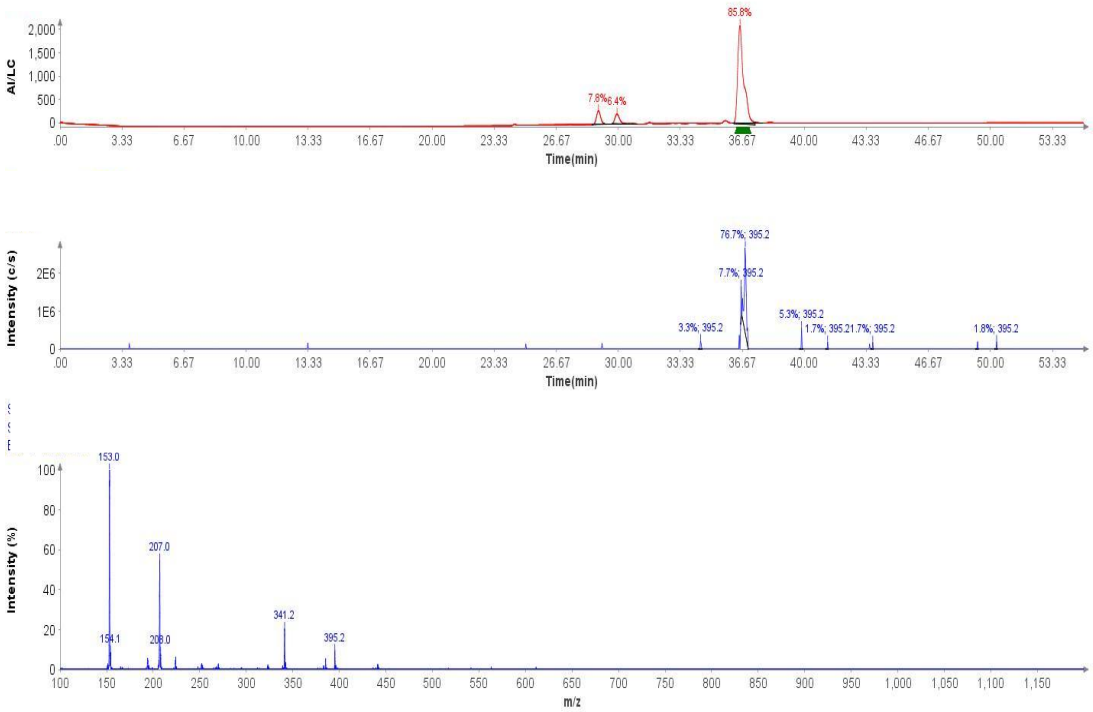

Figure S3.67: LCMS data for **3.11.**

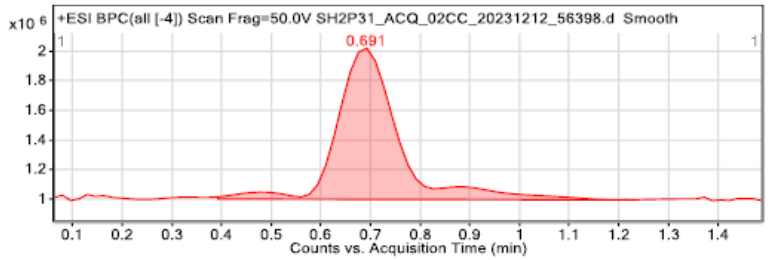

Figure 1: Base peak chromatogram

User Chromatogram Peak List

RT (min)	Area	Area %	Area Sum (%)	Base Peak (m/z)	Width (min)
0.69	8671686	100.00	100.00	563.2676	0.165

Compound Table

Compound Label	RT (min)	Observed mass (m/z)	Neutral observed mass (Da)	Theoretical mass (Da)	Mass error (ppm)	Isotope match score (%)	Error flag
Cpd 1: C23 H44 N4 O8	0.71	527.2898	504.3039	504.3159	-23.89	46.46	m/z tolerance
Cpd 2: C23 H34 N4 O8	0.70	517.2266	494.2366	494.2377	-2.13	90.78	No H adduct

Mass errors of between -5.00 and 5.00 ppm with isotope match scores above 60% are considered confirmation of molecular formulae

Figure: Full range view of Compound spectra and potential adducts.

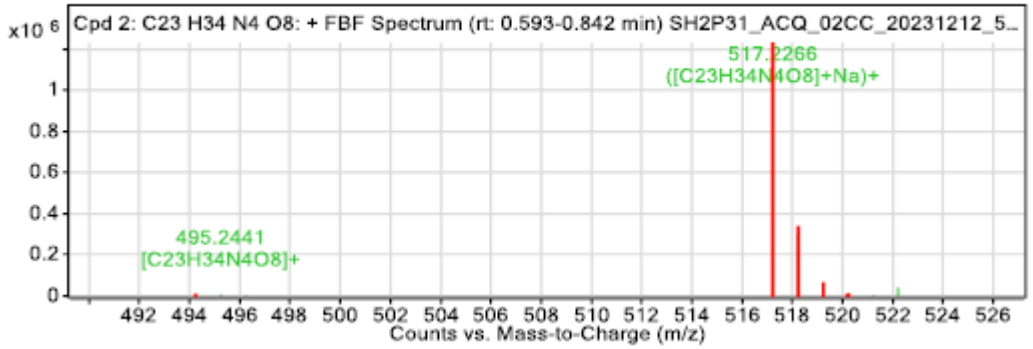

Figure S3.68: HRMS data for **3.11.**

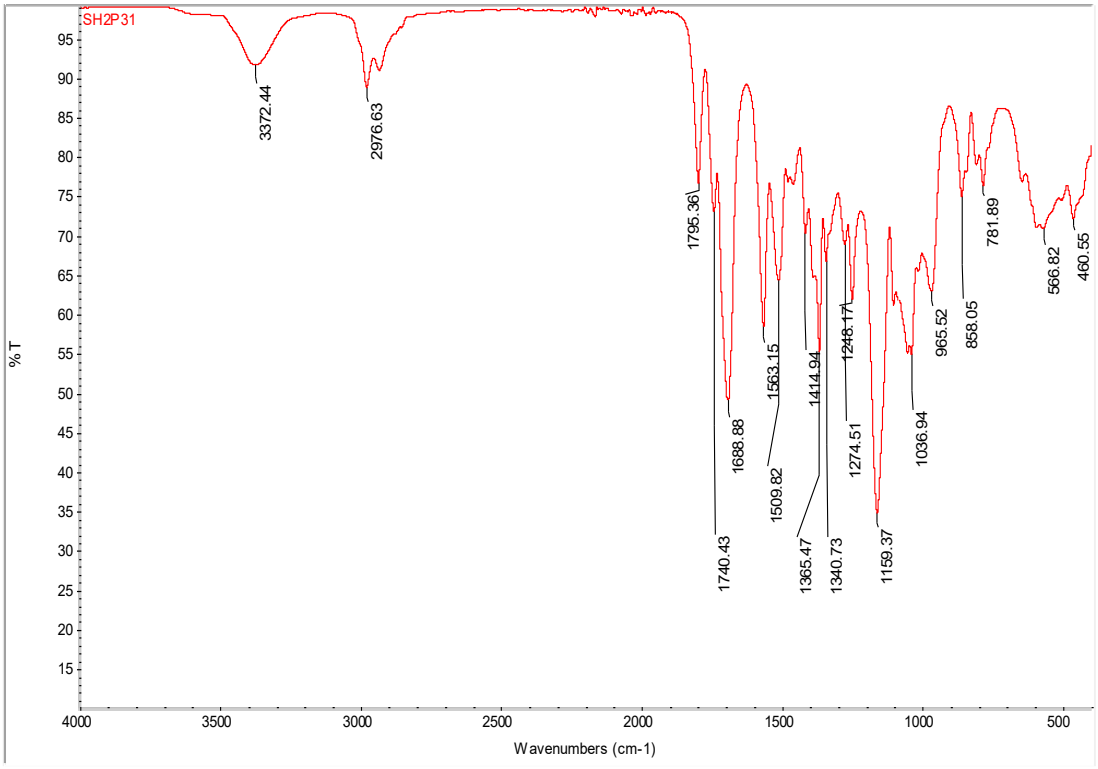

Figure S3.69: IR spectrum of **3.11.**

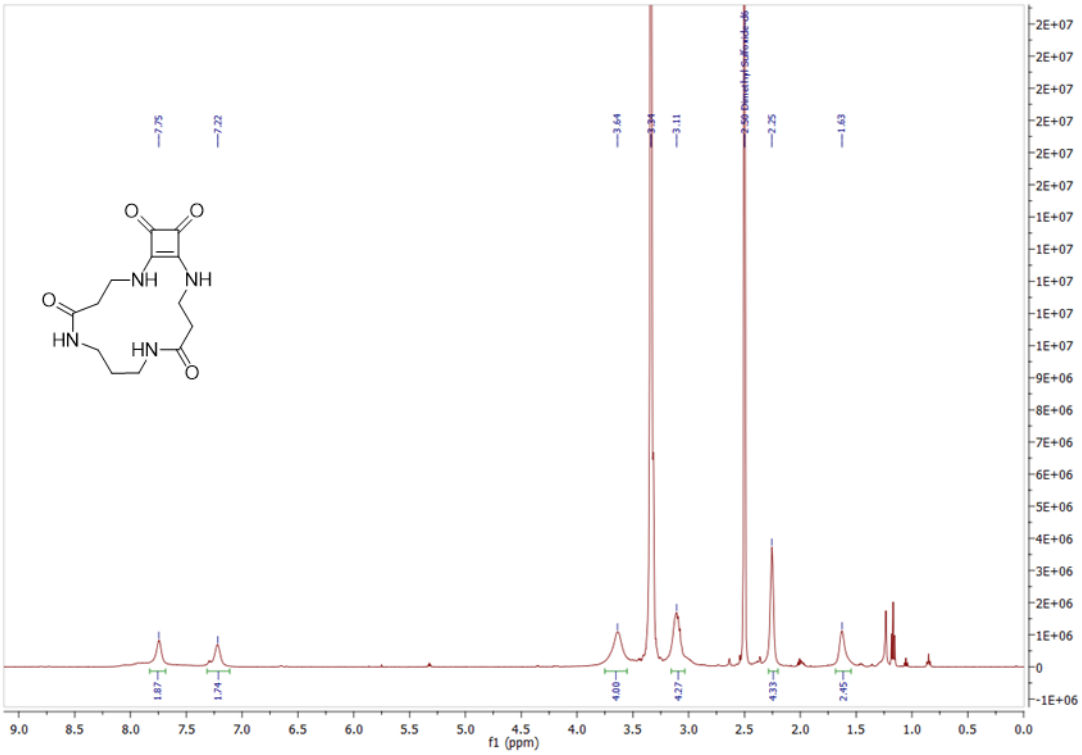

Figure S3.70: ^{1}H NMR spectrum of **3.12** in DMSO-d_6.

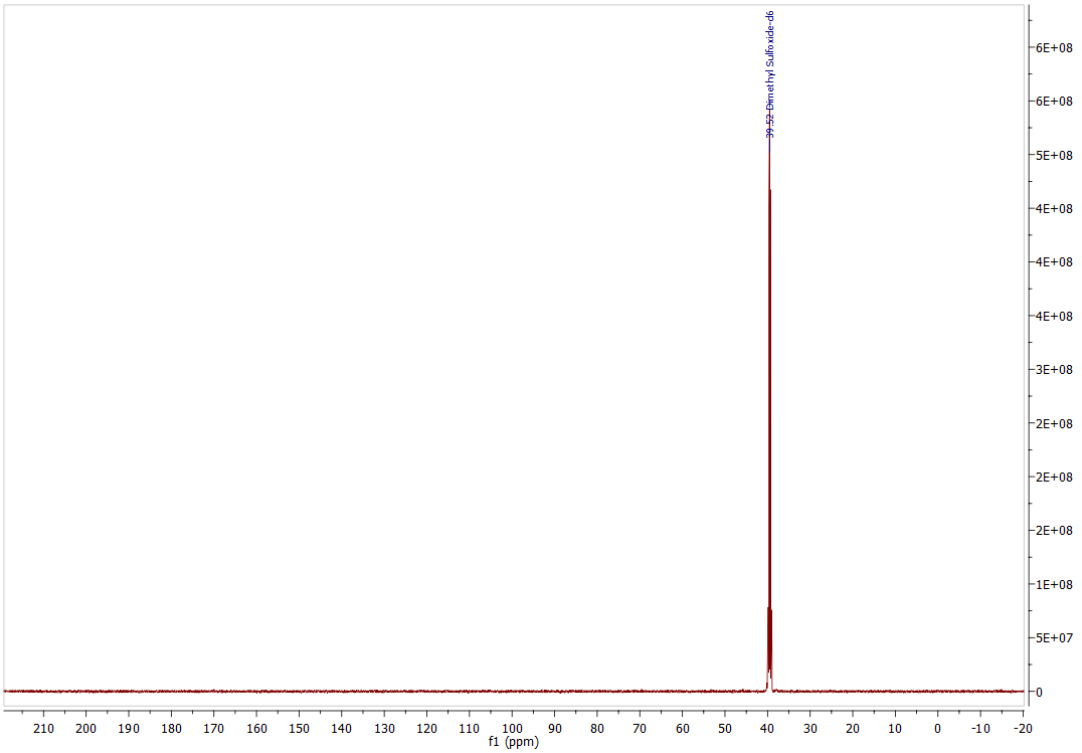

Figure S3.71: ^{13}C NMR spectrum of **3.12** in DMSO-d_6.

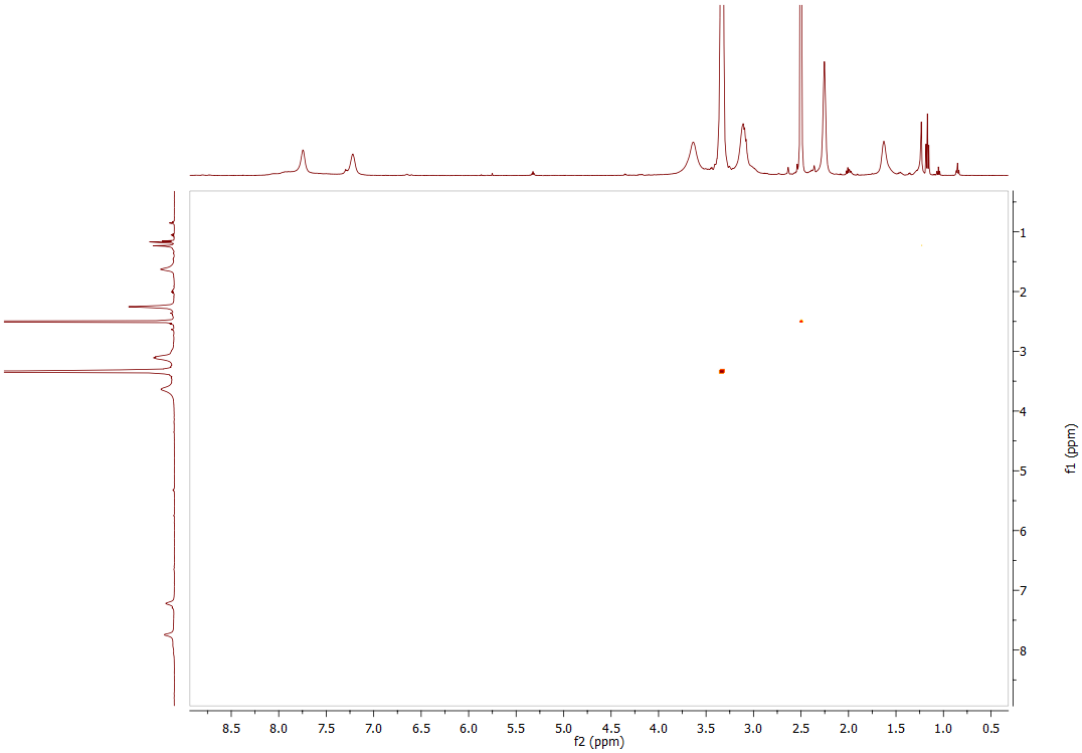

Figure S3.72: COSY spectrum of **3.12** in DMSO-d_6.

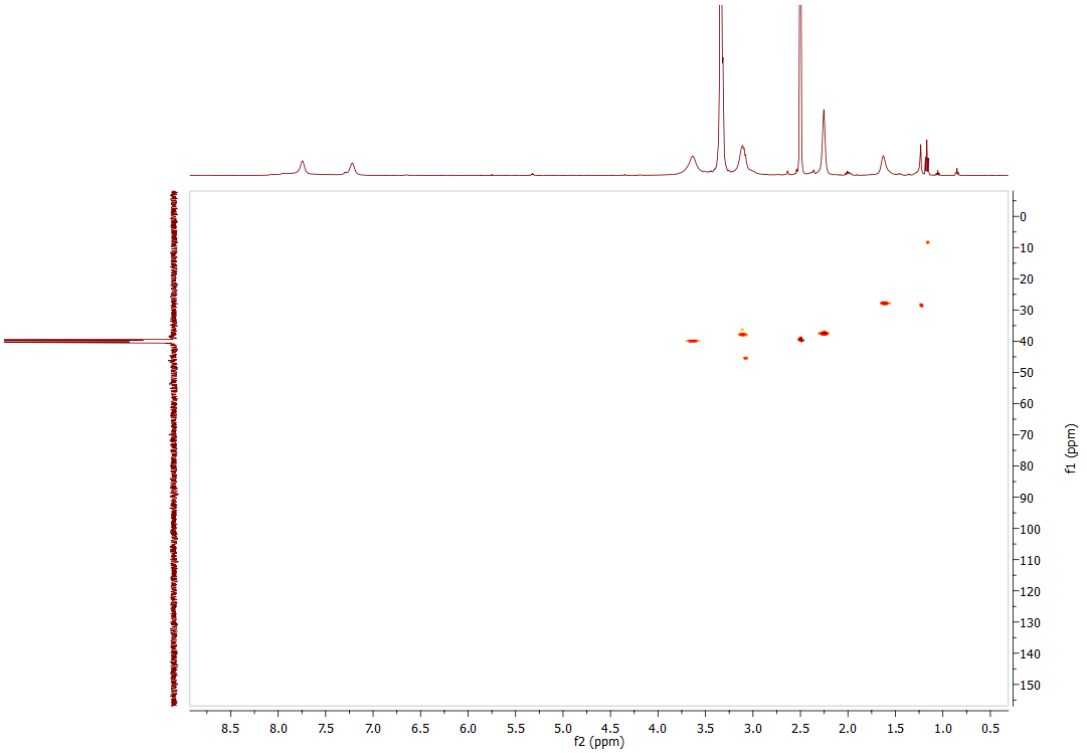

Figure S3.73: HSQC spectrum of **3.12** in DMSO-d_6.

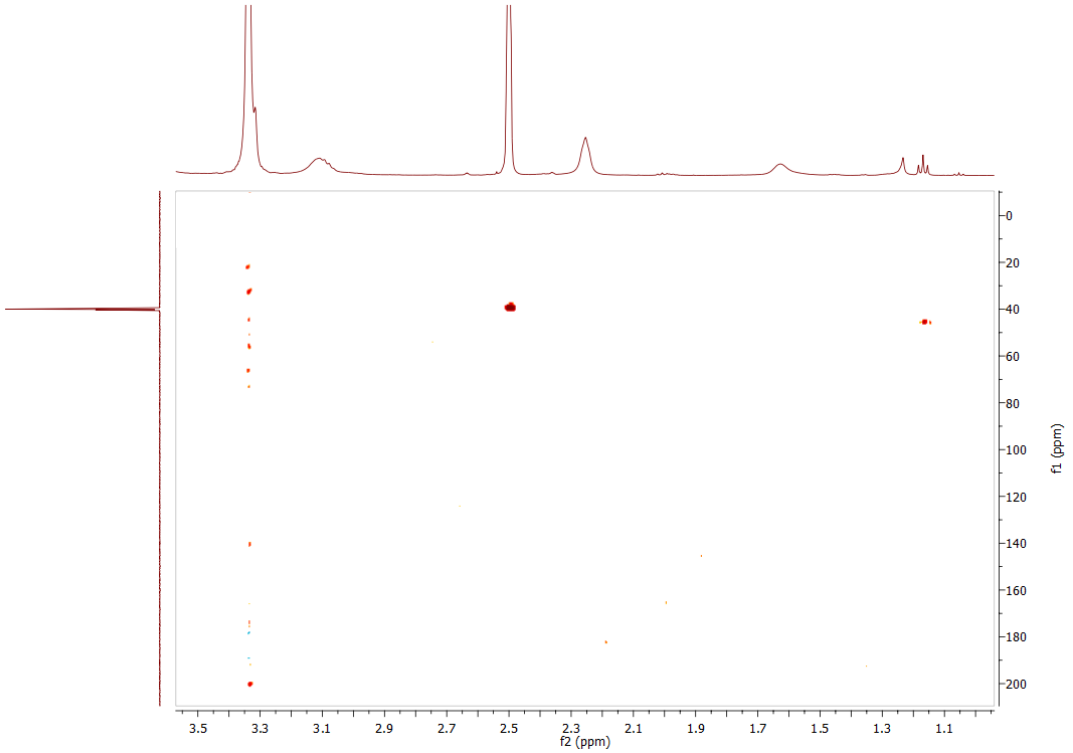

Figure S3.74: HMBC spectrum of **3.12** in DMSO-d_6.

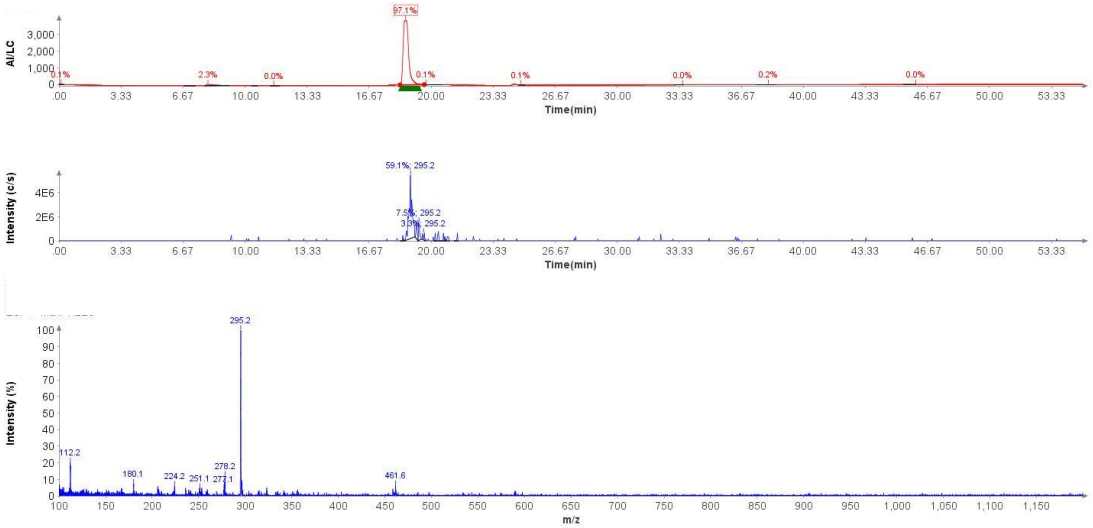

Figure S3.75: LCMS data for **3.12**.

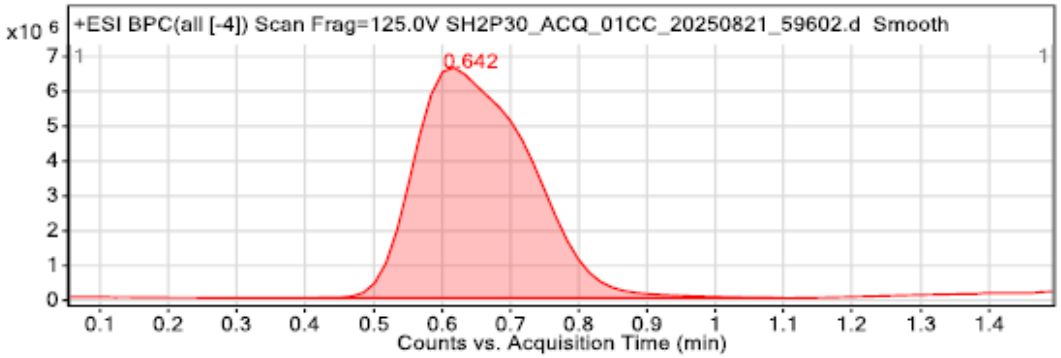

Compound Table

Compound Label	RT (min)	Observed mass (m/z)	Neutral observed mass (Da)	Theoretical mass (Da)	Mass error (ppm)	Isotope match score (%)
Cpd 1: C13 H18 N4 O4	0.65	295.1402	294.1317	294.1328	-3.64	87.24

Mass errors of between -5.00 and 5.00 ppm with isotope match scores above 60% are considered confirmation of molecular formulae

Figure: Full range view of Compound spectra and potential adducts.

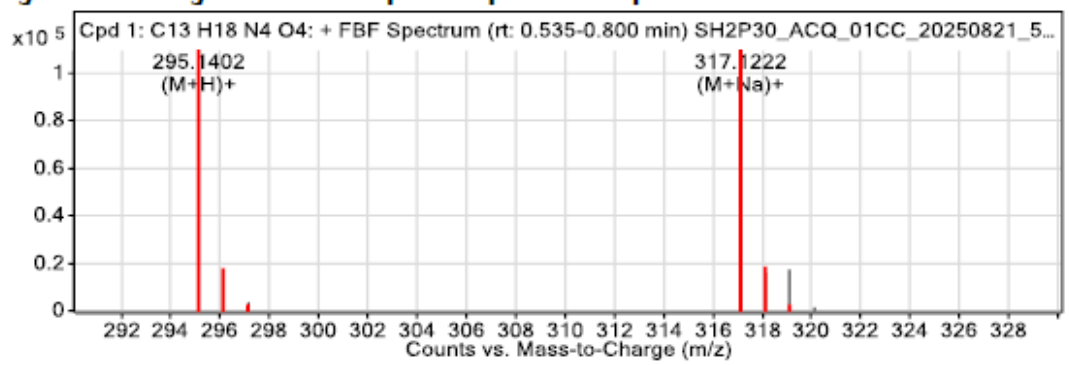

Figure S3.76: HRMS data for **3.12**.

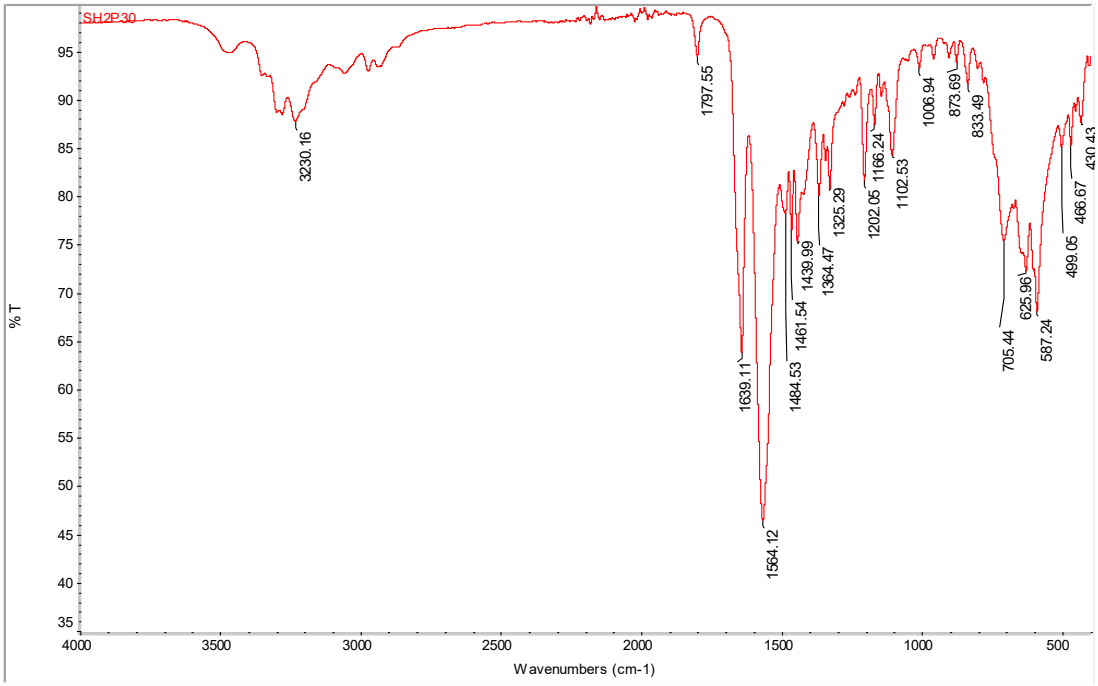

Figure S3.77: IR spectrum of **3.12**.

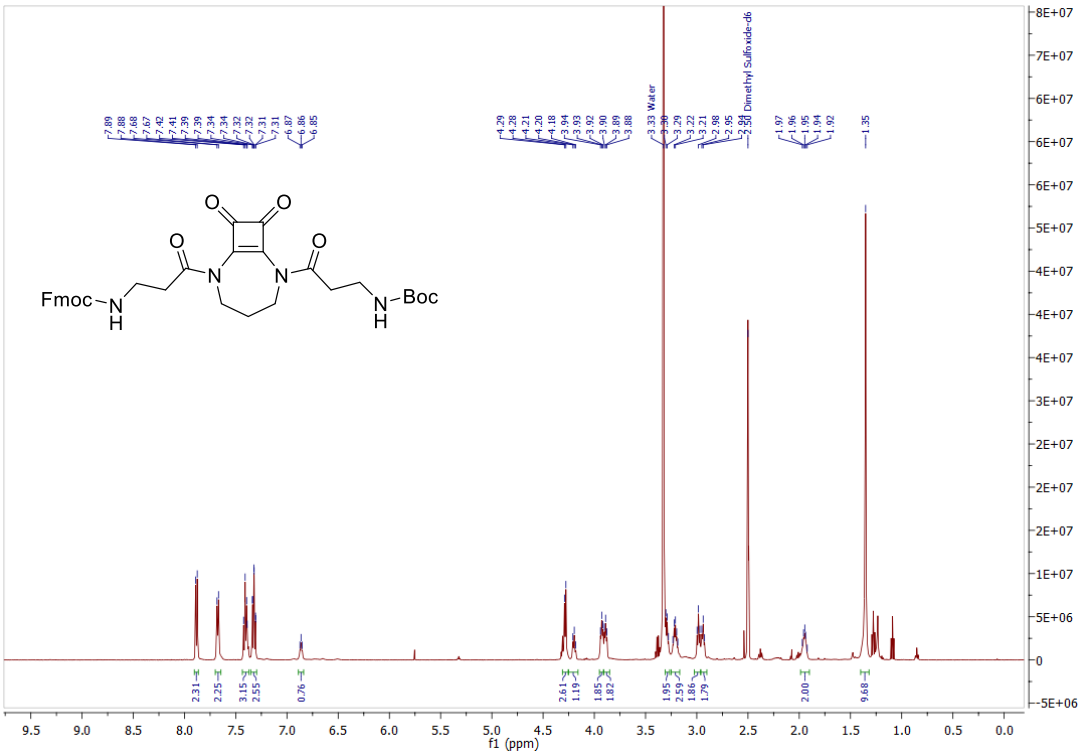

Figure S3.78: ^{1}H NMR spectrum of **3.13** in DMSO-d_6.

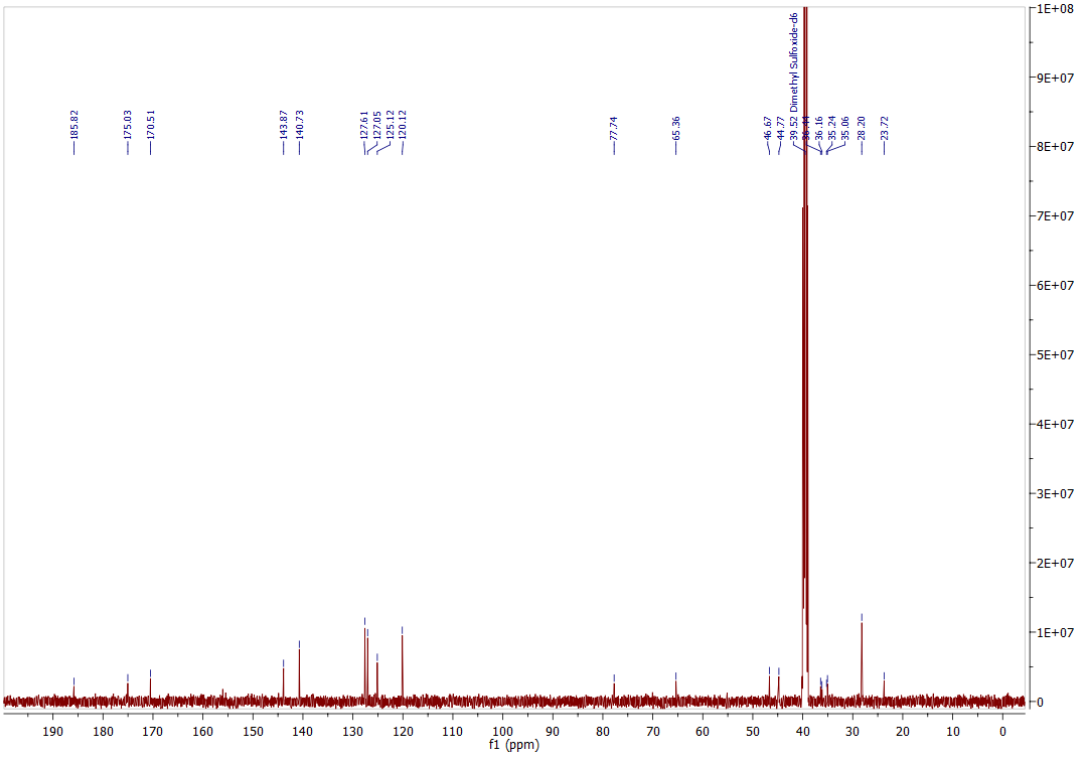

Figure S3.79: ^{13}C NMR spectrum of **3.13** in DMSO-d_6.

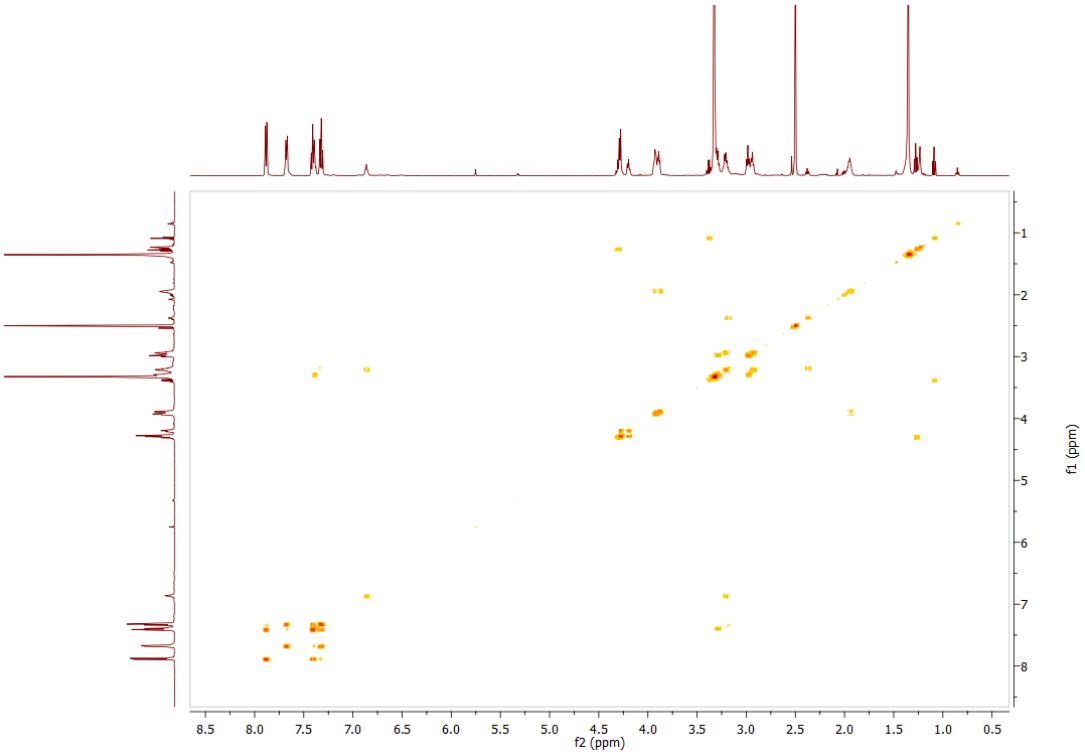

Figure S3.80: COSY spectrum of **3.13** in DMSO-d_6.

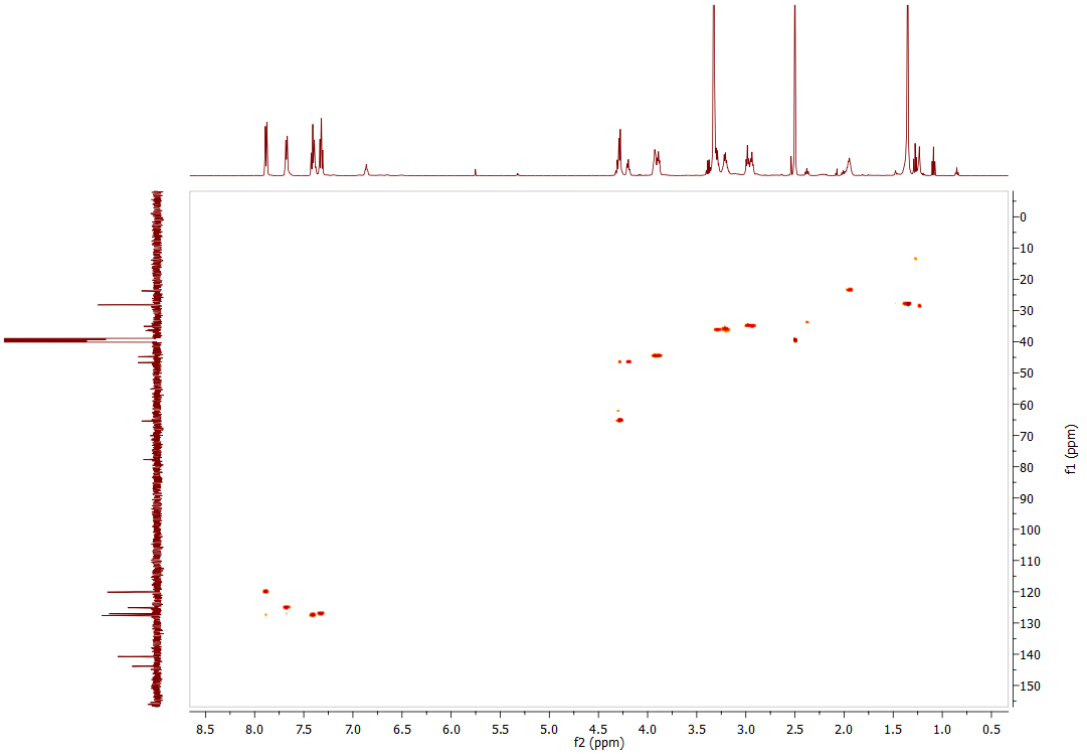

Figure S3.81: HSQC spectrum of **3.13** in DMSO-d_6.

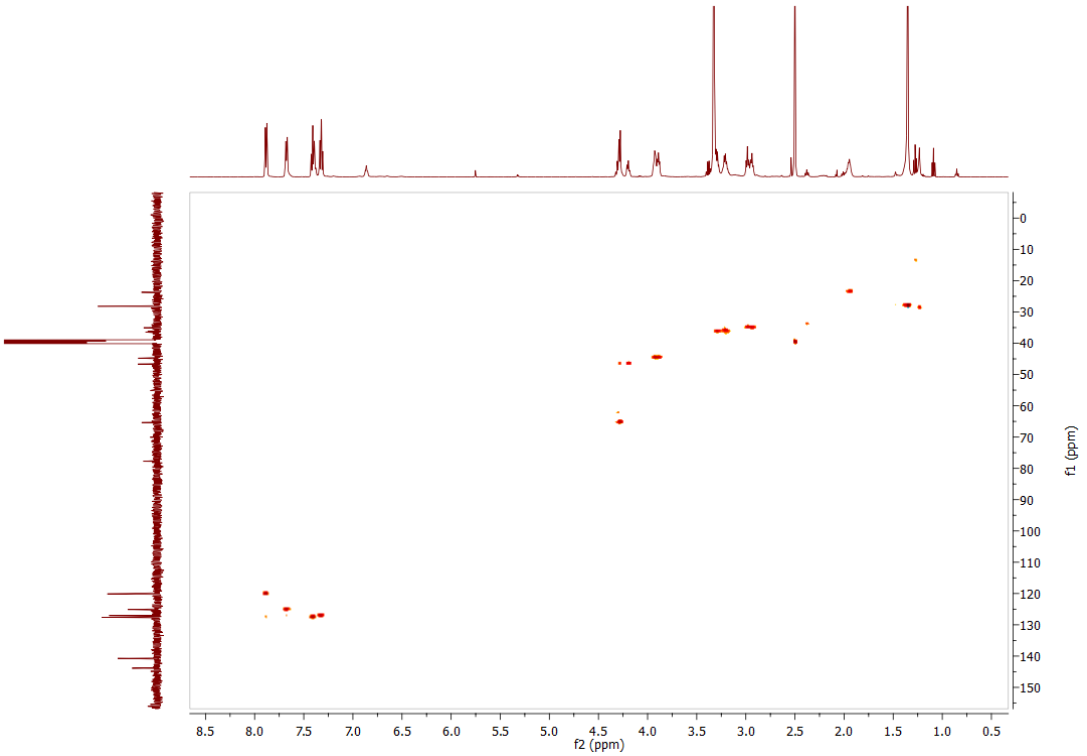

Figure S3.82: HMBC spectrum of **3.13** in DMSO-d_6.

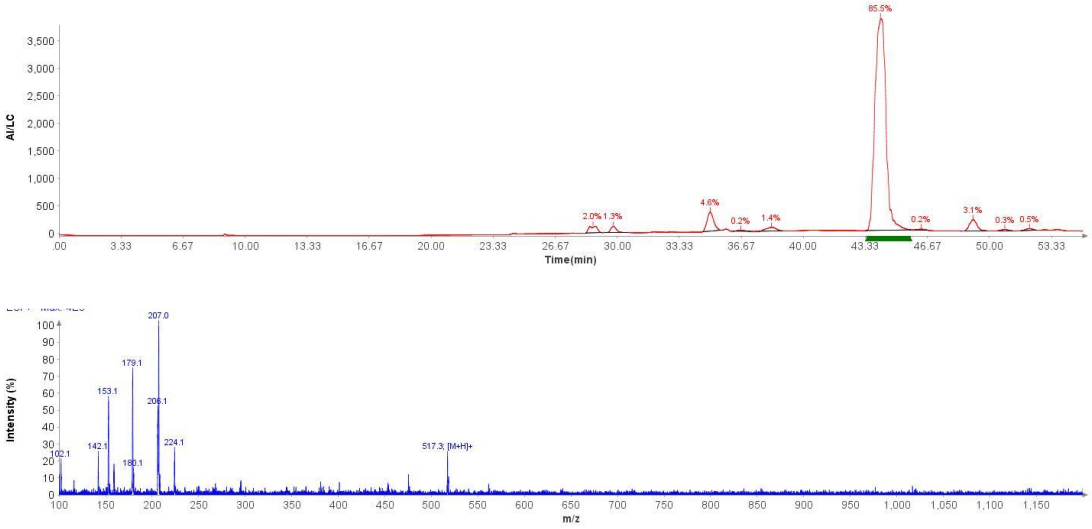

Figure S3.83: LCMS data for **3.13**

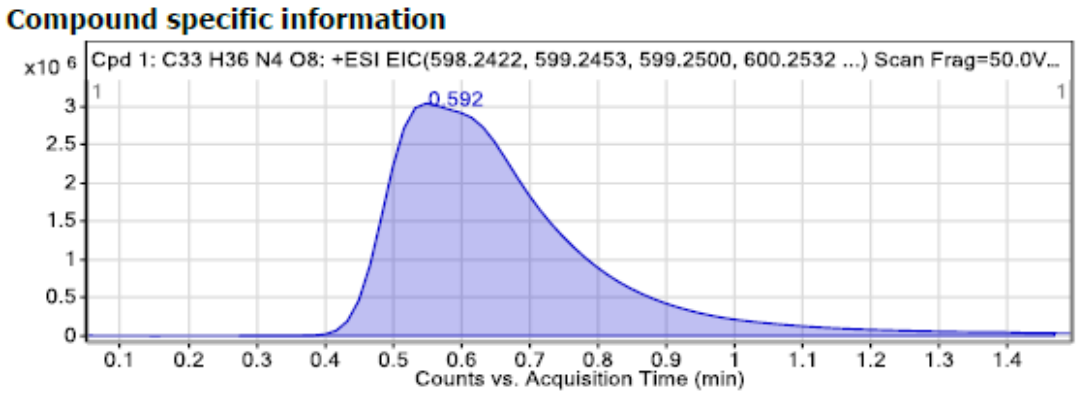

Compound Table

Compound Label	RT (min)	Observed mass (m/z)	Neutral observed mass (Da)	Theoretical mass (Da)	Mass error (ppm)	Isotope match score (%)
Cpd 1: C33 H36 N4 O8	0.59	639.2427	616.2532	616.2533	-0.12	97.82

Mass errors of between -5.00 and 5.00 ppm with isotope match scores above 60% are considered confirmation of molecular formulae

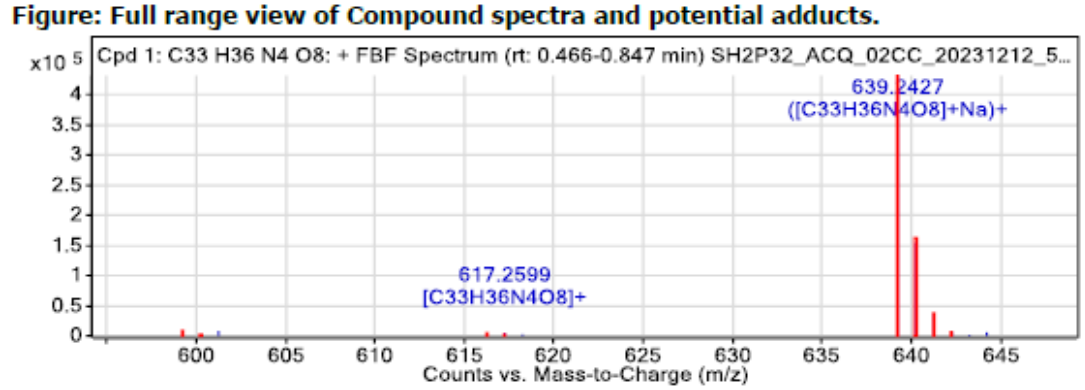

Figure S3.84: HRMS data for **3.13.**

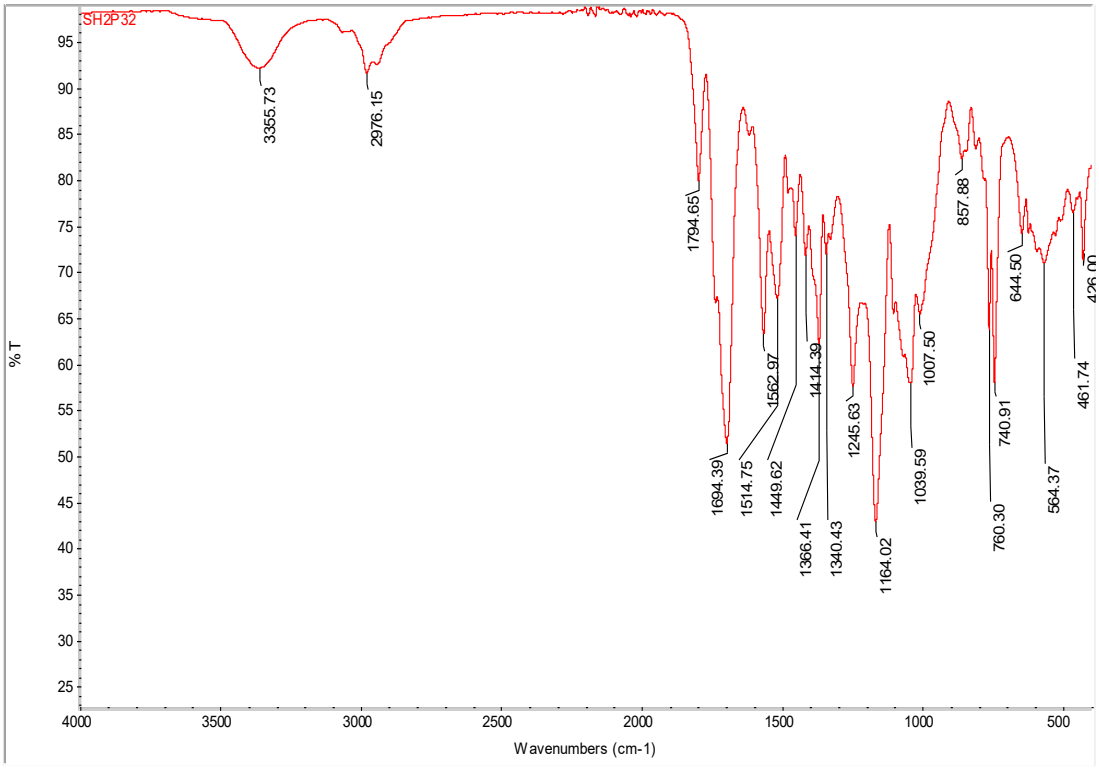

Figure S3.85: IR spectrum of **3.13**.

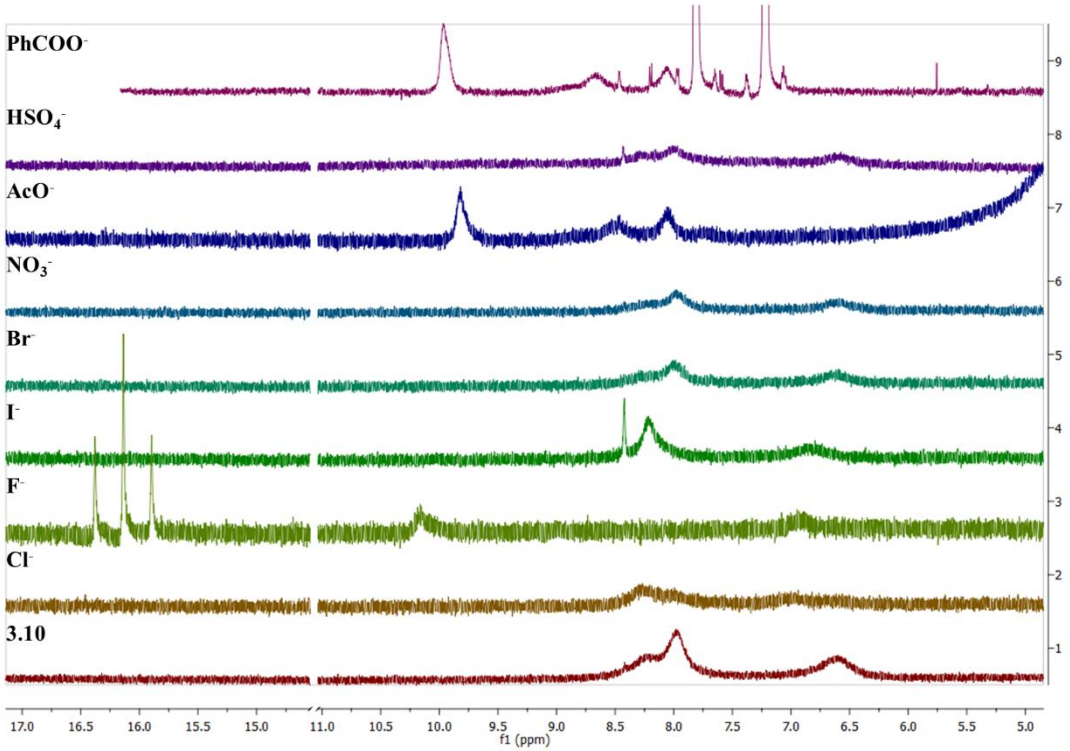

Figure S3.86: ^{1}H NMR stack plot of **3.10** (5 mM) in DMSO-d_6 treated with TBA salts of various anions (10 equiv.).

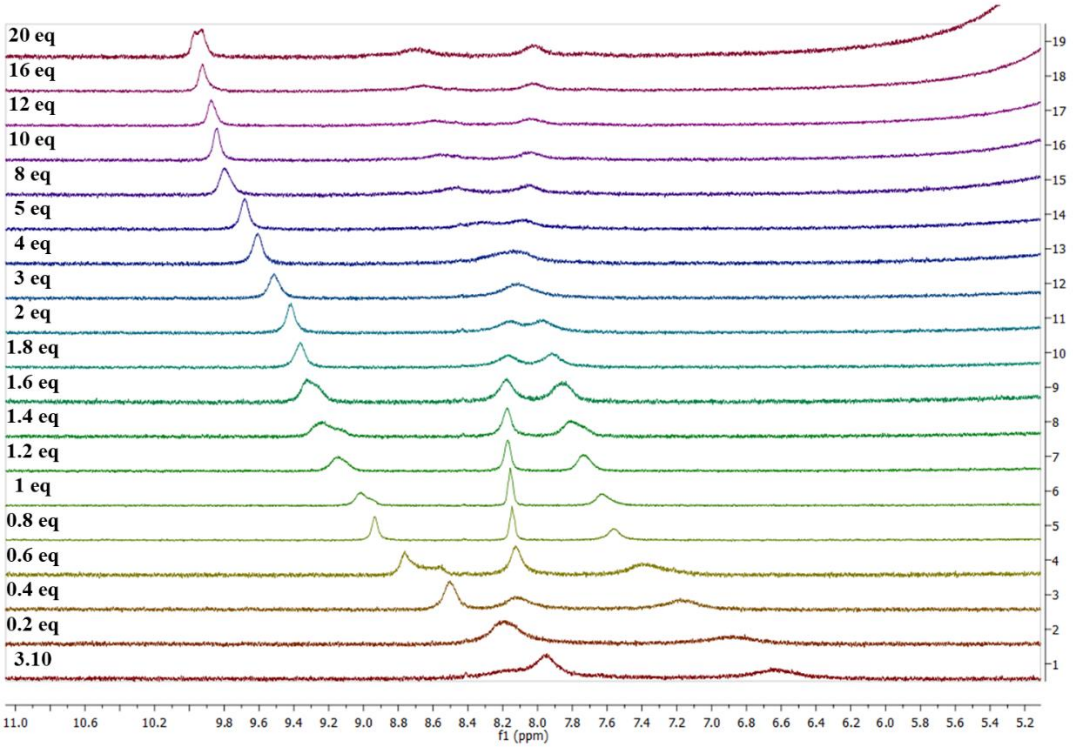

Figure S3.87: ^{1}H NMR stack plot of **3.10** (2.5 mM) and 0.0 – 20 eq. of TBA acetate in DMSO-d_6.

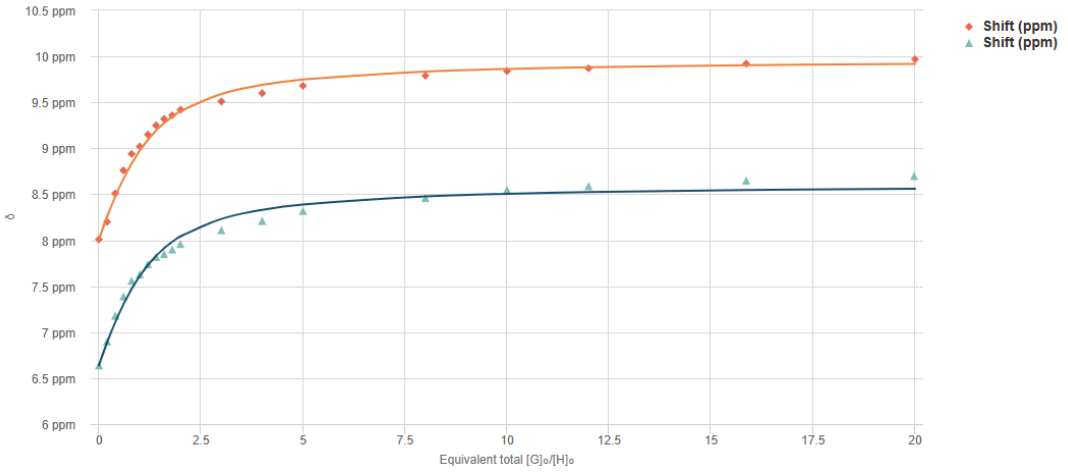

Figure S3.88: Fitted binding isotherm for the titration of **3.10** (2.5 mM) in the presence of increasing concentrations of AcO^- in DMSO-d_6. The data is fitted to 1:1 binding model and shows the chemicals shifts of the NH signals throughout the titration.

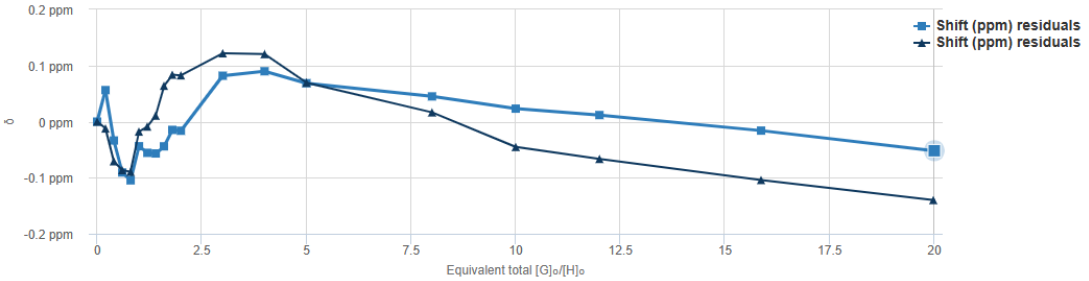

Figure S.89: Residual plot of **3.10** with AcO^-.

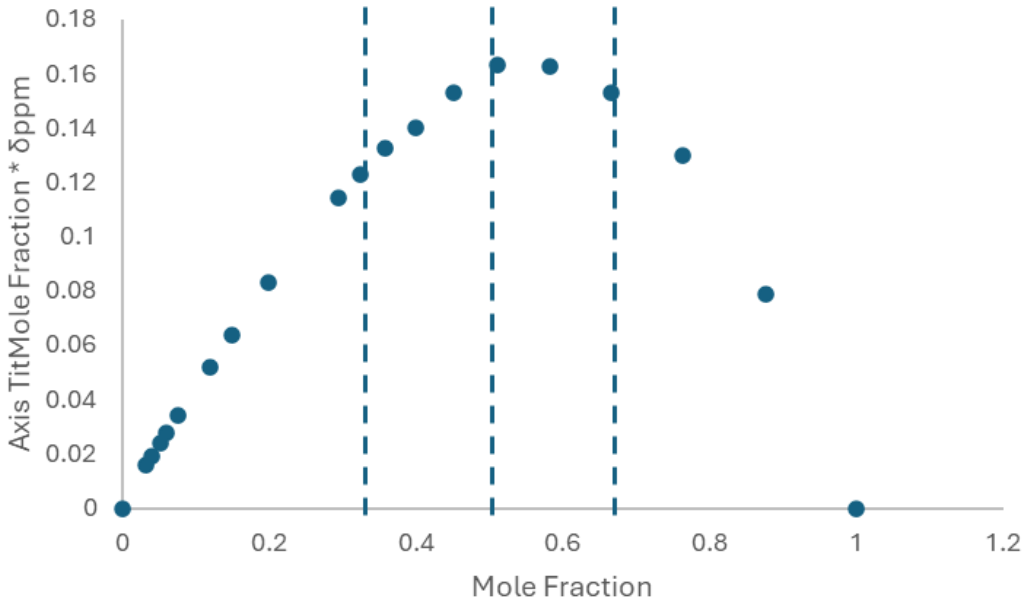

Figure S3.90: Jobs plot of ($\chi_o \times \Delta\delta_{nh}$) vs. mole fraction of host (χ_o) for the squaramide NH proton of **3.10** in titrations with acetate

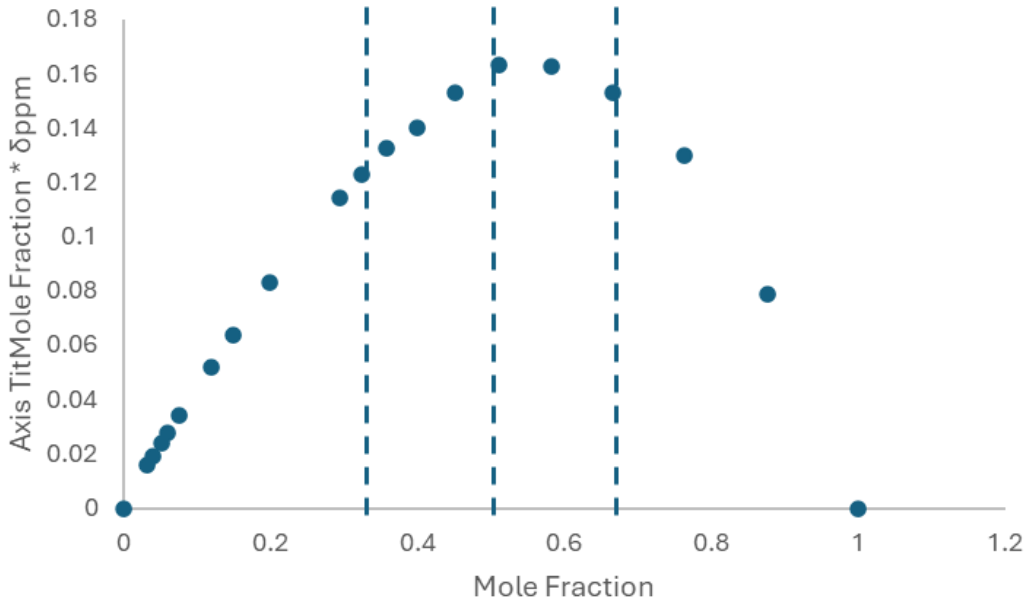

Figure S3.91: Job plot of ($\chi_0 \times \Delta\delta_{nh}$) vs. mole fraction of host (χ_0) for the amide NH proton of **3.10** in titrations with acetate.

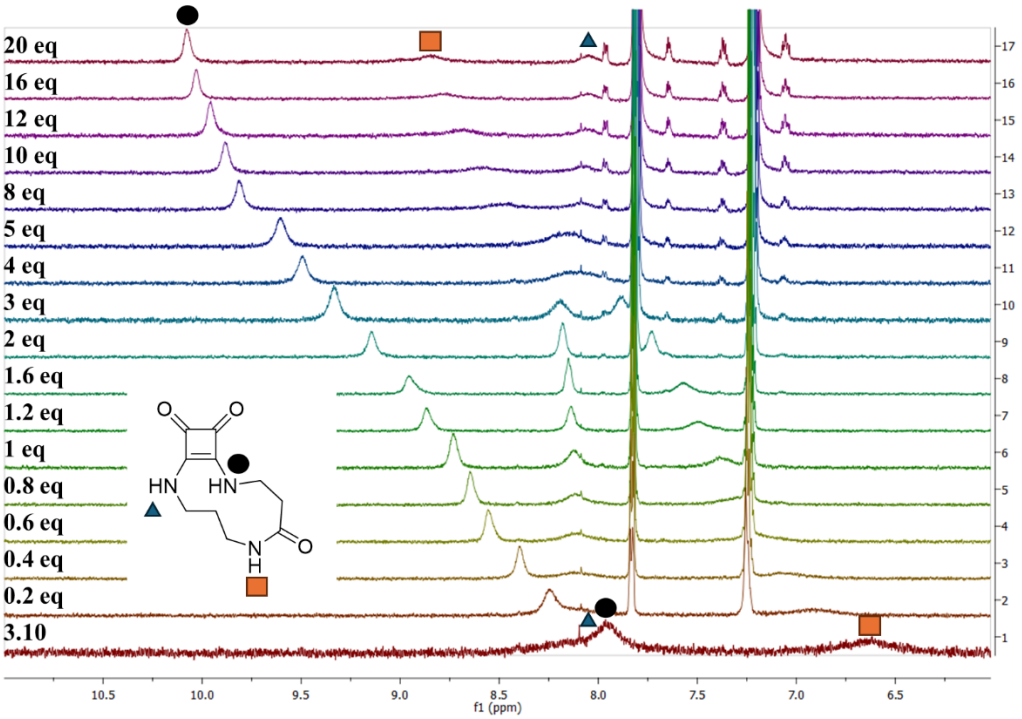

Figure S3.92: ^{1}H NMR stack plot of **3.10** (2.5 mM) and 0.0 – 20 eq. of TBA benzoate in DMSO-d_6.

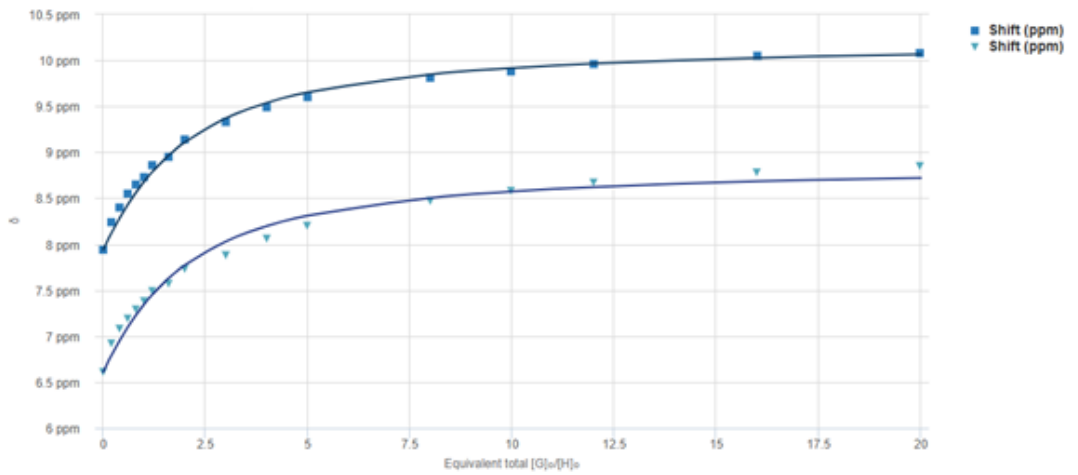

Figure S3.93: Fitted binding isotherm for the titration of **3.10** (2.5 mM) in the presence of increasing concentrations of $PhCOO^-$ in DMSO-d_6. The data is fitted to 1:1 binding model and shows the chemicals shifts of the NH signals throughout the titration.

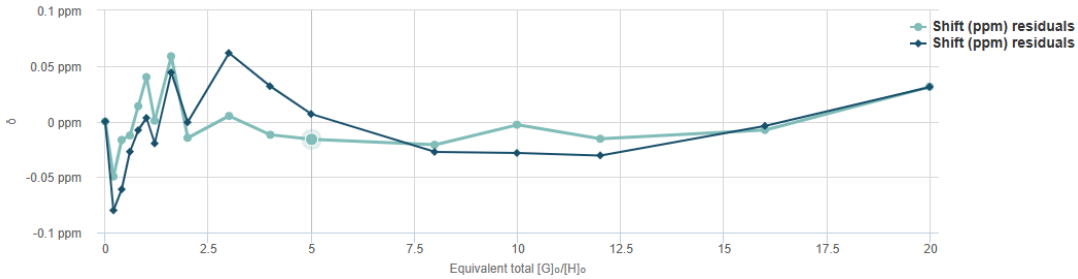

Figure S3.94: Residual plot of **3.10** with $PhCOO^-$.

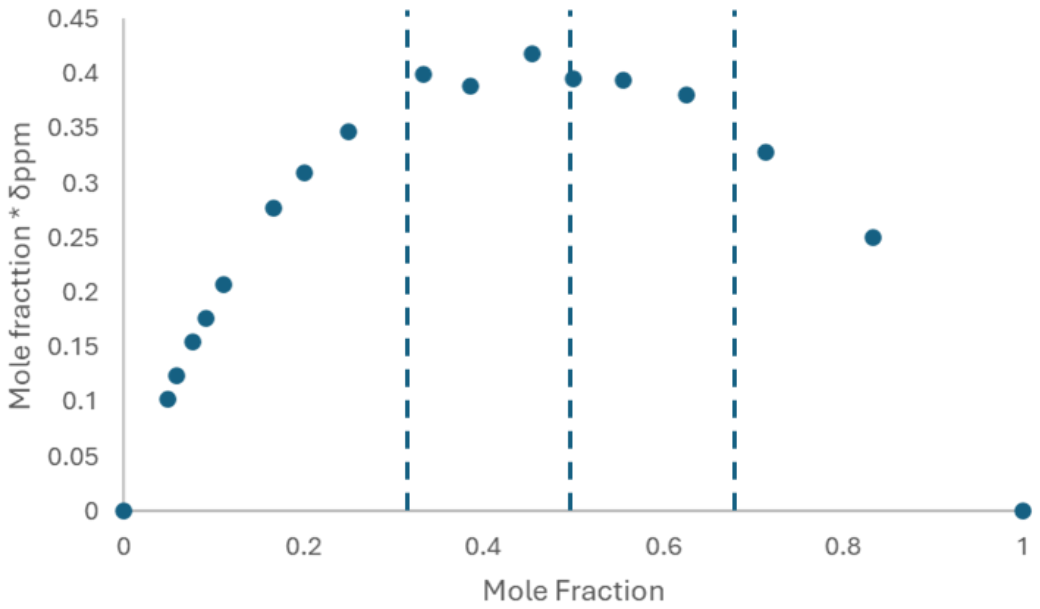

Figure S3.95: Jobs plot of ($\chi_0 \times \Delta\delta_{nh}$) vs. mole fraction of host (χ_0) for the squaramide NH proton of **3.10** in titrations with benzoate

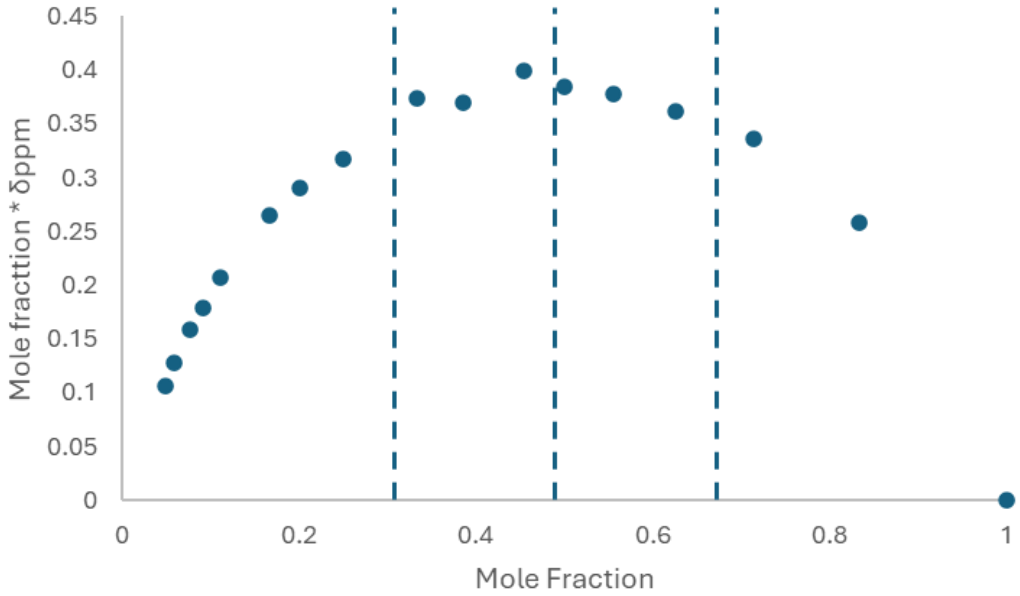

Figure S3.96: Job plot of ($\chi_0 \times \Delta\delta_{nh}$) vs. mole fraction of host (χ_0) for the amide NH proton of **3.10** in titrations with benzoate.

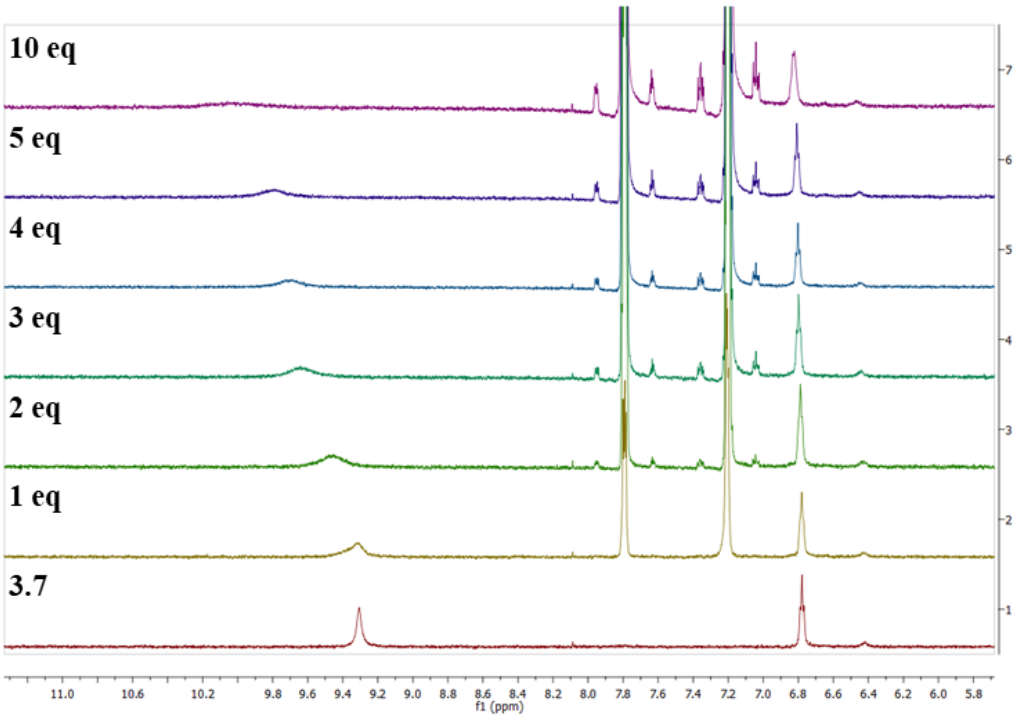

Figure S3.97: ^{1}H NMR stack plot of **3.7** (2.5 mM) and 0.0 – 20 eq. of TBA PhCOO$^-$ in DMSO-d_6.

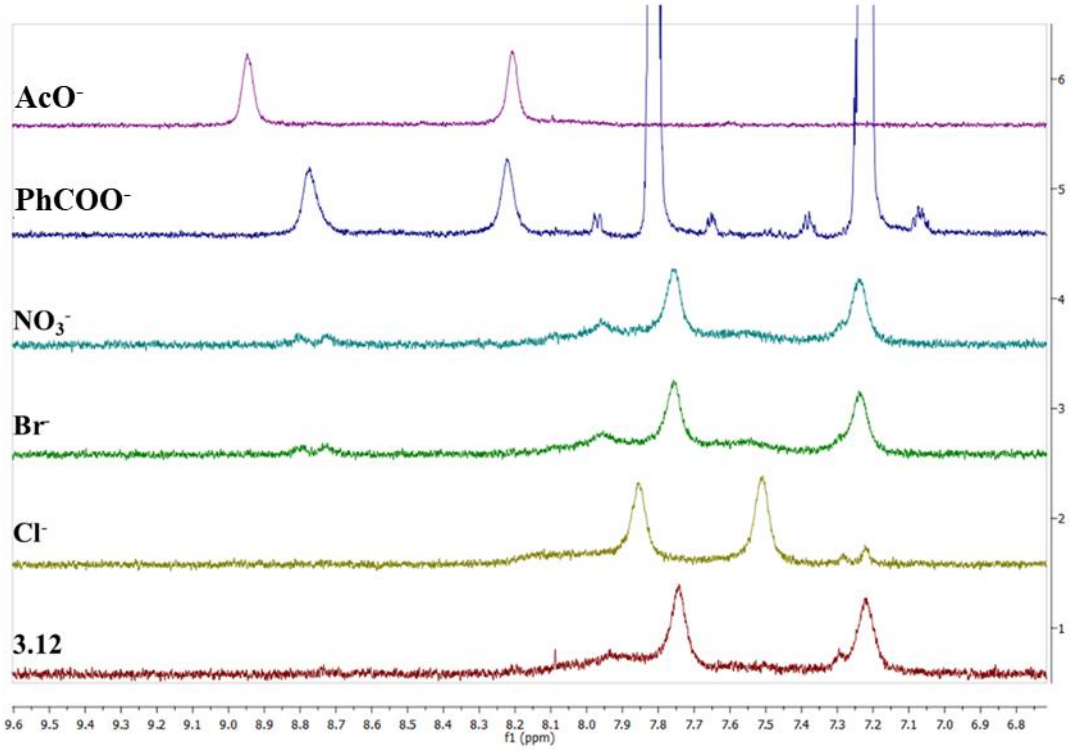

Figure S3.98: ^{1}H NMR stack plot of **3.12** (2.5 mM) in DMSO-d_6 treated with TBA salts of various anions (10 equiv.).

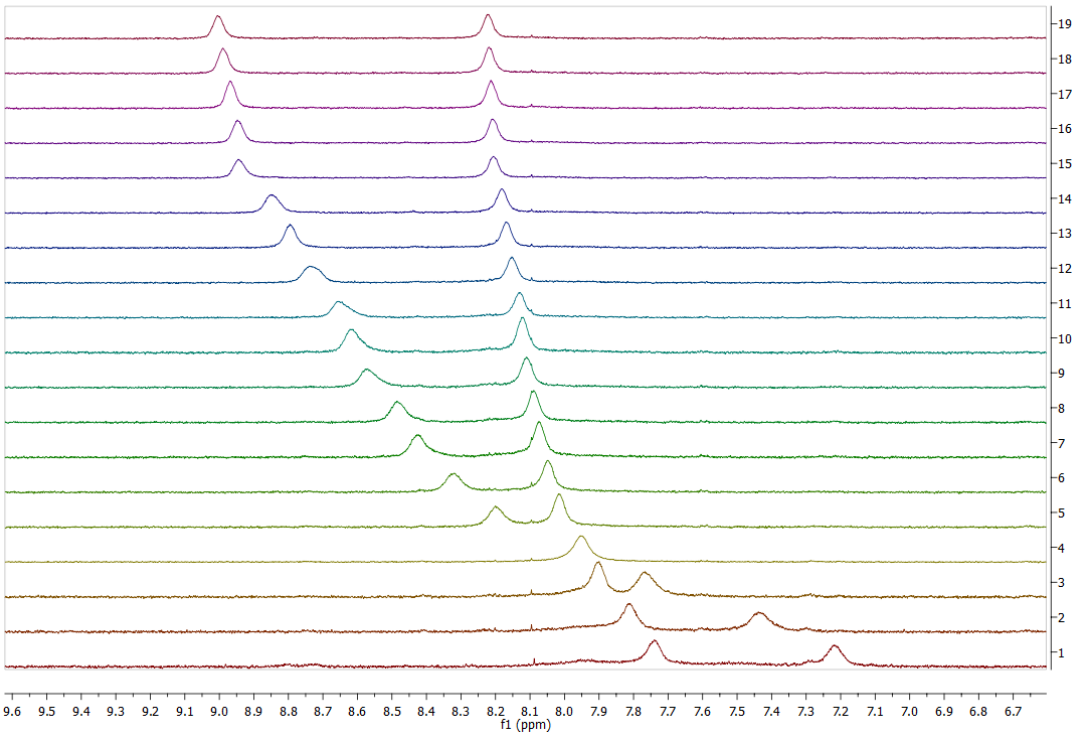

Figure S3.99: ^{1}H NMR stack plot of **3.12** (2.5 mM) and 0.0 – 20 eq. of TBA acetate in DMSO-d_6.

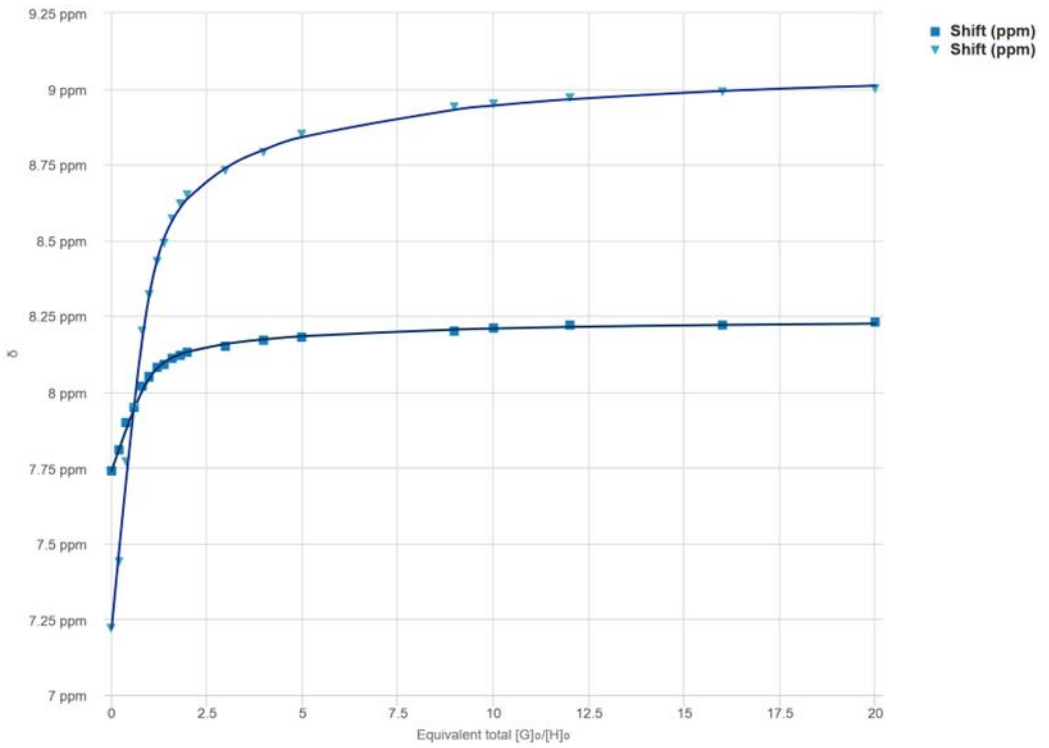

Figure S3.100: Fitted binding isotherm for the titration of **3.12** (2.5 mM) in the presence of increasing concentrations of AcO^- in DMSO-d_6. The data is fitted to 1:2 binding model and shows the chemicals shifts of the NH signals throughout the titration.

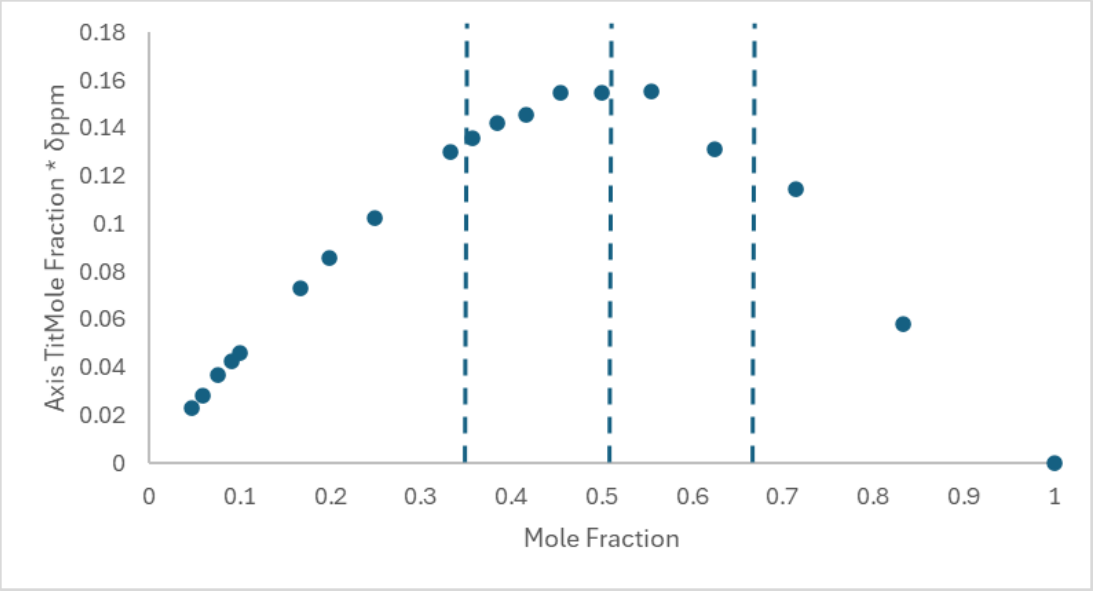

Figure S3.101: Jobs plot of ($\chi_0 \times \Delta\delta_{nh}$) vs. mole fraction of host (χ_0) for the squaramide NH proton of **3.12** in titrations with acetate

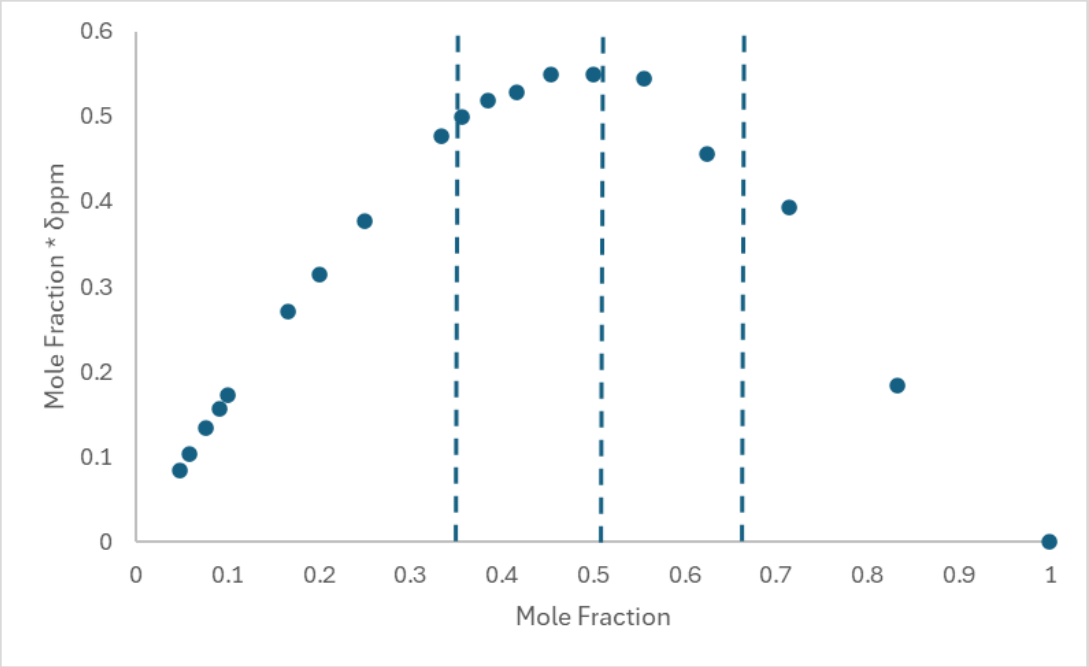

Figure S3.102: Jobs plot of ($\chi_0 \times \Delta\delta_{nh}$) vs. mole fraction of host (χ_0) for the amide NH proton of **3.12** in titrations with acetate

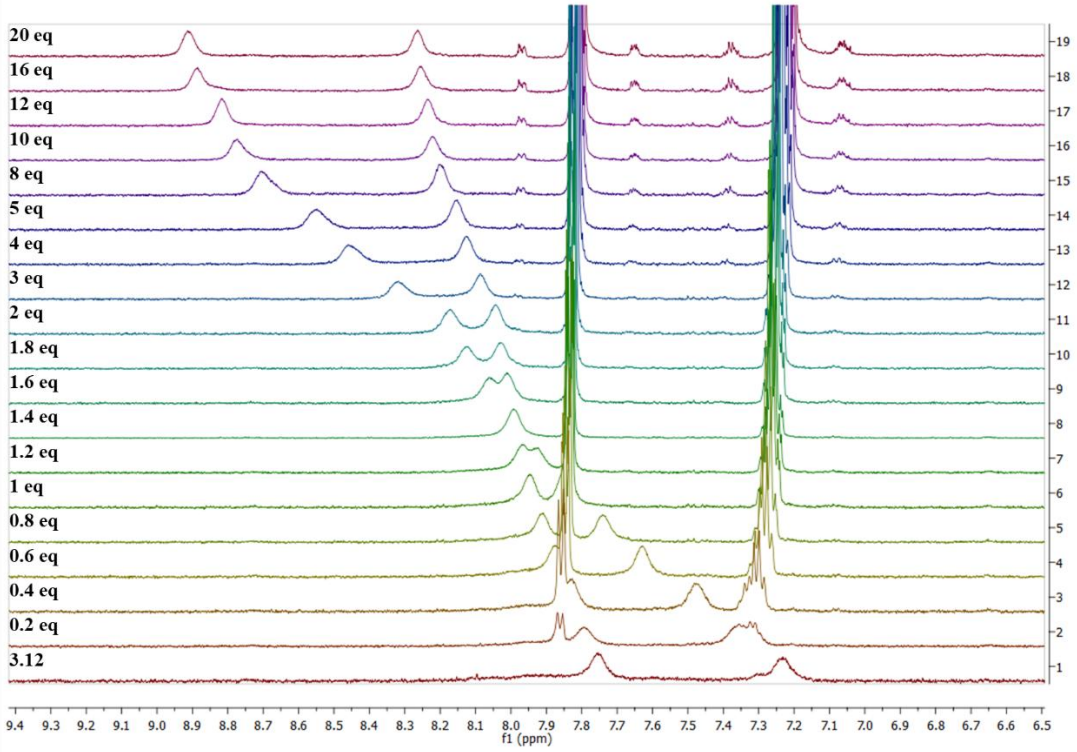

Figure S3.103: ^{1}H NMR stack plot of **3.12** (2.5 mM) and 0.0 – 20 eq. of TBA benzoate in DMSO-d_6.

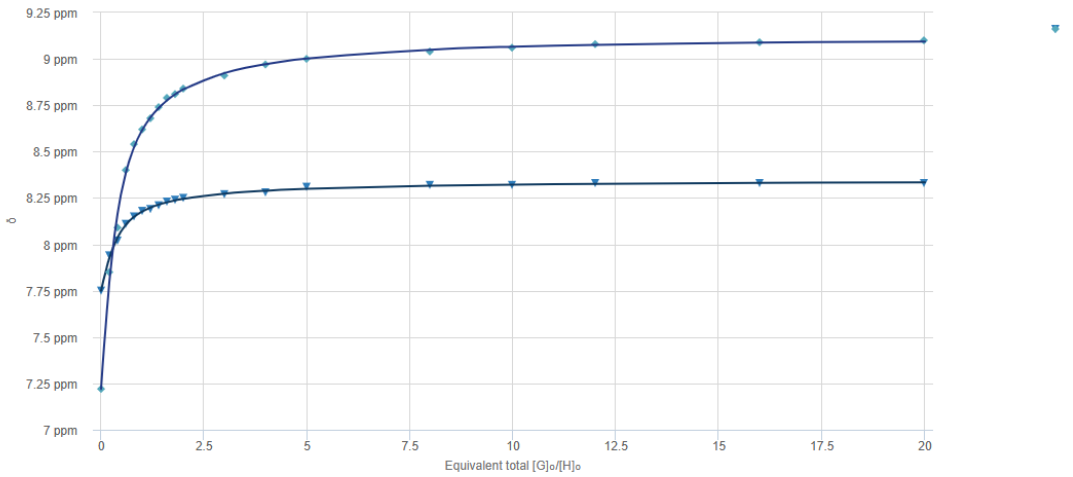

Figure S3.104: Fitted binding isotherm for the titration of **3.12** (2.5mM) in the presence of increasing concentrations of $PhCOO^-$ in DMSO-d_6. The data is fitted to 1:2 binding model and shows the chemicals shifts of the NH signals throughout the titration.

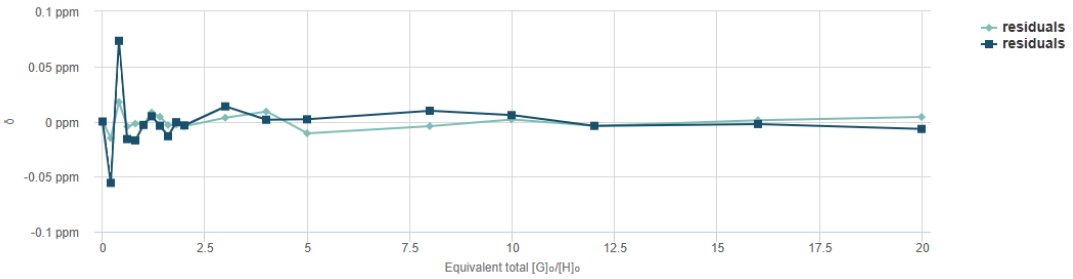

Figure S3.105: Residual plot of **3.12** with $PhCOO^-$.

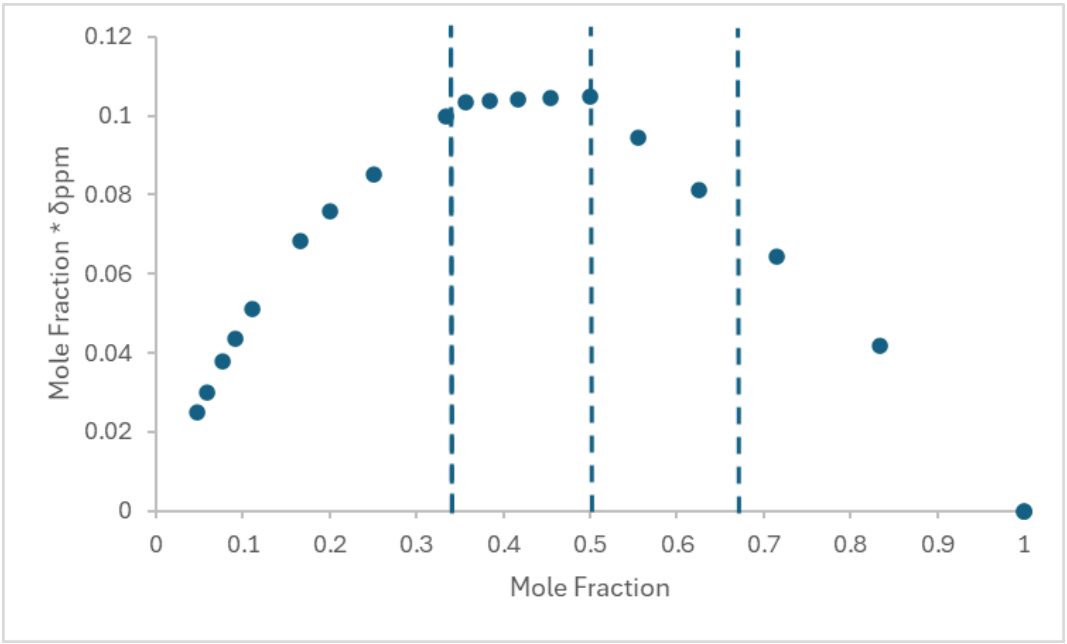

Figure S3.106: Jobs plot of ($\chi_0 \times \Delta\delta_{nh}$) vs. mole fraction of host (χ_0) for the squaramide NH proton of **3.12** in titrations with benzoate.

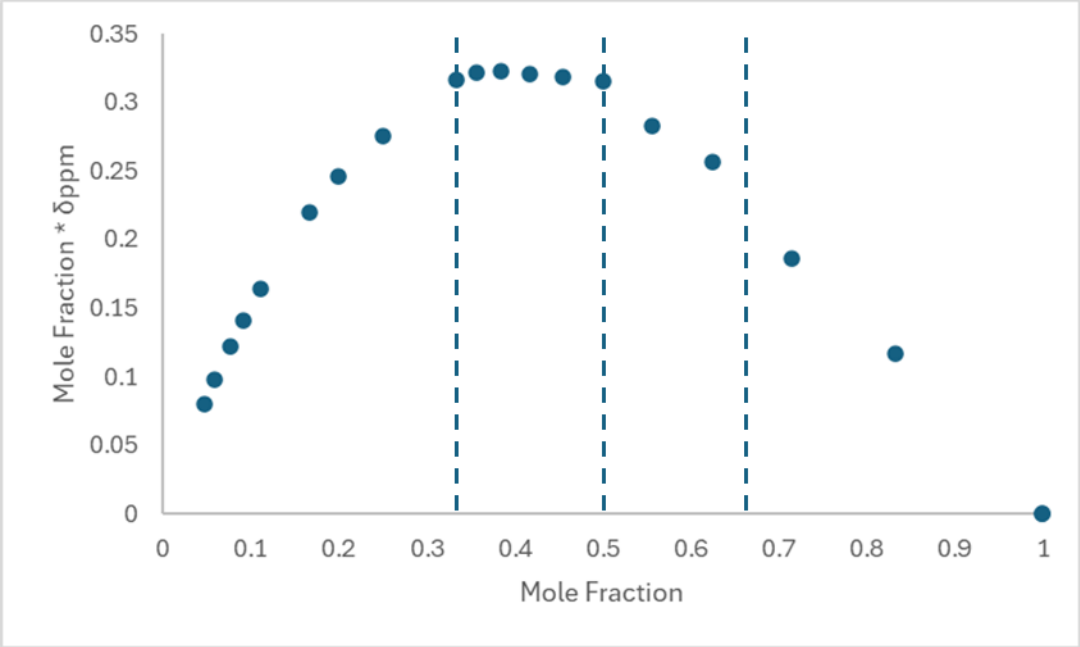

Figure S3.107: Jobs plot of ($\chi_0 \times \Delta\delta_{nh}$) vs. mole fraction of host (χ_0) for the amide NH proton of **3.12** in titrations with benzoate.

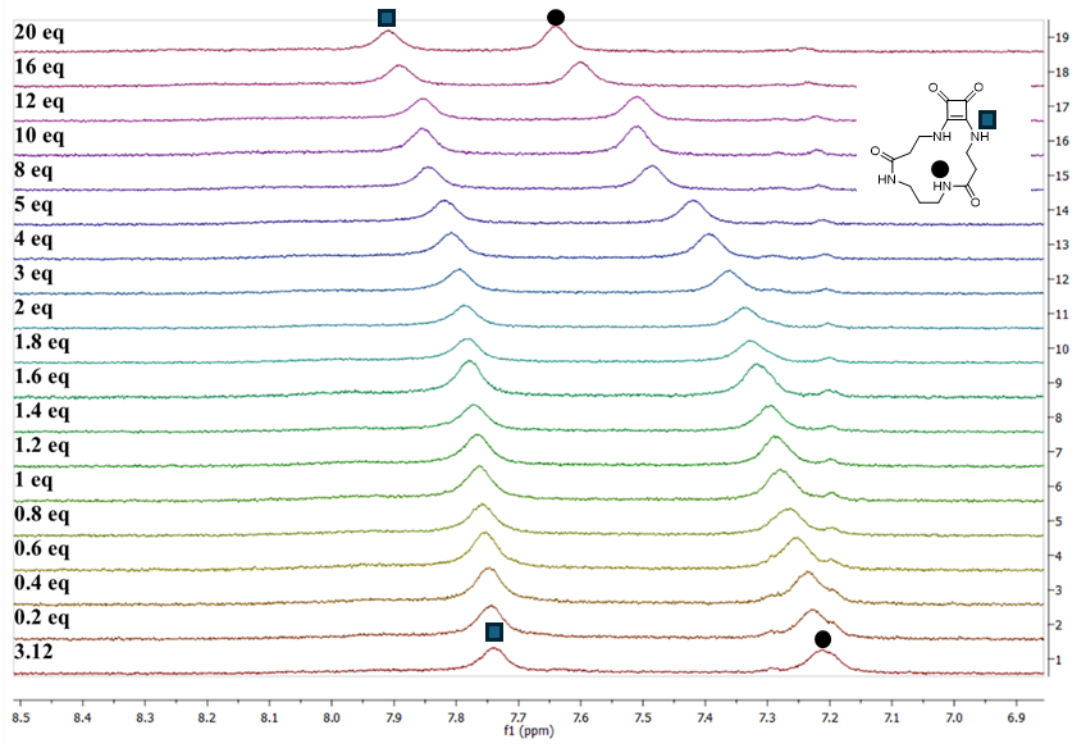

Figure S3.108: ^{1}H NMR stackplot of **3.12** (2.5 mM) and 0.0 – 20 eq. of TBA chloride in DMSO-d_6.

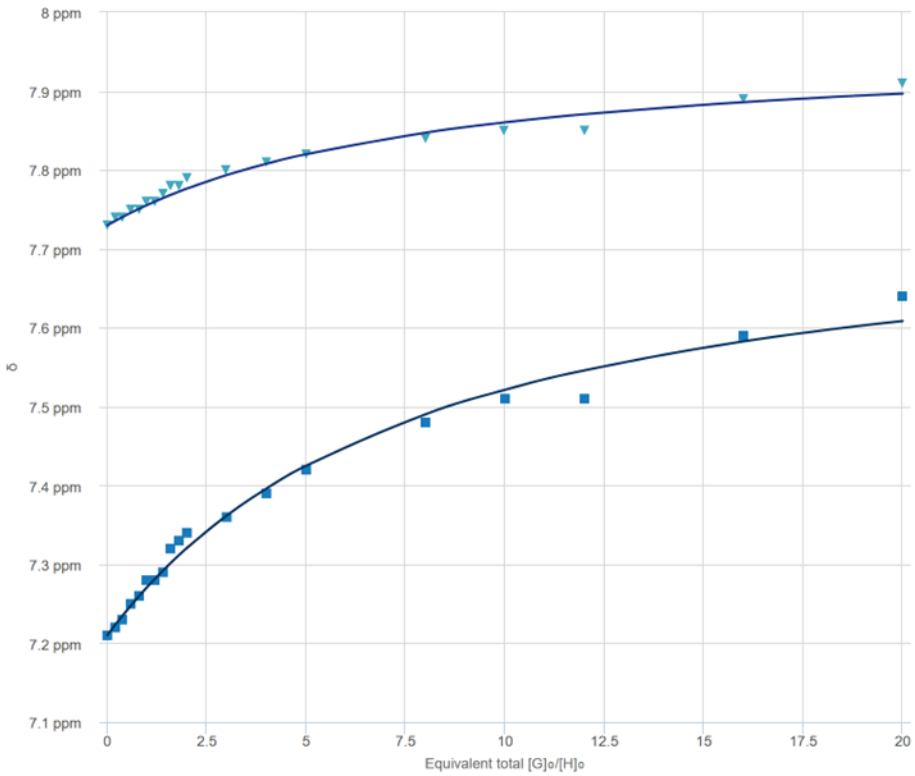

Figure S3.109: Fitted binding isotherm for the titration of **3.12** (2.5mM) in the presence of increasing concentrations of Cl^- in DMSO-d_6. The data is fitted to 1:1 binding model and shows the chemicals shifts of the NH signals throughout the titration.

Chapter 4 – Supplementary Characterisation Data

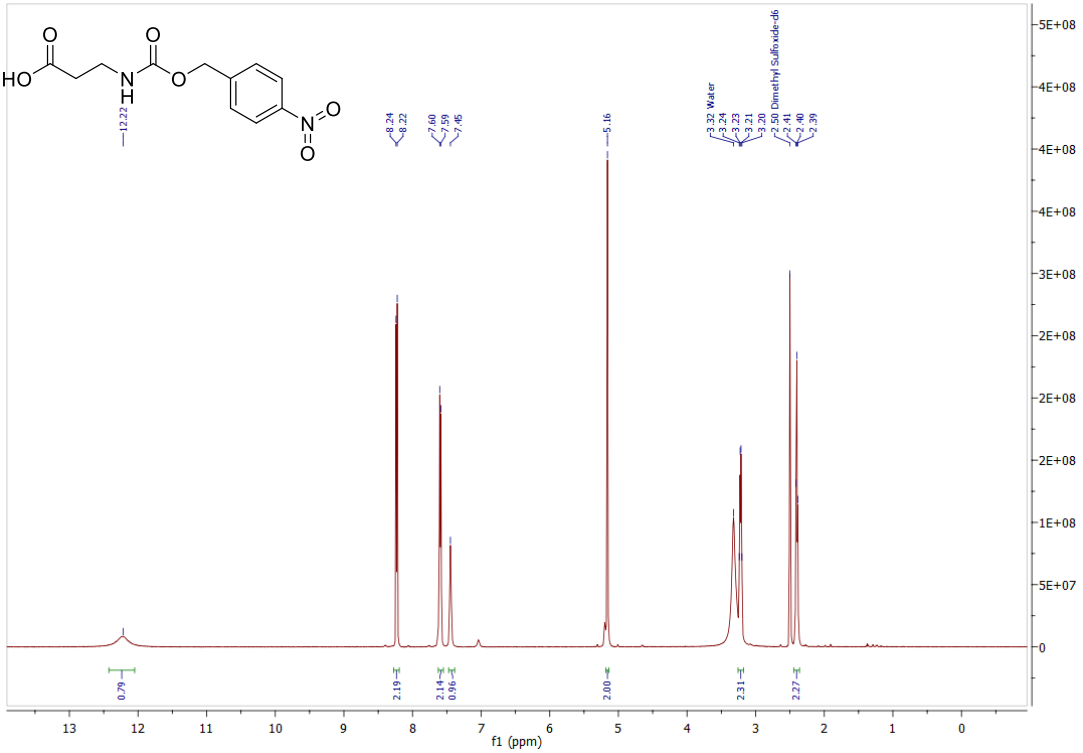

Figure S4.1: ^{1}H NMR spectrum of **4.8** in DMSO-d_6.

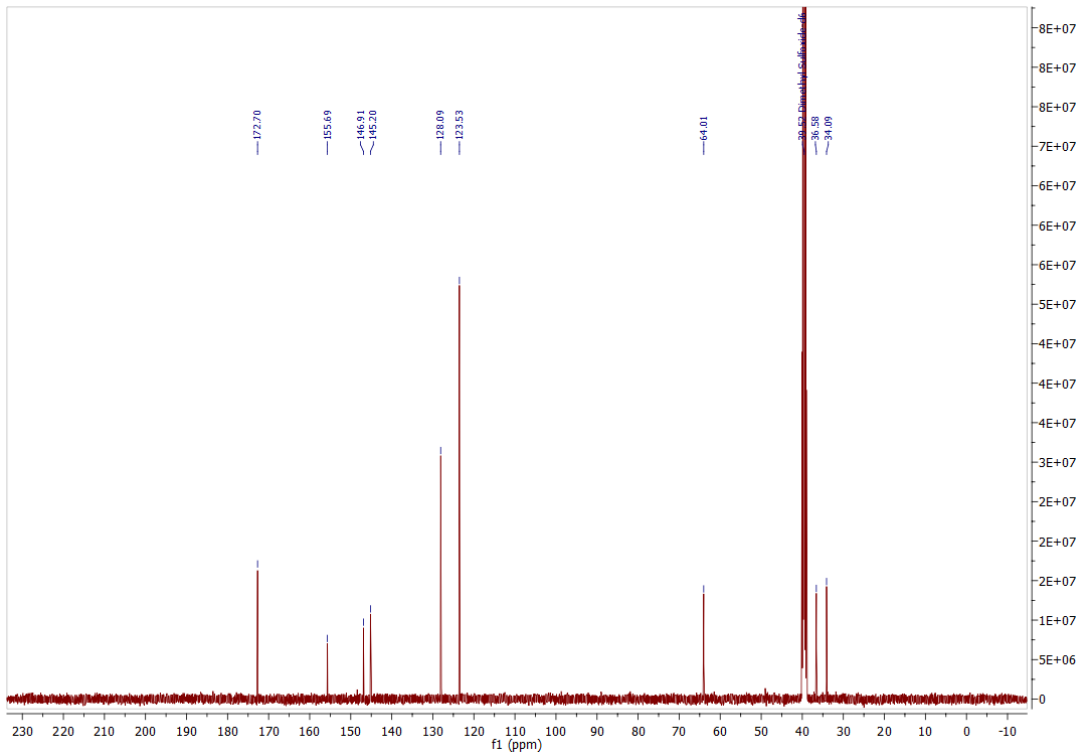

Figure S4.2: ^{13}C NMR spectrum of **4.8** in DMSO-d_6.

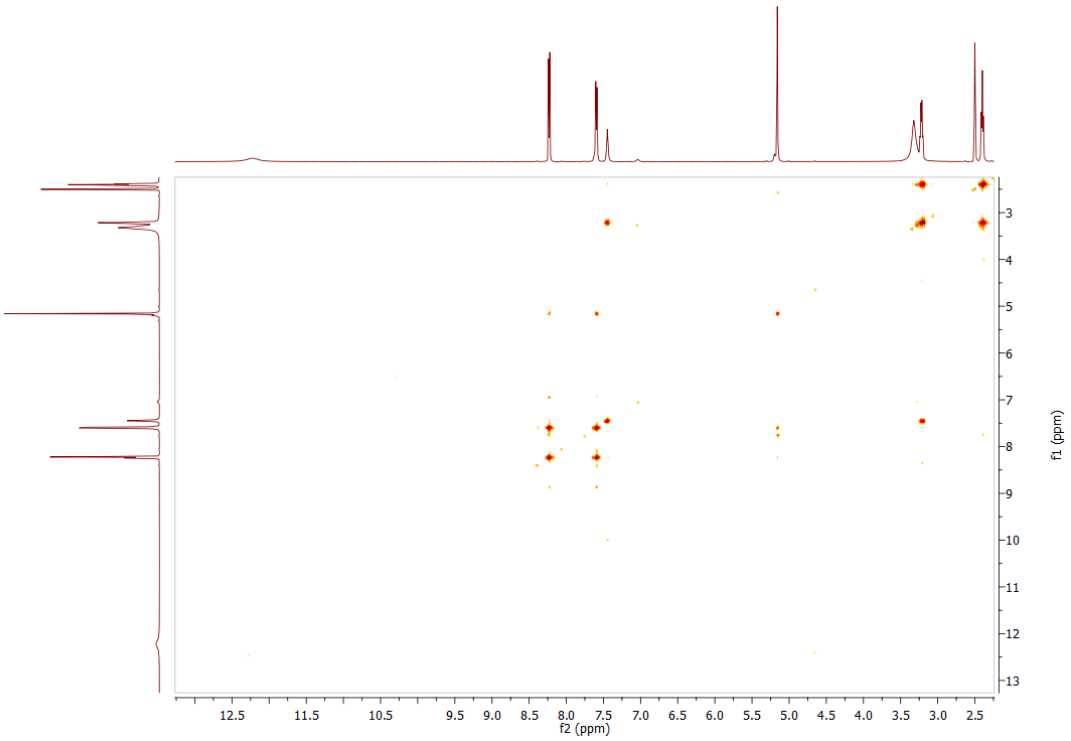

Figure S4.3: COSY spectrum of **4.8** in DMSO-d_6.

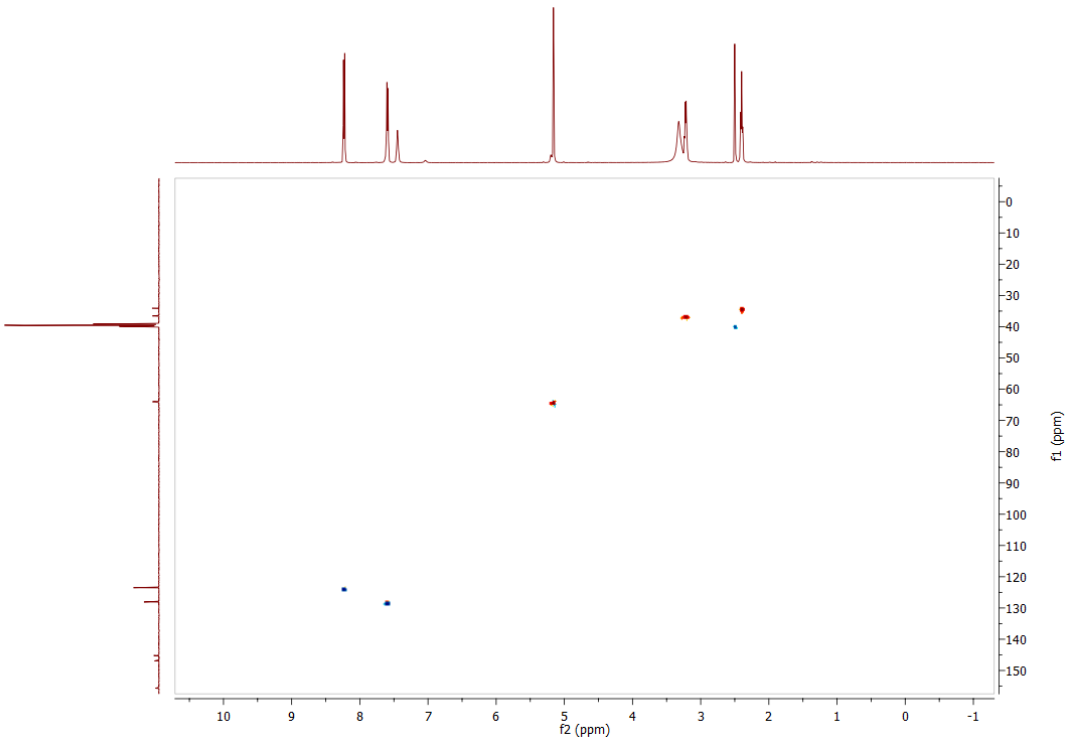

Figure S4.4: HSQC spectrum of **4.8** in DMSO-d_6.

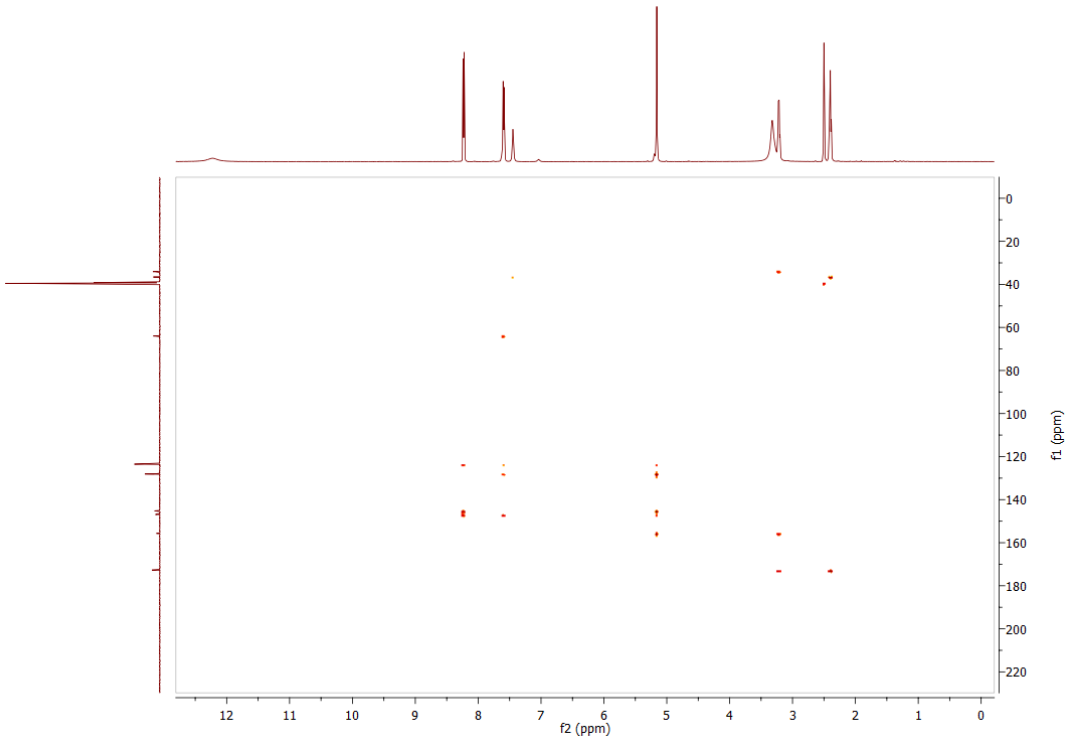

Figure S4.5: HMBC spectrum of **4.8** in DMSO-d_6.

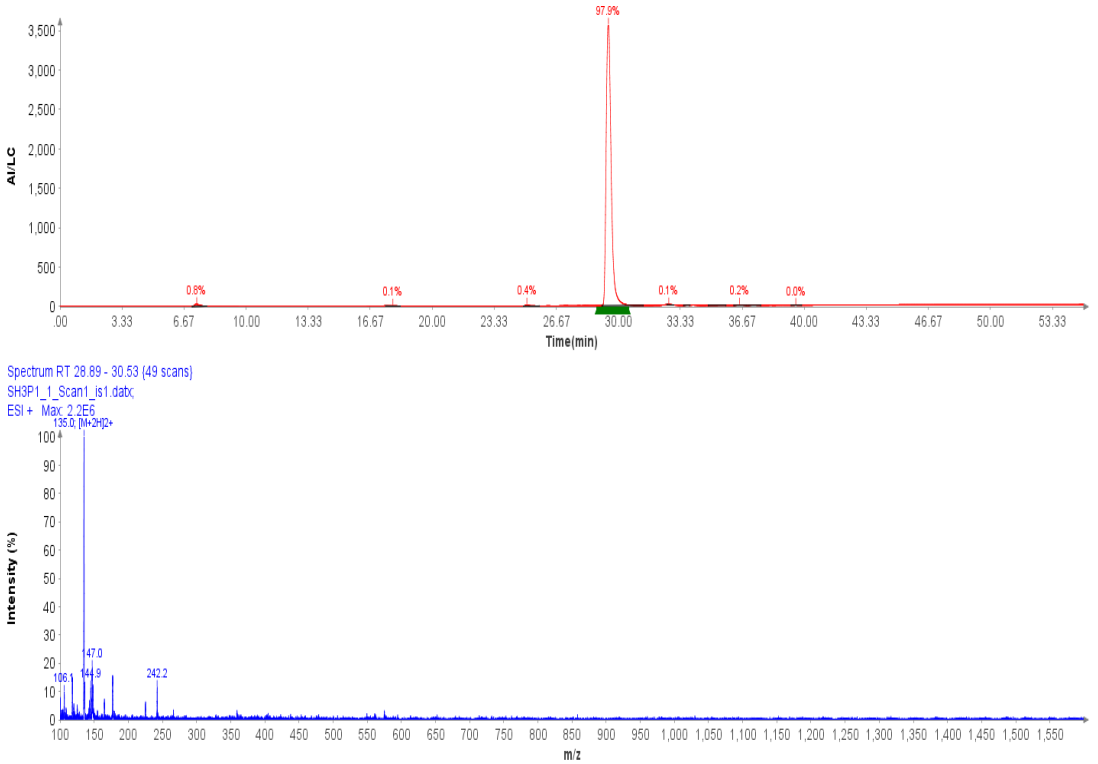

Figure S4.6: LC-MS data for **4.8.**

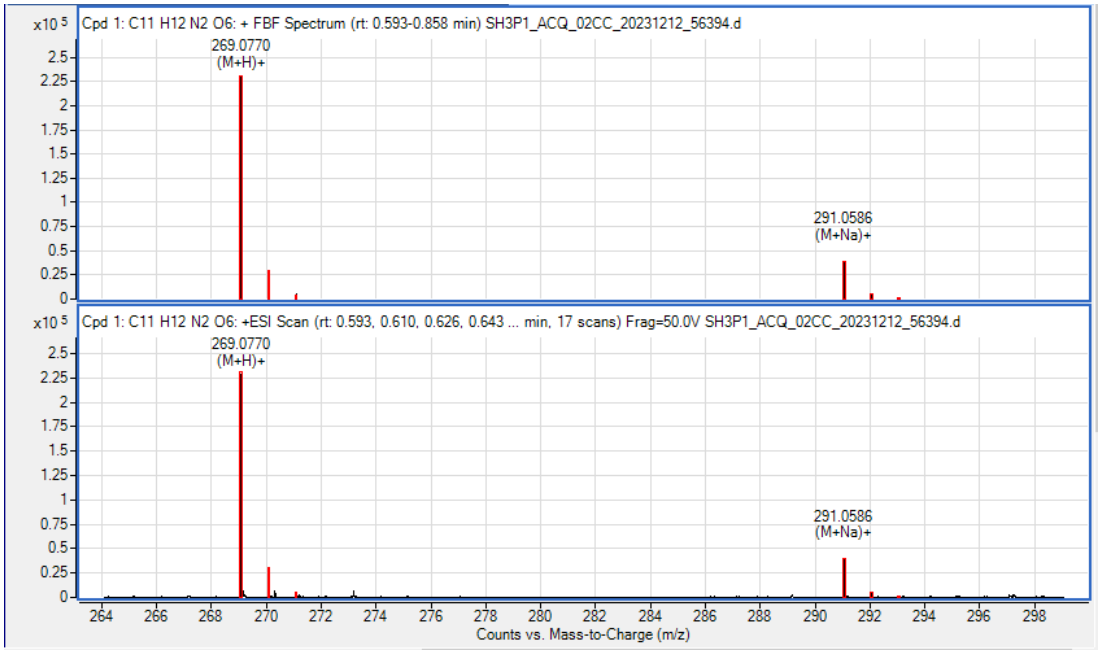

Figure S4.7: HRMS data for **4.8.**

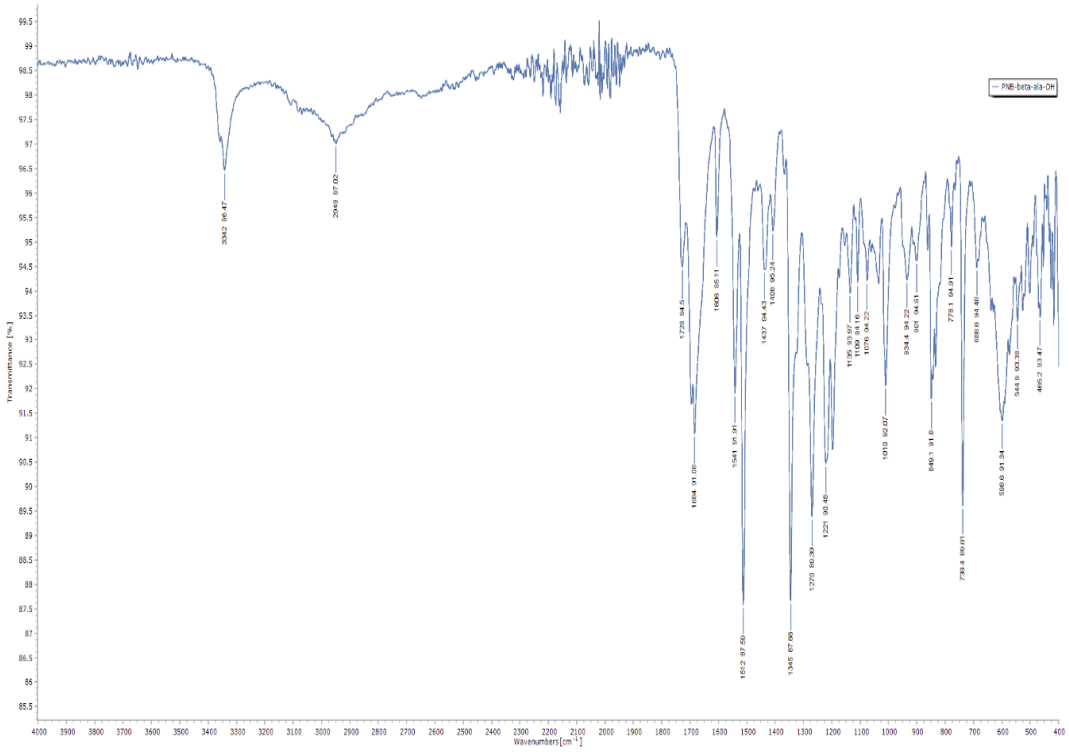

Figure S4.8: FTIR-ATR spectrum of **4.8.**

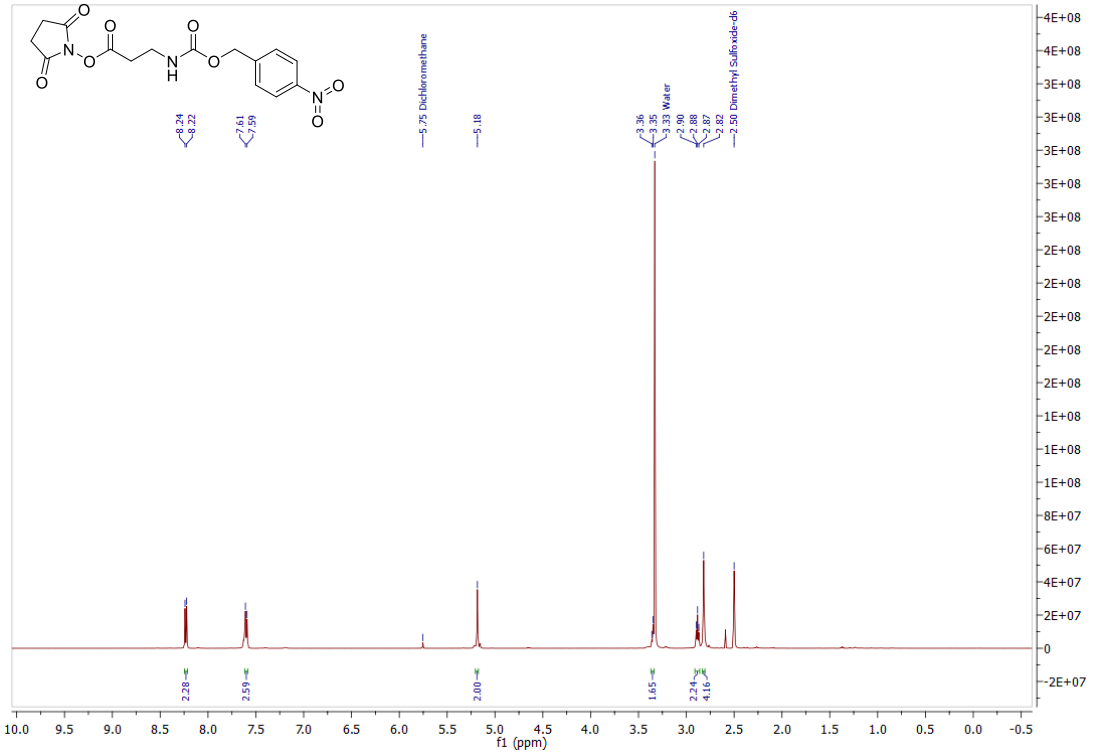

Figure S4.9: ^{1}H NMR spectrum of **4.9** in DMSO-d_6.

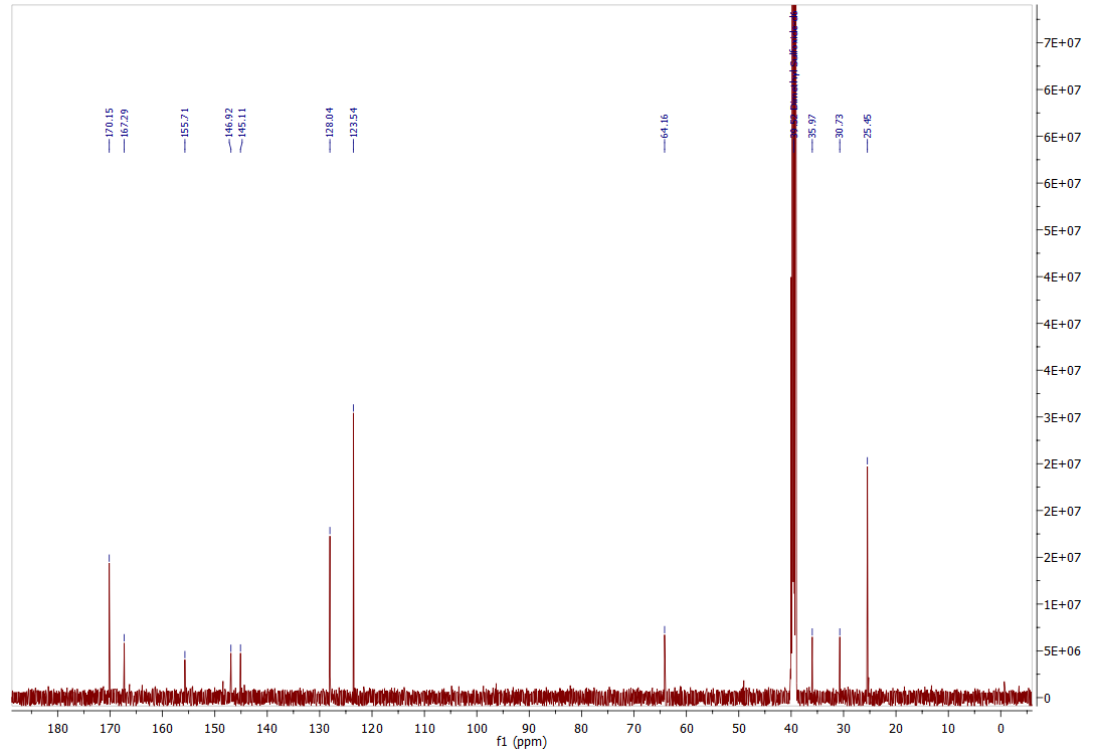

Figure S4.10: ^{13}C NMR spectrum of **4.9** in DMSO-d_6.

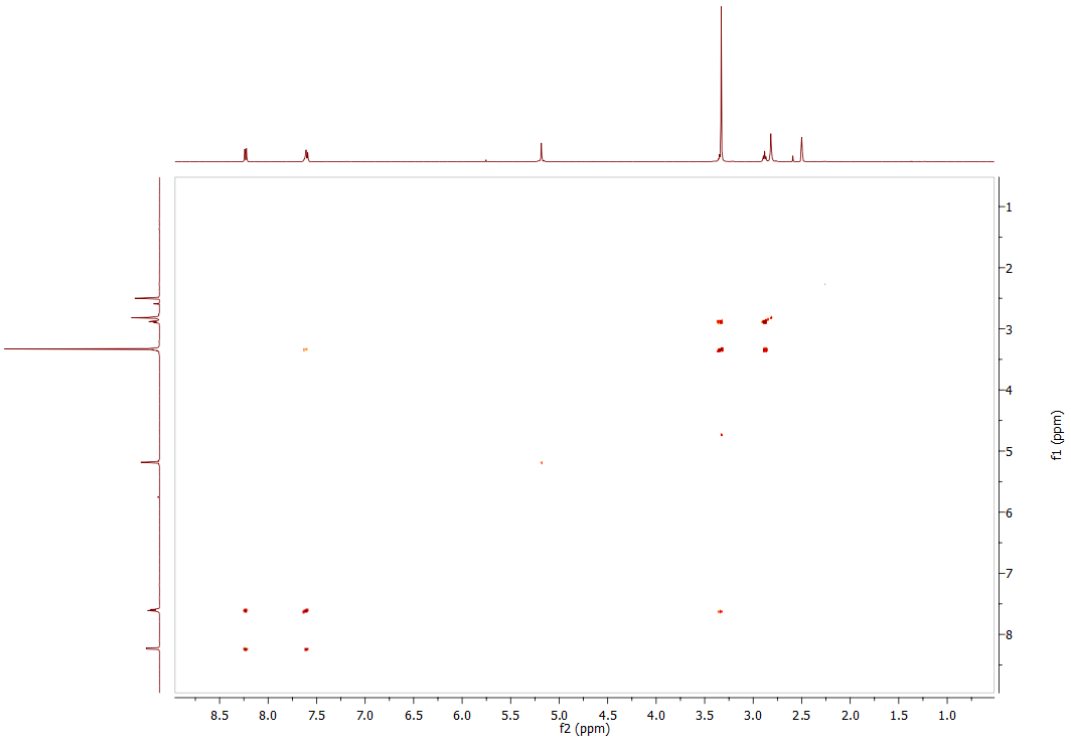

Figure S4.11: COSY spectrum of **4.9** in DMSO-d_6.

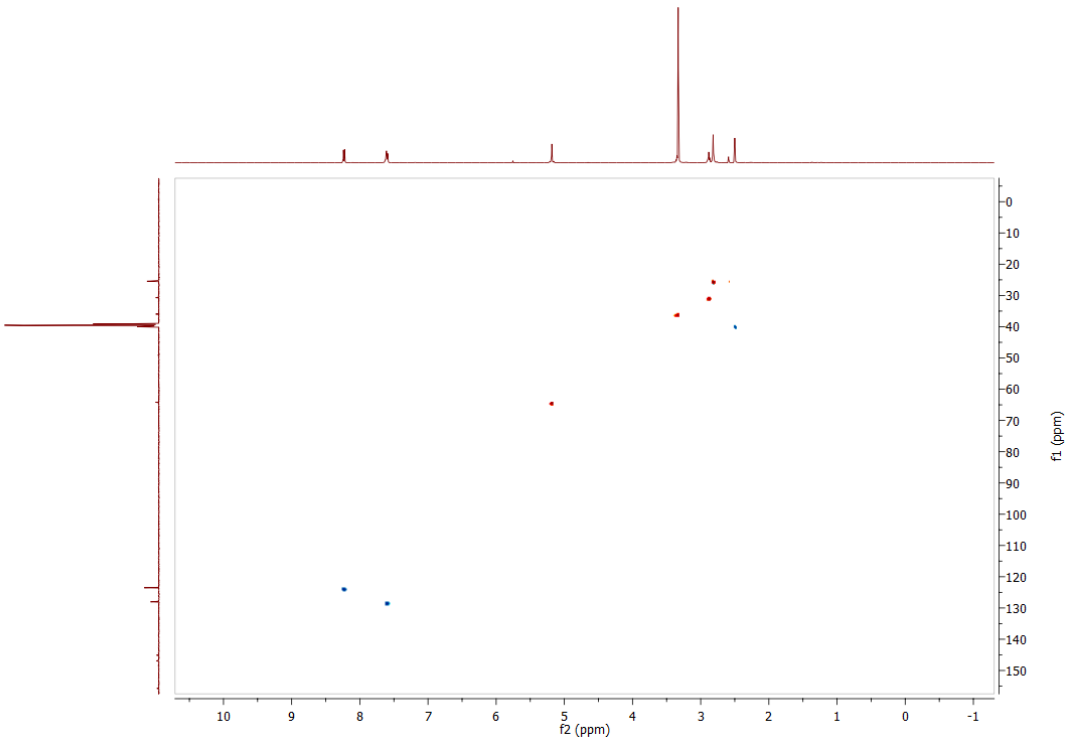

Figure S4.12: HSQC of **4.9** in DMSO-d_6.

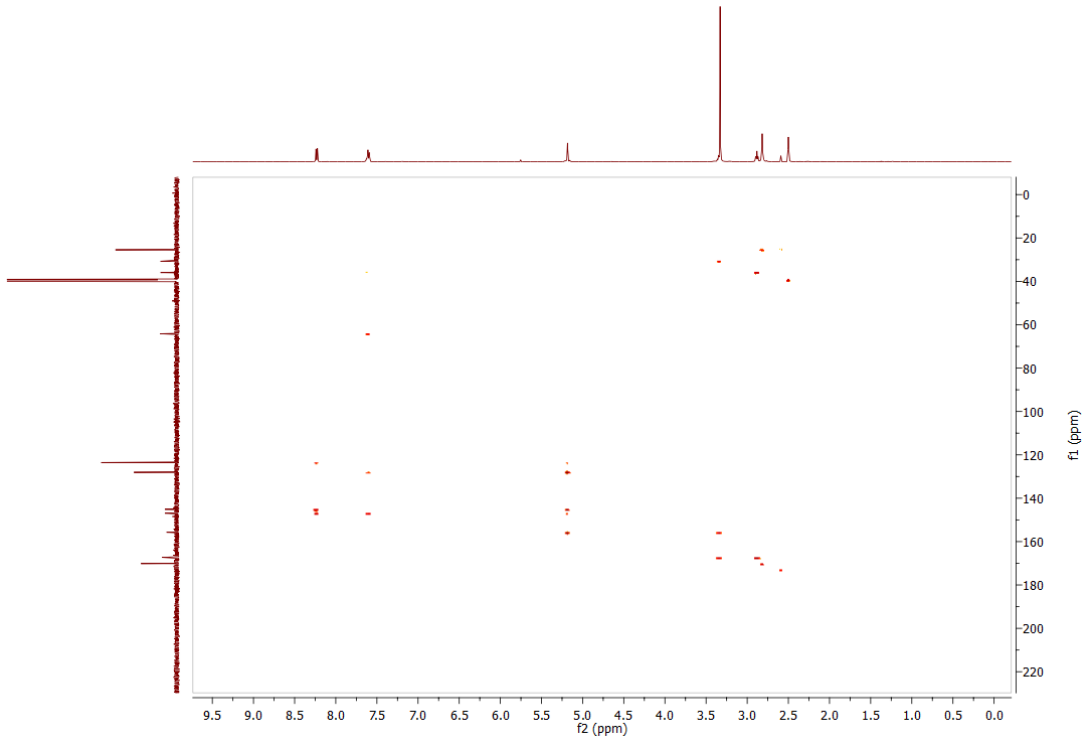

Figure S4.13: HMBC spectrum of **4.9** in DMSO-d_6.

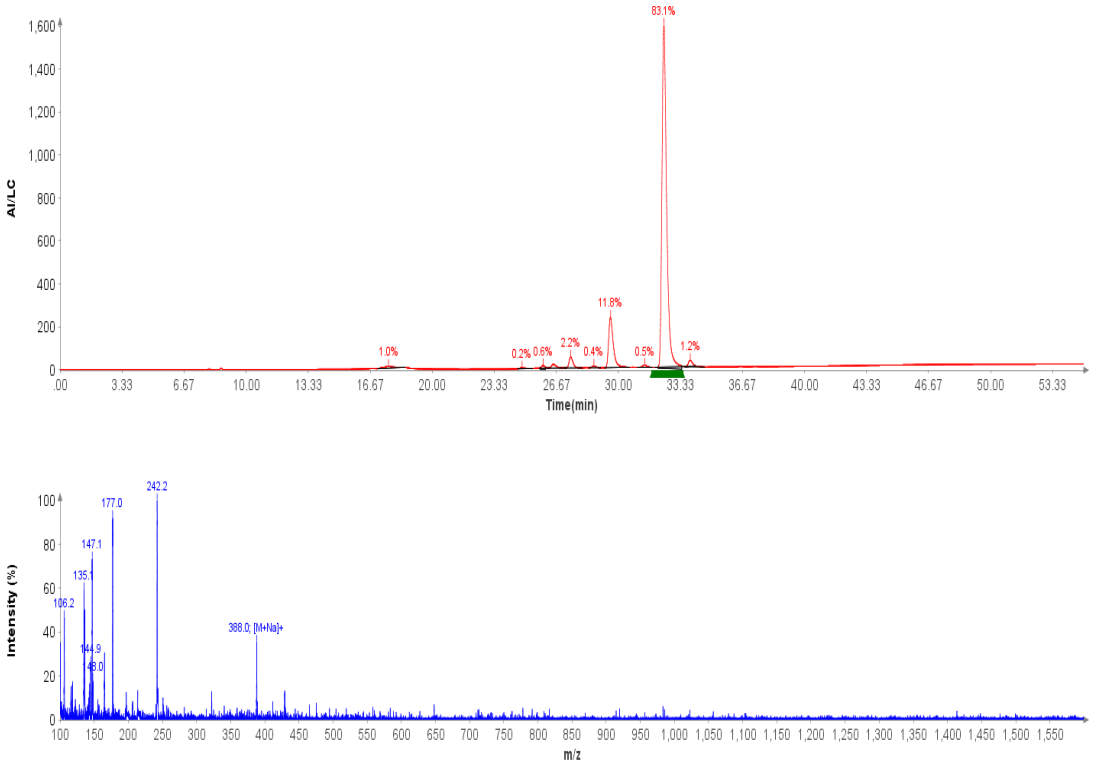

Figure S4.14: LC-MS data for **4.9.**

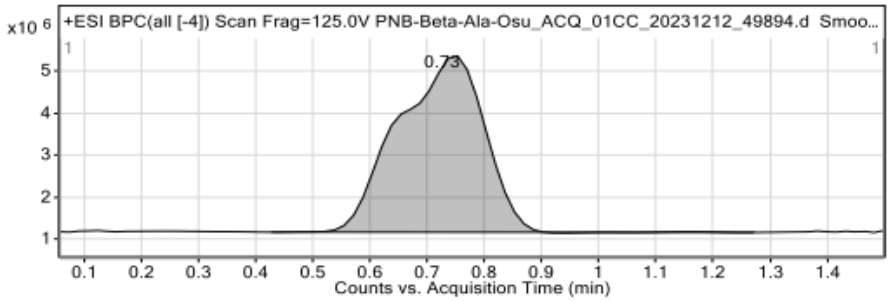

Figure 1: Base peak chromatogram

User Chromatogram Peak List

RT (min)	Area	Area %	Area Sum (%)	Base Peak (m/z)	Width (min)
0.73	44260024	100.00	100.00	388.0742	0.190

Compound Table

Compound Label	RT (min)	Observed mass (m/z)	Neutral observed mass (Da)	Theoretical mass (Da)	Mass error (ppm)	Isotope match score (%)
Cpd 1: C15 H15 N3 O8	0.73	388.0752	365.0861	365.0859	0.47	99.18

Mass errors of between -5.00 and 5.00 ppm with isotope match scores above 60% are considered confirmation of molecular formulae

Figure: Full range view of Compound spectra and potential adducts.

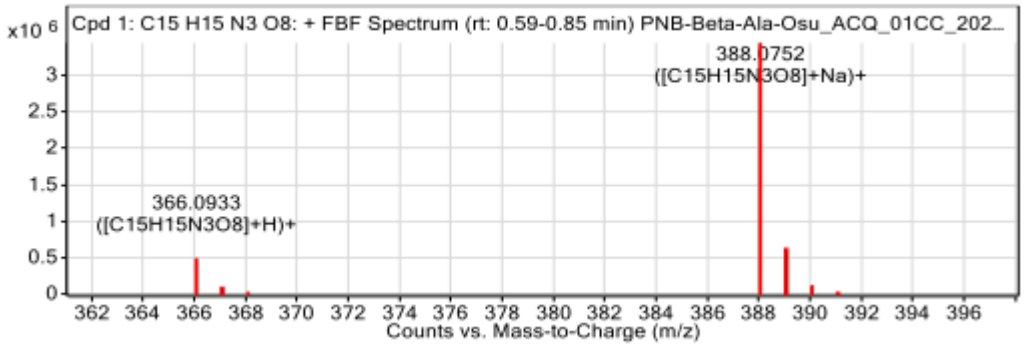

Figure S4.15: HRMS data for **4.9**

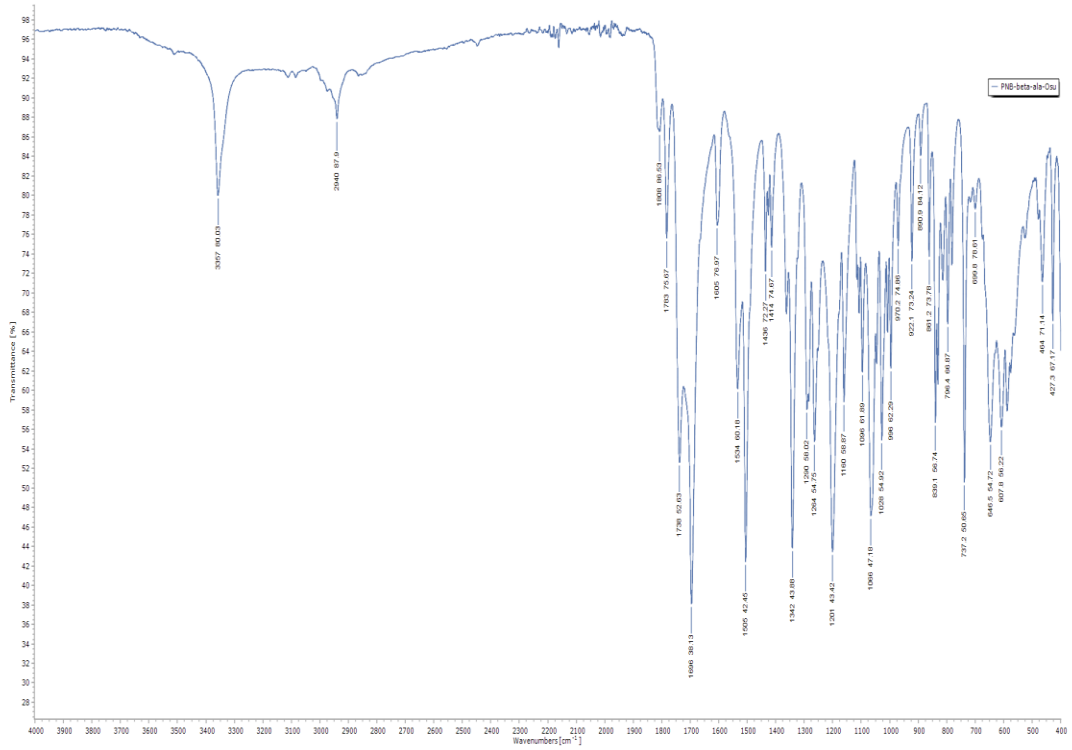

Figure S4.16: FTIR-ATR spectrum of **4.9.**

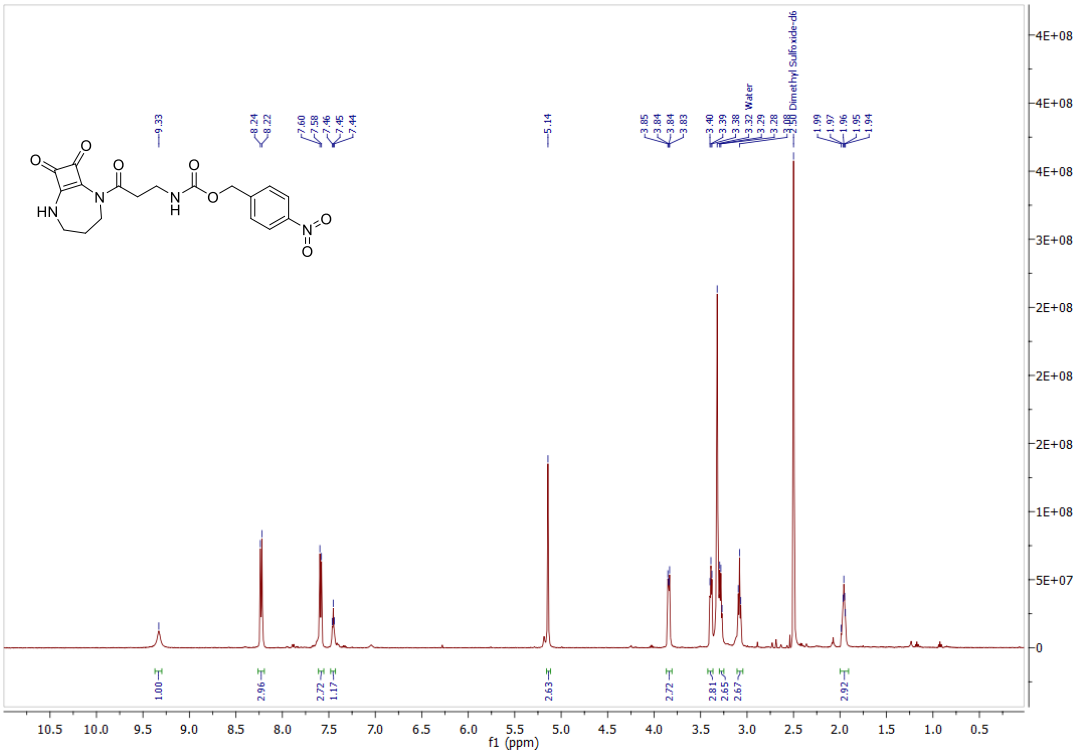

Figure S4.17: ^{1}H NMR spectrum of **4.5** in DMSO-d_6.

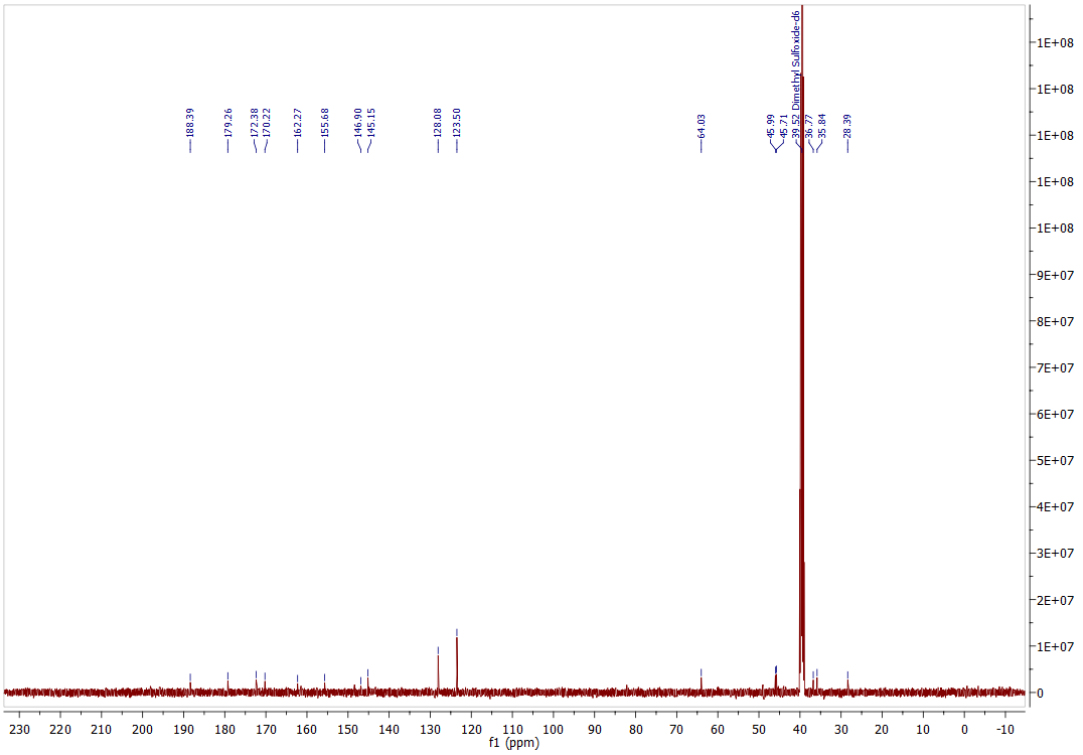

Figure S4.18: ^{13}C NMR of **4.5** in DMSO-d_6.

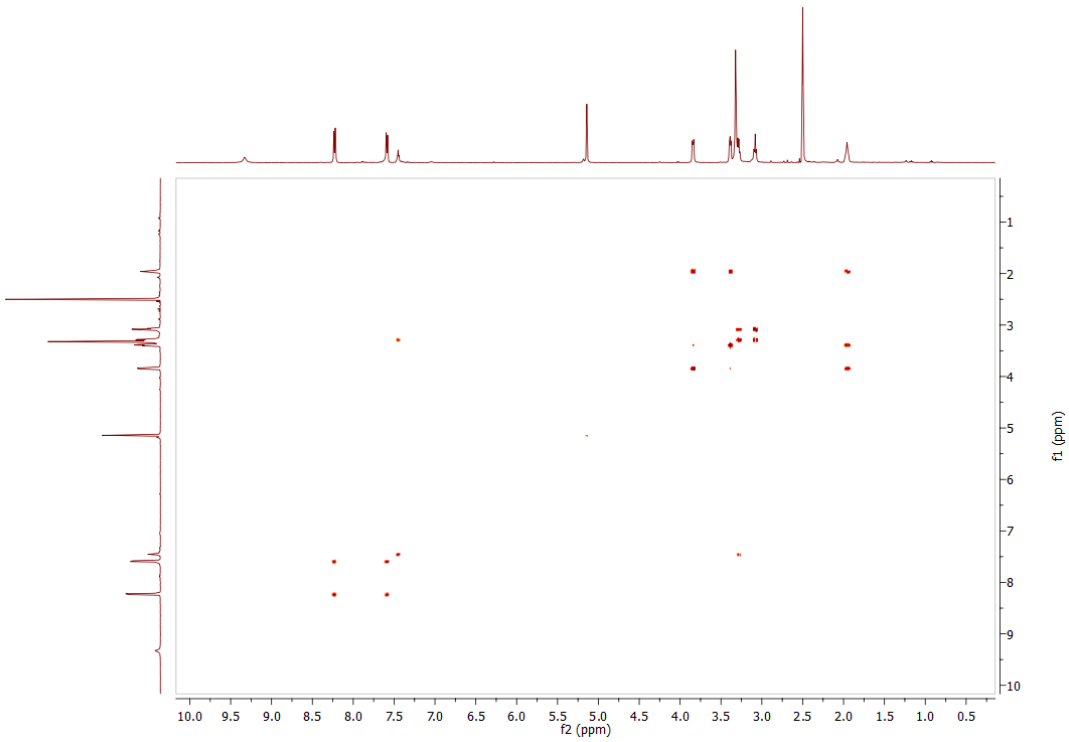

Figure S4.19: COSY spectrum of **4.5** in DMSO-d_6.

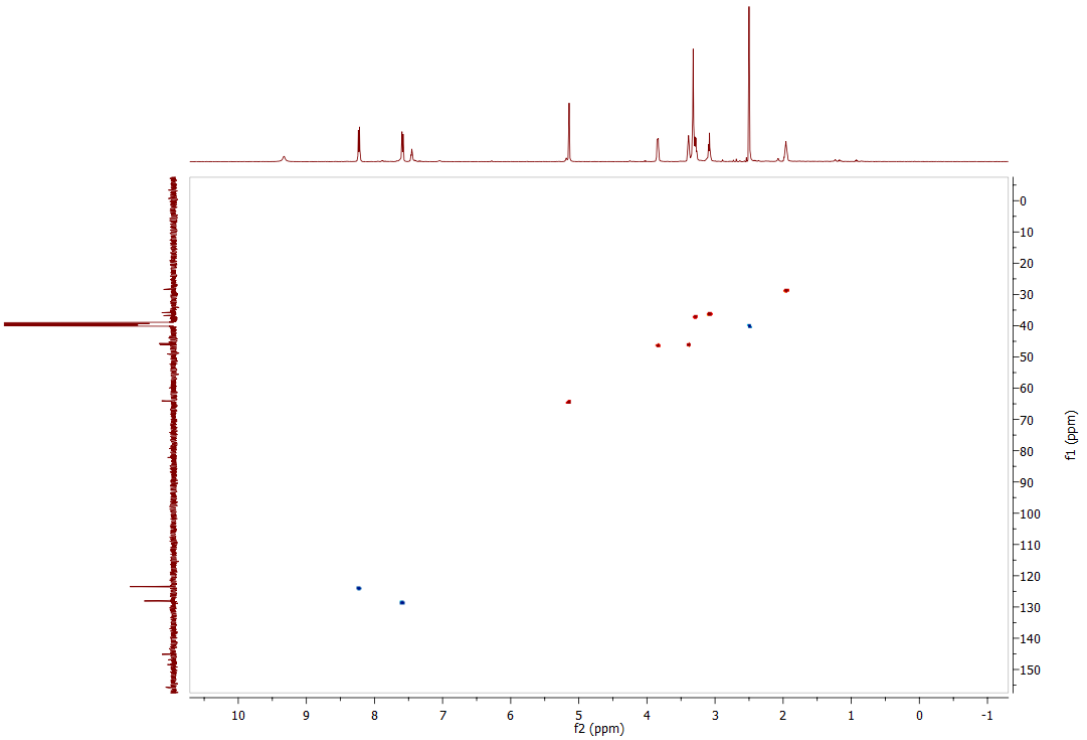

Figure S4.20: HSQC spectrum of **4.5** in DMSO-d_6.

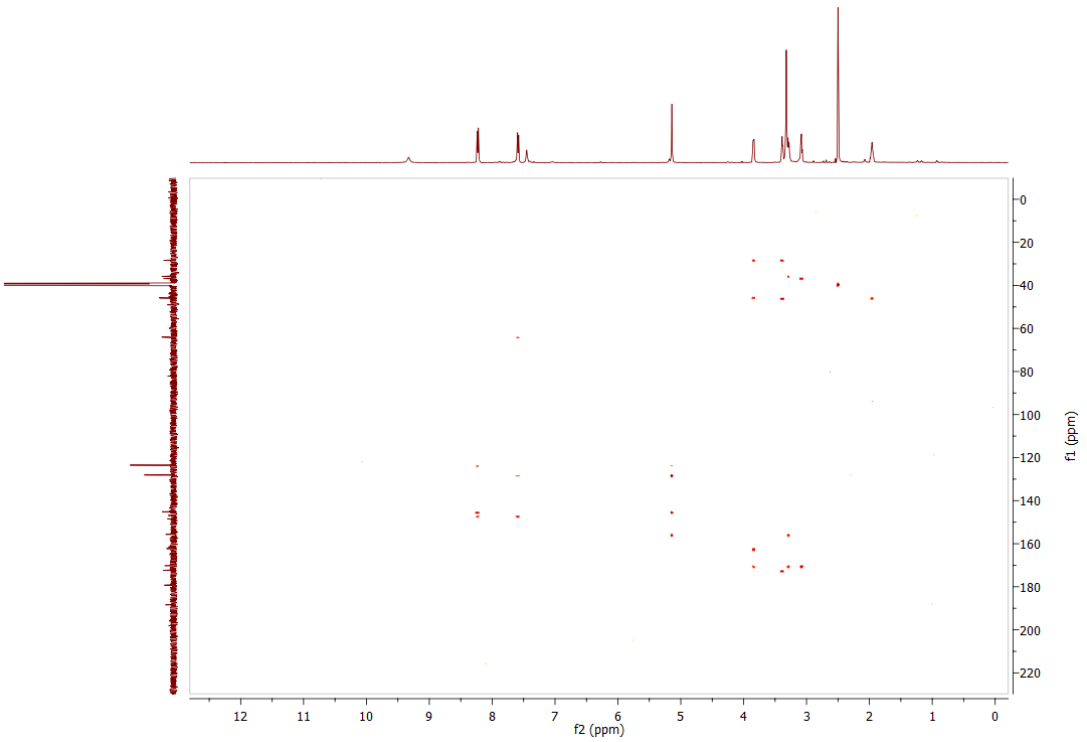

Figure S4.21: HMBC spectrum of **4.5** in DMSO-d_6.

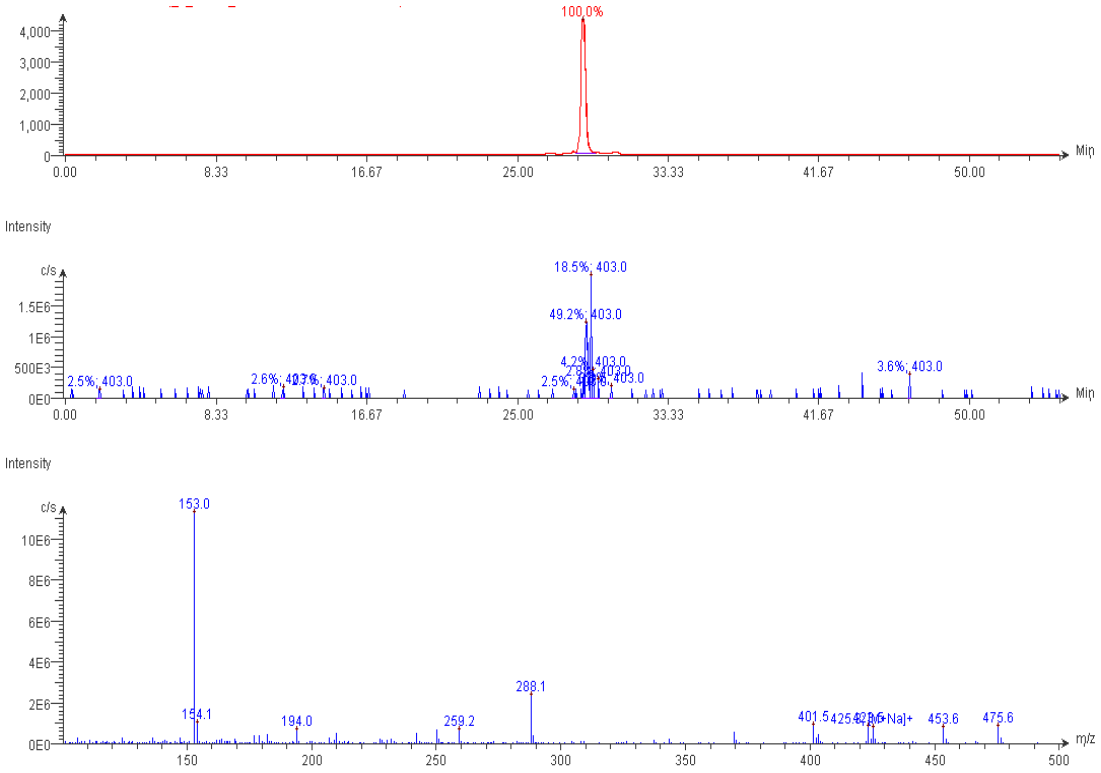

Figure S4.22: LC-MS data for **4.5.**

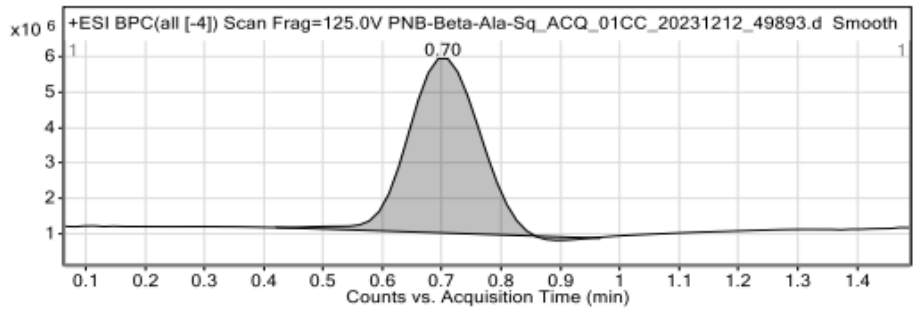

Figure 1: Base peak chromatogram

User Chromatogram Peak List

RT (min)	Area	Area %	Area Sum (%)	Base Peak (m/z)	Width (min)
0.70	41288128	100.00	100.00	441.0798	0.150

Compound Table

Compound Label	RT (min)	Observed mass (m/z)	Neutral observed mass (Da)	Theoretical mass (Da)	Mass error (ppm)	Isotope match score (%)
Cpd 1: C18 H18 N4 O7	0.74	403.1253	402.1177	402.1175	0.48	98.85

Mass errors of between -5.00 and 5.00 ppm with isotope match scores above 60% are considered confirmation of molecular formulae

Figure: Full range view of Compound spectra and potential adducts.

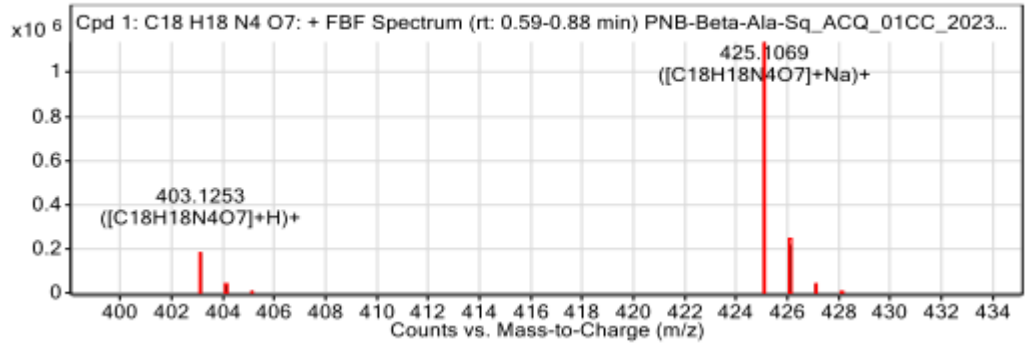

Figure S4.23: HRMS data for **4.5.**

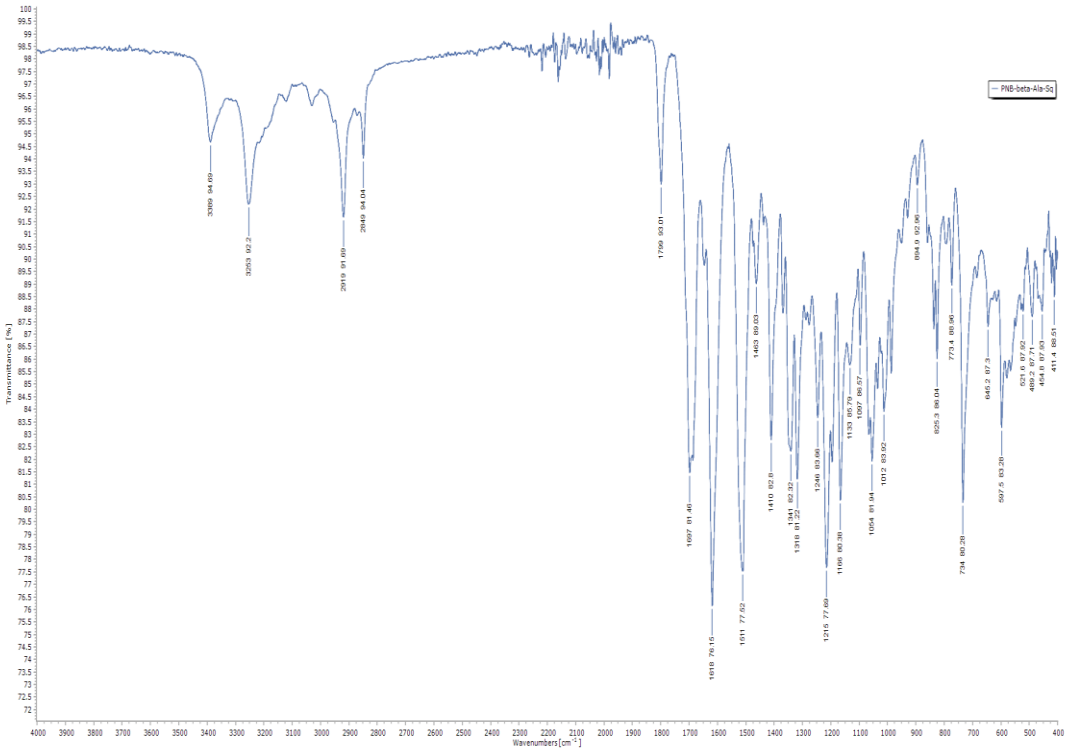

Figure S4.24: FTIR-ATR spectrum of **4.5.**

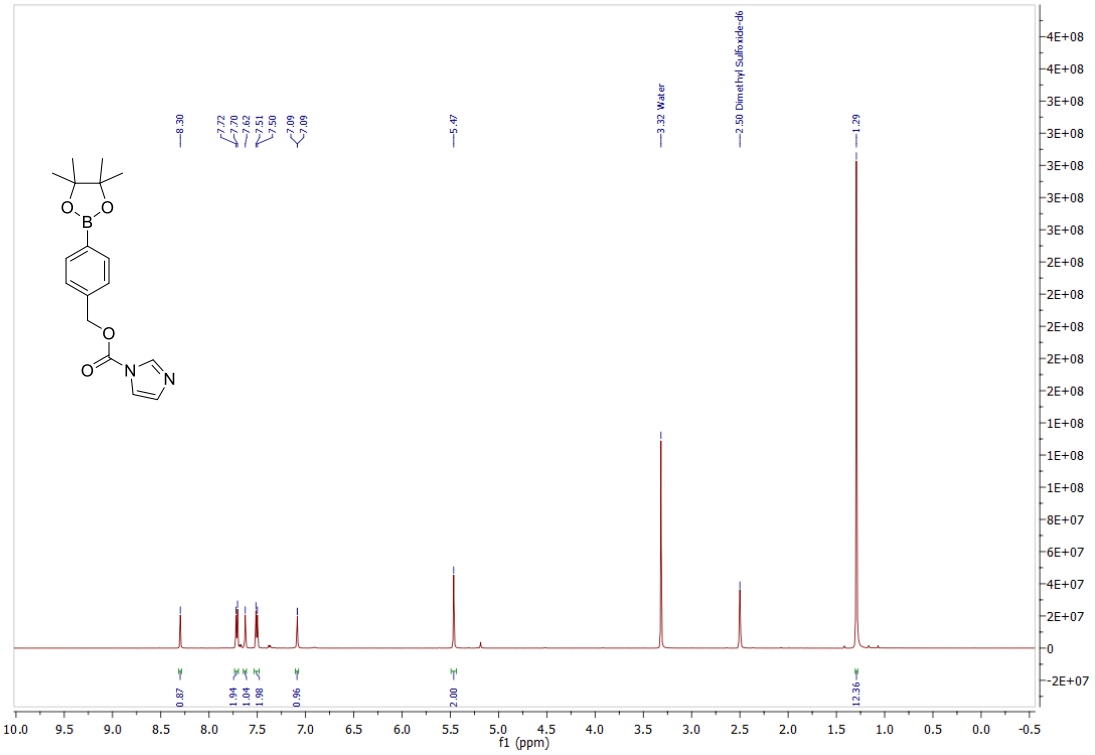

Figure S4.25: ^{1}H NMR spectrum of **4.10** in DMSO-d_6.

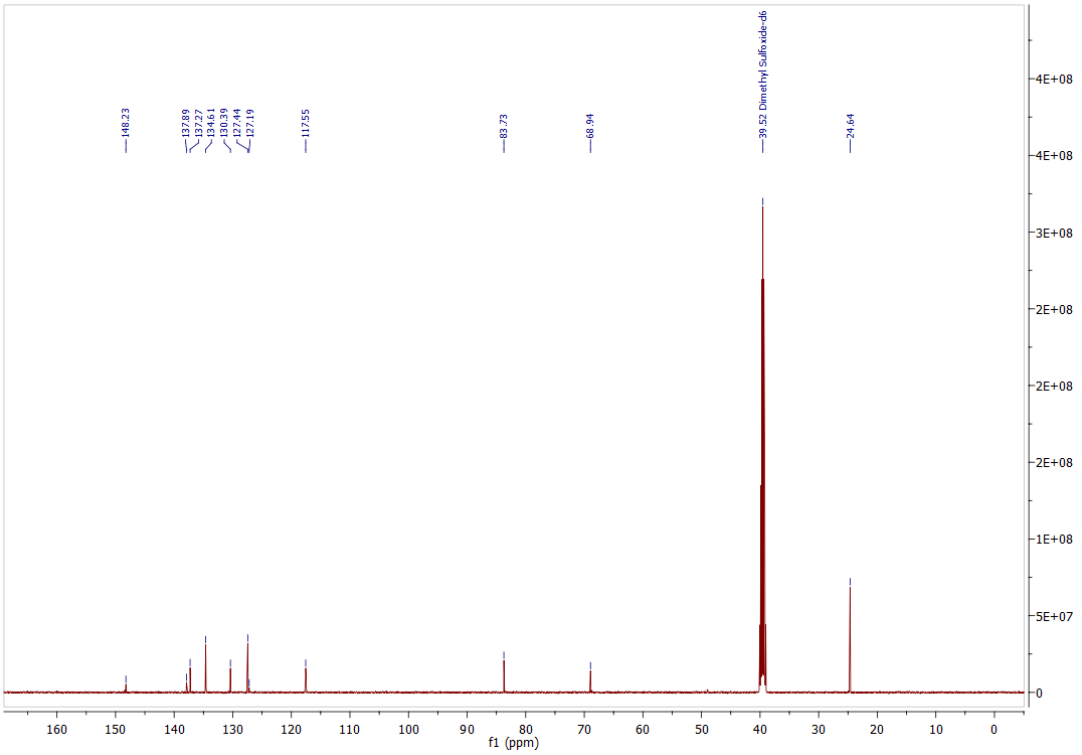

Figure S4.26: ^{13}C NMR spectrum of **4.10** in DMSO-d_6.

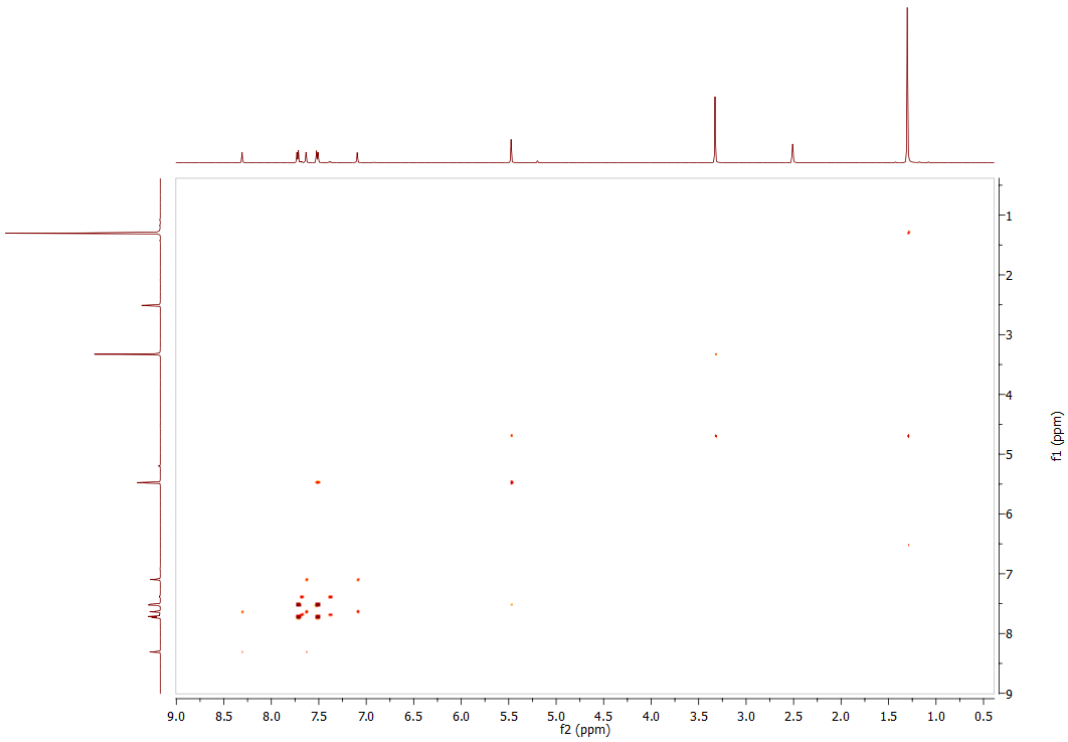

Figure S4.27: COSY spectrum of **4.10** in DMSO-d_6.

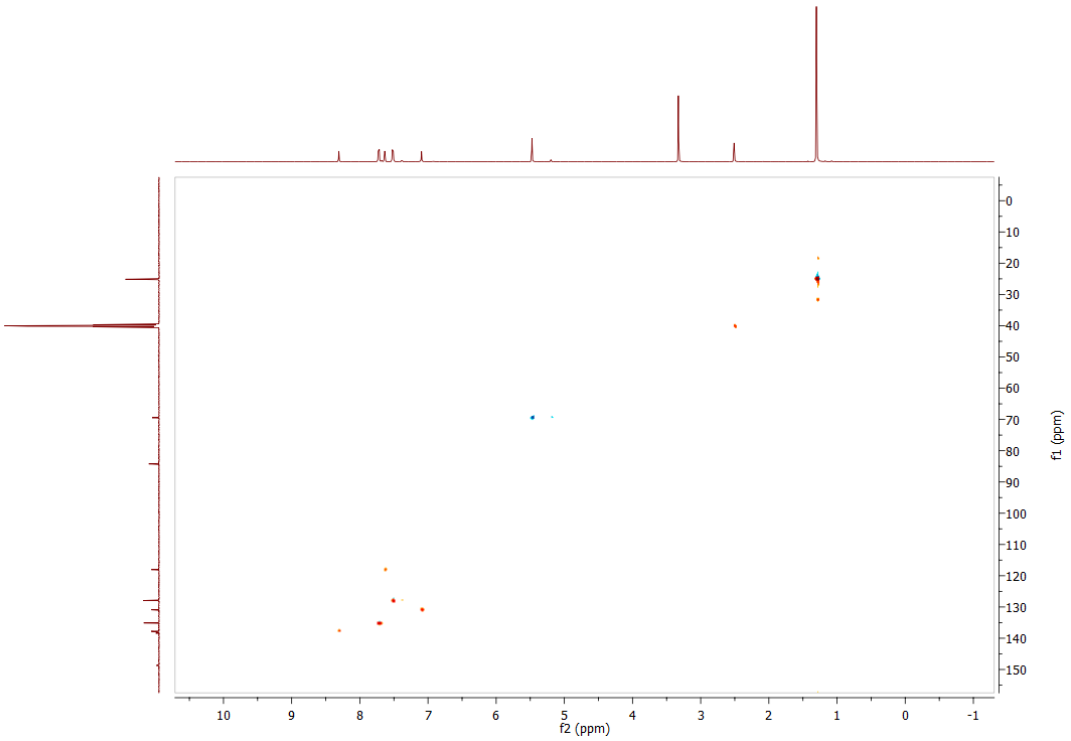

Figure S4.28: HSQC spectrum of **4.10** in DMSO-d_6.

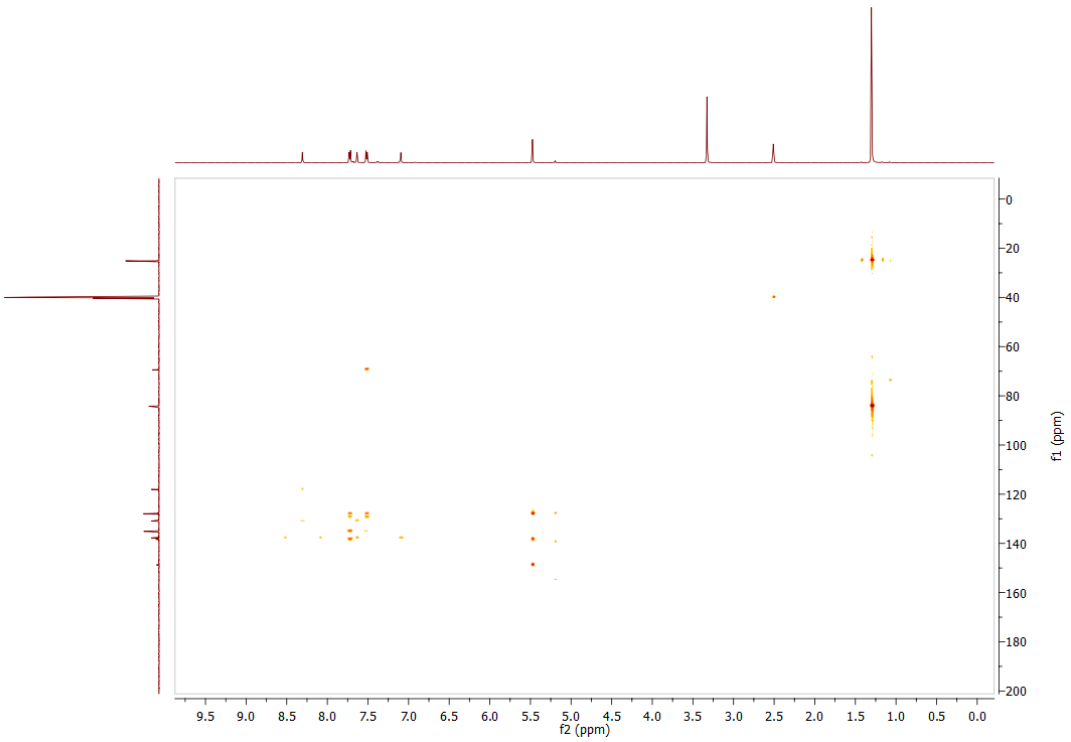

Figure S4.29: HMBC spectrum of **4.10** in DMSO-d_6.

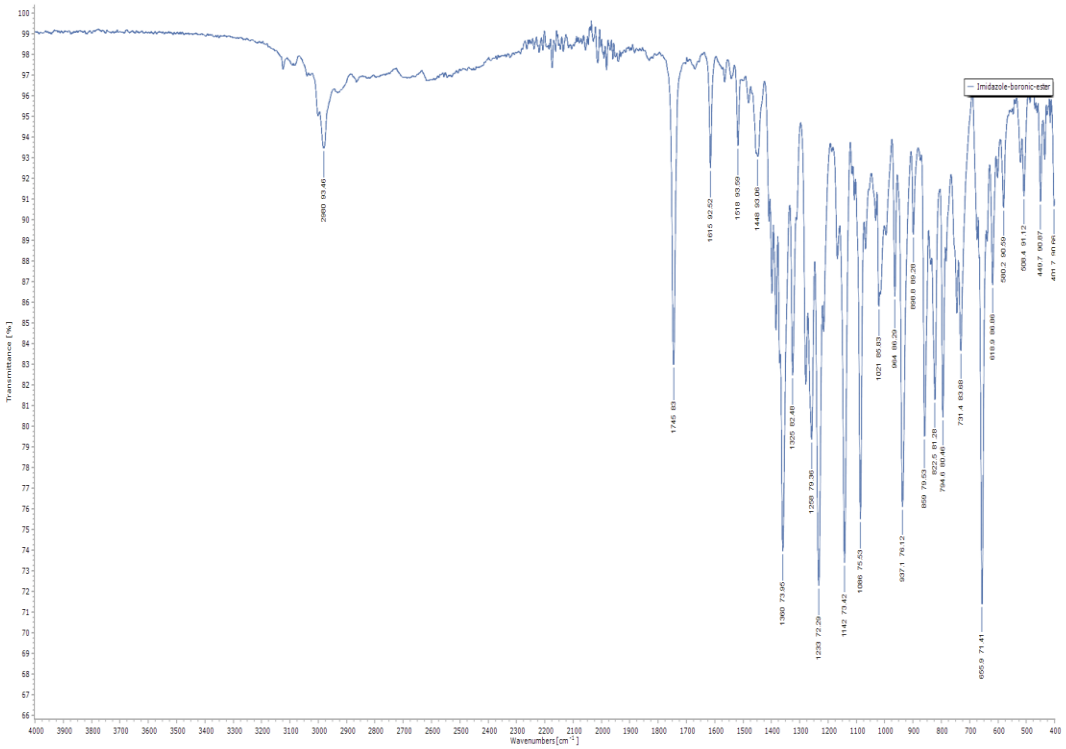

Figure S4.30: FTIR-ATR spectrum of **4.10.**

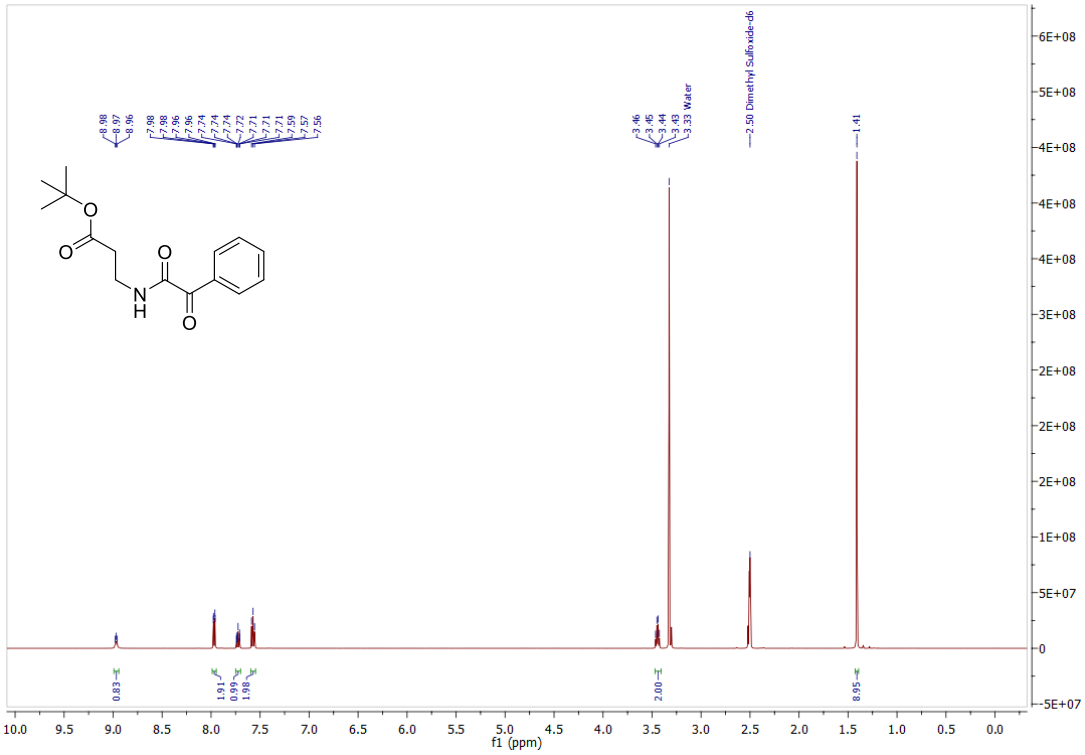

Figure S4.31: ^{1}H NMR spectrum of **4.12** in DMSO-d_6.

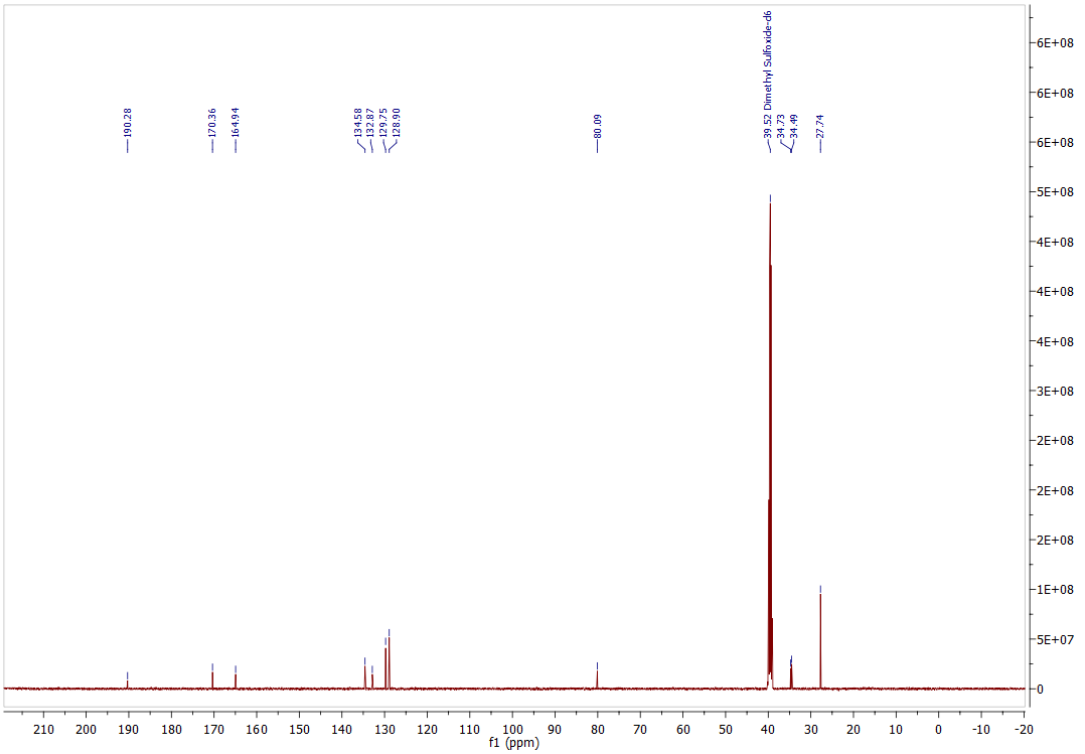

Figure S4.32: ^{13}C NMR spectrum of **4.12** in DMSO-d_6.

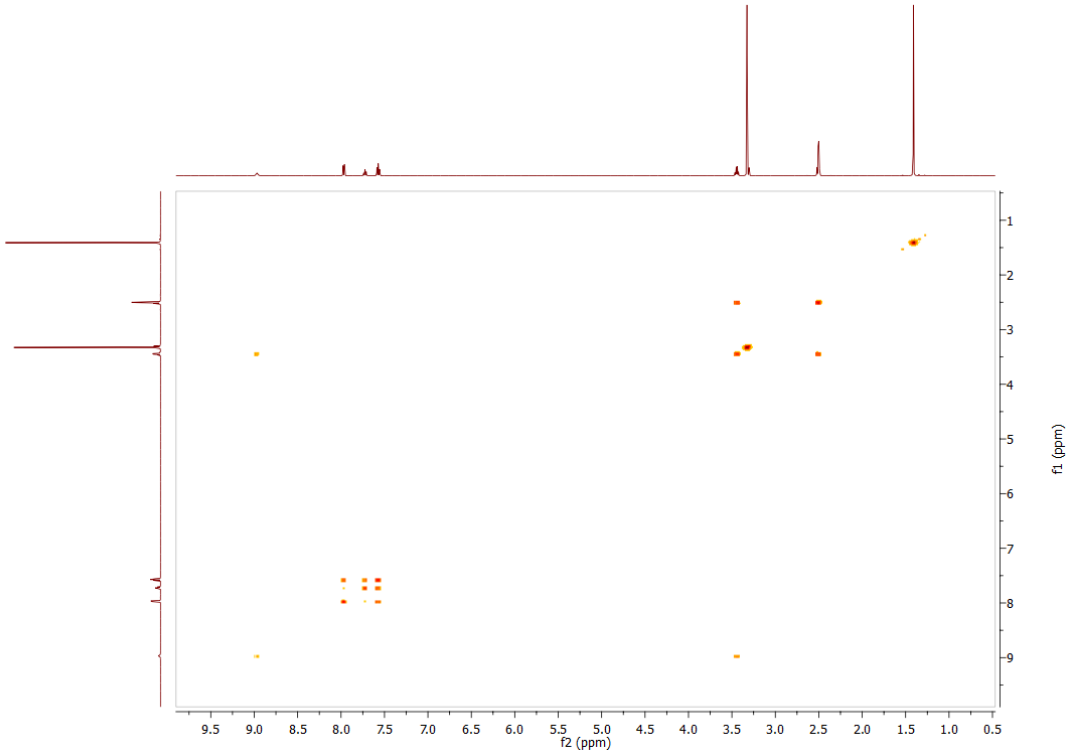

Figure S4.32: COSY spectrum of **4.12** in DMSO-d_6.

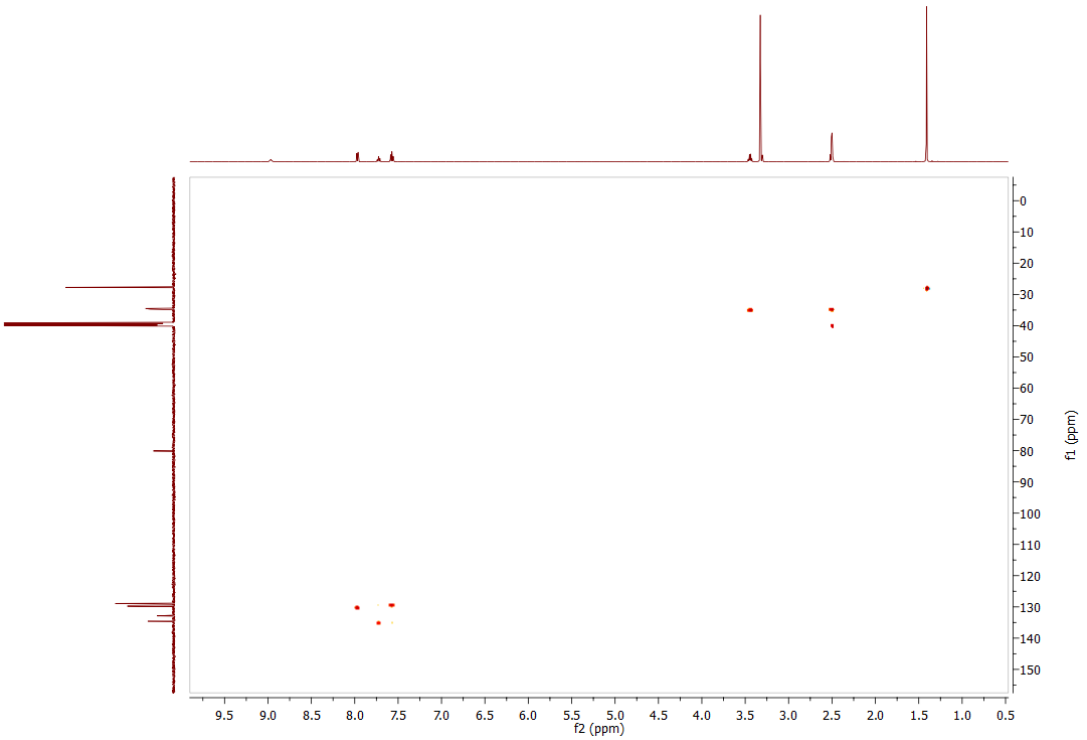

Figure S4.33: HSQC spectrum of **4.12** in DMSO-d_6.

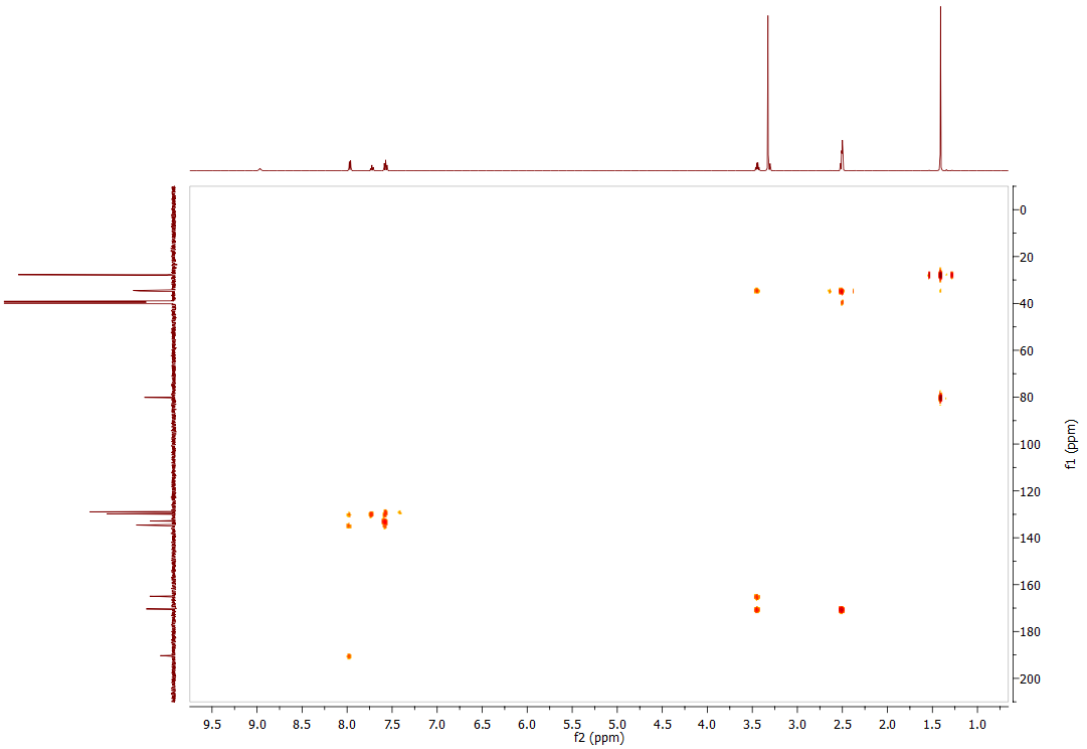

Figure S4.34: HMBC spectrum of **4.12** in DMSO-d_6.

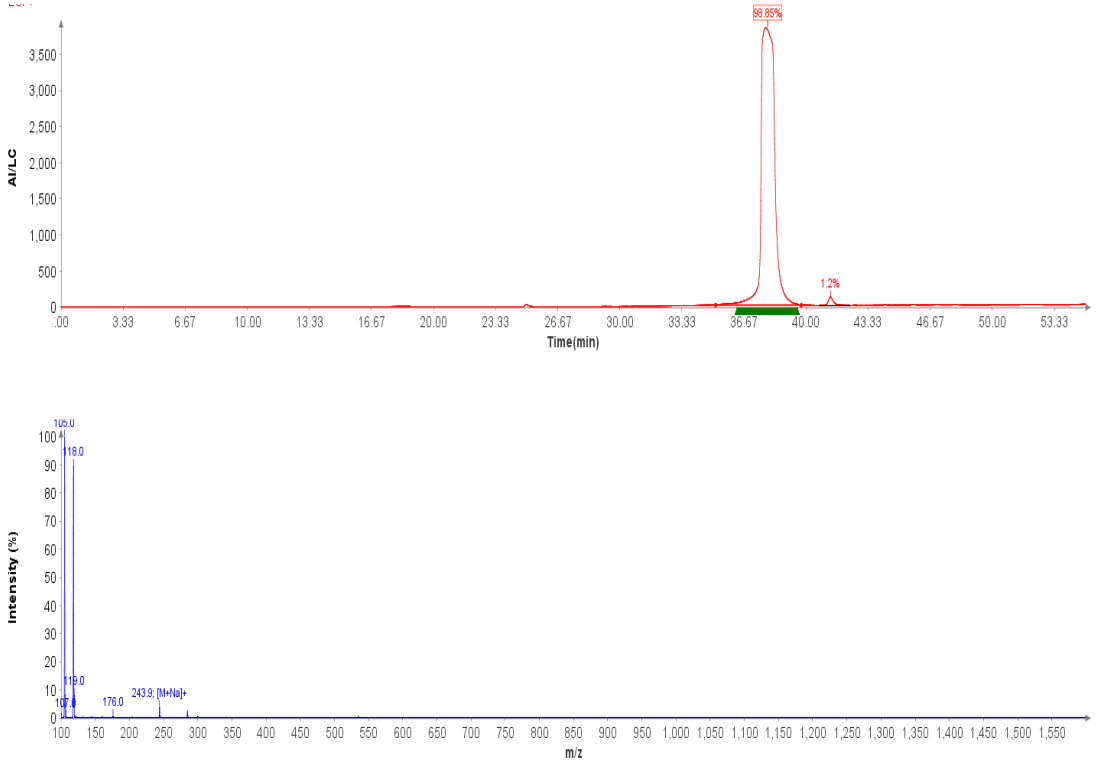

Figure S4.35: LC-MS data for **4.12.**

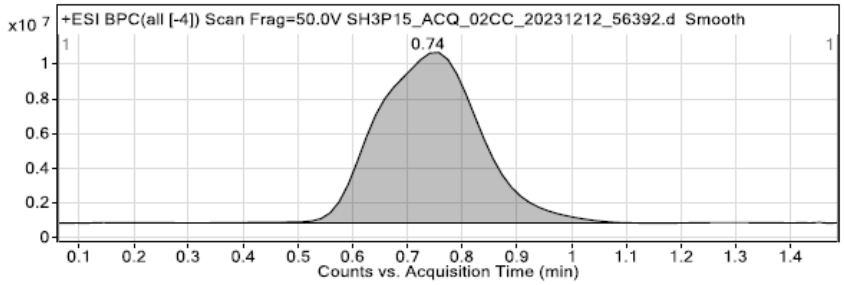

Figure 1: Base peak chromatogram

User Chromatogram Peak List

RT (min)	Area	Area %	Area Sum (%)	Base Peak (m/z)	Width (min)
0.74	130572535	100.00	100.00	222.0735	0.220

Compound Table

Compound Label	RT (min)	Observed mass (m/z)	Neutral observed mass (Da)	Theoretical mass (Da)	Mass error (ppm)	Isotope match score (%)
Cpd 1: C15 H19 N O4	0.71	300.1206	277.1314	277.1314	0.11	99.83

Mass errors of between -5.00 and 5.00 ppm with isotope match scores above 60% are considered confirmation of molecular formulae

Figure: Full range view of Compound spectra and potential adducts.

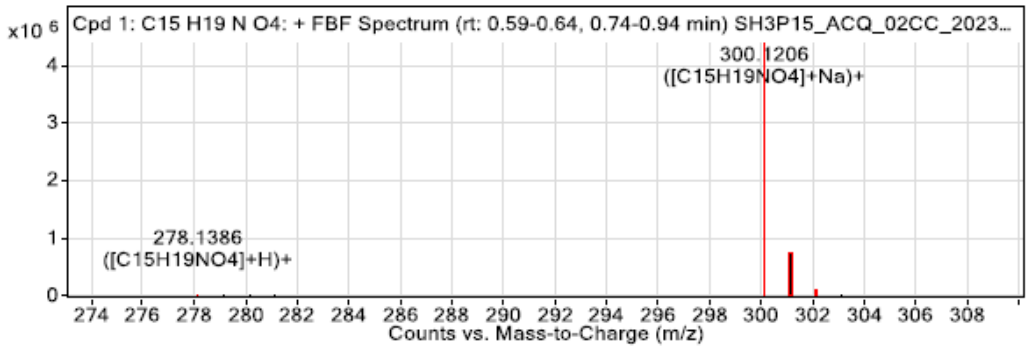

Figure S4.36: HRMS data for **4.12.**

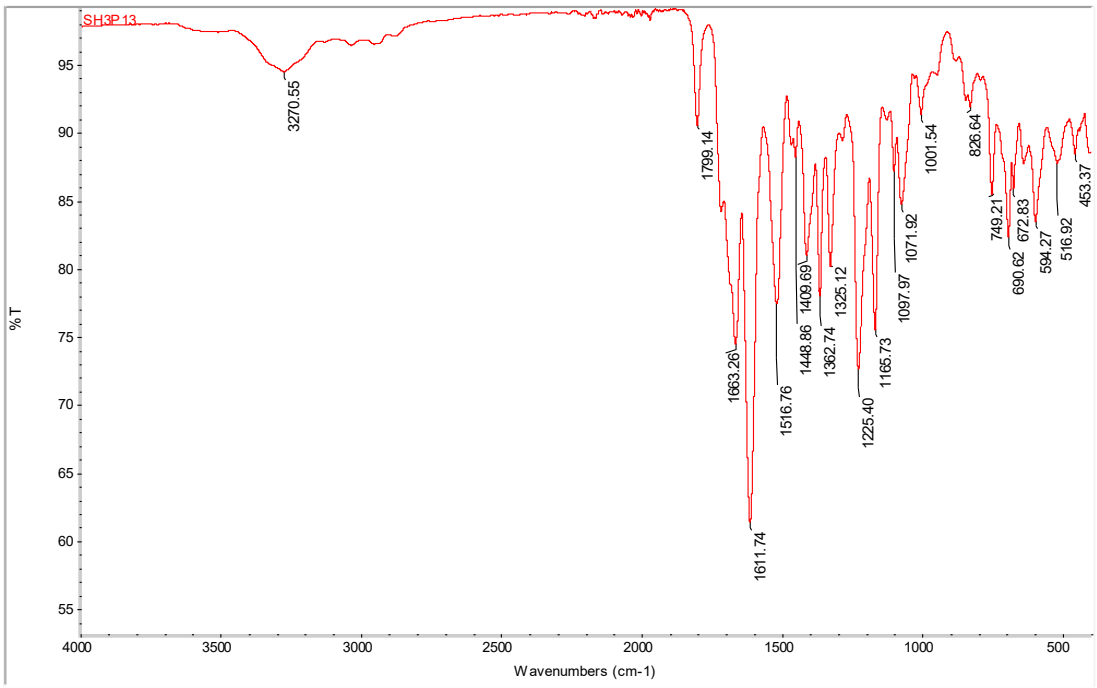

Figure S4.37: FTIR-ATR spectrum of **4.12.**

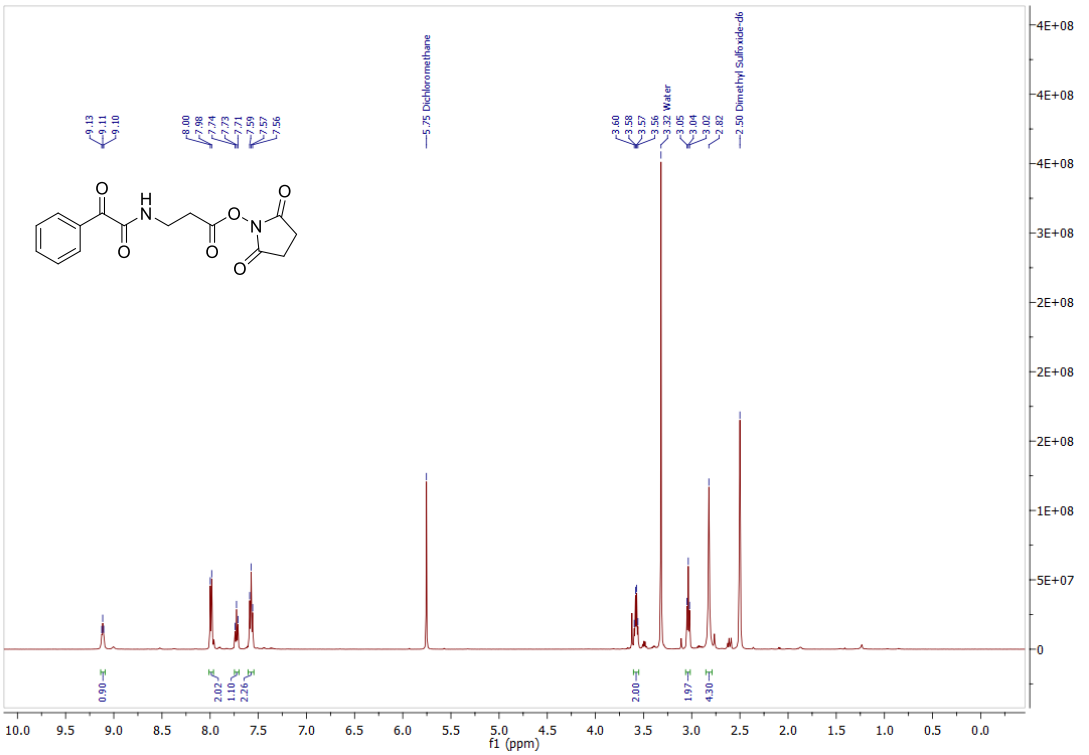

Figure S4.38: ^{1}H NMR spectrum of **4.13** in DMSO-d_6.

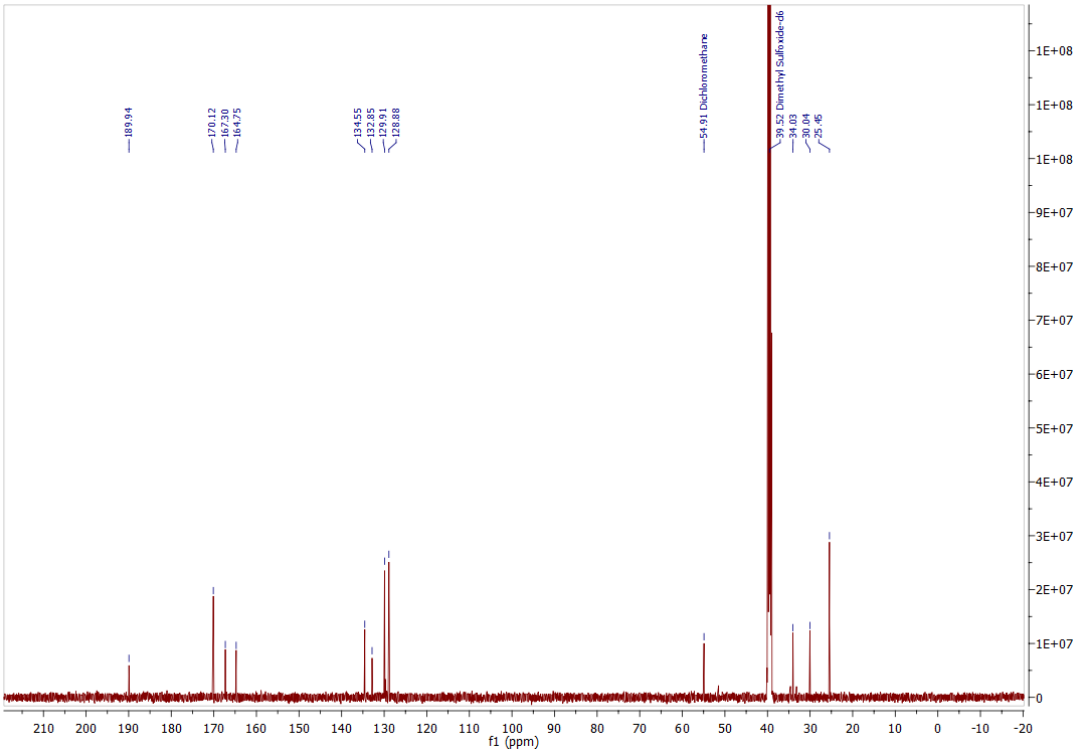

Figure S4.39: ^{13}C NMR spectrum of **4.13** in DMSO-d_6.

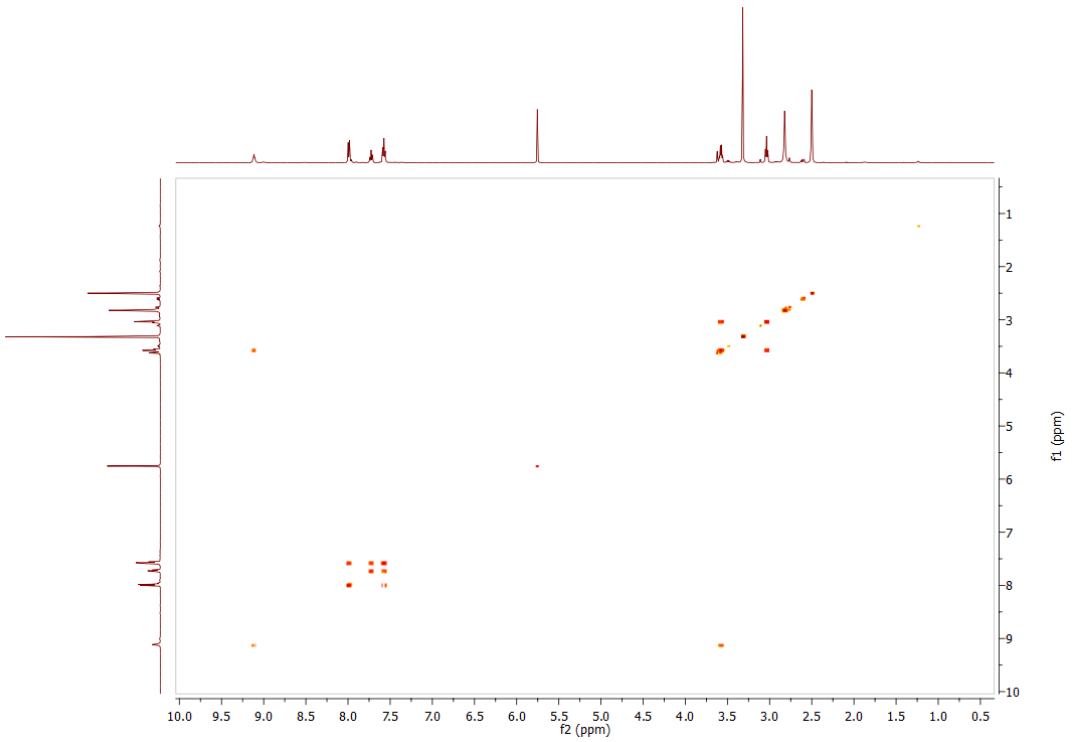

Figure S4.40: COSY spectrum of **4.13** in DMSO-d_6.

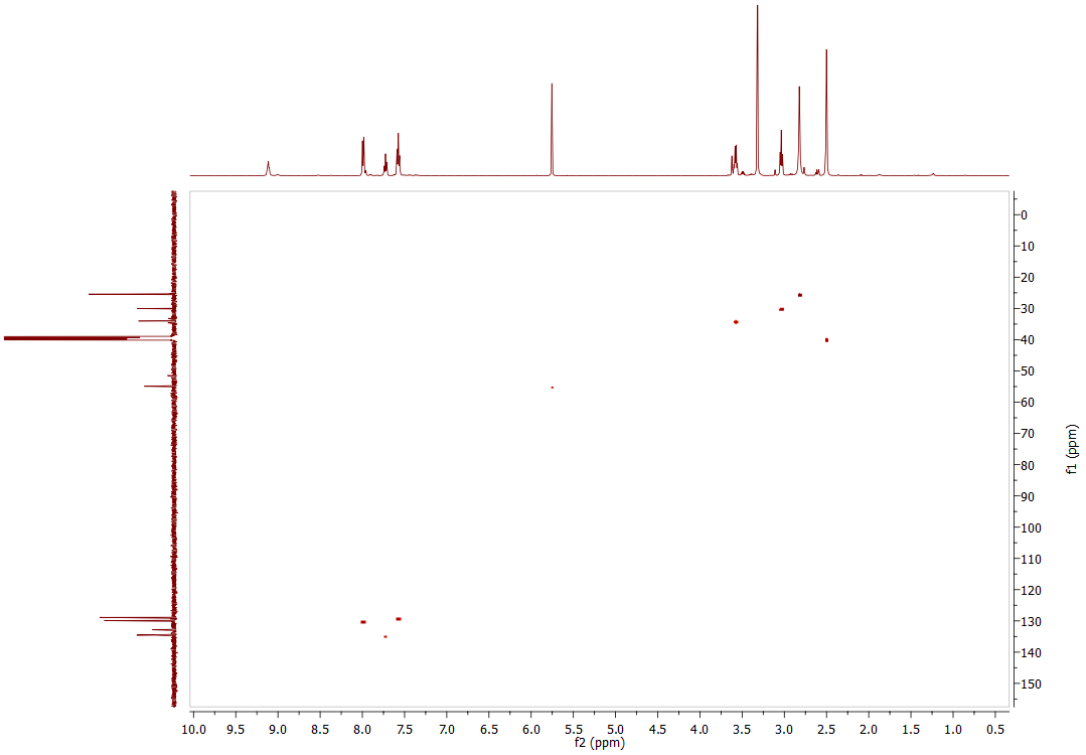

Figure S4.41: HSQC spectrum of **4.13** in DMSO-d_6.

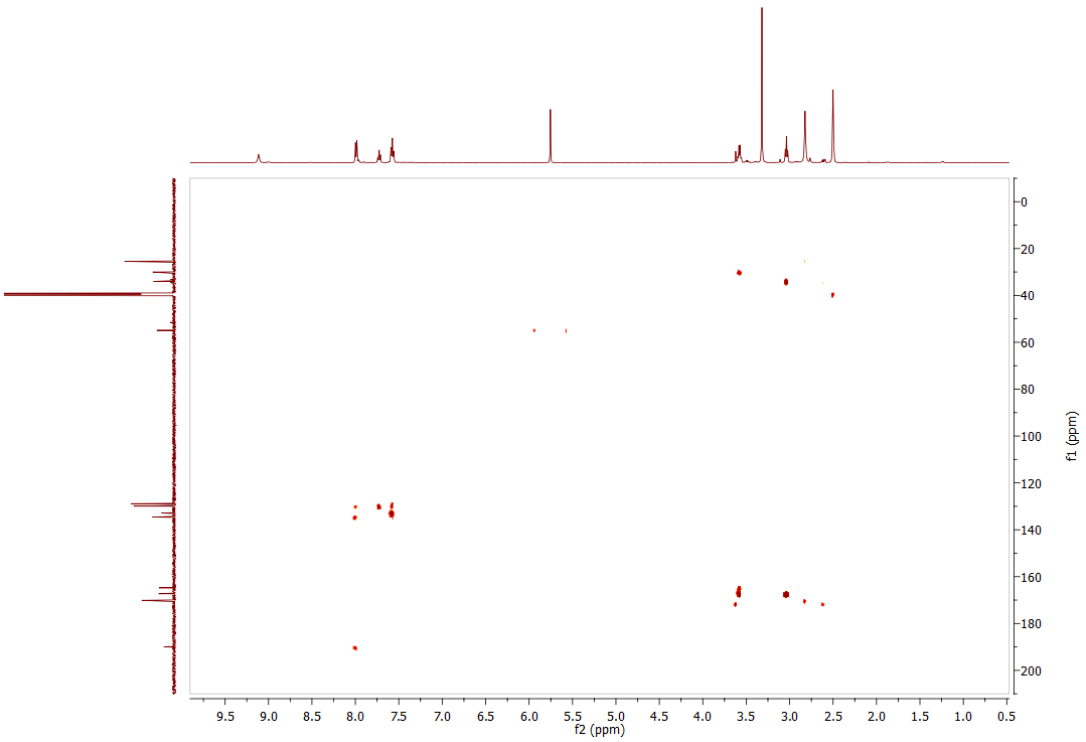

Figure S4.42: HMBC spectrum of **4.13** in DMSO-d_6.

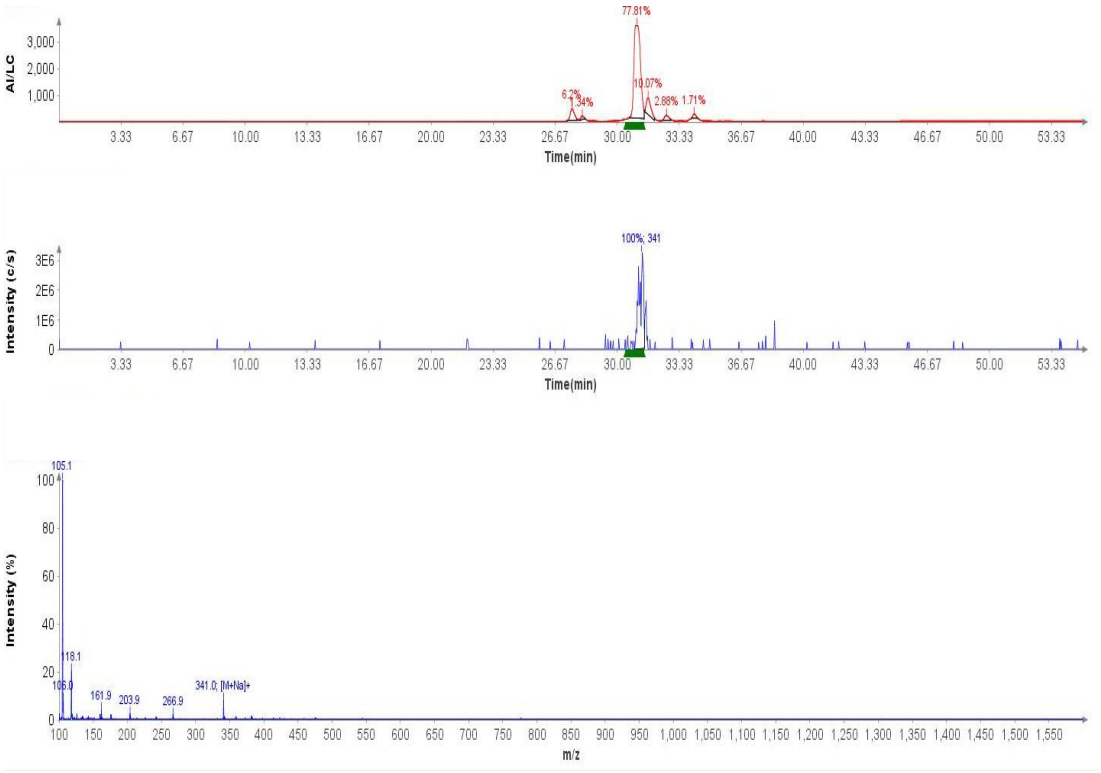

Figure S4.43: LC-MS data for **4.13.**

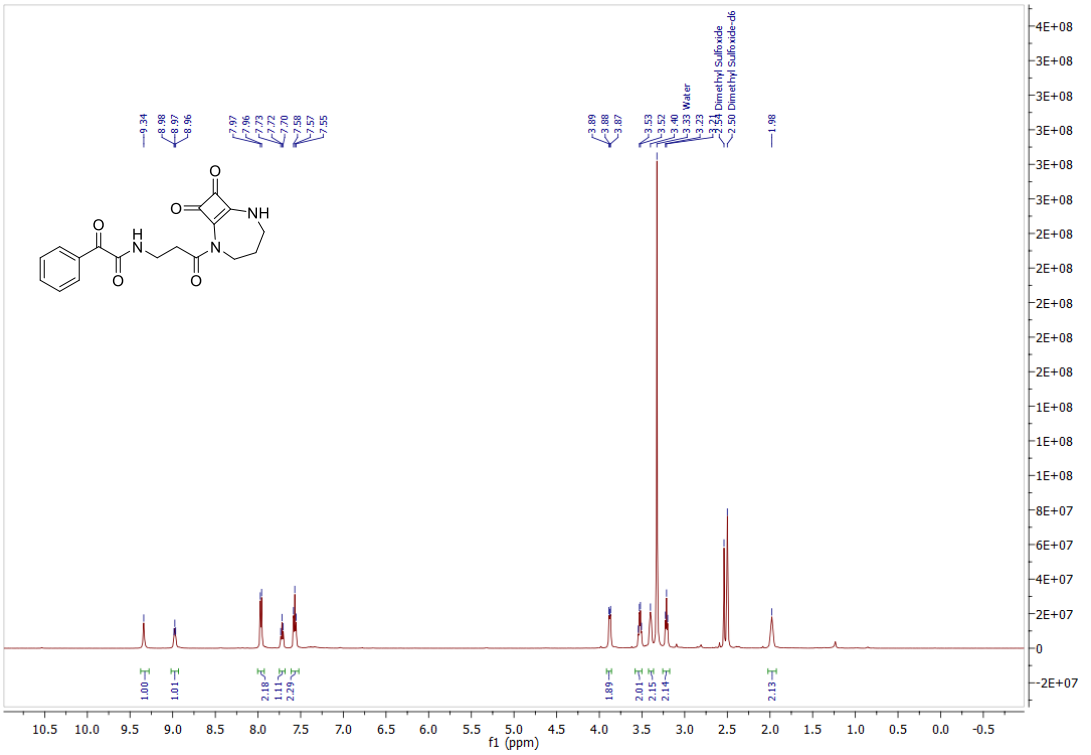

Figure S4.44: ^{1}H NMR spectrum of **4.11** in DMSO-d_6.

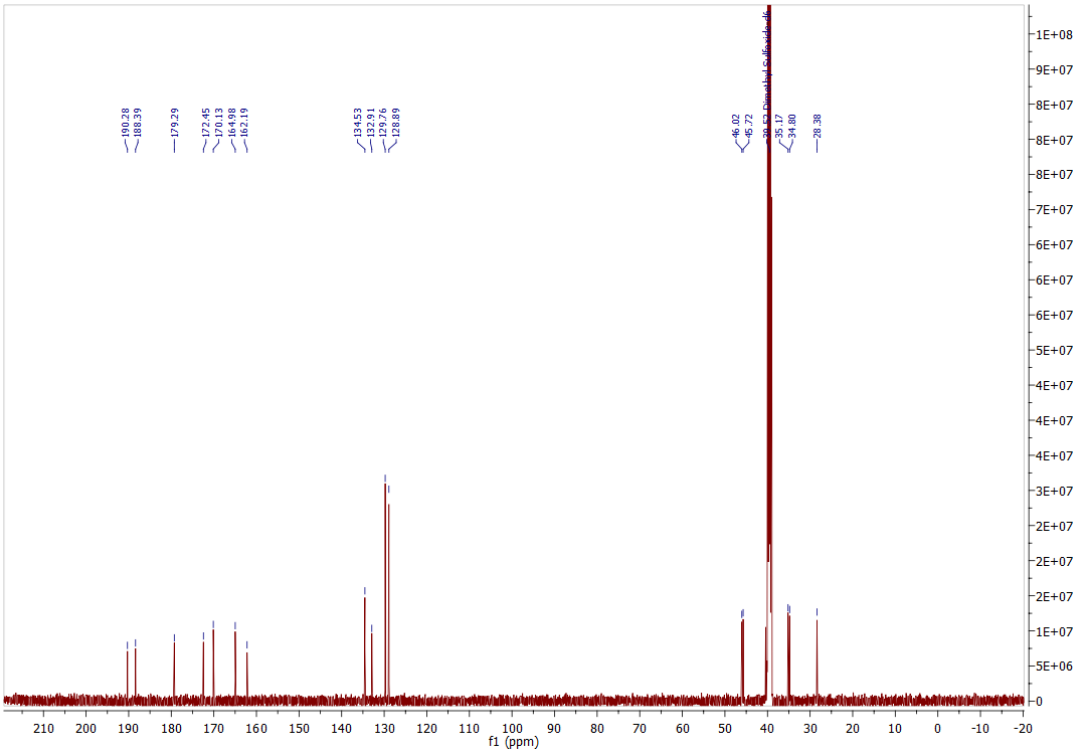

Figure S4.45: ^{13}C NMR spectrum of **4.11** in DMSO-d_6.

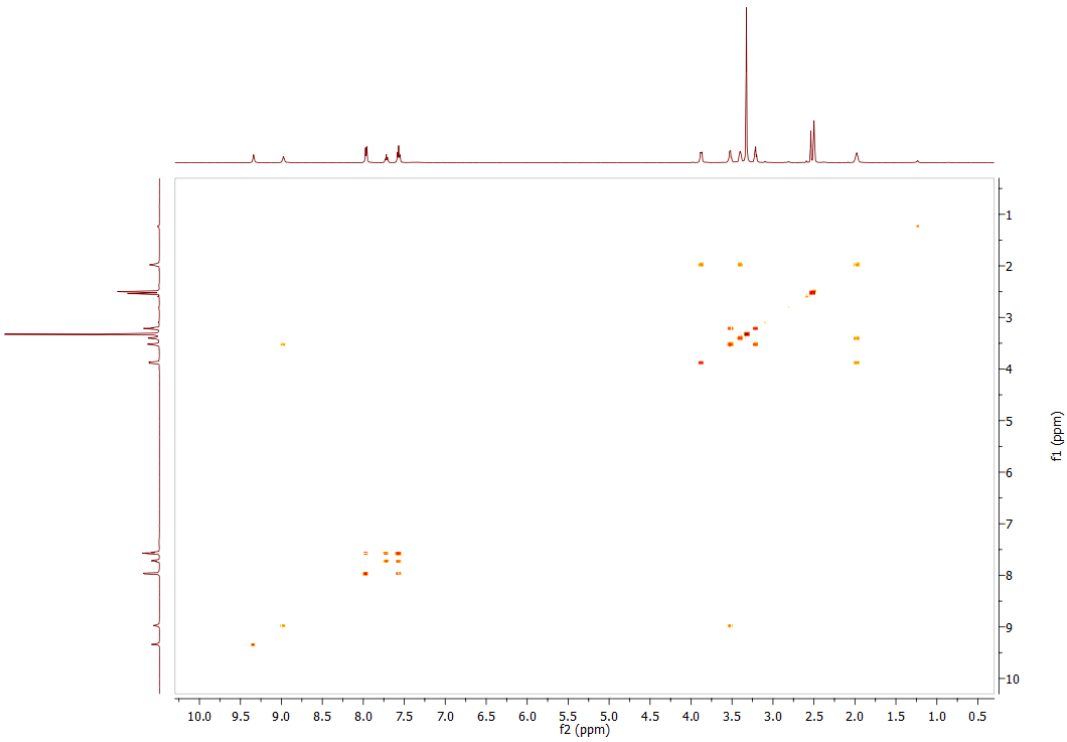

Figure S4.46: COSY spectrum of **4.11** in DMSO-d_6.

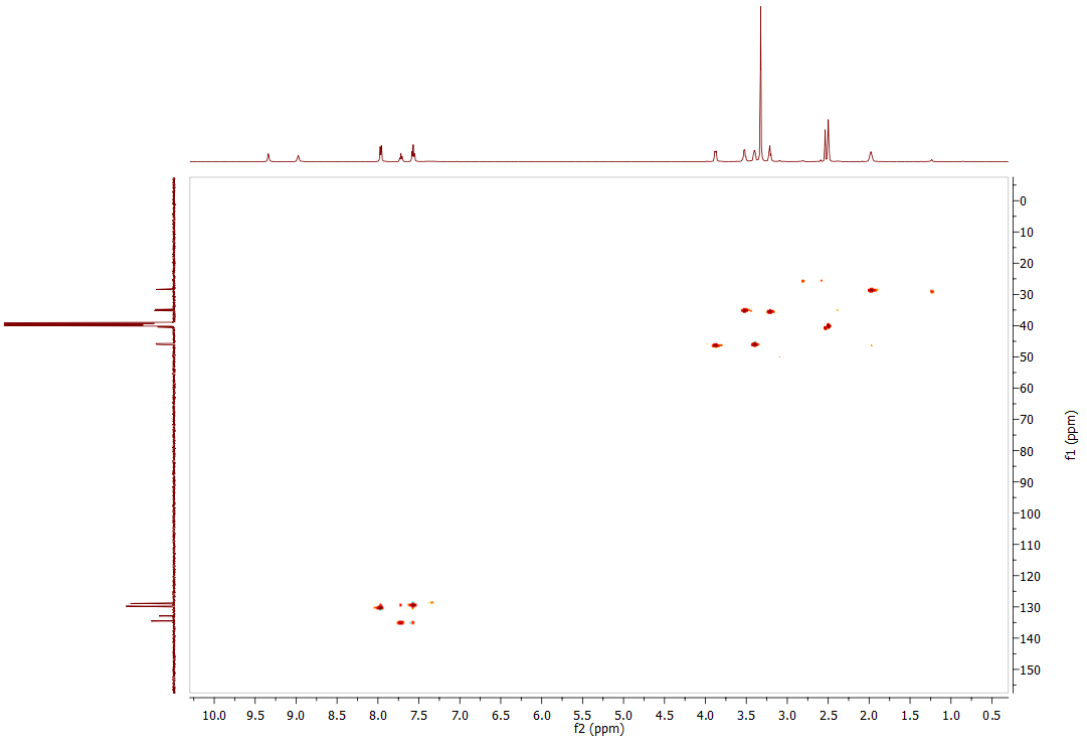

Figure S4.47: HSQC spectrum of **4.11** in DMSO-d_6.

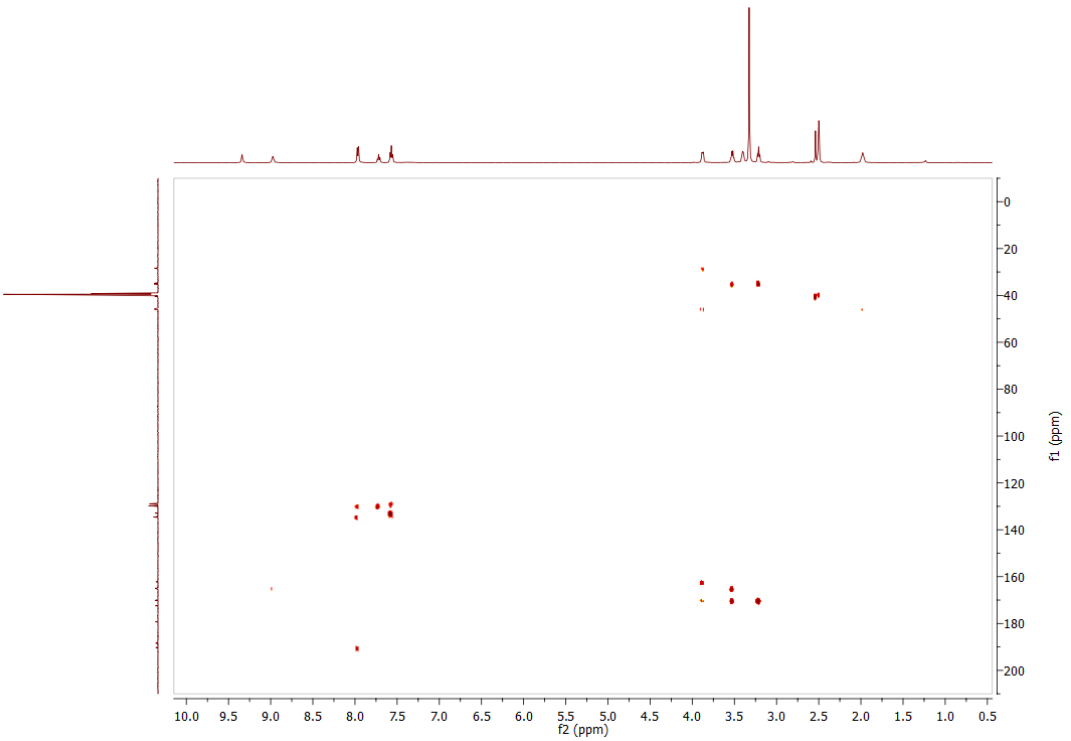

Figure S4.48: HMBC spectrum of **4.11** in DMSO-d_6.

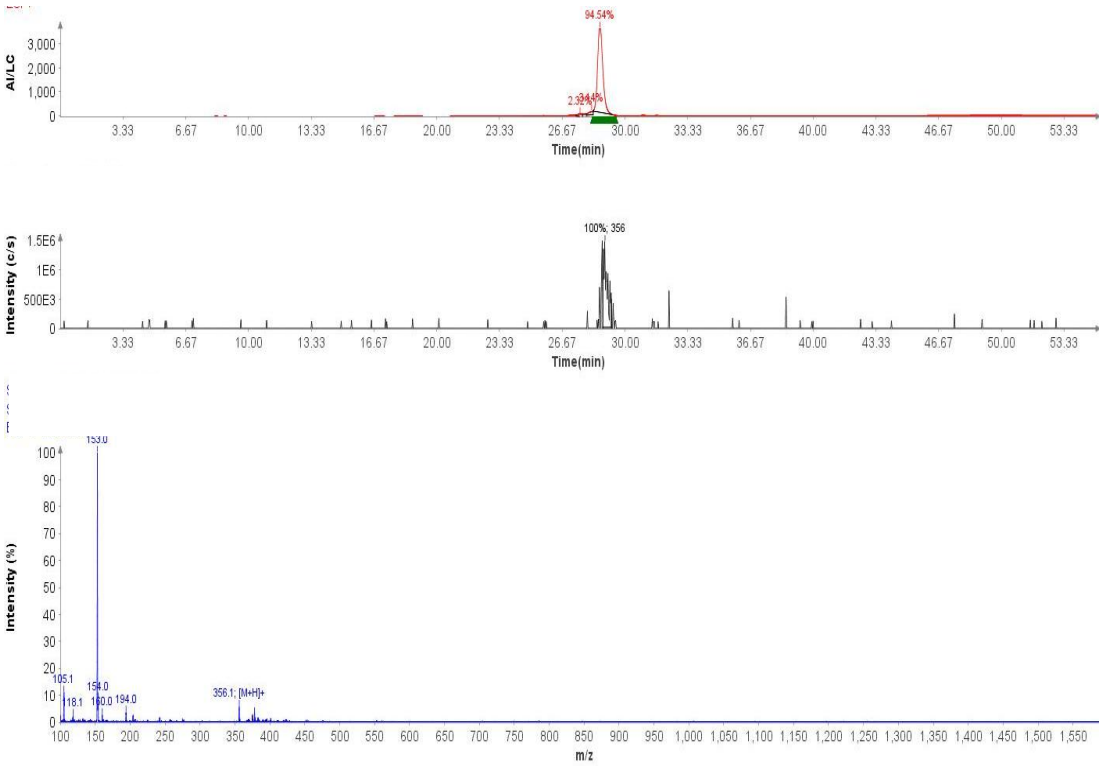

Figure S4.49: LC-MS data for **4.11.**

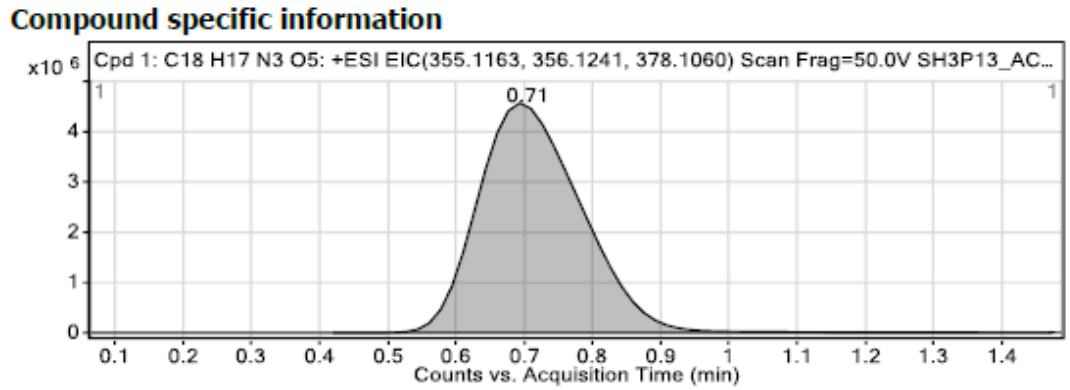

Compound Table

Compound Label	RT (min)	Observed mass (m/z)	Neutral observed mass (Da)	Theoretical mass (Da)	Mass error (ppm)	Isotope match score (%)	Error flag
Cpd 1: C18 H17 N3 O5	0.71	378.1060	355.1177	355.1168	2.52	99.71	No H adduct

Mass errors of between -5.00 and 5.00 ppm with isotope match scores above 60% are considered confirmation of molecular formulae

Figure: Full range view of Compound spectra and potential adducts.

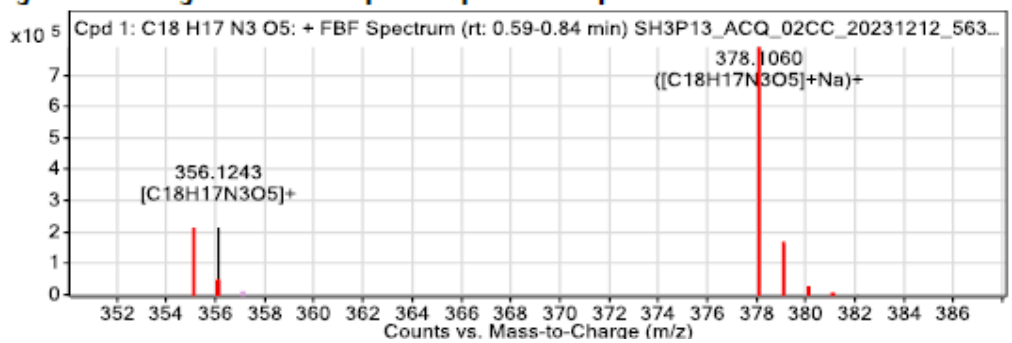

Figure S4.50: HRMS data for **4.11**

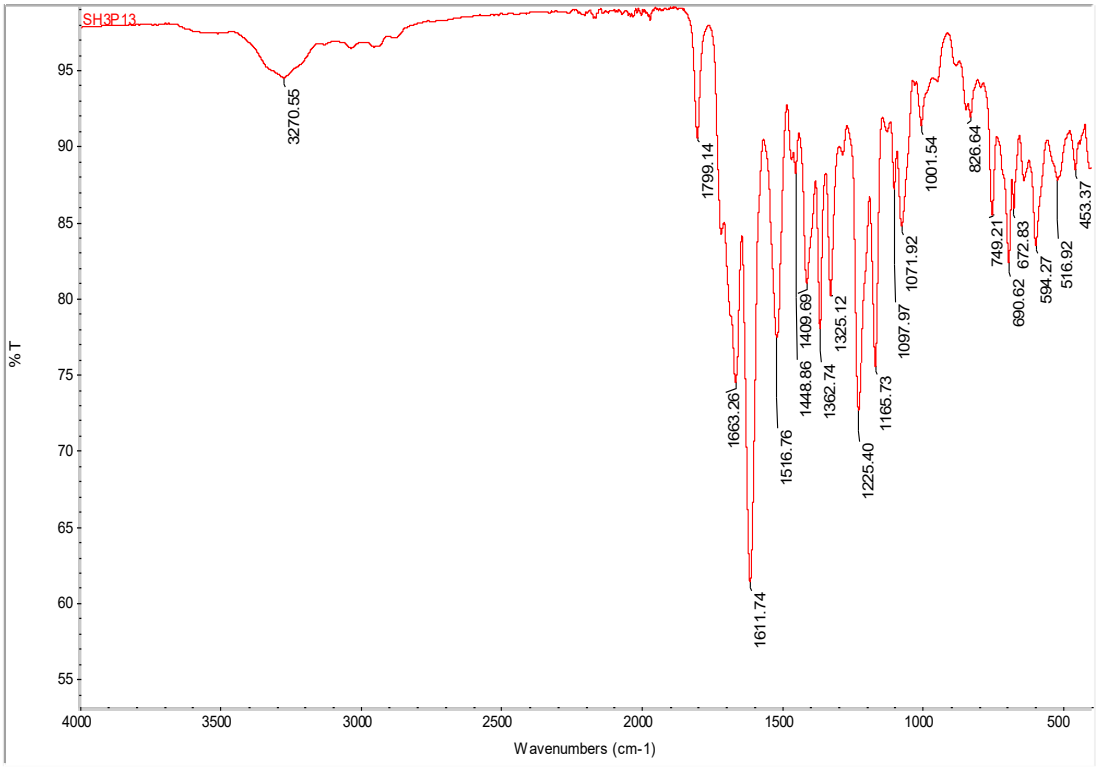

Figure S4.51: FTIR-ATR spectrum of **4.11**

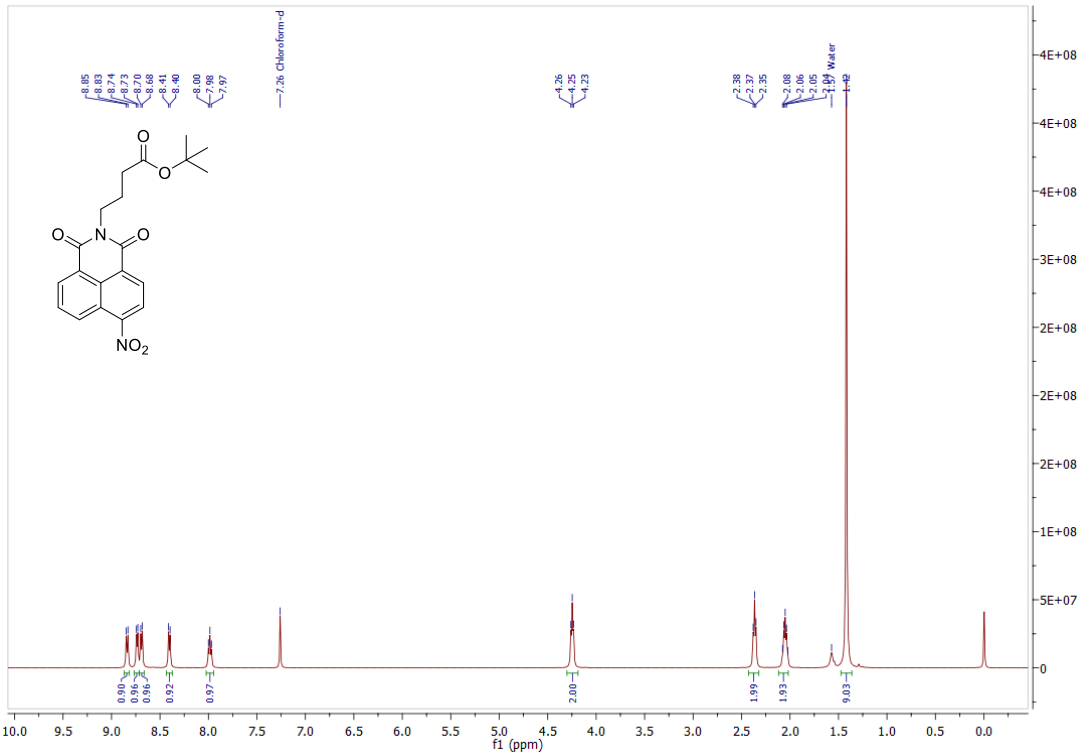

Figure S4.52: ^{1}H NMR spectrum of **4.14** in $CDCl_3$.

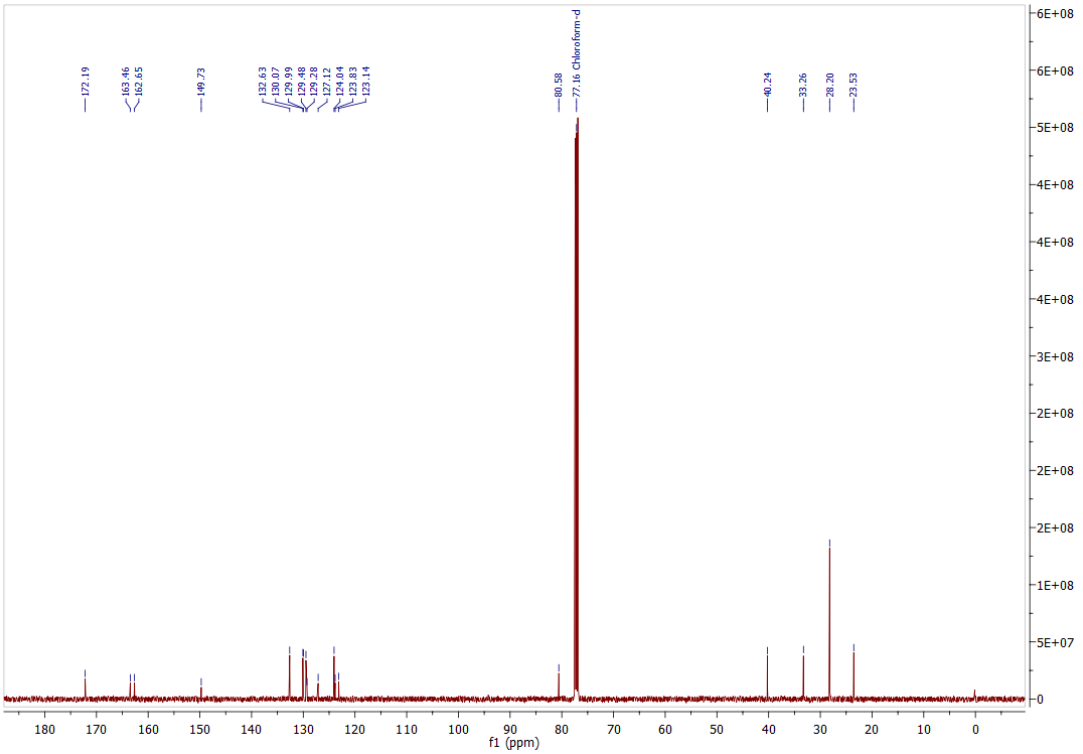

Figure S4.53: ^{13}C NMR spectrum of **4.14** in $CDCl_3$.

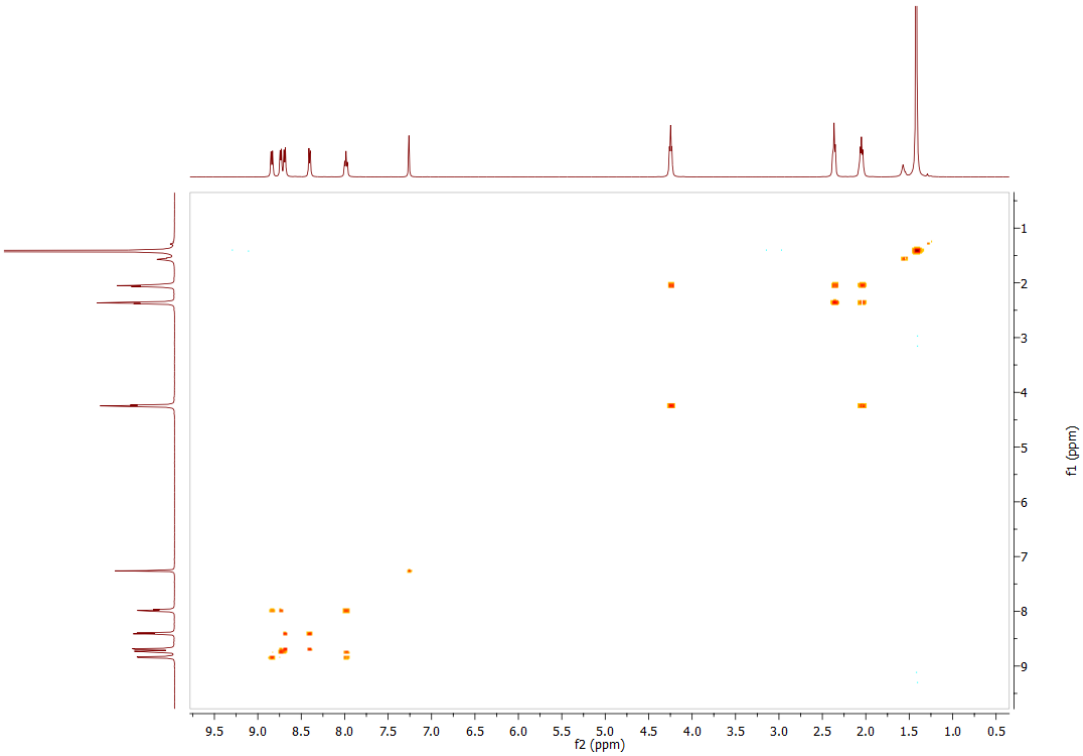

Figure S4.54: COSY spectrum of **4.14** in $CDCl_3$.

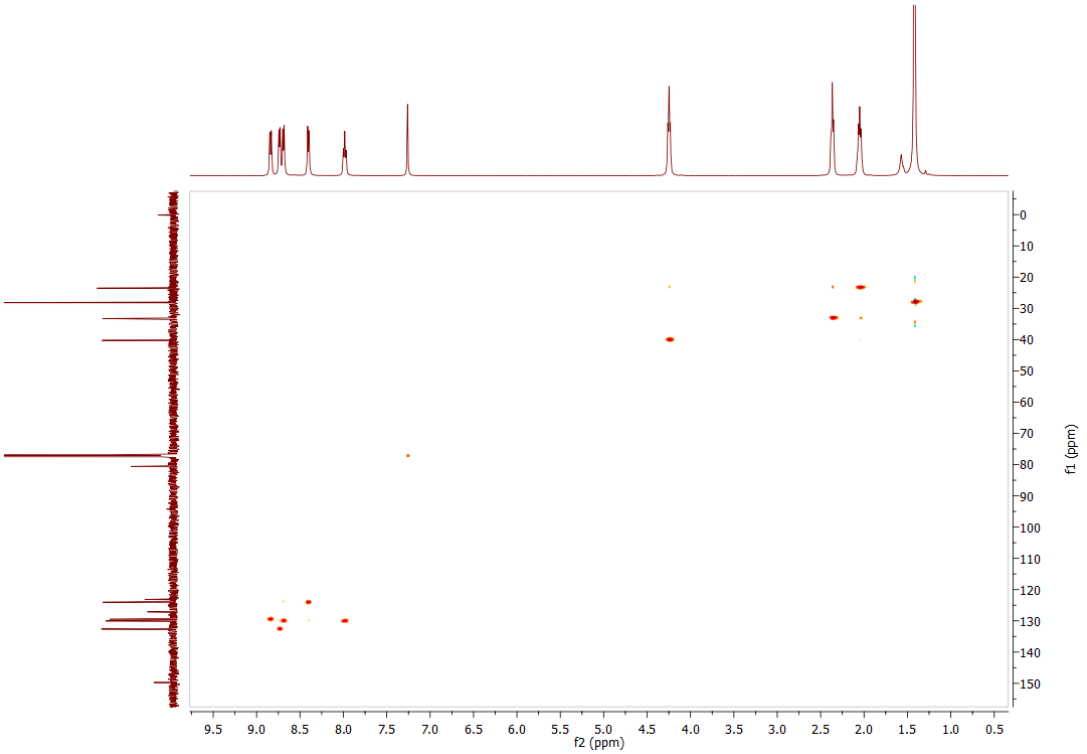

Figure S4.55: HSQC spectrum of **4.14** in $CDCl_3$.

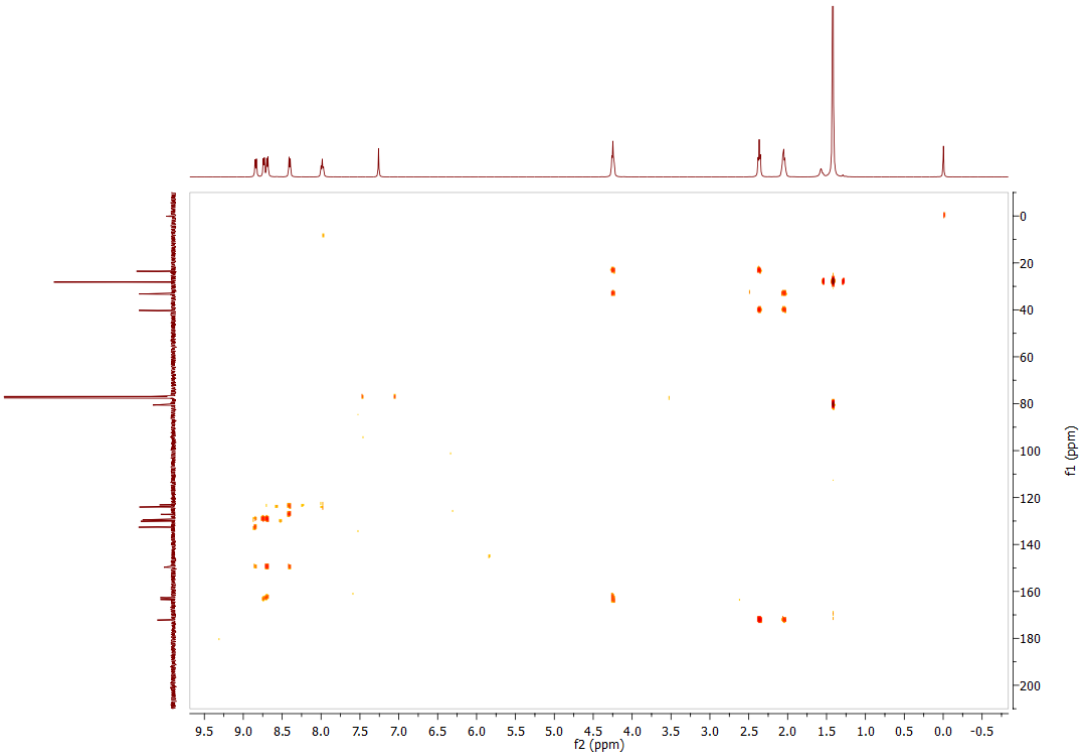

Figure S4.56: HMBC spectrum of **4.14** in $CDCl_3$.

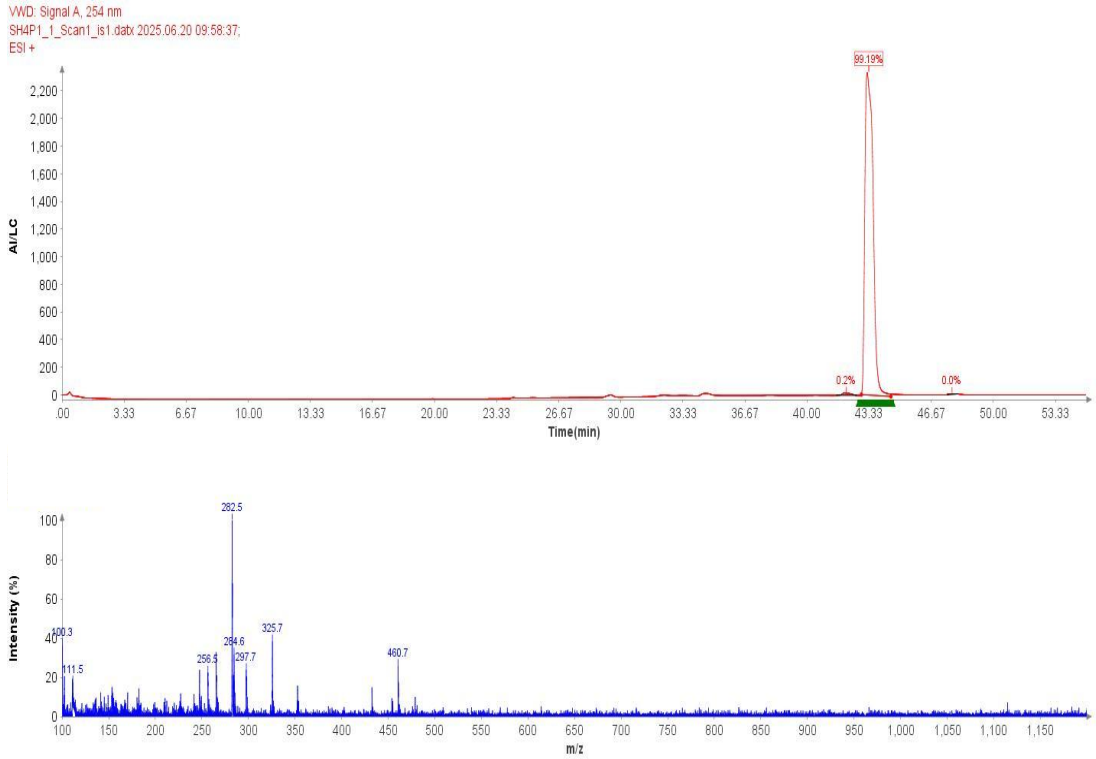

Figure S4.57: LCMS data for **4.14.**

Compound specific information

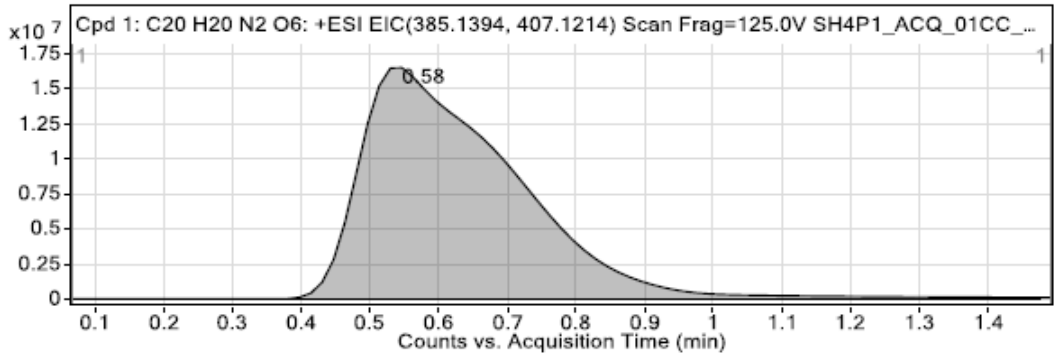

Compound Table

Compound Label	RT (min)	Observed mass (m/z)	Neutral observed mass (Da)	Theoretical mass (Da)	Mass error (ppm)	Isotope match score (%)
Cpd 1: C20 H20 N2 O6	0.58	407.1214	384.1322	384.1321	0.29	99.87

Mass errors of between -5.00 and 5.00 ppm with isotope match scores above 60% are considered confirmation of molecular formulae

Figure: Full range view of Compound spectra and potential adducts.

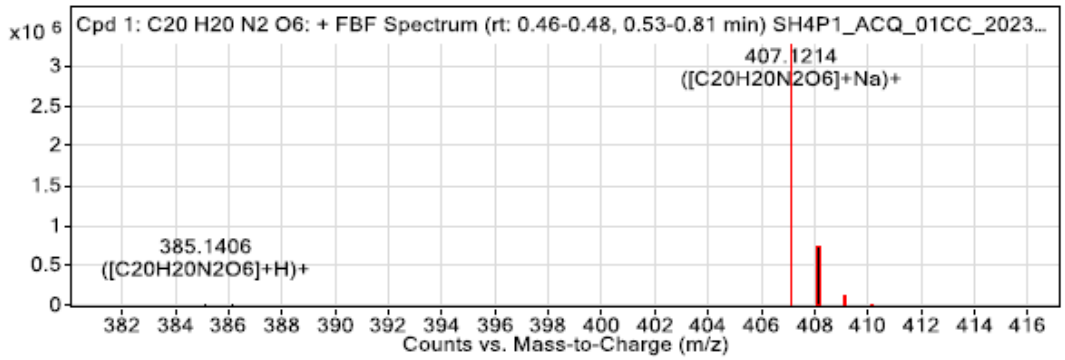

Figure S4.58: HRMS data for **4.14.**

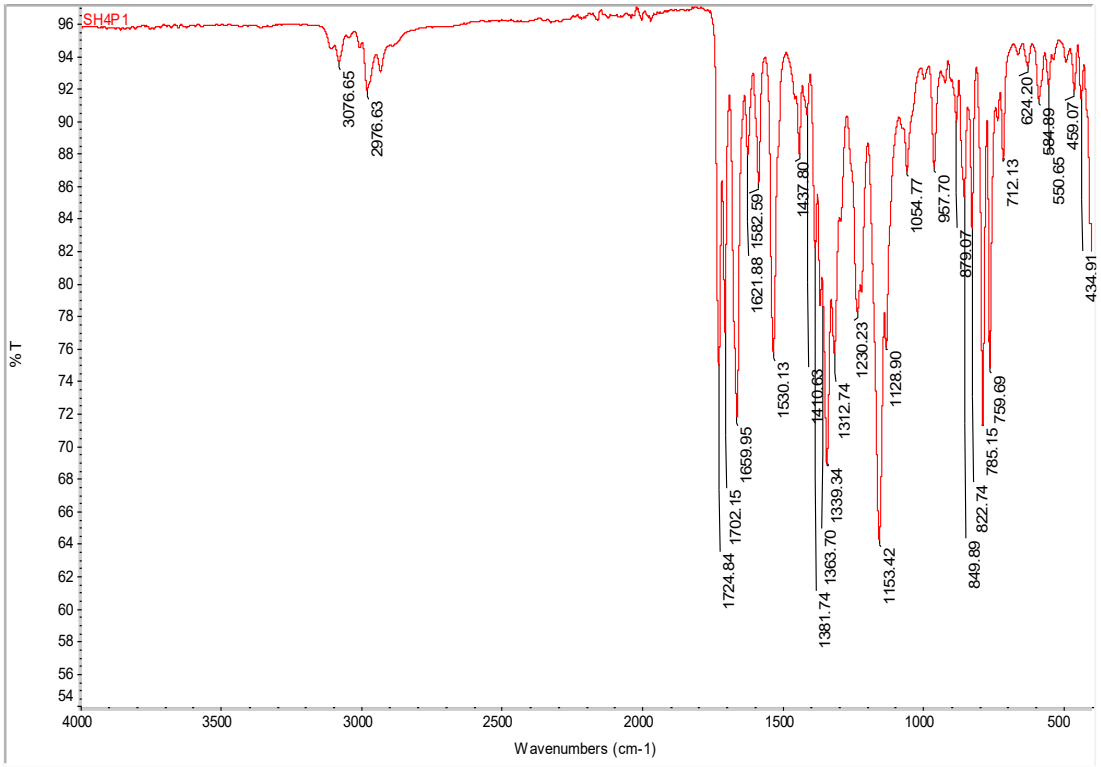

Figure 4.59: FTIR-ATR spectrum of **4.14.**

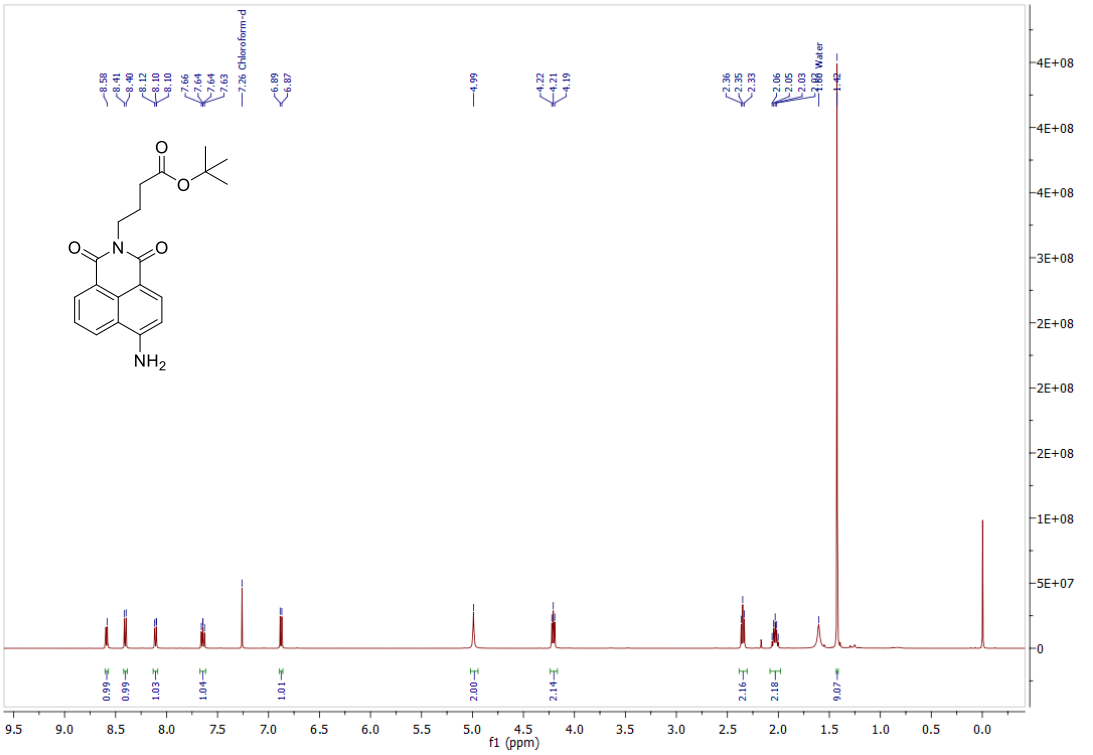

Figure S4.60: ^{1}H NMR spectrum of **4.15** in $CDCl_3$.

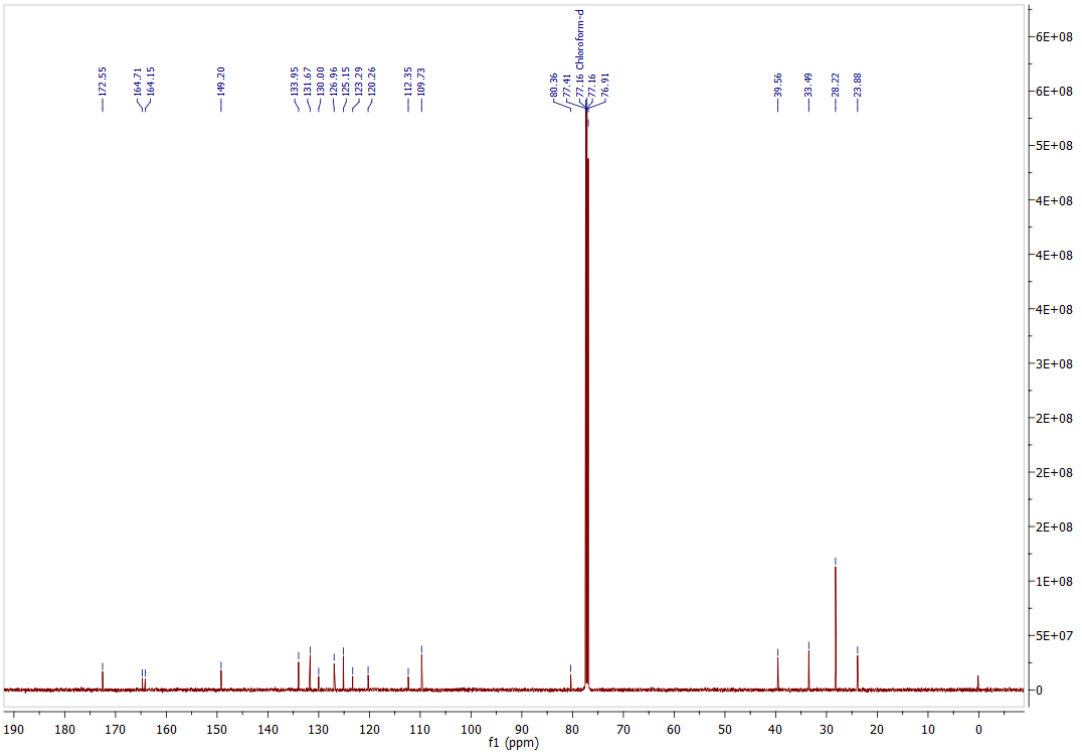

Figure S4.61: ^{13}C NMR spectrum of **4.15** in $CDCl_3$.

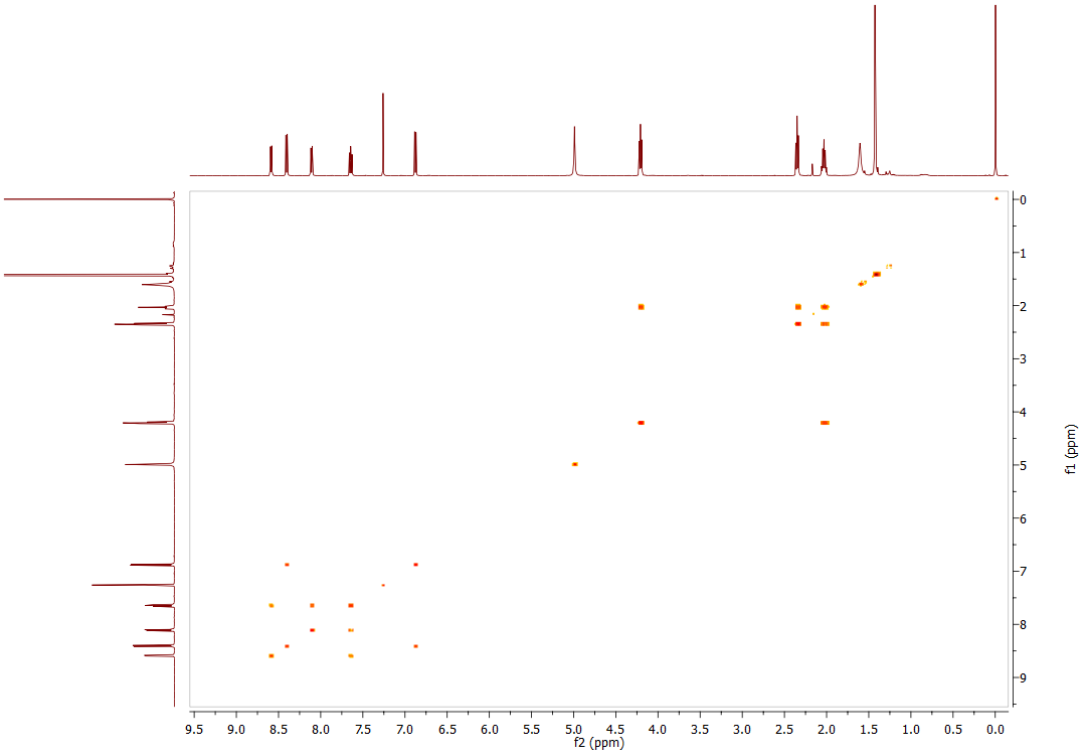

Figure S4.62: COSY spectrum of **4.15** in $CDCl_3$.

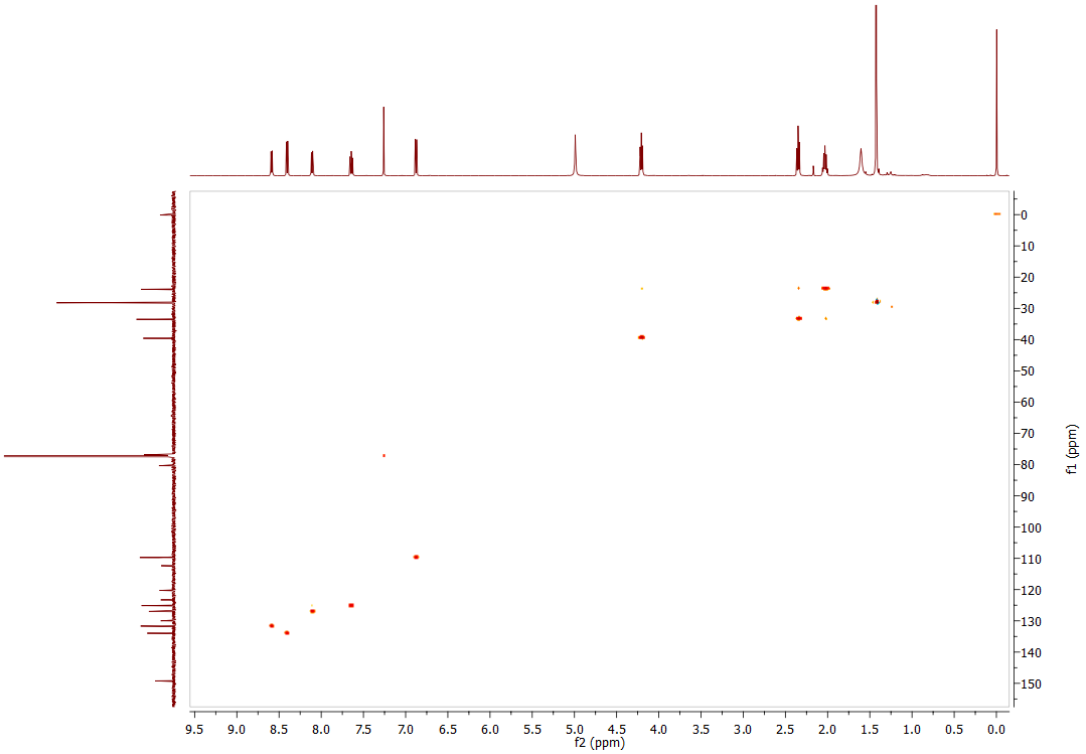

Figure S4.63: HSQC spectrum of **4.15** in $CDCl_3$.

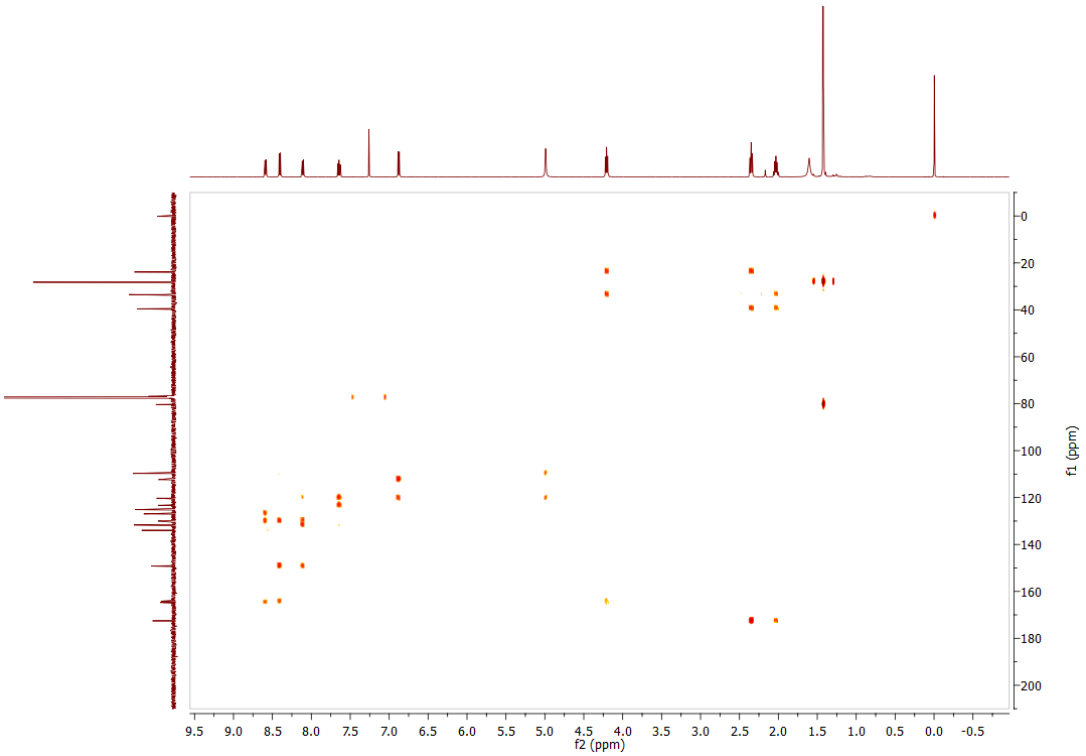

Figure S4.64: HMBC spectrum of **4.15** in $CDCl_3$.

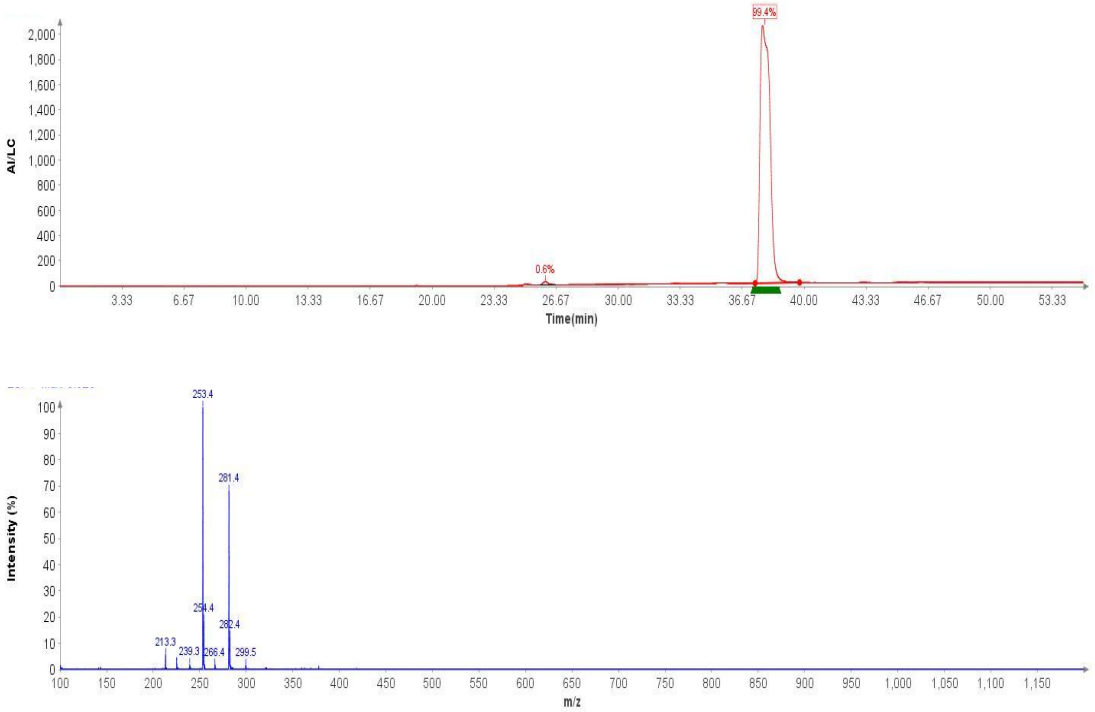

Figure S4.65: LCMS data for **4.15.**

Compound specific information

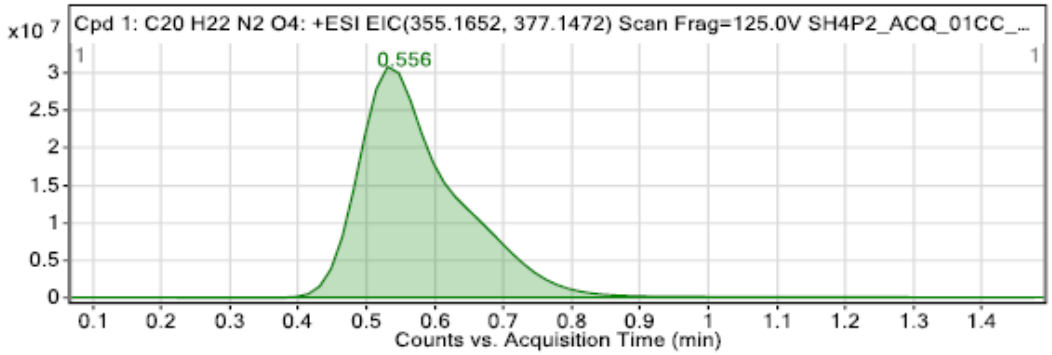

Compound Table

Compound Label	RT (min)	Observed mass (m/z)	Neutral observed mass (Da)	Theoretical mass (Da)	Mass error (ppm)	Isotope match score (%)
Cpd 1: C20 H22 N2 O4	0.56	377.1473	354.1582	354.1580	0.57	99.30

Mass errors of between -5.00 and 5.00 ppm with isotope match scores above 60% are considered confirmation of molecular formulae

Figure: Full range view of Compound spectra and potential adducts.

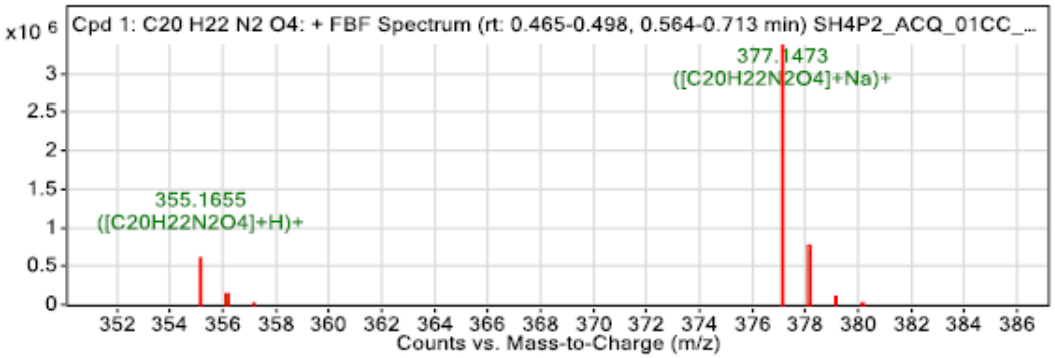

Figure S4.66: HRMS data for **4.15.**

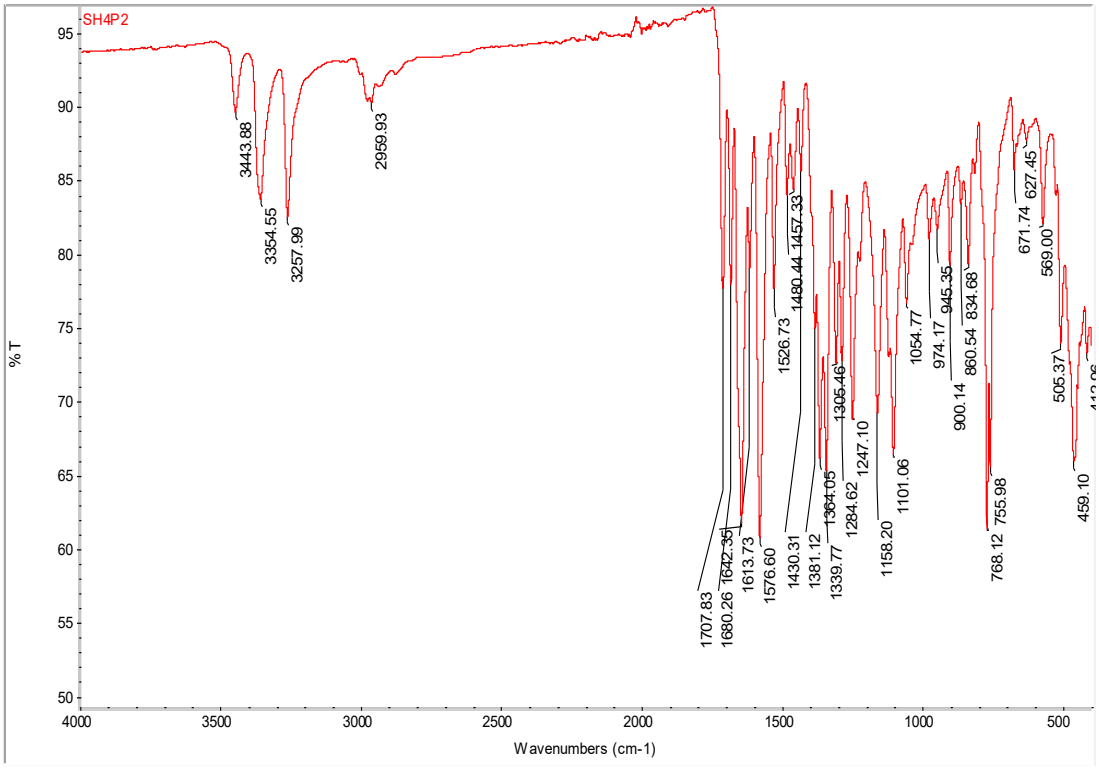

Figure S4.67: FTIR-ATR spectrum of **4.15.**

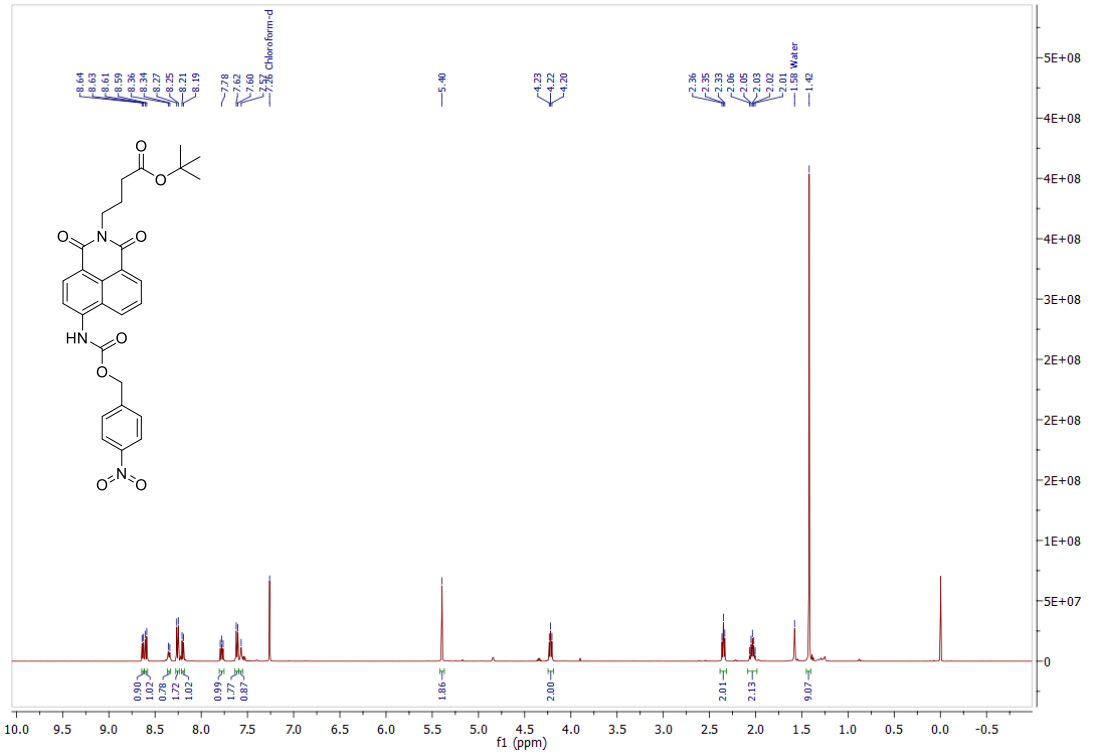

Figure S4.68: ^{1}H NMR spectrum for **4.16** in $CDCl_3$.

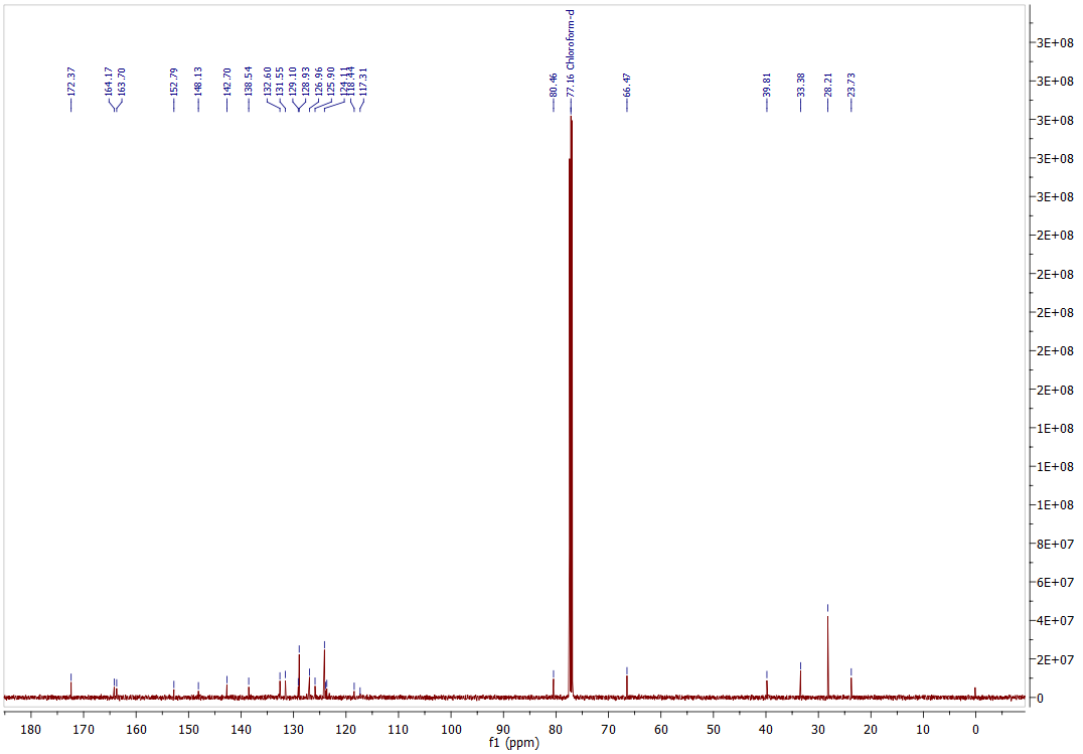

Figure S4.69: 13C NMR spectrum for **4.16** in $CDCl_3$.

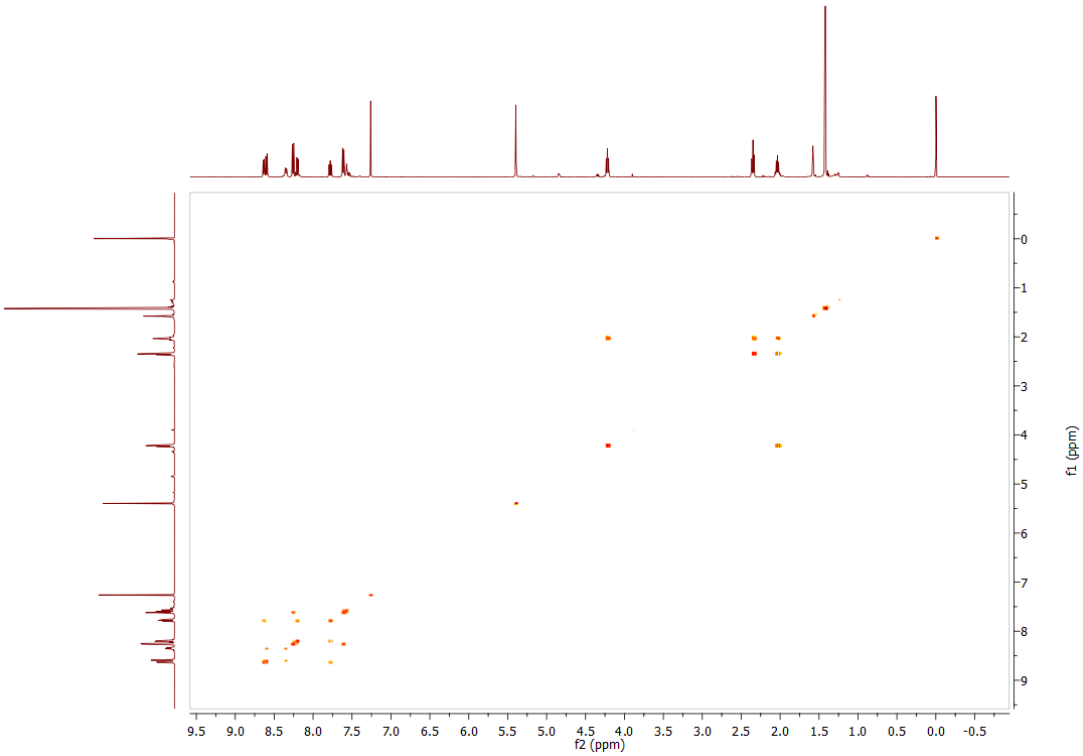

Figure S4.70: COSY NMR for **4.16** in $CDCl_3$.

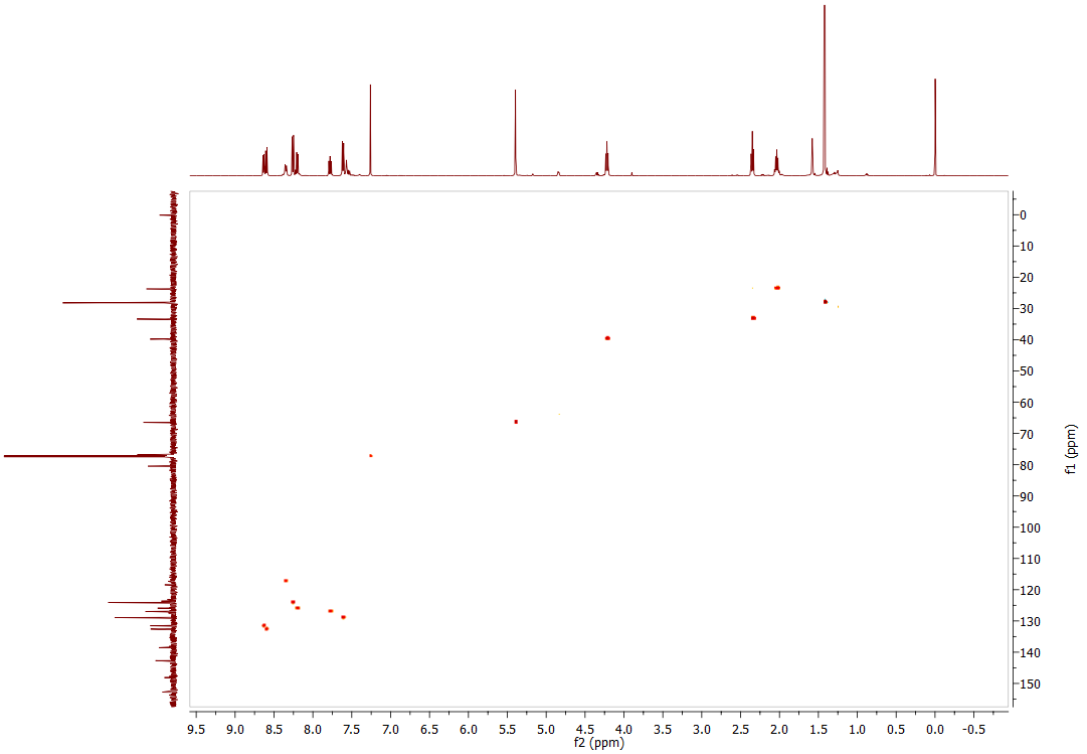

Figure S4.71: HSQC spectrum for **4.16** in $CDCl_3$.

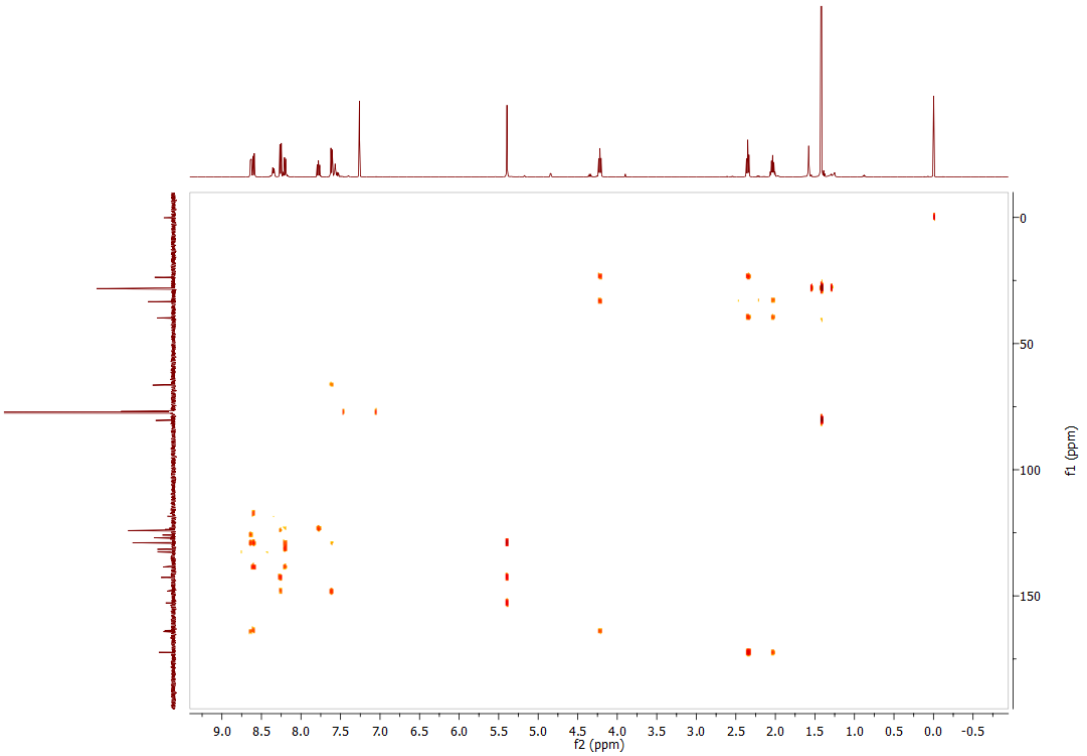

Figure S4.72: HMBC spectrum for **4.16** in $CDCl_3$.

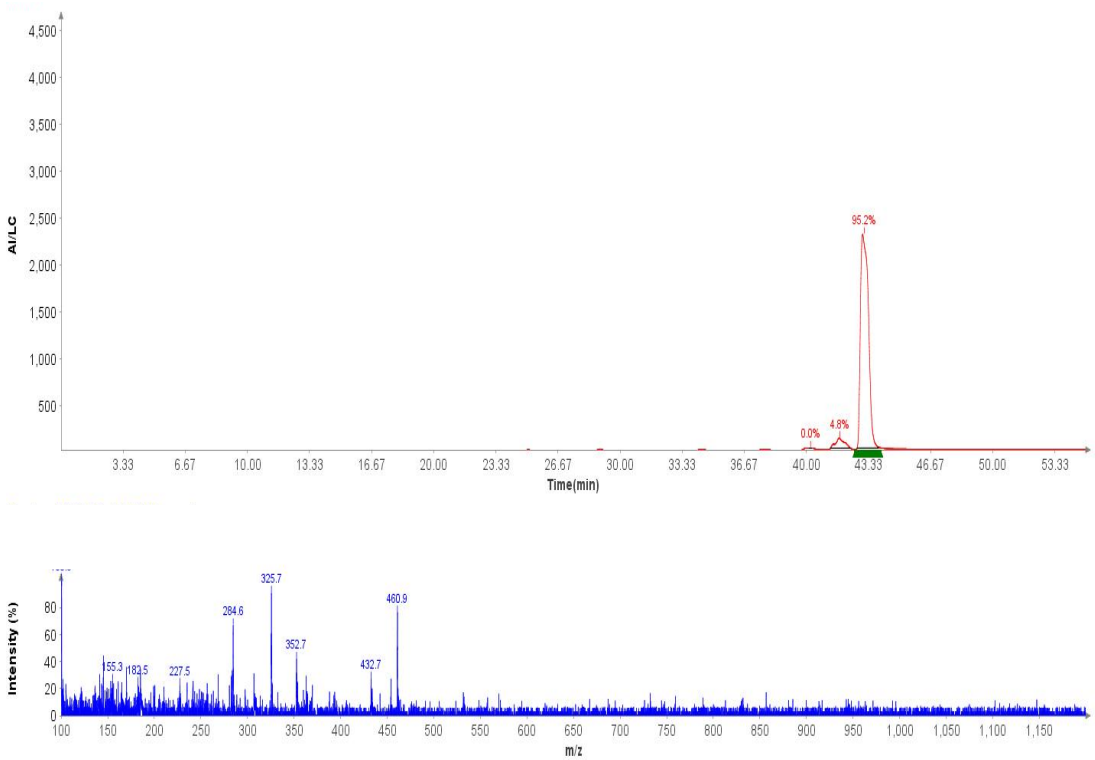

Figure S4.73: LCMS data for **4.16**

Compound specific information

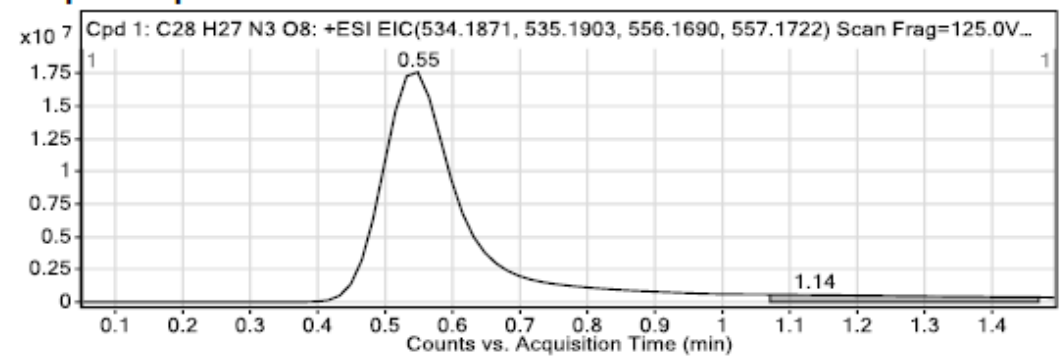

Compound Table

Compound Label	RT (min)	Observed mass (m/z)	Neutral observed mass (Da)	Theoretical mass (Da)	Mass error (ppm)	Isotope match score (%)	Error flag
Cpd 1: C28 H27 N3 O8	1.14	556.1687	533.1795	533.1798	-0.62	99.90	No H adduct

Mass errors of between -5.00 and 5.00 ppm with isotope match scores above 60% are considered confirmation of molecular formulae

Figure: Full range view of Compound spectra and potential adducts.

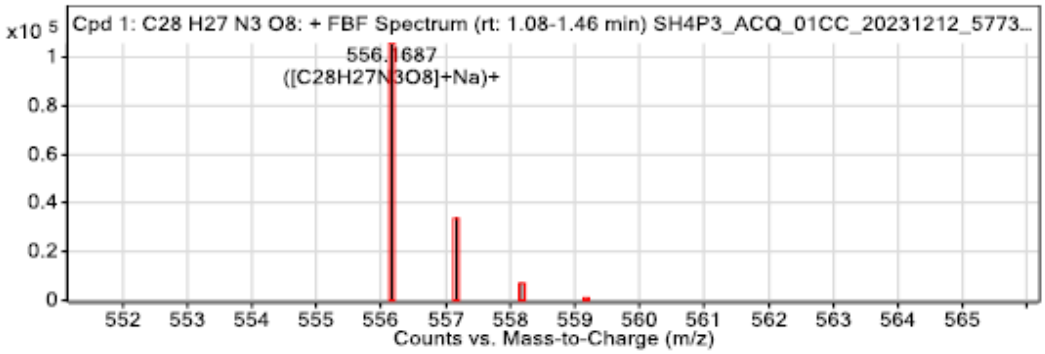

Figure S4.74: HRMS data for **4.16.**

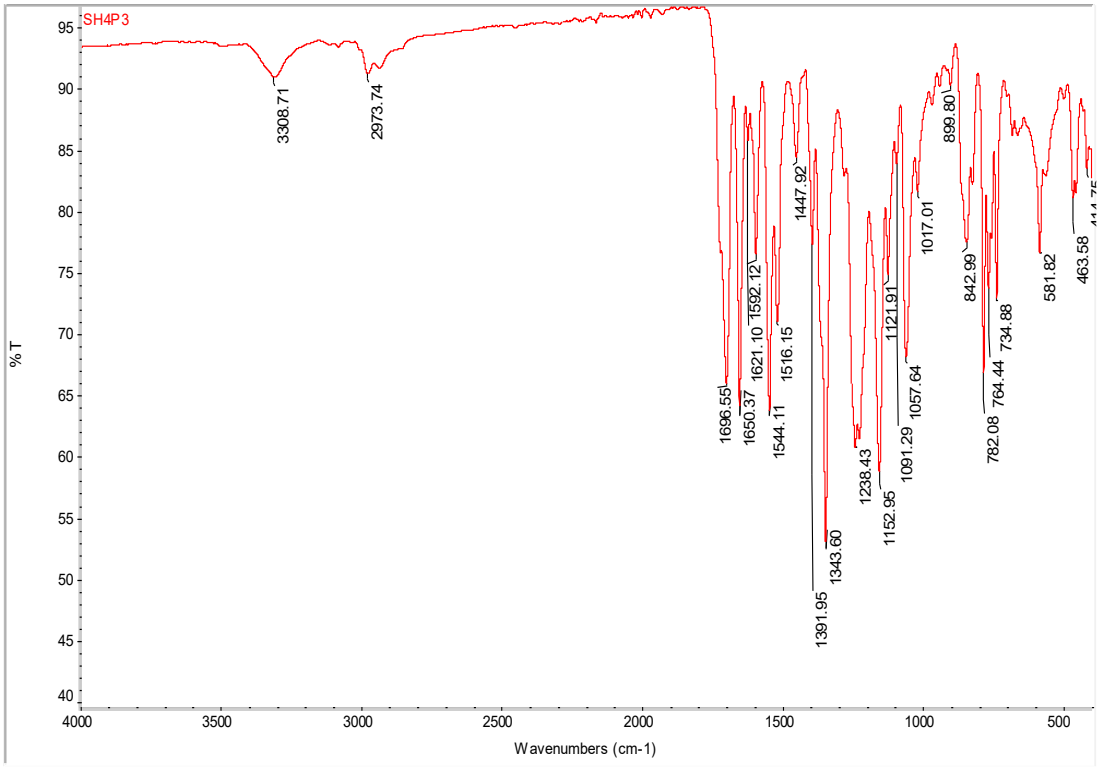

Figure S4.75: FTIR-ATR spectrum of **4.16.**

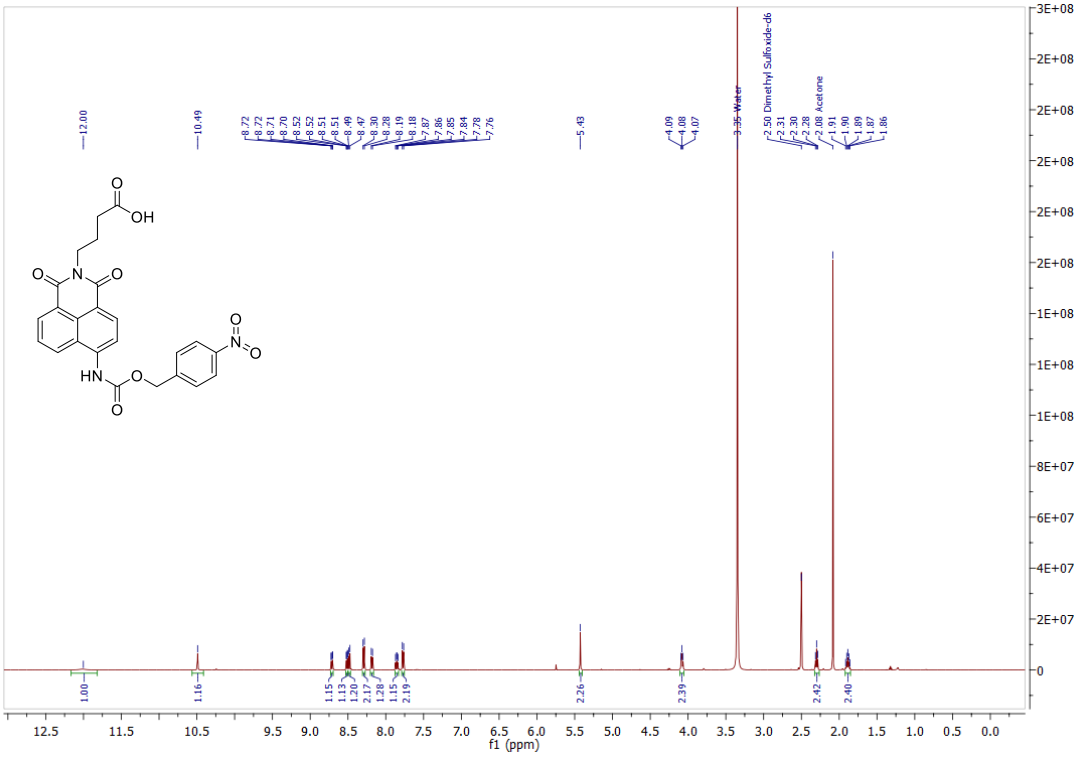

Figure S4.76: ^{1}H NMR spectrum of **4.17** in DMSO-d_6.

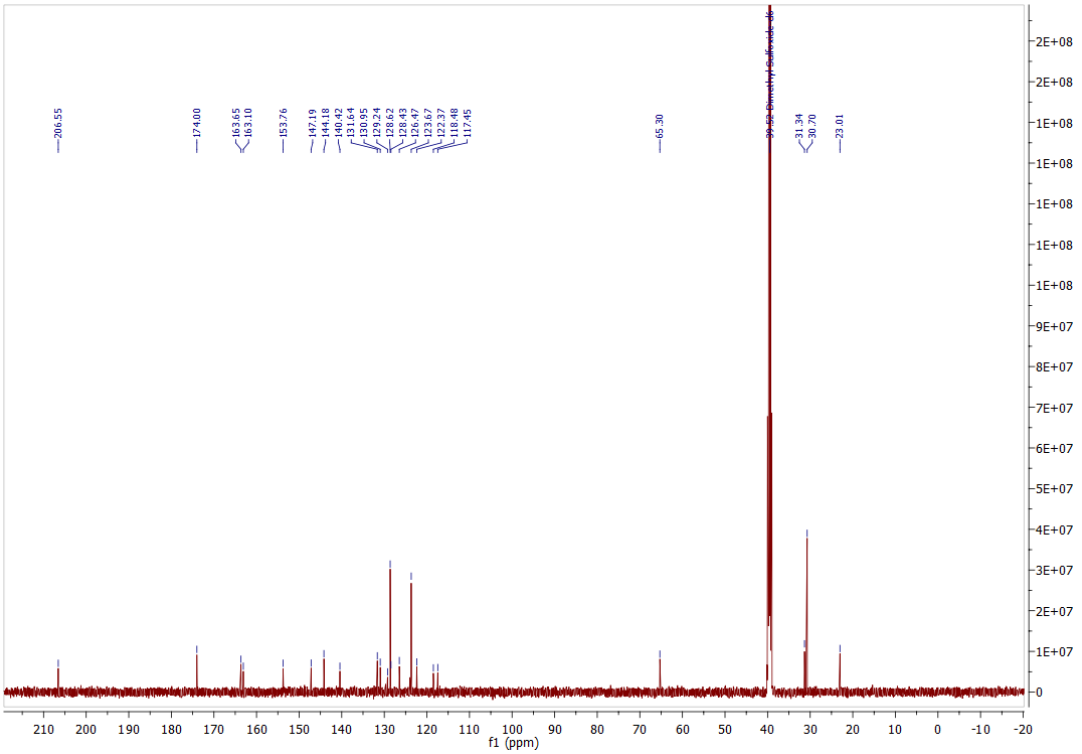

Figure S4.77: ^{13}C NMR spectrum of **4.17** in DMSO-d_6.

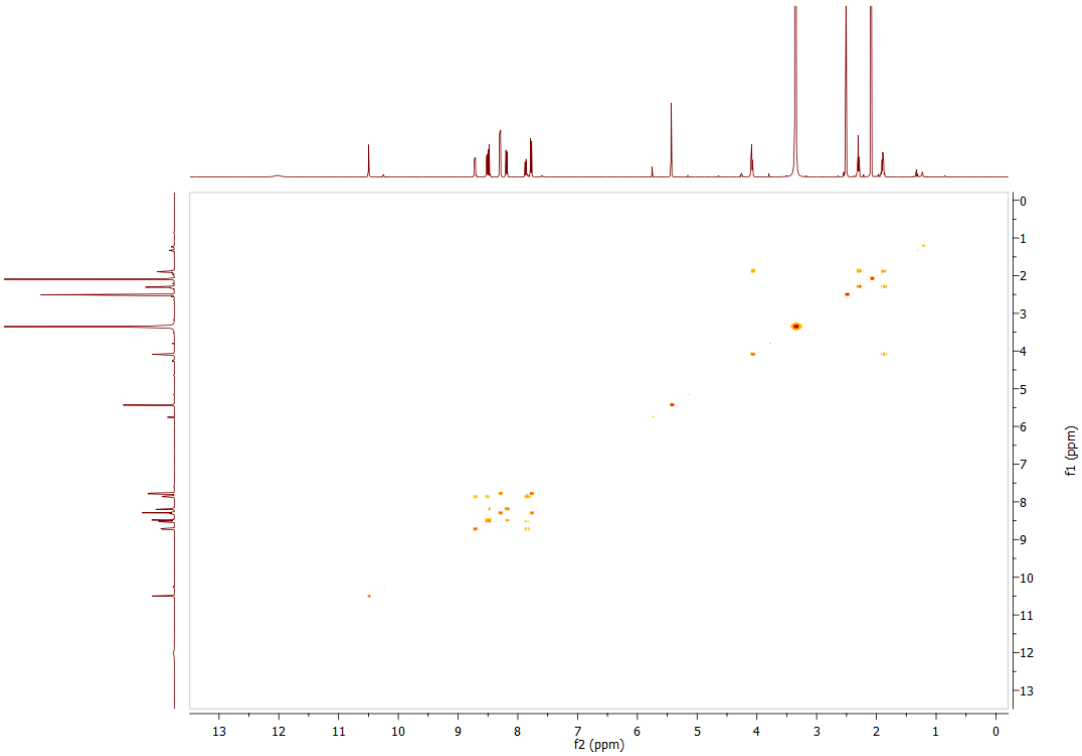

Figure S4.78: COSY spectrum of **4.17** in DMSO-d_6.

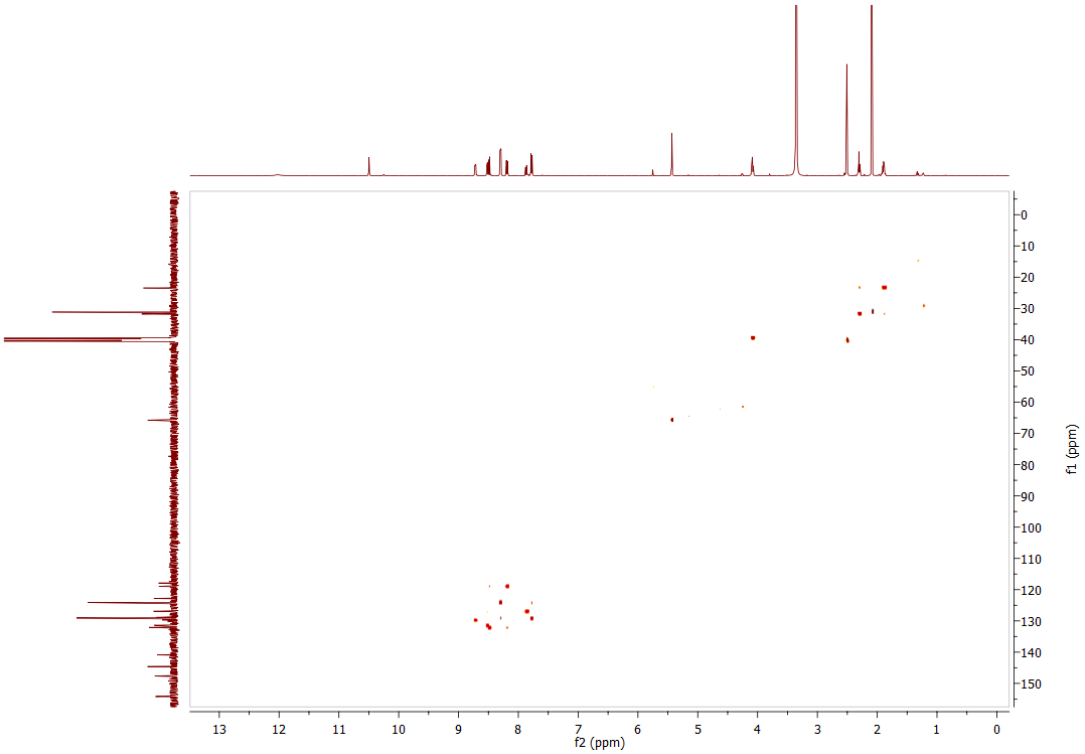

Figure S4.79: HSQC spectrum of **4.17** in DMSO-d_6.

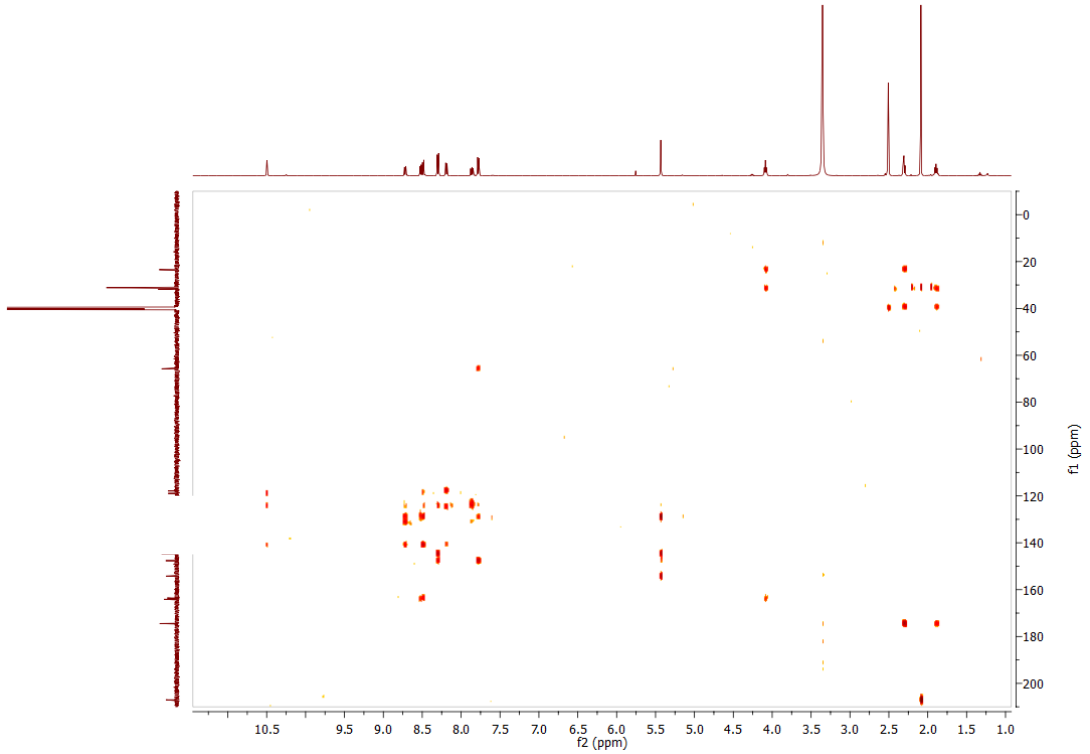

Figure S4.80: HMBC NMR of 4.17 in DMSO-d_6.

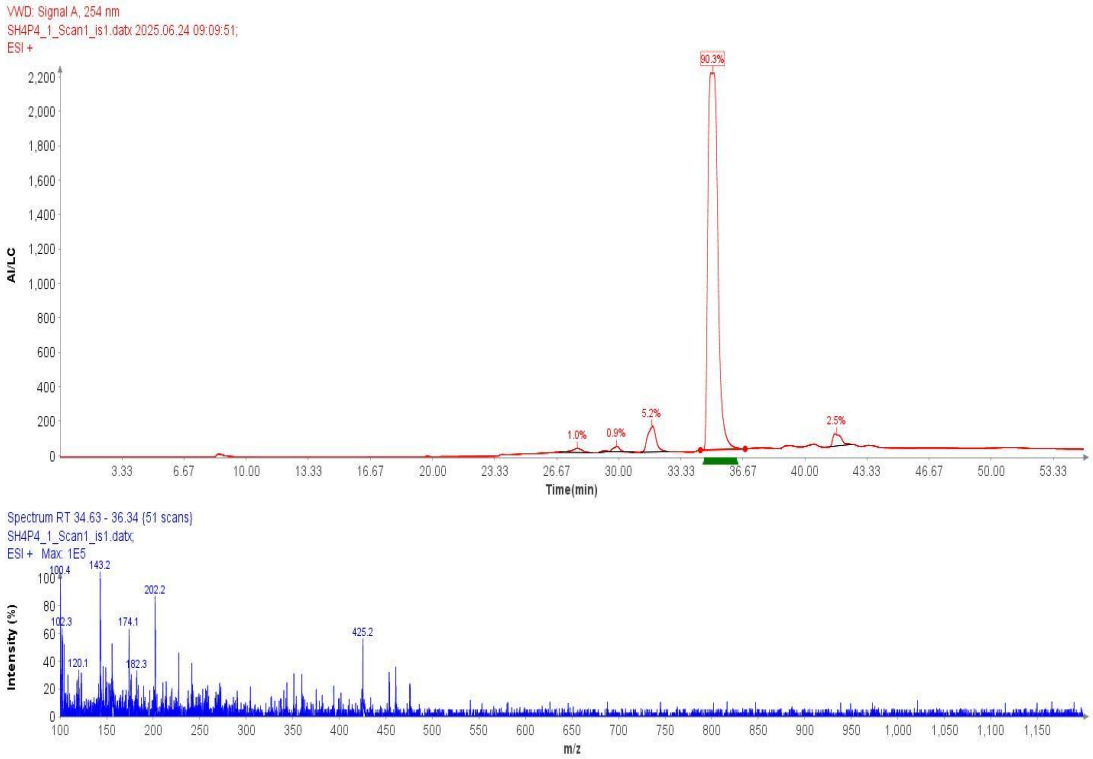

Figure S4.81: LCMS data for **4.17.**

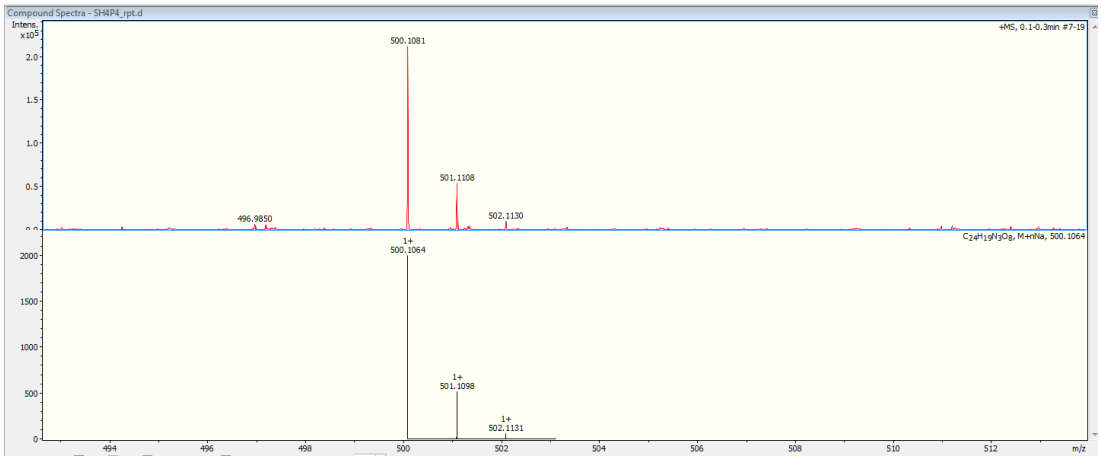

Figure S4.82: HRMS data for **4.17.**

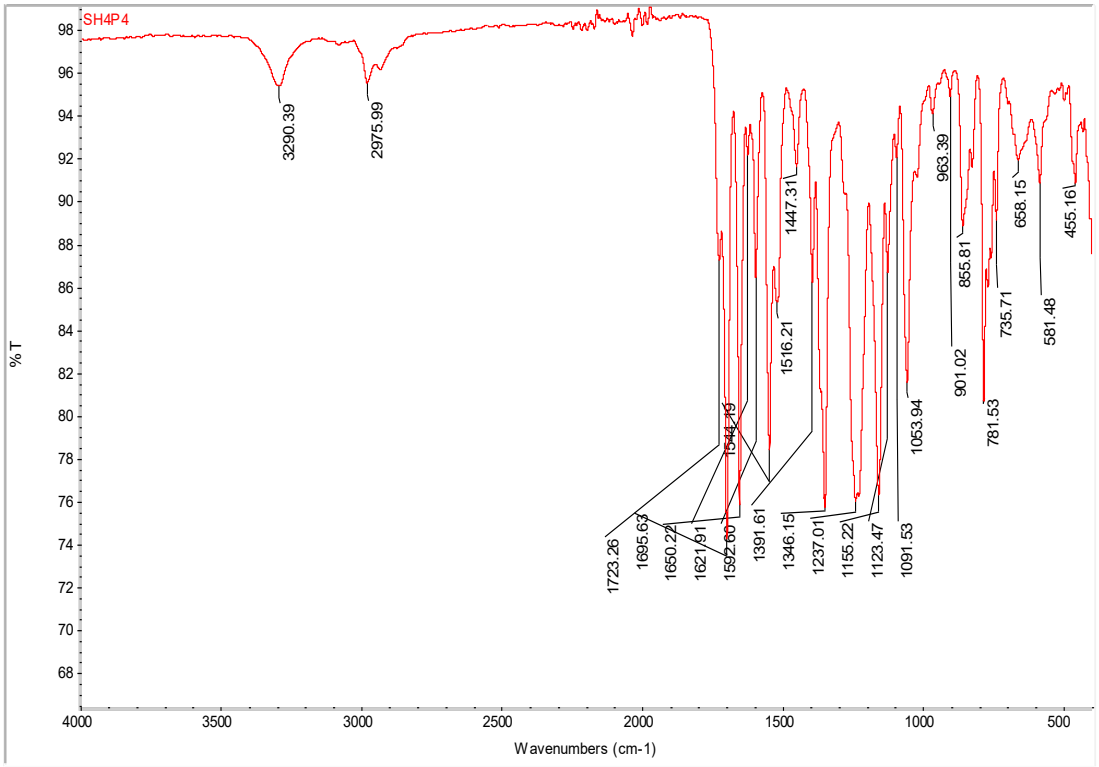

Figure S4.83: FTIR-ATR spectrum of **4.17.**